Physics of light depolarization, non-conventional polarimetric imaging, and optimal statistical processing of optical signals

Julien Fade

2017

UNIVERSITÉ DE RENNES 1

UNIVERSITE BRETAGNE LOIRE

UNIVERSITÉ DE RENNES 1

Habilitation à Diriger des Recherches

École doctorale SDLM

Mémoire présenté par

Julien Fade

Équipe DOP - Institut Foton - UMR 6082

Physics of light depolarization, non-conventional polarimetric imaging, and optimal statistical processing of optical signals

Habilitation soutenue à Rennes le 11 juillet 2017

devant le jury composé de :

Philippe ADAM
Responsable domaine scientifique photonique - Direction Générale de l'Armement - Invité

Mehdi ALOUINI
Professeur - Institut de Physique de Rennes, Univ. Rennes 1 - Examinateur

Gérard BERGINC
Directeur scientifique - Thales Optronique, Thales - Examinateur

Sophie BRASSELET
Directrice de recherche - Institut Fresnel, CNRS - Rapporteur

Christian BROSSEAU
Professeur - LabSTICC, Univ. Bretagne Occidentale - Examinateur

François GOUDAIL
Professeur - Lab. Ch. Fabry Institut d'Optique, Univ. Paris Saclay - Rapporteur

Meredith KUPINSKI
Associate Research Professor - College of Optical Sciences, Univ. of Arizona - Rapporteur

Remerciements

Je souhaite remercier ici toutes les personnes qui m'ont permis de produire ce document d'habilitation, à commencer par les membres du jury qui ont expertisé ce travail de synthèse. Je remercie en particulier les rapporteurs: Meredith Kupinski, Sophie Brasselet et François Goudail, pour leur relecture attentive et les discussions enrichissantes que nous avons pu avoir. Merci également à Gérard Berginc et Christian Brosseau d'avoir accepté de participer à ce jury.

Il convient surtout de remercier ici les membres de l'équipe DOP avec qui j'ai pu m'épanouir scientifiquement et participer à la construction d'une activité en imagerie physique non conventionnelle à Rennes. Merci à tous de la confiance et du soutien accordés à mon arrivée dans le laboratoire, et au support quotidien efficace de l'équipe technique (Ludovic Frein, Anthony Carré, Cyril Hamel, Steve Bouhier).

Je dois surtout adresser mes plus chaleureux remerciements à Mehdi Alouini, pour son soutien, ses conseils, sa disponibilité généreuse, et pour ses éclairages inspirants. Pour m'avoir mis le pied à l'étrier de l'expérimentation, du management de projets et de la valorisation, qui sont des atouts nécessaire aujourd'hui dans le métier de chercheur, et m'avoir permis de prendre une autonomie d'enseignant-chercheur "habilité", merci.

Je remercie aussi bien entendu les jeunes chercheurs avec qui j'ai pu travailler de près (en particulier Noé Ortega-Quijano, Swapnesh Panigrahi, François Parnet) et qui ont tant apporté à ces activités de recherche. J'adresse aussi un clin d'œil à l'ensemble des non-permanents, stagiaires, etc. qui au long de ces années ont animé la vie de notre laboratoire, et avec qui des amitiés ont pu se nouer.

Je veux également saluer l'ensemble des collègues de l'Institut de Physique de Rennes et de l'Institut FOTON avec qui j'ai partagé ces années d'expérience professionnelle en recherche et enseignement à Rennes. Merci aussi à Marie-Aude Lefeuvre, du service Culture de l'Université, et à Benoît Quéro et Yves Gomez, de Spectaculaires-Allumeurs d'images, pour la riche interaction culturelle que nous avons pu vivre ensemble en 2015, à l'occasion de l'année internationale de la lumière.

La richesse de ce métier doit également beaucoup aux rencontres, aux collaborations à l'extérieur du laboratoire. Même si la place manque ici pour citer tout le monde, je souhaite quand même remercier particulièrement Hema Ramachandran pour son accueil à Bangalore et pour les moments de collaboration passionnants. Merci à Philippe Adam pour son regard bienveillant et pertinent sur ces travaux. Merci enfin à Corinne Fournier, Matthieu Boffety, François Goudail et Vincent Devlaminck pour nos échanges amicaux et motivants pour l'organisation des Journées Imagerie Optique Non Conventionnelles.

Pour terminer, je voudrais saluer ma famille pour laquelle la destination Rennes n'était pas la plus proche, mais qui m'a toujours soutenu dans mes choix. Enfin, je remercie Marie-Anne pour son soutien quotidien dans les hauts et les bas du métier, mais surtout pour me permettre de partager avec elle les plus beaux moments qu'il soit à fonder une famille.

Table of contents

Curriculum Vitae étendu en français

Julien FADE

Maître de Conférences CNU 30

01-07-1981
Nationalité française
julien.fade@univ-rennes1.fr

Adresse professionnelle

Institut Foton – Équipe DOP
UMR 6082 Université Rennes 1 – CNRS – INSA
Bat 11B, Campus de Beaulieu
35042 Rennes Cedex
Tel : 02 23 23 52 15 / Port : 06 18 77 22 97

FORMATION-DIPLOMES

2009 Qualification aux fonctions de Maître de Conférences : section 30, 61

2009 Doctorat en Optique, Photonique et Traitement d'Image, Université Aix-Marseille III
« Caractérisation et extraction de l'information dans des signaux optiques polarimétriques ou issus d'états sous-poissoniens de la lumière. »

2006 Master 2 Optique & Traitement d'image, Univ. Aix-Marseille III, mention TB, Rang 1
Magistère EEA, ENS Cachan, Université Paris XI, mention TB

2004 Agrégation de Physique, option Physique Appliquée, Rang 3

2003 Maîtrise EEA, ENS Cachan, Université Paris XI, mention TB

2002 Licence EEA, ENS Cachan, Université Paris XI, mention TB

2001 CPGE MPSI/PSI*, Lycée Louis-le-Grand. Intégration de l'ENS Cachan

EXPERIENCES PROFESSIONNELLES

- **École Normale Supérieure de Cachan (Cachan)**

2001-2006 Élève de l'École Normale Supérieure de Cachan

- **Institut Fresnel, Université Aix-Marseille III (Marseille)**

2005-2006 Stage de recherche de M2 à l'Institut Fresnel
- Imagerie polarimétrique, imagerie de speckle

2006-2009 Thèse de doctorat, spécialité Optique, Photonique et Traitement d'Image
- Imagerie polarimétrique, imagerie de speckle
- Imagerie quantique, états quantiques non-classiques de la lumière
- Théorie de l'information

2006-2009 Moniteur d'enseignement
- Physique générale
- Électronique, automatique & instrumentation virtuelle (LabView)

- **Office National d'Études et de Recherches Aérospatiales (ONERA, Palaiseau)**

2009-2010 Ingénieur-chercheur, Dpt. Optique Théorique et Appliquée, Lab. Sources laser et Systèmes Lidar

- Spectroscopie atmosphérique par lidar à supercontinuum : modélisation, conception d'un logiciel de simulation de spectres et montage d'un banc expérimental.
- Conception de méthodes non supervisées pour la sélection optimale de modèle par approches MDL (*Miminum Description Length*).

- **Institut Foton/Institut de Physique de Rennes, Université de Rennes I (Rennes)**

2017 Depuis 1er juillet : Maître de Conférences, section CNU 30 à l'Institut Foton
2010-2017 Maître de Conférences, section CNU 30 à l'Institut de Physique de Rennes
2015-2017 En délégation à mi-temps au CNRS section 04
2010-2015 Titulaire d'une chaire CNRS section 04/ Enseignement Supérieur

- Imagerie polarimétrique avancée,
- Imagerie de speckle, imagerie de Stokes à l'échelle du grain de speckle,
- Imagerie de photons balistiques,
- Imagerie spectro-polarimétrique.

Enseignement : optique géométrique, optique anisotrope, physique des lasers.

PRODUCTION SCIENTIFIQUE

- 26 articles dans des revues internationales à comité de lecture
- 2 conférences invitées
- 21 conférences avec actes
- 4 brevets
- 6 contrats nationaux et internationaux financés (1 en cours).

ENCADREMENT

- Co-encadrement de deux thèses (2013-2016) et (2014-2017).
- Encadrement d'un post-doctorant (2014-2016) et un CDD (2013-2014).
- Encadrement de 12 stages dont 5 stages M2.

ACTIONS COLLECTIVES

- Membre du bureau de l'équipe DOP (Foton/IPR) (2012-2014/2016-2017).
- Président du Club « Physique et Imagerie Optique » de la Société Française d'Optique (depuis 2017).
- Organisateur des Journées Imagerie Optique Non Conventionnelle depuis 2013.
- Membre du comité d'organisation du Congrès Optique 2015 de la SFO regroupant les 5 grandes manifestations de l'Optique et de la Photonique (Horizons de l'Optique, COLOQ, JNOG, JNCO, JRIOA).
- Coordinateur pour Rennes de l'année Internationale de la Lumière en Bretagne.

ACTIVITES D'EVALUATION ET DE DIFFUSION DES CONNAISSANCES

- Responsable communication scientifique pour l'équipe DOP.
- Coordinateur du stand optique pour la Fête de la Science à Rennes.
- Referee pour les revues Optics Express, Optics Letters, Applied Optics et JOSA A.
- Expert pour l'ANR.

ANIMATION DE PROGRAMMES DE RECHERCHE, TRANSFERT TECHNOLOGIQUE, RELATIONS INDUSTRIELLES ET VALORISATION

Animation et participation à des contrats de recherche

- Contrat Défi Interne Mission Interdisciplinarité « PolarBio : IMagerie POLArimétrique par Brisure d'Orthogonalité pour la biologie cellulaire ».

Partenaire : IGDR-Biosit / Institut Foton UMR 6082
Financeur : Mission Interdisciplinarité CNRS
Montants : 26 k€
Durée : 1 an (2017)
Rôle : Partenaire scientifique

- Contrat ANR/DGA-ASTRID « Real-time Active Depolarization Imaging by OrthgonaLIty BREaking » (RADIO-LIBRE).

Partenaire : IPR UMR 6251/ Institut Fresnel UMR 7249
Financeur : Délégation Générale pour l'Armement / Agence Nationale pour la Recherche
Montants : 115 k€ pour la contribution IPR
Durée : 30 mois (fin 2013-2016)
Rôle : Coordinateur du projet

- Contrat Défi Instrumentation aux limites IMPOLABO « IMagerie POLArimétrique par Brisure d'Orthogonalité ».

Partenaire : IPR
Financeur : Mission Interdisciplinarité CNRS
Montants : 15 k€
Durée : 1 an (2013)
Rôle : Porteur de projet

- Contrat CEFIPRA « Real-time Imaging Through Fog Over Long Distances » (RITFOLD).

Partenaires: IPR UMR 6251/ RAMAN Research Institute (Bangalore, Inde)
Financeurs: CEFIPRA - Ministères des Affaires Etrangères Français et Indien
Montants : 56 k€ pour la contribution IPR
Durée : 3 ans (2012-2015)
Rôle: Contributeur scientifique associé

- Contrat ISI/OSEO « Vertically integrated Enhanced pRoducTs for Industrial Chain using Amplifier Lasers » (VERTICAL).

Partenaires: IPR UMR 6251/ 3S Photonics/ IXFiber/ Leukos/ Azur Light Systems/ Alphanov/ IMS UMR 5218/ Xlim UMR 7252/ CIMAP UMR 6252/ LPL UMR 7538
Financeur : OSEO
Montants : 215 k€ pour la contribution IPR
Durée : 24 mois (2013-2015) pour la contribution IPR
Rôle : Contributeur scientifique

- Contrat AIS Rennes-Métropole « Allocation d'Installation Spécifique ».

Partenaire : IPR UMR 6251
Financeur : Rennes Métropole

Montants : 40 k€
Durée : 1 an (2012-2013)
Rôle : Porteur de projet

Brevets

ORTEGA-QUIJANO N., FADE J., ALOUINI M., « Coherent light source with fully controllable state and degree of polarization », Brevet EP17165383.5 déposé le 06/04/2017, SATT Ouest Valorisation, 2017.

Document lié : ORTEGA-QUIJANO N., FADE J., ALOUINI M., « Source de lumière cohérente à état et degré de polarisation accordables dynamiquement à très haute cadence », Mémoire d'invention, SATT Ouest Valorisation, 01/2016.

PANIGRAHI S., RAMACHANDRAN H., FADE J., ALOUINI M., « Optical receiver for full-field optical quadrature demodulation », Brevet PCT/FR2016/051086, déposé le 10/05/2016, SATT Ouest Valorisation, 2016.

Document lié : PANIGRAHI S., RAMACHANDRAN H., FADE J., ALOUINI M., « Snapshot dual-quadrature optical demodulation for full-field imaging », Mémoire d'invention, SATT Ouest Valorisation, 01/2015.

RAMACHANDRAN H., BRETENAKER F., FADE J., ALOUINI M., « Dispositif et méthode d'imagerie temps-réel pour l'assistance aux transports en conditions de visibilité dégradées », Brevet EP 14 305269, déposé le 26/02/2014, SATT Ouest Valorisation, 2014.

Document lié : RAMACHANDRAN H., BRETENAKER F., FADE J., ALOUINI M., « Dispositif et méthode d'imagerie temps-réel pour l'assistance aux transports en conditions de visibilité dégradées », Mémoire d'Invention, Bretagne Valorisation, 10/2011.

ALOUINI M., FADE J., « Système et procédé d'analyse par détermination du caractère dépolarisant ou dichroïque d'un objet », Brevet déposé le 18/06/2011, Bretagne Valorisation, 2011.

Document lié : ALOUINI M., FADE J., « Principe et dispositif de mesure de dépolarisation avec ou sans déport par fibre optique en utilisant des états de polarisation orthogonaux et décalés en fréquence », Mémoire d'Invention, Bretagne Valorisation, 02/2011.

ACTIVITES D'ENSEIGNEMENT, FORMATION ET DIFFUSION DE LA CULTURE SCIENTIFIQUE

Formation d'étudiants en thèse

- Swapnesh PANIGRAHI, 2013-2016, « Real-time imaging through fog over long distances », Dir. thèse M. Alouini, co-encadrement à 50%, financement CEFIPRA.
- François PARNET, 2014-2017, « Imagerie spectro-polarimétrique temps réel à longue distance par approche optique-hyperfréquence et traitement avancé d'images spectro-polarimétriques», Dir. thèse M. Alouini, co-encadrement à 50%, financement DGA/Région Bretagne.

Encadrement d'un post-doctorant (Noé ORTEGA-QUIJANO) et un CDD (Julien LE MEUR), ainsi que 12 stagiaires M1/M2 dont 10 encadrés à 100%, et dont 5 étudiants de niveau M2.

Enseignement

- 2006-2009 : **Moniteur d'enseignement à l'Université Aix-Marseille III**, service d'enseignement de 64 HETD/an.
  Titularisation en qualité de professeur agrégé de Physique.

  - **Travaux dirigés d'Automatique & Travaux pratiques d'informatique industrielle**
    École Centrale de Marseille 2e Année
    TD : 36H / TP : 28H soit 19 HETD
    Automatique continue, correction, stabilité / acquisition, échantillonnage, quantification …

  - **Cours / TD : Module de préparation aux concours CCP/DEUG**
    Licence 2 Science de la Matière
    Cours 10H – TD 22H – soit 28 HETD
    Diffraction interférences, électromagnétisme, induction,…

  - **Travaux dirigés d'électrocinétique et électrostatique/magnétostatique**
    Licence 2 Science de la Matière
    TD 39H
    Electrostatique/magnétostatique, loi des circuits électrique, modèles équivalents,…

  - ***Cours / TDs / TPs :* Automatique & instrumentation virtuelle**
    IUT de Marseille
    Cours 3H – TD 20 H – TP 74H – soit 73 HETD
    Automatique, Stabilité, correction, LabView, interfaçage instruments,…

- 2009 (1 mois): Professeur Agrégé de physique titulaire sur zone de remplacement, Lycée Janetti, Saint-Saturnin, Var.

- 2010-2015 : Maître de Conférences, titulaire d'une chaire Enseignement Supérieur / CNRS, service d'enseignement de 64 HETD/an.
  2015-2017 : Maître de Conférences, en demi-délégation CNRS, service d'enseignement de 96 HETD/an.

- Cours d'Optique Anisotrope – Optique pour l'ingénieur (6 ans) : ***École Supérieur d'Ingénieurs de Rennes 2e Année - Cours : 14H – TD 2H***
- Cours Optique L1 (7 ans) : ***Cours 9H – TD 18H – TP 18 H soit 50 HETD***
- TPs de Physique des Lasers M1 (1 an) : ***Parcours M1/M2 Physique & Photonique : 18 HETD.***
- TPs de Mécanique L1 (1 an) : Licence Mathématiques-Informatique. ***TP 18 H***
- Interventions en M2 Préparation à l'Agrégation de Physique (1 an). 15 HETD.

AUTRES ACTIVITES (EXPERTISE, DIFFUSION DES CONNAISSANCES, ORGANISATION DE CONGRES, RESPONSABILITES COLLECTIVES…)

Séjours à l'étranger :

- Voyages d'échange scientifique au Raman Research Institute (Bangalore, Inde):

  -Jan 2013 : 2 sem.

  -July 2015 : 3 sem.

Activités d'expertise :

- Participation à un projet industriel ISI/OSEO « VERTICAL » (2013-2015, 24 mois, 215k€, collaboration 3S Photonics) : développement d'un système d'analyse spectro-polarimétrique temps-réel, en ligne, de diodes laser de pompe non packagées. Encadrement d'un ingénieur CDD.

- Referee pour des revues internationales d'optique à comité de lecture (11 articles sur la période).

- Expert pour l'ANR (1 projet reviewé sur la période) - membre d'un comité d'évaluation ANR (1 an).

Organisation de congrès et participations à des sociétés savantes :

- Président depuis début 2017 du club « Physique et Imagerie optique » de la Société Française d'Optique (~100 membres académiques et industriels dans le club).

- Co-organisateur depuis Mars 2013 des Journées GDR « Imagerie Optique Non Conventionnelle » (env. 120 participants annuels, 20 oraux, 20 posters)

- Co-Responsable depuis Mars 2013 de l'Action « Extraction d'information et physique des images » de l'Axe « Physique, Capteurs, Traitement », axe commun aux GDR ISIS et GDR ONDES.

- Membre du comité d'organisation du congrès national Optique Bretagne 2015 de la SFO à Rennes, 6-10 juillet 2015, regroupant les 5 grandes manifestations de l'Optique et de la Photonique.

Diffusion des connaissances :

- Co-Concepteur de l'installation art & science « LUMIÈRES », place du Parlement de Bretagne, été 2015, collab. Service Culturel Univ. Rennes 1 et la société Spectaculaires-Allumeurs d'images.

- Participation à la Fête de la Science 2011,2013 & 2015 (Village des Sciences à Rennes) sur un stand de démonstration de l'équipe DOP : *Transport de signal audio sur porteuse optique, fontaine laser, holographie, diffraction, interférométrie, démonstrateur d'imagerie spectro-polarimétrique,…*

- Membre du comité régional du projet LUMINEIZH, 2015, Année internationale de la lumière en Bretagne. Coordinateur pour le secteur de Rennes.

Responsabilités collectives :

- Depuis 2017, élu au conseil de laboratoire de l'Institut Foton.
- 2015-2017, élu au conseil de laboratoire de l'Institut de Physique de Rennes.
- Entre janvier 2012 et décembre 2014, puis depuis janvier 2016 : membre du bureau de l'équipe DOP.
- Depuis 2012, responsable communication scientifique de l'équipe DOP.

Curriculum Vitae

Julien FADE

Assistant Professor
Maître de conférences section CNU 30

Born 01-07-1981
French nationality
julien.fade@univ-rennes1.fr

Professional address

Institut Foton – DOP Team
UMR6082 Université Rennes 1 - CNRS - INSA
Bat 11B, Campus de Beaulieu
35042 Rennes Cedex - FRANCE
Tel : 02 23 23 52 15 / Cell : 06 18 77 22 97

TRAINING-DIPLOMAS

2009 PhD in Optics, Photonics and Image processing, Université Aix-Marseille III
« Characterization and extraction of information in polarimetric optical signals or in signals obtained from sub-Poissonian states of light »

2006 Master's degree Optics & Image processing, Univ. Aix-Marseille III
Magistère Electrical engineering, ENS Cachan, Université Paris XI

2004 Agrégation de Physique, option Applied Physics

2003 Master's degree Electrical engineering, ENS Cachan, Université Paris XI

2002 Bachelor's degree Electrical engineering, ENS Cachan, Université Paris XI

2001 CPGE MPSI/PSI*, Lycée Louis-le-Grand. Integrated ENS Cachan

PROFESSIONAL EXPERIENCE

- **École Normale Supérieure de Cachan (Cachan)**

2001-2006 Student at École Normale Supérieure de Cachan

- **Institut Fresnel, Université Aix-Marseille III (Marseille)**

2005-2006 Master's degree internship, Institut Fresnel
- Polarimetric imaging, speckle imaging

2006-2009 PhD in Optics, Photonics and Image processing
- Polarimetric imaging, speckle imaging
- Quantum imaging, non-classical quantum states of light
- Information theory

2006-2009 Teacher
- General physics
- Electronics, automation and virtual instrumentation (LabView)

- **Office National d'Études et de Recherches Aérospatiales (ONERA, Palaiseau)**

2009-2010 Engineer-Researcher at the French Aerospace Lab., Dpt. Theoretical and Applied Optics Dpt., Laser sources and Lidar Systems Lab.
- Supercontinuum lidar atmospheric spectroscopy
- Unsupervised methods for optimal model selection by *Miminum Description Length* approach

- **Institut Foton (since 01/07/17)/Institut de Physique de Rennes, Univ. Rennes 1**

2010- Assistant Professor (Maître de Conférences), section CNU 30
2015-2017 Half-time delegation at CNRS section 04
2010-2015 Holder of a CNRS chair, section 04
- Advanced polarimetric imaging,
- Speckle imaging, Stokes imaging at the speckle grain scale,
- Ballistic photons imaging,
- Statistical image processing.

Teaching: geometrical optics, anisotropic optics & polarization, laser physics.

SCIENTIFIC PRODUCTION

- 26 articles in international peer-reviewed journals
- 2 invited conferences
- 21 conferences with proceedings
- 4 patents
- 6 national/international funded research contracts.
- International collaboration with Raman Research Institute (Bangalore, India)

STUDENTS SUPERVISION

- Supervision of 2 PhDs (2013-16) et (2014-17). (50% supervision)
- Supervision of 1 post-doctoral student (2014-16) and fixed-term researcher (2013-14).
- Supervision of 12 internships, including 5 Master's degree internships.

INSTITUTIONAL RESPONSABILITIES & MEETINGS ORGANIZATION

- Member of the council of the DOP team (2012-14/2016-17).
- Elected member at the Lab. Council - Institut Foton (2017-).
- Elected member at the Lab. Council - Institut de Physique de Rennes (2015-17).
- Organizer of the *Journées Imagerie Optique Non Conventionnelle* workshop since 2013.
- President of the *Physics and Optical Imaging* club of the French Optical Society (SFO).
- Member of the organizing committee of the Congrès Optique 2015 of the SFO.

REVIEWING ACTIVITIES AND SCIENCE POPULARIZATION

- In charge of scientific communication for the DOP team.
- Local coordinator of LUMINEIZH project – International Year of Light 2015.
- Referee for journals Optics Express, Optics Letters, Applied Optics and JOSA A.
- Expert for the ANR (French National Research Agency)

List of publications

EXHAUSTIVE PUBLICATIONS LIST
Updated 01/07/2017

1. International peer-reviewed journals

[A29] FADE J., PERROTIN E., BOBIN J., « Two-pixel polarimetric camera by compressive sensing », submitted to IEEE Trans. in Computational Imaging (2017).

[A28] ORTEGA-QUIJANO N., FADE J., ROCHE M., PARNET F., ALOUINI M., « Orthogonality-breaking sensing model based on the instantaneous Stokes vector and the Mueller calculus: erratum », Journal of the Optical Society of America A, in press (2017).

[A27] ORTEGA-QUIJANO N , FADE J., PARNET F., ALOUINI M., « Generation of coherent light beam with precise and fast dynamic control of the state and degree of polarization », Optics Letters, in press (2017).

[A26] PARNET F., FADE J., ORTEGA-QUIJANO N., LOAS G., FREIN L., ALOUINI M., « Free-space active polarimetric imager operating at 1.55 µm by orthogonality breaking sensing », Optics Letters, 42 (4), 723-726 (2017).
http://dx.doi.org/10.1088/2040-8978/18/12/125604

[A25] FADE J., ORTEGA-QUIJANO N., « Differential description and irreversibility of depolarizing light-matter interactions », Journal of Optics, 18, 125604 (2016).
http://dx.doi.org/10.1088/2040-8978/18/12/125604

[A24] PANIGRAHI S., FADE J., RAMACHANDRAN H., ALOUINI M., « Theoretical optimal modulation frequencies for scattering parameter estimation and ballistic photon filtering in diffusing media », Optics Express, 24, (14), 16066-16083 (2016)
http://dx.doi.org/10.1364/OE.24.016066

[A23] SUDARSANAM S., MATHEW J., PANIGRAHI S., FADE J., ALOUINI M., RAMACHANDRAN H., « Real-time imaging through strongly scattering media: seeing through turbid media, instantly », Scientific Reports, 6, 25033 (2016)
http://dx.doi.org/10.1038/srep25033

[A22] PARNET F., FADE J., ALOUINI M., « Orthogonality breaking through few-mode optical fiber », Applied optics, 55, 2508-2520 (2016)
http://dx.doi.org/10.1364/AO.55.002508

[A21] ORTEGA-QUIJANO N., FADE J., ROCHE M., PARNET F., ALOUINI M., « Orthogonality-breaking sensing model based on the instantaneous Stokes vector and the Mueller calculus », Journal of the Optical Society of America A, 33, 434-446 (2016)
http://dx.doi.org/10.1364/JOSAA.33.000434

[A20] HUBY N., BIGEON J., LAGNEAUX Q., AMELA-CORTES M., GARREAU A., MOLARD Y., FADE J., DESERT A., FAULQUES E., BECHE B., DUVAIL J.-L., CORDIER S. « Facile design of red-emitting waveguides using hybrid nanocomposites made of inorganic clusters dispersed in SU8 photoresist host », Optical Materials, 52, 196-202 (2016)
http://dx.doi.org/10.1016/j.optmat.2015.12.034

[A19] FADE J., « Stochastic Complexity-Based Model Selection With False Alarm Rate Control in Optical Spectroscopy », Pattern Recognition Letters, 65, 152-156 (2015)
http://dx.doi.org/10.1016/j.patrec.2015.07.022

[A18] ORTEGA-QUIJANO N., FADE J., ALOUINI M., « Generalized Jones matrix method for homogeneous biaxial samples », Optics Express, 23 (16), 20428-20438 (2015)
http://dx.doi.org/10.1364/OE.23.020428

[A17] ORTEGA-QUIJANO N., FADE J., SCHAUB E., PARNET F. , ALOUINI M., « Full characterization of dichroic samples from a single measurement by circular polarization orthogonality breaking », Optics Letters, 40 (7), 1270-1273 (2015)
http://dx.doi.org/10.1364/OL.40.001270

[A16] PANIGRAHI S., FADE J., ALOUINI M., « Adaptive polarimetric image representation for contrast optimization of a polarized beacon through fog », Journal of Optics, 17, (6), 065703 (2015)
http://dx.doi.org/10.1088/2040-8978/17/6/065703

[A15] SCHAUB E., FADE J., ORTEGA-QUIJANO N., HAMEL C., ALOUINI M., « Polarimetric contrast microscopy by orthogonality breaking », Journal of Optics – Fast Track Communication, 16, (12), 122001 (2014)
http://dx.doi.org/10.1088/2040-8978/16/12/122001

[A14] FADE J., PANIGRAHI S., CARRE A., FREIN L., HAMEL C., BRETENAKER F., RAMACHANDRAN H., ALOUINI M., « Long-range polarimetric imaging through fog », Applied Optics, 53, (18), 3854-3865 (2014)
http://dx.doi.org/10.1364/AO.53.003854

[A13] FADE J., PANIGRAHI S., ALOUINI M., « Optimal estimation in polarimetric imaging in the presence of correlated noise fluctuations », Optics Express, 22 (5), 4920-4931 (2014)
http://dx.doi.org/10.1364/OE.22.004920

[A12] POUGET L., FADE J., HAMEL C., ALOUINI M., « Polarimetric imaging beyond the speckle grain scale », Applied Optics, 50, (30), 7345-7356 (2012)
http://dx.doi.org/10.1364/AO.51.007345

[A11] FADE J., ALOUINI M., « Depolarization Remote Sensing by Orthogonality Breaking », Physical Review Letters, 109, (4), 043901 (2012)
http://dx.doi.org/10.1103/PhysRevLett.109.043901

[A10] FADE J., ROCHE M., ALOUINI M., « Computational polarization imaging from a single speckle image », Optics Letters, 37, (3), 386-388 (2012)
http://dx.doi.org/10.1364/OL.37.000386

[A9] PINEL O., FADE J., BRAUN D., JIAN P., TREPS N., FABRE C., « Ultimate sensitivity of precision measurements with intense Gaussian quantum light: A multimodal approach », Physical Review A, 85, (1), 010101 (R) (2012)
http://dx.doi.org/10.1103/PhysRevA.85.010101

[A8] FADE J., LEFEBVRE S., CÉZARD N., « Minimum Description Length approach for unsupervised spectral unmixing of multiple interfering gas species », Optics express, 19, (15),

13863-13872 (2011)
http://dx.doi.org/10.1364/OE.19.013862

[A7] FADE J., « Optimal precision of contrast estimation between sub-Poissonian light beams », Journal of the Optical Society of America B, 28, (7), 1752-1759 (2011)
http://dx.doi.org/10.1364/JOSAB.28.001752

[A6] FADE J., RÉFRÉGIER P., TREPS N., FABRE C., « A gain criterion for the improvement of detection tasks with sub-Poissonian light », Journal of the Optical Society of America A, 26, (5), 1139-1146 (2009)
https://doi.org/10.1364/JOSAA.26.001139

[A5] FADE J., ROCHE M., RÉFRÉGIER P., « Precision of moment based estimation of the degree of polarization in coherent imagery without polarization device », Journal of the Optical Society of America A, 25, (2), 483-492 (2008)
https://doi.org/10.1364/JOSAA.25.000483

[A4] FADE J., RÉFRÉGIER P., ROCHE M., « Estimation of the degree of polarization from a single speckle intensity image with photon noise », Journal of Optics A : Pure and Applied Optics, 10, (11), 115301 (2008)
http://dx.doi.org/10.1088/1464-4258/10/11/115301

[A3] FADE J., TREPS N., FABRE C., RÉFRÉGIER P., « Optimal precision of parameter estimation in images with local sub-Poissonian quantum fluctuations », European Physical Journal D, 50, (2), 215-227 (2008)
http://dx.doi.org/10.1140/epjd/e2008-00211-3

[A2] RÉFRÉGIER P., FADE J., ROCHE M., « Estimation precision of the degree of polarization from a single intensity image », Optics Letters, 32, (7), 739-741 (2007)
https://doi.org/10.1364/OL.32.000739

[A1] ROCHE M., FADE J., RÉFRÉGIER P., « Parametric estimation of the square degree of polarization from two intensity images degraded by fully developed speckle noise », Journal of the Optical Society of America A, 24, (9), 2719-2727 (2007)
https://doi.org/10.1364/JOSAA.24.002719

2. Patents

[B4] ORTEGA-QUIJANO N., FADE J., ALOUINI M., « Coherent light source with fully controllable state and degree of polarization », EP17165383.5, 06/04/2017.

[B3] PANIGRAHI S., RAMACHANDRAN H., FADE J., ALOUINI M., « Optical receiver for full-field optical quadrature demodulation », PCT/FR2016/051086, 10/05/2016.

[B2] RAMACHANDRAN H., BRETENAKER F., FADE J., ALOUINI M., « System and method for navigation assistance in a scattering environment », European Patent Registration EP14305269.4, 26/02/2014.

[B1] ALOUINI M., FADE J., « Système et procédé d'analyse par détermination du caractère dépolarisant ou dichroïque d'un objet », Brevet déposé le 18/06/2011, Bretagne Valorisation, 2011. Extensions Europe et Etats-Unis début 2014.

3. Invited conferences in congresses

[CI2] FADE J., ALOUINI M., « Imagerie de dépolarisation par brisure d'orthogonalité: l'optique hyperfréquence au service de l'endoscopie polarimétrique », Assemblée Générale du GDR ONDES, (2013)

[CI1] FABRE C., PINEL O., JIAN P., TREPS N., FADE J., BRAUN D., « Ultimate sensitivity in precision optical measurements using intense gaussian quantum light: a multi-modal approach », Quantum Information and Measurements - Laser Optics, (Berlin), Germany (2012)

4. International conferences with proceedings

[AC21] PARNET F., FADE J., ALOUINI M., « Active infrared polarimetric imaging demonstrator by orthogonality breaking sensing », SPIE Optical Engineering + Applications, Polarization Science and Remote Sensing VII, San Diego, United States (2017).

[AC20] PARNET F., FADE J., ALOUINI M., « Polarimetric Imaging by Orthogonality Breaking: From Single-mode to Few-mode Fiber Polarimetric Endoscopy ? », Imaging and Applied Optics, Heidelberg, Germany (2016).

[AC19] PANIGRAHI S., FADE J., ALOUINI M., « Noise correlation-based adaptive polarimetric image representation for contrast enhancement of a polarized beacon in fog », SPIE Remote Sensing and Security + Defence, Image and Signal Processing for Remote Sensing, Toulouse, France (2015)

[AC18] FADE J., ROCHE M., ALOUINI M., « Polarizer-free degree of polarization computational imaging from a single speckle image », SPIE Optical Engineering + Applications, Polarization Science and Remote Sensing VII, San Diego, United States (2015)

[AC17] PANIGRAHI S., FADE J., ALOUINI M., « Optimal contrast enhancement in long distance snapshot polarimetric imaging through fog », SPIE Optical Engineering + Applications, Polarization Science and Remote Sensing VII, San Diego, United States (2015)

[AC16] ORTEGA-QUIJANO N., FADE J., SCHAUB E., PARNET F. , ALOUINI M., « Single-shot diattenuation imaging by circular polarization orthogonality breaking », SPIE Optical Engineering + Applications, Polarization Science and Remote Sensing VII, San Diego, United States (2015)

[A15] ORTEGA-QUIJANO N., FADE J., SCHAUB E., PARNET F. , ALOUINI M., « Single shot polarimetric contrast microscopy by circular polarization orthogonality breaking imaging », CLEO Europe, Munich, Germany (2015)

[AC14] PANIGRAHI S., FADE J., ALOUINI M., « Contrast enhancement in polarimetric imaging with correlated noise fluctuations », MaxEnt 2014, France (2014).

[AC13] FADE J., SCHAUB E., ALOUINI M., « Depolarization Sensing by Orthogonality Breaking: a microwave-photonics approach for snapshot polarimetric imaging », OPTRO 2014, OPTRO 2014 Proceedings, pp. 2967942, France (2014).

[AC12] FADE J., SCHAUB E., ALOUINI M., « Depolarization imaging by field orthogonality breaking for endoscopy applications », Frontiers in Optical Imaging 2013, (Mürten), Suisse (2013)

[AC11] ALOUINI M., FADE J., « Depolarization Sensing by Field Orthogonality Breaking », CLEO/Europe-IQEC, 12-16 May, (Munich), Allemagne (2013)

[AC10] FADE J., ROCHE M., ALOUINI M., « Snapshot computational imaging of the degree of polarization under coherent illumination », Frontiers In Optics - FIO, 14-18 octobre, (Rochester - NY), Etats-Unis (2012)

[AC9] FADE J., ALOUINI M., « Endoscopic depolarization sensing by polarization orthogonality breaking », Frontiers In Optics - FIO, 14-18 octobre, (Rochester - NY), Etats-Unis (2012)

[AC8] FABRE C., PINEL O., TREPS N., FADE J., BRAUN D., « General Cramer-Rao Bound for Parameter Estimation using Gaussian Multimode Quantum Resources », International Conference on Quantum Information, (Ottawa), Canada (2011)

[AC7] CÉZARD N., DOBROC A., CANAT G., DUHANT M., LEFEBVRE S., FADE J., « Supercontinuum laser absorption spectroscopy in the mid-infrared range for remote identification and concentration estimation of a multi-component atmospheric gas mixture », SPIE Remote Sensing Conference, 8182, 81820V, (Prague), Czech Republic (2011)

[AC6] PINEL O., FADE J., TREPS N., FABRE C., « General Cramer-Rao Bound for Parameter Estimation using Gaussian Multimode Quantum Resources », CLEO Europe/EQEC, (Munich), Germany (2011)

[AC5] FADE J., CÉZARD N., « Supercontinuum Lidar absorption spectroscopy for gas detection and concentration estimation », International Laser and Remote-sensing Conference ILRC 25, (St-Petersburg), Russia (2010)

[AC4] FADE J., ROCHE M., GALLAND F., RÉFRÉGIER P., « Estimation of the degree of polarization from a single image: characterization of the precision under various coherent imaging conditions », OPTO/IRS2 Conference, (Nuremberg), Germany (2008)

[AC3] ROCHE M., FADE J., RÉFRÉGIER P., « Comparaison de l'estimation de degré de polarisation à partir de 4, 2 et 1 images d'intensité entachées d'un speckle pleinement développé », GRETSI 2007, (Troyes), France (2007)

[AC2] FADE J., ROCHE M., RÉFRÉGIER P., « Polarization coherent imagery without polarization analyzing device », 3rd EOS Topical Meeting on Advanced Imaging Techniques, (Lille), France (2007)

[AC1] ROCHE M., FADE J., RÉFRÉGIER P., « Estimation of the degree of polarization from two intensity images degraded by speckle noise », Conference Speckle 06, (Nîmes), France (2006)

5. Communications in congresses, symposiums

[C25] FADE J., ORTEGA-QUIJANO N., «Description différentielle et irréversibilité des interactions dépolarisantes », Journées Imagerie Optique Non Conventionnelle, Paris, France (2017)

[C24] MIKHAILOVSKAYA A., FADE J., AMON A., CRASSOUS J., « Decorrelation with wavelength shift as a way to image transport mean free», Journées Imagerie Optique Non Conventionnelle, Paris, France (2017)

[C23] PARNET F., FADE J., ORTEGA-QUIJANO N., LOAS G., FREIN L., ALOUINI M., « Démonstrateur d'imagerie polarimétrique active par brisure d'orthogonalité à 1,55 µm », Journées Imagerie Optique Non Conventionnelle, Paris, France (2017)

[C22] PARNET F., FADE J., ALOUINI M., « Mesure de brisure d'orthogonalité à travers une fibre multimode », Journées Imagerie Optique Non Conventionnelle, Paris, France (2016)

[C21] PANIGRAHI S., FADE J., RAMACHANDRAN H., ALOUINI M., « Theoretical derivation of optimal operating frequencies for imaging through turbid media using intensity modulated light », Journées Imagerie Optique Non Conventionnelle, Paris, France (2016)

[C20] PANIGRAHI S., FADE J., ALOUINI M., « Adaptive polarimetric image representation for detection of polarized beacon of light embedded in fog », Horizons de l'optique, Rennes, France (2015)

[C19] ORTEGA-QUIJANO N., FADE J., SCHAUB E., PARNET F., ALOUINI M., « Imagerie rapide de contraste polarimétrique en une seule mesure par brisure d'orthogonalité », Horizons de l'optique, Rennes, France (2015)

[C18] ORTEGA-QUIJANO N., FADE J., SCHAUB E., PARNET F., ALOUINI M., « Derniers développements en imagerie par brisure d'orthogonalité », Journée du Club Optique Micro-ondes, Nantes, France (2015)

[C17] PARNET F., FADE J., SCHAUB E., ORTEGA-QUIJANO N., ALOUINI M., « Imagerie polarimétrique par brisure d'orthogonalité: un pas vers l'endoscopie polarimétrique », Journées Nationales de l'Optique Guidée, Rennes, France (2015)

[C16] ORTEGA-QUIJANO N., FADE J., PARNET F., SCHAUB E., ALOUINI M., « Imagerie polarimétrique d'échantillons dichroïques par brisure d'orthogonalité d'états de polarisation circulaires », Journées Imagerie Optique Non Conventionnelle, Mar 2015, Paris, France (2015)

[C15] PANIGRAHI S., FADE J., ALOUINI M., « Adaptive polarimetric image representation for contrast enhancement of a polarized beacon embedded in fog », Journées Imagerie Optique Non Conventionnelle, Paris, France (2015)

[C14] FADE J., LEDOT K., ALOUINI M., « Démonstrateur d'imagerie spectro-polarimétrique », Congrès Optique Bretagne 2015 - Session pédagogique, Rennes, France (2015)

[C13] FADE J., SCHAUB E., ALOUINI M., ORTEGA-QUIJANO N., « Towards real-time endoscopic depolarization sensing by orthogonally-polarized states mixing », Polarimetric Techniques and Technology Workshop, (Leiden), Pays-Bas 24-28 March (2014)

[C12] FADE J., PANIGRAHI S., ALOUINI M., « Performances optimales d'estimation en imagerie polarimétrique en présence de fluctuations de bruit corrélées », Journées d'Imagerie Optique Non Conventionnelle (19-20 Mars), (Paris), France (2014)

[C11] PANIGRAHI S., FADE J., CARRE A., HAMEL C., FREIN L., BRETENAKER F., RAMACHANDRAN H, ALOUINI M., « Imagerie polarimétrique à longue distance à travers le brouillard », Journées d'Imagerie Optique Non Conventionnelle (19-20 Mars), (Paris), France (2014)

[C10] FADE J., SCHAUB E., ALOUINI M., « L'optique hyperfréquence au service de l'endoscopie et de la microscopie de dépolarisation », Journée du Club Optique Micro-Ondes 2013, (Palaiseau), France (2013)

[C9] FADE J., SCHAUB E., ALOUINI M., « Depolarization Imaging by Field Orthogonality Breaking: towards polarimetric endoscopy », Horizons de l'Optique 2013, (Villetaneuse), France (2013)

[C8] FADE J., ALOUINI M., « Mesure hétérodyne de dépolarisation par brisure d'orthogonalité: vers une imagerie endoscopique polarimétrique temps-réel », OPTDIAG 2012 (9-11 Mai), (Paris), France

[C7] FADE J., ALOUINI M., « Mesure de dépolarisation hétérodyne par brisure d'orthogonalité », Journées d'Imagerie Optique Non Conventionnelle (20-21 Mars), (Paris), France (2012)

[C6] POUGET L., FADE J., HAMEL C., ALOUINI M., « Imagerie de Stokes à l'échelle du grain de speckle », Journées d'Imagerie Optique Non Conventionnelle (20-21 Mars), (Paris), France (2012)

[C5] FADE J., ROCHE M., ALOUINI M., « Imagerie computationnelle de degré de polarisation à une seule image de speckle », Journées d'Imagerie Optique Non Conventionnelle (21-21 Mars), (Paris), France (2012)

[C4] JIAN P., PINEL O., FADE J., BRAUN D., TREPS N., FABRE C., « Limite de Cramer-Rao quantique pour des états Gaussiens multimodes », COLOQ'12, (Marseille), France (2011)

[C3] FADE J., CÉZARD N., LEFEBVRE S., « Méthode non supervisée d'identification de composés gazeux pour la spectroscopie d'absorption », Horizons de l'optique, (Marseille), France (2011)

[C2] ROCHE M., FADE J., RÉFRÉGIER P., ALOUINI M., « Estimation du degré de polarisation à partir d'une seule image d'intensité », Journées d'Imagerie Optique Non Conventionnelle, (Paris), France (2008)

[C1] FADE J., RÉFRÉGIER P., FABRE C., TREPS N., « Précision optimale pour l'estimation de paramètres dans des images perturbées par des fluctuations quantiques sous-Poissoniennes », Journées d'Imagerie Optique Non Conventionnelle, (Paris), France (2008)

6. Seminars, workshops

[S10-S17] FADE J., seminar series (7) in « Introduction to Information Theory and tools for the engineer and the physicist »., Jan. 2016-Mar. 2017.

[S9] FADE J., « La « Brisure d'Orthogonalité », une technique hyper-fréquence pour l'imagerie polarimétrique optique : quels liens avec les approches RADAR ? », Journée du GDR ISIS Traitement du signal polarimétrique en imagerie Radar et Optique, Sept. (2016)

[S8] FADE J., « Recent developments in non-conventional polarimetric imaging at the Institut de Physique de Rennes », Séminaire Technicolor Rennes, Janv. (2015)

[S7] FADE J., « Non-conventional polarization-sensitive imaging techniques taking profit of polarized-light interferences », Séminaire au Raman Research Institute, Bangalore (Inde), (2013)

[S6] FADE J., ALOUINI M., « Mesure de dépolarisation hétérodyne par brisure d'orthogonalité d'états », Séminaire interne département Optique, Rennes (2012)

[S5] POUGET L., FADE J., HAMEL C., ALOUINI M., « Imagerie de Stokes à l'échelle du grain de speckle », Journée Electromagnétisme, Polarisation et Optique Statistique, (Marseille), France (2011)

[S4] FADE J., « Caractérisation et extraction de l'information dans des signaux optiques polarimétrique ou issus d'états sous-poissoniens de la lumière », Séminaire invité Équipe Photonique & Lasers, IPR (Rennes), France (2009)

[S3] FADE J., ROCHE M., RÉFRÉGIER P., ALOUINI M., « Estimation du degré de polarisation par analyse du contraste de speckle: principe et premiers résultats expérimentaux », Journées Thématiques Polarisation, (Marseille), France (2009)

[S2] FADE J., « Extraction et caractérisation de l'information dans des signaux optiques polarimétriques ou issus d'états sous-poissoniens de la lumière », Journées des Doctorants de l'Institut Fresnel, Giens, (2009)

[S1] FADE J., TREPS N., FABRE C., RÉFRÉGIER P., « Amélioration des performances de détection dans les images grâce à l'utilisation de lumière sous-poissonienne », Journées de l'École Doctorale Physique et Sciences de la Matière, Marseille, (2009).

7. Books and book chapters

[O1] FADE J., « Caractérisation et extraction de l'information dans des signaux optiques polarimétrique ou issus d'états sous-poissoniens de la lumière », Thèse de doctorat, 242 p., 02/10/09, Marseille, France
http://tel.archives-ouvertes.fr tel-00418557

[Ch1] FADE J., ALOUINI M., « Mesure hétérodyne de dépolarisation par brisure d'orthogonalité: vers une imagerie endoscopique polarimétrique temps-réel », Biophotonique générale: optique & imageries pour le diagnostic dans les sciences du vivant et en médecine - MRCT Editions, 1, 387-396 (2012)

8. Miscellaneous

ORTEGA-QUIJANO N., FADE J., ALOUINI M., « Source de lumière cohérente à état et degré de polarisation accordables dynamiquement à très haute cadence », Mémoire d'invention, SATT Ouest Valorisation, 01/2016.

FADE J., Tour report, CEFIPRA Project RITFOLD N° 4604-4, July 2014.

FADE J., Meeting report, ANR RADIO-LIBRE, March 2014.

FADE J., Intermediate scientific report, CEFIPRA Project RITFOLD N° 4604-4, 2013.

FADE J., Tour report, CEFIPRA Project RITFOLD N° 4604-4, January 2013.

FADE J., ALOUINI M., « Real-Time Imaging Through Fog Over Long Distances », Technical Report, 2012.

RAMACHANDRAN H., BRETENAKER F., FADE J., ALOUINI M., « Dispositif et méthode d'imagerie temps-réel pour l'assistance aux transports en conditions de visibilité dégradées », Enveloppe Soleau N°430334, Bretagne Valorisation, 14/11/2011.

RAMACHANDRAN H., BRETENAKER F., FADE J., ALOUINI M., « Dispositif et méthode d'imagerie temps-réel pour l'assistance aux transports en conditions de visibilité dégradées », Mémoire d'Invention, Bretagne Valorisation, 10/2011.

ALOUINI M., FADE J., « Principe et dispositif de mesure de dépolarisation avec ou sans déport par fibre optique en utilisant des états de polarisation orthogonaux et décalés en fréquence » Mémoire d'Invention, Bretagne Valorisation, 02/2011.

Summary of scientific activities and projects

Foreword

THIS manuscript is a condensed report of my scientific work in unconventional imaging techniques, including polarimetric imaging, quantum imaging and imaging through turbid media. Ranging from theory, through instrumental system design, to statistical signal processing, my scientific contribution aims at covering, as best as possible, the whole chain of understanding behind a physical imaging problem. This position is in phase with the recently celebrated "*co-design*" way of thinking which consists of jointly optimizing the hardware (physics of imaging, instrumental setup) and software (signal/image processing) building blocks required to provide the best image quality (of best processing performance) to an end-user for a dedicated application.

This work has been conducted over the last ten years, during my PhD at Institut Fresnel, in the Physics and Image Processing group (Phyti), then through a post-doctoral position at ONERA (the french aerospace lab) in the Lidar and Laser Sources group (DOTA-SLS), and finally at the Institute of Physics of Rennes, Optics and Photonics Department[1], where I actively contributed to create a recognized research activity in imaging (*Advanced imaging* axis).

In an attempt to present a unified vision of my scientific work, this document will be decomposed into two parts, corresponding to the two main aspects of my research activity. However, as imposed by any frontier, many connections between them are to be found, in terms of either applicative or scientific domains, which will be made appearant in this manuscript.

The first part, **Physics of light depolarization and non conventional polarimetric imaging**, is focused on polarimetric imaging, whose principles, methods and main topical challenges will be briefly recalled in Chapter 1. In spite of its long history, and of the huge number of contributors in this domain (either academic or industrial), this unconventional imaging technique still opens interesting scientific perspectives, in terms of physical understanding of the light-matter interaction, especially in random scattering media. As a result, there is still a topical debate about the clear definition and understanding of light depolarization, which is however one of the most used figure of merit in a wide number of polarimetric imaging applications. The theoretical and experimental developments conducted during these last years have allowed us to gain some physical insight in this domain, which will be summarized in Chapter 2.

The second challenge that I have tried to tackle in the polarimetric imaging domain concerns the simplification and robustness of the imaging processes. Indeed, full-Stokes or full-Mueller imaging polarimeters are very powerful and precise instruments, but to the expense of sometimes unaffordable price, time-consuming acquisitions, low wavelength tunability and complex calibration, correction and post-processing tasks in order to indirectly retrieve relevant polarimetric parameters. In that context, I will briefly present in Chapter 3 various simplified polarimetric imaging techniques, that aim at strongly reducing acquisition times, cost, and complexity of the image interpretation by providing a direct measurement of the desired polarimetric figure of merit. The first approach is

[1]At the date of the defense, and since July 1^{st} 2017, the Optics and Photonics Department in now part of Institut Foton, UMR 6082, University of Rennes 1, CNRS, INSA. The scientific activity of the former departement will continue as the DOP-team of the Institut Foton, which results from the merging of the Optics and Photonics Department of the IPR, and the former teams of the Foton laboratory, namely Foton-SP (Photonic Systems, Lannion, ENSSAT) and Foton-OHM (Optoelectronics, Heteroepitaxy and Materials, Rennes, INSA), in an attempt to federate the research in photonics at the University of Rennes 1.

very original with respect to standard polarimetric imaging techniques, as it relies on a specific dual-frequency dual-polarization laser illumination of the scene and on the detection of a radiofrequency (RF) beatnote component in the detected optical signal. The second approach represents the first proposal to my best knowledge of direct polarimetric sensing using a computational imaging approach, relying on the disseminating concept of compressed sensing. Lastly, the third technique that will be presented is based on the local analysis of the speckle intensity statistics in the image, and represents the utmost simplification for polarimetric sensing.

In the second part, titled **Optimal processing of optical signals in non conventional imaging approaches**, I will show how some of the well-known tools of information theory can be used in a scientific/engineering approach (i) to characterize the performance of an imaging setup and (ii) to develop efficient signal/image processing algorithms for specific tasks. In this document, the processing tasks considered will range from estimation of parameters, to contrast enhancement of active targets in images and unsupervised model selection in infrared spectroscopic data. After a brief reminder of the main information theoretic tools that have been used in my research (Shannon entropy, Fisher information, Kolmogorov complexity) in Chapter 4, the second part of this manuscript will address optimal extraction of information from non conventional optical signals, in different application domains. In Chapter 5, the issue of imaging through scattering media will be considered, relying on either a polarimetric approach or a fast intensity-modulation technique. I will illustrate how the Fisher information allowed us to define relevant gain criteria in terms of contrast enhancement of a remote target in turbid atmosphere, making it possible to evaluate the potentiality of these imaging setups for navigation assistance through fog.

Chapter 6 will present another example of information theory-based processing of unconventional optical signals. In the context of unsupervised wideband infrared spectroscopy, I will show how the principle of Minimum Description Length (MDL), inspired from the algorithmic definition of the information (Solomonoff-Kolmogorov's information theory), can be implemented to achieve unsupervised model selection, and how it can outperform standard penalized regression techniques for detection and estimation of atmospheric gas concentrations.

Lastly, a general conclusion along with scientific perspectives for future work will be provided in the last part of this manuscript.

Part I

Physics of light depolarization and non conventional polarimetric imaging

Chapter 1

Introduction: polarimetric imaging and depolarization

1.1 Polarization formalisms

Polarimetry and, by extension, polarimetric imaging aims at measuring the state of polarization of a light beam, i.e., the orientation of the electric field of the light as a function of time and space along its propagation, or at characterizing the polarimetric response of a sample when this latter is illuminated by a light with given polarization state (e.g., ellipsometry).

Among the mathematical descriptions and models of such (linear) light-matter interactions, Jones and Stokes/Mueller formalisms have always appeared as dual and often exclusive approaches, whose specific characteristics have been exploited for diverse applications. On the one hand, the description of field coherence in the Jones calculus, which relates the input and output 2-dimensional complex electric field through $\mathbf{E}_{out} = \mathbf{J}\mathbf{E}_{in}$ via a 2×2 complex Jones matrix, justifies its use in ellipsometry [Azz87, Web10], optical design [Chi89, Kam81, Col93, Kli12], spectroscopy [Kli12], astronomy [Cou94] or radar (PolSar) [Lee09]. On the other hand, Stokes/Mueller calculus is widely used in applications such as biophotonics [Pie11, Ala15], material characterization [Rog11, Mag14] or teledetection [Tyo06], as it is based on intensity measurements, relating the input and output 4-dimensional real Stokes vector through $\mathbf{s}_{out} = \mathbf{M}\mathbf{s}_{in}$, where $\mathbf{M}$ represents the 4×4 real Mueller matrix.

A consequence of the difference between these two mathematical representations is the way these approaches fundamentally differ in their capacity to characterize depolarizing light-matter interactions, as will be discussed below. However, as far as deterministic non depolarizing polarization transformations are concerned, the Jones and Stokes/Mueller descriptions are equivalent. In that case indeed, there is a clear one-to-one relationship between the Jones matrix $\mathbf{J}$ and the so-called Mueller-Jones matrix, denoted by $\mathbf{M}_{nd}$, through [Sim82, Kim87]

$$\mathbf{M}_{nd} = \mathbf{A}(\mathbf{J} \otimes \mathbf{J}^*)\mathbf{A}^\dagger, \text{ with } \mathbf{A} = \frac{1}{\sqrt{2}} \begin{bmatrix} 1 & 0 & 0 & 1 \\ 1 & 0 & 0 & -1 \\ 0 & 1 & 1 & 0 \\ 0 & i & -i & 0 \end{bmatrix}, \tag{1.1}$$

where $\otimes$ denotes Kronecker product. The unitary matrix $\mathbf{A}$ verifies $\mathbf{A}^{-1} = \mathbf{A}^\dagger$, and can also be rewritten in compact form as $\mathbf{A} = \left[\mathbf{vec}(\sigma_0)\ \mathbf{vec}(\boldsymbol{\sigma}_1)\ \mathbf{vec}(\boldsymbol{\sigma}_2)\ \mathbf{vec}(\boldsymbol{\sigma}_3)\right]^T/\sqrt{2}$, where $\mathbf{vec}(\boldsymbol{\sigma}_i)$ denotes the i^{th} Pauli matrix $\boldsymbol{\sigma}_i$ written in (column) vector form[2] Interestingly, if we restrict matrices $\mathbf{J}$ and $\mathbf{M}_{nd}$ to be unit-determinant, both descriptions appear to be isomorphic representations of the same 6-dimensional group, namely the proper orthochronous Lorentz group $SO^+(1,3)$ for Mueller matrices $\mathbf{M}_{nd}$ and the special linear group $SL(2,\mathbb{C})$ for Jones matrices $\mathbf{J}$ [Clo86, Han97]. As a result,

[2] In the remainder of this document, superscripts $*$, T and $\dagger$ will respectively denote complex conjugation, standard and Hermitian matrix transposition.

there is a well-known analogy between deterministic polarization transformations and special relativity [Han97, PF92, Mor03, Sim10, Lak12, Tud15, Fra15]. In particular, non-depolarizing interactions correspond to Lorentz transformations and must therefore preserve the Minkowski metric $\|\mathbf{s}\|_{1,3}$ of any input Stokes vector denoted by $\mathbf{s}$. This metric is defined by $\|\mathbf{s}\|_{1,3}^2 = \mathbf{s}^T G \mathbf{s} = I^2(1-\mathcal{P}^2)$, with $G = \mathrm{diag}[1,-1,-1,-1]$ and where $\mathcal{P} = \sqrt{s_1^2+s_2^2+s_3^2}/s_0$ denotes the light degree of polarization (DOP), and $I = s_0$ denotes the light intensity [Sim10]. By extension, this invariance property can be related to the preservation of the Shannon entropy[3] of the field, which is an informational measure of the disorder of the two-dimensional transverse electric field, as

$$H(\mathbf{s}) = -\int P_{\mathbf{E}}(\mathbf{E}) \ln P_{\mathbf{E}}(\mathbf{E}) = \ln \pi^2 e^2 \|\mathbf{s}\|_{1,3}^2 /4, \tag{1.2}$$

under the assumption of complex Gaussian circular fluctuations [Réf04]. Such an invariance property verified by non depolarizing deterministic polarization transformations will be put in perspective with a corresponding irreversibility property that we have established for depolarizing transformations, and which will be discussed in Chapter 2.

1.2 Polarimetric imaging

1.2.1 Standard polarimetric imaging techniques

Developed since a few decades, polarimetric imaging systems are still of growing interest for many applications like remote sensing [Tyo06], astronomy [Tin96], defense [Gou02, Dem97], biomedicine [Bue07, Gho11], synthetic-aperture radar [Lee01], and machine or enhanced vision [Mer08, Fad14b]. References [Tyo06, Sni14] provide recent reviews of the main applications of polarimetric imaging, either active or passive. Active polarimetric techniques are widely used to reveal contrasts that are not visible in standard intensity images, but can also provide valuable information of a given scene or sample from the measure of its anisotropic and depolarizing properties. Unlike ellipsometric techniques, which will not be addressed in this document, active polarimetric imaging is mostly often operated in a monostatic configuration, with co-located illumination source and polarization-analysing detector, either in the context of long range active imaging for defence applications, or in biomedical optics (tissue imaging, microscopy,...).

In that context, Mueller polarimetry is the most exhaustive active technique, as it completely characterizes the polarimetric response of an object. This technique typically implies registering 16 images, since four images must be acquired through four polarization analyzer configurations[4] and for four different illumination polarization states[5].

When it simply comes to analyzing the state of polarization of the light backscattered by an object, the so-called Stokes imaging is the recommended approach to be used. In that case, one can limit oneself to a single illumination state, while acquiring the same 4 images (Stokes images $\mathbf{s}_i, i \in \{0,3\}$) through various polarization analyzer configurations. These four measurements give access to the full polarization matrix defined as,

$$\Gamma = \langle \mathbf{E}(\mathbf{r},t)\mathbf{E}^{\dagger}(\mathbf{r},t) \rangle. \tag{1.3}$$

These "classical" techniques have proved efficient in many applications, but suffer from a number of practical limitations, which will be briefly enumerated below, and which justify the contributions about simplified polarimetry detailed in Chapter 3.

[3] See Chapter 4 for the definition of Shannon entropy.
[4] Linear horizontal, vertical, 45°, and circular polarization analyses.
[5] Identically, linear horizontal, vertical, 45°, and circular polarization states

1.2.2 Polarimetric parameters and figures of merit

To each polarimetric imaging modality, one can associate several polarization parameters, or contrasts, that could deliver relevant information to the end-user, revealing additional, enhanced or even new contrasts with respect to standard (reflectance) intensity imaging. In Stokes imaging, the most widely used parameter is the degree of polarization (DOP) $\mathcal{P}$ defined above, but also expressed from the polarization matrix Γ as

$$\mathcal{P} = \sqrt{1 - 4\frac{\det[\Gamma]}{\mathrm{tr}[\Gamma]^2}}. \tag{1.4}$$

A complementary polarization contrast is often obtained by the Angle of Linear Polarization map (AoLP) [Kup14], which basically provides the azimuth of the polarization state at each location of the scene.

As for Mueller imaging, the complete characterization of the sample polarimetric response gives access to a wide range of polarization parameters whose expressions will not be recalled here for the sake of conciseness: angle and amount of retardation, angle and amount of diattenuation, depolarization properties[6],... Regarding depolarization, it is customary in the Mueller/Stokes formalism to model purely depolarizing samples by a diagonal Mueller matrix

$$M_{\mathrm{puredep.}} = \begin{bmatrix} 1 & 0 & 0 & 0 \\ 0 & P_{L,1} & 0 & 0 \\ 0 & 0 & P_{L,2} & 0 \\ 0 & 0 & 0 & P_C \end{bmatrix} \tag{1.5}$$

, with $P_{L,1}$ and $P_{L,2}$ respectively denoting linear depolarization along X/Y and $+45°/-45°$ directions and P_C circular depolarization. In most situations, $P_{L,1} = P_{L,2}$, whereas P_C can be sometimes slightly different, though of the same order of magnitude [Bre99]. It can be noted here that many depolarization parameters have been defined and proposed from the expression of the Mueller matrix, as will be recalled in Chapter 2.

The variety and complementarity of the polarimetric maps obtained for each of these parameters often leads to one of the following situations:

- On the one hand, it can happen that only one, or very few parameters carry relevant information about the sample imaged. In that case, performing full-Mueller or full-Stokes measurements corresponds to oversampling the available information in the image, leading to largely redundant acquisitions. This situation is quite sub-optimal in terms of acquisition time, immunity to noise, calibration errors, etc.

- On the other hand, the information can be distributed over many polarimetric information channels (up to 16 in Mueller imaging), leading to a very difficult image interpretation by the end-user, who may not be an optics scientist in general, but a practicioner in a hospital, a soldier on the battlefield, or even an algorithm in an automated detection/navigation system. In that situation, it is highly desirable that the many polarimetric channels could be combined to provide a final synthetic image to the end-user with improved interpretability.

These two situations illustrate the reasons why these standard polarimetric imaging techniques are often replaced by simplified imaging systems, as will be described below. In addition, we can mention here that the complexity of these imaging techniques imply quite sophisticated calibration procedures (especially in the case of Mueller imaging, where calibration of instruments has given birth to an impressive literature) that are essential to guarantee physically acceptable results (See [Gil16b] for instance).

[6] Usually identified through the celebrated Lu-Chipman Mueller matrix decomposition [Lu96] (or similarly, through more recent types of decompositions).

1.3 Constraints and current challenges in polarimetric imaging

1.3.1 Simplification of the systems and real-time imaging

As recalled above, standard polarimetric approaches require that several images must be recorded for various illumination/analysis polarization states in order to provide a polarimetric image (potentially multi-dimensional). This is mainly due to the fact that optical techniques generally do not give access to a direct measurement of the electric field of the beam, as only intensity observables can be detected on an image sensor[7]. Historically, the acquisition of 16 – or 4 images depending on the technique – was initially operated sequentially, which causes a number of technical issues, such as long acquisition times, and complexity/cost of the imaging process[8]... In addition, these different images must then be combined together in order to provide the desired polarimetric parameters or contrasts listed above, implying possible image registration issues when imaging moving objects or living organisms, which can hinder the polarimetric consistency of the final polarimetric images obtained. These technological difficulties and constraints are probably largely responsible of the lack of diffusion of polarimetric approaches in real life imaging applications.

As a result, a topical challenge in polarimetric imaging is to avoid such sequential acquisitions by using different multiplexing "domains" such as spatially or spectrally multiplexed techniques [LaC11, Ale14, LG15], which appear as promising approaches to tackle the real-time challenge in Stokes or even Mueller imaging. Among the proposed setups, one can list various schemes including prisms [Bén09a], Savart plates [Luo08], polarization gratings [Kud12], liquid crystal modulators [Ala13], etc. In parallel, the recent development and commercialization of microgrid division-of-focal plane polarimetric cameras (Polaris, 4D-Technology, MoxTek,...) provide an appealing compromise towards mechanical reliability and real-time acquisition and processing, to the expense of course of spatial resolution. These commercial cameras are so far limited to measuring the degree and angle of linear polarization, but recent developments in laboratories have demonstrated the capacity of performing circular polarization measurements (S_3 Stokes parameter) [Hsu14].

However, the complexity of the systems and the loss of performance entailed by the different multiplexing methods listed above have led the community to propose several simplified polarimetric techniques which optimize the measurement of some specific polarimetric properties at a high performance [Ann12b, Ann12a, Tyo02, Tow01, Réf07b, Nan09, Jia05], without giving access to the whole polarimetric information (i.e., the Mueller matrix $\mathbf{M}$ for Mueller imaging, or the whole polarization matrix Γ for Stokes imaging). For instance, scalar polarimetric contrast images are commonly achieved from only two intensity measurements in the family of two-channel division-of-aperture imaging systems. Widely used in many applications due to its ease of implementation and simplicity of interpretation, the scalar polarimetric contrast imaging is mostly referred to as *Orthogonal States Contrast* (OSC) imaging [Gou04], or *Degree of Linear Polarization imaging* (DoLP) [Kup14]. The polarimetric contrast retrieved is given by

$$OSC = \frac{I_{\parallel} - I_{\perp}}{I_{\parallel} + I_{\perp}}, \tag{1.6}$$

where $I_{\parallel}$ and $I_{\perp}$ respectively denote the two polarimetric images acquired along linear directions of polarization, with orientation parallel (resp. perpendicular) to the illumination polarization direction. This polarimetric contrast is widely used in practice, as it correctly estimates the DOP of the backscattered light when the interaction with the sample is purely depolarizing (i.e., for samples exhibiting no diattenuation or birefringence). Such samples being modeled by a diagonal Mueller matrix as recalled above, it is quite obvious that the OSC parameter provides an estimate of the linear

[7] Let aside some interferometric polarization imaging techniques which can be of interest [Col02, Oka03], but to the expense of other kinds of technical complexity.

[8] Need of moving parts such as rotating polarizer, removable waveplate,... or use of electro-optic components (liquid crystal voltage-controlled retarders,...)

depolarization parameter[9] P_{L_1}. This hypothesis is mostly often valid in macroscopic imaging scenarii or when important light scattering occurs, which justifies the use of such a technique in remote sensing, target detection, imaging in turbid media and biological tissues imaging applications. We can also mention a recent scalar polarimetric imaging concept based on the acquisition of a single image through an optimized pair of illumination/analysis polarization states [Gou09, Ric09, Ann12b]. The technique has proved efficient in several situations, but the computation of the optimized states remains a non trivial problem which strongly depends on the noise statistics [Ann12a].

Generally speaking, these "incomplete" polarimetric techniques propose to operate a tradeoff between systems simplicity, rapidity, cost, and the polarimetric content of the final image provided to the user. As mentioned above, such a tradeoff is often justified by the context of the application addressed: in many situations, a single polarimetric contrast map will be provided to the end-user.

The work presented in Chapter 3 utterly corresponds to this last outlook on polarimetric imaging. In the various studies described in this chapter, our *motto* was also that, whatever be the polarimetric figure of merit relevant in the considered context, it would be highly desirable that it could be accessed within the smallest number of measurements/images/operations. Of course in some cases, extreme simplication can lead to a degradation of the performance with respect to standard complex techniques. However, it should make sense for the physicist that the most direct measure of a parameter must be the guarantee of the best immunity to crosstalk with other polarimetric parameters, but also to experimental noise, registration issues, calibration artifacts,... All such practical issues that limit the ease of Mueller imaging for instance. As will be detailed in Chapter 3, the three original simplified polarimetric imaging modalities studied allow the polarimetric contrast of interest for each modality to be obtained as far as possible from a direct measurement.

1.3.2 Endoscopic polarimetric imaging

Another ill-solved technological challenge in the field of polarimetric imaging is endoscopy for remote biomedical imaging and diagnosis. Indeed, the implementation of fiber-guided polarimetric imaging systems constitutes a challenging issue, due to the fact that the state of polarization of the illuminating beam is modified by the optical waveguide in an uncontrolled way. This is a remarkable aspect to be adressed for endoscopic applications, where the optical fiber stress-induced birefringence is the dominant effect on beam polarization [Woo10]. The feasibility of a multimodal endoscopic system including cross-polarized imaging has been demonstrated [The13]. However, such technique provides an orientation-dependent contrast, which entails some drawbacks for *in vivo* applications. Moreover, the fact that the polarimetric elements and the CCD camera are located at the distal end of the endoscope is quite restrictive in terms of miniaturization to access every organ of the human body. Regarding Mueller polarimetry, a narrow band 3×3 Mueller polarimetric endoscope was presented and validated with *ex vivo* experiments [Qi13]. However, the use of a rigid endoscope is unfeasible for most practical applications. Finally, a full Mueller endoscopic polarimeter was proposed in [Man15]. Nevertheless, this novel technique is still suboptimal in terms of acquisition time, as it is based on a first characterization of the optical fiber using a micro-switchable mirror before every Mueller matrix acquisition. A recent upgrade of the technique has permitted to lift the necessity of a movable mirror at the distal end of the endoscope by replacing it with a sharp dichroic spectral filter that reflects a first wavelength used to probe the Mueller matrix of the fiber itself, while a second wavelength transmitted by the filter probes the polarimetric response of the sample [Viz16]. However, as standard Mueller imaging systems, this technique necessitates a very precise calibration step, and requires ad hoc endoscopes to be developed with a specific optical architecture. As will be described in Chapter 3, the Depolarization/Dichroism Sensing by Orthogonality Breaking (DSOB) technique that we have developed at the Institute of Physics of Rennes can be seen as an alternative

[9] We can mention here the recent proposal of a *3-OSC* imaging approach, using three pairs of OSC images acquired along X/Y, $+45°/-45°$ and rcp/lcp, encoded in a composite RGB image, which allows the three depoalrization parameters $P_{L,1}$, $P_{L,2}$ and P_C to be measured. This technique seems promising for target detection applications [Van16].

approach to provide polarization-sensitive endoscopic measurements, while being compatible with standard monomode or few-mode fibers/endoscopes.

1.4 Light depolarization

As mentioned above, the DOP of the light on the one hand, and the depolarization parameter(s) of a sample on the other hand represent very relevant figures of merit that often provide contrasts able to reveal structures, objects or shapes that are not visible in a standard intensity image. Even though such parameters are in general quite straightforward to measure with the imaging systems listed above, the question of their physical meaning and interpretability is sometimes not so obvious, when departing from most standard imaging systems and/or experimental conditions, e.g. in the presence of speckle noise under coherent illumination, or in an endoscopic configuration through a spatially monomode waveguide, as will be discussed in Chapter 2. More generally – and quite problematically ! – the exact same scene characterized with different polarimetric imaging systems can yield different values of the DOP or of the sample depolarization parameters.

These observations illustrate the fact that in the most general case, the generic notion of light depolarization must encompass:

- (i) the optical anisotropic properties of the sample considered; but also (ii) its local structural organization, including spatial randomization effects;
- (iii) the properties of the illumination field (e.g. spectral bandwidth);
- and (iv) the characteristics of the detection setup (e.g. numerical aperture, spatial/spectral resolutions...).

Indeed, light depolarization occurs as the polarization state of the light analyzed undergoes a form of *randomization*.

This is clearly evidenced in the way the Stokes/Mueller and the Jones formalisms differ when non-deterministic polarization transformations are to be described. On the one hand, the Mueller formalism can model depolarization in a straightforward way, using depolarizing Mueller matrices $\mathbf{M}_{dep}$, whose elements can be any deterministic real values, as soon as the resulting Mueller matrix obeys standard physicality conditions. On the other hand, deterministic Jones matrices are unable to directly account for depolarizing interactions, which can only be apprehended under the Jones formalism using random sets of Jones matrices, i.e., $\mathbf{J}_{dep} = \langle \mathbf{J}_\lambda \rangle_\lambda$, where $\langle . \rangle_\lambda$ stands for ensemble averaging over statistical realizations λ. This discrepancy between both formalisms is mainly due to the fact that Jones formalism is a coherent description, as it models the evolution of the electrical field, whereas the Mueller formalism is incoherent. In fact, despite its apparent simplicity, the Mueller formalism implies such a randomization/averaging process when dealing with depolarizing Mueller matrices. As a result, the expression of a depolarizing Mueller matrix[10] implicitely assumes (at least partial) averaging over (at least) one of the above "dimensions" (spatial, spectral, temporal,...). However, in a broad range of experimental setups, the characteristics of the sensing/imaging system only lead to a partial averaging operation. As a result, the description of the sample by a diagonal depolarizing Mueller matrix can be no longer physically appropriate in such cases, as will be illustrated in Chapter 2.

Surprisingly at the beginning of the XXI$^{\text{th}}$ century, a deeper insight into the physical origins of depolarization is still a topical debate in the polarimetric imaging community [Bic92, Bro98, Aie05, Xu05, Set08, MR11, Sor11, Pou12, Dev13], as well as a consensual definition of depolarization parameters is still under discussion [Gil85, Fad16, OQ15b, Lip15, Gil16b, Gil16a]. In the next chapter, I will illustrate how I to strived through my research activity to contribute to the understanding of light depolarization, both from an theoretical and experimental standpoints.

[10] such as the matrix $\mathbf{M}_{\text{puredep.}}$ introduced above in Eq.(1.5) that models a purely depolarizing sample.

Chapter 2

Contribution to the physics of light depolarization

As mentioned in Chapter 1, the notion of light depolarization is quite subtle to define since it depends on almost all physical conditions of a light-matter experiment. Not only does it depends on the anisotropic optical properties of the sample illuminated and its local organization[11], but also on the way it is illuminated (wavelength, bandwidth, direction[12] of the illuminating light), and on the way it is detected (bandwidth, angular acceptance, resolution,... of the detector).

For instance in polarimetric imaging, the depolarization undergone when light is backscattered on the surface of a sample depends on the rugosity of the material, but also on the penetration depth of the wave in the sample. In this case, the depolarization mechanisms that occur for a surfacic or volumic interaction are today well understood when one considers ensemble averaged situations [Alo08, Amr08, Sor09]. That is to say when the illumination spectrum is wide enough; and/or when the illuminated surface is large with respect to the wavelength; and/or when the numerical aperture of the imaging system is large. In these conditions, the statistical description of the backscattered light field is well-known and can be used to probe the spatially-averaged degree of polarization (DOP) of the light with an extremely simple experimental setup, as will be described in Chapter 3.

Contrarily, as soon as the above conditions are not satisfied, the notion of depolarization must be handled with care. Indeed, even in the presence of a temporally frozen disorder (high temporal coherence of the light source and static object and detector, hence fixed speckle pattern during the analysis), the depolarization properties of the sample measured can vary dramatically as a function of the geometry of the imaging system. This observation has motivated the experimental study of the spatial repartition of the local state of polarization (SOP) in a static speckle pattern highly resolved on the camera. The results of this study are presented in the next section.

2.1 Polarimetric imaging at the speckle grain scale and spatial depolarization

Speckle is a ubiquitous phenomenon in all research fields studying the interaction between random media and propagating waves, whether electromagnetic [Goo07, Sko01, Jao84, Gar89] or acoustic [She06]. This phenomenon has been thoroughly investigated for decades [Goo07, Sko01, She06] but is still widely studied in very active research fields of physics, such as control of light through disordered media [Fre92, Pop10], optical non-linear effects in random media [Pee10] or polarization singularities [Ang02, Dup15]. In the optical imaging domain, speckle has often been considered as a noise detrimental to image quality [Alo09, Bén09a]. Nevertheless, speckle contrast imaging is known to be an efficient remote-sensing technique providing information on surface roughness properties

[11] at the scale of the volume probed by the light.

[12] i.e., temporal and spatial coherence properties of the incoming beam.

[Lég75, Leh95, Spr72], fluid velocity [And99], and biological activity [Nas14, Rou17] for instance. More recently, new applications involving speckle contrast images have been proposed to characterize polarization of light [Roc07, Réf07b, Fad12b] or diffusion properties of materials [Sor11, Cur11].

Despite this intense research activity, an open debate still remained about how the polarization state distribution of a speckle pattern can be clearly linked with a material's depolarization properties. This issue has occasioned a number of publications [Set08, Bro10, Bro11, Sor11, Li02, Amr08, Zer10, Ell04, Kor05, Ter09], questioning for instance the definition and the measurement of polarization correlation lengths in a spatial speckle pattern [Set08, Bro10, Bro11, Ell04, Kor05, Ter09], or the partial "repolarization" of unpolarized coherent light when backscattered by a depolarizing material [Sor11]. In order to link depolarization properties of a sample with the scattered light polarization distribution, former experimental studies were carried out using a spatial multiple-scale statistical analysis of the speckle polarization properties [Bro10, Li02, Amr08, Zer10]. In these experiments, light depolarization was studied from a "macroscopic" point of view, by conducting a statistical analysis of the DOP values or of the Orthogonal State Contrast (OSC), over a great number of coherence areas ("speckle grains"). These results tended to experimentally validate the fact that the polarization state is deterministic (light is fully polarized) at the "local" scale of a single speckle grain, whereas global depolarization induced by interaction (reflection or transmission) with the sample results from spatial averaging on the detector over several coherence areas [Bro10, Li02, Amr08, Zer10].

However, the various experimental devices used in these references were not able to study the polarization state of the speckle pattern at the local scale, i.e., beyond the speckle grain scale. To the best of our knowledge, an imaging setup capable of measuring the full Stokes vector (4 components) of light backscattered by a diffusive sample below the speckle grain scale in the optical wave domain had never been clearly addressed in the literature. Indeed, if such study could be carried out quite easily in the microwave range as suggested in [Zha09], it turned out to be a mere challenge when the wavelength is only a few hundreds of nanometers. Indeed, Stokes measurements require polarizers and wave plates (at least one) to be inserted and rotated in front of the imaging detector, thus inevitably modifying the optical wavefront of the scattered light and hence the speckle pattern itself. This experimental difficulty was mostly often eluded in the literature, suggesting that conventional experimental schemes based on the statistical analysis over many speckle grains were in fact not able to perform reliable Stokes measurements at an imaging scale well below the typical size of speckle grain.

It thus appeared to us that is was important to propose and develop a reliable and optimized experimental setup, cleared for all sources of instrumental bias that could easily hide the polarimetric effects by modifying (even very slightly) the wavefront of the light backscattered towards the detector. All the technical details about how we ensured the best immunity to turbulence, thermal drifts, sample heating, insertion/rotation of optical analyzing components in the path of light, etc. are detailed in [Pou12] (attached article (AA) I-1, p. 99). We used a 532 nm Coherent-Verdi pump laser to enlighten the sample, so as to ensure an extremely high temporal coherence to our illumination. This way, we could avoid any spectral/temporal depolarization effects in our experiment which was dedicated to probing the spatial depolarization. Using a 200 μm diameter objective lens in front of the detector, we were able to obtain highly resolved speckle grains on the camera (about 2000 pixels/speckle grain on the CCD). Polarization analysis was performed using a quarter-wave plate and a linear polarizer in a rotating mount, located in an intermediate image plane and finely oriented so as to minimize wavefront deformations. For the sake of conciseness, the details of the setup sketched in Fig. 2.1-[I] will not be given here but can be found in [Pou12] (AA I-1, p. 99). In Fig. 2.1-[II], we plot an example of speckle pattern imaged through various orientations of the polarization analysis element (each orientation corresponding to a different contour plot), showing fair spatial stability of the speckle pattern of the light backscattered on a non-depolarizing metallic surface.

This experimental setup has first permitted to confirm, without ambiguity for the first time at optical wavelengths, that the SOP of light is well defined (i.e., with unitary DOP) in all locations of a speckle field. This was expected theoretically, but deserved a clear experimental confirmation.

Moreover, this experiment has also confirmed what was hinted from previous statistical analyses: in coherent active polarimetric imaging with static objects (frozen disorder), the notion of depolarization results from a spatial averaging of the SOP over various coherence areas. In other words, a sample characterized as *non-depolarizing* in standard polarimetric experiments exhibits a constant SOP over all the speckle grains imaged: this is confirmed in Fig. 2.2 where the first two rows show the repartition on the Poincaré's sphere of the SOP of the pixels coming from three distinct speckle grains. It can be seen that all SOP's are located close to the one of the incident light. On the other hand, a *depolarizing* sample, as the one considered in the third row of Fig. 2.2 will have various SOP's across the different speckle grains of the pattern, as can be seen in the figure. The value of the DOP (0.4 for this last sample) measured from a standard polarimetric experiment is thus the result of a spatial averaging of these many SOPs across the Poincaré's sphere, as was confirmed by a statistical analysis over many grains [Pou12].

Lastly, this specific polarimetric imaging system has permitted an interesting observation to be made. On the depolarizing sample, we analyzed the polarimetric transition between two adjacent speckle grains, as sketched in Fig. 2.3-[I], by drawing a straight line between the centers of the grains, and plotting the evolution of the SOP across the Poincaré's sphere. The resulting "polarization trajectory" is plotted in Fig. 2.3-[II], which shows that the evolution is continuous (adiabatic) between the central SOPs of each grain, and seems to follow the shortest path on the sphere surface.

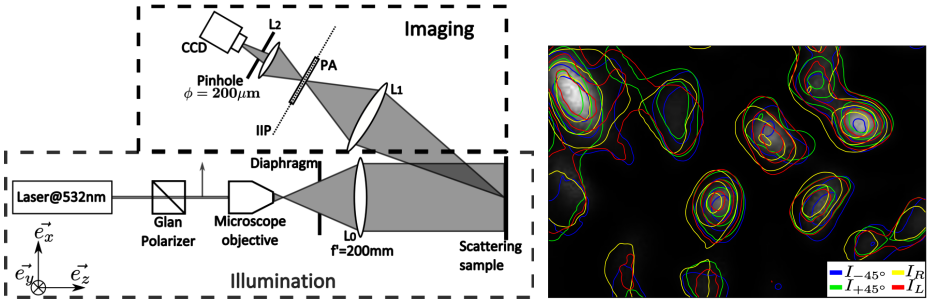

[I] [II]

Figure 2.1: [I] Experimental setup of Stokes imaging beyond the speckle grain scale. [II] In contour plots, the speckle intensity patterns observed after speckle registration for four Stokes images, superimposed on a grayscale image of the total intensity S_0.

This last observation would deserve a more thorough study to generalize or not such a behaviour. However, the exploitation of the setup proposed remained very limited due to the complexity of the measurement protocol required, and the acquisition time needed. As a result, the study of many interesting fundamental aspects that remain to be addressed with such an experimental setup has been temporarily postponed. In order to propose a more operational setup, we have upgraded it these last years by replacing the rotating polarization analyzer by a fixed system using liquid crystal retarder plates developed on purpose for this experiment. We are now close to having an automated setup allowing calibration and acquisition within reasonable acquisition times, and which will be used in the next years to push forward this interesting research field.

Lastly, it can be noted that this first measure of the spatial repartition of the SOP over a highly resolved speckle pattern has galvanized the community, as several french groups in Marseille and Toulouse have now developed similar optical benches, with higher precision and easier/faster acquisition, that confirm our seminal experimental results in this domain.

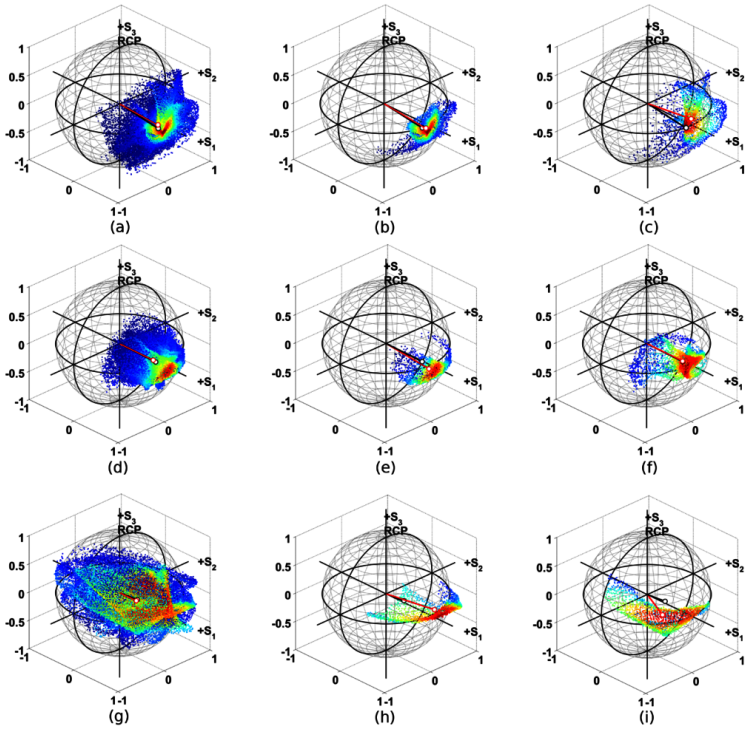

Figure 2.2: Repartition of the pixels SOP on Poincaré's sphere for a metallic sample (first row), a non-depolarizing red paint sample (second row), and a depolarizing green paint sample (third row). First column, SOP in the whole ROI; second and third column, SOP in two different speckle grains.

2.2 DOP tunable coherent source by temporal depolarization control

As seen above, light depolarization measured through its DOP must be defined with respect to a given spatial resolution (or spatial bandwidth) of the detector. As stated in the introduction, the temporal bandwidth of the detector should also be taken into account in the description of the experiment as it can influence the measure of the polarimetric properties of samples when depolarization effects are at stake. It is however hardly ever done in practice, as the temporal resolution of usual detectors is well below the typical time constants that characterize the temporal evolution of the light electric field.

In that context, we have shown that such temporal depolarization can be "tuned" by using a specific laser arrangment, making it possible to generate a coherent beam with precise control of its (temporal) DOP when the detector considered is sufficiently slow. The development of such a source presents a high potential for several applications like polarimetric imaging, interferometric sensing, gyroscopy, quantum communications, and instrument calibration. Several tunable sources based on different technologies have been demonstrated during the last decade, however, they entail a number of limitations (among others: single/fixed SOP, incomplete depolarization, or very long acquisition times). Moreover, all of them inherently provide a temporally incoherent beam, as they rely either on spectral dispersion of the SOP of light, or on temporal delays to make two fractions of the beam temporally incoherent with each other. They are thus incompatible with techniques requiring coherent beams, like interferometric systems.

In this context, we recently proposed a simple way of producing a coherent beam with full, precise and independent control on the SOP and DOP. This apparatus has been recently patented [OQ17a]. Our approach is based on an imbalanced dual-frequency dual-polarization (DFDP) light source exhibiting a potentially very fast temporal modulation of its SOP, which results in a partially depolarized beam when measured at the temporal scale of most standard optical detectors. The implementa-

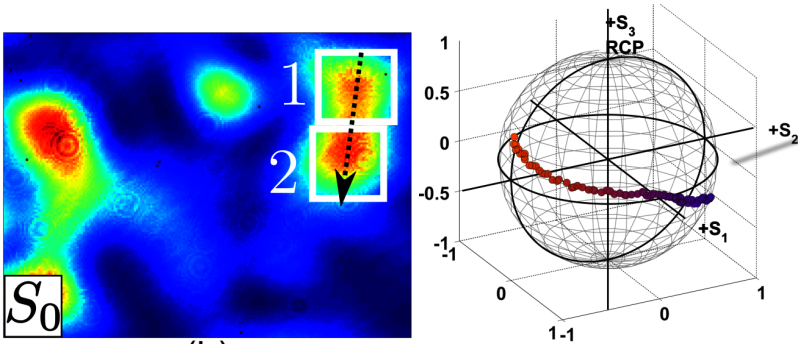

[I] [II]

Figure 2.3: [I] Speckle intensity (S_0) repartition on a depolarizing sample (green paint) allowing the definition of a linear path across two adjacent speckle grains. [II] Observation of an adiabatic polarization state transition along the geometrical path defined in [I] between two adjacent speckle grains on a depolarizing sample.

tion of this source can be easily done using fibered optical components, as sketched in Fig. 2.4, using a fibered polarization sensitive Mach-Zehnder architecture comprising a variable optical attenuator to tune the intensity imbalance between the two polarization states, and an acousto-optic modulator (AOM) that operates a frequency shift $\Delta\nu = 80$ MHz on one of the two states. The full details about the source implementation will be omitted here for the sake of concision, but can be found in [OQ17b] (AA I-2, p. 111). In addition, a very similar setup will be more thoroughly described in Chapter 3, as it is required to implement an original active polarimetric imaging technique that has been developed these last years in the laboratory.

It is more interesting here to focus on the mathematical description of this specific polarization state. In the case of linear input polarization states of azimuth α for the sake of clarity, it can be easily shown [OQ17b] that the Stokes vector describing such a beam can be written, as a function of time, as

$$\mathbf{S}(t) = S_0 \begin{bmatrix} 1 \\ \frac{\cos 2\alpha(1-\gamma) - 2\sqrt{\gamma}\sin 2\alpha \cos \Delta\omega t}{1+\gamma} \\ \frac{\sin 2\alpha(1-\gamma) + 2\sqrt{\gamma}\cos 2\alpha \cos \Delta\omega t}{1+\gamma} \\ \frac{2\sqrt{\gamma}\cos \Delta\omega t}{1+\gamma} \end{bmatrix}, \tag{2.1}$$

where γ is the intensity imbalance parameter such that $I^{\nu+\Delta\nu}/I^{\nu} = \gamma$. This expression shows that the Stokes parameters of the field evolve rapidly at the detuning frequency $\Delta\nu$, hence justifying the term *instantaneous* Stokes vector used in [OQ17b, OQ15b] (AA I-2, AA I-5). At a temporal scale faster than $\tau_{beam} = 1/\Delta\nu$, i.e., with a fast photodetector for instance, this SOP describes a circular trajectory across the Poincaré's sphere surface which indicates that the light is always temporally fully polarized. When the states are perfectly balanced, the SOP runs across a great circle (equator) of the sphere, whereas for $\gamma \neq 1$, the trajectory corresponds to a parallel line of the sphere, coming closer to the pole when $\gamma \gg 1$ or $\gamma \ll 1$.

On the other hand, a standard low frequency detector (which will be the case with imaging detectors that cannot resolve so far frequencies in the 10-100 MHz range) will observe a time-averaged Stokes vector

$$\langle \mathbf{S}(t) \rangle = S_0 \begin{bmatrix} 1 \\ \frac{1-\gamma}{1+\gamma}\cos 2\alpha \\ \frac{1-\gamma}{1+\gamma}\sin 2\alpha \\ 0 \end{bmatrix}, \tag{2.2}$$

from which expression it is obviously seen that the time-averaged degree of polarization is DOP=$\frac{1-\gamma}{1+\gamma}$. Therefore, an imbalanced DFDP source constitutes a pretty straightforward way of generating a beam with a fully tunable state and degree of polarization, with the sole condition that the frequency shift $\Delta\nu$ is much higher than the bandwidth of the detector to be used with. This behaviour is illustrated in Fig. 2.5-[I], where the overall DOP measured with a slow fibered polarimeter (Thorlabs PAT 9000, $\tau_{det} \simeq 0.03$ s) is plotted as a function of the imbalance parameter $\gamma(t)$ which is varied sinusoidally in time in the experiment with period τ_{mod}=20 s. The black curve demonstrates the ability of the source to provide a tunable DOP between 0 and 1 by adjusting γ (here γ can be set between $\gamma \ll 1$ and $\gamma = 1$), when the detector bandwidth is below the detuning frequency, i.e. for $\tau_{det} \ll \tau_{beam}$. At each time t, the partially polarized beam results from the time-averaging of a SOP describing a sphere parallel line. Interestingly, when γ is varied fast enough such that $\tau_{mod} \ll \tau_{det}$, the slow detector will "see" in that case a perfectly depolarized SOP, which results from the averaging of all possible SOPs across the Poincaré's sphere, thereby ensuring ideal depolarization model. This is illustrated by the red curve in Fig. 2.5-[I], where the overall DOP in this situation is measured to 0.44 (theoretical value $\simeq 0.4$), due to the fact that in our experimental setup, only one half of the sphere could be ran across by the SOP. Lastly, in the opposite situation where a fast photodetector is used that can resolve the time-evolution of the SOP, the exact same experimental setup makes it possible to generate interesting trajectories, at very fast rates, across the Poincaré's sphere. This is illustrated in Fig. 2.5-[II] where we have been able to measure and plot the SOP evolution on the Poincaré's sphere using a slow polarimeter. For that purpose, the trick consisted of using a frequency down-conversion of the fast SOP evolution at frequency $\Delta\nu$ to a very low frequency (well below $\ll 1/\tau_{det}$) by modulating the intensity of the front laser at a frequency close to $\Delta\nu$ with a 2-ports signal generator (see [OQ17b] AAI-2, p. 111 for details). The resulting trajectory when γ is time modulated is a spiral on the surface of the Poincaré's sphere. This demonstrated that such trajectories can be generated at radiofrequencies using a simple experimental scheme, which could find interesting applications in detectors characterization, optical communications, etc. but also for the developement of original polarimetric imaging approaches.

Besides its practical interest for generating coherent sources with finely tunable DOP, this experiment demonstrated that a strict analogy can be drawn between time depolarization and the spatial depolarization studied in the previous experiment. On the one hand, spatial depolarization can only be meaningful when the coherence area of the speckle pattern is well below the pixel size (spatial resolution of the detector). On the other hand, depolarization occurs when the instantaneous temporal evolution of the SOP cannot be probed by the detector used (temporal resolution of the detector). Again, these two experiments illustrate the strong interplay between the sample properties, the light used to probe it, and the illumination/detection conditions experimental conditions, that should be all encompassed to define depolarization on rigorous and sound bases in a polarimeric imaging experiment.

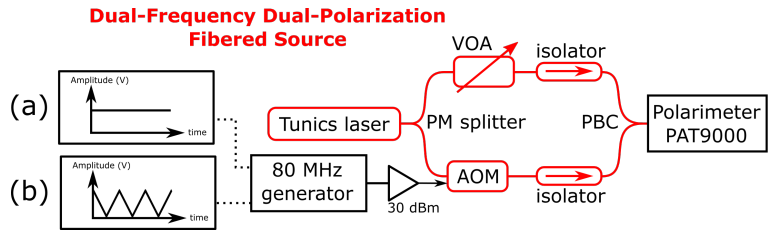

Figure 2.4: Production of a coherent light beam with (a) fixed, (b) time-modulated, precisely controlled DOP using an intensity-imbalanced DFDP source. The intensity imbalance can be obtained using a variable optical attenuator (VOA) in one arm of the Mach-Zehnder architecture, or (b) by modulating the RF power of the electrical signal on the acousto-optic modulator (AOM) used to operate the frequency shift.

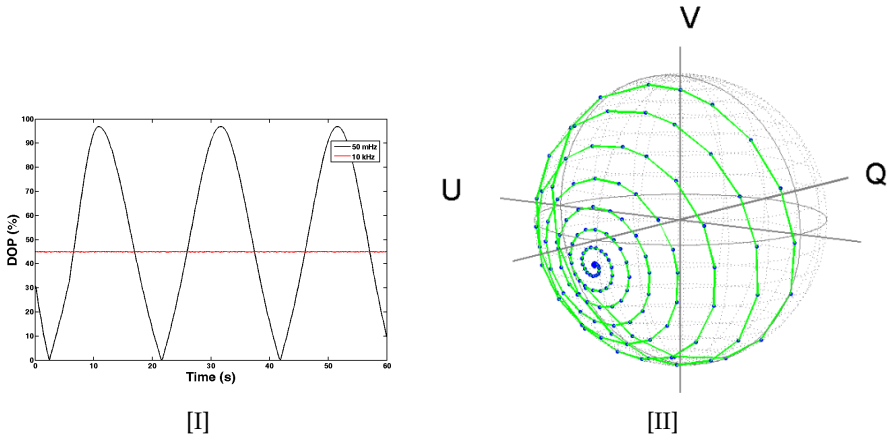

[I] [II]

Figure 2.5: [I] Temporal evolution of the DOP for slow (black dashed curve) and fast (red solid curve) AOM modulation signals. [II] Temporal evolution of the instantaneous DFDP state of polarization over the Poincaré's sphere.

2.3 Stochastic model of depolarizing Mueller matrix from random optical anisotropies

Let aside the spatial and temporal depolarization mechanisms discussed above that can occur due to limited bandwidth(s) of the detector, we shall now address in the next two sections of this chapter the question of modeling the depolarization properties of a sample from the random nature of its anisotropic properties. As mentioned above, depolarization arises from a randomization of the SOP of the light, as a result we proposed to describe a depolarizing sample by means of a stochastic model of random anisotropic optical properties. Our motivation was to lift the veil on depolarizing Mueller matrices, that most of the time dissimulate such randomization mechanisms as evoked in Chapter 1.

In this section, we briefly describe a stochastic model of a depolarizing anisotropic medium consisting of the action of random linear dichroic elements. Though simple, this model has a nice illustrative potential, as it makes it possible to characterize the progressive transition from a deterministic anisotropic sample to a strongly random one (characterized by a Mueller matrix of a diagonal depolarizer) as the averaging conditions evolve.

Let us thus model a dichroic depolarizing medium assuming that depolarization arises from the heterogeneity of its anisotropy properties at the spatial scale of the light illumination/collection[13]. For that purpose, we consider that the incoming beam urdergoes random local dichroic interactions, each polarization transformation having a Mueller matrix $\mathbf{M_{LD}}_{\mu}$ of a partial diattenuator with same diattenuation coefficient d, but randomly distributed linear dichroism angle ϕ_{μ}, and where the subscript μ denotes one realization of a random event. Consequently, the Mueller matrix of a single random event is not depolarizing (Mueller-Jones matrix), as the individual polarization transformation is purely deterministic.

When averaged over many random events, the (macroscopic) Mueller matrix reads $\bar{\mathbf{M}}_{\mathbf{LD}} = \langle \mathbf{M}_{\mathbf{LD}\mu} \rangle_{\mu}$. Using a convenient Wrapped-Gaussian Distribution (WGD) model for the statistical distribution of anisotropy angle [OQ16] (see AA I-5, p. 129 for further details), we have been able to

[13] i.e., at the scale of the focal volume of the excitation in microscopy, or the spatial resolution of the pixel/detector in most other imaging schemes.

provide a closed form expression of $\bar{\mathbf{M}}_{\mathbf{LD}}$ as

$$\bar{\mathbf{M}}_{\mathbf{LD}} = \rho \begin{bmatrix} 1 & d\,\xi\cos 2\bar{\phi} & d\,\xi\sin 2\bar{\phi} & 0 \\ d\,\xi\cos 2\bar{\phi} & \frac{1+T}{2} + \frac{1-\langle T\rangle}{2}\,\xi^4\cos 4\bar{\phi} & (1-T)\,\xi^4\cos 2\bar{\phi}\sin 2\bar{\phi} & 0 \\ d\,\xi\sin 2\bar{\phi} & (1-T)\,\xi^4\cos 2\bar{\phi}\sin 2\bar{\phi} & \frac{1+T}{2} - \frac{1-T}{2}\,\xi^4\cos 4\bar{\phi} & 0 \\ 0 & 0 & 0 & T \end{bmatrix}, \tag{2.3}$$

where ρ denotes the average isotropic absorption, and where $T = \rho\sqrt{T_{max}T_{min}}$ is the transmission parameter. It can be readily observed that this Mueller matrix is very similar to the Mueller matrix of a standard partial diattenuator with diattenuation parameter d, and average angle $\bar{\phi} = \langle\phi\rangle$, except for the presence of the parameter ξ, which only depends on the variance σ_ϕ^2 of the distribution of the anisotropy angle through $\xi = \exp(-2\sigma_\phi^2)$.

Interestingly, when $\sigma_\phi \to 0$, i.e., when no randomization occurs $\lim_{\sigma_\phi\to 0}\bar{\mathbf{M}}_{LD} = \mathbf{M}_{\mathbf{LD}}$, which corresponds to the trivial case of a deterministic diattenuating sample. In the intermediate case, the angular dispersion of ϕ naturally reduces the diattenuation capacity of the sample, since in that case the diattenuation coefficient, defined by $D = \sqrt{\sum_{j=2}^{4}(\bar{\mathbf{M}}_{\mathbf{LD}})_{1j}^2/(\bar{\mathbf{M}}_{\mathbf{LD}})_{11}}$ is equal to $D = d\,\xi \leq d$ [OQ15b]. The evolution of the "effective" diattenuation coefficient D is plotted in Fig. 2.6.(a) as a function of σ_ϕ and of $\log_{10} T_{max}/T_{min}$ (which is 0 for an isotropic sample and tends to infinity for a perfect polarizer). It can be seen that the diattenuation coefficient of the Mueller matrix rapidly decreases with σ_ϕ, whereas it increases for higher values of $\log_{10} T_{max}/T_{min}$ as expected. Now when the angular distribution becomes strongly randomized (i.e., $\sigma_\phi \gg 1$), the Mueller matrix tends to the form of a diagonal depolarizer:

$$\lim_{\sigma_\phi\gg 1}\bar{\mathbf{M}}_{\mathbf{LD}} = \rho\,\mathrm{diag}\big[1,\ (1+T)/2,\ (1+T)/2,\ T\big]. \tag{2.4}$$

Furthermore, if dichroism is perfect ($d = 1$), then $T = 0$ and the previous matrix corresponds to a sample that completely depolarizes the fourth element of the Stokes vector, and reduces by 0.5 the DOP of any linear input SOP. For other values of T, the depolarization strength of such a diagonal depolarizer varies for each Stokes vector element.

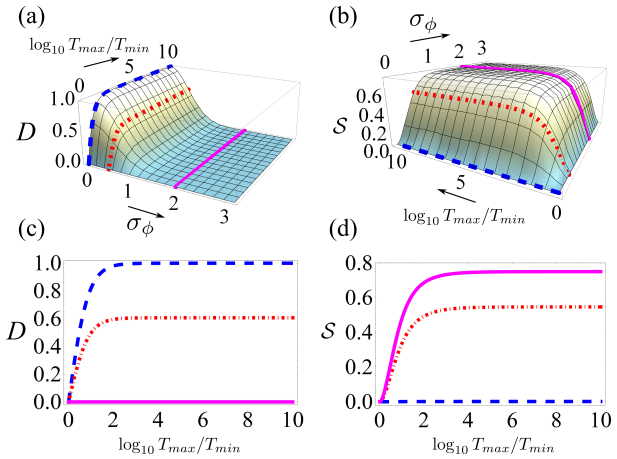

Figure 2.6: (a) Evolution of the effective diattenuation coefficient D as a function of angular dispersion σ_ϕ and of $\log_{10} T_{max}/T_{min}$. (b) Evolution of the Cloude entropy $\mathcal{S}$ as a function of angular dispersion σ_ϕ and of $\log_{10} T_{max}/T_{min}$. Evolution of the diattenuation coefficient D (c) and of the Cloude entropy $\mathcal{S}$ (d) as a function of $\log_{10} T_{max}/T_{min}$ for $\sigma_\phi = 0$ (blue), $\sigma_\phi = 1/2$ (red), and $\sigma_\phi = 2$ (magenta).

These features confirm that this model makes it possible to simply account for the continuous

transition from a non-depolarizing sample characterized by a deterministic polarization transformation on the one hand, to a fully depolarizing sample depending on the statistical properties of the random diattenuation parameters on the other hand. To confirm such behaviour, let us analyze the depolarizing properties of this matrix. Among the several depolarization metrics that can be used to quantify the depolarizing properties of a sample [Lu96, Clo86, Gil85, Chi05, Oss10, OQ15b], we relied on the Cloude entropy, which is a well-established metric to characterize the overall depolarizing nature of a given Mueller matrix [Clo86]. The Cloude entropy is given by $\mathcal{S} = -\sum_{i=1}^{4} \lambda'_i \log_4 \lambda'_i$, where $\lambda'_i = \lambda_i / \sum_{j=1}^{4} \lambda_j$ are the normalized eigenvalues of the 4×4 Cloude coherency matrix [Clo86], which is derived from $\bar{\mathbf{M}}_{\mathbf{LD}}$ by

$$\mathbf{C}(\bar{\mathbf{M}}_{\mathbf{LD}}) = \frac{\sum_{j,k=1}^{4} (\bar{\mathbf{M}}_{LD})_{jk}\, \mathbf{A}\big(\sigma_j \otimes \sigma_k^*\big)\mathbf{A}^\dagger}{4}, \tag{2.5}$$

where matrix $\mathbf{A}$ is given in Eq. (1.1). The Cloude entropy $\mathcal{S}$ is a measure of the dispersion of the relative magnitude of the four eigenvalues of $\mathbf{C}(\bar{\mathbf{M}}_{\mathbf{LD}})$, and varies between 0 for deterministic transformations and 1 for totally depolarizing interactions [Clo86]. The evolution of $\mathcal{S}$ is plotted in Fig. 2.6.b as a function of σ_ϕ and of $\log_{10} T_{max}/T_{min}$. It can be seen in Fig. 2.6.b that the Cloude entropy $\mathcal{S}$ increases with σ_ϕ, thus evidencing that depolarization is stronger as the angular dispersion grows. On the other hand, the Cloude entropy increases with $\log_{10} T_{max}/T_{min}$. For high σ_ϕ and significant anisotropy ($\log_{10} T_{max}/T_{min} \neq 0$), it can be noted that the Cloude entropy reaches a maximum value below unity ($\mathcal{S}_{max} = 0.75$), simply because the stochastic model of the sample considered does not lead to a complete depolarization of any input SOP, as we have only considered the subset of random linearly dichroic events without including elliptical dichroism.

Through this simple analytical example, we have illustrated how the intrinsic (local, microscopic) dichroic properties of the sample gradually vanish as more orientations of the dichroism are taken into account by increasing σ_ϕ, providing the sample with a "macroscopic" depolarizing nature. This situation could occur in practice as the transverse dimension of the beam used to probe a sample is increased with respect to scale of the microscopic structural organization of the sample responsible for its anistropic optical behaviour. The same reasoning could hold in the longitudinal (propagation) direction, where depolarization could occur gradually as the beam is propagated deeper in the sample. This latter situation is specifically addressed in the last section of this chapter, where we show how the so-called *differential* polarization formalisms allow to shed new light on the physics of light depolarization.

2.4 Description, characterization and irreversibility properties of depolarizing interaction from differential formalism

The differential formalisms were historically introduced in the domain of polarimetry by Jones himself [Jon48] and Azzam [Azz78], who respectively proposed to define a differential Jones matrix (dJm) $\mathbf{j}$ and a differential Mueller matrix (dMm) $\mathbf{m}_{nd}$, where the subscript nd still indicates a non-depolarizing transformation. Both approaches describe the local evolution of a transversally polarized wave along direction, say z, through the respective differential equations $d\mathbf{E}/d\hat{\mathbf{z}} = \mathbf{j}\,\mathbf{E}$, and $d\mathbf{s}/d\hat{\mathbf{z}} = \mathbf{m}_{nd}\,\mathbf{s}$, with

$$\mathbf{j} = \frac{1}{2}\begin{bmatrix} 2\kappa_i + \kappa_q - i(2\eta_i + \eta_q) & \kappa_u - \eta_v - i(\eta_u + \kappa_v) \\ \kappa_u + \eta_v - i(\eta_u - \kappa_v) & 2\kappa_i - \kappa_q - i(2\eta_i - \eta_q) \end{bmatrix}, \tag{2.6}$$

$$\text{and,} \quad \mathbf{m}_{nd} = \begin{bmatrix} 2\kappa_i & \kappa_q & \kappa_u & \kappa_v \\ \kappa_q & 2\kappa_i & -\eta_v & \eta_u \\ \kappa_u & \eta_v & 2\kappa_i & -\eta_q \\ \kappa_v & -\eta_u & \eta_q & 2\kappa_i \end{bmatrix}. \tag{2.7}$$

In the above matrices, the parameter κ_i denotes the isotropic extinction coefficient (in amplitude) induced by the sample or material, whereas parameter η_i stands for the isotropic (absolute) optical phase incurred by the interaction with the sample, and whose information is lost in the (incoherent) Mueller description [Jon47]. As for the other terms, the subscripts q, u, and v refer to linear x-y, linear $\pm 45°$ and circular left/right optical anisotropies, through $x_{q,u,v} = x_{x,45°,rcp} - x_{y,-45°,lcp}$, with $x = \kappa$ when describing absorption anisotropy (diattenuation), or $x = \eta$ when describing phase anisotropy (birefringence).

According to group theory, these differential descriptions lead to a representation of deterministic polarization transformations[14], either in group $SL(2,\mathbb{C})$ for $\widetilde{\mathbf{J}}$ or in $SO^+(1,3)$ for $\widetilde{\mathbf{M}}_{nd}$, by their counterpart in the corresponding Lie algebra $\mathfrak{sl}(2,\mathbb{C})$ for $\mathbf{j}$, or $\mathfrak{so}^+(1,3)$ for $\mathbf{m}_{nd}$, which latter verifies Minkowski G-antisymmetry, i.e., $\mathbf{m}_{nd} + \mathbf{G}\,\mathbf{m}_{nd}^T\,\mathbf{G} = 0$ [Lou01]. There is a clear equivalence between these four representations which are linked through a commutative diagram plotted in Fig. 2.7, the macroscopic and differential matrices being related by the exponential map, i.e., $\widetilde{\mathbf{J}} = \exp(\mathbf{j}\Delta z)$ and $\widetilde{\mathbf{M}}_{nd} = \exp(\mathbf{m}_{nd}\Delta z)$ when propagation over Δz through a homogeneous medium is assumed. As Lie algebras can be viewed as the tangent spaces to the corresponding Lie groups at the identity element [Lou01, Gal11], the differential Jones or Mueller formalisms allow polarization properties of a sample or a material to be described in a linearized geometry, which appears through the simple linear parameterizations of the differential matrices in terms of anisotropic optical properties of the sample[15].

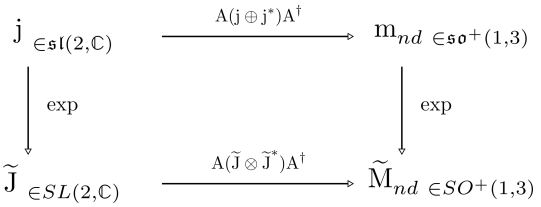

Figure 2.7: Commutative diagram verified by the macroscopic Jones matrix $\mathbf{J}$ and non-depolarizing Mueller matrix $\mathbf{M}_{nd}$ as elements of two isomorphic groups, and by the differential Jones matrix $\mathbf{j}$ and non-depolarizing differential Mueller matrix $\mathbf{m}_{nd}$ as corresponding elements of two isomorphic Lie algebras.

A few years ago, the differential Mueller formalism has been extended to the more intricate case of depolarizing transformations, by the introduction of depolarizing dMm's. This approach has permitted a number of interesting results to be obtained on depolarizing transformations [OQ12, Kum12, OQ14, Ell14, Vil14, Oss14b, OQ15b, Oss15, Aga15]. We recently proposed in [Fad16] (see AA I-3, p. 115) to shed new light on the recent developments on depolarizing dMms, by using an alternative description involving stochastic differential Jones matrices. For that purpose, we considered a stochastic differential Jones matrix $\mathbf{j} = \mathbf{j}_0 + \Delta\mathbf{j}$, modeling a random depolarizing local transformation of the field, where $\mathbf{j}_0 = \langle \mathbf{j} \rangle$ is the deterministic average polarization transformation, whose parametric form has been recalled in Eq. (2.6), and where the fluctuation matrix verifies $\langle \Delta\mathbf{j} \rangle = 0$. Assuming infinitesimal propagation over Δz in the considered medium, the Jones matrix for such a transformation can be written $\mathbf{J} = \exp(\mathbf{j}\Delta z) \simeq \underline{\mathrm{Id}} + \mathbf{j}\Delta z$ at first order in Δz. From Eq. (2.6), this relation can be conveniently rewritten in a vector form in the Pauli matrices basis $\{\sigma_i\}_{i=\{0,3\}}$ as $\mathbf{V}_\mathrm{J} \simeq \left[1 + \frac{\Delta z}{2} p^{(0)} \;\; \frac{\Delta z}{2}\mathbf{p}\right]^T$, with $p^{(0)} = p_0^{(0)} + \Delta p^{(0)}$, $\mathbf{p} = \mathbf{p}_0 + \Delta\mathbf{p}$. In these expressions, the deterministic

[14] In the remainder of this section, the notation $\widetilde{\mathbf{X}}$ will denote a normalized unit-determinant matrix.

[15] Contrarily to the parameterization of standard macroscopic Mueller matrices for instance, whose elements exhibit highly non linear (e.g., trigonometric) expressions as a function of the anisotropy parameters.

average values read

$$p_0^{(0)} = 2\kappa_i - 2\eta_i, \text{ and } \mathbf{p}_0 = \begin{bmatrix} \kappa_q - i\eta_q \\ \kappa_u - i\eta_u \\ \kappa_v - i\eta_v \end{bmatrix}, \tag{2.8}$$

whereas $\Delta p^{(0)}$ and $\Delta\mathbf{p}$ denote zero mean random variables describing the fluctuations of the anisotropy parameters.

The Cloude's coherency matrix (CCM) of the polarimetric transformation, which can be obtained from the Mueller matrix using relation (2.5), is also fundamentally defined as the second-order moment matrix of vector $\mathbf{V}_\mathrm{J}$, i.e., $\mathbf{C}(\mathbf{J}) = \langle \mathbf{V}_\mathrm{J}\mathbf{V}_\mathrm{J}^\dagger \rangle$ [Clo86]. With the above notations, it is readily seen that the CCM can be decomposed into a sum of two terms $\mathbf{C}(\mathbf{J}) = \langle \mathbf{V}_\mathrm{J}\mathbf{V}_\mathrm{J}^\dagger \rangle = \mathbf{C}_{nd} + \mathbf{C}_d$, where $\mathbf{C}_{nd} = \mathbf{V}_{\mathrm{J}_0}\mathbf{V}_{\mathrm{J}_0}^\dagger$ with $\mathbf{V}_{\mathrm{J}_0} \simeq \left[1 + \frac{\Delta z}{2} p_0^{(0)} \quad \frac{\Delta z}{2}\mathbf{p}_0\right]^T$, and where the covariance matrix $\mathbf{C}_d = \left\langle (\mathbf{V}_\mathrm{J} - \mathbf{V}_{\mathrm{J}_0})(\mathbf{V}_\mathrm{J} - \mathbf{V}_{\mathrm{J}_0})^\dagger \right\rangle$ reads

$$\mathbf{C}_d = \left(\frac{\Delta z}{2}\right)^2 \begin{bmatrix} c_0 & \mathbf{c}^\dagger \\ \mathbf{c} & \mathbf{\Sigma} \end{bmatrix}, \tag{2.9}$$

with $c_0 = \langle |\Delta p^{(0)}|^2 \rangle$, $\mathbf{c} = \langle \Delta p^{(0)*} \Delta\mathbf{p} \rangle$ and the 3×3 submatrix $\mathbf{\Sigma} = \langle \Delta\mathbf{p}\Delta\mathbf{p}^\dagger \rangle$.

From such a decomposition, it appears clearly that a deterministic transformation (with $\Delta p^{(0)} = 0$ and $\Delta\mathbf{p} = \mathbf{0}$, hence $\mathbf{C}_d = 0$) results in a CCM of rank one, $\mathbf{C}_{nd}$ being the matrix of a projector. As stated above, a CCM of rank one yields a null Cloude entropy, which is thus Cloude's condition for a polarimetric transformation to be non-depolarizing. Conversely, as soon as $\mathbf{\Sigma}$ is a non-null matrix, the rank of $\mathbf{C}(\mathbf{J})$ is greater than one, hence the corresponding transformation is depolarizing according to Cloude's criterion [Clo86, Clo90]. This decomposition allowed us to conclude that the depolarizing nature of a transformation appears to be completely comprehended by the 3×3 positive semi-definite Hermitian submatrix $\mathcal{C}$, i.e., by 9 independent real parameters consisting of variance/covariance terms of the random anistropic optical properties of the sample considered[16]. Such an observation had been previously reported with the Mueller formalism, using a model of stochastic dMm's for the first time in [Dev13], and then further improved in [Oss14a], but without offering the straighforward derivation obtained with Jones formalism. By identifying our result with these references, we interestingly showed that the nine depolarization terms that enter into the expression of the depolarizing dMm proposed simultaneously and independently in 2011 by Ortega-Quijano *et al.* [OQ11a, OQ11b] and Ossikovski [Oss11] can be directly linked to the second order statistical properties of random anisotropic parameters through the following set of equations

$$2d_{\mu_{q,u,v}} = \left\langle [(\Delta\eta)^2 + (\Delta\kappa)^2]_{u,v,q} + [(\Delta\eta)^2 + (\Delta\kappa)^2]_{v,q,u} \right\rangle, \tag{2.10}$$

$$2d_{\eta_{q,u,v}} = \left\langle \Delta\kappa_{u,v,q}\Delta\kappa_{v,q,u} + \Delta\eta_{u,v,q}\Delta\eta_{v,q,u} \right\rangle, \tag{2.11}$$

$$2d_{\kappa_{q,u,v}} = \left\langle \Delta\kappa_{u,v,q}\Delta\eta_{v,q,u} - \Delta\eta_{u,v,q}\Delta\kappa_{v,q,u} \right\rangle. \tag{2.12}$$

As depolarization properties seem to be comprehensively described by the 3×3 submatrix $\mathbf{\Sigma}$ introduced above, we then proposed in [Fad16] to define *intrinsic* depolarization metrics based on this matrix. Indeed, usual depolarization metrics are defined either on the macroscopic Mueller matrix of the medium (e.g., the standard depolarization index $P = \left\{(\mathrm{tr}[\mathbf{M}^T\mathbf{M}] - \mathbf{M}_{1,1}^2)/3\mathbf{M}_{1,1}^2\right\}^{1/2}$ [Gil86], which can vary between 0 – totally depolarizing – to 1 – non depolarizing), or on its CCM (e.g. the Cloude entropy recalled above). Though often used, such depolarization metrics can nevertheless be unsatisfactory in some situations since two interactions sharing identical fluctuations properties of the optical anisotropy parameters (i.e., same matrix $\mathbf{\Sigma}$) but with distinct principal (deterministic) po-

[16] Moreover, this first-order decomposition evidences the fact that depolarization effects must locally pile up quadratically in Δz, whereas deterministic anisotropy parameter classically evolve linearly with propagation distance. This interesting property of depolarization in samples has been recently verified experimentally on controlled test samples [Aga15], and it may have crucial implications in the analysis of depolarizing media in experimental polarimetry [Web10, Mar03]. However, current developemnts tend to show that such quadratic evolution of depolarization properties is not a general result, and could be different for varying illumination geometries [Cha16].

larization transformation vector $\mathbf{p}_0$ can have different depolarization indices or Cloude entropies in the general case. This is due to the fact that both metrics simultaneously depend on the deterministic polarization transformation and on the fluctuating parameters.

To solve this issue, we proposed to define intrinsic depolarization metrics, which only depend on the fluctuations of the anisotropy parameters of the sample, i.e., only on the submatrix $\mathbf{\Sigma}$. The *intrinsic differential depolarization metric* was first defined as $P_\delta = ||\mathbf{\Sigma}||_F$, where $||\mathbf{X}||_F = \sqrt{\mathrm{tr}[\mathbf{X}^\dagger \mathbf{X}]}$ denotes the Frobenius matrix norm [OQ15b, Fad16]. Such a quantity can vary from 0 – for non-depolarizing interactions – to (potentially) infinity and can be efficient in situations where standard approaches fail to correctly describe the depolarizing nature of a light-matter interaction. This property was emphasized with an illustrative example in Reference [OQ15b]. In addition, one can gain further physical insight into the depolarization properties of such interaction by analyzing other quantities, such as the determinant of $\mathbf{\Sigma}$ which can be interpreted as an intrinsic *depolarization volume*[17] $\mathcal{V}_\delta = \det[\mathbf{\Sigma}]$, or an intrinsic *Cloude entropy* $\mathcal{S}_\delta$ of the submatrix $\mathbf{\Sigma}$ itself where the subscript δ indicates that it is computed under the differential approach. These three differential depolarization metrics share the interesting property that they are defined irrespective of the propagation distance, and are invariant by deterministic unitary transformations, thus justifying their qualification of *intrinsic* metrics. This has the strong physical meaning that the sample or the light-matter interaction studied must keep the same depolarization properties whatever be its deterministic anisotropic properties [Fad16].

The combination of the differential formalism and of a stochastic model of anisotropic optical properties has thus permitted us to gain a fundamental insight on the origin of depolarization as a randomization of light polarization due to statistical fluctuations of the anisotropy parameters, giving access to meaningful intrinsic depolarization metrics. In addition, this work also allowed us to demonstrate a fundamental irreversibility property of depolarizing light-matter interactions, which is a clear counterpart of the invariance property for deterministic transformations briefly recalled in Section 1.1 of Chapter 1. This irreversibility property can be stated as follows:

Property 1 *For any admissible fully or partially polarized input Stokes vector $\mathbf{s}_{in}$, a physically realizable depolarizing non-singular and unit determinant Mueller matrix $\widetilde{\mathbf{M}}$ verifies* $\|\mathbf{s}_{out}\|_{1,3}^2 = \left\|\widetilde{\mathbf{M}}\,\mathbf{s}_{in}\right\|_{1,3}^2 \geq \|\mathbf{s}_{in}\|_{1,3}^2$.

The demonstration of this property in the general case of a standard Mueller matrix had never been reported to our best knowledge, and is provided in a general form in [Fad16] (AA I-3). A similar "local" property holds for a depolarizing dMm $\mathbf{m} = \mathbf{m}_{nd} + \mathbf{m}'_d$ with null trace ($\kappa_i = 0$). This property, which offers insightful physical interpretation, reads

$$\frac{d\,\|\mathbf{s}\|_{1,3}^2}{dz} = \mathbf{s}^T\left[\mathbf{m}'^T_d\,\mathbf{G} + \mathbf{G}\,\mathbf{m}'_d\right]\mathbf{s} \geq 0 \tag{2.13}$$

for any physical Stokes vector $\mathbf{s}$, with equality if and only if the dMm is non depolarizing ($\mathbf{m}'_d = 0$).

Property 1 and its "local" counterpart have a strong physical meaning since they reveal the irreversible effect of a depolarizing transformation on the propagating field. This irreversibility clearly appears through the necessary increase of the Minkowski metric of the Stokes vector defining the field polarization state. Interestingly, this irreversibility property has an informational or thermodynamical counterpart, under the hypothesis of complex Gaussian circular random fluctuations of the field. Indeed, as a consequence of Eq. (1.2), the Shannon entropy of the bidimensional electrical field vector must obey an irreversible evolution with depolarizing transformations, as

$$\frac{dH(\mathbf{s})}{dz} = \frac{2}{\|\mathbf{s}\|_{1,3}}\frac{d\,\|\mathbf{s}\|_{1,3}}{dz} \geq 0. \tag{2.14}$$

Such an irreversible behavior of the Minkowski metric $||\mathbf{s}||_{1,3}$ (or equivalently of the Shannon en-

[17] This quantity is equal to zero as soon as one polarimetric direction has null fluctuations, indicating perfect correlation between at least two polarization "directions"

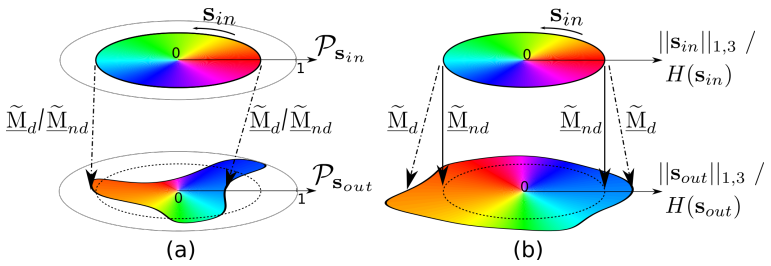

Figure 2.8: Schematic representation of the effect of a non-depolarizing ($\widetilde{M}_{nd}$) or a depolarizing ($\widetilde{M}_d$) transformation on (a) the standard DOP $\mathcal{P}$, and (b) the Minkowski metric $||\mathbf{s}||_{1,3}$ or Shannon entropy $H(\mathbf{s})$, for all possible input Stokes vectors $\mathbf{s}_{in}$ (represented around a chromatic disk for the sake of simplicity). Contrarily to the DOP, $||\mathbf{s}||_{1,3}$ or $H(\mathbf{s})$ are preserved for non-depolarizing (deterministic and reversible) transformations, and must necessarily grow for depolarizing (random and irreversible) transformations.

tropy $H(\mathbf{s})$) confirms that these quantities are best adapted to describe the polarimetric *randomization* (depolarization) of a propagating beam. Indeed, contrarily to the field intensity or the standard DOP $\mathcal{P}$, the quantities $\|\mathbf{s}\|_{1,3}$ and $H(\mathbf{s})$ are preserved through non-singular deterministic (and reversible) transformations as $\frac{dH(\mathbf{s})}{dz} = \frac{d\|\mathbf{s}\|_{1,3}}{dz} = 0$ in that case, but must necessarily grow with irreversible depolarizing transformations. This is schematically illustrated in Fig. 2.8 where it can be seen that, depending on the input Stokes vector $\mathbf{s}_{in}$, a non-depolarizing $\widetilde{\mathbf{M}}_{nd}$ or depolarizing $\widetilde{\mathbf{M}}_d$ polarimetric transformation can lead to an increase or a decrease of $\mathcal{P}$. An illustrative example can be found in [Fad16] (see AA I-3), but will not be detailed here for the sake of concision.

Conclusion

The different contributions briefly described in this chapter illustrate the fact that light depolarization is a complex notion, which cannot be defined rigorously without clearly stating the experimental conditions at hands (spectral bandwith, spatial/temporal bandwidth of the detector, illumination/detection geometry,...). Moreover, it fundamentally involves a randomization process of the SOP on either dimension (spectral, spatial, temporal...), and/or can result from the random aspect of the light/matter interaction considered due to the sample local random anisotropic properties. Treating light depolarization as a whole by encompassing clearly all the effects is still a very interesting challenge, both theoretically to define rigorous descriptions of all these randomization processes, or experimentally to confirm and guide the definition of operational theoretical tools.

Even though presented in a first chapter, the above contributions to the physics of light depolarization have in fact accompanied the development of original polarimetric imaging systems that will be detailed in the next chapter. Gathering experimental results and trying to interpret them has naturally led us to question light depolarization from a theoretical perspective. In turn, the physical insight gained from these fundamental studies has been leveraged to optimize the imaging systems developed, and to better interpret the unconventional polarimetric constrast images obtained with such systems.

Chapter 3

Non conventional approaches for simplified polarimetric imaging

This chapter will draw an overview of the scientific work conducted at the Optics and Photonics department of IPR towards the development of original unconventional simplified polarimetric imaging modalities.

Though very different from each other, the underling principles of the three imaging techniques described below are in agreement with the global approach presented in Chapter 1, which can be in a sense related to the currently famous *co-design* trend in imaging system/processing design. Indeed, in all these studies, we aimed at simplifying the acquisition process by radically departing from usual polarimetric techniques, in order to gain acquisition ease, speed, cost-effectiveness, etc. but also better image interpretation and easier calibration. Such simplifications were operated of course to the expense of a limited partial information on the full polarimetric response of the samples (i.e., their Mueller matrix), but as mentioned in Chapter 1, a direct access to a clearer polarimetric contrast image might sometimes be preferable for some applications.

Originally and remarkably, it can also be mentioned here that the three techniques presented below are very unconventional in the sense that they do not require any polarization analysis component at the detection. Indeed, the polarimetric sensitivity of these "polarizer-free" polarization sensing modalities is obtained by three different ways:

- The first technique was invented and patented in our laboratory in 2011 [Alo11], and relies on a very specific dual-frequency dual-polarization light illumination of the sample. As will be described below, the polarimetric information is based on the analysis of the spectral components of the light intensity signal detected on a fast photodetector. The technique is clearly inspired from microwave photonics approaches, microwave photonics being a reputed area of expertise of the Optics and Photonics Department. An important effort has been devoted to the study and development of this technique, which was supported by an ANR/DGA project that I managed, and which permitted to welcome Noé Ortega-Quijano for a two-year postdoctoral stay in our laboratory. In addition, a PhD student, François Parnet, is currently involved since more that two years on this research activity. His PhD, which I contribute to supervise, is funded by the DGA and the Région Bretagne.

- The second technique has been recently proposed through a collaboration with CEA Saclay, and consists of an original and new way of matching polarimetric imaging with the currently active domain of compressive sensing. Indeed, using a polarimetric "*defect*" of micromirrors MOEMS devices, we showed that an OSC image could be retrieved through a simultaneous signal acquisition on two single-pixel detectors.

- As for the last technique, the polarimetric sensitivity is gained by a statistical analysis of a speckle pattern intensity distribution under coherent polarized illumination. As will be seen

below, this technique, characterized during my PhD thesis at Institut Fresnel and validated experimentally at the IPR, provides the ultimate stage of simplification for a polarimetric imaging system while providing relevant polarimetric contrast[18].

3.1 Depolarization/Dichroism Sensing by Orthogonality Breaking

3.1.1 Principle

The concept of Depolarization/Dichroism Sensing by Orthogonality Breaking (DSOB) is based on the preparation of a specific probe light beam, which is used to enlighten the target (or sample) to characterize. This probe beam contains two light waves with respective optical frequencies ν_1 and ν_2 which are slightly detuned by a quantity $\Delta\nu = \nu_1 - \nu_2$. These two waves can have any deterministic states of polarization $\mathbf{e}_1$ and $\mathbf{e}_2$ (Jones vectors of fully polarized fields), but these two states have to be orthogonal to each other in a mathematical sense ($\mathbf{e}_1 \perp \mathbf{e}_2$). Such light field, that will be termed in the following as *dual-frequency dual polarization* (DFDP), can be written in the general form

$$\mathbf{E}_{in}(\mathbf{r},t) = \frac{E_0}{\sqrt{2}}\, e^{-j(2\pi\nu t - \mathbf{k}\cdot\mathbf{r})}\left[\mathbf{e}_1 + e^{-j2\pi\Delta\nu t}\mathbf{e}_2\right], \tag{3.1}$$

where $E_0/\sqrt{2}$ is the (equalized[19]) amplitude of the two polarization states emitted. The intensity of this field $I(\mathbf{r},t) = |\mathbf{E}_{in}(\mathbf{r},t)|^2 = |E_0|^2$ is constant in time since the two frequencies components of the light field oscillate along two orthogonal polarization states, and therefore, no interference beatnote can occur.

The underlying philosophy of the DSOB polarimetric sensing approach is the following: with such very specific probe beam used to illuminate a sample and made to interact with it (either in transmission or in reflection), a polarimetric information should be in principle retrieved by a simple analysis of the intensity of the light transmitted or backscattered by the sample and detected on a fast photodetector with bandwidth above the detuning frequency $\Delta\nu$ [Fad12a] (see AA I-4, p. 124). Let us illustrate the principle of the DSOB approach with Fig. 3.1: when the above beam E_{in} is made to interact with a sample that can be described with a deterministic unitary Jones matrix[20] $\mathbf{J_u}$, the intensity of the output field is given by $I_{out}(t) = \rho\,|E_0|^2$, which is still constant in time, since orthogonality (in the mathematical sense) between the two output field states $\mathbf{J_u}\mathbf{e}_1$ and $\mathbf{J_u}\mathbf{e}_2$ is maintained with unitary transformations[21] in spite of the polarization transformation undergone, as illustrated in Fig. 3.1.a. This situation occurs with birefringent samples or samples showing optical activity. Now, when the sample is dichroic (i.e., in the presence of absorption anisotropy), or depolarizing (only under very particular detection conditions, see below), the mathematical orthogonality is broken when light interacts with the sample, which is illutrated in Fig. 3.1.b. As soon as orthogonality breaking occurs, the light intensity is affected by an oscillating interference term (intensity beatnote at frequency $\Delta\nu$). As a result, the dichroic (or in some conditions the depolarizing) nature of the target can be easily and directly detected on the output beam intensity itself, without requiring any polarization analysis component at the detection level.

It can be noted at this level that the DSOB approach is in essence insensitive to birefringence and polarization rotation, thus enabling in principle remote sensing through optical fibers. In addition, the technique does not require any component to be inserted at the distal fiber end, and it may thus be directly adapted to commercial endoscopes in which stress or torsion-induced birefringences are

[18] To the expense of course of spatial resolution and estimation precision.

[19] Contrarily to the generation of coherent light beam with controllable DOP presented in Chapter 2, where the intensity imbalance between the two polarization states makes it possible to control the DOP of the light, it was shown that a perfectly balanced DFDP beam is optimal for the application of the DSOB imaging techniques.

[20] or proportional to a unitary Jones matrix, up to an isotropic absorption factor ρ.

[21] This affirmation is valid provided no significant dispersion of the birefringence appears between frequencies ν_1 and ν_2, which is very unlikely to occur in practice since $\Delta\nu$ will not exceed tens of gigahertz for the beatnote to be detectable on a photodetector

usually highly detrimental to usual polarimetric measurements. Moreover, this technique offers a direct characterization of some polarimetric properties of a sample with high sensitivity and rapidity ($< 1\ \mu$s/pixel is feasible with high frequency detuning and optimized demodulation electronics). As will be shown below, such capacity is exploited towards the development of real-time long-range polarimetric imaging systems with high sensitivity and rapidity.

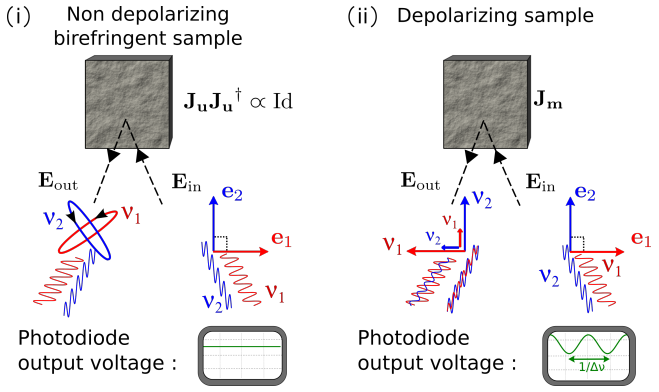

Figure 3.1: General principle of depolarization/dichroism sensing by orthogonality breaking (DSOB).

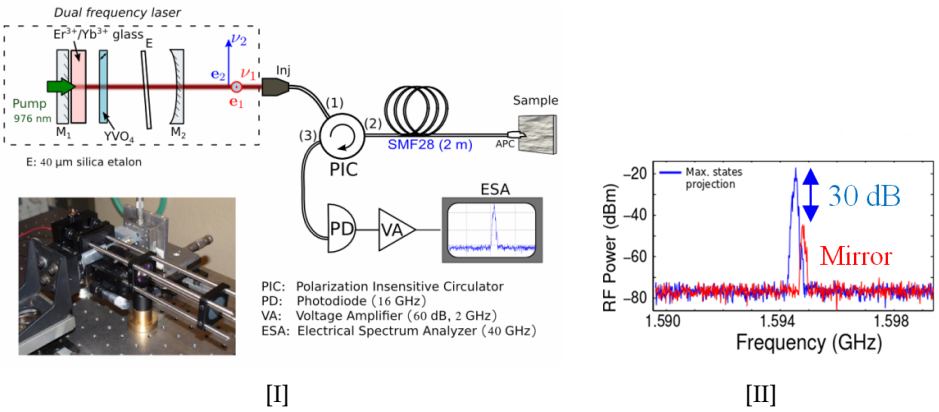

Figure 3.2: [I] Schematic representation of the first DSOB setup. Dashed box and photograph: Er,Yr;Glass dual-frequency laser. [II] Measurement of the RF contrast obtained on a fibred mirror and a perfect dichroic element (NIR polarizer).

The first experimental implementation of the DSOB technique was performed using a diode-pumped (Er,Yb)-doped glass 4-cm-long external cavity laser emitting at 1550 nm, and specially adjusted to emit a DFDP laser beam as described in Eq. (3.1) [Fad12a]. Indeed, a 500-μm-thick YVO_4 crystal, cut at 45° of its optical axis, was inserted into the laser cavity in order to favor dual-frequency operation of the laser by inducing a slight spatial walk-off between the two eigen polarization modes in the gain medium [Bru97, Bai09][22]. In this configuration sketched in Fig. 3.2-[I], the output field is generated along two linear polarization eigenstates defined by the eigen axes of the YVO_4 crystal, each of it oscillating at a given frequency, the frequency difference $\Delta\nu$ being proportional to the cavity

[22]Dual-frequency lasers is a reknowned research activity of the Optics and Photonics Department, finding various applications in Lidar-Radar, microwave photonics and metrology. Contarily to these applications where a polarizer is used at the laser output to readily create a RF modulation an optical carrier, the DSOB approach requires absorption/reflection anisotropies to be minimized in the path of light towards and from the sample. For instance, this prevented us from using an optical isolator at the output of the cavity, hence hindering the stability of the laser.

free-spectral-range and to the intracavity phase anisotropy between the two eigenstates [Bru97]. By slightly tilting an intracavity 40-μm silica etalon used to ensure single-longitudinal mode oscillation, it was possible to set this frequency difference to a value compatible with the detection setup, namely within the radio-frequency (RF) range, i.e., $\Delta\nu < 2$ GHz. In this configuration, the laser provided an output power of 1.8 mW equally distributed on two orthogonal states of polarization (horizontal and vertical), with a pump power of approximately 130 mW [Fad12a].

Using this homemade laser, which provides a direct and elegant solution to output the desired DFDP beam, we tested the DSOB approach in a fibred configuration which is represented in Fig. 3.2-[I]. For that purpose, the dual-frequency probe beam was injected and guided into a 2 m-long single-mode optical fiber (SMF28) before illuminating a target. The backscattered light was back propagated into the same fiber, and analyzed through a polarization-insensitive circulator (PIC) and directed on a high-band pass (16 GHz) photodiode (PD). A high-gain voltage amplifier and an electrical spectrum analyzer (ESA) were finally used to analyze the detected signal. We estimated the available dynamics of such polarimetric measurement by comparing the residual beatnote power when light was reflected on a perfect Faraday mirror[23] to the maximum beat note power obtained when the two eigen polarization states are maximally projected on a perfect infrared polarizer oriented at a 45° angle with respect to the illumination polarization directions. A contrast of about 30 dB was measured from the corresponding electrical spectra analyzed around frequency $\Delta\nu$ on the ESA, as illustrated in Fig. 3.2-[II]. Additional measurements showed that orthogonality was fairly well maintained during propagation in a single-mode fiber over tens of kilometers, which was encouraging for endoscopic operation [Fad12a].

During this first experimental work, we also tried the DSOB technique on several samples that were assumed to be purely depolarizing in order to validate its capacity to measure depolarization. These results can be found in [Fad12a] (AA I-4), where the orthogonality breaking contrast measured through a single-mode fiber as described above seemed to be in agreement with control values of the DOP of the light backscattered by the samples under polarized illumination. These results thus seemed to validate the capacity of the DSOB approach to gauge depolarization in a direct way.

However, a thorough theoretical modeling and understanding of the physical origins of the orthogonality breaking signatures was still necessary at this time. Within the course of an ANR/DGA collaborative project "Radio-Libre" which I managed and conducted in collaboration with M. Roche from Institut Fresnel (PHYTI team), such a theoretical investigation was rigorously performed using the *instantaneous* Stokes/Mueller formalism presented in Chapter 2. This theoretical work allowed us to confirm that orthogonality breaking is produced by the sample diattenuation, and that it is immune to birefringence [OQ15a] (see AA I-5, p. 129). As for depolarization however, the predictions were in contradiction with the conclusions of our first experimental work described above. Indeed, according to the theory, the DSOB technique should be totally insensitive to pure diagonal depolarization[24].

Yet, more fundamental studies on light depolarization were conducted in the laboratory in parallel with the study of the DSOB technique, which allowed us to finally lift the apparent contradiction between experiments and theory, and to better interpret our initial measurements in [Fad12a]. Indeed, according to the discussions presented in Section 2.3 of Chapter 2, a difference in experimental conditions can have strong consequences on the notion and on the measured values of depolarization. On the one hand, the reference Stokes polarimetry measurements were carried out in free-space in [Fad12a], with a relatively high spot size on the sample and high numerical aperture for the light collection. Such an experimental configuration effectively implied a spatial averaging operation over the sample surface and over several spatial coherence areas (speckle grains). On the other hand, the OB signals detected on the same samples were collected through a standard single-mode SMF28 optical fiber whose FC-APC connector end was placed in vicinity of the samples. Under such con-

[23] This residual beatnote was caused by imperfect orthogonality between the polarization states emitted, due to fiber coupling, circulator component, etc.

[24] i.e., unable to produce any beatnote signal on samples exhibiting a diagonal Mueller matrix.

ditions, the spatial or angular averaging was very moderate. This presumably corresponded to an intermediate position in the transition from a non-depolarizing sample to a depolarizing one, which was conveniently modeled using the stochastic model of depolarizing Mueller matrix from random optical anisotropies presented in the previous chapter and in [OQ15a]. Therefore, in light of the modelization proposed in [OQ15a], we finally concluded that the orthogonality breking signatures measured in [Fad12a] were most likely due to a moderate spatial averaging of the local diattenuation properties of the samples rather than due to pure depolarization.

3.1.2 Dichroism imaging for microscopy and active infrared imaging

The theoretical investigation of the physical origins of orthogonality has also permitted us to identify optimal polarization states to fully characterize the anisotropy parameters (magnitude and orientation angle) of a linear dichroic sample in a single measurement. This feature encouraged us to transpose the initial pointwise measurement to imaging, by implementing the DSOB technique on a confocal microscope for biological microscopy first, and then by developing an near infrared (NIR) active imaging demonstrator for defence applications in the context of the ANR/DGA project. Let us indeed consider a DFDP beam emitting orthogonal right $\mathbf{e}_R$ and left $\mathbf{e}_L$ circular polarization states. In that case, using Jones calculus, it is straightforward to show that when such beam interacts with a sample showing linear dichroism of magnitude d, with anisotropy axis orientation ϕ, the output intensity $\mathrm{I}_{out}(t)$ measured by a fast photodetector is the sum of a DC term and a radiofrequency (RF) term oscillating at the beatnote frequency $\Delta\nu$ between the two modes. These intensity components respectively read

$$\mathrm{I}^{0}_{out} = \rho\,\mathrm{I}_0, \tag{3.2}$$

$$\mathrm{I}^{\Delta\nu}_{out}(t) = \rho\,d\,\mathrm{I}_0\cos(2\pi\Delta\nu t + 2\phi + p\pi), \tag{3.3}$$

with p=0 for transmission measurements, and p=1 in reflexion/backscattering configuration. The above epxressions show that the measurement of the DC and the RF beatnote components of the output intensity directly gives access indeed to all the sample parameters[25]. A so-called orthogonality breaking contrast (OBC) parameter was defined to directly provide a measure of the sample diattenuation through

$$\mathrm{OBC} = \frac{|\mathrm{I}^{\Delta\nu}_{out}(t)|}{\mathrm{I}^{0}_{out}(t)} = d, \tag{3.4}$$

and the anisotropy orientation ϕ is directly given by the beatnote signal phase, up to a π factor, since $\mathrm{Arg}\big[\mathrm{I}^{\Delta\nu}_{out}(t)\big] = 2\phi + p\pi$. It is a remarkable property that the different parameters of interest that characterize the sample anisotropy are obtained in an uncoupled and straightforward way, which considerably simplifies the determination and analysis of the acquired data.

The imaging setup that was developped to validate this approach is shown in Figs. 3.3-[I] and 3.3-[II]. To ensure stable operation in the visible range, we had to replace the former homemade dual-frequency laser that was operating in the NIR range. For that purpose, since no dual frequency laser was available in the laboratory at the required wavelength, we developped an optical setup allowing to produce intense stable DFDP laser illumination. This setup depicted in Fig. 3.3-[I] comprises a 40 mW commercial monomode source emitting at 488 nm, which is injected into a polarization splitting/combining Mach-Zehnder architecture, where one of the two arms comprises an acousto-optical modulator (AOM) which shifts the beam frequency by a fixed frequency shift of $\Delta\nu$ = 80 MHz. The two orthogonal linearly-polarized modes obtained at the output after recombination are spatially filtered using a pinhole – or a section of single-mode polarization maintaining (PM) fiber. A quarter wave plate (QWP) oriented at 45 degrees with respect to the linear polarization directions turns them into two orthogonal right and left circular SOP's. A portion of the output signal is detected through a polarizer on a fast silicon photodiode at the exit of the Mach-Zehnder architecture to produce a

[25]Obviously, the isotropic absorption ρ can be directly obtained from the DC intensity, as in conventional non-polarimetric techniques.

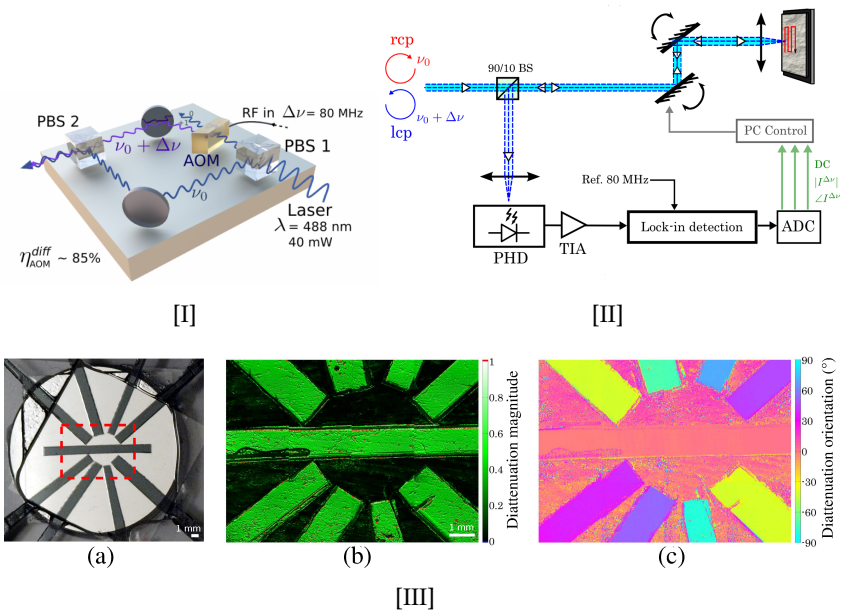

Figure 3.3: [I] Dual-frequency dual-polarization (DFDP) source based on a Mach-Zehnder architecture used for orthogonality breaking imaging at $\lambda = 488$ nm. [II] Sketch of the laser scanning imaging setup in reflection configuration. [III] Synthetic dichroic sample (made of polaroid sheets on a mirror) used for validation (intensity image). DSOB measurements results: linear diattenuation magnitude (b) and orientation (c) of the measured sample. Each image is 10×7.5 mm.

reference signal used for demodulation. The produced DFDP beam is then sent into the confocal microscope and imaging is performed by laser beam scanning using galvanometric mirrors, which enable to acquire a 256×256 pixels image of a 2.5 mm side sample in about 4 s (see Fig. 3.3-[II]). The DFDP beam is focused on the sample with an objective lens and the reflected light is collected by a beamsplitter on a high-speed PIN photodiode, whose output is connected to a lock-in amplifier to retrieve amplitude and phase of the beatnote signal. Further details about the imaging system can be found in [OQ15a, Sch14].

The very first images were obtained on a controlled dichroic sample made of several polaroid rectangular cuts radially placed around a central one [OQ15a]. Each polaroid piece was cut along its dichroic axis and glued on a microscope slide placed on the surface of a mirror. The measured diattenuation magnitude, obtained from the measurement of the DC component and 80 MHz beatnote as described above, is shown in Fig. 3.3-[III].b. The most relevant characteristic is that the contrast is homogeneous all over the image, diattenuation being actually close to 1 for each polaroid fragment whatever its orientation, and almost 0 elsewhere, as expected.[26] The linear dichroism angle is presented in Fig. 3.3-[III](c). It can be observed that the measured parameter enables to succesfully discriminate the orientation of each dichroic segment. The value in each of them is almost constant, the uniformity of the results being indeed greater than that observed in the diattenuation magnitude image. This behaviour is a consequence of the fact that phase is usually less prone to be affected by noise and other fluctuations than amplitude[27]. This setup is currently being deployed on a cell biology platform (mRic-BIOSIT) of the University of Rennes 1 in order to evaluate the interest of such

[26] This is a strong asset of the proposed method when compared to standard simplified polarimetric approaches such as OSC imaging, which contrast values depends on the orientation of the dichroism in that case.

[27] Another interesting feature of this approach is that the calculated parameters are not affected by variations in the sample illumination, being either a ratio, or a phase value. In this example, the background of the DC intensity image (not included here) indeed showed strong inhomogeneity in the sample illumination and a mosaicing pattern which is not visible in the polarimetric images [OQ15a].

unconventional polarimetric approach for biological samples. One of the potential interest of this technique could be to provide marker-free structural or functional imaging of cell constituents, such as actin network.

In the context of active imaging for defense applications and within the course of the "Radio-Libre" project, we have also recently developed an infrared active polarimetric imaging demonstrator based on the orthogonality breaking technique to investigate its potential for long range target detection and decamouflage [Par17]. We showed that a DFDP source using acousto-optic frequency shift could be easily built up using commercially available fibred components from the telecommunication domain around 1.5 μm (a spectral range of great interest of defence application, since it allows furtivity and eye-safe operation). The source developped is very similar to the one depicted in Fig. 2.4 in Chapter 2, and we refer the reader to it or to [Par17] for further details about the source optimization. We designed an original laser scanning imaging system prototype depicted in Figs. 3.4-[I] and 3.4-[II]. The signal is detected on an avalanche photodiode in a confocal configuration, and then demodulated using a dedicated synchronous quadrature demodulation electronics allowing images of the amplitude and phase of the beatnote to be built-up within limited acquisition time (< 1 s). An example of experimental result at 1.5 μm is given in Fig. 3.4-[III], which confirms the ability of this "circular" DSOB approach to fully characterize the diattenuation properties of a scene/sample in a single acquisition.

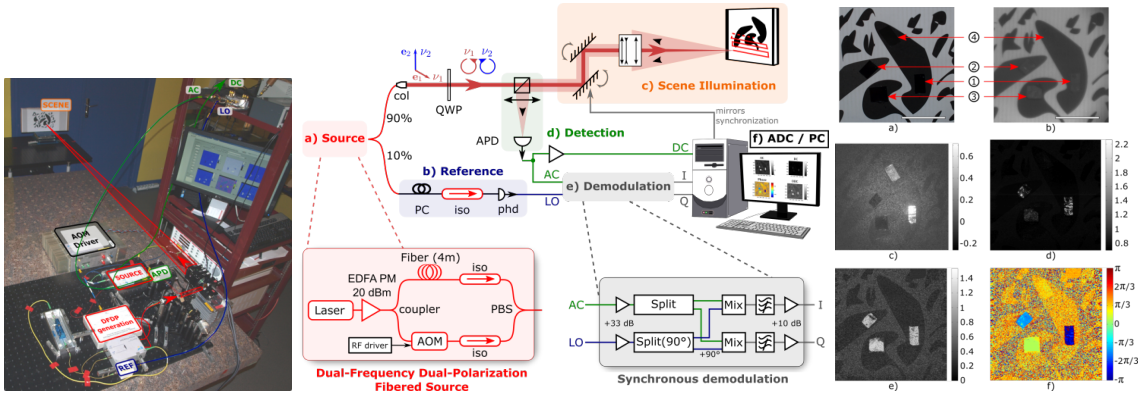

Figure 3.4: [I] Photograph and [II] schematic of the active infrared imaging demonstrator based on the DSOB technique. [III] Visible (a) and NIR (b) intensity pictures of the sample made of three IR polarizers on dark patterns printed on a white sheet. NIR OSC image is acquired for reference (c). Acquisitions with the demonstrator of the DC image (c), OBC contrast (d) and phase (e) maps.

3.1.3 Towards polarimetric endoscopy ? – DSOB sensing through few-mode fibers

Due to its insensitivity to birefringence (a property which is not commonplace among existing polarimetric imaging techniques), and its simple operation through single-mode fibers [Fad12a], the DSOB approach was expected since its invention in 2011 to be a good candidate for enabling polarimetric endoscopic imaging. However, among commercially available endoscopes used for medical diagnosis, an important subset of them guide the light through slightly multimode fiber bundles or multicore fibers.[28] Hence, it was necessary to investigate the feasibility of polarimetric orthogonality breaking sensing through few-mode optical fibers, a question which was not obviously solvable beforehand.

[28] In these cases, the image can be formed either by laser beam scanning of the multiple fibers/cores at the endoscope proximal end, or using a scanning optomechanical stage at the distal end of the bundle.

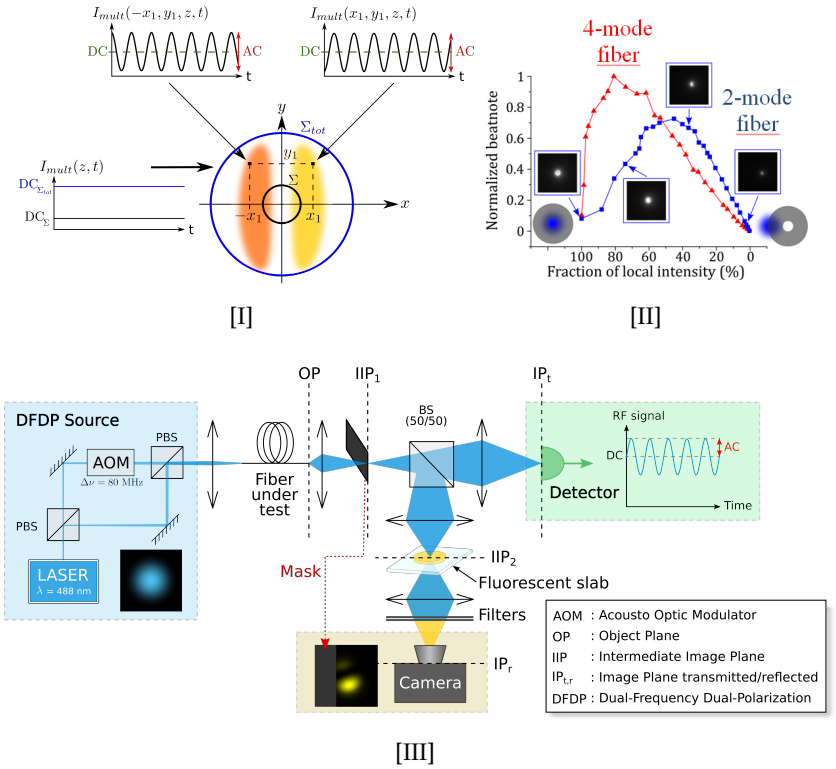

Figure 3.5: [I] Illustration of local polarimetric orthogonality breaking and global orthogonality preservation in a two-mode configuration with fundamental mode LP01 (not repre- sented) and mode LP11. [II] Evolution of the beatnote amplitude versus the fraction of cropped intensity after optimization of the injection in the fiber (squares) and for the non optimized injection (triangles). [III] Experimental scheme used to study the propagation of a DFDP beam in an optical fiber multimode at 488 nm.

Indeed, injecting a DFDP beam into a multimode fiber results in the distribution of the incident orthogonal pair of polarizations onto n guided modes. The birefringence modal dispersion of the fiber changes the SOP of each mode independently. As a result, the superimposition of the n modes at the exit of the multimode fiber generates locally a beatnote in the detector plane (transverse plane), hence indicating local breaking of the polarimetric orthogonality which *a priori* should forbid any DSOB measurement. Nevertheless, we demonstrated that the orthogonality can be recovered, and the intensity delivered by a detector can be kept constant provided the entire beam is integrated on the detector active area [Par16]. Indeed, due to the spatial modal orthogonality of the guided modes in the fiber, adding intensity contributions in a coherent manner over the entire beam leads to the perfect compensation of the locally produced beatnotes.[29] This property is illustrated in Fig. 3.5-[I] where we considered a simple example of a two-mode beam in the detector plane. At each location of the transvers plane, the intensity is modulated by the overlap of the two modes, yielding local breaking of the polarimetric orthogonality. However, in that simple two-mode case, the symmetrical distribution of the non-fundamental mode leads to modulations in antiphase with respect to the Y axis as illustrated on the figure, and total integration over the beam does cancel out these local beatnote contributions.

We experimentally checked this result using the experimental setup depicted in Fig. 3.5-[II]. For that purpose, a DFDP beam (at λ=488 nm) was injected into the fiber under test. The output of the

[29]Note that if the beam is partially integrated over the detector surface, the orthogonality can still be kept provided a symmetric detection geometry of the beam is ensured.

fiber was imaged simultaneously on a fast photodiode and a camera. A mask was placed in a first conjugated plane to simulate an imperfect detection of the beam. As a convenient way to obtain an interference/speckle-free image of the multimode beam repartition at the fiber output, we used a fluorescent slab so as to break the coherency of the beam, which fluorescent image was finally imaged on the camera through appropriate dichroic filters. Two-mode and four-mode fibers were tested and the experiments confirmed that a significant beatnote was detected when the beam was partially cropped, as illustrated in Fig. 3.5-[II]. Nevertheless, the complete symmetric integration of the beam on the detector yielded a low residual beatnote, as expected. As a consequence, the detection geometry is crucial to avoid bias in the beatnote measurements when propagating a DFDP beam in few-mode fibers. We also studied the limits of the DSOB technique when a few-mode fiber is used to probe a sample in reflection. The experimental results obtained showed that measurements through few-mode fibers were limited to a smaller angular excursion when compared to single-mode operation. In addition, we also identified a decrease of the measurement dynamics with the number of guided modes [Par16]. Despite these operational constraints when used through few-mode fibers, the DSOB technique still appears as a potential solution to polarimetric endoscopy, for instance to enhance contrast between diseased and healthy tissues or organs that are not accessible in free-space with conventional polarimetric imaging systems. A perspective for future work will of course consist of adapting the DSOB sensing to a multimode endoscopic imaging system using galvanometric scan system, and investigate the interest of DSOB for endoscopic biomedical imaging.

3.2 Two pixel polarimetric contrast imaging by compressive sensing

In this section, we briefly present an original *compressive imaging* architecture offering a way to perform OSC imaging with only two single-pixel detectors, and based on an algorithmic image reconstruction step following the recently introduced principle of compressive sensing, which is recalled below.

3.2.1 Context

Compressive sensing (CS) is a very recent field of research in signal/image processing which has gained enormous popularity during the last decade due to its appealing theoretical results, but most of all due to innumerable potential applications. The CS theory basically states that a signal $\mathbf{x}$ written as a row vector of dimension N can be in principle recovered mathematically or algorithmically through a reconstruction procedure from a limited number of $M \ll N$ measurements[30] with reasonable quality, provided the two following conditions are fulfilled [Can06, Don06]:

- *Sparsity condition:* the signal $\mathbf{x}$ must be *sparse* in a given representation, i.e., there should exist a signal basis transformation $\mathbf{\Psi}$ (Fourier transform, wavelets,...) such that $\mathbf{x} = \mathbf{s}\mathbf{\Psi}$, with the vector of expansion coefficients $\mathbf{s}$ having exactly K non-null terms (K-sparsity) or K dominant terms (approximate K-sparsity). This condition is most of the time largely fulfilled in the context of image processing, as evidenced by the huge compressibility obtained with wavelet-based compression techniques (e.g., JPEG2000 standard);

- *"Incoherent" measurements:* information about $\mathbf{x}$ must be acquired in an "incoherent" manner with respect to the sparse basis representation. Classically, usual (pixel-wise) measurements on $\mathbf{x}$ are thus replaced by linear projections of $\mathbf{x}$ through a sensing operator $\mathbf{\Phi}$ verifying[31] $\max_{i,j} |\langle \Phi_i, \Psi_j \rangle| \leq 1$. It was notably shown that using pseudo-random projections could lead in general to fairly incoherent measurements, particularly in the context of image processing.

[30] hence, the term *compressive*.

[31] An example in image processing of optimally incoherent signal representation/sensing bases is the pixel basis (Dirac) (well adapted to represent an image with punctual objects) and the Fourier basis that will represent the best sensing basis in the CS framework.

With these two ingredients, it remains to reconstruct the initial signal $\mathbf{x}$ from the limited number of measurements, which is now classically performed using non linear iterative procedures that enforce the sparsity, in a given basis Ψ, of the reconstructed signal $\widehat{\mathbf{x}}$, by minimizing the ℓ_1 norm[32] of the expansion coefficients vector $\mathbf{s}$. During the last decade also, intense work was indeed carried out on a class of iterative algorithms dedicated to solving non differentiable convex optimization problems (so-called *proximal* algorithms). It has enabled fast (accelerated) optimized iterative algorithms to be developed, such as the celebrated FISTA algorithm [Bec09], which was used in this work.

Few months after the initial results and predictions of the CS theory were issued [Can06, Don06], CS-derived original imaging concepts had already been proposed such as the single-pixel camera (SPC), which has attracted much attention these past years [Bar08, Cha08]. With this latter approach, the imaging process relies on the spatial sampling of the image of interest with a Digital Micromirror Device (DMD), and on numerical reconstruction of the image from intensity measurements on a single photodetector for different sampling patterns on the DMD, allowing a compressed version of the image to be recovered from the photocurrent signal acquired. More recently, the concept of SPC has been applied to a number of domains including, among others, multi/hyperspectral imaging [Wag08, Ram10, Stu12, Aug13], THz imaging [Cha08], or random media-assisted CS [Liu14]. However, despite the swarming interest in CS, only few attempts were reported so far to perform polarimetric CS imaging [Ram10, Dur12, Sol13, Wel15, Fu15]. The imaging setups proposed in these references are all directly based on the SPC concept, where polarimetric sensitivity was simplistically gained by detecting the optical signals through appropriate polarization analyzing devices during sequential acquisitions. Moreover, they solved as many CS reconstruction problems as polarimetric channels were considered (2 or 4) thereby inducing a two-fold (respectively four-fold) increase in the measurement/reconstruction time, while at the same time suffering from the loss in intensity due to the use of a polarization analyzer.

3.2.2 2-pixel CS polarimetric sensing

In collaboration with J. Bobin (CEA Saclay, Palaiseau, France), we recently proposed to revisit the problem of 2-channel polarimetric CS by proposing an original polarimetric imaging architecture using two single-pixel detectors [Fad17] (see AA I-7, p. 146). The proposed setup is still inspired from the initial concept of SPC, but does not require any polarization analyzing element as it relies on imperfections of the DMD itself, more precisely, on the variation of the Fresnel's reflection coefficients with incidence angle, and polarization direction of light. Contrarily to previous attempts in polarimetric CS, the polarimetric information is obtained through a single temporal data acquisition on the two photodetectors, and the polarimetric channels are recovered simultaneously from a single reconstruction step. It also offers in principle the best detectivity tradeoff, as all the light directed towards the DMD is involved in the imaging process without passing through any polarization analysis component. As we will show below through simulations, this approach is in principle able to provide a compressive sensing of the total intensity image, denoted $\mathbf{x}_T$ in the remainder of this section, and of the OSC map, that will be rewritten with a specific notation throughout this section as

$$OSC = \frac{\mathbf{x}_S - \mathbf{x}_P}{\mathbf{x}_S + \mathbf{x}_P}, \tag{3.5}$$

where we have replaced subscript $\parallel$ (resp. $\perp$) by S (resp. P) with respect to the initial definition in Eq. (1.6).

The proposed setup is described in Fig. 3.6-[I]. An object enlightened by a fully (horizontally) polarized light is imaged onto the surface of a DMD, which spatially samples it by applying a controlled

[32]Minimizing the ℓ_1 norm $\|\mathbf{s}\|_1 = \sum_{i=1}^{N} |s_i|$ of $\mathbf{s}$ is in fact an approximation that allows the optimization problem to be convex (and thus algorithmically tractable). The ℓ_1 norm is in that case used as an approximation of the ℓ_0 norm of $\mathbf{s}$ (i.e., the number of non-null coefficients in $\mathbf{s}$) that would of course naturally enforce sparsity, but that leads to non-convex minimization problems.

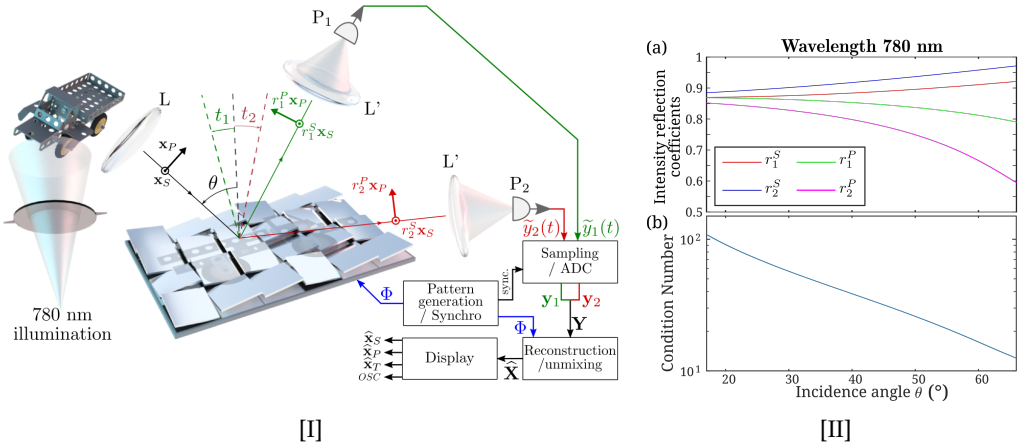

Figure 3.6: [I] CS polarimetric imaging setup proposed. It is inspired from the concept of SPC where the image is first spatially sampled by a DMD which reflects light in two directions, and where the total photon flux is detected on a single photodetector in each direction. [II] Evolution of (a) the reflection coefficients in intensity, and (b) of the condition number of mixing matrix $\mathbf{A}$ for two tilt directions and two polarimetric components S and P, as a function of incidence angle θ on the DMD surface at wavelength 780 nm.

binary pattern on the micromirrors. The light reflected in direction 1 is integrated and detected on a first photodetector (P_1), whereas photodetector P_2 detects the light reflected in the second direction of the tilted mirrors (instead of being discarded as in the original SPC scheme), thereby producing two temporal signals $\mathbf{y}_1$ and $\mathbf{y}_2$. After a few simplifications (see [Fad17]), one can show that these signals can be written as

$$\mathbf{Y} = \begin{bmatrix} \mathbf{y}_1 \\ \mathbf{y}_2 \end{bmatrix} = \mathbf{A}\mathbf{X}\mathbf{\Phi} + \mathbf{b} = \mathbf{Y}^{\circ}\mathbf{\Phi} + \mathbf{b}, \tag{3.6}$$

where the $M \times N$ sampling matrix $\mathbf{\Phi}$ contains the M binary patterns applied on the DMD. The matrix $\mathbf{X}$ contains the two polarimetric components of the image to recover, with $\mathbf{X}^T = [\mathbf{x}_S^T \; \mathbf{x}_T^T]^T$, and where $\mathbf{x}_S$ (resp. $\mathbf{x}_P$) represents the polarization component parallel (resp. perpendicular) to the incident illumination. In the above equation, $\mathbf{b}$ accounts for a noise contribution that we assume additive Gaussian, while the mixing matrix $\mathbf{A}$ depends on the Fresnel's reflection coefficients (in intensity) of the two polarimetric components, for the two incidence angles considered:

$$\mathbf{A} = \frac{1}{2}\begin{bmatrix} r_1^S & r_1^P \\ -r_2^S & -r_2^P \end{bmatrix}. \tag{3.7}$$

This parameterization indeed shows that the polarimetric sensitivity only relies in this setup on the diversity of the reflection coefficients[33] which slightly depend on the incidence angle and polarization direction, as illustrated in Fig. 3.6-[II] [Fad17].

Assuming that the polarimetric components are sparse in the same basis $\{\Psi_i\}$, i.e., $\mathbf{x}_{S,P} = \mathbf{s}_{S,P}\,\mathbf{\Psi}$, it is easily seen that Eq. (3.6) can be treated as a CS reconstruction problem consisting of recovering a mixture $\mathbf{Y}^{\circ} = \mathbf{A}\mathbf{X}$ of the polarimetric components of the image. As a result, it should be in principle possible to recover the data $\mathbf{X}$ containing $2N$ pixels (N pixels per component) from a limited number $2M$ ($M \ll N$) of measures. Contrarily to most CS inverse problems that have been considered so far, we are facing an additional difficulty in this particular situation, as the signals to recover are strongly mixed in the measurement process via the mixing matrix $\mathbf{A}$. Indeed, as illustrated in Fig. 3.6-[II], the reflection coefficients of metals are usually quite similar for polarization directions S and P, causing

[33] hence, justifying the notation S and P for the polarimetric components in this study.

a strong crosstalk between the two components of interest. As a consequence, the signals detected at photodetectors P_1 and P_2 are almost perfectly anticorrelated, the polarimetric information lying in the tiny discrepancies between these two signals. This is illustrated in Fig. 3.7.a (lower inset), where simulated intensity signals are plotted.

3.2.3 Reconstruction algorithms and numerical results

We proposed and implemented several approaches to tackle this unmixing/CS reconstruction problem, either by considering the two problems independently, or by solving them simultaneously in the recovery process [Fad17]. A first simple two-step approach consisted of first solving the CS problem to recover the mixture $\mathbf{Y}^\circ$, using an accelerated forward-backward algorithm (namely a reweighted FISTA algorithm). Under this form, the CS reconstruction problem can be written very classically as

$$\widehat{\mathbf{Y}^\circ} = \text{Argmin}_{\mathbf{Y}^\circ} \quad \left\|\mathbf{\Lambda} \odot \left(\mathbf{Y}^\circ \mathbf{\Psi}^T\right)\right\|_{\ell_1} + \frac{1}{2}\left\|\mathbf{Y} - \mathbf{Y}^\circ \mathbf{\Phi}\right\|_F^2. \tag{3.8}$$

Basically, such iterative algorithm will aim at optimizing fidelity between the measured signal $\mathbf{Y}$ and the reconstructed signal $\mathbf{Y}^\circ\mathbf{\Phi}$ (by minimizing the square Frobenius norm of their difference, with $\|\mathbf{X}\|_F^2 = \text{Trace}(\mathbf{X}\mathbf{X}^T)$), while enforcing the sparsity of the reconstructed mixture by minimizing the ℓ_1 norm above of its wavelet expansion coefficients vector $\mathbf{Y}^\circ\mathbf{\Psi}^T$. In the above equation, the $2 \times N$ matrix $\mathbf{\Lambda}$ stands for a weight matrix used in the implementation of the reweighted FISTA algorithm, the symbol $\odot$ standing for the Hadamard matrix product (see [Fad17] for more details).

Then, in the second step, the signal $\mathbf{X}$ is recovered by matrix inversion, i.e., $\widehat{\mathbf{X}} = \mathbf{A}^{-1}\widehat{\mathbf{Y}^\circ}$ since $\mathbf{A}$ is invertible. Despite its simplicity, this two-stage approach suffers from a major drawback: the mixed components $\mathbf{Y}^\circ$ will not be perfectly estimated, especially when only few measurements in $\mathbf{Y}$ are available and when noise contaminates the data. These estimation errors will be amplified in the unmixing stage. Since the mixing matrix $\mathbf{A}$ is likely to be ill-conditioned[34] due to the similarity of the reflection coefficients, these errors will largely impact the reconstruction accuracy of the reconstruction process.

A more effective strategy consisted in jointly tackling both the compressed sensing recovery and the unmixing problems. Extending standard reconstruction procedures yielded the following optimization problem

$$\widehat{\mathbf{X}} = \text{Argmin}_{\mathbf{X}} \quad \left\|\mathbf{\Lambda} \odot \left(\mathbf{X}\mathbf{\Psi}^T\right)\right\|_{\ell_1} + \frac{1}{2}\left\|\mathbf{Y} - \mathbf{A}\mathbf{X}\mathbf{\Phi}\right\|_F^2, \tag{3.9}$$

that can also be solved using a reweighted FISTA procedure.

Further improvement in the components recovery was obtained by imposing additional constraints on $\mathbf{X}$ (see [Fad17] AA I-7) , that reflect the specific physical constraints that hold in active polarimetric imaging: each component $\mathbf{x}_S$ and $\mathbf{x}_P$ must have non-negative values, and under the assumption of purely depolarizing samples illuminated by fully polarized light, the components must verify the following inequality: $\mathbf{x}_S \geq \mathbf{x}_P$. As a result of these new constraints, the optimization problem to tackle is now described as follows

$$\begin{aligned} \widehat{\mathbf{X}} = \text{Argmin}_{\mathbf{X}} \quad & \left\|\mathbf{\Lambda} \odot \left(\mathbf{X}\mathbf{\Psi}^T\right)\right\|_{\ell_1} + i_{\mathbf{X}\succeq 0}(\mathbf{X}) \\ + i_{\mathbf{D}\mathbf{X}\succeq 0}(\mathbf{X}) + \frac{1}{2}\left\|\mathbf{Y} - \mathbf{A}\mathbf{X}\mathbf{\Phi}\right\|_F^2, & \end{aligned} \tag{3.10}$$

where $i_{\mathbf{X}\succeq 0}(\mathbf{X})$ stands for the characteristic function of the positive orthant $\{\mathbf{X};\ \forall i,j,\ [\mathbf{X}]_{ij} \geq 0\}$ and $i_{\mathbf{D}\mathbf{X}\succeq 0}(\mathbf{X})$ for the characteristic function of the convex set $\{\mathbf{X};\ \forall i,j,\ [\mathbf{D}\mathbf{X}]_{ij} \geq 0\}$ where $\mathbf{D} = [1, -1]$.

[34] The condition number of a matrix $\mathbf{A}$ reads $\kappa(\mathbf{A}) = \|\mathbf{A}^{-1}\|_2 \cdot \|\mathbf{A}\|_2$, and is basically the ratio of the highest to the lowest eigen value of $\mathbf{A}$. The condition number $\kappa(\mathbf{A})$ is plotted at the bottom of Fig. 3.6-[II] as a function of the incidence angle θ of the light on the DMD. The influence of θ and of the wavelength on $\kappa(\mathbf{A})$ and on the reconstruction quality have been throughly addressed in [Fad17] (AA I-7).

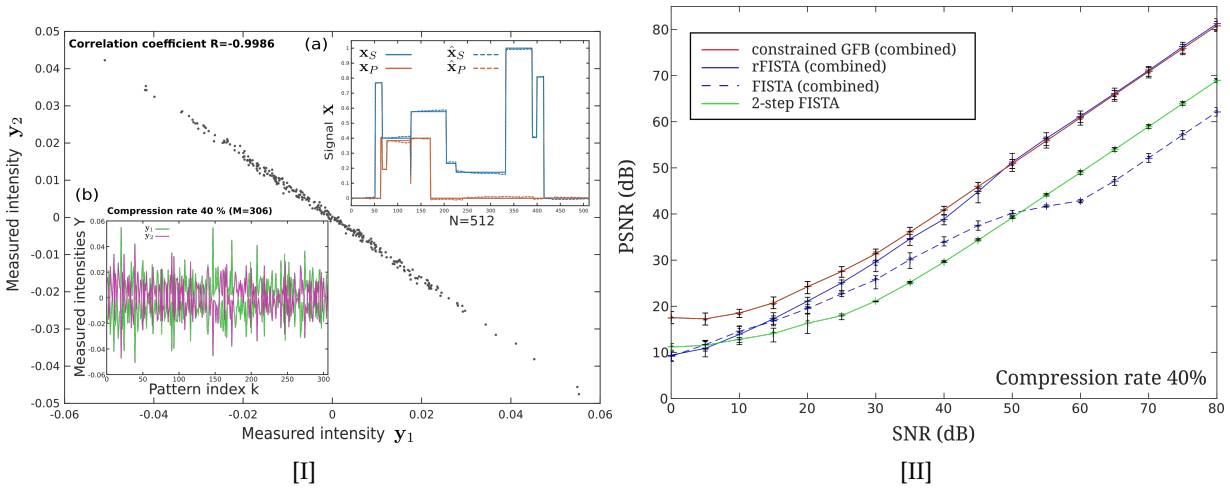

Figure 3.7: [I] Main figure: plot of intensity $\mathbf{y}_2$ as a function of $\mathbf{y}_1$ revealing strong anticorrelation between the two detected signals. Inset (a): Synthetic 1D polarimetric test signal used to assess recontruction algorithms performance, and example of reconstructed signal. Inset (b): example of measured intensities on photodetectors P_1 and P_2 for $M = 306$ different binary patterns (Hadamard) applied on the DMD. [II] Evolution of the PSNR of the signal $\widehat{\mathbf{X}}$ reconstructed with the 4 compared algorithms as a function of detected signal SNR for a compression rate of 40 %.

In contrast to the standard problem in Eq. (3.9), the problem in Eq. (3.10) is composed of a sum of convex penalizations that cannot be tackled with the FISTA algorithm. Multiple convex penalizations can be handled using a specific implementation of the Generalized Forward Backward (GFB) algorithm [Rag13] that was developed on purpose for the considered problem, and which is detailed in [Fad17]. The main drawback of the GFB algorithm lies in its lack of acceleration, thus leading to weak convergence rates and hence slower implementation[35]. Optimization of the parameters of the three algorithms mentioned is a quite subtle task, but we refer the interested reader to [Fad17] for the sake of conciseness.

To compare the performance of these algorithms with reasonable computation times, we first considered a synthetic 1D polarimetric data described in Fig. 3.7. In Fig. 3.7.b, we plot the evolution of the PSNR[36] of $\widehat{\mathbf{X}}$, for a moderate compression rate of 40 %, as a function of the SNR of the simulated data $\mathbf{Y}$. It can first be seen that all the algorithms asymptotically exhibit a linear evolution of their PSNR as a function of the SNR. Then, it is interesting to note that for intermediate values of SNR (10 dB<SNR<50 dB), the 2-step approach underperforms with respect to the simplest implementation of the combined reconstruction approach (denoted by combined-FISTA). However, as soon as a reweighted procedure is implemented, solving the CS and the unmixing problems simultaneously (algorithm denoted as combined-rFISTA) provides an asymptotical gain of about 12 dB in PSNR with respect to the 2-step algorithm. Lastly, imposing physical positivity constraints on $\widehat{\mathbf{x}}_S$, $\widehat{\mathbf{x}}_P$ and $\widehat{\mathbf{x}}_S - \widehat{\mathbf{x}}_P$ through the implementation of the GFB algorithm (denoted as combined-GFB) does not bring any additional gain in performance for highest values of SNR. However, in noisy situations, for SNR < 50 dB, the positivity constraints prove efficient to improve the reconstruction quality. A maximum gain of almost 10 dB is obtained for SNR = 0 dB. These simulation results are further detailed in [Fad17],

[35] In practice, the proposed GFB-based algorithm was initialized with the result of the reweighted FISTA algorithm in order to accelerate convergence and minimize computation time.

[36] The Peak Signal to Noise Ratio (PSNR) is a standard measure used in image processing to assess the quality of a reconstructed or compressed image with respect to the original image. It is defined as $PSNR_{dB} = 10\log_{10}\frac{[\max(\mathbf{X})]^2}{\mathrm{MSE}(\widehat{\mathbf{X}},\mathbf{X})}$, with mean square error $\mathrm{MSE}(\widehat{\mathbf{X}},\mathbf{X}) = \frac{1}{N}\sum_{i=1}^{N}\left(\widehat{X}_i - X_i\right)^2$.

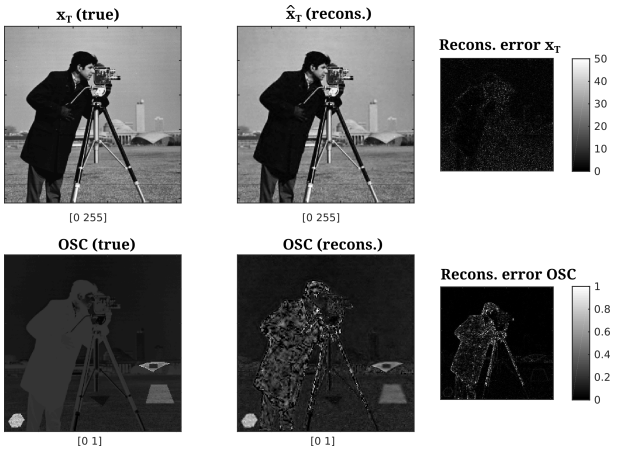

Figure 3.8: Example of numerical polarimetric imaging experiment. First row: total intensity image $\mathbf{x}_T$, reconstruction $\widehat{\mathbf{x}}_T$ and error map. Second row: true OSC image, reconstructed OSC image and error map.

but suffice to demonstrate the validity and interest of the joint reconstruction approaches proposed.

Lastly, we present below an example of reconstructed polarimetric image on a more realistic imaging scenario to validate the potential of the technique for polarimetric imaging. For that purpose, we considered a true intensity image $\mathbf{x}_T$ (the *cameraman* image, famous in the image processing community) with size $N = 512 \times 512$, as plotted in Fig. 3.8. Appropriate polarimetric components $\mathbf{x}_S$ and $\mathbf{x}_P$ were generated so that a true OSC map would reveal four hidden objects (three in the grass, one in the buildings) over a depolarizing background, as can be seen in Fig. 3.8. The reconstruction results with the combined reweighted-FISTA approach are also displayed in Fig. 3.8, along with reconstruction error maps. The total intensity image is almost perfectly reconstructed, as would be the case with a SPC imaging system. The four hidden objects remain of course invisible in the reconstructed image $\widehat{\mathbf{x}}_T$. Contrarily, the reconstructed OSC map makes it possible to identify the presence of the four hidden objects by revealing their polarimetric contrast over the background. The analysis of the reconstruction error map of OSC shows that the polarimetric information about the four hidden objects is fairly retrieved, despite significant reconstruction errors in the darkest regions of the image (cameraman body and tripod).

These numerical simulations have permitted to validate the possibility of obtaining fairly compressed polarimetric contrast images with good reconstruction quality using optimized reconstruction algorithms. This is done in principle with an extremely simple sensing setup, which does not require any polarization analysis component, hence offering optimal tradeoff in terms of photon budget and spectral operating range. A perspective to this work is to implement such an imaging setup in a laboratory experiment, and further investigate the application of CS theory to the polarimetric imaging domain.

3.3 Computational snapshot DOP imaging from a single speckle image

Lastly, let us briefly present in this chapter an alternative computational technique that allows DOP imaging to be performed with an experimental setup showing the most extreme simplification, as it only requires an illumination laser source and a standard grayscale camera. This technique was theoretically thoroughly characterized during my PhD thesis work in terms of ultimate estimation performance [Réf07b, Fad08c], practical estimators [Fad08c], robustness to Poisson noise in low flux situations [Fad08a], etc., and since validated experimentally in the Optics and Photonics Department [Fad12b]. A summary of this work is given below.

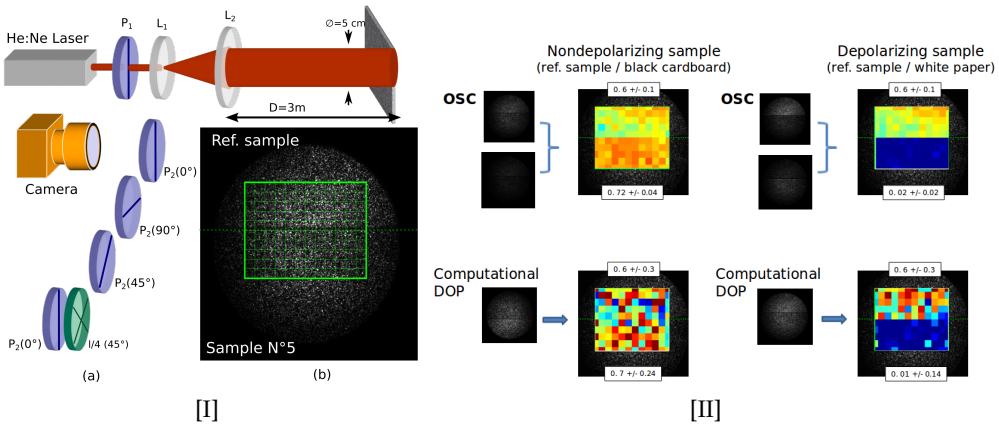

Figure 3.9: [I] Schematic standard measurement setup for measuring the DOP of the light in active coherent imagery. The incoming polarized laser light is backscattered by the scene. The backscattered light is acquired on a CCD camera through a polarization analyzing component (Stokes imaging). An additional image without any polarization analyzing component provides a speckle image which is were partitioned (green grid) to obtain homogeneous zones of 20x20 pixels on which the DOP is estimated. [II] Example of imaging contrasts obtained with OSC (upper row) and single-image computational DOP estimation (lower row) on a slightly depolarizing sample (left), and a strongly depolarizing sample (right).

3.3.1 DOP inference from speckle statistics

As recalled in Chapter 2, a rough surface illuminated by a coherent light will produce a highly contrasted speckle pattern when imaged on a detector, which results from interferences of the backscattered light at each location of the sample. Though often treated in classical coherent imaging as a source of noise that must be get rid of, we will show that one can take advantage of these perturbations, in particular since they contain information on the degree of polarization of the reflected light [Goo85, Bro98, Réf07b, Fad12b]. This technique can be interesting for polarization imaging applications that require the greatest simplicity and the shortest acquisition time. Indeed, after enlightenment of the scene by laser light, the proposed method only requires a single image acquisition and a very short processing time to provide a DOP map of the scene, to the expense of a loss in spatial resolution.

The proposed estimation technique assumes a standard model of speckle statistics for a partially polarized light, whose second order statistical parameters are completely described by the polarization matrix Γ introduced in Chapter 1. This matrix allows one to define the degree of polarization (DOP), referred to as $\mathcal{P}$, by Eq. (1.4). The intensity of an image degraded by speckle noise can be considered as a random variable I of mean value μ_I. Moreover, it is well-known from statistical optics developments [Goo85] that when light is partially polarized with DOP $\mathcal{P}$, the intensity can be decomposed as an incoherent sum of a fully polarized component with mean intensity $\mu_I\mathcal{P}$ and a totally unpolarized component with mean intensity $\mu_I(1-\mathcal{P})$. Such decomposition can also be conveniently rewritten into a sum of two incoherent polarized components denoted here $I_\mathcal{X}$ and $I_\mathcal{Y}$, which correspond to two fictitious orthogonal polarization states of the electric field, whose respective mean values $\mu_\mathcal{X} = (1+\mathcal{P})/2$ and $\mu_\mathcal{Y} = (1-\mathcal{P})/2$ correspond to the eigenvalues of the polarization matrix Γ. If the speckle is fully developed[37], each of these two components follows an independent exponential probability density function (pdf) [Goo85]. From this decomposition, it is then straightforward to show that the pdf of the speckle pattern intensity follows a specific law, being

[37]Speckle can be termed as fully developed when random phases undergone by light – upon scattering on a rough surface or transmission through a disordered medium – are uniformly distributed across $[0; 2\pi[$, and when speckle grains are not averaged on the detector (i.e., a pixel covers at most one spatial coherence area of the field).

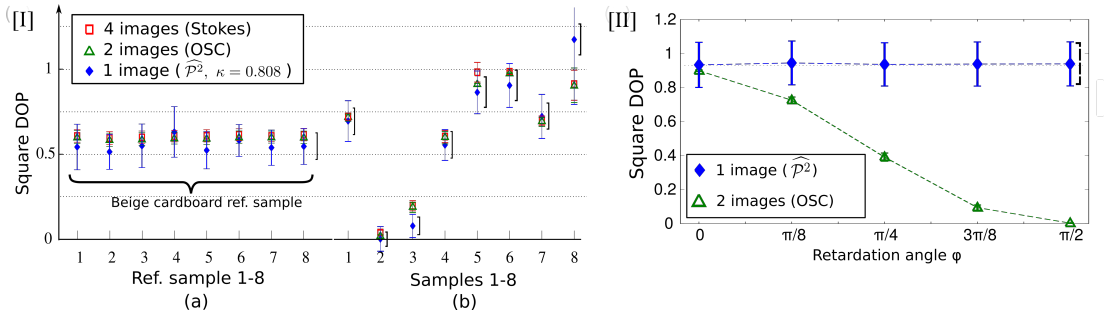

Figure 3.10: [I] Comparison of the DOP estimated from a single speckle image (blue diamond symbols) and from standard DOP estimation techniques (Stokes (red squares) and OSCI (green triangles)) on (a) a reference test sample (8 realizations) and (b) 8 distinct test samples. [II] Square DOP estimated from two images (OSC) and from one speckle image on a birefringent sample, showing the robustness of the speckle estimation method.

the convolution of two exponential pdfs of different means, which basically reads as a difference of exponentials [Goo85, Réf07b] and whose shape strongly depends on $\mathcal{P}$. From the shape of this intensity distribution, it is quite clear that $\mathcal{P}$ can in principle be retrieved easily. A part of my PhD thesis work has been dedicated to studying the optimal estimation precision for the estimation of $\mathcal{P}$ from a single speckle image. The remainder of this section will briefly mention some of these contributions, but also detail the experimental validation that has been conducted at IPR since 2010.

For the sake of generality, we have proposed to extend the above statistical description by adopting a more general model of speckle [Fad08c]. For that purpose, we assumed that $I_{\mathcal{X}}$ and $I_{\mathcal{Y}}$ are still independent random variables with the same multiplicative probability law of general form $P_{\mathcal{Z}}(z) = 1/\mu_{\mathcal{Z}} f(z/\mu_{\mathcal{Z}})$, with $\mathcal{Z} = \mathcal{X}, \mathcal{Y}$. The pdf of the total intensity I is still obtained from the convolution of the two marginal pdfs with different means. This more general model accounts for speckles of higher order[38] L (i.e., with a gamma law of order L) or even less standard models of speckle, when f belongs to a different family of pdfs such as Weibull laws for instance[39] [Fad12b]. With such model, it is quite straightforward to show that the variance of the intensity distribution reads $\mathrm{var}(I) = (1 + \mathcal{P}^2)\kappa_2 \mu_I^2/2$, where κ_i represents the statistical cumulant of order i of the pdf f (κ_2 being the reduced variance of f, equal to 1 when f is an exponential law). This relation demonstrates that the DOP can be estimated as soon as the mean value and the variance of the intensity have been measured and provided the cumulant κ_2 of f is known. This latter quantity can be either deduced from theoretical considerations or measured from a calibration step as shown below.

This estimation approach requires an analysis of the speckle pattern intensity statistics, typically on N pixels of a homogeneous region χ in the image[40]. One of the outcomes of the theoretical study of this technique during my PhD is that homogeneous regions of about $N = 20 \times 20$ pixels is a good tradeoff between precision (10% precision on $\mathcal{P}$) and resolution of the final DOP image, when $\kappa_2 \simeq 1$.

3.3.2 Experimental validation

Among the experimental work that I have conducted at IPR, I have undertaken the experimental validation of this imaging technique on various samples in a reflection configuration, in collaboration with M. Roche (Institut Fresnel, Marseille, France). This experimental study allowed us to analyze its precision in regard to the theory, and to test its robustness with illumination wavelength or with

[38] which situation occurs when L speckle grains are averaged in one pixel of the detector.

[39] Such laws (Weibull, lognormal, K-laws) are commonly used to model non uniform reflectivity of materials, and widely used for instance to model ground clutter in radar signal processing.

[40] A simple sliding window moved along the image dimensions can be used, as shown here, but segmentation algorithms can be used in a preprocessing step to get statistically homogeneous regions χ_j of maximum size in the image [Fad08b].

non purely depolarizing samples [Fad12b] (see AA I-8, p. 158). A sketch of the experimental setup is given in Fig. 3.9-[I]: a vertically-polarized, 15 mW, collimated 633 nm He:Ne laser beam was used to illuminate the samples, located at a 3 m distance from the emission/reception setup. As for the imaging part, the samples were imaged through a 50 mm objective on a 12-bit Basler CCD camera (782 x 582 pixels) selected for its good noise properties under low illumination levels. As shown in Fig. 3.9-[I].a, four Stokes images could be recorded with appropriate configurations of a polarization analyzer ($P2$) and a quarter-wave plate. These 4 Stokes images were processed to estimate the DOP at each pixel of the scene, and provide a reference DOP map, used as benchmark for the validation of the single speckle image technique. In addition, OSC images could be derived from the first two Stokes images acquired for comparison.

The snapshot polarizer-free computational estimation of the DOP from speckle contrast was performed using another image acquisition, obtained by removing any polarization analyzing device in front of the camera objective. In that case, the DOP image resulted from a statistical analysis of the speckle intensity fluctuations at a local scale, using the simplest estimator that can be derived from the above statistical description, i.e.,

$$\hat{\mathcal{P}^2} = \frac{2}{\kappa_2}\left[\frac{\langle I^2\rangle_\chi}{\langle I\rangle_\chi^2} - 1\right] - 1, \tag{3.11}$$

which basically boils down to estimating mean and variance of the pixels graylevels in a homogeneous region χ. Local estimation was performed over homogeneous zones of 20x20 pixels represented by the green grid in Fig. 3.9-[I].b, superimposed over an example of speckle image acquisition. The parameter κ_2 in Eq. (3.11) was directly linked to the geometry of the imaging setup as $L = 1/\kappa_2$ is an indication of the mean number of speckle grains that were averaged per pixel, and which was controlled by the objective aperture. Calibration of κ_2 was easily operated by measuring the reduced variance of a fully polarized light field (i.e., on the Stokes images acquired). For the experimental conditions at hand (wavelength, objective aperture, geometry,...), we obtained a final estimation of $\kappa_2 = 0.808 \pm 0.003$ (see [Fad12b] (AA I-8) for further details).

Once calibrated, the snapshot computational DOP estimation technique can be operated on the speckle image acquisitions recorded over 8 realizations of the reference sample and a variety of 8 distinct samples with varying depolarization properties. As can be checked in Fig. 3.10.[I], the estimator given in Eq. (3.11) provides a correct value of the square DOP, in agreement with standard techniques (Stokes or OSC imaging). As shown in [Fad12b], it can be checked that the precision of this estimator is in good agreement with theoretical predictions of the variance, which had been shown to depend only on $\mathcal{P}$ and on the first four cumulants of the marginal law f [Fad08c]. Other experiments were conducted which demonstrate the robustness of the technique over several operating wavelengths and various imaging geometries (and thus various speckle order). We also checked that, contrarily to OSC imaging, the snapshot computational imaging technique addressed here is able to estimate the DOP in the presence of birefringent samples, as evidenced in Fig. 3.10.[II].

The above results can also be presented in an alternative way, as shown in Fig. 3.9-[II] to provide an insight on the imaging capabilities of the described technique. In this figure, each of the $20x20$ pixels homogeneous regions provides a local estimate of the degree of polarization of the two objects imaged, which is color-encoded in Fig. 3.9-[II] as "macro-pixels". In the first row, the estimation is performed using OSC whereas the lower row corresponds to an estimation performed using the polarizer-free, single image technique presented here. The DOP values are rendered using a colormap where null DOP appears in blue, while unitary DOP corresponds to dark red. From this figure, it can be observed that the OSC enables clear discrimination of the two regions in the case of the depolarizing sample (white paper, on the right), and a slight contrast remains between the two objects in the left case (black cardboard), allowing two objects with DOP values separated by $10\ \%$ to be discriminated. This is not the case with the computational technique presented in the lower row when only 20x20 pixels regions are considered. However, one can notice that a clear discrimi-

nation is possible when DOP values are frankly different, as in the case of the depolarizing sample on the right. As a result, provided the loss in resolution is acceptable for a given application, using the single-shot polarizer-free DOP imaging technique presented in this work can be an interesting alternative for cheap, instantaneous and robust object inspection, only requiring a coherent illumination with a laser source. Recently, this extremely simple approach has been used for food inspection applications [Rou17], in conjonction with other metrics derived from the same speckle acquisition, such as the biospeckle activity [Nas14]. To facilitate its transfer to practical applications, it would be very interesting to further investigate the potentialities of this approach for discrimination/detection tasks, for it is important to provide some quantitative results, and to determine the best statistical processing strategies adapted to the situation at hand. This will be explored in forthcoming works.

Conclusion

In this chapter, I have summarized the work conducted towards the development of original polarimetric imaging modalities offering strong simplification of the systems, but also direct and immediate access to specific polarimetric figures of merit (DOP, OSC, diattenuation magnitude/angle). Of course, these techniques only provide partial information about the polarimetric properties of the samples, and therefore may be confined to specific applications that require fast acquisitions (DSOB, DOP from single speckle image), large spectral range of use (DSOB, OSC compressive imaging, DOP from single speckle image), or long range operation (DSOB), or acquisitions in spectral bandwidths where polarization analysis elements or array detectors are unavailable (OSC compressive imaging).

From the reading of Chapters 2 and 3, it should appear to the reader that these developments were conducted in conjunction with experimental and theoretical developments about the physical origins and interpretation of light depolarization. Such an interplay between fundamental works and applicative developments have permitted us to contribute to the clarification of a number of issues that were still pending about depolarization and polarimetric imaging. We believe that this unconventional point of view on polarimetric imaging, between fundamental polarization physics, laser/microwave photonics and advanced signal processing will continue to open interesting scientific questions and supply original experimental schemes to answer it.

Part II

Optimal processing of optical signals with information theoretic tools

Chapter 4

A (very) succinct introduction to information theory

In the second part of this manuscript, I will describe the work that I have conducted since my PhD on two other research domains about optimal processing of optical signals in non conventional imaging approaches. First, the development of original experimental facilities and processing tools for long range ballistic photons imaging in turbid atmosphere will be described in Chapter 4. Then, Chapter 5 will briefly summarize the numerical implementation of an original technique for unsupervised model selection in the context of wideband infrared optical spectroscopy based on the Minimum Description Length principle.

In these two chapters, I will make use of a number of tools derived from information theory that are offered to the physicist to design optimal processing strategies. Though very well known to most physicists nowadays, these tools derived from either *probabilistic*[41] (Shannon's) information theory or *algorithmic* (Solomonoff-Kolmogorov's) information theory are very briefly recalled in the remainder of this chapter, at least for notational purposes.

4.1 General definition of information theory

Information theory is a rather recent science whose development started since the early XX$^{\text{th}}$ century, following important developments in thermodynamical physics. However, the most important breakthrough that gave rise to the wide spread of these concepts in all areas of science and technology occured in the 1940's, with Shannon's seminal contributions that founded the *probabilistic* information theory. Later, tremendous progress in computer science led to the development of an alternative *algorithmic* information theory, notably through Solomonoff, Kolmogorov and Chaitin's work.

Generally speaking, information theory corresponds to an attempt to measure and quantify *information* on a rational basis[42]. Remarkably, as soon as such information measures were proposed, information theory provided an impressively large number of theoretical mathematical results with important practical consequences for many areas of science and technology. Without claiming exhaustivity, we can cite coding/compression/cryptography theories, communications theory, statistical inference (estimation & decision theories), gambling & portfolio theories, model selection, etc. which have found many applications in physics, computer science, telecommunications, but also biology and economy [Cov91]...

For the physicist, information theory provides for instance reliable guidelines for the development of optimal estimation procedures, and for assessing the best estimation precision expectable from a given experiment. It also offers efficient approaches to design unsupervised sparse model selection strategies. These two aspects are briefly introduced below.

[41] We use the term *probabilistic* here to distinguish Shannon's theory from the *algorithmic* information theory.

[42] without restriction to the information support: binary sequence, text, image, audio record, DNA chain, ...

4.2 Shannon information theory and tools for statistical image processing

4.2.1 Definition of entropy

Shannon's definition of information requires that a probability measure $P(\omega)$ can be assigned to an observation or event ω considered as random. When such probability is known *a priori* (or measured, or hypothesized), the opposite logarithm of P defines the information carried by the observation of ω, $\mathcal{I}(\omega) = -\log(P(\omega))$ where $\log(.)$ will denote the base 2 logarithm ($\log(.) = \ln(.)/\ln(2)$), so that $\mathcal{I}(\omega)$ is expressed in bits. With such definition, the information $\mathcal{I}(\omega)$ can be regarded as a "measure of improbability" with a number of interesting properties[43]. The well-known Shannon entropy then simply consists of the information averaged over all possible outcomes of the random event ω, i.e., assuming P is a continuous probability distribution,

$$H(P) = \langle \mathcal{I}(\omega) \rangle = -\int_{\mathcal{S}} P(x) \log P(x) dx, \tag{4.1}$$

where $\mathcal{S}$ is the support of the probability density function (pdf) P. This quantity indicates the average amount of information, in bits, obtained when observing one outcome of the random event ω.

Kullback-Leibler divergence (KLD) (termed *relative entropy* in the case of discrete probability distributions) is a closely related quantity which can be defined in a similar way as

$$D(P||Q) = -\int_{\mathcal{S}} P(x) \log \frac{P(x)}{Q(x)} dx, \tag{4.2}$$

where $P(x)$ and $Q(x)$ denote two continuous pdf's. This non-negative quantity interestingly acts as a measure of "distance" between two probability distributions (even though not a distance mathematically speaking) since $D(P||Q) = 0$ if and only if $\forall x,\ P(x) = Q(x)$.

4.2.2 Consequences of information theory for parameter estimation

Let us now consider a probability distribution $P_X(x;\theta)$ on a random variable x that depends on a parameter θ, assumed – in a non-Bayesian framework – to have a fixed yet unknown value. When inference about the value of parameter θ is performed from the observation of K samples of the random variable x (through K various experiments), the probability of the set of K independent observations reads $P_\chi(\chi;\theta) = P_{X_1,\ldots,X_K}(x_1,\ldots,x_K;\theta) = \prod_{i=1}^{K} P_X(x;\theta)$. This quantity is referred to as the likelihood of the observed data χ under the hypothesis that the parameter value is θ.

In that case, a *local* measure of information content about θ is given by the Fisher information (FI), which is defined as

$$I_F^\chi(\theta) = \left\langle \left(\frac{\partial \ln P_X(x_1,\ldots,x_K;\theta)}{\partial \theta} \right)^2 \right\rangle = K \times \int_{\mathcal{S}} P_X(x;\theta) \left(\frac{\partial \ln P_X(x;\theta)}{\partial \theta} \right)^2 dx. \tag{4.3}$$

This quantity has a strong physical meaning, as it represents the amount of information that can be maximally retrieved about θ from the set of observations χ. In other words, the Fisher information is a measure of the "sensitivity" of the pdf $P_X(x;\theta)$ to the variations of parameter θ. This can be readily understood by analyzing the following approximation

$$I_F(\theta) \sim \frac{2}{(\delta\theta)^2} D(P_X(x;\theta)||P_X(x;\theta+\delta\theta)), \tag{4.4}$$

where the KLD $D(P_X(x;\theta)||P_X(x;\theta+\delta\theta))$ measures the local variation of the pdf with small incre-

[43] such as non-negativity, monotonicity and continuity with P, and additivity for independent events.

ments $\delta\theta$ of the parameter of interest.

A direct and very important consequence of the definition of the FI is the well-known Cramer-Rao theorem which states that the variance of any unbiased estimator $\hat{\theta}$ of the parameter θ from the dataset $\chi = \{x_1, \ldots, x_K\}$ must verify[44]

$$\mathrm{var}(\hat{\theta}) \geq \frac{1}{I_F^{\chi}(\theta)} = CRB^{\chi}(\theta), \tag{4.5}$$

where $CRB^{\chi}(\theta)$ denotes the Cramer-Rao lower bound[45] (CRB) on the estimation of θ. This is a very strong fundamental result, as it makes it possible to compute a lower bound on the minimum variance of estimation of a parameter, regardless of the estimation strategy adopted, as it does not depend specifically on $\hat{\theta}$. Due to its "universality" property, the CRB (or equivalently the FI) will be used in the next chapter to assess the quality of the practical estimators proposed and tested. But most importantly, the computation of the FI will be leveraged to quantify and study the best precision expectable in a physical experiment as a function of all the parameters regardless of the estimation strategy. As a result, this information theoretic tool is in phase with the *co-design* strategy presented in Chapter 3: it allows the performances of an optical or physical system to be assessed (to a certain extent) independently from the processing strategy, which can in turn be optimized to reach or approach the estimation bound.

Unfortunately, there is no guarantee in the most general case that an *efficient* estimator exists (i.e., an estimator whose precision reaches the CRB), nor that there exists a systematic "recipe" to build such an optimal estimator. However, if the pdf $P_X(x;\theta)$ from which the data was drawn belongs to the exponential family of distributions[46], the well-known Maximum-Likelihood estimation (MLE) procedure often leads to an optimal estimator[47]. The ML estimator is very simply defined as the value of θ that maximizes the likelihood of the observed data, i.e.,

$$\hat{\theta}_{ML} = \mathrm{argmax}_{\theta}\big\{P_X(x_1, \ldots, x_K; \theta)\big\}, \tag{4.6}$$

but its practical implementation can sometimes be a bit tedious, requiring an iterative optimization procedure. For instance, in the context of single speckle computational DOP imaging presented in Chapter 3, a ML estimation technique was proved to be efficient during my PhD work [Réf07b], even though the distribution does not belong to the exponential family. Unfortunately, this estimator required a slow iterative solving procedure.

As a result, the MLE strategy and the CRB theorem provide interesting guidelines to design optimal estimation strategies, as will be illustrated in the next chapter. However, they both share the general drawback of Shannon's probabilistic definition of information: all the concepts derived within this theory strongly depend on the pdf of the data, which most of the time is hypothesized. An incorrect estimation or hypothesis can thus be highly detrimental in that case to the validity of the theoretical predictions, and thus caution should be taken to check the actual data distribution on the experimental acquisitions.

[44] This theorem holds under proper regularity conditions on the pdf $P_X(x;\theta)$ [Gar95] which are assumed verified here. It can also be noted that a version of the theorem holds for a biased estimator $\hat{\theta}$, but which does not share the "estimator-independent" property.

[45] Similarly, a lower bound on estimation covariance matrix can be derived from the Fisher information matrix (FIM) in the case of a multivariate parameter vector $\boldsymbol{\theta}$ [Réf07a].

[46] i.e., if it can be written as $P_X(x;\theta) = \exp\big\{\sum_{j=1}^{m} A_j(\theta)B_j(x) + C(x) + D(\theta)\big\}$.

[47] Provided the MLE is unbiased, it is minimum-variance among all estimators for samples of limited sizes, and asymptotically efficient for large samples [Gar95].

4.3 Algorithmic information theory and Minimum Description Length principle

4.3.1 Algorithmic information theory and Kolmogorov complexity

As mentioned above, an alternative definition of information, and an alternative information theory can be built on an algorithmical basis. The algorithmic definition of the information content of a message is also termed *descriptive* information, since it aims at quantifying the amount of information needed to describe a sequence, without any reference to the underlying probabilistic model that generated it, contrarily to Shannon's notion of information. As a result, this approach circumvents the main drawback of the probabilistic information theory briefly sketched above.

Within this framework, the Kolmogorov complexity, denoted $\mathcal{K}(x)$, is a measure of information contained in a message x, and defined as the size, in bits, of the shortest binary computer program that can describe (or output) the sequence when processed by a computer [Cov91]. Despite the extreme simplicity of its formal definition, the Kolmogorov complexity remains however a very conceptual (and barely practical) notion. Indeed, it can be shown that the Kolmogorov complexity is in general not computable. Such impossibility is related to the halting problem in computer science, i.e., for any computer model, there is no general algorithm to decide whether a program will halt in a finite time or not[48] [Cov91]. As a result, practical use of algorithmic information theory requires approximations of the Kolmogorov complexity. Nevertheless, this conceptual definition of information gave rise to several fundamental notions, such as algorithmically random sequences[49], or universal probability[50] which find use in universal source coding theory [Cov91].

4.3.2 Minimum Description Length principle

An interesting concept which originated from the algorithmic information theory is the Minimum Description Length (MDL) principle which has found many applications in various research domains. It is based on a parcimony principle[51], which is a rationally acceptable heuristic belief stating that between two possible explanations of the same phenomenon, same data or same message, one should favour the simplest one, i.e., the one that has the minimum complexity (i.e., the one requiring the least hypotheses, parameters, variable, etc.).

MDL is simply a formal application of this principle to practical issues in data processing where one wants to decide, in an automated way, between several hypotheses that can fairly explain the observations. This is a common problem in many data processing areas, such as data clustering, detection/classification, inverse problems, regression/model selection, image segmentation,... Generally denoting by $\mathcal{H}$ the set of possible hypotheses at hand, the MDL principle consists in finding and selecting the hypothesis $H \in \mathcal{H}$ that minimizes the length $L_H(X_1, \ldots, X_n)$ (in bits) of the description of the observed data $\chi = \{X_1, \ldots, X_n\}$ under hypothesis H, i.e.,

$$\text{select } H = \underset{\mathcal{H}}{\operatorname{argmin}} \Big\{ L_H(X_1 \ldots X_n) = \mathcal{K}(H) + \ell_H^{data} \Big\}. \tag{4.7}$$

In this equation, the total length is given by the sum of two terms: on the one hand, the Kolmogorov complexity $\mathcal{K}(H)$ of the model (pdf, parameter vector, class decision boundaries, segmentation map...) retained by hypothesis H – i.e., the number of bits required to describe the

[48] This halting problem is directly related to Gödel's incompleteness theorem.

[49] A sequence of length N bits is said algorithmically random if it cannot be described in less than N bits (simple enumeration), i.e., $\mathcal{K}(x_1 x_2 \ldots x_N | N) \geq N$.

[50] Being also an extremely conceptual notion, the universal probability of a message is the probability that a program randomly drawn as fair coin flips will issue such message.

[51] This pinciple, often quoted as *Occam's razor* from Occam's writing (1285-1347), has important implications in philosophy, epistemology, etc. but can be connected to algorithmic information theory which provides mathematical justifications of this principle [Cov91].

selected model – and on the other hand, the number of bits ℓ_H^{data} required to encode the residuals of the data not described by the model H. This latter quantity can be generally expressed as $\ell_H^{data} = -\log P_X(X_1 \dots X_n; H)$, which is the opposite loglikelihood of the data under hypothesis H. This quantity can also be regarded as the length of the optimal (Shannon's) code that describes the data residuals, when the data set $\chi = \{X_1, \dots, X_n\}$ is supposed distributed according to the pdf assumed under the selected hypothesis H.

Due to the non-computability of Kolmogorov complexity, Rissanen suggested in the early 1970's to replace the first term in the above minimization problem by an approximation, termed (Rissanen's) *stochastic complexity* [Ris78, Ris89, Ris07]. Under such an approximation, the minimization problem now reads

$$\text{select } H = \underset{\mathcal{H}}{\operatorname{argmin}} \left\{ \ell_H^{model} + \ell_H^{data} \right\} \tag{4.8}$$

and solving it will naturally consist of making a balance between the complexity of the model (described with ℓ_H^{model} bits) and the fidelity to the observed data (requiring ℓ_H^{data} bits to be described under hypothesis H). The approach may look very similar to other penalization approaches (very well-known in regression, inverse problem issues, etc.), however, an important feature of MDL is that the two contributions are naturally expressed in the same unity (bits). This automatically circumvents the common problem of selecting a regularization parameter (the famous "λ") which weights the penalization term and the data fidelity term, and which may depend on the data set. As a result, MDL approaches have proved to be very interesting in applications where supervision by an operator was impossible or had to be minimized [Gal03]. Since Rissanen's seminal contribution, a lot of work has been conducted on that topic to propose refined and more general, robust versions of the MDL, some of which will be used and compared in Chapter 6 in the context of unsupervised optical spectroscopy. These advanced MDL implementations are based for instance on Bayesian approaches (with universal priors) or using universal distributions. For the sake of concision, we will not delve into such approaches and we refer the reader to [Ris96, Ris07] for further reading on that techniques.

Chapter 5

Long distance imaging through turbid atmosphere

5.1 Objectives and motivations

Imaging through and within turbid media is an area of interest that has tremendous application in medical diagnostics [Boa01], underwater vision [Sch04, Bof12, Dub13], imaging through colloids [Ram98] and transportation and navigational aids [Wat00, Hau07]. Light traveling through a complex medium with randomly distributed positions and refractive indices undergoes absorption and random scattering and loses the spatial and temporal information of its source. The photons that undergo such multiple scattering are labeled as diffused photons. A small fraction of the total photons called ballistic (and quasi-ballistic photons) undergo no (or very few) forward scattering events before they reach the detector, and they retain the information of their source (direction, polarization state, modulation,...). It is of wide interest to discriminate the ballistic/quasi-ballistic photons from the diffused photons for resolution enhanced imaging through turbid media. However, the diffuse light that strongly depends on the properties of the scattering medium can be used to deduce various parameters related to the medium itself. Thus, imaging in turbid media can be classified into two broad categories: parameter estimation using only diffused light to obtain image of heterogeneities in turbid media, and filtering of ballistic photons from diffused light for high resolution imaging through turbid media.

In this chapter, we will be more focused on this latter issue, for applications of navigational aid through turbid atmosphere, and for relatively long distances of typically one kilometer. In typical fog, light propagation is diffusive rather than ballistic with the diffusive photons overwhelmingly large. To image through such media several techniques have been developed in the last few decades. Optical Diffusion Tomography [Gon95, Sch97] uses image reconstruction strategies based on the inverse-source algorithm to recover the hidden objects from the scattered photons detected. The numerical algorithms used to solve such inverse problems are usually sophisticated, computationally intensive and time-consuming, prohibiting real-time imaging. Other approaches aim at isolating the few ballistic photons, i.e., photons that have not been (significantly) scattered along their trajectory through the scattering medium. A first category of ballistic imaging is based on time-gating techniques [Wan91, Dun91], which employ a pulsed light source (typically, pulse durations ranging from few tens of femto-seconds to few picoseconds) to illuminate the scattering medium. The technique is based on the use of a time-gated ultra-fast camera to detect ballistic photons, which, unlike scattered photons, are not delayed by multiple scattering. In spite of their efficiency and their depth-scanning capability, such techniques are not easily implemented due to their complexity and the prohibitive cost of both the light source and the detection equipment.

On the other hand, ballistic photon imaging can also be attempted with continuous-wave approaches, using either polarization of light [Hor95, Emi96, Ram98], or intensity modulation techniques. The use of polarized light and polarization imaging has been long used for image contrast

enhancement in turbid media (see for example [Dem96, Row95, San97]). These investigations mainly conducted in laboratory short-range experiments, have given interesting results on the influence of the polarization state of the incident light [Sch92, Kar05], or of the particles size [Sch98], anisotropy [Muj04], or of the noise properties [Bén09a, Bén09b] on the image quality. Other techniques based on light intensity modulation have also been experimentally studied in the laboratory [O'l92, Mul04]. However, real-time imaging in real fog conditions has not been demonstrated so far, especially for application to navigation due to the inability of most of the techniques to handle long-range media.

The main objective of the work reported in this chapter was thus to implement these two techniques in real-field conditions (in real atmospheric conditions and over long distances), while aiming at real-time operability. These developments have mainly been conducted within a collaborative project with the Raman Research Institute (Bangalore, India), during more than 3 years (CEFIPRA project "RITFOLD"). This project offered us the opportunity to supervise an indian student, Swapnesh Panigrahi during his PhD thesis in Rennes. The motivation of this project was to propose cheap, and low-complexity solutions for assistance to aerial navigation and landing[52] in low visibility conditions, which could appear as an alternative to cost-prohibitive pulsed approaches, or electromagnetic guidance systems such as ILS which are not available on small airports and small aircrafts. Even with ILS, international aviation regulation rules require a minimum visibility for landing, often expressed in terms of Runway Visual Range (RVR), defining the distance over which the centreline of the runway can be visually identified by the pilot [Ric00, ICA96][53]. Below this minimal visibility, aircrafts are not authorized to land and have to be rerouted to another airport, one of the reasons for that being that ILS is not able to provide a visual real-time representation of the landing scene. As a result, it appeared to us that it would be very beneficial to develop cheap, portable and easy-to-implement alternative systems, which could be easily installed on small aircrafts, and introduced on the vast majority of small airports that are not equipped with ILS[54].

During this project, we first addressed a simple solution allowing efficient background rejection and contrast enhancement of an active beacon (as the ones that could be implemented on a landing area) over long distances and through turbid atmosphere. Such contrast enhancement is illustrated in the drawing of Fig. 5.1.b, where it can be seen that wiping out the contribution of the ambient illumination can significantly improve the visibility of light beacons, demarcating a landing area with respect to the initial image provided to a pilot as sketched in Fig. 5.1.a. The corresponding work and results about optimal contrast enhancement using polarized light are summarized below in the first section of this chapter. Though such efficient background rejection can be interesting for practical application and visual aid to a pilot, it does not constitute however a true "ballistic" photon imaging. Indeed, ballistic filtering would allow for instance a clear suppression of the diffuse light contribution of the emitter itself on the final image[55], as sketched in Fig. 5.1.c. To address this issue without resorting to pulsed illumination, we then considered modulated-light techniques, which could be an interesting cost-effective alternative. This raises however two issues which are (i) what is the miminum frequency ω_{min} that should be advocated to achieve ballistic filtering ?, and (ii) how to perform full-field image demodulation in real time at such high frequencies ? These questions are addressed below in the second section of this chapter, which details the first theoretical and experimental developements that were conducted on this topic at the Optics and Photonics Department of the IPR.

[52] Other areas of application could be envisaged of course, such as coastal navigation or road transportation...

[53] The minimum visibility requirements vary with the ILS categories and regulation, (from 800 m for Cat. I ILS system, up to 91 m for a Cat. III-b ILS, nowadays the most sophisticated equipment on commercial airplanes) [ICA96].

[54] e.g., only about 160 runways were equipped with ILS among the 1100 landing areas in the state of California in 2010 [Ils10].

[55] and hence also provide better spatial resolution of the emitter.

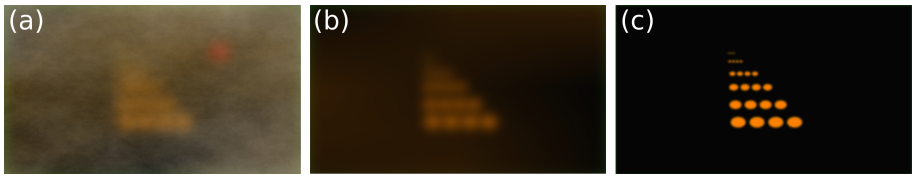

Figure 5.1: (a) Illustration of an aircraft landing scenario in low visibility conditions due to the presence of intense background illumination (ambiant spurious light) and strong light scattering causing reduction of the visibility and of the spatial resolution of the light beacons. (b) Illustration of the resulting image after perfect background removal processing. (c) Illustration of the resulting image expected after ideal ballistic photon imaging process.

5.2 Polarimetric approach for optimal contrast enhancement

5.2.1 Polarimetric imaging facilities for long-distance imaging through fog

During the first years of my work at IPR, I have contributed to the design and settling of an original polarimetric imaging facility in Rennes, to perform experiments in real-field conditions trough fog and over long distances. The facility consists of a highly linearly polarized incoherent source, located on a telecommunication tower (about 80 m in height), belonging to the TDF company, represented in Figs. 5.2 and 5.3.a, imaged from a distance of about 1.3 km with a polarization-sensitive camera. The source used is a 300 W halogen incandescent lamp with a linear vertical polarizer (LCD projector polarizer replacement sheets for heat tolerance), both placed inside a weatherproof steel housing as shown in Fig. 5.3.a. The light source is connected to a GSM switch enabling easy remote control of the emitter. The distance of the tower from the laboratory site in the campus of University of Rennes 1 is 1.3 km, which is optimal for the aerial navigation application addressed with this long-range imaging through fog experiment.

Figure 5.2: Left: View of the TDF telecommunication tower from the laboratory, distant from 1.3 km. The red arrow indicates the location of the polarized beacon. Center: View of the reception site (red ellipse) from the top of the telecommunication tower. Right: Close view of the TDF tower from the ground.

At the reception site, the polarimetric sensitivity is obtained with a modular optical add-on attached to a grayscale camera. As sketched in Figs. 5.3.b and 5.3.c, the polarimetric add-on first comprises an arrangement of lenses L1 and L2 after a monochromatic filter F (at 612 nm, FWHM = 12 nm). The image is partly masked by a slit (FM) in an intermediate image plane, then collimated and passed through a Wollaston prism (WP) to produce, on a single detector (C) and using lens L3, two images $I_{\parallel}$ and $I_{\perp}$ corresponding to two orthogonal polarization directions (with $I_{\parallel}$ aligned with the direction of polarization of the source). The camera used is a low noise, high dynamics Andor NEO sCMOS camera (5.5 Mpixels , 16-bits, 0.015 e-/pixel/s dark noise at -30°C sensor temperature). The high dynamics detector enables fine sampling of the intensity levels and noise statistics in the

acquired images. The whole acquisition has been made autonomous by designing a specific LabView acquisition program, able to acquire series of images over long periods of time (> 10h), and with varying imaging conditions (day/night, clear sky/fog/etc.). This has required a number of acquisition parameters to be automated, such as the exposure time, or the frame grabbing mode[56]. All details about the Wollaston prism-based polarimetric add-on and its calibration can be found in [Bén09a, Fad14b], whereas all the technical details about the whole long-distance polarimetric imaging facility and interfacing are detailed in [Fad14b] (see AA II-1, p 162), and are not reproduced here for the sake of conciseness. The whole setup for application to navigation assistance in obscured weather has been patented in 2014 [Ram16].

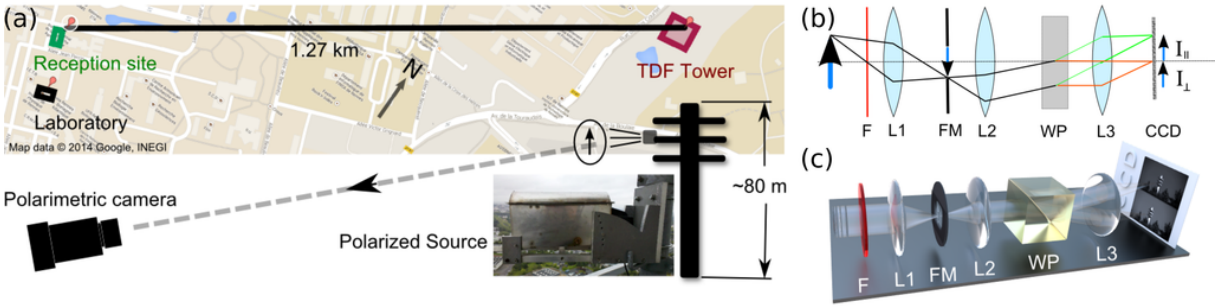

Figure 5.3: (a) Schematic of the long range imaging setup. The source and the camera are separated by a distance of 1.3 km. Sketch (b) and 3D view (c) of the Wollaston prism-based optical setup allowing snapshop polarimetric imaging.

An example of raw image acquisition in a clear sky condition is shown in Fig. 5.4-[I], where the polarized source can be clearly seen in the parallel polarimetric channel (upper image), whereas it appears dark in the perpendicular channel (lower image). After extracting the two polarimetric images, one obtains a set of two-dimensional pixels, such that the polarimetric image $\mathbf{I}_P = \{\mathbf{X}_i^P\}_{i\in[1,N]} = [\mathbf{I}_\parallel\ \mathbf{I}_\perp]^T$, is formed by the set of pixels $\mathbf{X}_i^P = [x_{\parallel,i}\ x_{\perp,i}]^T$. In this work, as a unique polarized beacon was considered, with a priori known location in the image, we were mainly focused on the central region of the image (light-blue dashed square in Fig. 5.4-[I]) as the source usually spreads between 1×1 up to about 5×5 pixels depending on the weather conditions. A relevant contrast measure allowing the visibility of the polarized beacon to be evaluated has been defined as the contrast-to-noise ratio (CNR) of a central 3×3 region, denoted by s (signal region) (red square in Fig. 5.4-[II]), with respect to its surrounding neighbourhood χ_k of size N_k pixels (region delineated between the two blue squares in Fig. 5.4-[II].b). The CNR expression then reads

$$CNR = \frac{\gamma_s - \langle\gamma\rangle_{\chi_k}}{\sqrt{\frac{1}{N_k-1}\sum_{i\in\chi_k}^{N_k}\left(\gamma_i - \langle\gamma\rangle_{\chi_k}\right)^2}}, \tag{5.1}$$

where γ stands for a given representation fo the polarimetric data in the image, for instance, the total intensity $\gamma_\Sigma = x_\parallel + x_\perp$ that would be acquired on a standard camera.[57]

This setup that has necessitated more than two years of work to settle it completely, and to reach full remote operability from any location, at any time. This allowed us to launch long-term acquisitions during day or night, and allowed our colleagues in Bangalore (India) to also have access to it. These efforts turned out to be crucial, and the development of such an experimental facility was

[56] For instance, we implemented a so-called cumulative grab mode (CGM) to avoid recording the 100 Hz intensity fluctuations due to the 50 Hz modulation of the electrical supply network when exposure time was lower than 10 ms (see [Fad14b]).

[57] As can be seen in Fig. 5.4-[II].b, the spatial average $\langle\gamma\rangle_{\chi_k} = \sum_{i=1}^{N_k}\gamma_i/N_k$ is performed on a set of 320 pixels defined by the region χ_k comprised between the 21×21 square region around the source location, excluding a 11×11 central region to prevent the spatial extent of the light source from perturbing computation of the background statistical properties.

indeed an important milestone for our collaborative project, as very few experiments can be found in the litterature concerning polarimetric imaging over long distances in real fog conditions. Indeed, most research groups have focused, for simplicity reasons, on toy models of atmospheric proapagation in turbid water, or in water vapor chambers inside the laboratory. However, one of the main outcomes of our work was to understand that such short-distance models were poorly efficient at reproducing the behaviour of light scattering, absorption, or depolarization in real fog over long distances. After three years of exploitation of this setup, we have gathered important quantities of data over long time series, and in all possible conditions of illumination (day-time, twilight, dawn, night-time) or atmospheric visibility (clear sky, haze, fog, clouds, rain, snow...). A subset of long time-series acquisitions is reported and commented thoroughly in [Fad14b] (see AA II-1, p. 162). We shall here only summarize the most important outcomes of this experimental campaign:

- In our experiments in real conditions, either during day-time or night-time due to city lighting, the presence of a very important amount of ambient illumination cannot be neglected, contrarily to usual in-laboratory experiments were spurious illumination is generally avoided. This has the strong consequence that visibility of the beacon is further decreased, as the observer (or a standard camera) is always completely overwhelmed – dazzled – by the bright ambient light.

- Due to the long propagation distance considered, and due to the small numerical aperture of the imaging system (at least for the few pixels corresponding to the polarized beacon), our system already operates a kind of ballistic filtering of the photons emitted by the source by filtering the photons direction of arrival. This may explain why we were never able to observe any *depolarization halo* around the central pixel, contrarily to what was expected initially from previous laboratory studies.

- Another remarkable observation was that as soon as a thin layer of haze or fog was present in the sky, the whole scene including tower structures, ground, sky (excluding the polarized beacon of course) appeared totally depolarized, with a measured DOP very close to zero. According to the previous remark above, the DOP of the light detected from the source was always perfectly unitary.

- Most importantly, a comparison of standard polarimetric representations of the two-component polarimetric data recorded by the camera showed quite clearly that the best visibility contrast (evaluated with the CNR) was not always provided by the same representation, i.e., no standard poalrimertic representation could be considered as a *uniformly optimal* representation [Fad14b].

Table 5.1: Polarimetric representations and gains in CNR.

Representation	Symbol	$(u=1, v=)$	$g^{\Sigma}=\mathcal{C}(\gamma)/\mathcal{C}(\gamma_{\Sigma})$
Intensity-summed	γ_{Σ}	1	1
Pol. filtered	$\gamma_{\parallel}$	0	$\sqrt{2(1+\rho)}$
Pol. difference	γ_{Δ}	-1	$\sqrt{(1+\rho)/(1-\rho)}$
Computational	γ_{CS}	v_{CS}	$-$
Max. Likelihood	γ_{ML}	$-\rho$	$\sqrt{2/(1-\rho)}$

This last observation, which has motivated the search and derivation of an optimal polarimetric representation for maximum contrast enhancement, is illustrated in Fig. 5.4-[II].b. It provides the contrast image and CNR figure of the polarized beacon with three simple and standard polarimetric representations, which are recalled in the upper part of Table 5.1, among which the polarization differnce γ_{Δ} or the polarization filtered image $\gamma_{\parallel}$ for two different acquired frames labeled as [A]

and [B]. It can be readily seen that the best CNR is obtained with $\gamma_{||}$ in situation [A] (low visibility), whereas γ_δ provide better CNR in situation [B][58].

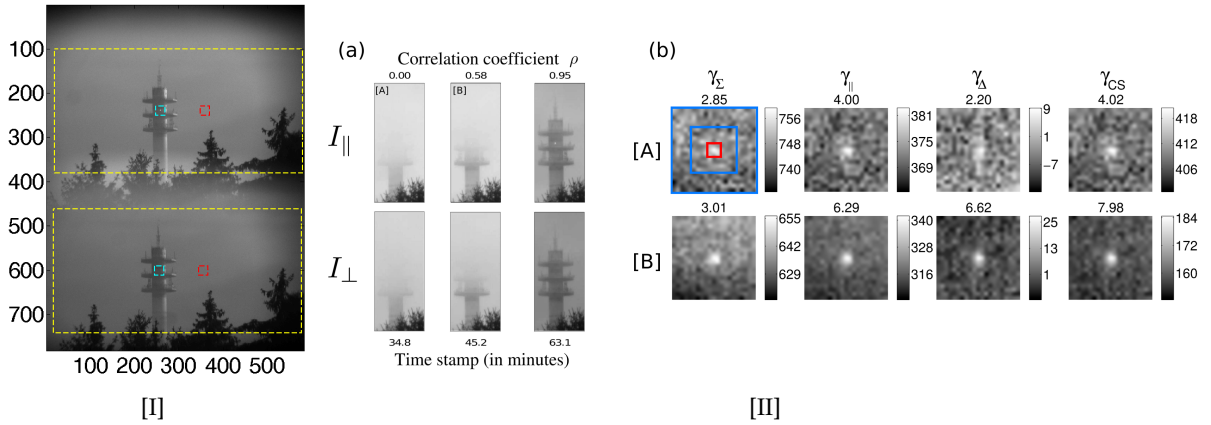

Figure 5.4: [I] Raw image obtained from the camera with 782 × 582 pixels. Extraction of two image channels after applying image registration process is demarcated in yellow dashed box. The cyan square delineates the 21 × 21 pixels region-of-interest around the source location. [II] (a) Examples of raw images from the polarimetric camera, showing the tower and the source with varying conditions of fog density and visibility. The time stamp of acquisition and measured correlation coefficient of noise at the source pixel location are respectively indicated below and above each image. (b) Comparison of four polarimetric representations for two frames labeled as [A] and [B].

5.2.2 Contrast gain and optimal representations from information theory

In light of the above observation, it appeared interesting for the application at hand to derive an optimal signal representation that could ensure best contrast maximization in any weather and visibility condition. Moreover, we also aimed at quantifying theoretically the gain in visibility offered by polarimetric imaging, either with standard representations, or with the optimal one. Before summarizing the theoretical study that we carried out for the derivation of such optimal representation using information theory, let us illustrate on real data that a contrast-maximizing adaptive polarimetric representation can indeed be found. In the last column of Fig. 5.4-[II].b, we have represented the image of the polarized beacon obtained with an optimized polarimetric representation, denoted $\gamma_{CS} = u\,x_{||} + v\,x_\perp$. Such representation consisting of a linear combination of the two polarimetric channels acquired, is computed so as to provide maximum CNR of the polarized beacon with respect to its surrounding neighbourhood. The optimal weights of the linear combination were obtained here by a computational search (hence the subscript CS) over all possible values of u and v, with $u \in [0;1]$[59] and $v \in [-1;1]$. The CNR figures provided in Fig. 5.4-[II] show that γ_{CS} does outperform the standard representations. More interestingly, the 2D search map over u and v plotted in Fig. 5.5-[I] reveals that the optimal representation lies in general between the two standard polarimetric representations, namely the polarization filtered image $\gamma_{||}$ and the polarization-difference image γ_Δ. Such an optimization over all possible weigth values – which is further described in [Pan15a] (see AA II-3, p. 186) – needs be realized at each pixel of the image in a practical situation where the location

[58] One can notice that the OSC contrast map has not been represented. This is indeed another outcome of the experimental work described in [Fad14b] to observe that the normalization step (division by total intensity) incurred by the expression of the OSC appears to be highly detrimental to its robustness to noise. This is the reason why OSC is not relevant and not considered here for a task of optimal contrast enhancement of an active polarimetric target through fog.

[59] Since under the hypotheses considered the CNR metric is invariant by multiplication with a scalar, it suffices in practice to fix $u = 1$ and optimize v. This is why $u = 1$ in the expressions of the representations in Table 5.1. The display of the 2D search has been retained in Fig. 5.5-[I] for the sake of better visual illustration.

and number of polarized sources to be detected will be unknown. As a result, may the technique be efficient, it may fall down well beyond the requirements for real-time imaging and processing with limited computation resources such as the ones that could be embarked in a light aircraft.

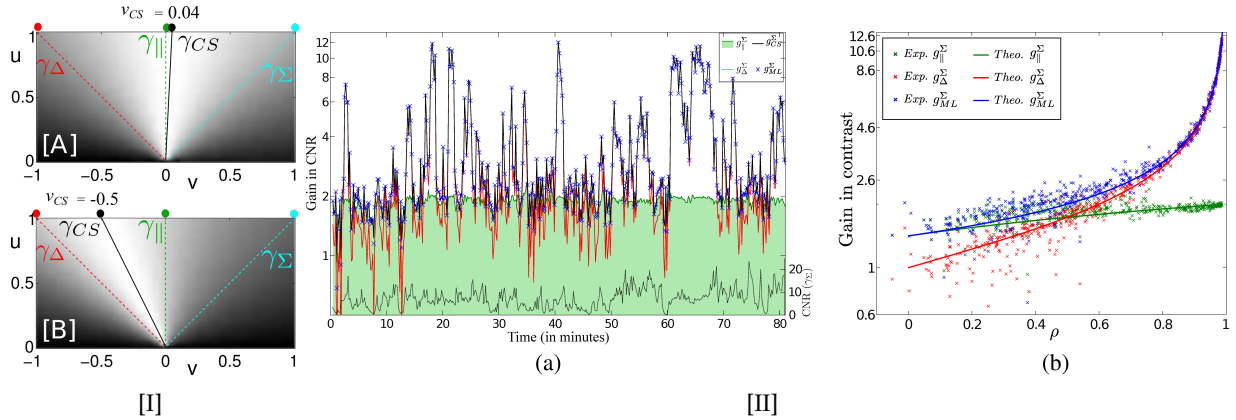

Figure 5.5: [I] Example on frames [A] and [B] of the computational search for an optimum contrast-maximizing linear combination of polarimetric images. [II] (a) Time evolution over a 80 minutes dataset of the gain in CNR of various polarimetric representations, with respect to a standard intensity image. (b) Gain in CNR represented as a function of estimated correlation coefficient ρ (symbols, same dataset), and comparison with theoretical gain expressions (solid curves) for two standard polarimetric representations $\gamma_{||}$ and γ_{Δ} and the optimal adaptive representation Γ_{ML}.

As a consequence, it can be interesting to investigate whether a closed-form expression of an optimal representation suited to the conditions at hand can be obtained using an information theoretical approach . In an anterior theoretical work [Fad14a] (see AA II-2, p. 174), we have shown that a simple Gaussian noise model including partial correlation in the noise features of the polarimetric channels could lead to interesting results in terms of optimal variance bounds – obtained by computing the Fisher Information of the estimation problem at hand – and on optimal estimation strategies in the Maximum-Likelihood (ML) sense [Fad14a], as recalled in Chapter 4. Indeed, it appeared on the experimental data gathered that the noise corrupting the images was well modeled by gaussian fluctuations, and that significant correlation could be identified between the two polarimetric channels. Such partial correlation is understandable as the polarimetric camera used in our setup operates in a snapshot mode, and therefore the spatio-temporal fluctuations of the turbid atmosphere (due to wind, turbulence, etc.) and possible temporal source fluctuations are identically reproduced on the two images acquired simultaneously.

Considering the most general case of a partially polarized beacon of DOP P and a partially polarized background of DOP β, we therefore modeled the bidimensional measurement vector $\mathbf{X}_i^P$ at pixel i by a bivariate Gaussian random variable with covariance matrix

$$\Gamma_i = \left\langle \left(\mathbf{X}_i^P - \langle \mathbf{X}_i^P \rangle\right)\left(\mathbf{X}_i^P - \langle \mathbf{X}_i^P \rangle\right)^T \right\rangle = \begin{bmatrix} \frac{1+\beta}{2}\epsilon_i^2 & \rho\frac{\sqrt{1-\beta^2}}{2}\epsilon_i^2 \\ \rho\frac{\sqrt{1-\beta^2}}{2}\epsilon_i^2 & \frac{1-\beta}{2}\epsilon_i^2 \end{bmatrix}, \tag{5.2}$$

and mean value $\langle \mathbf{X}_i^P \rangle = \begin{bmatrix} \frac{1+P}{2}s_i + \frac{1+\beta}{2}b_i \\ \frac{1-P}{2}s_i + \frac{1-\beta}{2}b_i \end{bmatrix}$. The correlation parameter ρ accounts for the partial correlation of noise between the two polarimetric channels, and the source (respectively background) mean intensity is denoted by s (respectively b). The detector electronic noise contribution has been neglected here for the sake of simplicity[60].

[60] See [Fad14a] for further discussion about the influence of the detector electronic noise.

For the sake of brevity and to favour the physical insight about the theoretical results derived from this model, we refer the reader to [Fad14a] (AA II-2) for the full details of their derivation. A first outcome of these results is the demonstration that the optimal representation, in the sense that it derives from a ML estimation procedure known to be minimum-variance under Gaussian fluctuations, corresponds to a simple linear combination of the two polarimetric images, according to the computational search procedure implemented above. In the most general case of possibly unperfectly polarized beacon $P \in [0,1]$ and partially polarized background $\beta \in [0,1]$, the optimal polarimetric representation indeed reads:

$$\gamma_{ML} = \left[\sqrt{\frac{1-\beta}{1+\beta}} - \rho\frac{1-P}{1+P}\right] x_{\parallel} + \left[\frac{1-P}{1+P}\sqrt{\frac{1+\beta}{1-\beta}} - \rho\right] x_{\perp}, \tag{5.3}$$

with ρ denoting the background noise correlation coefficient, estimated in practice over region χ_k. Interestingly, in the actual physical conditions of the experiments conducted in real fog for which we checked that we always had $P = 1$ and $\beta = 0$, the optimal estimator has a very simple expression [Pan15a] $\gamma_{ML} = x_{\parallel} - \rho\, x_{\perp}$, i.e., it suffices to weight the perpendicular image with the opposite noise correlation coefficient $\hat{\rho}$ estimated empirically in the image.

As detailed in [Pan15a] (see AA II-3, p. 186), we checked the optimality of this representation on actual data, by comparing the evolution of the CNR gain $g^{\Sigma}_{ML} = CNR(\gamma_{ML})/CNR(\gamma_{\Sigma})$ obtained with the γ_{ML} representation with respect to a standard intensity image γ_{Σ} in Fig. 5.5-[II].a. The time evolution of g^{Σ}_{ML} is plotted in Fig. 5.5-[II].a with blue crosses symbols, and can be seen to closely follow the best possible gain obtained with γ_{CS} (plotted in black solid line), i.e., with a computational search over all possible linear combinations. This is an interesting result, confirming on the one hand the efficiency of the ML approach, and on the other hand, allowing the optimal representation to be obtained in an analytical way. Moreover, this simple representation behaves adaptively to present the best source contrast in the final image for any fog density condition, since it was shown to depend on the actual experimental conditions which are assessed by the estimation of the correlation parameter ρ [Pan15a].

We were also interested in studying the behaviour of the gain in CNR for each representation in relation with the noise statistics in the polarimetric images. According to the theoretical developments presented in [Fad14a], the gain in CNR of each standard representation with respect to standard intensity imaging can be readily obtained, and the expressions are recalled in Table 5.1. As for the maximum expectable gain in CNR (obtained with the ML representation as it saturates Cramer-Rao inequality), we showed in [Fad14a, Pan15a] that it can be derived from the ratio of the Fisher information ${\mathrm{I_F}}^{P}(s)$ accessible with polarimetric measurements for the estimation of the source mean intensity s, to the Fisher information accessible with standard intensity measurements ${\mathrm{I_F}}^{I}(s)$. In the most general case of arbitrary P and β, and with neglegible detector noise, the expression of the gain is

$$\mu_{opt}(P,\beta,\rho) = \frac{{\mathrm{I_F}}^{P}(s)}{{\mathrm{I_F}}^{I}(s)} = \frac{(1-2\beta P+P^2) - \rho(1-P^2)\sqrt{1-\beta^2}}{(1-\rho^2)(1-\beta^2)}. \tag{5.4}$$

This theoretical expression has been extensively analyzed in [Fad14a] (see AA II-2). From this result, it is quite straightforward to derive the theoretical optimal gain in CNR with respect to the intensity-summed image γ_{Σ}, which in our conditions for $P = 1$ and $\beta = 0$, yields $g^{\Sigma}_{opt} = \sqrt{2/(1-\rho)}$, as recalled in Table 5.1[61].

We found very relevant to analyze the evolution of the gain in CNR for each representation as a function of the estimated background correlation ρ. This is plotted in Fig. 5.5-[II].b, where it can be seen that the CNR gain for each representation depends on ρ in an orderly fashion which was not

[61] The comparison between the expression of g^{Σ}_{opt} and $\mu_{opt}(P=1,\beta=0,\rho)$ reveals that $g^{\Sigma}_{opt} = \sqrt{(1+\rho)\mu_{opt}(1,0,\rho)}$. The correction factor $\sqrt{1+\rho}$ in the expression of g^{Σ}_{opt} accounts for the fact that a true intensity image as considered in the information theoretic treatment when computing ${\mathrm{I_F}}^{I}(s)$ is not strictly equivalent in terms of noise variance to a intensity-summed image $\gamma_{\Sigma} = I_{\parallel} + I_{\perp}$.

obvious in the "noisy" time-series data in Fig. 5.5-[II].a, and which fairly coincides with the theoretical expressions of the gains in CNR derived and recalled in Table 5.1. In this figure, the optimality of the ML representation appears clearly, since it approaches the best contrast representations for all values of ρ. It is interesting to notice that the polarization difference image γ_Δ is outperformed by the polarization-filtered image $\gamma_\parallel$ as the value of ρ falls bellow 0.5, but as soon as $\rho \geq 0.5$, the gain in CNR provided by γ_Δ rises steeply when $\rho \to 1$, leading in this experiment to gains of more than twelve-fold. This is easily interpreted as the main benefit of γ_Δ relies in its ability to suppress highly structured (and thus correlated) background in the final image. On the other hand, with uncorrelated background ($\rho = 0$), the perpendicular image $I_\perp$ does not bring any further information, making $\gamma_\parallel$ optimal in very low visibility conditions [Fad14a, Pan15a].

5.2.3 Conclusion

Such a study about the optimal contrast-enhancement of a polarized beacon through turbid atmosphere over long distances has permitted an original experimental facility to be settled on the campus of the University of Rennes 1. The large amount of experimental data gathered has revealed interesting features about propagation of polarized light in fog, which in turn motivated the development of original signal processing strategies for all-weather adaptive contrast enhancement. Clever software implementations of the simple optimal polarimetric representation have also been proposed [Pan15b], demonstrating that such computationally-efficient representation could be easily implemented in real-time applications as a pre-processing task for automated detection/localization on wide field images.

More generally, this study has shown that such a polarimetric approach could be an efficient, simple and cost-effective way to obtain clear background rejection, and hence better detectivity of polarized beacon in obscured weather conditions. However, despite the significant gain in contrast obtained with this polarimetric system, this approach fails to perform true ballistic photon filtering. Indeed, it was observed that light polarization was not relevant in the context of long-range imaging to effectively discriminate ballistic photons from diffused photons. In the next section, we shall consider intensity-modulation as a possible way to achieve true ballistic photon imaging.

5.3 Ballistic photon imaging through turbid media using intensity-modulated light

This section summarizes the first contributions and results obtained at the Optics and Photonics Department in the domain of ballistic photon imaging through turbid media using intensity-modulated light. Indeed, this technique appears as an interesting compromise between efficiency and cost-effectiveness. On the one hand, using of pulsed lasers and time-gated cameras provide very efficient means of performing 3D imaging with time-of-flight measurements along with true ballistic filtering by detecting only the *fastest* photons corresponding to ballistic propagation. However, this is achieved to the expense of very complex and costly imaging systems, which are hardly compatible with the application initially aimed at, namely, the assistance to navigation in obscured weather conditions.

On the other hand, with the recent development of light sources such as LEDs that are easy to modulate at relatively high frequencies, and with the availability of first generation of demodulating image sensors such as the time-of-flight (ToF) cameras, using continuous wave intensity modulation (as a counterpart to time-gated imaging) appears as an interesting way to achieve ballistic imaging at relatively low cost.

In the remainder of this section, we shall first briefly describe an experimental work conducted in Bangalore in collaboration with our colleague Hema Ramachandran. This experiment illustrates how low-frequency intensity-modulation and an accelerated implementation of a software demodulation technique can allow real-time contrast enhancement through turbid media to be achieved in a simple

and efficient way. However, to achieve true ballistic filtering, high modulation frequency operation is needed. We analyzed this issue in a theoretical work relying on information theory and diffusion approximation to derive the optimal modulation frequencies for ballistic photon filtering in diffusing media. The main aspects and results of this study will be summarized below ina second section. Lastly, we shall conclude this chapter by presenting a novel imaging system architecture that we recently patented in 2016 [Pan16b], and which allows full-field snapshot quadrature demodulation of high-frequency components of an image to be performed without requiring any synchronization with the emitter. This last original contribution opens a large number of scientific perspectives in terms of instrument developement but also in the field of biomedical imaging.

5.3.1 Contrast enhancement by low-frequency quadrature software demodulation

Within the course of the collaborative CEFIPRA project with Prof. Hema Ramachandran, from the Raman Research Institute (Bangalore, India), I had the opportunity to travel several times to India for 2-week periods each time, allowing me to participate to a number of experiments that were to be developed in India within the project. One of these experiments consisted of performing contrast enhancement of an active beacon in strongly scattering medium, by efficient background rejection using an intensity-modulated light. The main objective of this study was to demonstrate the feasibility of such background rejection in real-time (i.e., faster than the natural human eye flicker), using low-frequency modulation and hence a cheap apparatus including (almost) standard laptop computation resources. Assuming that the modulation frequency is known, we showed how a quadrature demodulation scheme could outperform a simple spectral (Fourier) analysis of the temporal evolution of the graylevel at each pixel in the image, either in terms of demodulation performance or in terms of computation speed.

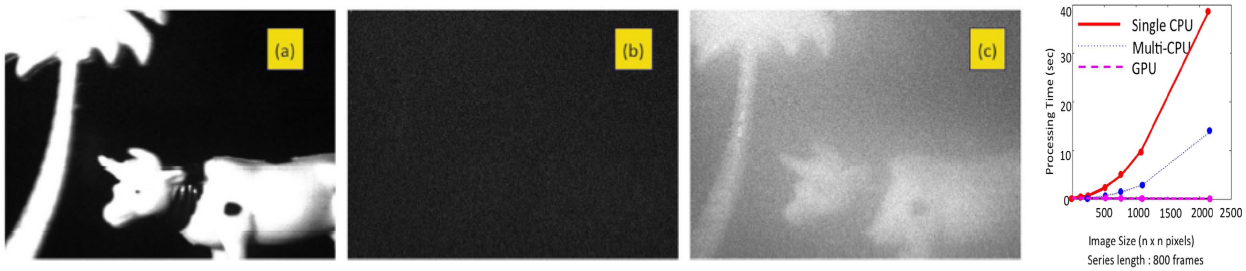

[I] [II]

Figure 5.6: [I] Illustration of the efficient background removal reachable using a low frequency intensity-modulated illumination and a real-time software quadrature demodulation: (a) original scene without scattering medium; (b) scene observed with a standard intensity camera; and (c) demodulated image allowing visibility of the scene to be partly recovered. [II] Illustration of the computational speed-up offered by multithreading and GPU programming.

One of the main contribution of our work was to show that the quadrature demodulation, which could be operated here by software at low modulation frequencies ($\sim$ 10-100 Hz), could be highly accelerated to reach real-time acquisition, computation and display by using multithreading programming and parallel computation on graphical processing units (GPUs). These results will not be detailed here for the sake of conciseness, but can be found in [Sud16]. We simply comment here a convincing example of experimental acquisition and final processed image in Fig. 5.6-[I]. When imaged by a standard camera through a thick scattering medium (in laboratory, milk suspension in small tank), the objects in the scene (a palm tree and a cow, see Fig. 5.6-[I].a) which are enlightened by modulated light ($f_{mod} = 17$ Hz) are absolutely indiscernable, as can be observed in Fig. 5.6-[I].b. However, after quadrature demodulation at f_{mod}, the two objects appear clearly in the final image,

which is demodulated and displayed in real time with the optimized processing proposed in [Sud16]. In addition, Fig. 5.6-[II] shows the huge acceleration offered by multithreading and GPU computation approaches for this demodulation issue.

These results appear already very interesting for practical applications to ensure highly efficient background rejection of ambiant, unmodulated light and to disciminate active sources (or passive targets, but enlightened as in the above example) in strongly scattering media or atmosphere. However, the very low frequency operation of the modulated illumination does not permit any true ballistic filtering. Indeed, in this case and for the short propagation distances considered here (and even for the kilometric range we aim at, in the final scenario), the ballistic photons as well as the diffuse photons arrive at the detector with the same modulation index, and without any discernable phase difference. In the next section however, we briefly summarize a theoretical study that we conducted using information theoretic tools and diffusion theory to quantify the minimum modulation frequency that would be required for given optical properties (scattering, absorption) of the scattering medium.

5.3.2 Optimal modulation frequencies for ballistic photon filtering in turbid media

The diffusion theory for photon transport provides a simple, fast and analytical method for modeling light propagation through turbid media. The properties of intensity modulated light through a diffusing medium have been well studied and reviewed [Pat89, Mar97, Fis93, Gra97]. The diffusion model arises when the photons are allowed to perform a random walk, diffusing from high photon density regions to low photon density regions. The theory has proved efficient when modeling light in a predominantly scattering medium where the source and the detector are far from boundaries of the medium and when detection is carried out sufficiently away from a point source, in a supposed infinite geometry.

For the problem at hand, we considered an intensity modulated source of light having modulation angular frequency ω and amplitude modulation index M (also termed *modulation depth*), whose intensity reads $i(t) = I_0(1 + M\cos\omega t)$. After propagation through a scattering medium, the ballistic light that follows Beer-Lambert's law is only attenuated and reaches the detector with instantaneous intensity $i_b(t) = I_B(1 + m_B\cos\omega t)$ without any change in received modulation index, $m_B = M$, but with reduced mean intensity $I_B \ll I_0$. The attenuation I_B/I_0 mainly depends on the total extinction coefficient $\mu+\mu_s$ (inverse value of the mean free path MFP), where μ and μ_s respectively stand for the absorption coefficient and the scattering coefficient of the medium. Consequently, for a propagation distance of r, we can define an effective attenuation factor for the ballistic light as $R_b = r/MFP$, such that $I_B/I_0 \sim e^{-R_b}$.

On the other hand, using the model of the propagation of sinusoidally modulated light through a scattering medium as derived in [Tro93, Fis93, Jac08], it can be analytically shown that the modulated light is received at the detector with reduced modulation index and additional phase [Tro93]. Within the framework of diffusion theory, the instantaneous diffuse light intensity received at the detector is shown to read $i_d(t) = I_D(1 + m_D\cos\omega t + \Delta\phi)$, where the condensed expression of the reduced modulation index m_D and the phase $\Delta\phi$ respectively read[62]

$$m_D = Me^{-R_\delta(q-1)}, \tag{5.5a}$$

$$\Delta\phi = R_\delta\sqrt{q^2-1}. \tag{5.5b}$$

The parameter R_δ corresponds to the reduced propagation distance, normalized by the optical penetration depth $\delta = \left[3\mu(\mu + (1-g)\mu_s\right]^{-1/2}$ in the scattering medium, i.e., $R_\delta = r/\delta$, with g standing for the scattering anisotropy factor[63]. If R_δ only depends on the medium properties, the dimensionless

[62] As for the mean attenuation of the diffuse light component, one can show that $\alpha = I_B/I_D$ is related to the geometry of the illumination source and to the scattering parameters of the medium (see [Pan16a] for further details).

[63] Defined as the mean cosine of the scattering phase function [Ish78] (see [Pan16a] for further details about the derivation of these results and the problem parameterization).

parameter $q = \sqrt{(1+\sqrt{1+(\omega/\mu c)^2})/2}$ appearing in the above equation, is related to the angular frequency of modulation, and ranges between $[1,\infty)$ when $\omega \in [0,\infty)$. Although the physical interpretation of this parameter is not straightforward, we were able to interpret qR_δ as a dimensionless, frequency-dependent, effective attenuation of the modulation index of the diffused light. More precisely, in the following we denote by $\beta = m_B/m_D$ the ratio of the modulation indices of ballistic light to diffuse light. It can now be clearly understood from this analytical model how intensity-modulated light can be used to achieve ballistic-photon filtering and imaging: it suffices to select a modulation frequency ω sufficiently high such that the modulation index of the diffused light contribution fades out after demodulation of light at the detector location.

To complement this physical propagation model and to describe the imaging system, we considered a classical noise model [Muf11] describing the intensity fluctuations of a possible demodulating imaging scheme. More precisely, we assumed that the detector was able to perform, at each pixel location, a so-called *4-bucket* temporal sampling of the modulated signal, as represented in Fig. 5.7-[I] [Pan16a] (see AA II-4, p. 193). With such noise model, we were able to compute and compare the Fisher information (FI) for the estimation of the modulation index M with ballistic photons on the one hand, and with diffuse photons on the other hand. We were then in a position to define the gain in information by the ratio of the FI when observing diffused and ballistic photons to the FI when observing diffused photons only. The expression of the gain thus reads

$$\mathcal{G}_{bf} = \frac{I_{\mathcal{B}\oplus\mathcal{D}}(M)}{I_{\mathcal{D}}(M)} \sim K_1 e^{2(qR_\delta - R_b)}\Big(1 + K_2 e^{-(qR_\delta - R_b)}\cos[\sqrt{2(q^2-1)}R_\delta]\Big), \tag{5.6}$$

where K_1 and K_2 in the right-hand-side asymptotic expression of $\mathcal{G}_{bf}$ are polynomials expressions of the imaging geometry and scattering parameters [Pan16a]. From the above approximate expression of the gain, it appeared clearly that a significant gain could occur only if

$$q > R_b/R_\delta = \frac{\delta}{MFP}, \tag{5.7}$$

i.e., if the effective attenuation of the modulation index of the diffused light is greater than the effective attenuation for ballistic photons. The minimum frequency condition – which interestingly appears to be independent of the propagation distance r – has a simple expression when expressed in terms of the parameter q, since it only depends on the relative magnitude of the mean free path (MFP) and of the optical penetration depth δ defined above. When expressed in terms of angular frequency ω, the expression is more involved, but the gain condition can be plotted as the red dashed line on the contour maps in Fig. 5.7-[II] and seems to provide a well-defined condition for attaining ballistic gain. Further simplification holds under the validity conditions of the diffusion theory, where $\sigma > 10\mu$. In this case, the condition for achieving ballistic filtering reduces to $\omega/c > 2\sigma/3(1-g)^2$, and is insensitive to the value of the absorption coefficient μ. This clearly indicates that filtering of ballistic photons using an imaging demodulation technique will be more difficult, and hence require higher modulation frequency, in forward anisotropically scattering media with $g > 0$. Indeed, this can be physically understood, as diffused photons will be less likely to deviate from the ballistic path in a significantly forward scattering medium.

According to the above results, ballistic filtering in biomedical applications would require very high (if not unrealistic) modulation frequencies, as for typical values of $\sigma = 10$ cm^{-1}, refraction index $n = 1.33$, and a propagation distance $r = 5$ cm, one obtains $f_{min} = 23.9$ GHz (respectively $f_{min} = 597$ GHz) when $g = 0$ (respectively $g = 0.8$)! The expression derived above can also serve conversely to provide the range of visibilities that can be handled by a ballistic filtering device working at any fixed modulation-demodulation frequency. For instance, for transport safety in foggy weather, if we consider $r = 1$ km, $n = 1.33$, and a modulation frequency of $f = 10$ MHz, the above rule of thumb indicates that ballistic filtering can be obtained when $\mu_s \leq 0.42$ m^{-1} (respectively $\mu_s \leq 0.084$ m^{-1}) when $g = 0$ (respectively $g = 0.8$). According to the World Meteorological Or-

ganization's recommendations [WMO08], such values of μ_s correspond to very low visibilities (in terms of meteorological optical range $MOR = 3/\mu_s$) of 7.5 m (respectively 36 m), still assuming a homogeneous, mostly scattering medium ($\mu_s \gg \mu$).

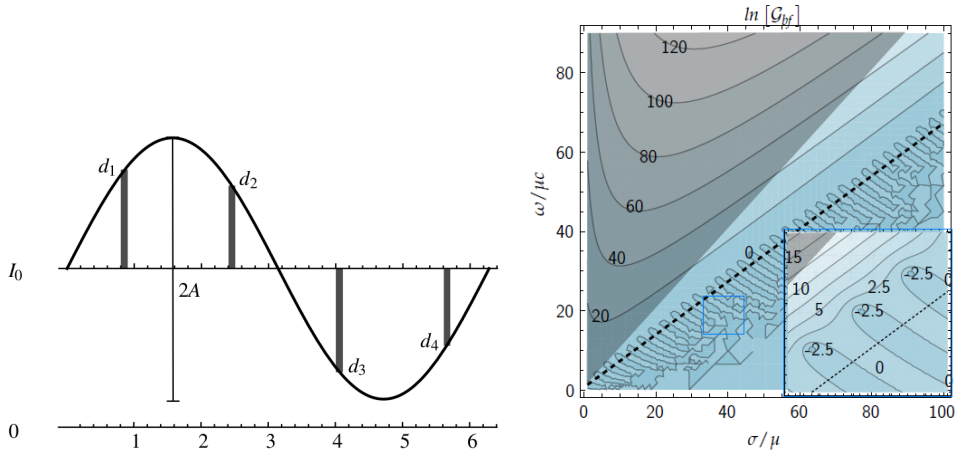

Figure 5.7: [I] Illustration of the *four-bucket* temporal sampling of a signal. I_0 stands for the average intensity, wheras A denotes the amplitude of the modulation. [II] Contour plot of the logarithm of the gain $\mathcal{G}_{bf}$ expressed in Eq. (5.6) for range $\sigma/\mu \in [1, 100]$ and $\omega/\mu c \in [0.01, 90]$, with anisotropy factor $g = 0$. The inset shows a zoomed-in section of the plot where the effect of the cosine term is clearly visible. The condition of Eq. (5.7) for expecting a gain is displayed as the black dashed line. The diffusion approximation remains valid in the unshaded region.

In addition to these interesting indications about the feasibility of ballistic photon filtering using intensity-modulated light, we also studied the optimal modulation frequency for parameter estimation in scattering media/tissues. This issue is of great interest in the biomedical imaging domain, since estimating and imaging the scattering parameters makes it possible to produce inhomogeneity maps revealing internal structures or inclusions in the biological tissues. By deriving the Fisher information matrix (and hence the corresponding Cramer-Rao lower bounds on estimation variance) for the estimation of the scattering parameters (see [Pan16a], AA II-4), we analytically demonstrated the existence of an optimal modulation frequency, which had already been predicted through numerical simulations, and observed experimentally. This optimal modulation frequency is shown to be solely a function of optical penetration depth δ and the source-detector distance r through

$$\omega_{opt} = \mu c \sqrt{\frac{2}{R_\delta^4}} \sqrt{1 + \sqrt{1 + 4R_\delta^2} + R_\delta^2 \left(3 + \sqrt{1 + 4R_\delta^2}\right)}. \tag{5.8}$$

These theoretical results allowed us to evaluate the range of frequency at which one should operate to perform optimal scattering parameter estimation/imaging or ballistic filtering/imaging. Providing an analytical form of these optimal frequencies, these results are in agreement with previous experiments and numerical simulations implementing more complex photon propagation models (typically, Monte-Carlo solving of Boltzmann's transport equation) [Tor03, Kim08]. The minimum frequencies required for efficient ballistic filtering appear to be relatively high, and beyond the capabilities of standard full-field imaging systems. This raised the question of developing an optical setup able to answer such technological issue at relatively low cost and complexity. This issue is addressed in the last section of this chapter, were we report the first modeling and experimental developments of a full-field quadrature demodulating camera.

5.3.3 Prototype of an all-optical full-field quadrature demodulating camera

As seen above, for typical distances encountered in aerial navigation (kilometric range) and for typical scattering parameters of fog, it turns out that the minimum modulation frequency required should lie above 10 to 100 MHz. Such figures, which could have seemed unrealistic a few years ago, are now perfectly conceivable, at least from the emitter side, with the availability of cost-effective and energy-effective semiconductor LED lamps which can be potentially modulated at such high frequencies (in the radiofrequency RF range) as evidenced by the development of LIFI[64] communication systems with low-power LEDs. To reach long range imaging capabilities, there is no major technological bottleneck preventing from modulating high-power LEDs in the RF domain, or at least large arrays of smaller LEDs. As a result, there is a strong need to design and develop an imaging system able to demodulate and detect such high-frequency modulated sources in real-time and with limited cost and bulk, which could be embarked in small aircrafts or drones to help in navigation/target detection tasks. Demodulation of light at radio frequencies and higher poses practical challenges like phase synchronization, timing jitters etc., and no existing technology is currently able to answer it perfectly:

- Scanning single pixel imaging systems like LIDARs (LIght Detection And Ranging) – which have been used since many decades as demodulation imagers and are still in active use in both military and civil applications – do not offer full-field instantaneous demodulation;
- Modulated gain intensifier cameras (iCCDs) have also been tested as full-field demodulating cameras. Indeed, the voltage controlled gain can act as a fast shutter that may be used to demodulate multiple pixels at the same time [Pay08]. However, they require synchronization with the emitter(s) and high voltage (4 kV - 8 kV) electronics. Moreover, they are bulky and rather expensive for a very poor spatial resolution and dynamics;
- Time-of-Flight (ToF) cameras provide a compact and inexpensive means of correlating an optical source signal with an internal reference electronic signal to estimate the intensity, amplitude and phase received at each pixel for frequencies typically between 5 to 30 MHz so far [Muf11, Li14]. However, ToF cameras suffer from a number of limitations, in terms of maximum operating frequency (limited commercially to 40 MHz until now) and frequency tunability (no continuous tunability), low resolution (typically 320×240 pixels) and dynamics. Moreover, ToF cameras have different architecture and fabrication from standard cameras, which prevents the use of conventional, high quality cameras.

The limitations of the above mentioned state-of-the-art techniques thus pave way for a technological advancement to fill the gap in the high frequency full-field optical demodulation area. Owing to this, and within the course of the CEFIPRA project conducted in collaboration with Pr. Hema Ramachandran, we recently proposed and patented an innovative system inspired from the well-known quadrature ("I/Q")demodulation approach in electronics [Pan16b]. Such an approach is robust to timing jitters and provides demodulation without a need of a synchronization signal. This last advantage is especially important when the source and detector are far apart and a synchronization signal may not be available. For example, when using modulated light for assisting in aircraft landing and taxiing, the source on the ground and the on-board demodulating camera should preferably be independent and demodulation be operated without synchronization. In a quadrature detection scheme, both the received amplitude and the relative phase of the signal can be estimated without need of a synchronized source. We very recently established the proof-of-concept of such a full-field quadrature demodulation camera (referred to as ffQDC in the following) by designing and building a preliminary low-frequency version, in the visible range, of a stand-alone all-optical modular device which could be inserted in front of any conventional camera in order to offer full-field demodulation of spatially distributed modulated sources, without requiring synchronization. The sketch of

[64] or VLC (visible light communication).

the setup and a photograph of our initial prototype are given in Figs. 5.8-[I] and 5.8-[II]. The modularity of the optical setup offers strong versatility and potential use in numerous domains, as a user could choose between inexpensive web-cameras and HD cameras to EMCCDs and low-noise, high dynamics cameras depending on the application area.

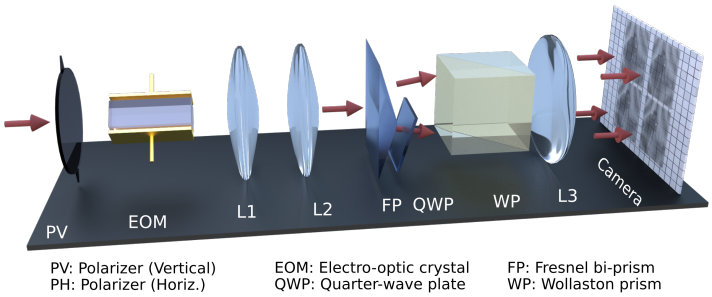

[I]

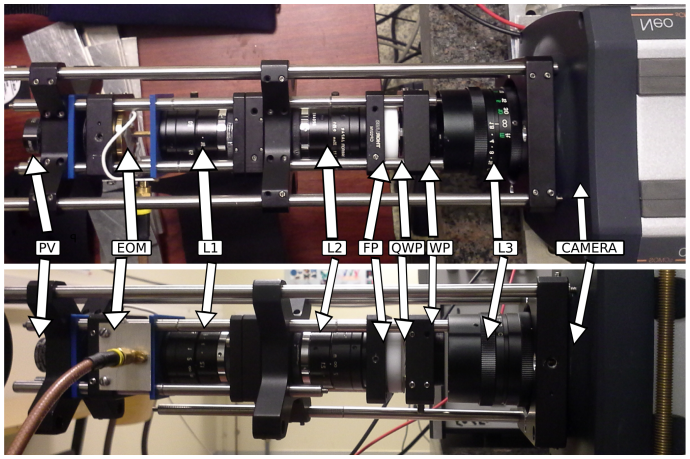

[II]

Figure 5.8: Schematic 3D view [I] and photograph [II] of the first prototype of a full-field quadrature demodulating camera proposed and developed in the laboratory. At the heart of the system, an EOM is driven by an external high voltage source, and appropriate beam separating prisms are used to retrieve four images simultaneously with four distinct demodulation phases, allowing four-bucket sampling to be performed instantaneously on a single detector.

Our technique, unlike in electrical shuttering approaches, first preserves the average incoming optical power, and second, it does not require any image intensifier but only a basic camera. Moreover, the demodulation is performed directly in the optical domain, (it does not rely on specific electronics embedded in the pixel matrix as in ToF cameras). Thus our invention has the potential to be portable with moderate power requirement. Most importantly, this new concept is not limited by the camera speed and is able to handle demodulation frequencies ranging from a few Hz up to several GHz, without requiring synchronization between the modulating and demodulating parts (source and receiver). At the heart of the imaging system proposed lies an electro-optic (EO) modulator. Based on a specific arrangement of a birefringent electro-optic crystal (such as Lithium Niobate) and two crossed polarizers oriented at 45° from the crystal optical axes, it is possible to obtain a voltage-controlled optical gate. The transfer function created is a cosine function of the phase induced in the EOM by the input voltage. When a ramp voltage of $V_\pi \times \omega t/\pi$ is applied as a function of time t,

the transfer function is oscillatory with an angular frequency of ω, which should correspond to the angular frequency of the sources to be demodulated in the image. As a result, such a sinusoidal optical transfer function operates a product demodulation of the incoming light passing through such arrangement at angular frequency ω. With a simple modification of this optical configuration, it is possible to detect simultaneously the quadrature component of the modulated light, still with a single electro-optic crystal (to limit the requirements in electronics and optical components). Indeed, a transfer function that is in quadrature with the above described configuration can be achieved easily by introducing a quarter-wave plate (QWP) before the exit polarizer. As a result, splitting the beam at the exit of the EO crystal allows one to obtain the in-phase and in-quadrature information simultaneously, by passing the first split beam into a polarizer and the second split beam through the juxtaposition of a QWP and the exit polarizer. Finally, a last step of polarization-insensitive beam splitting, provided by a Fresnel biprism arrangement, allows four images to be detected simultaneously on the same sensor. As a result, it can be shown that these four images sample the modulated signals in each pixel of the image with four equidistant phases, allowing an equivalent "four-bucket detection" to be achieved in a snapshot acquisition by spatial multiplexing [Pan16b].

A sketch of the optical setup enabling all-optical quadrature image demodulation is provided in Fig. 5.8-[I]. The last stage of classical quadrature demodulating electronic circuits that consists of temporal integration via a low-frequency low-pass filter is here automatically performed by the integration time of the camera itself. Any conventional camera with exposure time longer than the time period of modulation can be used, thereby ensuring high versatility of the proposed optical setup utilisable with any commercially available camera. It must be noted that in the presence of intense background illumination, acquiring the four images as described above also enables the spurious background illumination to be suppressed, along with quadrature demodulation of the signals of interest in a single frame. Finally, the magnitude and phase of the detected signals in the image is then directly obtained by squaring each image, and adding them together. In this case of single-shot I/Q demodulation, the relative phase stability required between emitter and receiver is limited to the integration time of a single frame on the camera, which can be of the order of 100 μs. This figure is very interesting for the application aimed at in this project, namely the assistance to a pilot for landing through obscured atmosphere. The relative motion of the airplane with respect to the light beacon will indeed impose lowest time stability requirements on the demodulation.

Currently, preliminary experimental acquisitions and results (that will not be described here for the sake of concision) obtained with our first prototype (see Fig. 5.8-[II]) allowed us to initiate the proof-of-concept of the setup at low-frequency (200 kHz). This imaging setup requires an important calibration step which has been developed within the PhD thesis of S. Panigrahi to compensate for all experimental imperfections, amplitude/phase mismatches at each pixel, etc. As a function of the exposure time, we were able to measure quality factors of about $\Delta f = 5$ Hz for an exposure time of 200 ms, whereas $\Delta f \simeq 1Hz$ for an exposure time of about 1.5 s, for a central modulation frequency of 15 kHz. These figures appear to be compatible with efficient frequency discrimination with standard camera exposure times. This new concept of a demodulating add-on for standard camera has been patented in 2016 [Pan16b], and an article is in preparation about the optical design, calibration, and first experimental validation of this full-field quadrature demodulating camera. The development of this new camera constitutes an important perspective for future work, as will be more precisely described in the next part of this document.

Conclusion

The contributions to imaging through turbid atmosphere that have been described in this chapter showed that efficient contrast enhancement of an active polarized beacon could be performed at low-cost, with a simple imaging device, and algorithmically efficient processing enabling real-time capabilities. On the other hand, performing true ballistic filtering using intensity-modulated light appears as a more difficult challenge, requiring high frequency operation, and thus the development

of original imaging systems able to perform reference-free image demodulation at such high frequencies. A concept of a novel imaging setup has been described to solve this technical issue, which is currently being tested and validated in the laboratory.

Besides these achievements, this chapter has permitted to show how the interplay between the physical modeling of light propagation in turbid media and of the image formation, the statistical description of the noise properties, and some basic concepts of information theory made it possible to design efficient processing strategies, and to derive relevant figures of merit for the design of future experiments. Closing the loop, these theoretical results have been sucessfully validated on experimental results in the first study using light polarization, whereas they motivated the design of an original optical setup for image demodulation in quadrature at high speed in the second study.

Chapter 6

MDL model selection for unsupervised optical spectroscopy

The context of the work described in this last chapter is unsupervised optical absorption spectroscopy in the infrared range for air pollution monitoring or noxious gas remote detection in the atmosphere. This work has been initiated and mostly conducted during my post-doctoral stay at ONERA (the French aerospace Lab) in Palaiseau, as a post-doctoral engineer. In a monitoring context, a single instrument should ideally be able to detect and quantify numerous gas species, thus imposing wide spectral range operability. Narrow-line tunable lasers have been used in multi-wavelength systems like DIfferential Absorption Lidars (DIAL) [Wei04, Qua97] and Tunable-Diode Laser Absorption Spectroscopy (TD-LAS) [Wys08], however, the recent development of mi-infrared instantaneous broadband sources such as supercontinuum fiber lasers has motivated the design of experimental supercontinuum lidar systems for wideband absorption spectroscopy [Kaa07, Bro08, Cez11, Cez14].

All these techniques provide multi-spectral absorption data that can be processed by standard multivariate statistical analysis in order to characterize the gas mixture [War96, Yin06, Fad10], provided the number and nature of the chemical species are a priori known. In practice however, in a monitoring system, the number, nature, and concentration of gas components are all likely to be unknown. It is therefore necessary to design unsupervised methods enabling model selection (to identify the gas components) and concentrations estimation simultaneously. As described in Chapter 4, the MDL approach appears as a good candidate for designing unsupervised model selection algorithms. During my post-doctoral stay at ONERA (French Aerospace Laboratory), I have thus proposed to apply MDL techniques to optical absorption spectroscopy, and I benchmarked their potential with respect to usual penalization criteria on simulated data. In the meanwhile, the development of an experimental supercontinuum lidar facility (in the visible) initiated during my work at ONERA has permitted to obtain first experimental validations on the technique on real data. More recently, I have proposed a slightly modified version of the most efficent MDL approach for optical spectroscopy (so called nMDL, see below) so as to provide control of the probability of false alarm (Pfa), which can be very interesting for the implementation of such algorithm on a real monitoring system. These contributions are briefly summarized in the remainder of this chapter.

6.1 Active optical absorption spectroscopy in the mid-infrared range

Let us first model an active optical absorption spectroscopy experiment, which is sketched in Fig. 6.1-[I]. We shall denote by a M-dimensional column vector $\mathbf{X}$ the intensities detected on M spectral slits (or wavelengths, not necessarily adjacent). In the presence of absorbing gas species, these spectral measurements reveal specific absorption patterns depending on the nature and concentration of the chemicals encountered by the probe light beam. Considering small absorption optical depths, the Beer-Lambert's absorption law can be linearized to obtain a simple linear regression model of the

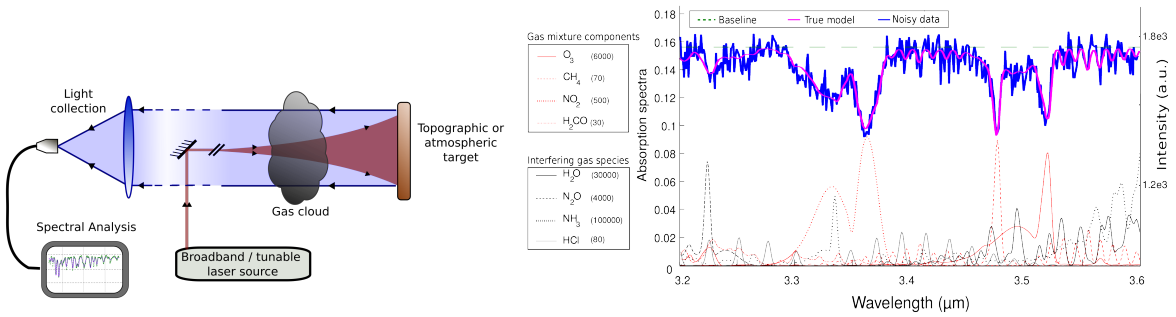

[I] [II]

Figure 6.1: [I] Sketch of an atmospheric optical absorption spectroscopy experiment. [II] Absorption spectra of the 4 gas components present in the mixture (red curves) and of 4 other chemicals of the spectral database (black and green curves).

following form:

$$\tilde{\mathbf{Y}} = \mathbf{b}_0 - \mathbf{H} \cdot \mathbf{c} + \mathbf{n}, \tag{6.1}$$

where $\mathbf{b}_0$ denotes a known spectral baseline[65], and where the absorption features depend on a K-dimensional gas concentrations vector $\mathbf{c}$, and a $M \times K$ matrix $\mathbf{H} = [\mathbf{h}_1, \mathbf{h}_2, \ldots, \mathbf{h}_K]$ contains the absorption spectra of the K gas species[66], an example of which is represented in Fig. 6.1-[II].

For the sake of simplicity, the M-dimensional zero-mean random vector $\mathbf{n}$ modelling the experimental noise is assumed centered Gaussian with unknown variance, and with no correlation between two distinct spectral slits. In that case, given a mixture model $\mathbf{H}$, a simple and optimal estimator for the concentration vector $\mathbf{c}$ is the minimum mean squared error (MMSE) estimator $\hat{\mathbf{c}} = (\mathbf{H}\mathbf{H}^T)^{-1}\mathbf{H}^T(\tilde{\mathbf{Y}} - \mathbf{b}_0)$, which corresponds here to the maximum likelihood estimator (MLE). Indeed, this estimator minimizes the Residual Sum of Squares $RSS = \left\| \tilde{\mathbf{Y}} - \left(\mathbf{b}_0 - \mathbf{H}\hat{\mathbf{c}}\right) \right\|^2$, which can be shown to be related to the loglikelihood of the observed data through the following equation

$$\ell_{\tilde{\mathbf{Y}}}(\tilde{\mathbf{Y}}|\mathbf{H}) = \ln P_{\tilde{\mathbf{Y}}}(\tilde{\mathbf{Y}}|\mathbf{H}) = -\frac{M}{2} \ln RSS + ct, \tag{6.2}$$

where ct denotes an additive constant independent of the measured data.

6.2 Penalized model selection using MDL principle

Although the estimation problem is trivial, the main issue in this data processing task is model selection: how many gas components (regressors) are needed to describe the experimental data, and which regressors have to be selected in the linear regression model of Eq.(6.1) to best explain the observations ? Using the full spectral database of absorbing species in $\mathbf{H}$ would lead to misleading and incorrect results, due to noise overfitting. For that purpose, many penalization methods can be implemented, which basically consist of minimizing the sum of the RSS (data fidelity) and an additive penalization term $\mathcal{C}$. The most classical penalization criteria (so-called *information criteria*) are the Akaike Information Criterion (AIC) [Aka74] ($\mathcal{C}^{(a)} = K$) and its refinements such as AICc[67] and the Bayesian Information Criterion (BIC) $\mathcal{C}^{(b)} = (K/2)\ln M$ [Sch78]. Other information criteria can

[65] This baseline being the spectrum of the active illumination source, possibly modified by the spectral response of a topographic or atmospheric reflecting target as depicted in Fig. 6.1-[I].

[66] Here we assumed that the $\mathbf{h}_i$ are directly convolved by the spectral slit function of the system for the sake of notational simplicity.

[67] In the case of samples of limited size, AIC is commonly replaced by the AICc: $\mathcal{C}^{(a)} = (M+K)/2[M-(K+2)]$ [Han01].

be found in abundance in the literature, suggesting that an appropriate "most efficient" criterion at hand can be designed for a given statistical problem.

As described in Chapter 4, the MDL principle proposes a quite general and systematic framework to interpret model complexity. Interestingly, under Gaussian hypothesis, the BIC corresponds to the simplest form of the MDL: the so-called *two-stage description length*. Indeed, with a M-dimensional data, the code length needed to describe a parametric model H_K with K components can be shown to be equal to approximately $K/2 \ln M$ [Ris07, Han01], whereas one needs a codelength of $-\ell(\tilde{\mathbf{Y}}; H_K) = RSS$ to encode the data residuals under the parametric model H_K. More recently, sophisticated forms of the MDL principle have been proposed, with a constant effort towards loosening the assumptions held on the observed data. For instance, the *mixture* MDL [Ris89] uses a prior distribution on the parameters vector in order to extend the MDL approach to an entire model class (e.g., family of pdf's) instead of restricting it to a single element of the class. Using Zellner's "g-prior", one obtains the so-called $gMDL$ [Han01] whose closed-form expression $\mathcal{C}^{(g)}$ is recalled in [Fad10] (see AA II-5, p. 211) and which was applied to spectroscopic data.

The most recent MDL version pushes forward the generalization of this principle to entire families of distributions [Ris96], relying on the *normalized maximized likelihood* coding scheme [Sht87] which is subtended by the notion of *universal distributions* [Cov91, Myu06]. This approach has proved efficient in various practical problems [Han01, Grü05] and has shown several optimality properties [Ris07, Han01]. The details of the implementation of the so-called nMDL penalization $\mathcal{C}^{(n)}$ are given in [Fad10, Ris07] and omitted here for the sake of conciseness. Though complex, the expressions of $\mathcal{C}^{(g)}$ and $\mathcal{C}^{(n)}$ are analytically computable, hence offering fast processing capabilities.

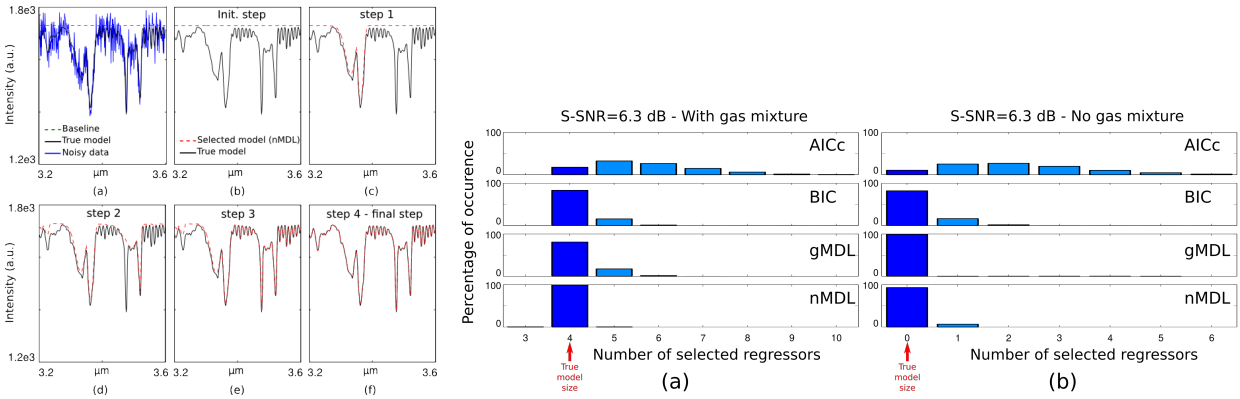

Figure 6.2: [I] Example of simulated noisy data (blue curve) superimposed with the true spectrum (black curve). (b)-(f) Reconstructed signal after various steps of nMDL-based stepwise model selection (red dotted curve). [II] Histograms of the number of regressors selected by AICc, BIC, gMDL and nMDL criteria for S-SNR=6.3 dB, (a): with a 4-component gas mixture; (b): without gas mixture.

Whatever be the penalization selected, solving the minimization issue to reach optimal model selection is operated with a forward stepwise algorithm for the sake of computational speed, instead of performing an exhaustive search among all possible models. At each step of the algorithm, the regressor (i.e., the gas species) that most diminishes the criterion is included in the model, until any further increase in the model complexity leads to an increase of the criterion[68]. An example of iterative model selection is illustrated in Fig.6.2-[I].

To assess the performances of MDL based model selection in spectroscopy, we simulated a typical absorption spectroscopy experiment by numerically generating spectral measurements over $M = 400$ adjacent spectral slits, spanning between 3.2 and 3.6 μm, with a simulated instrumental spectral

[68] This algorithm could be further refined for future developments, for instance by including backward elimination steps to reduce the risk of reaching local minima.

Table 6.1: Percentage of correct models selected by the stepwise algorithm with four information criteria (AICc, BIC, gMDL, nMDL) and for various values of the SNR (a), or for various amounts of outliers measurements (b). The scenario simulated corresponds to a gas mixture with 4 components among a database of 16 interfering species.

(a)					(b)				
S-SNR	AICc	BIC	gMDL	nMDL	% outliers	AICc	BIC	gMDL	nMDL
20.3 dB	16.5	83.6	96.0	>99.9	[S-SNR=6.3 dB]				
14.3 dB	18.6	83.7	92.8	99.9	0 %	17.7	83.1	80.8	98.9
9.8 dB	18.5	83.8	87.6	99.8	5 %	13.7	80.0	75.7	97.4
6.3 dB	17.7	83.1	80.8	98.9	20 %	7.3	62.2	53.6	90.1
4.3 dB	18.0	82.5	76.6	90.0					
2.0 dB	16.4	74.0	63.5	53.5					

resolution of 2.3 nm (Gaussian slit function) and flat baseline. We assumed propagation through a gas mixture with 4 components, namely O_3 (6000 ppm.m), NO_2 (500 ppm.m), CH_4 (70 ppm.m) and H_2CO (30 ppm.m), whose absorption features were significantly overlapping over the spectral bandwidth considered (see Fig. 6.1-[II]). The full spectral database considered in this simulation contained $K_{max} = 16$ gas species, including the 4 gases of the "true" model and 12 spectrally interfering species (such as H_2O, N_2O, NH_3, HCl, etc.).

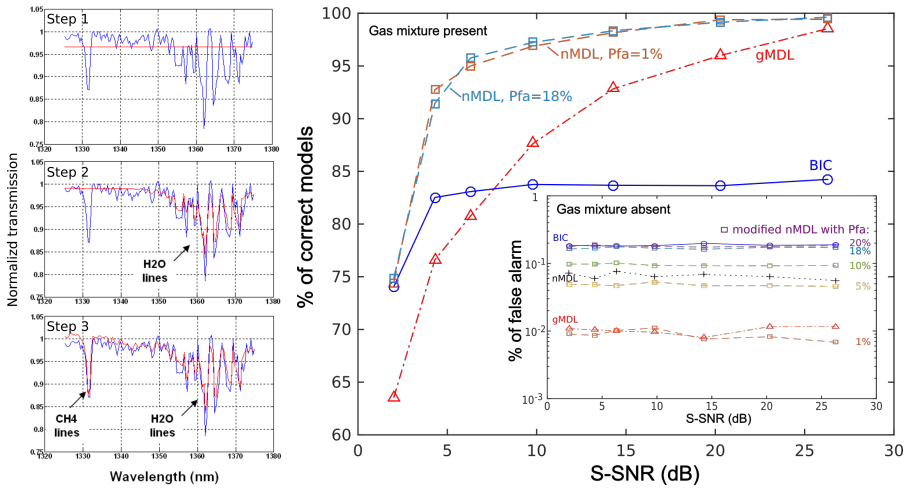

[I] [II]

Figure 6.3: [I] Blue curve: experimental supercontinuum absorption spectrum around 1.3-1.4 μm. Red curves: nMDL-estimated models at iterations 1, 2 and 3 (final). [II] Percentage of correct model selections as a function of the S-SNR with a simulated gas mixture, for two fixed values of Pfa for the nMDL. Inset: Comparison of the Pfa obtained with BIC, gMDL, original nMDL and modified nMDL with various fixed values of Pfa.

The results of the numerical simulations ($N = 20$ acquisitions, $R = 10^4$ Monte-Carlo realizations) are summarized in Table 6.1.a, where the percentage of correct model selections is given for the 4 information criteria compared in this paper and for different SNRs. This table clearly reveals that in the context of unsupervised spectral unmixing, the MDL approaches implemented outperform the classical information criteria such as AICc or BIC, for reasonably high values of the SNR. The nMDL is by far the most efficient criterion, with less than 2% erroneous selected models for reasonable SNR

values (S-SNR ≥ 6.3 dB)[69], while the standard BIC selects approximately 17% of erroneous models and AICc is strongly inefficient. In Fig. 6.2-[II].a, the histogram of the selected model sizes is plotted for the 4 criteria and for an S-SNR=6.3 dB, revealing that the AICc is prone to overfitting. The size distributions for BIC and gMDL are very similar, with approximately 16% of overestimated models ($K = 5$), but the nMDL appears very efficient at avoiding overfitting, with only 1% of overestimated selections and 0.4% of selections with only $K = 3$ components. This tendency to enforce sparse models had already been observed in previous implementations of nMDL in other application fields [Ris07], and seems interesting in the context of absorption spectroscopy, as it decreases the probability of erroneously detecting a gas component in excess, and consequently strengthens the confidence in the components selected with nMDL. This behavior remains valid in the situation where no absorption occurred on the optical beam (i.e., null model), which is represented in Fig. 6.2-[II].b. With approximately 99% of correct models, the gMDL criterion leads to the lowest probability of false gas detection (probability of false alarm) $\mathrm{Pfa} \simeq 1 - 0.99 = 1\%$, whereas the nMDL criterion appears at first sight less efficient with a $\mathrm{Pfa} \simeq 6.5\%$.

The promising capabilities of nMDL to operate efficient unsupervised model selection was confirmed by its robustness to outliers measurements. Indeed, in practical situations of in-field experiments, measurement artifacts may exist, that were simulated here by averaging among the $N = 20$ independent measures a varying proportion of outliers, corresponding to the simulated noisy absorption spectrum of a single interferent gas species (HCl [80 ppm.m]). Once again, it can be clearly seen from Table 6.1.b that the nMDL criterion outperforms the other methods, with still 90% of correct models for a significant amount of outliers (20%). Moreover, contrarily to the other criteria implemented, the inclusion of 20% of outliers did not significantly influence the Pfa obtained with nMDL (approximately $1 - 0.933 \simeq 6,7\%$).

The outcomes of this theoretical and numerical study have motivated the use of the nMDL model selection algorithm in the first experimental implementation of optical spectroscopy at ONERA using supercontinuum sources. An example of acquisition and efficient model selection with the stepwise algorithm presented above in given in Fig. 6.3-[I] in the simple situation of two interfering gases [Cez11].

6.3 False alarm rate control with nMDL criterion

In a more recent theoretical work [Fad15] (see AA II-6, p. 222), I have investigated the possibility of slightly modifying the nMDL criterion by adding a supplementary parameter in the selection stage in order to gain tunability on the probability of false alarm. The main objective would be to control the tendency of the automated model selection procedure to include at least one gas in the model, i.e., rejecting the null hypothesis in which no gas is present. Such a feature can be of great interest in practice in the context of unsupervised optical spectroscopy for air pollution monitoring and detection or noxious gas detection.

For that purpose, I have proposed a modified version of the nMDL criterion, which is not reported here for the sake of concision, but which is detailed in [Fad15]. It turns out that the modified nMDL criterion for discrimination between null/non-null hypotheses leads to the following decision rule:

$$\begin{aligned} & -\ell_{\tilde{\mathbf{Y}}}(\tilde{\mathbf{Y}}; H_K) + \mathcal{C}'^{(n)}_{H_K} \underset{H_1}{\overset{H_0}{\gtrless}} -\ell_{\tilde{\mathbf{Y}}}(\tilde{\mathbf{Y}}; H_0) + \mathcal{C}'^{(n)}_{H_0} + \delta_{\mathrm{Pfa}} \\ \Leftrightarrow \quad & \Delta\mathcal{C}'^{(n)}(\tilde{\mathbf{Y}}, M, K) \overset{\triangle}{=} -\ell_{glrt}(\tilde{\mathbf{Y}}) + \mathcal{C}'^{(n)}_{H_K} - \mathcal{C}'^{(n)}_{H_0} \underset{H_K}{\overset{H_0}{\gtrless}} \delta_{\mathrm{Pfa}}, \end{aligned} \tag{6.3}$$

where the additional parameter is denoted δ_{Pfa}. The second formulation of the decision rule illus-

[69] The S-SNR denotes a *spectral* signal-to-noise ratio, quantifying the amount of noise with respect to the of the "strength" of the absorption features in the mixture, and defined such that $\text{S-SNR}^2 = \|\mathbf{Hc}\|^2 / M\sigma^2$.

trates that the nMDL criterion rejects the null hypothesis H_0 (no gas mixture) if $\Delta C'^{(n)}(\ell_{glrt}, M, K)$ is lower than a threshold δ_{Pfa} that fixes the probability of false alarm. Indeed, with such formulation, the thresholded nMDL criterion can be seen as an equivalent implementation of a *generalized likelihood ratio test* (glrt) which is optimal in the Neyman-Pearson sense [The89]. Indeed, taking the logarithm of the likelihood ratio yields $\ell_{glrt}(\tilde{\mathbf{Y}}) = -\ell_{\tilde{\mathbf{Y}}}(\tilde{\mathbf{Y}}; H_K) + \ell_{\tilde{\mathbf{Y}}}(\tilde{\mathbf{Y}}; H_0) = \ln P_{\tilde{\mathbf{Y}}}(\tilde{\mathbf{Y}}; H_0)/P_{\tilde{\mathbf{Y}}}(\tilde{\mathbf{Y}}; H_K)$. In [Fad15], we detail how the threshold δ_{Pfa} can be determined as a function of the desired Pfa and of the pdf of the data.

Let us now simply summarize here some simulation results that demonstrate the ability of this modified nMDL to operate efficient model selection while offering false alarm control capability. With some necessary precautions in the implementation that are detailed in [Fad15], numerical results have been obtained on the same simulated data as presented in Fig. 6.2-[I], which are presented in Fig. 6.3-[II]. These results allow us to check the validity of the proposed approach for Pfa control: indeed, it can be clearly seen in the inset of Fig. 6.3-[II] that tuning the parameter δ_{Pfa} allows one to adjust the Pfa of the nMDL selection criterion at will. In addition, the main plot of Fig. 6.3-[II] confirms the efficiency of the nMDL criterion for sparse model selection for sufficiently high values of the S-SNR (typically > 5 dB). The comparison with the gMDL approach shows that the nMDL is less sensitive to a degradation of the SNR, and is thus better adapted for practical implementation in real field scenarios.

Conclusion

The work described in this last chapter has permitted to reveal the interest of unsupervised model selection procedure using most advanced refinements of the MDL principle. Namely, the nMDL approach has proved very efficient in selecting sparse models in unsupervised wideband optical absorption spectroscopy, while showing significant robustness with respect to the presence of measurement outliers. Even though the criterion requires little more involved calculations, it can be readily computed from an analytical expression, hence allowing fast processing, especially when using an iterative approach such as the stepwise implementation proposed. Lastly, this criterion can be easily modified so as to ensure direct control of the probability of false alarm. This potentiality offers great flexibility of use for practical real-field implementations of unsupervised optical spectroscopy, which remains a current environmental issue for air pollution monitoring and noxious gas detection for defence applications.

General conclusion and scientific perspectives

General conclusion

THROUGHOUT this document, I have made my best to present a condensed and structured vision of my scientific contribution in the domain of unconventional imaging. I hope that in spite of the apparent diversity of the studies conducted, and of the aspects studied (physical and statistical optics, instrumentation, algorithmics, information processing), the coherence of the whole research project conducted during the last ten years distinctly reveals itself while reading this manuscript. More precisely, I wish that it will be apparent to the reader that the originality, the coherence and the fertility of the work conducted so far in the Optics and Photonics Departement (DOP) of the IPR lie in the permanent exchange between three domains of interest, namely (i) physical interpretation; (ii) design of original systems that match specific uses; and (iii) rigorous search for optimum statistical processing within the framework of information theory.

The willpower to develop a dynamic and original research axis in advanced imaging within the Optics and Photonics Department of the IPR was supported in 2010 by my recruitment as an assistant professor. This position provided me reduced teaching duty, as I was holder of a "CNRS chair" during the first five years, and of CNRS "delegations" for the next two years. Since then, I had the opportunity to benefit from the research environment of the DOP, which is very conducive to scientific exchanges between research axes (notably with microwave photonics or vectorial lasers). Such advantageous work conditions as a young researcher at the University have allowed me to devote myself to the success of this project. Once cleared the initial difficulties and delays inherent to the birth of new research activities in a laboratory (experimental rooms layout, search for fundings, equipement purchases, valorization/patenting, building of setups, collaborations and recruitments,...), these efforts have been rewarded by the present existence of various original research axes (at a national, or even international scale for some of them). Today, material and scientific means (equipment, laboratory rooms, collaborations, fundings,...) are at the disposal of these research axes, which turns the "Advanced imaging" axis into an enduring and recognized research field of the Optics and Photonics Department of the IPR. In the near future, this research domain will be at the heart of one the main axes of the Institut Foton, which results, starting from July 2017, from the merging of the Optics and Photonics Department of the IPR, and the former teams of the Foton laboratory, namely Foton-SP (Photonic Systems, Lannion, ENSSAT) and Foton-OHM (Optoelectronics, Heteroepitaxy and Materials, Rennes, INSA).

Scientific perspectives

Bibliography

[Aga15] Agarwal N., Yoon J., Garcia-Caurel E., Novikova T., Vanel J.C., Pierangelo A. *et al.* "Spatial evolution of depolarization in homogeneous turbid media within the differential mueller matrix formalism." *Optics Letters*, **40** (23), pp. 5634–5637 (2015).

[Aie05] Aiello A. and Woerdman J. "Physical bounds to the entropy-depolarization relation in random light scattering." *Physical Review Letters*, **94** (9), p. 090406 (2005).

[Aka74] Akaike H. "A new look at the statistical model identification." *IEEE Trans. on Automatic Control*, **19** (6), pp. 716–723 (1974).

[Ala13] Alali S., Yang T. and Vitkin I. "Rapid time-gated polarimetric stokes imaging using photoelastic modulators." *Optics letters*, **38** (16), pp. 2997–3000 (2013).

[Ala15] Alali S. and Vitkin A. "Polarized light imaging in biomedicine: emerging mueller matrix methodologies for bulk tissue assessment." *Journal of Biomedical Optics*, **20** (6), p. 061104 (2015).

[Ale14] Alenin A.S. and Tyo J.S. "Generalized channeled polarimetry." *JOSA A*, **31** (5), pp. 1013–1022 (2014).

[Alo08] Alouini M., Goudail F., Roux N., Le Hors L., Hartemann P., Breugnot S. and Dolfi D. "Active spectro-polarimetric imaging: signature modeling, imaging demonstrator and target detection." *The European Physical Journal - Applied Physics*, **42** (02), pp. 129–139 (2008).

[Alo09] Alouini M., Goudail F., Grisard A., Bourderionnet J., Dolfi D., Bénière A. *et al.* "Near-infrared active polarimetric and multispectral laboratory demonstrator for target detection." *Appl. Opt.*, **48** (8), pp. 1610–1618 (2009).

[Alo11] Alouini M. and Fade J. "System and method of analysis by determining a depolarizing or dichroic character of an object." Patent FR11.55527 - PCT/EP2012/061585 (2011).

[Amr08] Amra C., Zerrad M., Siozade L., Georges G. and Deumié C. "Partial polarization of light induced by random defects at surfaces or bulks." *Opt. Express*, **16** (14), pp. 10372–10383 (2008).

[And99] Andrés N., Arroyo M.P., Hinrichs H. and Quintanilla M. "Digital speckle-pattern interferometry as a full-field fluid-velocimetry technique." *Optics Letters*, **24**, pp. 575–577 (1999).

[Ang02] Angelsky O.V., Mokhun I.I., Mokhun A.I. and Soskin M.S. "Interferometric methods in diagnostics of polarization singularities." *Phys. Rev. E*, **65**, p. 036602 (2002).

[Ann12a] Anna G., Bertaux N., Galland F., Goudail F. and Dolfi D. "Joint contrast optimization and object segmentation in active polarimetric images." *Optics letters*, **37** (16), pp. 3321–3323 (2012).

[Ann12b] Anna G., Sauer H., Goudail F. and Dolfi D. "Fully tunable active polarization imager for contrast enhancement and partial polarimetry." *Applied optics*, **51** (21), pp. 5302–5309 (2012).

[Aug13] August Y. and Stern A. "Compressive sensing spectrometry based on liquid crystal devices." *Optics letters*, **38** (23), pp. 4996–4999 (2013).

[Azz78] Azzam R. "Propagation of partially polarized light through anisotropic media with or without depolarization: a differential 4×4 matrix calculus." *JOSA*, **68** (12), pp. 1756–1767 (1978).

[Azz87] Azzam R.M. and Bashara N.M. *Ellipsometry and polarized light*. Elsevier (1987).

[Bai09] Baili G., Morvan L., Alouini M., Dolfi D., Bretenaker F., Sagnes I. and Garnache A. "Experimental demonstration of a tunable dual-frequency semiconductor laser free of relaxation oscillations." *Opt. Lett.*, **34** (21), pp. 3421–3423 (2009).

[Bar08] Baraniuk R.G. "Single-pixel imaging via compressive sampling." *IEEE Signal Processing Magazine* (2008).

[Bec09] Beck A. and Teboulle M. "Fast iterative shrinkage-thresholding algorithm for linear inverse problems." *SIAM journal on imaging science*, **2**. 183–202 (2009).

[Bén09a] Bénière A., Alouini M., Goudail F. and Dolfi D. "Design and experimental validation of a snapshot polarization contrast imager." *Appl. Opt.*, **48** (30), pp. 5764–5773 (2009).

[Bén09b] Bénière A., Goudail F., Dolfi D. and Alouini M. "Target detection in active polarization images perturbed with additive noise and illumination nonuniformity." *JOSA A*, **26** (7), pp. 1678–1686 (2009).

[Bic92] Bicout D. and Brosseau C. "Multiply scattered waves through a spatially random medium: entropy production and depolarization." *Journal de Physique I*, **2** (11), pp. 2047–2063 (1992).

[Boa01] Boas D.a., Brooks D.H., Miller E.L., Dimarzio C.a., Kilmer M., Gaudette R.J. and Zhang Q. "Imaging the body with diffuse optical tomography." *IEEE Signal Processing Magazine*, **18** (6), pp. 57–75 (2001).

[Bof12] Boffety M., Galland F. and Allais A.G. "Influence of polarization filtering on image registration precision in underwater conditions." *Opt. Lett.*, **37** (15), pp. 3273–3275 (2012).

[Bof14] Boffety M., Hu H. and Goudail F. "Contrast optimization in broadband passive polarimetric imaging." *Optics letters*, **39** (23), pp. 6759–6762 (2014).

[Bre99] Breugnot S. and Clémenceau P. "Modeling and performances of a polarization active imager at λ=806 nm." *Laser Radar technology and applications IV*, **3707**, pp. 449–460 (1999).

[Bro98] Brosseau C. *Fundamentals of polarized light - A statistical Optics approach*. John Wiley (1998).

[Bro08] Brown D.M., Shi K., Liu Z. and Philbrick C.R. "Long-path supercontinuum absorption spectroscopy for measurement of atmospheric constituents." *Optics express*, **16** (12), pp. 8457–8471 (2008).

[Bro10] Broky J. and Dogariu A. "Complex degree of mutual polarization in randomly scattered fields." *Opt. Express*, **18** (19), pp. 20105–20113 (2010).

[Bro11] Broky J. and Dogariu A. "Correlations of polarization in random electro-magnetic fields." *Opt. Express*, **19** (17), pp. 15711–15719 (2011).

[Bru97] Bruniquel J. and Lopès A. "Multi-variate optimal speckle reduction in polarimetric SAR imagery." *International Journal of Remote Sensing*, **18** (3), pp. 603–627 (1997).

[Bue07] Bueno J.M., Hunter J.J., Cookson C.J., Kisilak M.L. and Campbell M.C. "Improved scanning laser fundus imaging using polarimetry." *JOSA A*, **24** (5), pp. 1337–1348 (2007).

[Can06] Candes E.J. and Tao T. "Near-optimal signal recovery from random projections: Universal encoding strategies ?" *IEEE transactions on information theory*, **52** (12), pp. 5406–5425 (2006).

[Cez11] Cezard N., Dobroc A., Canat G., Duhant M., Renard W., Alhenc-Gelas C., Lefebvre S. and Fade J. "Supercontinuum laser absorption spectroscopy in the mid-infrared range for identification and concentration estimation of a multi-component atmospheric gas mixture." In *SPIE Remote Sensing*, pp. 81820V–81820V. International Society for Optics and Photonics (2011).

[Cez14] Cezard N., Canat G., Dobroc A., Duhant M., Renard W. and Besson C. "Fast and wideband supercontinuum absorption spectroscopy in the mid-ir range." In *Imaging and Applied Optics 2014*, p. LW4D.4. Optical Society of America (2014).

[Cha08] Chan W.L., Charan K., Takhar D., Kelly K.F., Baraniuk R.G. and Mittleman D.M. "A single-pixel terahertz imaging system based on compressed sensing." *Applied Physics Letters*, **93** (12), p. 121105 (2008).

[Cha16] Charbois J.M. and Devlaminck V. "Stochastic model for the differential mueller matrix of stationary and nonstationary turbid media." *J. Opt. Soc. Am. A*, **33** (12), pp. 2414–2424 (2016).

[Chi89] Chipman R.A. "Polarization analysis of optical systems." *Optical Engineering*, **28** (2), p. 280290 (1989).

[Chi05] Chipman R.A. "Depolarization index and the average degree of polarization." *Applied optics*, **44** (13), pp. 2490–2495 (2005).

[Clo86] Cloude S. "Group theory and polarisation algebra." *Optik*, **75** (1), pp. 26–36 (1986).

[Clo90] Cloude S.R. "Conditions For The Physical Realisability Of Matrix Operators In Polarimetry." In *Polarization Considerations for Optical Systems II, Proc. SPIE*, vol. 1166, pp. 177–185 (1990).

[Col93] Collett E. *Polarized light: fundamentals and applications*. Dekker (1993).

[Col02] Colomb T., Dahlgren P., Beghuin D., Cuche E., Marquet P. and Depeursinge C. "Polarization imaging by use of digital holography." *Applied optics*, **41** (1), pp. 27–37 (2002).

[Cou94] Coulson D., Crittenden R.G. and Turok N.G. "Polarization and anisotropy of the microwave sky." *Physical Review Letters*, **73**, pp. 2390–2393 (1994).

[Cov91] Cover T.M. and Thomas J.A. *Elements of Information Theory*. Wiley-interscience, New York (1991).

[Cur11] Curry N., Bondareff P., Leclercq M., van Hulst N.F., Sapienza R., Gigan S. and Grésillon S. "Direct determination of diffusion properties of random media from speckle contrast." *Opt. Lett.*, **36** (17), pp. 3332–3334 (2011).

[Dem96] Demos S.G. and Alfano R. "Temporal gating in highly scattering media by the degree of optical polarization." *Optics letters*, **21** (2), pp. 161–163 (1996).

[Dem97] Demos S.G. and Alfano R.R. "Optical polarization imaging." *Appl. Opt.*, **36** (1), pp. 150–155 (1997).

[Dev13] Devlaminck V. "Physical model of differential mueller matrix for depolarizing uniform media." *JOSA A*, **30** (11), pp. 2196–2204 (2013).

[Don06] Donoho D.L. "Compressed sensing." *IEEE Transactions on information theory*, **52** (4), pp. 1289–1306 (2006).

[Dub13] Dubreuil M., Delrot P., Leonard I., Alfalou A., Brosseau C. and Dogariu A. "Exploring underwater target detection by imaging polarimetry and correlation techniques." *Applied optics*, **52** (5), pp. 997–1005 (2013).

[Dun91] Duncan M.D., Mahon R., Tankersley L.L. and Reintjes J. "Time-gated imaging through scattering media using stimulated raman amplification." *Optics letters*, **16** (23), pp. 1868–1870 (1991).

[Dup15] Dupont J. and Orlik X. "Polarized vortices in optical speckle field: observation of rare polarization singularities." *Optics express*, **23** (5), pp. 6041–6049 (2015).

[Dur12] Durán V., Clemente P., Fernández-Alonso M., Tajahuerce E. and Lancis J. "Single-pixel polarimetric imaging." *Optics letters*, **37** (5), pp. 824–826 (2012).

[Ell04] Ellis J. and Dogariu A. "Complex degree of mutual polarization." *Opt. Lett.*, **29**, pp. 536–538 (2004).

[Ell14] Ellingsen P.G., Aas L.M.S., Hagen V.S., Kumar R., Lilledahl M.B. and Kildemo M. "Mueller matrix three-dimensional directional imaging of collagen fibers." *Journal of Biomedical Optics*, **19** (2), p. 026002 (2014).

[Emi96] Emile O., Bretenaker F. and Floch A.L. "Rotating polarization imaging in turbid media." *Optics letters*, **21** (20), pp. 1706–1708 (1996).

[Fad08a] Fade J., Réfrégier P. and Roche M. "Estimation of the degree of polarization from a single speckle intensity image with photon noise." *Journal of Optics A: Pure and Applied Optics*, **10** (11), p. 115301 (2008).

[Fad08b] Fade J., Roche M., Galland F. and Réfrégier P. "Estimation of the degree of polarization from a single image: characterization of the precision under various coherent imaging conditions." In *OPTO/IRS^2 Conference Proceedings, Nürnberg (Germany)*, pp. 69–74 (2008).

[Fad08c] Fade J., Roche M. and Réfrégier P. "Precision of moment based estimation of the degree of polarization in coherent imagery without polarization device." *Journal of the Optical Society of America A*, **25** (2), pp. 483–492 (2008).

[Fad10] Fade J. and Cézard N. "Supercontinuum lidar absorption spectroscopy for gas detection and concentration estimation." In *Proc. 25th International Laser and Remote-sensing Conference*, pp. 798–801 (2010).

[Fad12a] Fade J. and Alouini M. "Depolarization remote sensing by orthogonality breaking." *Physical review letters*, **109** (4) (2012).

[Fad12b] Fade J., Roche M. and Alouini M. "Computational polarization imaging from a single speckle image." *Optics Letters*, **88** (3) (2012).

[Fad14a] Fade J., Panigrahi S. and Alouini M. "Optimal estimation in polarimetric imaging in the presence of correlated noise fluctuations." *Optics Express*, **22** (5), pp. 4920–4931 (2014).

[Fad14b] Fade J., Panigrahi S., Carré A., Frein L., Hamel C., Bretenaker F., Ramachandran H. and Alouini M. "Long-range polarimetric imaging through fog." *Applied optics*, **53** (18), pp. 3854–3865 (2014).

[Fad15] Fade J. "Stochastic complexity-based model selection with false alarm rate control in optical spectroscopy." *Pattern Recognition Letters*, **65**, pp. 152–156 (2015).

[Fad16] Fade J. and Ortega-Quijano N. "Differential description and irreversibility of depolarizing light–matter interactions." *Journal of Optics*, **18** (12), p. 125604 (2016).

[Fad17] Fade J., Perrotin E. and Bobin J. "Two-pixel compressive sensing polarimetric camera." *submitted to IEEE Tran. on Computational Imaging* (2017).

[Fis93] Fishkin J.B. and Gratton E. "Propagation of photon-density waves in strongly scattering media containing an absorbing semi-infinite plane bounded by a straight edge." *Journal of the Optical Society of America. A*, **10** (1), pp. 127–140 (1993).

[Fra15] Franssens G.R. "Relativistic kinematics formulation of the polarization effects of jones–mueller matrices." *JOSA A*, **32** (2), pp. 164–172 (2015).

[Fre92] Freund I. "Time-reversal symmetry and image reconstruction through multiple-scattering media." *J. Opt. Soc. Am. A*, **9** (3), pp. 456–463 (1992).

[Fu15] Fu C., Arguello H., Sadler B.M. and Arce G.R. "Compressive spectral polarization imaging by a pixelized polarizer and colored patterned detector." *J. Opt. Soc. Am. A*, **32** (11), pp. 2178–2188 (2015).

[Gal03] Galland F., Bertaux N. and Réfrégier P. "Minimum description length synthetic aperture radar image segmentation." *IEEE Trans. Image Process.*, **12** (9), pp. 995–1006 (2003).

[Gal11] Gallier J. *Geometric methods and applications: for computer science and engineering*. Springer Science & Business Media (2011).

[Gar89] Garcia N. and Genack A.Z. "Crossover to strong intensity correlation for microwave radiation in random media." *Phys. Rev. Lett.*, **63**, pp. 1678–1681 (1989).

[Gar95] Garthwaite P., Jolliffe I. and Jones B. *Statistical Inference*. Prentice Hall Europe, London (1995).

[Gho11] Ghosh N. and Vitkin I.A. "Tissue polarimetry: concepts, challenges, applications, and outlook." *Journal of biomedical optics*, **16** (11), p. 110801 (2011).

[Gil85] Gil J.J. and Bernabeu E. "A depolarization criterion in mueller matrices." *Journal of Modern Optics*, **32** (3), pp. 259–261 (1985).

[Gil86] Gil J.J. and Bernabeu E. "Depolarization and polarization indices of an optical system." *Journal of Modern Optics*, **33** (2), pp. 185–189 (1986).

[Gil16a] Gil J.J. "Structure of polarimetric purity of a mueller matrix and sources of depolarization." *Optics Communications*, **368**, pp. 165–173 (2016).

[Gil16b] Gil J.J.G. and Ossikovski R. *Polarized Light and the Mueller Matrix Approach*. CRC Press (2016).

[Gon95] Gonatas C., Ishii M., Leigh J.S. and Schotland J.C. "Optical diffusion imaging using a direct inversion method." *Physical Review E*, **52** (4), p. 4361 (1995).

[Goo85] Goodman J.W. *Statistical Optics*. John Wiley and Sons, Inc., New York (1985).

[Goo07] Goodman J.W. *Speckle phenomena: Theory and Applications*. Roberts & Company Publishers, Greenwood village (2007).

[Gor03] Gori F., Santarsiero M., Simon R., Piquero G., Borghi R. and Guattari G. "Coherent-mode decomposition of partially polarized, partially coherent sources." *J. Opt. Soc. Am. A*, **20**, pp. 78–84 (2003).

[Gou02] Goudail F. and Réfrégier P. "Target segmentation in active polarimetric images by use of statistical active contours." *Appl. Opt.*, **41** (5), pp. 874–883 (2002).

[Gou04] Goudail F. and Réfrégier P. *Statistical image processing techniques for noisy images: an application oriented approach*. Kluwer, New York (2004).

[Gou09] Goudail F. and Bénière A. "Optimization of the contrast in polarimetric scalar images." *Optics letters*, **34** (9), pp. 1471–1473 (2009).

[Gra97] Gratton E., Fantini S., Franceschini M.a., Gratton G. and Fabiani M. "Measurements of scattering and absorption changes in muscle and brain." *Philosophical transactions of the Royal Society of London. Series B, Biological sciences*, **352** (1354), pp. 727–735 (1997).

[Grü05] Grünwald P.D., Myung I.J. and Pitt M.A. *Advances in minimum description length: Theory and applications*. MIT press Cambridge (2005).

[Han97] Han D., Kim Y. and Noz M.E. "Stokes parameters as a minkowskian four-vector." *Physical Review E*, **56** (5), p. 6065 (1997).

[Han01] Hansen M. and Yu B. "Model selection and the principle of minimum description length." *Journal of the American Statistical Association*, **96** (454), pp. 746–774 (2001).

[Hau07] Hautière N., Tarel J.P. and Aubert D. "Towards fog-free in-vehicle vision systems through contrast restoration." In *Proceedings of the IEEE Computer Society Conference on Computer Vision and Pattern Recognition* (2007).

[Hor95] Horinaka H., Hashimoto K., Wada K., Cho Y. and Osawa M. "Extraction of quasi-straightforward-propagating photons from diffused light transmitting through a scattering medium by polarization modulation." *Optics letters*, **20** (13), pp. 1501–1503 (1995).

[Hsu14] Hsu W.L., Myhre G., Balakrishnan K., Brock N., Ibn-Elhaj M. and Pau S. "Full-stokes imaging polarimeter using an array of elliptical polarizer." *Optics express*, **22** (3), pp. 3063–3074 (2014).

[ICA96] ICAO J. "International standards and recommended practices, annex 10 to the convention on international civil aviation, volume 1, radio navigation aids." (1996).

[Ils10] Ilslist.com. `https://sites.google.com/site/ilsapproaches/` (2010).

[Ish78] Ishimaru A. *Wave propagation and scattering in random media*, vol. 2. Academic press New York (1978).

[Jac08] Jacques S.L. and Pogue B.W. "Tutorial on diffuse light transport." *Journal of Biomedical Optics*, **13** (4), p. 041302 (2008).

[Jao84] Jao J.K. "Amplitude distribution of composite terrain radar clutter and the K-distribution." *IEEE Trans. on Antennas and Propagation*, **AP-32** (10), pp. 1049–1062 (1984).

[Jia05] Jiao S., Todorović M., Stoica G. and Wang L.V. "Fiber-based polarization-sensitive mueller matrix optical coherence tomography with continuous source polarization modulation." *Applied optics*, **44** (26), pp. 5463–5467 (2005).

[Jon47] Jones R.C. "A new calculus for the treatment of optical systemsv. a more general formulation, and description of another calculus." *J. Opt. Soc. Am.*, **37** (2), pp. 107–110 (1947).

[Jon48] Jones R.C. "A new calculus for the treatment of optical systems. vii. properties of the n-matrices." *J. Opt. Soc. Am.*, **38** (8), pp. 671–685 (1948).

[Kaa07] Kaasalainen S., Lindroos T. and Hyyppa J. "Toward hyperspectral lidar: Measurement of spectral backscatter intensity with a supercontinuum laser source." *IEEE Geoscience and Remote Sensing Letters*, **4** (2), pp. 211–215 (2007).

[Kam81] Kaminow I.P. "Polarization in optical fibers." *IEEE Journal of Quantum Electronics*, **17**, pp. 15–22 (1981).

[Kar05] Kartazayeva S., Ni X. and Alfano R. "Backscattering target detection in a turbid medium by use of circularly and linearly polarized light." *Optics letters*, **30** (10), pp. 1168–1170 (2005).

[Kim87] Kim K., Mandel L. and Wolf E. "Relationship between Jones and Mueller matrices for random media." *J. Opt. Soc. Am. A*, **4** (3), pp. 433–437 (1987).

[Kim08] Kim H.K., Netz U.J., Beuthan J. and Hielscher A.H. "Optimal source-modulation frequencies for transport-theory-based optical tomography of small-tissue volumes." *Optics Express*, **16** (22), pp. 18082–18101 (2008).

[Kli12] Kliger D.S. and Lewis J.W. *Polarized light in optics and spectroscopy*. Elsevier (2012).

[Kor05] Korotkova O. and Wolf E. "Generalized Stokes parameters of random electromagnetic beams." *Opt. Lett.*, **30** (2), pp. 198–200 (2005).

[Kud12] Kudenov M.W., Escuti M.J., Hagen N., Dereniak E.L. and Oka K. "Snapshot imaging mueller matrix polarimeter using polarization gratings." *Opt. Lett.*, **37** (8), pp. 1367–1369 (2012).

[Kum12] Kumar S., Purwar H., Ossikovski R., Vitkin I.A. and Ghosh N. "Comparative study of differential matrix and extended polar decomposition formalisms for polarimetric characterization of complex tissue-like turbid media." *Journal of Biomedical Optics*, **17** (10), p. 105006 (2012).

[Kup14] Kupinski M., Chipman R. and Clarkson E. "Relating the statistics of the angle of linear polarization to measurement uncertainty of the stokes vector." *Optical Engineering*, **53** (11), p. 113108 (2014).

[LaC11] LaCasse C.F., Chipman R.A. and Tyo J.S. "Band limited data reconstruction in modulated polarimeters." *Optics express*, **19** (16), pp. 14976–14989 (2011).

[Lak12] Lakshminarayanan V., Calvo M.L. and Alieva T. *Mathematical Optics: Classical, Quantum, and Computational Methods*. CRC Press (2012).

[Lee01] Lee J.S., Grunes M.R. and Pottier E. "Quantitative comparison of classification capability: Fully polarimetric versus dual and single-polarization sar." *IEEE Transactions on Geoscience and Remote Sensing*, **39** (11), pp. 2343–2351 (2001).

[Lee09] Lee J.S. and Pottier E. *Polarimetric radar imaging: from basics to applications*. CRC Press (2009).

[Lég75] Léger D., Mathieu E. and Perrin J.C. "Optical surface roughness determination using speckle correlation technique." *Appl. Opt.*, **14**, pp. 872–877 (1975).

[Leh95] Lehman M., Pomarico J.A. and Torroba R.D. "Digital speckle pattern interferometry applied to a surface roughness study." *Optical Engineering*, **34**, pp. 1148–1152 (1995).

[LG15] Le Gratiet A., Rivet S., Dubreuil M. and Le Grand Y. "100 khz mueller polarimeter in reflection configuration." *Optics letters*, **40** (4), pp. 645–648 (2015).

[Li02] Li J., Yao G. and Wang L.V. "Degree of polarization in laser speckles from turbid media: implication in tissue optics." *Journal of Biomedical Optics*, **7**, pp. 307–312 (2002).

[Li14] Li L. "Time-of-flight camera–an introduction." *Tech. Rep. SLOA190B*, Texas Instruments Dallas, Tex, USA (2014).

[Lip15] Lippok N., Villiger M. and Bouma B.E. "Degree of polarization (uniformity) and depolarization index: unambiguous depolarization contrast for optical coherence tomography." *Optics letters*, **40** (17), pp. 3954–3957 (2015).

[Liu14] Liutkus A., Martina D., Popoff S., Chardon G., Katz O., Lerosey G., Gigan S., Daudet L. and Carron I. "Imaging with nature: Compressive imaging using a multiply scattering medium." *Scientific reports*, **4**, p. 5552 (2014).

[Lou01] Lounesto P. *Clifford algebras and spinors*. Cambridge University Press (2001).

[Lu96] Lu S.Y. and Chipman R.A. "Interpretation of mueller matrices based on polar decomposition." *J. Opt. Soc. Am. A*, **13** (5), pp. 1106–1113 (1996).

[Luo08] Luo H., Oka K., Edward D., Kudenov M., Schiewgerling J. and Dereniak E. "Compact and miniature snapshot imaging polarimeter." *Applied optics*, **47** (24), pp. 4413–4417 (2008).

[Mag14] Magnusson R., Birch J., Sandström P., Hsiao C.L., Arwin H. and Järrendahl K. "Optical mueller matrix modeling of chiral al x in 1- x n nanospirals." *Thin Solid Films*, **571**, pp. 447–452 (2014).

[Man15] Manhas S., Vizet J., Deby S., Vanel J.C., Boito P., Verdier M., De Martino A. and Pagnoux D. "Demonstration of full $4\times$ 4 mueller polarimetry through an optical fiber for endoscopic applications." *Optics express*, **23** (3), pp. 3047–3054 (2015).

[Mar97] Martelli F., Contini D., Taddeucci A. and Zaccanti G. "Photon migration through a turbid slab described by a model based on diffusion approximation. I. Theory." *Appl. Opt.*, **36**, pp. 4587–4599 (1997).

[Mar03] Marinopoulos A.G., Reining L., Rubio A. and Vast N. "Optical and loss spectra of carbon nanotubes: Depolarization effects and intertube interactions." *Phys. Rev. Lett.*, **91**, p. 046402 (2003).

[Mer08] Meriaudeau F., Ferraton M., Stolz C., Morel O. and Bigué L. "Polarization imaging for industrial inspection." In *Electronic Imaging 2008*, pp. 681308–681308. International Society for Optics and Photonics (2008).

[Mor03] Morales J.A. and Navarro E. "Minkowskian description of polarized light and polarizers." *Physical Review E*, **67** (2), p. 026605 (2003).

[MR11] Macias-Romero C., Foreman M. and Török P. "Spatial and temporal variations in vector fields." *Optics Express*, **19** (25), pp. 25066–25076 (2011).

[Muf11] Mufti F. and Mahony R. "Statistical analysis of signal measurement in time-of-flight cameras." *ISPRS journal of photogrammetry and remote sensing*, **66** (5), pp. 720–731 (2011).

[Muj04] Mujumdar S. and Ramachandran H. "Imaging through turbid media using polarization modulation: dependence on scattering anisotropy." *Optics communications*, **241** (1), pp. 1–9 (2004).

[Mul04] Mullen L., Laux A., Concannon B., Zege E.P., Katsev I.L. and Prikhach A.S. "Amplitude-modulated laser imager." *Applied optics*, **43** (19), pp. 3874–3892 (2004).

[Myu06] Myung J.I., Navarro D.J. and Pitt M.A. "Model selection by normalized maximum likelihood." *Journal of Mathematical Psychology*, **50** (2), pp. 167–179 (2006).

[Nan09] Nan Z., Xiaoyu J., Qiang G., Yonghong H. and Hui M. "Linear polarization difference imaging and its potential applications." *Applied optics*, **48** (35), pp. 6734–6739 (2009).

[Nas14] Nassif R., Nader C.A., Afif C., Pellen F., Le Brun G., Le Jeune B. and Abboud M. "Detection of golden apples' climacteric peak by laser biospeckle measurements." *Applied optics*, **53** (35), pp. 8276–8282 (2014).

[Oka03] Oka K. and Kaneko T. "Compact complete imaging polarimeter using birefringent wedge prisms." *Opt. Express*, **11** (13), pp. 1510–1519 (2003).

[O'l92] O'leary M., Boas D., Chance B. and Yodh A. "Refraction of diffuse photon density waves." *Physical Review Letters*, **69** (18), p. 2658 (1992).

[OQ11a] Ortega-Quijano N. and Arce-Diego J.L. "Depolarizing differential mueller matrices." *Optics Letters*, **36** (13), pp. 2429–2431 (2011).

[OQ11b] Ortega-Quijano N. and Arce-Diego J.L. "Mueller matrix differential decomposition." *Optics Letters*, **36** (10), pp. 1942–1944 (2011).

[OQ12] Ortega-Quijano N., Haj-Ibrahim B., Garcia-Caurel E., Arce-Diego J.L. and Ossikovski R. "Experimental validation of mueller matrix differential decomposition." *Optics Express*, **20** (2), pp. 1151–1163 (2012).

[OQ14] Ortega-Quijano N., Fanjul-Vélez F. and Arce-Diego J.L. "Polarimetric study of birefringent turbid media with three-dimensional optic axis orientation." *Biomedical Optics Express*, **5** (1), pp. 287–292 (2014).

[OQ15a] Ortega-Quijano N., Fade J., Schaub E., Parnet F. and Alouini M. "Full characterization of dichroic samples from a single measurement by circular polarization orthogonality breaking." *Optics letters*, **40** (7), pp. 1270–1273 (2015).

[OQ15b] Ortega-Quijano N., Fanjul-Vélez F. and Arce-Diego J.L. "Physically meaningful depolarization metric based on the differential mueller matrix." *Optics letters*, **40** (14), pp. 3280–3283 (2015).

[OQ16] Ortega-Quijano N., Fade J., Roche M., Parnet F. and Alouini M. "Orthogonality-breaking sensing model based on the instantaneous stokes vector and the mueller calculus." *JOSA A*, **33** (4), pp. 434–446 (2016).

[OQ17a] Ortega-Quijano N., Fade J. and Alouini M. "Coherent light source with fully controllable state and degree of polarization." Patent EP17165383.5 (2017).

[OQ17b] Ortega-Quijano N., Fade J., Parnet F. and Alouini M. "Generation of coherent light beam with precise and fast dynamic control of the state and degree of polarization." *submitted to Opt. Lett.* (2017).

[Oss10] Ossikovski R. "Alternative depolarization criteria for mueller matrices." *JOSA A*, **27** (4), pp. 808–814 (2010).

[Oss11] Ossikovski R. "Differential matrix formalism for depolarizing anisotropic media." *Optics Letters*, **36** (12), pp. 2330–2332 (2011).

[Oss14a] Ossikovski R. and Arteaga O. "Statistical meaning of the differential mueller matrix of depolarizing homogeneous media." *Optics Letters*, **39** (15), pp. 4470–4473 (2014).

[Oss14b] Ossikovski R. and Devlaminck V. "General criterion for the physical realizability of the differential mueller matrix." *Optics Letters*, **39** (5), pp. 1216–1219 (2014).

[Oss15] Ossikovski R. and De Martino A. "Differential mueller matrix of a depolarizing homogeneous medium and its relation to the mueller matrix logarithm." *JOSA A*, **32** (2), pp. 343–348 (2015).

[Pan15a] Panigrahi S., Fade J. and Alouini M. "Adaptive polarimetric image representation for contrast optimization of a polarized beacon through fog." *Journal of Optics*, **17** (6), p. 065703 (2015).

[Pan15b] Panigrahi S., Fade J. and Alouini M. "Optimal contrast enhancement in long distance snapshot polarimetric imaging through fog." In *Proc. SPIE*, vol. 9613, p. 96130V (2015).

[Pan16a] Panigrahi S., Fade J., Ramachandran H. and Alouini M. "Theoretical optimal modulation frequencies for scattering parameter estimation and ballistic photon filtering in diffusing media." *Optics express*, **24** (14), pp. 16066–16083 (2016).

[Pan16b] Panigrahi S., Ramachandran H., Fade J. and Alouini M. "Optical receiver for full-field optical quadrature demodulation." Patent PCT/FR2016/051086 (2016).

[Par16] Parnet F., Fade J. and Alouini M. "Orthogonality breaking through few-mode optical fiber." *Applied optics*, **55** (10), pp. 2508–2520 (2016).

[Par17] Parnet F., Fade J., Ortega-Quijano N., Frein L., Alouini M. *et al.* "Free-space active polarimetric imager operating at 1.55 μm by orthogonality breaking sensing." *Optics Letters*, **42** (4), pp. 723–726 (2017).

[Pat89] Patterson M.S., Chance B. and Wilson B.C. "Time resolved reflectance and transmittance for the non-invasive measurement of tissue optical properties." *Applied Optics*, **28** (12), pp. 2331–2336 (1989).

[Pay08] Payne A.D., Dorrington A.A., Cree M.J. and Carnegie D.A. "Characterizing an image intensifier in a full-field range imaging system." *IEEE Sensors Journal*, **8** (11), pp. 1763–1770 (2008).

[Pee10] Peeters W.H., Moerman J.J.D. and van Exter M.P. "Observation of two-photon speckle patterns." *Phys. Rev. Lett.*, **104**, p. 173601 (2010).

[PF92] Pellat-Finet P. and Bausset M. "What is common to both polarization optics and relativistic kinematics?" *Optik*, **90** (3), pp. 101–106 (1992).

[Pie11] Pierangelo A., Benali A., Antonelli M.R., Novikova T., Validire P., Gayet B. and De Martino A. "Ex-vivo characterization of human colon cancer by mueller polarimetric imaging." *Optics Express*, **19** (2), pp. 1582–1593 (2011).

[Pop10] Popoff S.M., Lerosey G., Carminati R., Fink M., Boccara A.C. and Gigan S. "Measuring the transmission matrix in optics: An approach to the study and control of light propagation in disordered media." *Phys. Rev. Lett.*, **104**, p. 100601 (2010).

[Pou12] Pouget L., Fade J., Hamel C. and Alouini M. "Polarimetric imaging beyond the speckle grain scale." *Applied Optics*, **51** (30), pp. 7345–7356 (2012).

[Qi13] Qi J., Ye M., Singh M., Clancy N.T. and Elson D.S. "Narrow band 3$\times$ 3 mueller polarimetric endoscopy." *Biomedical optics express*, **4** (11), pp. 2433–2449 (2013).

[Qua97] Quagliano J.R., Stoutland P.O., Petrin R.R., Sander R.K., Romero R.J., Whitehead M.C., Quick C.R., Tiee J.J. and Jolin L.J. "Quantitative chemical identification of four gases in remote infrared (9-11 μm) differential absorption lidar experiments." *Appl. Opt.*, **36** (9), pp. 1915–1927 (1997).

[Rag13] Raguet H., Fadili J. and Peyre G. "A Generalized Forward-Backward Splitting." *SIAM Journal on Imaging Sciences*, **6** (3), pp. 1199–1226 (2013).

[Ram98] Ramachandran H. and Narayanan A. "Two-dimensional imaging through turbid media using a continuous wave light source." *Optics Communications*, **154** (5), pp. 255–260 (1998).

[Ram10] Ramos A.A. and Ariste A.L. "Compressive sensing for spectroscopy and polarimetry." *Astronomy & Astrophysics*, **509**, p. A49 (2010).

[Ram16] Ramachandran H., Bretenaker F., Fade J. and Alouini M. "System and method for navigation assistance in scattering environment." Patent EP14305269.4 (2016).

[Réf04] Réfrégier P., Goudail F., Chavel P. and Friberg A. "Entropy of partially polarized light and application to statistical processing techniques." *J. Opt. Soc. Am. A*, **21**, pp. 2124–2134 (2004).

[Réf05a] Réfrégier P. "Polarization degree of optical waves with non gaussian probability density functions: Kullback relative entropy-based approach." *Opt. Lett.*, **30** (10), pp. 1090–1092 (2005).

[Réf05b] Réfrégier P. and Goudail F. "Invariant degrees of coherence of partially polarized light." *Opt. Express*, **13** (16), pp. 6051–6060 (2005).

[Réf07a] Réfrégier P. "Symmetries in coherence theory of partially polarized light." *J. of Math. Physics*, **48** (3), p. 033303 (2007).

[Réf07b] Réfrégier P., Fade J. and Roche M. "Estimation precision of the degree of polarization from a single speckle intensity image." *Opt. Lett.*, **32** (7), pp. 739–741 (2007).

[Ric00] Richman I. "Real time imaging system and method for use in aiding a landing operation of an aircraft in obscured weather conditions." US Patent 6,119,055 (2000).

[Ric09] Richert M., Orlik X. and De Martino A. "Adapted polarization state contrast image." *Optics express*, **17** (16), pp. 14199–14210 (2009).

[Ris78] Rissanen J. "Modeling by shortest data description." *Automatica*, **14**, pp. 465–471 (1978).

[Ris89] Rissanen J. *Stochastic Complexity in Statistical Inquiry*, *Series in Computer Science*, vol. 15. World Scientific, Singapore (1989).

[Ris96] Rissanen J. "Fisher information and stochastic complexity." *IEEE Trans. Inform. Theory*, **42**, pp. 48–54 (1996).

[Ris07] Rissanen J. *Information and Complexity in Statistical Modeling*. Springer, New-York (2007).

[Roc07] Roche M., Fade J. and Réfrégier P. "Parametric estimation of the square degree of polarization from two intensity images degraded by fully developed speckle noise." *J. Opt. Soc. Am. A*, **24**, pp. 2719–2727 (2007).

[Rog11] Rogers P., Kang T., Zhou T., Kotelyanskii M. and Sirenko A. "Mueller matrices for anisotropic metamaterials generated using $4\times$ 4 matrix formalism." *Thin Solid Films*, **519** (9), pp. 2668–2673 (2011).

[Rou17] Rousseau D., Berthelon X. and Frindel C. "BRP imaging a multicomponent speckle imaging." In *Journée Imagerie Optique Non-Conventionnelle* (2017).

[Row95] Rowe M.P., Pugh E.N., Tyo J.S. and Engheta N. "Polarization-difference imaging : a biologically inspired technique for observation through scattering media." *Opt. Lett.*, **20**, pp. 608–610 (1995).

[San97] Sankaran V., Schnenberger K., Walsh J.T. and Maitland D.J. "Polarization discrimination of coherently propagating light in turbid media." *Appl. Opt.*, **38** (19), pp. 4252–4261 (1997).

[Sch78] Schwartz G. "Estimating the dimension of a model." *Annals of Statistics*, **9**, pp. 461–464 (1978).

[Sch92] Schmitt J., Gandjbakhche A. and Bonner R. "Use of polarized light to discriminate short-path photons in a multiply scattering medium." *Applied optics*, **31** (30), pp. 6535–6546 (1992).

[Sch97] Schotland J.C. "Continuous-wave diffusion imaging." *JOSA A*, **14** (1), pp. 275–279 (1997).

[Sch98] Schilders S., Gan X. and Gu M. "Effect of scatterer size on microscopic imaging through turbid media based on differential polarisation-gating." *Optics communications*, **157** (1), pp. 238–248 (1998).

[Sch04] Schechner Y. and Karpel N. "Clear underwater vision." *Proceedings of the 2004 IEEE Computer Society Conference on Computer Vision and Pattern Recognition, 2004. CVPR 2004.*, **1** (2004).

[Sch14] Schaub E., Fade J., Ortega-Quijano N., Hamel C. and Alouini M. "Polarimetric contrast microscopy by orthogonality breaking." *Journal of Optics*, **16** (12), p. 122001 (2014).

[Set08] Setälä T., Shevchenko A., Kaivola M. and Friberg A.T. "Polarization time and length for random optical beams." *Physical Review A*, **78** (3), p. 033817 (2008).

[She06] Sheng P. *Introduction to wave scattering, localization and mesoscopic phenomena, 2nd ed.* Springer (2006).

[Sht87] Shtar'kov Y.M. "Universal sequential coding of single messages." *Problemy Peredachi Informatsii*, **23** (3), pp. 3–17 (1987).

[Sim82] Simon R. "The connection between mueller and jones matrices of polarization optics." *Optics Communications*, **42** (5), pp. 293–297 (1982).

[Sim10] Simon B., Simon S., Mukunda N., Gori F., Santarsiero M., Borghi R. and Simon R. "A complete characterization of pre-mueller and mueller matrices in polarization optics." *JOSA A*, **27** (2), pp. 188–199 (2010).

[Sko01] Skolnik M.I. *Introduction to Radar Systems : Third Edition*. Mc Graw-Hill (2001).

[Sni14] Snik F., Craven-Jones J., Escuti M., Fineschi S., Harrington D., De Martino A., Mawet D., Riedi J. and Tyo J.S. "An overview of polarimetric sensing techniques and technology with applications to different research fields." In *SPIE Sensing Technology+ Applications*, pp. 90990B–90990B. International Society for Optics and Photonics (2014).

[Sol13] Soldevila F., Irles E., Durán V., Clemente P., Fernández-Alonso M., Tajahuerce E. and Lancis J. "Single-pixel polarimetric imaging spectrometer by compressive sensing." *Applied Physics B*, **113** (4), pp. 551–558 (2013).

[Sor09] Sorrentini J., Zerrad M. and Amra C. "Statistical signatures of random media and their correlation to polarization properties." *Opt. Lett.*, **34** (16), pp. 2429–2431 (2009).

[Sor11] Sorrentini J., Zerrad M., Soriano G. and Amra C. "Enpolarization of light by scattering media." *Opt. Express*, **19** (22), pp. 21313–21320 (2011).

[Spr72] Sprague R.A. "Surface roughness measurement using white light speckle." *Appl. Opt.*, **11**, pp. 2811–2817 (1972).

[Stu12] Studer V., Bobin J., Chahid M., Mousavi H.S., Candes E. and Dahan M. "Compressive fluorescence microscopy for biological and hyperspectral imaging." *Proceedings of the National Academy of Sciences*, **109** (26), pp. E1679–E1687 (2012).

[Sud16] Sudarsanam S., Mathew J., Panigrahi S., Fade J., Alouini M. and Ramachandran H. "Real-time imaging through strongly scattering media: seeing through turbid media, instantly." *Scientific reports*, **6**, p. 25033 (2016).

[Ter03] Tervo J., Setälä T. and Friberg A.T. "Degree of coherence for electromagnetic fields." *Opt. Express*, **11**, pp. 1137–1142 (2003).

[Ter09] Tervo J., Setälä T., Roueff A., Réfrégier P. and Friberg A.T. "Two-point stokes parameters: interpretation and properties." *Opt. Lett.*, **34** (20), pp. 3074–3076 (2009).

[The89] Therrien C.W. *Decision, Estimation, and Classification*. John Wiley and Sons, Inc., New York (1989).

[The13] Thekkek N., Pierce M.C., Lee M.H., Polydorides A.D., Flores R.M., Anandasabapathy S. and Richards-Kortum R.R. "Modular video endoscopy for in vivo cross-polarized and vital-dye fluorescence imaging of barrett's-associated neoplasia." *Journal of biomedical optics*, **18** (2), pp. 026007–026007 (2013).

[Tin96] Tingerben J. *Astronomical polarimetry*. Cambridge University Press (1996).

[Tor03] Toronov V., D'Amico E., Hueber D., Gratton E., Barbieri B. and Webb A. "Optimization of the signal-to-noise ratio of frequency-domain instrumentation for near-infrared spectro-imaging of the human brain." *Optics Express*, **11** (21), pp. 2717–2729 (2003).

[Tow01] Tower T.T. and Tranquillo R.T. "Alignment maps of tissues: Ii. fast harmonic analysis for imaging." *Biophysical journal*, **81** (5), pp. 2964–2971 (2001).

[Tro93] Tromberg B.J., Svaasand L.O., Tsay T.T. and Haskell R.C. "Properties of photon density waves in multiple-scattering media." *Applied optics*, **32** (4), pp. 607–616 (1993).

[Tud15] Tudor T. "On a quasi-relativistic formula in polarization theory." *Optics Letters*, **40** (5), pp. 693–696 (2015).

[Tyo02] Tyo J.S. "Design of optimal polarimeters: Maximization of snr and minimization of systematic errors." *Appl. Opt.*, **41**, pp. 619–630 (2002).

[Tyo06] Tyo J.S., Goldstein D.L., Chenault D.B. and Shaw J.A. "Review of passive imaging polarimetry for remote sensing applications." *Appl. Opt.*, **45**, pp. 5453–5469 (2006).

[Van16] Vannier N., Goudail F., Plassart C., Boffety M., Feneyrou P., Leviandier L., Galland F. and Bertaux N. "Comparison of different active polarimetric imaging modes for target detection in outdoor environment." *Applied optics*, **55** (11), pp. 2881–2891 (2016).

[Vil14] Villiger M. and Bouma B.E. "Practical decomposition for physically admissible differential mueller matrices." *Optics Letters*, **39** (7), pp. 1779–1782 (2014).

[Viz16] Vizet J., Manhas S., Tran J., Validire P., Benali A., Garcia-Caurel E., Pierangelo A., Martino A.D. and Pagnoux D. "Optical fiber-based full mueller polarimeter for endoscopic imaging using a two-wavelength simultaneous measurement method." *Journal of Biomedical Optics*, **21** (7), p. 071106 (2016).

[Wag08] Wagadarikar A., John R., Willett R. and Brady D. "Single disperser design for coded aperture snapshot spectral imaging." *Applied optics*, **47** (10), pp. 44–51 (2008).

[Wan91] Wang L., Ho P. *et al.* "Ballistic 2-d imaging through scattering walls using an ultrafast optical kerr gate." *Science*, **253** (5021), p. 769 (1991).

[War96] Warren E.R. "Optimum detection of multiple vapor materials with frequency-agile lidar." *Appl. Opt.*, **35** (21), pp. 4180–4193 (1996).

[Wat00] Watkins W.R., Tofsted D.H., CuQlock-Knopp V.G., Jordan J.B. and Merritt J.O. "Navigation through fog using stereoscopic active imaging." In *Enhanced and Synthetic Vision 2000*, vol. SPIE-4023, pp. 20–28 (2000).

[Web10] Weber J., Calado V. and Van de Sanden M. "Optical constants of graphene measured by spectroscopic ellipsometry." *Applied Physics Letters*, **97**, p. 091904 (2010).

[Wei04] Weibring P., Abrahamsson C., Sjöholm M., Smith J.N., Edner H. and Svanberg S. "Multi-component chemical analysis of gas mixtures using a continuously tuneable lidar system." *Appl. Phys. B*, **79**, pp. 525–530 (2004).

[Wel15] Welsh S.S., Edgar M.P., Bowman R., Sun B. and Padgett M.J. "Near video-rate linear stokes imaging with single-pixel detectors." *Journal of Optics*, **17** (2), p. 025705 (2015).

[WMO08] WMO. *Guide to meteorological instruments and methods of observation (7th ed.)*. Secretariat of the World Meteorological Organization (2008).

[Wol03] Wolf E. "Unified theory of coherence and polarization of random electromagnetic beams." *Phys. Lett. A*, **312**, pp. 263–267 (2003).

[Woo10] Wood T.C. and Elson D.S. "Polarization response measurement and simulation of rigid endoscopes." *Biomedical optics express*, **1** (2), pp. 463–470 (2010).

[Wys08] Wysocki G., Lewicki R., Curl R., Tittel F., Diehl L., Capasso F. *et al.* "Widely tunable mode-hop free external cavity quantum cascade lasers for high resolution spectroscopy and chemical sensing." *Appl. Phys. B: Lasers and Optics*, **92** (3), pp. 305–311 (2008).

[Xu05] Xu M. and Alfano R. "Circular polarization memory of light." *Physical Review E*, **72**, p. 065601 (2005).

[Yin06] Yin S. and Wang W. "Novel algorithm for simultaneously detecting multiple vapor materials with multiple-wavelength differential absorption lidar." *Chinese Opt. Lett.*, **4** (6), pp. 360–363 (2006).

[Zer10] Zerrad M., Sorrentini J., Soriano G. and Amra C. "Gradual loss of polarization in light scattered from rough surfaces: Electromagnetic prediction." *Opt. Express*, **18** (15), pp. 15832–15843 (2010).

[Zha09] Zhang S., Lockerman Y.D., Park J. and Genack A.Z. "Interplay between generic and mesoscopic speckle statistics in transmission through random media." *Journal of Optics A: Pure and Applied Optics*, **11** (9), p. 094018 (2009).

Selection of publications

Selection of publications - Part I

- Lucien Pouget, Julien Fade, Cyril Hamel, Mehdi Alouini. "Polarimetric imaging beyond the speckle grain scale". Applied Optics, 51 (30), pp. 7345-7356 (2012).

- Noe Ortega-Quijano, Julien Fade, François Parnet, Mehdi Alouini. "Generation of coherent light beam with precise and fast dynamic control of the state and degree of polarization". Submitted to Optics Letters. (2017).

- Julien Fade, Noe Ortega-Quijano. "Differential description and irreversibility of depolarizing light-matter interactions". Journal of Optics, 2016, 18, pp. 125604 (2016).

- Julien Fade, Mehdi Alouini. "Depolarization remote sensing by orthogonality breaking". Physical Review Letters, 109 (4), pp. 043901 (2012).

- Noe Ortega-Quijano, Julien Fade, Muriel Roche, François Parnet, Mehdi Alouini. "Orthogonality-breaking sensing model based on the instantaneous Stokes vector and the Mueller calculus". Journal of the Optical Society of America A, 33 (4), pp. 434-446 (2016).

- Noe Ortega-Quijano, Julien Fade, Emmanuel Schaub, François Parnet, Mehdi Alouini. "Full characterization of dichroic samples from a single measurement by circular polarization orthogonality breaking". Optics Letters, 40 (7), pp. 1270-1273 (2015).

- Julien Fade, Esteban Perrotin, Jérôme Bobin. "Two-pixel compressive sensing polarimetric camera". Submitted to IEEE Transactions in Computational Imaging. (2017).

- Julien Fade, Muriel Roche, Mehdi Alouini. "Computational polarization imaging from a single speckle image". Optics Letters, 37 (3), pp. 386-388 (2012).

Polarimetric imaging beyond the speckle grain scale

Lucien Pouget, Julien Fade,* Cyril Hamel, and Mehdi Alouini

Institut de Physique de Rennes, CNRS, Université de Rennes 1, Campus de Beaulieu, Rennes 35042, France

*Corresponding author: julien.fade@univ-rennes1.fr

Received 12 June 2012; revised 14 September 2012; accepted 14 September 2012;
posted 18 September 2012 (Doc. ID 170496); published 18 October 2012

We address an experimental Stokes imaging setup allowing one to explore the polarimetric properties of a speckle light field with spatial resolution well beyond the speckle grain scale. We detail how the various experimental difficulties inherent to such measurements can be overcome with a dedicated measurement protocol involving a careful *speckle registration* step. The setup and protocol are then validated on a metallic reference sample, and used to measure the state of polarization (SOP) of light in each pixel of highly resolved speckle patterns (>2000 pixels per speckle grain) resulting from the scattering of an incident coherent beam on samples exhibiting different polarimetric properties. Evolution of the SOP with spatial averaging and across adjacent speckle grains is eventually addressed.

OCIS codes: 110.5405, 260.5430, 110.6150, 030.0030, 220.4830.

1. Introduction

Speckle is a ubiquitous phenomenon in all research fields studying the interaction between random media and propagating waves, whether electromagnetic [1–4] or acoustic [5]. Since speckle intensity patterns often represent the simplest and most accessible observables to gauge such interaction, this phenomenon has been thoroughly investigated for decades [1,2,5] but is still widely studied in very active research fields of physics, such as wave localization [5], control of light through disordered media [6,7], optical nonlinear effects in random media [8], or polarization singularities [9]. In the optical imaging domain, speckle has often been considered as a noise detrimental to image quality [10,11]. Nevertheless, speckle contrast imaging is known to be an efficient remote-sensing technique providing information on surface roughness properties [12–14] or fluid velocity [15], for instance. More recently, new applications involving speckle contrast images have been proposed to characterize polarization of light [16–19] or diffusion properties of materials [20,21].

Despite this intense research activity, an open debate still remains about how the polarization state distribution of a speckle pattern can be clearly linked with materials depolarization properties. Recently, this issue has occasioned a number of publications [20,22–30], questioning, for instance, the definition and measurement of polarization correlation lengths in a spatial speckle pattern [22–24,28–30], or the partial "repolarization" of unpolarized coherent light backscattered by a depolarizing material [20]. In order to link depolarization properties of a sample with the scattered light polarization distribution, experimental studies have been carried out using a spatial multiple-scale analysis of the speckle polarization properties [23,25–27]. In these experiments, light depolarization has been studied from a "macroscopic" point of view, by conducting a statistical analysis of a scalar parameter {degree of polarization (DOP) [31] or orthogonal state contrast (OSC) [32]}, over a great number of coherence areas (speckle "grains"). These results tended to experimentally validate that the polarization state is deterministic (light is fully polarized) at the "local" scale of a single speckle grain, whereas global depolarization induced by interaction (reflection or transmission) with the sample results from spatial averaging on the detector over several coherence areas [23,25–27].

1559-128X/12/307345-12$15.00/0

However, the various experimental devices used in these references were not specifically dedicated to studying the polarization state of the speckle pattern at the local scale, i.e., beyond the speckle grain scale. To the best of our knowledge, an imaging setup capable of measuring the full Stokes vector (four components) of light scattered by a diffusive sample below the speckle grain scale in the optical wave domain has not been clearly addressed in the literature. If such study could be carried out quite easily in the microwave range as suggested in [33], it turns out to be a mere challenge when the wavelength is only a few hundred nanometers, as already noticed in [9]. Indeed, Stokes measurements require polarizers and wave plates (at least one) to be inserted and rotated in front of the imaging detector, thus inevitably modifying the optical wavefront of the scattered light and hence the speckle pattern itself, as will be evidenced in the next section. This experimental difficulty is mostly often eluded in the literature, suggesting that conventional experimental schemes are not suitable to perform Stokes imaging at the speckle grain level. In this paper, we tackle this problem by proposing a rigorous experimental setup as well as the methodology allowing one to acquire Stokes images of a speckle pattern, where each grain covers several hundreds or thousands of pixels on the detector surface. The paper is organized as follows: in Section 2, the experimental setup and measurement protocol proposed to achieve Stokes imaging beyond the speckle grain scale are described and calibrated. Test samples are then described and characterized in Section 3. Lastly, we report in Section 4 experimental Stokes imaging of highly resolved speckle patterns obtained with this setup. The processing and analysis of these results are also addressed and commented in this section. Conclusions and future work directions are finally given in Section 5.

2. Experimental Setup

Analyzing the polarization properties of a speckle field beyond the speckle grain scale requires performing a measurement of the Stokes vector of light at any point of a highly resolved speckle pattern. Before detailing the experimental setup used, let us briefly recall the Stokes vector formalism and the principle of Stokes imaging.

A. Stokes Imaging Principle

Stokes formalism is commonly used to characterize the light state of polarization (SOP) [31]. According to this formalism, the polarization state of light is fully described by a four-component vector:

$$\mathcal{S} = \begin{pmatrix} \mathcal{S}_0 = I_x + I_y \\ \mathcal{S}_1 = I_x - I_y \\ \mathcal{S}_2 = I_{+45^\circ} - I_{-45^\circ} \\ \mathcal{S}_3 = I_R - I_L \end{pmatrix}. \quad (1)$$

The four components of the Stokes vector $\mathcal{S}_i$ can thus be simply obtained from intensity measurements $(I_x, I_y, I_{+45^\circ}, I_{-45^\circ}, I_R, I_L)$ through six configurations of a polarization analyzer (PA). In the context of polarimetric imaging considered in the paper, the PA is used to record six intensity images on a detector matrix. From these six images, the SOP (i.e., the four-component Stokes vector) in each pixel of the image is then determined. A global and scalar characterization of the SOP in each pixel is classically obtained by computing the DOP image, given by [31]

$$\mathrm{DOP} = \frac{\sqrt{\mathcal{S}_1^2 + \mathcal{S}_2^2 + \mathcal{S}_3^2}}{\mathcal{S}_0} = \sqrt{S_1^2 + S_2^2 + S_3^2}, \quad (2)$$

or the OSC, given by

$$\mathrm{OSC} = \frac{\mathcal{S}_1}{\mathcal{S}_0} = S_1, \quad (3)$$

where the $S_i = \mathcal{S}_i/\mathcal{S}_0$ stand for the normalized Stokes components.

This method has been preferred to a Fourier analysis technique involving a rotating quarter-wave plate [31]. Indeed, this one implies recording multiple intensity snapshots through a moving plate, which is inconsistent with the extreme stability required for the experimental setup, as will be evidenced below. Another alternative would be using a liquid-crystal variable retarder, but it would be necessary to check that no wavefront distortion is introduced when its configuration is changed during the measurement.

Indeed, to ensure validity of the polarimetric data recorded at the speckle grain scale, one needs to prevent any modification in the wavefront of the scattered light during the measurement procedure. Understandably, this last condition is not easily achieved since speckle is nothing but an interference pattern, and therefore any change in the optical path of the order of a fraction of wavelength will modify the speckle pattern. As will be detailed afterward, unwanted wavefront distortions can be caused by air turbulence within the optical path, thermal expansions of the sample, or mechanical vibrations, but the main difficulty is to keep the wavefront unchanged while switching between the six different configurations of the PA. In the remainder of this section, we will address these technical issues in detail and propose an optimized experimental setup and measurement protocol allowing one to perform Stokes imaging beyond the speckle grain scale.

B. Description of the Experimental Setup

The experimental setup proposed is depicted in Fig. 1. Stokes imaging of the speckle pattern is performed in a reflection geometry (quasi-monostatic configuration). Indeed, the polarimetric imaging system analyzes light scattered by the sample in a direction close to backscattering direction. Consequently,

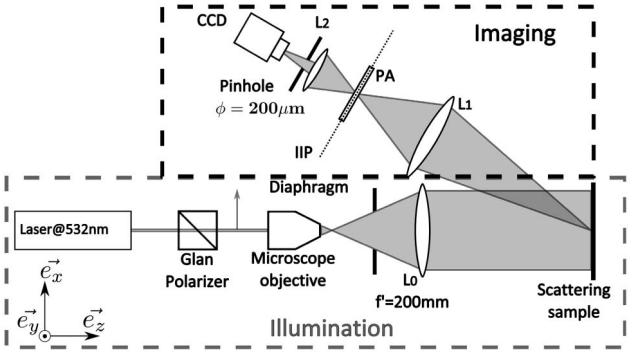

Fig. 1. Experimental setup (see text for details).

it has to be noted that in the remainder of this paper, the word *backscattering* will not refer to the strict sense of scattering in the incident beam direction. The setup comprises several building blocks, which are described in detail below.

Illumination: In the experimental configuration chosen, the scattering sample is enlightened with a frequency-doubled Nd:YVO_4 laser (Coherent Verdi) emitting a maximum output power of 2 W at $\lambda = 532$ nm. Although the light emitted by the laser is linearly polarized, we use a Glan polarizer to ensure high-contrast horizontal linear polarization of the illumination beam. The laser beam is then expanded and collimated with the association of a microscope objective (×10, 0.25 NA) and a convex lens L_0 ($f'_0 = 200$ mm). A diaphragm is used to adjust the beam diameter and suppress unwanted diffusions or reflections on the edges of the collimation lens (L_0). Finally, this beam forms a 2.5 cm diameter illumination spot on the scattering sample under test.

Imaging optics: A set of two converging lenses L_1 ($f_1' = 80$ mm) and L_2 ($f_2' = 40$ mm) is used to image the surface of the sample on the detector plane. Such optical configuration makes it possible to position the PA between the two lenses, in the intermediate image plane (IIP). The distance between the two lenses is 22.5 cm and the distance between L_2 and the IIP is set to 12 cm.

Though unusual in polarimetric imaging setups, positioning of the polarization analysis components in a conjugate plane of the sample and of the CCD is justified here since it helps minimizing wavefront deformations when the PA configuration is changed. Indeed, the beam has a minimum size in the IIP, forming an intermediate image of diameter 6.2 mm on the PA. Provided the beam is well centered with the rotation axis of the PA, such configuration minimizes any spurious effect of planarity imperfections of the polarization analysis components (see paragraph "Polarization analyzer" below).

Imaging pinhole: To ensure a sufficient size of the coherence area on the detector, such that a speckle grain covers a few thousands of pixels, the aperture of the imaging system is shrunk by inserting a circular pinhole of diameter $\phi = 200$ μm on the imaging lens L_2. The typical size of a speckle grain on the detector is then given by

$$\delta = 1.22\lambda\frac{2D}{\phi} \simeq 0.4 \text{ mm}, \tag{4}$$

where $D = 6$ cm corresponds to the distance between imaging lens L_2 and the detector plane. In this configuration, each speckle grain of circular shape covers in the final image approximately 2300 square pixels of dimension 7.4 μm.

Imaging detector: Due to the tiny imaging aperture used in the experiment, the camera must exhibit good noise properties under low illumination levels. Consequently, we choose to record the images on a 12 bit monochromatic 659 × 494 pixels CCD camera (Basler scA640-70 fm). Moreover, to enhance the dynamic range, a dual exposure with two different acquisition times ($T_2 = 10T_1$) is used to extract data from the low intensity areas. Image processing is necessary to recombine the two snapshots, finally providing an intensity image with higher dynamics than the 4096 grayscale levels of the 12 bit camera [see pixels grayscale values of Fig. 9(a), for instance].

Polarization analyzer (PA): Most conventional polarimetric imaging experiments use a single adjustable polarizer to measure $I_x, I_y, I_{+45°}, I_{-45°}$, and then add a quarter-wave plate to access the two images I_R and I_L associated with circular polarization of light. This simple and natural approach is not satisfactory in our experiment. Indeed, inserting an optical element between the sample and the CCD detector will necessarily modify the optical path of the backscattered light and modify the speckle pattern, thus inevitably spoiling the measurement as will be evidenced below. To maintain a constant optical path during the six intensity measurements, the PA used consists of a nanoparticles linear film polarizer plate (2 mm thickness) and an achromatic quarter-wave plate (400–700 nm, $\lambda/10$ wavefront distortion, 1 mm thick) closely packed together. These components are inserted in a single rotating optical mount with the axes of the polarizer and of the quarter-wave plate forming an angle of 45°. The relative positioning of the polarizer and quarter-wave plate, as well as the calibration of the PA axes, were operated preliminary to any measurement, using the vertically polarized illumination laser beam. Calibration is an important step in the design of a polarimeter due to possible polarization artifacts introduced by the optical elements of the system [34].

To switch from a linear polarization analysis to a circular polarization analysis, the whole mount is turned around so that the analyzed light enters the polarizer first, or the quarter-wave plate first, respectively. To this aim, the PA is set on a motorized rotating stage for precise and repeatable positioning. This configuration allows us to access the whole six intensity measurements needed to determine the full Stokes vector [31]. In addition, two angular degrees of freedom are added to the PA mount to enable fine adjustment of the orientation of the polarization analysis plates with respect to the optical axis (one rotation about $\vec{e}_x$ and one about $\vec{e}_y$). The lens L_1

($f_1' = 80$ mm) is also placed on a micrometric translation mount allowing fine positioning of the focal spot on the polarization analysis plates. These mechanical degrees of freedom associated to the PA are sketched in Fig. 2. As will be evidenced in the next subsection, these additional degrees of freedom are indispensable to refine the relative positioning between the center of the PA and the focal spot in the IIP and thus minimize wavefront deformations between two successive acquisitions with different configurations of the PA.

Mechanical stability and housing: As will be detailed below, mechanical stability and air turbulence must be taken into account to ensure stability of the speckle pattern. To this end, the optical setup is compactly built on an optical table and breadboard. The whole setup (apart from laser) is inserted within a Plexiglas housing to protect it from air flows.

C. Measurement Protocol and Speckle Pattern Registration

A crucial point to achieve Stokes imaging beyond the speckle grain scale is to ensure that the wavefront is not modified by the movement of the PA during the complete Stokes measurement. In other words, when the configuration of the PA is switched to measure the different Stokes components, the speckle pattern must not change. As the PA is neither strictly plane nor placed in a plane strictly perpendicular to the optical axis, this condition is not *a priori* satisfied. This is evidenced in Fig. 3, where a first Stokes intensity image I_x is plotted [Fig. 3(a)] and can be compared with a second intensity image $I_{+45°}$ obtained after rotating the polarizer by a 45° angle [Fig. 3(b)]. As can be clearly seen, the speckle intensity pattern observed is obviously different. At this level, if wavefront distortions caused by PA rotation were to be ignored, such modification of the speckle intensity repartition could erroneously be interpreted as a signature of different SOPs across the speckle grains observed. Indeed, the images of Fig. 3 were recorded on a metallic slab sample. For such nondepolarizing material, we have checked that the SOP after reflection

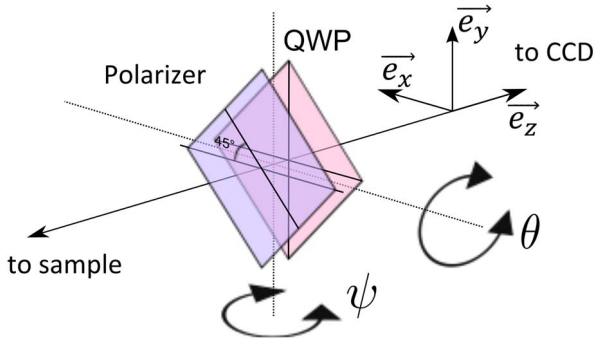

Fig. 2. (Color online) Schematic description of the PA in a linear analyzer configuration. The PA mechanical mount provides two angular degrees of freedom (rotation θ about axis $\vec{e}_x$ and rotation ψ about axis $\vec{e}_y$) used during the speckle registration procedure.

is strictly identical to the illumination state. Consequently, the speckle intensity pattern must have different intensity levels but the same spatial repartition for each Stokes intensity measurement. Since this is clearly not the case in Fig. 3(b), one has to act on the fine PA orientation adjustments to recover the initial wavefront (or at least minimize the distortions). Acting very slightly and accurately on the three degrees of freedom of the PA (two rotations about $\vec{e}_x$ and $\vec{e}_y$ and the translation of the lens L_1 along $\vec{e}_z$), it is indeed possible to recover the initial speckle pattern reasonably well, as can be seen in Fig. 3(c). Such procedure will be referred to in the remainder of this article as *speckle pattern registration*.

Once the possibility of experimental speckle pattern registration is evidenced, let us now detail the measurement protocol proposed to achieve Stokes imaging beyond the speckle grain scale. This protocol is based on the use of a metallic reference slab sample as follows:

- After a first intensity measurement, say I_x, is operated on a given sample, the metallic reference slab is inserted in front of the sample, in the vicinity of the sample surface. The speckle intensity pattern formed by the light backscattered on the metallic slab is temporarily stored as a reference.
- Then the PA is rotated to the next configuration to measure, say $I_{+45°}$, thus inevitably causing wavefront distortions and hence modifying the current speckle intensity pattern.
- Registration of the speckle pattern is then carried out as described above, until the previously stored reference pattern is recovered. A coarse registration is first operated by trying to adjust the bright speckle grains; then a fine tuning is done by minimizing numerical criteria [spatial average of the whole difference image between the reference speckle pattern image and the current image (normalized in terms of average intensity) on the one hand, and root mean square of this difference image on the other hand]. Once these two indicators are minimized, we can warrant that the initial wavefront has been recovered with minimum distortion.
- The metallic slab is then removed and the next image ($I_{+45°}$ in this example) can be eventually acquired on the sample under test.

To get a full characterization of the Stokes vector in each point of a highly resolved speckle pattern, the above protocol has to be followed between each Stokes intensity measurement to ensure that the same speckle pattern is analyzed all along the six acquisitions. This registration protocol can be quite long and tedious but is unavoidable. It must be noted that the speckle pattern might sometimes not be recovered if the mechanical or thermal drifts are not properly cancelled, as will be shown in the following subsection.

An illustration of the quality of speckle registration obtained during four successive Stokes measurements $I_{+45°}$, $I_{-45°}$, I_R, I_L is given in Fig. 4. It can be

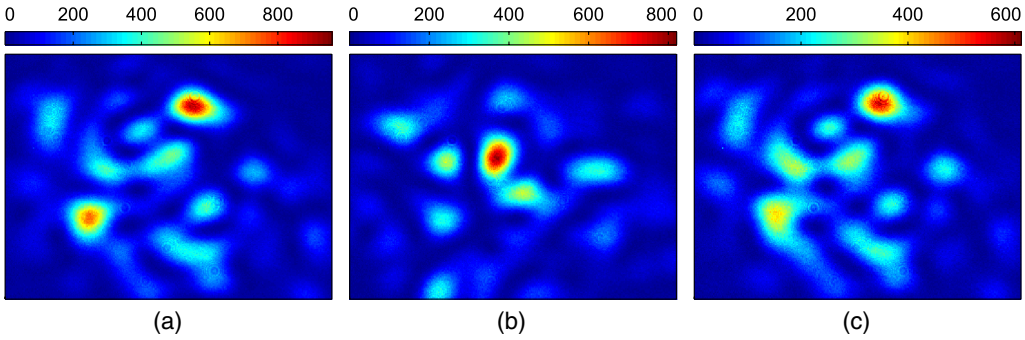

Fig. 3. (Color online) Reference speckle intensity pattern (a) acquired on a metallic slab, (b) wavefront distortions caused by rotation of the PA modify the speckle intensity pattern, and (c) the reference speckle pattern can be fairly recovered after speckle registration.

observed that the registration procedure allows the speckle pattern to be recovered when the sample is nondepolarizing (metallic reference) with various orientations of the PA.

D. Air Flow and Thermal Effects

To minimize wavefront aberrations caused by air turbulence, the whole setup (apart from the laser) is packaged in a Plexiglas housing. However, modifications of the PA configuration and adjustment of the mount during speckle registration are done manually and it is thus necessary to keep a part of the housing open during the measurement process. The evolution during half an hour of the intensity of 10 pixels arbitrarily chosen on a resolved speckle intensity pattern obtained on a metallic sample is plotted in Fig. 5. During this experiment, the setup has been disturbed by some actions at various times indicated with vertical dotted lines in Fig. 5. It can be seen that the speckle pattern is highly sensitive to these actions, indicating that handling of the PA mechanical mount must be operated with care. Moreover, we were able to measure a typical stabilization time of 50 s for the speckle field to stabilize to its initial pattern. This time was then considered as the typical time to wait between any intervention on the setup and the next measurement.

Besides, since imaging of the sample is operated through a small aperture (200 μm pinhole), it is thus necessary to illuminate the sample with a laser power of a few hundreds of milliwatts to warrant sufficient signal-to-noise ratio on the detector. Taking into account the illumination spot diameter of 3.5 cm, the illumination intensity is around 10 mW/cm^2. Despite this relatively moderate value, we found that thermal effects occur in the samples that undergo sufficient mechanical dilatation at a microscopic scale to alter the speckle interference intensity pattern acquired on the detector. It can indeed be seen in Fig. 5 that thermalization of the sample takes some time on a metallic slab (typically >10 min). This thermalization can be longer or even never reached on other samples, as illustrated in Fig. 6 on a cardboard sheet sample. In this figure, the time evolution of the intensity of 10 pixels in a resolved speckle intensity pattern is recorded during 30 min. As one can see, the speckle intensity pattern shows important variations during all the experiment, which are also imputed to bad mechanical stability of the sample.

These experimental results indicate that the measurement of Stokes parameters on a highly resolved speckle intensity pattern requires a sufficient preliminary illumination time for the sample to

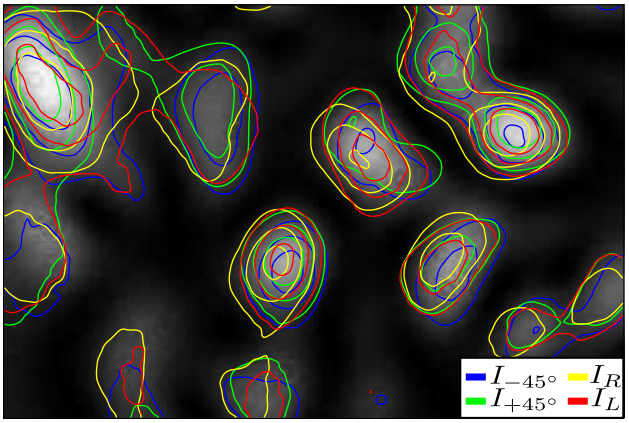

Fig. 4. (Color online) Contour plots: speckle intensity patterns observed after speckle registration with four orientations of the PA on a metallic reference slab. Grayscale background image: total intensity image $\mathcal{S}_0$.

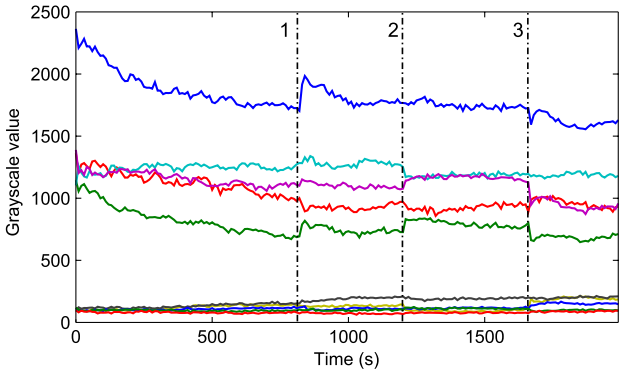

Fig. 5. (Color online) Time evolution of the intensity of 10 pixels in a speckle intensity pattern with perturbations when the sample is a metallic slab. (1) Cover is opened and air is blown inside, (2) 360° rotation about $\vec{e}_z$ of the PA, and (3) 360° rotation about $\vec{e}_y$ of the PA.

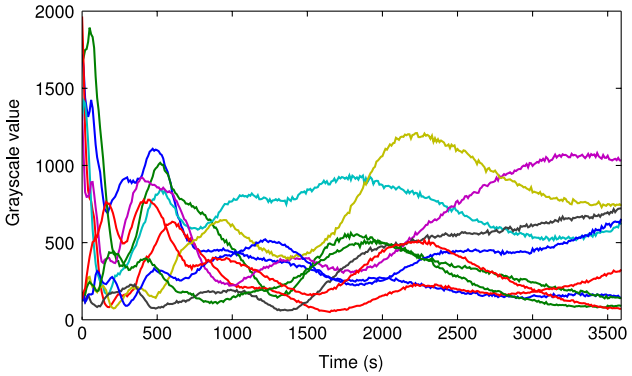

Fig. 6. (Color online) Time evolution (30 min) of the intensity of 10 pixels when the sample is a cardboard sheet sample.

thermalize (and the speckle pattern to stabilize). In addition, the samples have to show good thermal and mechanical stability to optimize the stability of the observed speckle pattern. For these reasons, the samples used in the following experiments have been deposited on a heavy marble block to help heat dissipation and to ensure mechanical stability. In these conditions, an acceptable stability of the speckle pattern can be obtained, which has been checked experimentally. It can indeed be observed in Fig. 7 that after a 14 min (840 s) thermalization of a diffusive red paint sample deposited on a heavy marble block, the grayscale values of the 10 pixels do not evolve by more than 5% for 6 min.

3. Description of the Experiment

To illustrate the possibilities offered by the experimental setup and protocol described in the previous section, different experiments have been carried out by considering different samples with distinct scattering properties. Before displaying the experimental results obtained in Section 4, we describe the samples considered as well as their "macroscopic" (large spatial scale) depolarization properties given by the measurement of the Stokes parameters on unresolved speckle patterns.

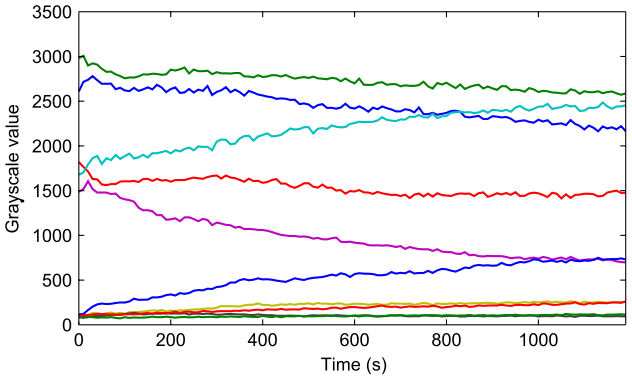

Fig. 7. (Color online) Time evolution (20 min) of the intensity of 10 pixels when the sample is a red paint deposited on a heavy marble block.

A. Sample Selection

The samples considered have been selected for their distinct depolarization properties. First, a metallic slab has been used as a reference sample to check the validity of the method because of the well-known polarimetric behavior of such material. Next, two samples with distinct scattering characteristics have been designed for the purpose of the experiment by depositing a red and a green paint on a heavy marble block to warrant heat dissipation and mechanical stability as mentioned in the previous section.

On the one hand, in the case of the red paint sample, the green illuminating light ($\lambda = 532$ nm) is rapidly absorbed at the sample surface. As a consequence, the small amount of backscattered light predominantly comes from surface reflection with a quasi-normal incidence angle and the incident SOP is thus maintained [35]. This is sketched in Fig. 8(a), and this sample can thus be considered as nondepolarizing. On the other hand, in the case of the green paint sample, incident light is much less absorbed, enabling multiple scattering to occur in the bulk of the material, as illustrated in Fig. 8(b) [35]. Such a volume scattering regime highly depolarizes the incident light, as will be checked in the next subsection. These two samples will make it possible to compare the effect of two different types of scattering on the local polarization below the speckle grain scale in the next section.

B. Large-Scale Polarimetric Characterization of Speckle Patterns

Large-scale polarimetric characterization of the speckle fields backscattered by each sample has been carried out by measuring the values of the DOP and of the OSC in a measurement configuration where the speckle is not resolved, i.e., with each pixel of

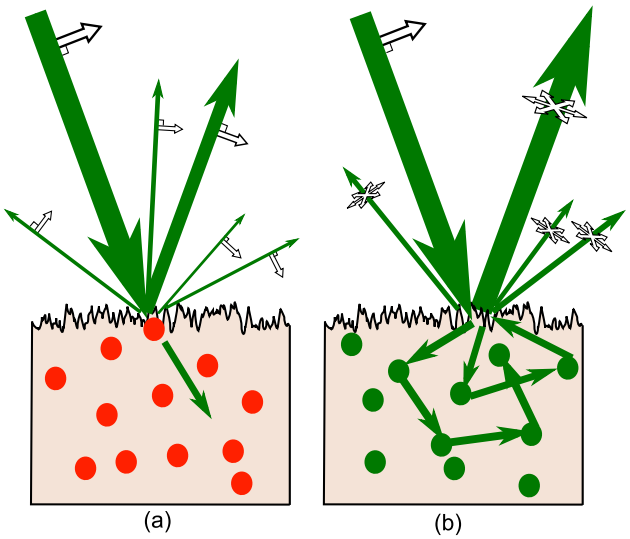

Fig. 8. (Color online) Schematic illustration of (a) surface and (b) volume scattering regimes obtained by scattering of a green illumination on red and green samples, respectively. The white arrows symbolize the electric field polarization direction.

the camera averaging several speckle grains, as in standard coherent polarimetric imaging setups. For this purpose, we removed the pinhole in order to decrease speckle grains dimension below the pixel size. In this configuration, one can estimate how many speckle grains are averaged per pixel by determining the speckle contrast when backscattered light is fully polarized, which is given by [1]

$$c = \frac{\langle I \rangle}{\sigma_I}, \tag{5}$$

where $\langle I \rangle = \langle \mathcal{S}_0 \rangle$ is the mean intensity computed over the whole image and $\sigma_I = \sigma_{\mathcal{S}_0}$ is the standard deviation of the intensity. In this configuration, we measured a speckle contrast of 2.5, meaning that each pixel contains 2.5 speckle grains on average. We emphasize that in that case, as in standard coherent polarimetric imaging setups, the measurement of the Stokes parameters can be operated without the need of any speckle registration procedure. Indeed, uncontrolled wavefront distortions occurring during the measurement are wiped out by spatial averaging of several speckle grains in each pixel. Moreover, the Stokes vectors were estimated on homogeneous regions of 100 pixels (square regions of 10 × 10 pixels), thus increasing the effect of spatial averaging. Table 1 gives the results of the estimation on 420 subregions of 100 pixels of the normalized Stokes parameters $S_1 = \mathrm{OSC}$, S_2, S_3 for each sample.

It can be noted that the values of the DOP and the OSC are similar for the metallic reference and the red paint sample. This confirms that these two materials share a similar nondepolarizing action and thus illustrates that light does not undergo multiple scattering in a surface scattering regime. For the green sample, the value of the DOP and of the OSC are much lower, which is in agreement with the expected depolarizing behavior of this sample due to volume scattering of light in the bulk of the material.

This large scale polarimetric characterization given in Table 1 will now be compared in the next section with polarimetric measurements beyond the speckle grain scale obtained with the setup and protocol presented in Section 2. More particularly, this preliminary characterization will allow us to analyze how "global" depolarization occurs from a spatial averaging of locally well-defined polarization states.

Table 1. Large Scale Polarimetric Characterization of Light Backscattered by the Three Samples Considered[a]

Sample	DOP	$S_1 = \mathrm{OSC}$	S_2	S_3
Metal slab	0.97	0.96	0.12	0
Red paint	0.95	0.94	0.16	−0.01
Green paint	0.44	0.43	0.07	−0.01

[a]A maximum standard deviation of 0.02 was obtained over these 12 estimated values (estimation on 420 homogeneous regions of 100 pixels).

4. Results and Discussion

A. Stokes Imaging Beyond the Speckle Grain Scale

Let us now present the experimental results of Stokes imaging beyond the speckle grain scale obtained with the setup and protocol detailed in Section 2. These experimental acquisitions were conducted on the three samples described in the previous section. For each sample, six intensity images were recorded with a careful speckle registration step between each image acquisition, as described in Section 2.

Reference metallic slab: For the sake of concision, we only present the raw images obtained on the reference metallic slab sample in Fig. 9. An example of raw image I_x acquired with a horizontal linear polarization direction is given in Fig. 9(a). A region of interest (ROI) of 200 × 150 pixels is then selected in the initial image. In Fig. 9(b), the first Stokes image $\mathcal{S}_0$ is plotted and represents the total intensity of the speckle pattern as $\mathcal{S}_0 = I_x + I_y$. One can notice that each speckle grain covers

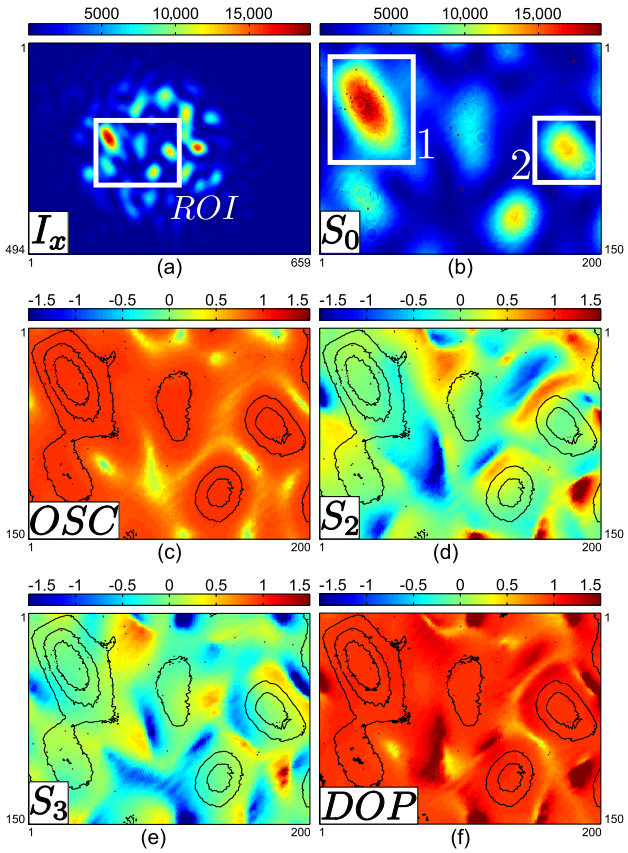

Fig. 9. (Color online) Stokes imaging of a speckle intensity pattern obtained on the metallic reference slab. (a) Example of raw image acquisition (I_x) and selection of the ROI. From the six acquisitions, the four Stokes images are determined. (b) First Stokes image $\mathcal{S}_0$ (total intensity). Two sub-ROIs are defined to compare the SOP in distinct speckle grains. (c) Second normalized Stokes image S_1. (d) Third normalized Stokes image S_2. (e) Fourth normalized Stokes image S_3. (f) DOP. Total intensity repartition is indicated in contour plots in (c), (d), (e), and (f) thumbnails.

approximately 1000 pixels. Figure 9(c) shows the computed second normalized Stokes parameter S_1, which is equal to the OSC, as shown in Eq. (3). The third and fourth Stokes images are respectively plotted in Figs. 9(d) and 9(e), and are finally used to determine the experimental DOP map, which is given in Fig. 9(f).

As expected, the values of the OSC and of the DOP are close to 1 across the ROI considered, while S_2 and S_3 maps are close to null values. This is particularly well verified in areas exhibiting a high intensity (bright speckle spots). Conversely, it decreases in the low-intensity areas where DOP values exceeding 1 can be observed, thus revealing experimental biases in the measurement in spite of experimental care in the speckle registration procedure. As a consequence, these areas in the image should not be analyzed since the signal-to-noise ratio is too low to draw any conclusion.

Other samples: The experimental results obtained on the two other samples considered are given in Fig. 10, which provides the total intensity image (Stokes parameter $\mathcal{S}_0$) as well as the computed OSC and DOP maps on a 200 × 150 pixels ROI. It can be checked in Figs. 10(a), 10(c), and 10(e) that the red sample exhibits a behavior strongly similar to the metallic sample with DOP and OSC values close to 1 in high-intensity areas. This nondepolarizing behavior is in agreement with the expected surface scattering regime, and with the large-scale polarimetric measurements presented in Subsection 3.B. Moreover, this figure thus confirms experimentally that incident polarization is maintained during interaction with the material in a surface scattering regime.

In the case of the green paint sample, it can first be observed in Fig. 10(d) that the SOP of light is well-defined within each coherence area (speckle grain) since the value of the DOP remains close to 1 in each pixel in a bright speckle spot. This is in agreement with theoretical predictions and previous experimental hints obtained from multiple-scale analyses of nonresolved speckle intensity patterns [23,25–27]. By contrast, unlike the red paint and metallic samples, it can be seen in Fig. 10(f) that for the green paint sample, the initial polarization is not necessarily maintained in all the coherence areas since OSC values significantly lower than unity can be observed in areas corresponding to bright speckle spots with DOP values close to 1.

In the next subsection, these experimental results are analyzed with more detail through the mapping of the spatial repartition of the SOPs on Poincaré's sphere.

B. Analysis of Polarization States Spatial Repartition

To complement the study of the spatial repartition of local SOPs within the speckle pattern, it is possible to map the normalized Stokes components of each pixel on a Poincaré sphere as shown in Fig. 11. In Fig. 11(a), the repartition of the pixels SOP obtained

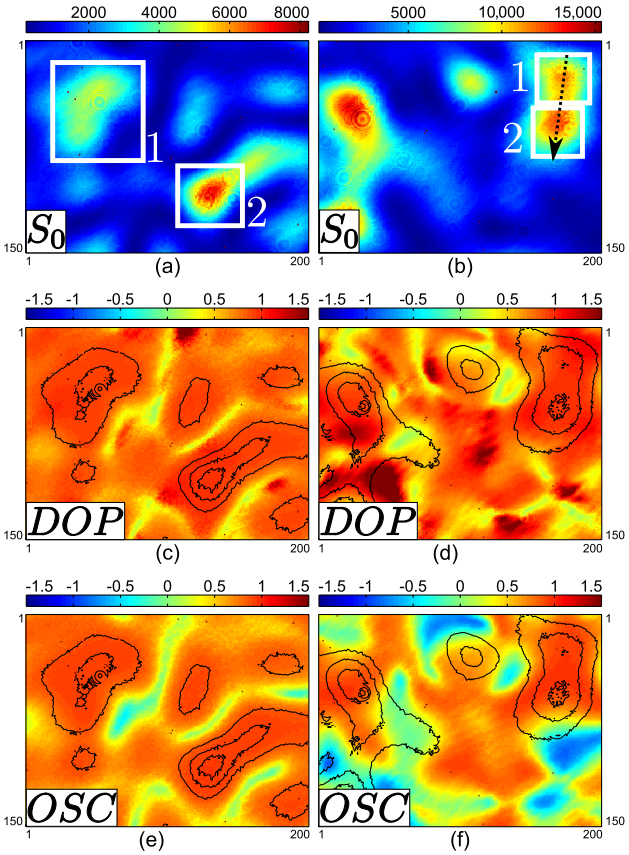

Fig. 10. (Color online) Stokes imaging beyond the speckle grain scale of a speckle intensity pattern obtained on a red paint sample [(a), (c), and (e)] and a green paint sample [(b), (d), and (f)]. (a), (b) First Stokes image $\mathcal{S}_0$ (total intensity). Two sub-ROIs are defined to compare the SOP in distinct speckle grains. (c), (d) Map of the computed DOP. (e), (f) Map of the computed OSC. Total intensity repartition is indicated in contour plots in (c), (d), (e), and (f) thumbnails.

on the reference metallic slab in the whole ROI defined in Fig. 9(a) is plotted on Poincaré's sphere, whereas Figs. 11(b) and 11(c) represent the pixels SOP in sub-ROIs 1 and 2 defined in Fig. 9(b). The colors associated with each point on the sphere denote the total intensity (parameter $\mathcal{S}_0$) of the corresponding pixel, in agreement with pixel colors of Fig. 9(b). As a consequence, a larger degree of confidence can be granted to the red points, corresponding to the pixels of the bright speckle grains, but the SOPs for the darkest pixels plotted in blue must be interpreted warily due to significant experimental noise. In addition, the red circle corresponds to the mean value of the Stokes vector estimated in the whole ROI, whereas the black circle shows the value of the Stokes vector determined from the preliminary large-scale polarimetric characterization presented in Subsection 3.B. and given in Table 1. From Figs. 11(b) and 11(c), it can be observed that the two speckle grains share the same SOP, corresponding almost perfectly to the incident illumination polarimetric state and to the "global" polarimetric state observed after spatial averaging [Fig. 11(a)]. This

confirms the nondepolarizing behavior of this metallic reference sample as every single speckle is in the same polarization state. We highlight again that the important dispersion of the SOPs plotted in blue is due to important experimental noise in darkest regions of the speckle patterns.

A similar behavior is confirmed for the red paint sample by analyzing the polarimetric repartition over Poincaré's sphere given in Fig. 11(d) for the whole ROI and in Figs. 11(e) and 11(f) for sub-ROIs 1 and 2 defined in Fig. 10(a). As is the case for the metallic sample, the two speckle grains selected in sub-ROIS 1 and 2 share the same SOP, matching with the illumination polarization, and the "global" polarimetric state measured after spatial averaging.

In the case of the green paint sample, the analysis of the spatial mapping of SOPs over Poincaré's sphere is more interesting. It can first be checked that after averaging over the whole ROI, the mean polarimetric state represented by the red circle in Fig. 11(g) is in agreement with the "global" polarization measured in Subsection 3.B. after spatial averaging (black circle). Averaging over the ROI indeed yields a globally depolarized state (DOP = 0.44 in average from Table 1), corresponding to a point lying inside Poincaré's sphere. However, at a single speckle grain scale, the SOP is well defined. Indeed, as can be seen in Figs. 11(h) and Fig. 11(i), which correspond respectively to the SOP of the pixels in sub-ROIs 1 and 2 defined in Fig. 10(b), the DOP is close to 1

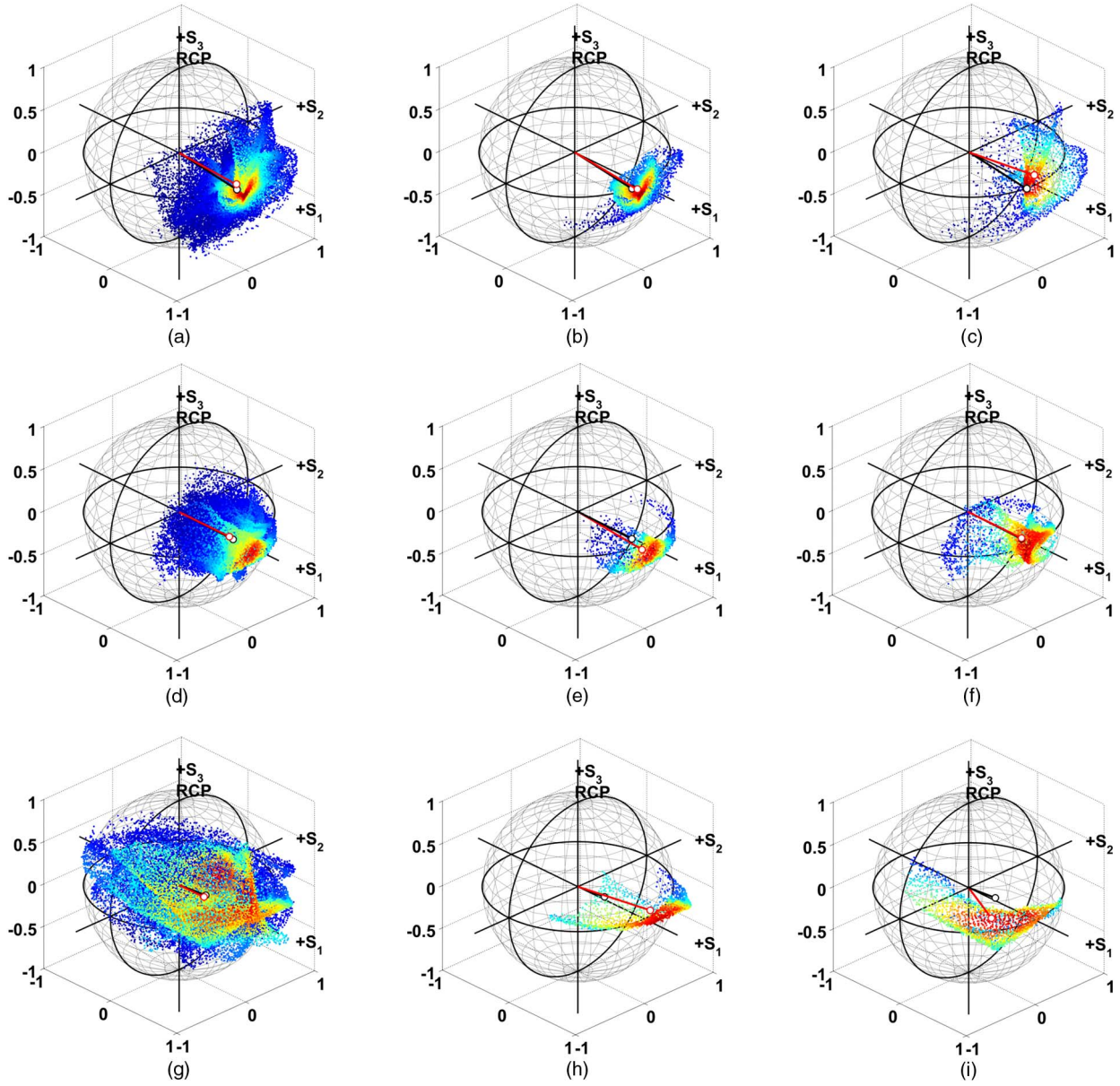

Fig. 11. (Color online) Repartition of the pixels SOP on Poincaré's sphere for a metallic sample (first line), a red paint sample (second line), and a green paint sample (third line). First column, SOP in the whole ROI; second column, SOP in sub-ROI 1; third column, SOP in sub-ROI 2. Sub-ROIs are respectively defined in Figs. 9(b), 10(a), and 10(b).

and the polarization state lies on the surface of Poincaré's sphere. In addition, contrarily to the previous samples, one can see that the two speckle grains considered exhibit different SOPs, which do not exactly resemble the illumination polarization state. Such behavior is a consequence of multiple scattering occurring in the bulk of the sample in the case of the green paint sample, as explained in Subsection 3.A.

These results thus represent clear experimental evidence in the optical domain and beyond the speckle grain scale that light is fully polarized at a local scale, whatever the scattering regime considered (surface or bulk). As suggested by previous results obtained from a statistical analyses of polarization states on nonresolved speckle patterns [23,27], global depolarization properties stem from a spatial averaging of local SOPs over several coherence areas. Using the experimental results gathered, we analyze this property in the next subsection.

C. Multiple-Scale Analysis of the DOP

A multiple-scale analysis of the DOP has been conducted on the highly resolved Stokes images measured. The results are summarized in Table 2, which contains the values of the DOP and the OSC averaged over the whole ROI after local binning with different binning pitches. For instance, a binning pitch of 30 means that 33 blocks of 30×30 pixels have been averaged in a ROI of 200×150 pixels. As the binning pitch is increased, it can be seen that DOP and OSC values tend to the values measured in Subsection 3.B (see Table 1), which is in agreement with previous works [23,27]. This result, which is better evidenced in the case of the green paint sample, thus tends to confirm that the global depolarizing behavior emerges from a spatial averaging of varying polarization states, well-defined at a local scale.

D. SOP Mapping Across Speckle Pattern: Observation of an Adiabatic Polarization Transition

To illustrate the potentialities offered by the setup and protocol proposed in this paper, let us lastly present how the spatial evolution of the SOP can be mapped along a geometrical path across the speckle pattern studied. Let us, for instance, consider the two contiguous speckle grains corresponding to the sub-ROIs defined for the green paint sample in Fig. 10(b). This case is indeed interesting since it has been checked in the previous section and in Fig. 11 that these two speckle grains exhibit different SOPs but a DOP close to unity. With the setup proposed, it is possible to study how this polarization evolves from one speckle grain to the other. The data plotted in Fig. 12(a) on Poincaré's sphere correspond to the evolution of the SOP along the black dotted line drawn in Fig. 10(b). On the sphere, the dark points correspond to the pixels located at the beginning of the line and the bright points to those located at the tip of the black dashed arrow of Fig. 10(b). The OSC and DOP measured along this line are also plotted respectively with dashed and plain lines in Fig. 12(b). From these results, we can see that the spatial SOP transition between two speckle grains is continuous, which is consistent with previous works [9,36]. In the situation considered, the incident illumination SOP, which is almost maintained in the first speckle grain, then rapidly evolves toward a distinct polarization state, which does not resemble the initial laser polarization. Nevertheless, this evolution is shown to be adiabatic so that the SOP follows a continuous trajectory along the surface of Poincaré's sphere.

Table 2. Average Value of the DOP and of the OSC for Different Binning Pitches[a]

Sample	Bin. Pitch	Binned Areas	DOP		OSC	
			$\langle\cdot\rangle$	σ	$\langle\cdot\rangle$	σ
Metal slab	3	3333	1.00	0.23	0.85	0.17
	10	300	0.97	0.16	0.86	0.14
	30	33	0.93	0.06	0.91	0.07
Red paint	3	3333	0.80	0.18	0.69	0.23
	10	300	0.80	0.16	0.71	0.21
	30	33	0.80	0.10	0.77	0.12
Green paint	3	3333	0.78	0.30	0.38	0.47
	10	300	0.76	0.28	0.39	0.45
	30	33	0.61	0.24	0.41	0.36

[a]The estimated value and the corresponding standard deviations were estimated in the whole ROI on a varying number of binned regions.

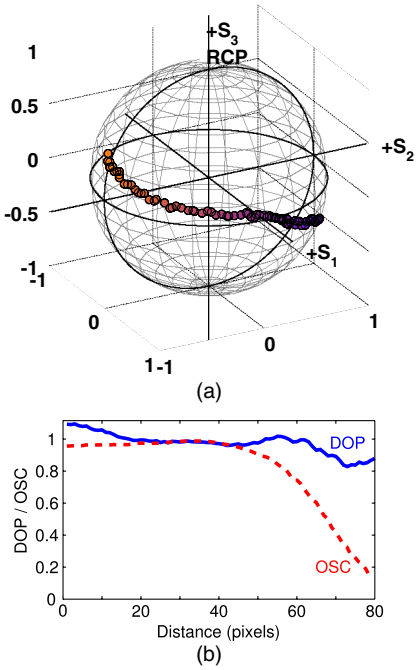

Fig. 12. (Color online) Observation of the adiabatic polarization state transition along the geometrical path defined in Fig. 10(b) between two adjacent speckle grains on the green paint sample exhibiting bulk scattering regime. (a) Evolution of the SOP on Poincaré's sphere. (b) Evolution of the OSC (dotted curve) and DOP (plain curve).

5. Conclusion

In this article, we addressed the experimental issue of coherent active Stokes imaging beyond the speckle grain scale, i.e., on a highly resolved speckle pattern with each speckle grain covering several hundreds or thousands of pixels. The numerous experimental difficulties encountered to achieve such a measurement have been identified and solved to design the first realization, to the best of our knowledge, of a polarimetric imaging setup dedicated to such measurement. In addition, we proposed an experimental protocol able to warrant a constant wavefront during the entire measurement process. We demonstrated that the setup and the speckle registration protocol proposed allow the measurement of the full Stokes vector to be achieved in each pixel of a highly resolved speckle pattern. After a validation of the technique on a metallic reference sample exhibiting a well-known nondepolarizing behavior, experimental Stokes imaging beyond the speckle grain scale has been demonstrated on two scattering samples exhibiting different scattering regimes (surface and bulk). The influence of these distinct scattering regimes on the local polarization state of light has been studied and commented, and the conclusions obtained are in agreement with previous experimental works using a statistical analysis on moderately resolved speckle pattern. Lastly, these experiments allowed us to experimentally demonstrate in the optical domain that the polarization transition between two contiguous speckles follows a continuous and adiabatic evolution.

There are various perspectives to this work among which we can cite a more thorough study of SOP transitions between adjacent speckle grains and the analysis of polarimetric correlation lengths in regard to speckle intensity coherence areas. The investigation of the influence of the source wavelength and coherence on polarization beyond the speckle grain scale is currently in progress. Besides, the analysis of specific samples exhibiting nonstandard scattering properties is also an interesting perspective. From an applicative point of view, we are quite convinced that exploring the polarization properties at a microscopic scale could lead to a more accurate understanding of the physics happening in optical systems or techniques using the speckle [6,7,16–19,21] and thus might help in optimizing these systems. All these perspectives would benefit from the development of more robust experimental designs, by automating the speckle registration optimization stage, for instance (programmable actuators, liquid-crystal polarimetric devices, etc.), or even using a four-arm division of amplitude system with appropriate phase plates/polarizers and calibration in order to perform simultaneous imaging of the four Stokes components.

References

1. J. W. Goodman, *Speckle Phenomena: Theory and Applications* (Roberts & Company, 2007).
2. M. I. Skolnik, *Introduction to Radar Systems*, 3rd ed. (McGraw-Hill, 2001).
3. J. K. Jao, "Amplitude distribution of composite terrain radar clutter and the K-distribution," IEEE Trans. Antennas Propag. **AP-32**, 1049–1062 (1984).
4. N. Garcia and A. Z. Genack, "Crossover to strong intensity correlation for microwave radiation in random media," Phys. Rev. Lett. **63**, 1678–1681 (1989).
5. P. Sheng, *Introduction to Wave Scattering, Localization and Mesoscopic Phenomena*, 2nd ed. (Springer, 2006).
6. I. Freund, "Time-reversal symmetry and image reconstruction through multiple-scattering media," J. Opt. Soc. Am. A **9**, 456–463 (1992).
7. S. M. Popoff, G. Lerosey, R. Carminati, M. Fink, A. C. Boccara, and S. Gigan, "Measuring the transmission matrix in optics: an approach to the study and control of light propagation in disordered media," Phys. Rev. Lett. **104**, 100601 (2010).
8. W. H. Peeters, J. J. D. Moerman, and M. P. van Exter, "Observation of two-photon speckle patterns," Phys. Rev. Lett. **104**, 173601 (2010).
9. O. V. Angelsky, I. I. Mokhun, A. I. Mokhun, and M. S. Soskin, "Interferometric methods in diagnostics of polarization singularities," Phys. Rev. E **65**, 036602 (2002).
10. M. Alouini, F. Goudail, A. Grisard, J. Bourderionnet, D. Dolfi, A. Béniére, I. Baarstad, T. Løke, P. Kaspersen, X. Normandin, and G. Berginc, "Near-infrared active polarimetric and multispectral laboratory demonstrator for target detection," Appl. Opt. **48**, 1610–1618 (2009).
11. A. Béniére, M. Alouini, F. Goudail, and D. Dolfi, "Design and experimental validation of a snapshot polarization contrast imager," Appl. Opt. **48**, 5764–5773 (2009).
12. D. Léger, E. Mathieu, and J. C. Perrin, "Optical surface roughness determination using speckle correlation technique," Appl. Opt. **14**, 872–877 (1975).
13. M. Lehman, J. A. Pomarico, and R. D. Torroba, "Digital speckle pattern interferometry applied to a surface roughness study," Opt. Eng. **34**, 1148–1152 (1995).
14. R. A. Sprague, "Surface roughness measurement using white light speckle," Appl. Opt. **11**, 2811–2817 (1972).
15. N. Andrés, M. P. Arroyo, H. Hinrichs, and M. Quintanilla, "Digital speckle-pattern interferometry as a full-field fluid-velocimetry technique," Opt. Lett. **24**, 575–577 (1999).
16. I. Freund, "Stokes-vector reconstruction," Opt. Lett. **15**, 1425–1427 (1990).
17. M. Roche, J. Fade, and P. Réfrégier, "Parametric estimation of the square degree of polarization from two intensity images degraded by fully developed speckle noise," J. Opt. Soc. Am. A **24**, 2719–2727 (2007).
18. P. Réfrégier, J. Fade, and M. Roche, "Estimation precision of the degree of polarization from a single speckle intensity image," Opt. Lett. **32**, 739–741 (2007).
19. J. Fade, M. Roche, and M. Alouini, "Computational polarization imaging from a single speckle image," Opt. Lett. **37**, 386–388 (2012).
20. J. Sorrentini, M. Zerrad, G. Soriano, and C. Amra, "Enpolarization of light by scattering media," Opt. Express **19**, 21313–21320 (2011).
21. N. Curry, P. Bondareff, M. Leclercq, N. F. van Hulst, R. Sapienza, S. Gigan, and S. Grésillon, "Direct determination of diffusion properties of random media from speckle contrast," Opt. Lett. **36**, 3332–3334 (2011).
22. T. Setälä, A. Shevchenko, M. Kaivola, and A. T. Friberg, "Polarization time and length for random optical beams," Phys. Rev. A **78**, 033817 (2008).
23. J. Broky and A. Dogariu, "Complex degree of mutual polarization in randomly scattered fields," Opt. Express **18**, 20105–20113 (2010).
24. J. Broky and A. Dogariu, "Correlations of polarization in random electro-magnetic fields," Opt. Express **19**, 15711–15719 (2011).
25. J. Li, G. Yao, and L. V. Wang, "Degree of polarization in laser speckles from turbid media: implication in tissue optics," J. Biomed. Opt. **7**, 307–312 (2002).
26. C. Amra, M. Zerrad, L. Siozade, G. Georges, and C. Deumié, "Partial polarization of light induced by random defects at surfaces or bulks," Opt. Express **16**, 10372–10383 (2008).

27. M. Zerrad, J. Sorrentini, G. Soriano, and C. Amra, "Gradual loss of polarization in light scattered from rough surfaces: electromagnetic prediction," Opt. Express **18**, 15832–15843 (2010).
28. J. Ellis and A. Dogariu, "Complex degree of mutual polarization," Opt. Lett. **29**, 536–538 (2004).
29. O. Korotkova and E. Wolf, "Generalized Stokes parameters of random electromagnetic beams," Opt. Lett. **30**, 198–200 (2005).
30. J. Tervo, T. Setälä, A. Roueff, P. Réfrégier, and A. T. Friberg, "Two-point stokes parameters: interpretation and properties," Opt. Lett. **34**, 3074–3076 (2009).
31. E. Collett, *Polarized Light: Fundamentals and Applications* (Dekker, 1993).
32. S. Breugnot and P. Clémenceau, "Modeling and performances of a polarization active imager at $\lambda = 806$ nm," Opt. Eng. **39**, 2681–2688 (2000).
33. S. Zhang, Y. D. Lockerman, J. Park, and A. Z. Genack, "Interplay between generic and mesoscopic speckle statistics in transmission through random media," J. Opt. A **11**, 094018 (2009).
34. E. Compain, S. Poirier, and B. Drevillon, "General and self-consistent method for the calibration of polarization modulators, polarimeters, and Mueller-matrix ellipsometers," Appl. Opt. **38**, 3490–3502 (1999).
35. M. Alouini, F. Goudail, N. Roux, L. Le Hors, P. Hartemann, S. Breugnot, and D. Dolfi, "Active spectro-polarimetric imaging: signature modeling, imaging demonstrator and target detection," Eur. Phys. J. Appl. Phys. **42**, 129–139 (2008).
36. M. S. Soskin, V. Denisenko, and I. Freund, "Optical polarization singularities and elliptic stationary points," Opt. Lett. **28**, 1475–1477 (2003).

Generation of coherent light beam with precise and fast dynamic control of the state and degree of polarization

NOE ORTEGA-QUIJANO[1], JULIEN FADE[1], FRANÇOIS PARNET[1], MEHDI ALOUINI[1]

[1]*Institut de Physique de Rennes, CNRS, Université de Rennes 1, Campus de Beaulieu, 35 042 Rennes, France*
**Corresponding author: julien.fade@univ-rennes1.fr*

Received XX Month XXXX; revised XX Month, XXXX; accepted XX Month XXXX; posted XX Month XXXX (Doc. ID XXXXX); published XX Month XXXX

Recent developments of polarized light sources with tunable state and degree of polarization (SOP and DOP) inherently provide a temporally incoherent beam, which makes them unsuitable for applications like interferometry. We present a method for generating a coherent beam with full, precise and independent control of the SOP and DOP. Our approach is based on an imbalanced dual-frequency dual-polarization light source. We demonstrate that it offers three different working regimes, respectively providing perfectly depolarized light, DOP modulated light, or fully polarized light with a deterministic SOP trajectory. A simple implementation of this versatile approach is described and experimentally validated. © 2017 Optical Society of America

OCIS codes: *(260.5430) Polarization; (110.2945) Illumination design; (120.2130) Ellipsometry and polarimetry.*

http://dx.doi.org/10.1364/OL.99.099999

Precise polarization control constitutes an essential aspect in many optic and photonic techniques. A polarized beam is characterized by its state of polarization (SOP) and degree of polarization (DOP). Modifying the state of polarization of a beam is a common task that can be readily achieved by using conventional polarization elements like polarizers and waveplates, or dynamically-configurable elements like liquid crystal variable retarders or photo-elastic and electro-optic modulators [1]. Regarding the degree of polarization, one can use depolarizers to convert a fully polarized beam into a completely depolarized one. Such depolarizers are based on different approaches whose common characteristic is the fact that depolarization is achieved by ensemble-averaging a diversity of states of polarization in either the spatial, temporal, or spectral domain [2-7].

The development of tunable sources capable of performing both state and degree of polarization precise control within the source presents a high potential. Several tunable sources based on different technologies have been demonstrated during the last decade [8-15] for applications like polarimetric imaging, interferometric sensing, gyroscopy, quantum communications, and instrument calibration. However, they entail a number of limitations. Some of them are constrained to a single fixed state of polarization [8-10]. Other proposals do not reach completely depolarized beams [11,12], and are limited to systems with a minimum detection time of about 1 s due to the long response time of liquid crystals [12]. Nonetheless, recent proposals enable to achieve a full tunability of both DOP and SOP [13-15]. However, all of them inherently provide a temporally incoherent beam, as they rely either on spectral dispersion of the SOP of light, or on temporal delays to make two fractions of the beam temporally incoherent with each other. They are thus incompatible with techniques requiring coherent beams, like interferometric systems. Moreover, they show some additional limitations: the need for two separate sources [13] and the fact of being limited to sources with small coherence length or time [14,15].

In this work, we present a simple way of producing a coherent beam with full, precise and independent control on the SOP and DOP. Our approach is based on an imbalanced dual-frequency dual-polarization (DFDP) light source exhibiting a potentially very fast temporal modulation of its SOP, which results in a partially depolarized beam when measured at the temporal scale of most standard optical detectors. A simple implementation of this principle is described and experimentally validated in this Letter. We will also illustrate that depending on the relative magnitude of the characteristic frequencies of the proposed source (modulation frequencies) and of the detector used (cut-off frequency), this setup allows one to access three different working regimes, providing respectively perfectly depolarized light, DOP modulated light, or fully polarized light with a deterministic trajectory on the Poincaré sphere.

We first describe the principle of such a source theoretically. For that purpose, let us define a DFDP source as a superposition of two optical beams, perfectly polarized along two orthogonal modes $\vec{\mathbf{e}}_1$ and $\vec{\mathbf{e}}_2$, and propagating along direction z, whose yields a transversal electric field

$$\vec{\mathbf{E}}(t)=\begin{bmatrix} E_1(t) \\ E_2(t) \end{bmatrix} = \frac{E_0}{2} e^{-i\omega t}\left(\vec{\mathbf{e}}_1 + \sqrt{\gamma} e^{-i\Delta\omega t}\vec{\mathbf{e}}_2\right), \qquad (1)$$

with $\Delta\omega = 2\pi\Delta\nu$ being the angular frequency shift between the two modes, and where parameter γ describes their intensity imbalance [16]. If the polarization ellipse azimuth and ellipticity of

the first polarization mode $\vec{\mathbf{e}}_1$ are respectively denoted α and ε, the general parametrized forms of the DFDP source modes are

$$\vec{\mathbf{e}}_1 = \begin{bmatrix} \cos\alpha\cos\varepsilon - i\sin\alpha\sin\varepsilon \\ \sin\alpha\cos\varepsilon + i\cos\alpha\sin\varepsilon \end{bmatrix}, \quad (2)$$

$$\vec{\mathbf{e}}_2 = \begin{bmatrix} -\sin\alpha\cos\varepsilon + i\cos\alpha\sin\varepsilon \\ \cos\alpha\cos\varepsilon + i\sin\alpha\sin\varepsilon \end{bmatrix}. \quad (3)$$

The instantaneous Stokes vector $\vec{\mathbf{S}}(t)$ is linked to the complex electric field components by [17]

$$\vec{\mathbf{S}}(t) = \begin{bmatrix} E_1(t)E_1^*(t) + E_2(t)E_2^*(t) \\ E_1(t)E_1^*(t) - E_2(t)E_2^*(t) \\ E_1(t)E_2^*(t) + E_1^*(t)E_2(t) \\ i\{E_1(t)E_2^*(t) - E_1^*(t)E_2(t)\} \end{bmatrix}. \quad (4)$$

Introducing Eq. (1) into (4), and normalizing by the total beam intensity, the instantaneous Stokes vector $\vec{\mathbf{S}}(t)$ of a DFDP source is

$$\vec{\mathbf{S}}(t) = \begin{bmatrix} 1 \\ \dfrac{C_{2\alpha}\left[(1-\gamma)C_{2\varepsilon} - 2\sqrt{\gamma}S_{2\varepsilon}S_{\Delta\omega t}\right] - 2\sqrt{\gamma}S_{2\alpha}C_{\Delta\omega t}}{1+\gamma} \\ \dfrac{S_{2\alpha}\left[(1-\gamma)C_{2\varepsilon} - 2\sqrt{\gamma}S_{2\varepsilon}S_{\Delta\omega t}\right] + 2\sqrt{\gamma}C_{2\alpha}C_{\Delta\omega t}}{1+\gamma} \\ \dfrac{(1-\gamma)S_{2\varepsilon} + 2\sqrt{\gamma}C_{2\varepsilon}S_{\Delta\omega t}}{1+\gamma} \end{bmatrix}, \quad (5)$$

where the compact notation $C_X = \cos(x)$ and $S_X = \sin(x)$ has been used. Such an instantaneous Stokes vector corresponds to a totally polarized beam whose SOP follows a periodical temporal evolution governed by the azimuth, ellipticity, and imbalance of the orthogonal modes, and by the frequency shift. Relevantly, the time period of the SOP evolution $\tau_{\text{beam}} = 1/\Delta\nu$ can be tuned by adjusting the frequency shift Δν. Typically, DFDP sources can be easily implemented with a frequency shift in the tens of megahertz [20, 22] to tens of gigahertz radio-frequency (RF) range [18]. Now, if the DFDP beam is detected on a photodetector whose bandwidth is smaller than the source frequency shift, then $\tau_{\text{detector}} >> \tau_{\text{beam}}$, and a time-averaged Stokes vector will thus be measured instead of the instantaneous one. Time-averaging Eq. (5) results in the following Stokes vector:

$$\vec{\mathbf{S}} = \left\langle \vec{\mathbf{S}}(t) \right\rangle = \begin{bmatrix} 1 \\ \dfrac{1-\gamma}{1+\gamma}\cos(2\alpha)\cos(2\varepsilon) \\ \dfrac{1-\gamma}{1+\gamma}\sin(2\alpha)\cos(2\varepsilon) \\ \dfrac{1-\gamma}{1+\gamma}\sin(2\varepsilon) \end{bmatrix}. \quad (6)$$

A direct comparison of this vector with the parametric expression of a Stokes vector in the Poincaré sphere [17] shows that the azimuth and ellipticity of the measured state of polarization is that of the DFDP source modes ($\vec{\mathbf{e}}_1$ and $\vec{\mathbf{e}}_2$), while the degree of polarization (DOP) is fully determined by the modes imbalance:

$$DOP = \frac{1-\gamma}{1+\gamma}. \quad (7)$$

Therefore, an imbalanced DFDP source constitutes a straightforward way of generating a beam with a fully tunable state and degree of polarization, with the sole condition that the frequency shift is much higher than the bandwidth of the detector to be used with.

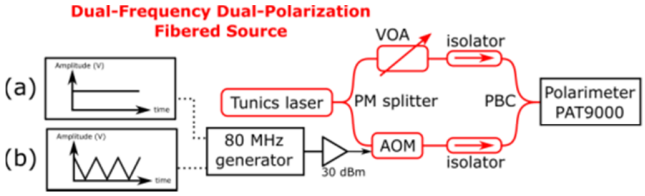

Fig. 1. Production of a coherent light beam with (a) fixed, (b) time-modulated, precisely controlled DOP using an intensity-imbalanced DFDP source. The intensity imbalance can be obtained using a variable optical attenuator (VOA) in one arm of the Mach-Zehnder architecture, or (b) by modulating the RF power of the electrical signal on the acousto-optic modulator (AOM) used to operate the frequency shift.

Such DFDP sources can be implemented by tailored solid-state or semiconductor laser cavities [18, 19] that output dual-frequency beams with detuning frequency Δν fixed by the intracavity phase anisotropy and polarization modes corresponding to the eigenaxes of the intracavity birefringence. Another solution that can be advantageously adapted on commercial light sources consists of using beam splitting/combination setups to obtain two orthogonal polarization states with a small wavelength shift operated with acousto-optics effects. Regarding this latter solution, we have recently reported the realization of DFDP sources based on free-space and fiber-based Mach-Zehnder architectures and acousto-optic modulators for visible and near-infrared wavelengths [20-22]. Let us consider the fibered DFDP source depicted in Fig. 1. It is based on a commercial single-mode fiber laser tunable from 1.5 to 1.63 μm (Yenista Tunics 100HP-CL), which is operated at 1.55 μm in this work. The polarization-maintaining (PM) fibered output of the laser is connected to a PM splitter, so as to separate the beam intensity into two arms. An isolator in each arm enhances the polarization purity and avoids any back-reflection towards the laser source. The acousto-optic modulator (AOM) inserted in one of the arms introduces a frequency shift on the light optical frequency of 80 MHz. The 80 MHz electrical signal applied on the AOM is obtained from a waveform generator with constant voltage amplitude, as illustrated by configuration (a) in Fig. 1, followed by a voltage amplifier (4 GHz bandwidth) producing a RF power of 30 dBm. A variable optical attenuator (VOA) is inserted in the other arm to enable the control of the intensity imbalance γ.

We now focus on the DOP of the generated DFDP beam, which has been measured with a commercial fibered polarimeter (Thorlabs PAT9000B) placed at the Mach-Zehnder architecture

output. The polarimeter bandwidth is a few tens ofhertz ($\tau_{detector} \approx 0.03$ s), which is much smaller than the 80 MHz detuning introduced by the AOM ($\tau_{beam} = 12.5$ ns=1/fbeam), so $\tau_{detector} >> \tau_{beam}$ and a time-averaged beam like the one described in Eq. (6) is expected. According to Eq. (7), a DOP of 0 should be obtained for a perfect balancing of both modes ($\gamma = 1$), while a complete vanishing of one of the modes ($\gamma = 0$) would naturally yield a completely polarized beam ($DOP = 1$) at the DFDP source output. The VOA was manually tuned between 0 and 40 dB attenuation to sweep the complete range of γ . The value of γ was experimentally controlled by measuring the total power at the output and the power after the VOA. The DOP measurements are plotted versus the intensity imbalance in Figure 2. In practice, we were able to achieve a maximum DOP of 96%, whereas the minimum one was roughly 0.2%. Despite these minor experimental imperfections, it can be observed that the agreement of the measured DOP with the predicted behavior is very good, which demonstrates the DOP tunability of this source, obtained with a simple fibered apparatus. Finally, the SOP of the output beam could be easily controlled by varying the state of polarization of the orthogonally-polarized modes at the output of the Mach-Zehnder architecture. Such polarization control can be obtained by using a fibered polarization controller/modulator after the proposed setup, or a photo-elastic or electro-optic device in a free-space design.

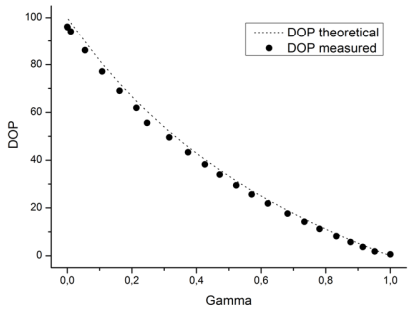

Fig. 2. Degree of polarization of the generated beam as a function of the modes intensity imbalance.

To ensure faster control of the intensity imbalance γ between the two arms, the manual tuning of the VOA attenuation can be replaced by a modification of the amplitude of the RF electrical signal used to drive the AOM. In the remainder of this Letter, we use this technique to temporally modulate the intensity imbalance $\gamma(t)$ as a function of time, accordingly yielding a modulation of the DOP ($DOP(t) = [1+\gamma(t)]/[1-\gamma(t)]$). This will allow us to illustrate the versatility of this source architecture to generate a beam with custom DOP.

For that purpose the VOA is removed from the experimental setup, and the AOM is driven with a triangle sweep modulation waveform of time constant τ_{mod} , as illustrated by configuration (b) in Fig. 1, so that a time varying $\gamma(t)$ between 0 and 1 is achieved. As a result, the DFDP source is gradually and periodically tuned from a completely polarized beam ($DOP = 1$) to a totally unpolarized one ($DOP = 0$) with time period $\tau_{modulation}$. Firstly, we have fixed a very low modulation frequency for the triangle signal on the AOM, namely 50 mHz ($\tau_{mod} = 20$ s). In this case, $\tau_{mod} >> \tau_{detector} >> \tau_{beam}$, so the polarimeter can effectively follow the DOP fluctuation as a function of $\gamma(t)$. This is shown in Fig. 3, where it can be observed that the DOP varies between a minimum and a maximum values during the period of the triangular modulation signal, thus confirming the easy and precise control of the source DOP with such a system.

However, if we now consider a second regime with a faster triangle sweep signal of 10 kHz, then $\tau_{detector} >> \tau_{mod} >> \tau_{beam}$. In that case, the detector response is very slow with respect to AOM and intensity imbalance modulation periods, and the detector measures a time-averaged DOP of 0.44, which is not far from the theoretically expected value $\langle DOP(t) \rangle = \int_{\tau_{mod}} \frac{1+\gamma(t)}{1-\gamma(t)} dt \approx 0.39$.

The discrepancy between the theoretical and experimental values can be attributed to possible slight non-linearity of the triangle modulation waveform after electrical amplification.

It is interesting to note here that if one could achieve full modulation of γ between -1 and +1, the same temporal modulation of $DOP(t)$ as in Fig. 3 would be observed with a fast detector (black dashed curve), whereas a low bandwidth detector would perceive the light as totally depolarized with $\langle DOP(t) \rangle = 0$. As a result, the proposed setup makes it possible to obtain a totally depolarized light beam, even with a very coherent source of light. Moreover, such depolarized beam would result from the complete temporal averaging of all polarization states across the Poincaré sphere as will be illustrated below, thereby providing ideal depolarization model.

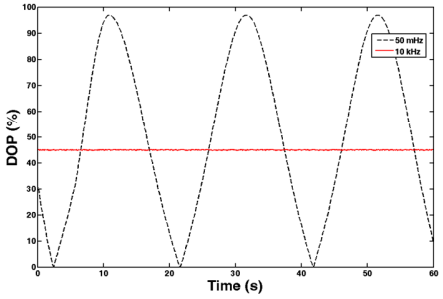

Fig. 3. Temporal evolution of the DOP for slow (black dashed curve) and fast (red solid curve) AOM modulation signals.

So far, we have only shown the DOP variation capabilities of this source resulting from controlled temporal averaging. Regarding the evolution of the instantaneous SOP, Eq. (5) shows that the SOP of the output light evolves dynamically at shortest time scales following a spiral trajectory across the Poincaré sphere Being able to address specific temporal trajectories of the SOP of a light beam across the Poincaré sphere at very high speed could find interesting applications in various domains, such as telecommunications or calibration of imaging systems [23]. In order to experimentally validate this potentiality through a direct observation, we would need a high bandwidth polarimeter (above 80 MHz with the fibered setup described above). We propose instead to operate a frequency down-conversion of the SOP evolution at 80 MHz, for it to be observable with the standard low

bandwidth polarimeter available in our laboratory. This can be achieved by using a temporal modulation of the front laser intensity at a frequency $f_{\text{intensity}}$ close to that of the RF signal used to drive the AOM (f_{beam}). In fact, the combination of the laser intensity modulation and of the AOM frequency shift allows the evolution of the DFDP SOP on the Poincaré sphere to be transposed at the frequency difference $f'_{\text{beam}} = f_{\text{beam}} - f_{\text{intensity}}$. It must be noted that the RF modulation is also replicated at high frequency ($f_{\text{AOM}} + f_{\text{intensity}}$) though the 80 MHz and 160 MHz modulations are filtered by the narrow bandwidth of the sensor.

We have accordingly modified our setup by inserting a fibered intensity modulator between the front laser and the Mach-Zehnder setup. To ensure synchronization of the two modulation signals, the intensity modulation of the front laser and the AOM were driven by the same 2-channel waveform generator (Tektronix AFG3252C) with a frequency detuning of 0.5 Hz. The frequency transposition f'_{beam} and the modulation of the source balancing f_{mod} are respectively set to 0.5 Hz ($\tau'_{\text{beam}} = 2$ s) and 30 mHz ($\tau_{\text{mod}} = 33$ s). Consequently, the polarimeter is now able to follow the temporal evolution of the generated state of polarization, as $\tau_{\text{mod}} >> \tau'_{\text{beam}} >> \tau_{\text{detector}}$.

On the one hand, for perfectly balanced horizontal and vertical source states, the generated beam is expected to oscillate between ± 45° linear to left/right completely circular states of polarization, as predicted by Eq. (5) and shown in previous work [16]. On the other hand, complete attenuation of the vertical state would produce a static linear SOP along the horizontal direction. Fig. 6 shows the dynamic transition between both extremes following a spiral trajectory across the Poincaré sphere. It can be appreciated that the SOP of the output beam rotates gradually from the horizontal polarization to the prime meridian of the sphere as the DFDP source gets well-balanced. Again, it should be noted that only half of the sphere is swept, since the optical power tuning is limited to the frequency shifted arm. If γ was varied between -1 and +1, the generated SOP would vary over the whole surface of the Poincaré sphere, and thus temporally occupy all accessible SOPs. Such a source would be well suited to scan the full Poincaré sphere, provided that the operating regime condition ($\tau_{\text{mod}} >> \tau'_{\text{beam}} >> \tau_{\text{detector}}$) is fulfilled.

As a conclusion, we have demonstrated a versatile coherent source architecture based on a dual-frequency dual-polarization laser enabling the generation of a custom beam with fully tunable degree of polarization obtained by temporal depolarization. The capacity of such a source to operate in different temporal regimes depending on both the source configuration and the detector bandwidth adds potential for this approach to be used in various applications requiring precise polarization control and tunable degree of polarization. The same approach could also be applied to less coherent light sources (laser diodes, superluminescent LEDs/LEDs,...), and offer similar DOP and SOP control potentialities.

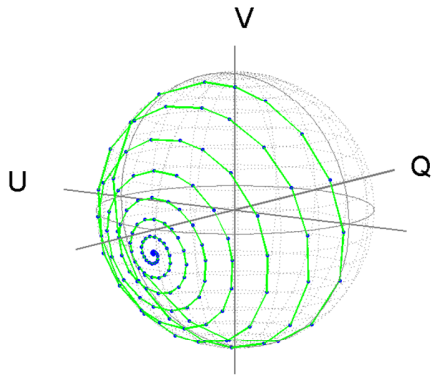

Fig. 6. Temporal evolution of the instantaneous DFDP state of polarization over the Poincaré sphere.

Funding. Agence Nationale de la Recherche (ANR) (ANR-13-ASTR-0001); Direction Générale de l'Armement (DGA).

Acknowledgment. F.P.'s Ph.D. is supported by the DGA-MRIS scholarship and by Région Bretagne.

References

1. R. M. A. Azzam and N. M. Bashara, Ellipsometry and Polarized Light (Elsevier, 1996).
2. B. H. Billings, J. Opt. Soc. Am. 41, 966–75 (1951).
3. W. Burns, J. Lightw. Technol. LT-1, 475–9 (1983).
4. F. Heismann and K. L. Tokuda, Opt. Lett. 20, 1008–10 (1995).
5. W. Jin, G. Stewart, K. Crawford, and B. Culshaw, Opt. Lett. 20, 1737–9 (1995).
6. G. Biener, A. Niv, V. Kleiner, and E. Hasman, Opt. Lett. 28, 1400–2 (2003).
7. P. Schau, L. Fu, K. Frenner, M. Schäferling, H. Schweizer, H. Giessen, L. M. G. Venancio, and W. Osten, Opt. Express 20, 22700–11 (2012).
8. M. Honma and T. Nose, Appl. Opt. 43, 4667–71 (2004).
9. G. Puentes, D. Voigt, A. Aiello, and J. P. Woerdman, Opt. Lett. 31, 2057–9 (2006).
10. A.-B. Mahler and R. A. Chipman, Appl. Opt. 50, 1726–34 (2011).
11. C. Vena, R. Massarelli, F. Carbone, and C. Versace, J. Op. 16, 065705 (2014).
12. A. Peinado, A. Lizana, and J. Campos, Opt. Lett. 39, 659–62 (2014).
13. R. D. Ramkhalawon, T. G. Brown, and M. A. Alonso, Opt. Express 21, 4106–15 (2013).
14. A. Shaham and H. S. Eisenberg, Opt. Lett. 37, 2643–5 (2012).
15. A. Lizana, I. Estévez, F. A. Torres-Ruiz, A. Peinado, C. Ramirez, and J. Campos, Opt. Lett. 40, 3790–3 (2015).
16. N. Ortega-Quijano, J. Fade, M. Roche, F. Parnet, and M. Alouini, J. Opt. Soc. Am. A 33, 434–46 (2016).
17. C. Brosseau, Fundamentals of Polarized Light (Wiley, 1998).
18. M. Alouini, B. Benazet, M. Vallet, M. Brunel, P. Di Bin, F. Bretenaker, A. Le Floch, P. Thony, IEEE Photon. Technol. Lett. 13, 367–9 (2001).
19. G. Baili, L. Morvan, M. Alouini, D. Dolfi, F. Bretenaker, I. Sagnes, and A. Garnache, Opt. Lett. 34, 3421–3 (2009).
20. E. Schaub, J. Fade, N. Ortega-Quijano, C. Hamel, and M. Alouini, J. Opt. 16, 122001 (2014).
21. N. Ortega-Quijano, J. Fade, E. Schaub, F. Parnet, and M. Alouini, Opt. Lett. 40, 1270–3 (2015).
22. F. Parnet, J. Fade, N. Ortega-Quijano, G. Loas, L. Frein, and M. Alouini, Opt. Lett. 42, 723–6 (2017).
23 J. Dupont, X. Orlik, A. Ghabbach, M. Zerrad, G. Soriano, and C. Amra, Opt. Express 22, 24133-41 (2014).

IOP Publishing Journal of Optics
J. Opt. 18 (2016) 125604 (9pp) doi:10.1088/2040-8978/18/12/125604

Differential description and irreversibility of depolarizing light–matter interactions

Julien Fade and Noé Ortega-Quijano

Institut de Physique de Rennes, CNRS, Université de Rennes 1, Campus de Beaulieu, F-35 042 Rennes, France

E-mail: julien.fade@univ-rennes1.fr

Received 17 July 2016, revised 27 September 2016
Accepted for publication 10 October 2016
Published 11 November 2016

Abstract

The widely used Jones and Mueller differential polarization calculi allow non-depolarizing deterministic polarization interactions to be described in an efficient way. Recently, the differential Mueller formalism has been successfully extended to the case of depolarizing transformations. In this article, a stochastic differential Jones formalism is shown to provide a clear physical insight on light depolarization, which arises when the interaction of polarized light with a medium involves randomized anisotropic properties. Based on this formalism, several intrinsic depolarization metrics which naturally arise to efficiently characterize light depolarization in a random medium are presented, and an irreversibility property of depolarizing transformations is finally established.

Keywords: polarimetry, depolarization, irreversibility, differential polarization formalisms

(Some figures may appear in colour only in the online journal)

1. Introduction

In the field of polarimetry, Jones and Stokes/Mueller formalisms have always appeared as dual and often exclusive approaches, whose specific characteristics have been exploited for diverse applications. On the one hand, the description of field coherence in the Jones calculus, which relates the input and output two-dimensional complex electric field through $\mathbf{E}_{\text{out}} = \underline{\mathbf{J}}\mathbf{E}_{\text{in}}$, justifies its use in ellipsometry [1, 2], optical design [3–6], spectroscopy [6], astronomy [7] or radar (PolSar) [8]. On the other hand, Mueller calculus is widely used in applications such as biophotonics [9, 10], material characterization [11, 12] or teledetection [13], as it is based on optical field observables (intensity measurements), relating the input and output four-dimensional real Stokes vector through $\mathbf{s}_{\text{out}} = \underline{\mathbf{M}}\mathbf{s}_{\text{in}}$. As a consequence, these approaches fundamentally differ in their capacity to characterize depolarizing light–matter interactions (i.e., non-deterministic polarization transformations yielding a partial randomization of the input electric field). As Jones already pointed out in one of his seminal papers [14], deterministic Jones matrices are unable to directly describe depolarizing interactions, which can however be handled in the Mueller formalism via depolarizing Mueller matrices. This discrepancy between both standpoints takes part in the debate, still topical in the scientific community, about the physical origin of light depolarization [15–23].

In this article, after recalling some well-known properties of non-depolarizing Mueller matrices and the differential Jones and Mueller formalisms in section 2, we show in section 3 that these differential polarization formalisms, which naturally arise from group theory, provide new physical insight on depolarizing light–matter interactions. This approach allows us to define new intrinsic depolarization metrics which are described in section 4, before an irreversibility property for depolarizing transformations is demonstrated in section 5, as a counterpart to the well-known invariance property verified by deterministic interactions, which is recalled below.

2. Properties of non-depolarizing light–matter interactions and differential polarization formalisms

Let us first review some well-known properties of deterministic polarization transformations, which can be described by a 2×2 complex Jones matrix $\underline{\mathbf{J}}$, or equivalently, by a 4×4 real-valued non-depolarizing Mueller matrix denoted $\underline{\mathbf{M}}_{\text{nd}}$,

where the subscript nd indicates a non-depolarizing transformation. In that case, there is a clear one-to-one relationship between $\underline{\mathbf{J}}$ and the so-called Mueller–Jones matrix $\underline{\mathbf{M}}_{\mathrm{nd}}$ through [24, 25]

$$\underline{\mathbf{M}}_{\mathrm{nd}} = \underline{\mathbf{A}}(\underline{\mathbf{J}} \otimes \underline{\mathbf{J}}^{*})\underline{\mathbf{A}}^{\dagger}, \text{ with } \underline{\mathbf{A}} = \frac{1}{\sqrt{2}}\begin{bmatrix} 1 & 0 & 0 & 1 \\ 1 & 0 & 0 & -1 \\ 0 & 1 & 1 & 0 \\ 0 & \mathrm{i} & -\mathrm{i} & 0 \end{bmatrix}, \quad (1)$$

where $\otimes$ denotes Kronecker product. The matrix $\underline{\mathbf{A}}$ verifies $\underline{\mathbf{A}}^{-1} = \underline{\mathbf{A}}^{\dagger}$, and can also be rewritten in compact form as $\underline{\mathbf{A}} = [\mathrm{vec}(\underline{\boldsymbol{\sigma}}_0)\ \mathrm{vec}(\underline{\boldsymbol{\sigma}}_1)\ \mathrm{vec}(\underline{\boldsymbol{\sigma}}_2)\ \mathrm{vec}(\underline{\boldsymbol{\sigma}}_3)]^{T}/\sqrt{2}$, where $\mathrm{vec}(\underline{\boldsymbol{\sigma}}_i)$ denotes the ith Pauli matrix $\underline{\boldsymbol{\sigma}}_i$ written in (column) vector form. In the remainder of this article, superscripts $*$, T and $\dagger$ respectively denote complex conjugation, standard and Hermitian matrix transposition. Interestingly, when one considers normalized unit-determinant matrices, respectively denoted $\widetilde{\underline{\mathbf{J}}}$ and $\widetilde{\underline{\mathbf{M}}}_{\mathrm{nd}}$, both descriptions appear to be isomorphic representations of the same six-dimensional group, namely the proper orthochronous Lorentz group $SO^{+}(1, 3)$ for unit-determinant Mueller matrices $\widetilde{\underline{\mathbf{M}}}_{\mathrm{nd}}$ and the special linear group $SL(2, \mathbb{C})$ for unit-determinant Jones matrices $\widetilde{\underline{\mathbf{J}}}$ [26, 27]. As a result, there is a well-known analogy between deterministic polarization transformations and special relativity [27–33]. In particular, non-depolarizing interactions correspond to Lorentz transformations and must therefore preserve the Minkowski metric $\|\mathbf{s}\|_{1,3}$ of the input Stokes vector $\mathbf{s}_{\mathrm{in}}$. This metric is defined by $\|\mathbf{s}\|_{1,3}^{2} = \mathbf{s}^{T}G\mathbf{s} = I^{2}(1 - \mathcal{P}^{2})$, with $G = \mathrm{diag}[1, -1, -1, -1]$ and where $\mathcal{P} = \sqrt{s_1^2 + s_2^2 + s_3^2}/s_0$ denotes the light degree of polarization (DOP), and $I = s_0$ denotes the light intensity [30]. By extension, this invariance property can be related to the preservation of the Shannon entropy of the field, which is an informational measure of the disorder of the two-dimensional transverse electric field, as

$$H(\mathbf{s}) = -\int P_{\mathbf{E}}(\mathbf{E})\ln P_{\mathbf{E}}(\mathbf{E}) = \ln\pi^{2}e^{2}\|\mathbf{s}\|_{1,3}^{2}/4, \quad (2)$$

under the assumption of complex Gaussian circular fluctuations [34]. As pointed out in [33], such an invariance property is neither verified by the light intensity, I, nor by its DOP, $\mathcal{P}$.

Historically, Jones [35] and Azzam [36] respectively introduced the so-called differential Jones and Mueller calculi, with a corresponding differential Jones matrix (dJm) $\underline{\mathbf{j}}$ and a differential Mueller matrix (dMm) $\underline{\mathbf{m}}_{\mathrm{nd}}$, where the subscript nd still indicates a non-depolarizing transformation. Both approaches describe the local evolution of a transversally polarized wave along direction $\hat{\mathbf{n}}$ through the respective differential equations $\mathrm{d}\mathbf{E}/\mathrm{d}\hat{\mathbf{n}} = \underline{\mathbf{j}}\mathbf{E}$, and $\mathrm{d}\mathbf{s}/\mathrm{d}\hat{\mathbf{n}} = \underline{\mathbf{m}}_{\mathrm{nd}}\,\mathbf{s}$. According to group theory, these differential descriptions lead to a representation of deterministic polarization transformations, either in group $SL(2, \mathbb{C})$ for $\widetilde{\underline{\mathbf{J}}}$ or in $SO^{+}(1, 3)$ for $\widetilde{\underline{\mathbf{M}}}_{\mathrm{nd}}$, by their counterpart in the corresponding Lie algebra $\mathfrak{sl}(2, \mathbb{C})$ for $\underline{\mathbf{j}}$, or $\mathfrak{so}^{+}(1, 3)$ for $\underline{\mathbf{m}}_{\mathrm{nd}}$, the latter verifying Minkowski G-antisymmetry, i.e., $\underline{\mathbf{m}}_{\mathrm{nd}} + \underline{\mathbf{G}}\,\underline{\mathbf{m}}_{\mathrm{nd}}^{T}\,\underline{\mathbf{G}} = 0$ [37]. There is a clear equivalence between these four representations, which are linked through the following commutative diagram

$$\begin{array}{ccc} \underline{\mathbf{j}} \in \mathfrak{sl}(2,\mathbb{C}) & \xrightarrow{\underline{\mathbf{A}}(\underline{\mathbf{j}}\oplus\underline{\mathbf{j}}^{*})\underline{\mathbf{A}}^{\dagger}} & \underline{\mathbf{m}}_{\mathrm{nd}} \in \mathfrak{so}^{+}(1,3) \\ \exp\downarrow & & \downarrow\exp \\ \widetilde{\underline{\mathbf{J}}} \in SL(2,\mathbb{C}) & \xrightarrow{\underline{\mathbf{A}}(\widetilde{\underline{\mathbf{J}}}\otimes\widetilde{\underline{\mathbf{J}}}^{*})\underline{\mathbf{A}}^{\dagger}} & \widetilde{\underline{\mathbf{M}}}_{\mathrm{nd}} \in SO^{+}(1,3) \end{array}, \quad (3)$$

the macroscopic and differential matrices being related by the exponential map, through $\widetilde{\underline{\mathbf{J}}} = \exp(\underline{\mathbf{j}}\Delta z)$ and $\widetilde{\underline{\mathbf{M}}}_{\mathrm{nd}} = \exp(\underline{\mathbf{m}}_{\mathrm{nd}}\Delta z)$ when propagation over Δz through a homogeneous medium is assumed.

As Lie algebras can be viewed as the tangent spaces to the corresponding Lie groups at the identity element [37, 38], the differential Jones or Mueller formalisms allow polarization properties of a sample or a material to be described in a linearized geometry. One of the powerful consequences of such a linearization lies in the simple linear parameterizations of the differential matrices in terms of anisotropic optical properties of the sample. Indeed, the dJm $\underline{\mathbf{j}}$ and dMm $\underline{\mathbf{m}}_{\mathrm{nd}}$, that both characterize the polarimetric properties of an infinitesimal plane-parallel slab of a deterministic linear optical medium, read

$$\underline{\mathbf{j}} = \frac{1}{2}\begin{bmatrix} 2\kappa_i + \kappa_q - \mathrm{i}(2\eta_i + \eta_q) & \kappa_u - \eta_v - \mathrm{i}(\eta_u + \kappa_v) \\ \kappa_u + \eta_v - \mathrm{i}(\eta_u - \kappa_v) & 2\kappa_{\mathrm{i}} - \kappa_q - \mathrm{i}(2\eta_i - \eta_q) \end{bmatrix}, \quad (4)$$

$$\text{and,} \quad \underline{\mathbf{m}}_{\mathrm{nd}} = \begin{bmatrix} 2\kappa_i & \kappa_q & \kappa_u & \kappa_v \\ \kappa_q & 2\kappa_i & -\eta_v & \eta_u \\ \kappa_u & \eta_v & 2\kappa_i & -\eta_q \\ \kappa_v & -\eta_u & \eta_q & 2\kappa_i \end{bmatrix}. \quad (5)$$

This choice of notation conventions implies that the considered monochromatic plane wave can be written as $\mathbf{E}(z, t) = \mathbf{E}_0\exp(\mathrm{i}\omega t + pz)$ where $p = \kappa - \mathrm{i}\eta$, with propagation constants $\kappa = 2\pi k/\lambda$ and $\eta = 2\pi n/\lambda$ respectively related to the imaginary and real part of the complex refractive index $\tilde{n} = n + \mathrm{i}k$ [35, 39]. By analogy, in the above matrices parameter κ_i denotes the isotropic extinction coefficient (in amplitude) induced by the sample or material. Parameter η_i stands for the isotropic (absolute) optical phase incurred by the interaction with the sample, and whose information is lost in the Mueller description [14]. As for the other terms, the subscripts q, u, and v refer to linear x–y, linear $\pm 45°$ and circular left/right optical anisotropies, through $x_{q,u,v} = x_{x,45°,\mathrm{rcp}} - x_{y,-45°,\mathrm{lcp}}$, with $x = \kappa$ when describing absorption anisotropy (diattenuation), or $x = \eta$ when describing phase anisotropy (birefringence).

3. Stochastic Jones and Mueller differential formalisms for depolarizing interactions

After having recalled the polarization differential formalisms and these well-established properties of deterministic non

depolarizing transformations, it is naturally motivating to question whether such differential formalisms can deepen the physical understanding of depolarizing light–matter interactions. In fact, it has recently been proposed to extend the differential Mueller formalism to the more intricate case of depolarizing transformations, by the introduction of depolarizing dMm's. This approach has paved the way for a number of interesting results obtained on depolarizing transformations [40–48]. We propose below to shade new light on the recent developments on depolarizing dMms, by using an alternative description involving stochastic differential Jones matrices. For that purpose, let us consider a stochastic dJm $\underline{\mathbf{j}} = \underline{\mathbf{j}}_0 + \Delta\underline{\mathbf{j}}$, modeling a random depolarizing local transformation of the field, where $\underline{\mathbf{j}}_0 = \langle\underline{\mathbf{j}}\rangle$ is the deterministic average polarization transformation, whose form has been recalled in equation (4), and where the fluctuations matrix verifies $\langle\Delta\underline{\mathbf{j}}\rangle = 0$. Assuming infinitesimal propagation over Δz in the considered medium, the Jones matrix for such a transformation can be written $\underline{\mathbf{J}} = \exp(\underline{\mathbf{j}}\Delta z) \simeq \underline{\mathrm{Id}} + \underline{\mathbf{j}}\Delta z$ at first order in Δz. From equation (4), this relation can be conveniently rewritten in a vector form in the Pauli matrices basis $\{\boldsymbol{\sigma}_i\}_{i=\{0,3\}}$ as $\mathbf{V}_\mathrm{J} \simeq \left[1 + \frac{\Delta z}{2}p^{(0)} \quad \frac{\Delta z}{2}\mathbf{p}\right]^T$, with $p^{(0)} = p_0^{(0)} + \Delta p^{(0)}$, $\mathbf{p} = \mathbf{p}_0 + \Delta\mathbf{p}$. In these expressions, the deterministic average values read

$$p_0^{(0)} = 2\kappa_i - 2\eta_i, \text{ and } \mathbf{p}_0 = \begin{bmatrix} \kappa_q - \mathrm{i}\eta_q \\ \kappa_u - \mathrm{i}\eta_u \\ \kappa_v - \mathrm{i}\eta_v \end{bmatrix}, \tag{6}$$

whereas $\Delta p^{(0)}$ and $\Delta\mathbf{p}$ denote zero mean random variables describing the fluctuations of the anisotropy parameters.

From $\mathbf{V}_\mathrm{J}$, one can derive the Cloude's coherency matrix (CCM) of the polarimetric transformation, defined as the second-order moment matrix of vector $\mathbf{V}_\mathrm{J}$, i.e., $\underline{\mathbf{C}}(\underline{\mathbf{J}}) = \langle\mathbf{V}_\mathrm{J}\mathbf{V}_\mathrm{J}^\dagger\rangle$ [26]. The CCM can also be directly computed from a Mueller matrix $\underline{\mathbf{M}}$ through

$$\underline{\mathbf{C}}(\underline{\mathbf{M}}) = \frac{1}{2}\sum_{j=0}^{3}\sum_{k=0}^{3}\underline{\mathbf{M}}\underline{\mathbf{A}}(\underline{\boldsymbol{\sigma}}_j \otimes \underline{\boldsymbol{\sigma}}_k^*)\underline{\mathbf{A}}^\dagger, \tag{7}$$

with $\underline{\boldsymbol{\sigma}}_i$ denoting the ith Pauli matrix [26, 49]. The CCM is widely used in the field of Mueller polarimetry as it provides relevant criteria to assess the physical realizability of macroscopic Mueller matrices [26, 49]. With the above notations, the CCM can be decomposed into a sum of two terms $\underline{\mathbf{C}}(\underline{\mathbf{J}}) = \langle\mathbf{V}_\mathrm{J}\mathbf{V}_\mathrm{J}^\dagger\rangle = \underline{\mathbf{C}}_\mathrm{nd} + \underline{\mathbf{C}}_d$, where $\underline{\mathbf{C}}_\mathrm{nd} = \mathbf{V}_{\mathrm{J}_0}\mathbf{V}_{\mathrm{J}_0}^\dagger$ with $\mathbf{V}_{\mathrm{J}_0} \simeq \left[1 + \frac{\Delta z}{2}p_0^{(0)} \quad \frac{\Delta z}{2}\mathbf{p}_0\right]^T$, and where the covariance matrix $\underline{\mathbf{C}}_d = \langle(\mathbf{V}_\mathrm{J} - \mathbf{V}_{\mathrm{J}_0})(\mathbf{V}_\mathrm{J} - \mathbf{V}_{\mathrm{J}_0})^\dagger\rangle$ reads

$$\underline{\mathbf{C}}_d = \left(\frac{\Delta z}{2}\right)^2\begin{bmatrix} c_0 & \mathbf{c}^\dagger \\ \mathbf{c} & \underline{\mathcal{C}} \end{bmatrix}, \tag{8}$$

with $c_0 = \langle|\Delta p^{(0)}|^2\rangle$, $\mathbf{c} = \langle\Delta p^{(0)*}\Delta\mathbf{p}\rangle$ and the 3×3 submatrix $\underline{\mathcal{C}} = \langle\Delta\mathbf{p}\Delta\mathbf{p}^\dagger\rangle$. From such a decomposition, it is clear that a deterministic transformation (with $\Delta p^{(0)} = 0$ and $\Delta\mathbf{p} = \mathbf{0}$, hence $\underline{\mathbf{C}}_d = 0$) results in a CCM of rank one, $\underline{\mathbf{C}}_\mathrm{nd}$ being the matrix of a projector. A CCM of rank one is precisely known as the Cloude's condition for a polarimetric transformation to be non-depolarizing [26, 49]. Conversely, as soon as $\underline{\mathcal{C}}$ is a non-null matrix, the rank of $\underline{\mathbf{C}}(\underline{\mathbf{J}})$ is greater than one, hence the corresponding transformation is depolarizing according to Cloude's criterion [26, 49]. As a result, the depolarizing nature of a transformation appears to be completely comprehended by the 3×3 positive semi-definite Hermitian (PSDH) submatrix $\underline{\mathcal{C}}$, i.e., by 9 independent real parameters. As will be seen below, this submatrix also allows one to define interesting intrinsic depolarization metrics.

It is now quite straightforward to identify the two terms of the CCM, namely $\underline{\mathbf{C}}_\mathrm{nd}$ and $\underline{\mathbf{C}}_d$, with the CCM's of, respectively, the non-depolarizing and the depolarizing dMm's introduced in earlier works [50–52]. Indeed, in the dMm formalism, the Mueller matrix for the considered local transformation reads $\underline{\mathbf{M}} = \exp(\underline{\mathbf{m}}\Delta z) \simeq \underline{\mathrm{Id}} + \underline{\mathbf{m}}\Delta z$ at first order in Δz. As suggested in [52], the dMm $\underline{\mathbf{m}}$ can be decomposed into a G-antisymmetric part, namely $\underline{\mathbf{m}}_\mathrm{nd}$ given in equation (5), and a G-symmetric part $\underline{\mathbf{m}}_d'$ which corresponds to the depolarizing contribution. With such a decomposition, it can be checked that the 3×3 lower-right submatrix of the CCM of $\underline{\mathbf{M}}$ is only due to the G-symmetric (depolarizing) part of $\underline{\mathbf{m}}$. As a result, since equation (8) indicates that this submatrix must have a quadratic behavior in Δz, the parameterization of the dMm must be written $\underline{\mathbf{m}} = \underline{\mathbf{m}}_\mathrm{nd} + \underline{\mathbf{m}}_d' = \underline{\mathbf{m}}_\mathrm{nd} + \underline{\mathbf{m}}_d\Delta z$, with the 9-parameters G-symmetric part reading [50–52]

$$\underline{\mathbf{m}}_d = \begin{bmatrix} 0 & d_{\kappa_q} & d_{\kappa_u} & d_{\kappa_v} \\ -d_{\kappa_q} & -d_{\mu_q} & d_{\eta_v} & d_{\eta_u} \\ -d_{\kappa_u} & d_{\eta_v} & -d_{\mu_u} & d_{\eta_q} \\ -d_{\kappa_v} & d_{\eta_u} & d_{\eta_q} & -d_{\mu_v} \end{bmatrix}. \tag{9}$$

The proposed decomposition of the dMm $\underline{\mathbf{m}}$ has an important physical meaning: the depolarization properties of light propagating in a sample must pile up quadratically with Δz, whereas deterministic anisotropy parameters classically evolve linearly with propagation distance. Such a decomposition of $\underline{\mathbf{m}}$ involving a quadratic behavior of the depolarizing dMm has been recently proposed in [53], but without a clear physical justification that is brought by the above approach. This interesting property of depolarization in samples has been recently verified experimentally on controlled test samples [48], and it may have crucial implications in the analysis of depolarizing media in experimental polarimetry [2, 54].

With such parameterizations of $\underline{\mathbf{m}}_\mathrm{nd}$ and $\underline{\mathbf{m}}_d$, respectively described through equations (5) and (9), the CCM of $\underline{\mathbf{M}} \simeq \underline{\mathrm{Id}} + \underline{\mathbf{m}}\Delta z$ can be obtained using the relationship recalled in equation (7). A direct calculus yields

$$\underline{\mathbf{C}}(\underline{\mathbf{M}}) = \begin{bmatrix} 1 + 2\kappa_i\Delta z & \frac{\Delta z}{2}\mathbf{p}_0^\dagger \\ \frac{\Delta z}{2}\mathbf{p}_0 & \left(\frac{\Delta z}{2}\right)^2\underline{\boldsymbol{\Sigma}} \end{bmatrix}, \text{ with}$$

$$\underline{\boldsymbol{\Sigma}} = 2\begin{bmatrix} \frac{-d_{\mu_q} + d_{\mu_u} + d_{\mu_v}}{2} & d_{\eta_v} + \mathrm{i}d_{\kappa_v} & d_{\eta_u} - \mathrm{i}d_{\kappa_u} \\ d_{\eta_v} - \mathrm{i}d_{\kappa_v} & \frac{d_{\mu_q} - d_{\mu_u} + d_{\mu_v}}{2} & d_{\eta_q} + \mathrm{i}d_{\kappa_q} \\ d_{\eta_u} + \mathrm{i}d_{\kappa_u} & d_{\eta_q} - \mathrm{i}d_{\kappa_q} & \frac{d_{\mu_q} + d_{\mu_u} - d_{\mu_v}}{2} \end{bmatrix}.$$

It can be observed that $\underline{\mathbf{C}}(\underline{\mathbf{M}})$ corresponds to an approximation of the CCM obtained above with the Jones formalism, where each element has been truncated to the first non-null term of its Taylor expansion in Δz, and where all information about the absolute phase delay η_i has been lost. However, the lower-right 3×3 submatrix $\underline{\mathbf{\Sigma}}$ and its previous expression $\underline{\mathcal{C}} = \langle \Delta\mathbf{p}\Delta\mathbf{p}^{\dagger} \rangle$ given in equation (8) can be identified, as they correspond to the same order of approximation (in Δz^2) yielding the following set of equations:

$$2d_{\mu_{q,u,v}} = \langle [(\Delta\eta)^2 + (\Delta\kappa)^2]_{u,v,q} + [(\Delta\eta)^2 + (\Delta\kappa)^2]_{v,q,u} \rangle,$$
$$2d_{\eta_{q,u,v}} = \langle \Delta\kappa_{u,v,q}\Delta\kappa_{v,q,u} + \Delta\eta_{u,v,q}\Delta\eta_{v,q,u} \rangle,$$
$$2d_{\kappa_{q,u,v}} = \langle \Delta\kappa_{u,v,q}\Delta\eta_{v,q,u} - \Delta\eta_{u,v,q}\Delta\kappa_{v,q,u} \rangle.$$

This clearly shows that the nine depolarization parameters $d_{\mu_{q,u,v}}$, $d_{\eta_{q,u,v}}$ and $d_{\kappa_{q,u,v}}$ of the dMm $\underline{\mathbf{m}}_d$ are physically related to the second-order statistical properties (variance/covariance terms) of the anisotropy parameters, hence implying specific relationships between their nine respective values. Such an observation was reported for the first time in [23] through a somewhat intricate calculus involving stochastic dMm's. In addition, these specific relationships imply necessary conditions on the elements of $\underline{\mathbf{M}}_d$ so that it is physically admissible. In that perspective, it can be shown [45, 53] that a physically admissible depolarizing dMm $\underline{\mathbf{m}}_d$ must belong (up to double cosetting by Lorentz transformations) to one of the two canonical forms derived in [55, 56]:

$$\underline{\mathbf{m}}_d^{(\mathrm{I})} = \mathrm{diag}[d_1 + d_2 + d_3;\ d_1 - d_2 - d_3;\ -d_1 + d_2 - d_3;\ -d_1 - d_2 + d_3], \tag{10}$$

$$\underline{\mathbf{m}}_d^{(\mathrm{II})} = \begin{bmatrix} d_1 + d_2 & d_2 & 0 & 0 \\ -d_2 & d_1 - d_2 & 0 & 0 \\ 0 & 0 & -d_1 & 0 \\ 0 & 0 & 0 & -d_1 \end{bmatrix}, \tag{11}$$

with the following conditions on the *canonical* depolarization parameters: $d_i \geqslant 0$, for $i \in \{1, 3\}$.

4. Intrinsic depolarization metrics

These previous results evidence the fact that the depolarization properties of light propagating in a medium at an infinitesimal level are intrinsically described by the matrix $\underline{\mathbf{\Sigma}}$ (or equivalently $\underline{\mathcal{C}}$), which contains the 9 depolarization parameters described above. However, usual depolarization metrics are defined either on the macroscopic Mueller matrix of the medium, or on its CCM. For instance, the standardly used depolarization index is defined as $P = \{(\mathrm{tr}[\underline{\mathbf{M}}^T\underline{\mathbf{M}}] - \underline{\mathbf{M}}_{\mathrm{l},1}^2)/3\underline{\mathbf{M}}_{\mathrm{l},1}^2\}^{1/2}$ [57], and can vary between 0 (totally depolarizing) to 1 (non depolarizing). Another description of depolarization uses the so-called Cloude *entropy* [26, 49, 58], derived from the eigenvalues λ_i, $i \in \{1, 4\}$ of the CCM $C(\underline{\mathbf{M}})$ by $\mathcal{S} = -\sum_{i=1}^{4} \lambda_i' \log_4 \lambda_i'$ with $\lambda_i' = \lambda_i \Big/ \left(\sum_{j=1}^{4} \lambda_j\right)$ or, written in compact form, $\mathcal{S} = -\mathrm{tr}[(\underline{\mathbf{M}}/||\underline{\mathbf{M}}||_{\mathrm{l}}) \log_4 (\underline{\mathbf{M}}/||\underline{\mathbf{M}}||_{\mathrm{l}})]$, where $||\underline{\mathbf{M}}||_{\mathrm{l}} = \mathrm{tr}\sqrt{\underline{\mathbf{M}}^{\dagger}\underline{\mathbf{M}}}$ denotes the *trace* norm [59], with $\sqrt{\underline{\mathbf{X}}}$ and $\log_4(\underline{\mathbf{X}}) = \ln(\underline{\mathbf{X}})/\ln(4)$ respectively referring to square root and logarithm of a matrix $\underline{\mathbf{X}}$. Fundamentally differing from the Shannon entropy $H(\mathbf{s})$ of a Stokes vector $\mathbf{s}$ introduced in equation (2), the Cloude *entropy* (denoted by $\mathcal{S}$ to avoid any confusion) is essentially a measure of the dispersion of the relative magnitude of the CCM eigenvalues, ranging from 0 (non depolarizing sample) to 1 (perfect depolarizer). Though often useful, such depolarization metrics can nevertheless be unsatisfactory in some situations. Indeed, two interactions sharing identical fluctuations properties of the optical anisotropy parameters (i.e., same matrix $\underline{\mathbf{\Sigma}}$) but with distinct principal polarization transformation vector $\mathbf{p}_0$ can have different depolarization indices or Cloude entropies in the general case. This is due to the fact that the depolarization index is calculated from the entire Mueller matrix, and that the Cloude entropy depends on the four eigenvalues of the CCM, i.e., both metrics simultaneously depend on the deterministic polarization transformation and on the fluctuating parameters.

Contrarily, the new insight brought by the differential Jones and Mueller calculi allows one to naturally define intrinsic depolarization metrics, which only depend on the fluctuations of the anisotropy parameters of the sample . One can first define the *intrinsic differential depolarization metric* as $P_\delta = ||\underline{\mathbf{\Sigma}}||_F$, where $||\underline{\mathbf{X}}||_F = \sqrt{\mathrm{tr}[\underline{\mathbf{X}}^{\dagger}\underline{\mathbf{X}}]}$ denotes the Frobenius matrix norm [46]. Such a quantity can vary from 0 (for non-depolarizing interactions) to (potentially) infinity and can be efficient in situations where standard approaches fail to correctly describe the depolarizing nature of a light–matter interaction. This property is emphasized with an illustrative example in [46]. In addition, one can gain further physical insight into the depolarization properties of such interaction by analyzing other quantities on the submatrix $\underline{\mathbf{\Sigma}}$. For instance, the determinant of $\underline{\mathbf{\Sigma}}$ can be interpreted as a *depolarization volume* $\mathcal{V}_\delta = \det[\underline{\mathbf{\Sigma}}]$. This quantity is equal to zero as soon as one polarimetric direction has null fluctuations, indicating perfect correlation between at least two polarization 'directions'. Another interesting approach is to analyze the Cloude *entropy* of the submatrix $\underline{\mathbf{\Sigma}}$ itself, i.e., $\mathcal{S}_\delta = -\mathrm{tr}[(\underline{\mathbf{\Sigma}}/||\underline{\mathbf{\Sigma}}||_{\mathrm{l}}) \log_3 (\underline{\mathbf{\Sigma}}/||\underline{\mathbf{\Sigma}}||_{\mathrm{l}})]$, where the subscript δ indicates that the Cloude *entropy* is computed under the differential approach. This Cloude *entropy* varies between 0 and 1 with the relative distribution of the eigenvalues of $\underline{\mathbf{\Sigma}}$, thus revealing possible depolarization anisotropy.

It is interesting to note that the quantities P_δ, $\mathcal{V}_\delta$ and $\mathcal{S}_\delta$ are defined irrespective of the propagation distance, and are invariant by deterministic unitary transformations, thus justifying their qualification of *intrinsic* metrics. This has the strong physical meaning that the sample or the light–matter interaction studied must keep the same depolarization properties regardless of its deterministic anisotropic properties. Moreover, combining these three depolarization parameters, one can get direct information on the number and degeneracy of non-null canonical parameters, as evidenced in table 1. Such a procedure, which does not require reducing $\underline{\mathbf{m}}_d$ to its canonical form, also allows one to identify type-(I) canonical family from type-(II) when all three canonical parameters are non-null. It is important to note that, in practice, the intrinsic

Table 1. Intrinsic differential depolarization metric, volume and Cloude entropy for the two canonical dMm's of equation (10).

Parameters $d_{i,i\in\{1,3\}}$		P_δ^2	$\mathcal{V}_\delta$	$\mathcal{S}_\delta$
(I)	$d_i = d_j = d_k$	$3d_i$	d_i^3	1
	$d_i = d_j \neq d_k$	$2d_i + d_k$	$d_i^4 d_k$	$\frac{\ln 2}{\ln 3} < \mathcal{S}_\delta < 1$
	$d_i \neq d_j \neq d_k$	$d_i + d_j + d_k$	$d_i d_j d_k$	$0 < \mathcal{S}_\delta < 1$
(I/II)	$d_i = d_j \quad 0$	$2d_i$	0	$\frac{\ln 2}{\ln 3}$
	$d_i \neq d_j \quad 0$	$d_i + d_j$	0	$0 < \mathcal{S}_\delta < \frac{\ln 2}{\ln 3}$
	$d_i \quad 0 \quad 0$	d_i^2	0	0

depolarization metrics proposed above can be computed directly from the Mueller matrix $\underline{\mathbf{M}}$ using the following procedure: (i) compute the matrix logarithm of $\underline{\mathbf{M}}$; (ii) identify $\underline{\mathbf{m}}_d$ by taking the G-symmetric part of $\log(\underline{\mathbf{M}})$ and normalizing by the square sample thickness Δz^2; (iii) compute the CCM of $\underline{\mathbf{m}}_d$ to identify the submatrix $\underline{\mathbf{\Sigma}}$; (iv) and finally compute the above metrics P_δ, $\mathcal{V}_\delta$ and $\mathcal{S}_\delta$.

5. Irreversibility property of depolarizing light–matter interactions

These considerations provide a fundamental insight on the origin of depolarization as a randomization of light polarization due to statistical fluctuations of the anisotropy parameters, giving access to meaningful intrinsic depolarization metrics. Finally they also allow us to demonstrate the following irreversibility property of depolarizing light–matter interactions:

Property 1. For any admissible fully or partially polarized input Stokes vector $\mathbf{s}_{\text{in}}$, a physically realizable depolarizing non-singular and unit determinant Mueller matrix $\underline{\widetilde{\mathbf{M}}}$ verifies $\|\mathbf{s}_{\text{out}}\|_{\text{I},3}^2 = \|\underline{\widetilde{\mathbf{M}}}\,\mathbf{s}_{\text{in}}\|_{\text{I},3}^2 \geqslant \|\mathbf{s}_{\text{in}}\|_{\text{I},3}^2$.

The demonstration of this property in the general case of a standard Mueller matrix has never been reported before to our best knowledge, and is provided in a more general form in appendix (property A.1). For the sake of conciseness, we provide the demonstration of an equivalent 'local' property for a depolarizing dMm $\underline{\mathbf{m}} = \underline{\mathbf{m}}_{nd} + \underline{\mathbf{m}}'_d$ with null trace ($\kappa_i = 0$), which reads

$$\frac{\mathrm{d}\|\mathbf{s}\|_{\text{I},3}^2}{\mathrm{d}z} = \mathbf{s}^T[\underline{\mathbf{m}}'^T_d\,\underline{\mathbf{G}} + \underline{\mathbf{G}}\underline{\mathbf{m}}'_d]\mathbf{s} \geqslant 0 \tag{12}$$

for any physical Stokes vector $\mathbf{s}$, with equality if and only if the dMm is non depolarizing ($\underline{\mathbf{m}}'_d = 0$). The above expression of $\mathrm{d}\|\mathbf{s}\|_{\text{I},3}^2/\mathrm{d}z$ is easily obtained by computing the first order Taylor expansion of $\|\mathbf{s}(z+\Delta z)\|_{\text{I},3}^2 = \|(\underline{\mathrm{Id}} + \underline{\mathbf{m}}\Delta z)\mathbf{s}(z)\|_{\text{I},3}^2$ and using the G-antisymmetry of $\underline{\mathbf{m}}_{\text{nd}}$ when $\kappa_i = 0$. The positivity can then be easily shown on the two canonical forms of $\underline{\mathbf{m}}'_d$ recalled above. One indeed has $\mathrm{d}\|\mathbf{s}\|_{\text{I},3}^2/\mathrm{d}z = \Delta z[2s_0^2(d_1+d_2+d_3) - s_1^2(d_1-d_2-d_3) - s_2^2(d_2-d_3-d_1) - s_3^2(d_3-d_1-d_2)]$ for type-(I) depolarizing dMm, whereas, for type-(II), $\mathrm{d}\|\mathbf{s}\|_{\text{I},3}^2/\mathrm{d}z = \Delta z[2d_2(s_0^2+s_1^2) + d_1(s_0^2 - s_1^2 + s_2^2 + s_3^2)]$. These two quantities are obviously non negative under the physicality conditions recalled above (i.e., $\forall i \in \{1,3\}$, $d_i \geqslant 0$) and for admissible Stokes vectors (i.e., $\|\mathbf{s}\|_{\text{I},3} \geqslant 0$).

Property 1 and its 'local' counterpart have a strong physical meaning since they reveal the irreversible effect of a depolarizing transformation on the propagating field. This irreversibility clearly appears through the necessary increase of the Minkowski metric of the Stokes vector defining the field polarization state. Interestingly, this irreversibility property has an informational or thermodynamical counterpart, under the hypothesis of complex Gaussian circular random fluctuations of the field. Indeed, as a consequence of equation (12), the Shannon entropy of the bidimensional electrical field vector must obey an irreversible evolution with depolarizing transformations, as $\frac{\mathrm{d}H(\mathbf{s})}{\mathrm{d}z} = \frac{2}{\|\mathbf{s}\|_{\text{I},3}}\frac{\mathrm{d}\|\mathbf{s}\|_{\text{I},3}}{\mathrm{d}z} \geqslant 0$. Such an irreversible behavior of the Minkowski metric $\|\mathbf{s}\|_{\text{I},3}$ (or equivalently of the Shannon entropy $H(\mathbf{s})$) confirms that these quantities are best adapted to describe the polarimetric *randomization* (depolarization) of a propagating beam. Indeed, contrarily to the field intensity or the standard DOP $\mathcal{P}$, the quantities $\|\mathbf{s}\|_{\text{I},3}$ and $H(\mathbf{s})$ are preserved through non-singular deterministic (and reversible) transformations as $\frac{\mathrm{d}H(\mathbf{s})}{\mathrm{d}z} = \frac{\mathrm{d}\|\mathbf{s}\|_{\text{I},3}}{\mathrm{d}z} = 0$ in that case, but must necessarily grow with irreversible depolarizing transformations. This is schematically illustrated in figure 1 where it can be seen that, depending on the input Stokes vector $\mathbf{s}_{\text{in}}$, a non-depolarizing $\underline{\widetilde{\mathbf{M}}}_{\text{nd}}$ or a depolarizing $\underline{\widetilde{\mathbf{M}}}_d$ polarimetric transformation can lead to an increase or a decrease of $\mathcal{P}$.

This can be also quantitatively illustrated with the following simple example. Let us consider the Mueller matrix $\underline{\widetilde{\mathbf{M}}} = \underline{\widetilde{\mathbf{M}_\alpha}}\,\underline{\widetilde{\mathbf{M}_\beta}}$ formed by the sequential combination of a (unit-determinant) diagonal depolarizer $\underline{\widetilde{\mathbf{M}_\beta}} = \mathrm{diag}[1, \beta, \beta, \beta]/\beta^{3/4}$ with $\beta \in [0, 1]$, followed by a partial polarizer along the X axis with (unit-determinant) Mueller matrix:

$$\underline{\widetilde{\mathbf{M}_\alpha}} = \frac{1}{\sqrt{1-\alpha^2}}\begin{bmatrix} 1 & \alpha & 0 & 0 \\ \alpha & 1 & 0 & 0 \\ 0 & 0 & \sqrt{1-\alpha^2} & 0 \\ 0 & 0 & 0 & \sqrt{1-\alpha^2} \end{bmatrix},$$
$$\text{with } \alpha \in [0, 1].$$

Let us now consider for instance that the fully polarized Stokes vector $\mathbf{s}_{\text{in},1} = [1, 1, 0, 0]^T$, with DOP $\mathcal{P}(\mathbf{s}_{\text{in},1}) = 1$ and Minkowski metric $\|\mathbf{s}_{\text{in},1}\|_{\text{I},3} = 0$, interacts with a sample described by $\underline{\widetilde{\mathbf{M}}}$. In that case, the DOP of the output Stokes vector $\mathbf{s}_{\text{out},1} = \underline{\widetilde{\mathbf{M}}}\mathbf{s}_{\text{in},1}$ reads $\mathcal{P}(\mathbf{s}_{\text{out},1}) = (\alpha+\beta)/(1+\alpha\beta)$ which is clearly lower than the unit DOP of the input light, seemingly indicating a depolarizing interaction. This is confirmed by the evolution of the Minkowski metric which verifies property 1 as $\|\mathbf{s}_{\text{out},1}\|_{\text{I},3}^2 = (1-\beta^2)/\beta^{3/2} \geqslant 0$. This is also the case with the Stokes vector $\mathbf{s}_{\text{in},2} = [1, 0, 0, 0]^T$ of a totally unpolarized light, as

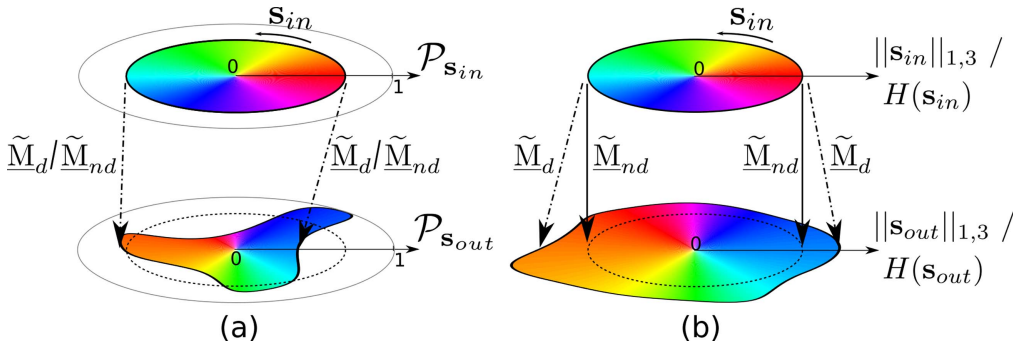

Figure 1. Schematic representation of the effect of a non-depolarizing ($\widetilde{M}_{\mathrm{nd}}$) or a depolarizing ($\widetilde{M}_d$) transformation on (a) the standard DOP $\mathcal{P}$, and (b) the Minkowski metric $||\mathbf{s}||_{\mathrm{l},3}$ or Shannon entropy $H(\mathbf{s})$, for all possible input Stokes vectors $\mathbf{s}_{\mathrm{in}}$ (represented around a chromatic disk for the sake of simplicity).

$\|\mathbf{s}_{\mathrm{out},2}\|_{\mathrm{l},3}^2 = 1/\beta^{3/2} \geqslant \|\mathbf{s}_{\mathrm{in},2}\|_{\mathrm{l},3}^2 = 1$. However in that case, the polarimetric transformation described by $\widetilde{\underline{\mathbf{M}}}$ leads to an increase of the DOP since $\mathcal{P}(\mathbf{s}_{\mathrm{out},2}) = \alpha$, whereas $\mathcal{P}(\mathbf{s}_{\mathrm{in},2}) = 0$, which could be apparently in contradiction with the depolarizing nature of $\widetilde{\underline{\mathbf{M}}}$. This simple example thus confirms that the evolution of the standard DOP does not share the same irreversibility behavior, described in property 1, that is followed by the Minkowski metric or the field Shannon entropy.

6. Conclusion

As a conclusion, we have illustrated in this article how differential polarimetric formalisms could provide a clear physical picture of the origins of depolarization of light when interacting with a medium. The derivation conducted from the differential Jones formalism approach provides a straighforward derivation of the CCM of a depolarizing polarimetric transformation, from which we have been able to confirm that 9 independent parameters are required to describe depolarization. Moreover, the statistical analysis presented has evidenced the fact that depolarization properties locally grow up quadratically with propagation distance, contrarily to deterministic anisotropy properties which pile up linearly. We have also proposed to define new *intrinsic* depolarization metrics, which are able to describe how a polarization transformation will randomize the input field components, independently of the main deterministic polarization transformation. Lastly, a physically meaningful implication regarding an irreversibility property of the Minkowski metric of the Stokes vector under depolarizing transformations has been established, with an insightful interpretation in terms of growth of the beam Shannon entropy under the hypothesis of complex Gaussian circular fluctuations.

Appendix

In this appendix, we provide the demonstration of the following property, which is a generalized version of property 1 for non unit-determinant Mueller matrices.

Property A.1. For any admissible fully or partially polarized input Stokes vector $\mathbf{s}_{\mathrm{in}}$, a physically realizable non-singular Mueller matrix $\underline{\mathbf{M}}$ with $\det(\underline{\mathbf{M}}) > 0$ verifies

$$\|\mathbf{s}_{\mathrm{out}}\|_{\mathrm{l},3}^2 = \|\underline{\mathbf{M}}\,\mathbf{s}_{\mathrm{in}}\|_{\mathrm{l},3}^2 \geqslant [\det(M)]^{1/2}\,\|\mathbf{s}_{\mathrm{in}}\|_{\mathrm{l},3}^2. \qquad \text{(A.1)}$$

It can be readily checked that when $\det(\underline{\mathbf{M}}) = 1$, one obtains the formulation of the property 1 given in the article.

Before providing the demonstration of this property, let us recall the definitions of Stokes realizability and Cloude realizability for general Mueller matrices [60, 61]:

Stokes realizability: A Mueller matrix $\underline{\mathbf{M}}$ is said *Stokes realizable* if, for any fully polarized Stokes vector $\mathbf{s}_{\mathrm{in}}$ verifying $\|\mathbf{s}_{\mathrm{in}}\|_{\mathrm{l},3} = 0$ and $\mathbf{s}_0 > 0$, one has $\|\mathbf{s}_{\mathrm{out}}\|_{\mathrm{l},3} = \|\underline{\mathbf{M}}\,\mathbf{s}_{\mathrm{in}}\|_{\mathrm{l},3} \geqslant 0$. It must be noted that this last inequality is a particular case of the condition of equation (A.1). In that sense, property A.1 can be seen as a generalized version of the Stokes realizability condition.

Cloude realizability: A Mueller matrix $\underline{\mathbf{M}}$ is said *Cloude realizable* (or Jones realizable in [60, 61]) if and only if its CCM $\underline{\mathbf{C}}(\underline{\mathbf{M}})$ is PSDH [26, 49, 61]. The Cloude realizability implies the Stokes realizability whereas the converse is not true.

The demonstration of the above property A.1, which has never been reported so far to our best knowledge, is largely based on the work conducted by Rao *et al* [60, 61], which has permitted to exhibit two canonical forms of Stokes realizable non-singular Mueller matrices, under double cosetting by $SO^+(1, 3)$ elements. Their main result can be summarized through the following theorem:

Theorem 1. *(Rao et al [60]) If a non-singular Mueller matrix* $\underline{\mathbf{M}}$ *verifying* $\det(\underline{\mathbf{M}}) > 0$ *is Stokes realizable then* $\exists\,\underline{\mathbf{L}}_L, \underline{\mathbf{L}}_R \in SO^+(1, 3)$ *such that* $\underline{\mathbf{M}} = \underline{\mathbf{L}}_L\,\underline{\mathbf{M}}^{(\mathrm{I})}\,\underline{\mathbf{L}}_R$ *with*

$$\underline{\mathbf{M}}^{(\mathrm{I})} = \mathrm{diag}[\sqrt{\rho_0}, \sqrt{\rho_1}, \sqrt{\rho_2}, \sqrt{\rho_3}]$$

with $\rho_0 \geqslant \rho_1 \geqslant \rho_2 \geqslant \rho_3 > 0$; *or* $\underline{\mathbf{M}} = \underline{\mathbf{L}}_L\,\underline{\mathbf{M}}^{(\mathrm{II})}\,\underline{\mathbf{L}}_R$ *with*

$$\underline{\mathbf{M}}^{(\mathrm{II})} = \begin{bmatrix} \sqrt{n_0} & (\rho_0 - n_0)/\sqrt{n_0} & 0 & 0 \\ 0 & \rho_0/\sqrt{n_0} & 0 & 0 \\ 0 & 0 & \sqrt{\rho_2} & 0 \\ 0 & 0 & 0 & \sqrt{\rho_3} \end{bmatrix}$$

with $n_0 > \rho_0 > \rho_2 > \rho_3 > 0$.

It can be noted that additional constraints on the canonical parameters apply in order to ensure Cloude realizability [61], leading to the same canonical forms and constraints derived by Bolshakov *et al* in [62], where the authors analyzed the physical realizability of Mueller matrices from the viewpoint of the so-called *G*-polar decomposition. However, these additional constraints are not required here for the following demonstration.

We now come to the demonstration of property A.1. The condition of equation (A.1) is obviously a sufficient condition for Stokes realizability since it implies the usual Stokes realizability condition. To demonstrate that it is a necessary condition, it suffices to show that the two canonical forms of Stokes realizable non-singular Mueller matrices (recalled in theorem 1) verify the condition of equation (A.1). The generalization to any Stokes realizable non-singular Mueller matrix is then straightforward since the double cosetting by $SO^+(1, 3)$ elements does not modify the Minkowski metric.

Without loss of generality, we consider an input Stokes vector with unit intensity $\mathbf{s}_{\text{in}} = [1 \quad \mathbf{s}']^T$, with $\mathbf{s}' = [s_1\ s_2\ s_3]^T$ and $\|\mathbf{s}'\|_2^2 = \mathcal{P}^2$. In that case, one has $\|\mathbf{s}_{\text{in}}\|_{1,3}^2 = 1 - \mathcal{P}^2$ where $\mathcal{P} \in [0, 1]$ denotes the DOP of the input light.

Canonical form $\underline{\mathbf{M}}^{(\text{I})}$: In that case, one has $\det[\underline{\mathbf{M}}^{(\text{I})}] = [\rho_0\rho_1\rho_2\rho_3]^{1/2}$ and $\|\mathbf{s}_{\text{out}}\|_{1,3}^2 = \mathbf{s}_{\text{in}}^T(\underline{\mathbf{M}}^{(\text{I})})^T\underline{\mathbf{G}}\,\underline{\mathbf{M}}^{(\text{I})}\mathbf{s}_{\text{in}} = \rho_0 - [s_1^2\rho_1 + s_2^2\rho_2 + s_3^2\rho_3]$. We now compute

$$\begin{aligned}\mathcal{D}_{(\text{I})}(\mathbf{s}_{\text{in}}) &= \|\mathbf{s}_{\text{out}}\|_{1,3}^2 - [\det(\underline{\mathbf{M}}^{(\text{I})})]^{1/2}\,\|\mathbf{s}_{\text{in}}\|_{1,3}^2\\ &= \rho_0 - \left[s_1^2\rho_1 + s_2^2\rho_2 + s_3^2\rho_3\right]\\ &\quad - [\rho_0\rho_1\rho_2\rho_3]^{1/4}(1 - \mathcal{P}^2)\\ &\geqslant \rho_0 - \rho_0[s_1^2 + s_2^2 + s_3^2] - \rho_0(1 - \mathcal{P}^2) = 0,\end{aligned}$$

since $\rho_i \leqslant \rho_0,\ \forall\ i \in \{1, 3\}$.

Canonical form $\underline{\mathbf{M}}^{(\text{II})}$: The demonstration for the second canonical form is a little more involved. In that case, one has $\det[\underline{\mathbf{M}}^{(\text{II})}] = \rho_0[\rho_2\rho_3]^{1/2}$ and

$$\begin{aligned}\mathcal{D}_{(\text{II})}(\mathbf{s}_{\text{in}}) &= \|\mathbf{s}_{\text{out}}\|_{1,3}^2 - [\det(\underline{\mathbf{M}}^{(\text{II})})]^{1/2}\,\|\mathbf{s}_{\text{in}}\|_{1,3}^2\\ &= n_0(1 - s_1)^2 + 2\rho_0 s_1(1 - s_1) - (\rho_2 s_2^2 + \rho_3 s_3^2)\\ &\quad - \rho_0^{1/2}[\rho_2\rho_3]^{1/4}(1 - \mathcal{P}^2).\end{aligned}$$

Since $\rho_2 \geqslant \rho_3 \geqslant 0$, and noticing that $s_2^2 + s_3^2 = \mathcal{P}^2 - s_1^2$, it is easy to show that

$$\begin{aligned}\mathcal{D}_{(\text{II})}(\mathbf{s}_{\text{in}}) &\geqslant n_0(1 - s_1)^2 + 2\rho_0 s_1(1 - s_1)\\ &\quad - \rho_2(\mathcal{P}^2 - s_1^2) - [\rho_0\rho_2]^{1/2}(1 - \mathcal{P}^2).\end{aligned}$$

As a result, it now suffices to prove the positivity of the term at the right-hand side of the above inequality, for any input Stokes vector $\mathbf{s}_{\text{in}}$.

For that purpose, we first notice that this quantity is a polynomial function of order 2 in s_1, which we shall rewrite $f(s_1)$. For the input Stokes vector to be physically admissible, one must have $s_1 \in [-\mathcal{P}, \mathcal{P}]$. Let us first show that $f(s_1) \geqslant 0$ at its boundaries:

$$\begin{aligned}f(-\mathcal{P}) &= (1 + \mathcal{P})\\ &\quad \times [n_0(1 + \mathcal{P}) - 2\rho_0\mathcal{P} - [\rho_0\rho_2]^{1/2}(1 - \mathcal{P})]\\ &\geqslant (1 + \mathcal{P})^2(n_0 - \rho_0), \quad \text{since } \rho_0 > \rho_2\\ &\geqslant 0, \quad \text{since } n_0 > \rho_0 \text{ and } \mathcal{P} \geqslant 0.\end{aligned}$$

$$\begin{aligned}f(\mathcal{P}) &= (1 - \mathcal{P})\\ &\quad [n_0(1 - \mathcal{P}) + 2\rho_0\mathcal{P} - [\rho_0\rho_2]^{1/2}(1 + \mathcal{P})]\\ &\geqslant (1 - \mathcal{P})^2(n_0 - \rho_0), \quad \text{since } \rho_0 > \rho_2\\ &\geqslant 0, \quad \text{since } n_0 > \rho_0 \text{ and } \mathcal{P} \in [0, 1].\end{aligned}$$

Lastly, a parabolic function verifying $f(-\mathcal{P}) \geqslant 0$ and $f(\mathcal{P}) \geqslant 0$ is necessarily non-negative over the interval $[-\mathcal{P}, \mathcal{P}]$ if the function is concave, i.e., if

$$\begin{aligned}\frac{\mathrm{d}^2 f(s_1)}{\mathrm{d}s_1^2} &= 2[(n_0 - \rho_0) - (\rho_0 - \rho_2)] = 2[U - V] \leqslant 0\\ &\Leftrightarrow \quad U \leqslant V\end{aligned}$$

with $U = (n_0 - \rho_0) > 0$ and $V = (\rho_0 - \rho_2) > 0$.

On the other hand, if the function is convex, one has $U \geqslant V$ and $f(s_1)$ can be negative over $[-\mathcal{P}, \mathcal{P}]$ only if its minimum $s_1^* \in [-\mathcal{P}, \mathcal{P}]$. However, it is easy to show that solving $\mathrm{d}f(s_1)/\mathrm{d}s_1 = 0$ leads to $s_1^* = U/(U - V) \geqslant 1 \geqslant \mathcal{P}$ since $U > 0$, $V > 0$ and $U - V \geqslant 0$, thus implying that the function $f(s_1)$ cannot admit a minimum value in the interval $[-\mathcal{P}, \mathcal{P}]$. This finally proves the positivity of $f(s_1)$ for $s_1 \in [-\mathcal{P}, \mathcal{P}]$, and thus of $\mathcal{D}_{(\text{II})}(\mathbf{s}_{\text{in}})$ for any admissible input Stokes vector $\mathbf{s}_{\text{in}}$, hence achieving the proof of property A.1.

References

[1] Azzam R M and Bashara N M 1987 *Ellipsometry and Polarized Light* (Amsterdam: Elsevier)

[2] Weber J, Calado V and Van de Sanden M C M 2010 Optical constants of graphene measured by spectroscopic ellipsometry *Appl. Phys. Lett.* **97** 091904

[3] Chipman R A 1989 Polarization analysis of optical systems *Opt. Eng.* **28** 280290

[4] Kaminow I P 1981 Polarization in optical fibers *IEEE J. Quantum Electron.* **17** 15–22

[5] Collett E 1993 *Polarized Light: Fundamentals and Applications* (New York: Dekker)

[6] Kliger D S and Lewis J W 2012 *Polarized Light in Optics and Spectroscopy* (Amsterdam: Elsevier)

[7] Coulson D, Crittenden R G and Turok N G 1994 Polarization and anisotropy of the microwave sky *Phys. Rev. Lett.* **73** 2390–3

[8] Lee J-S and Pottier E 2009 *Polarimetric Radar Imaging: From Basics to Applications* (Boca Raton, FL: CRC Press)

[9] Pierangelo A, Benali A, Antonelli M-R, Novikova T, Validire P, Gayet B and De Martino A 2011 Ex-vivo characterization of human colon cancer by Mueller polarimetric imaging *Opt. Express* **19** 1582–93

[10] Alali S and Vitkin A 2015 Polarized light imaging in biomedicine: emerging Mueller matrix methodologies for bulk tissue assessment *J. Biomed. Opt.* **20** 061104

[11] Rogers P, Kang T, Zhou T, Kotelyanskii M and Sirenko A A 2011 Mueller matrices for anisotropic metamaterials generated using 4×4 matrix formalism *Thin Solid Films* **519** 2668–73
[12] Magnusson R, Birch J, Sandström P, Hsiao C-L, Arwin H and Järrendahl K 2014 Optical Mueller matrix modeling of chiral al x in 1- x n nanospirals *Thin Solid Films* **571** 447–52
[13] Tyo J S, Goldstein D L, Chenault D B and Shaw J A 2006 Review of passive imaging polarimetry for remote sensing applications *Appl. Opt.* **45** 5453–69
[14] Jones R C 1947 A new calculus for the treatment of optical systemsv. A more general formulation, and description of another calculus *J. Opt. Soc. Am.* **37** 107–10
[15] Bicout D and Brosseau C 1992 Multiply scattered waves through a spatially random medium: entropy production and depolarization *J. Phys.* I **2** 2047–63
[16] Brosseau C 1998 *Fundamentals of polarized light—A statistical Optics approach* (New York: Wiley)
[17] Aiello A and Woerdman J P 2005 Physical bounds to the entropy-depolarization relation in random light scattering *Phys. Rev. Lett.* **94** 090406
[18] Xu M and Alfano R R 2005 Random walk of polarized light in turbid media *Phys. Rev. Lett.* **95** 213901
[19] Setälä T, Shevchenko A, Kaivola M and Friberg A T 2008 Polarization time and length for random optical beams *Phys. Rev.* A **78** 033817
[20] Macias-Romero C, Foreman M R and Török P 2011 Spatial and temporal variations in vector fields *Opt. Express* **19** 25066–76
[21] Sorrentini J, Zerrad M, Soriano G and Amra C 2011 Enpolarization of light by scattering media *Opt. Express* **19** 21313–20
[22] Pouget L, Fade J, Hamel C and Alouini M 2012 Polarimetric imaging beyond the speckle grain scale *Appl. Opt.* **51** 7345–56
[23] Devlaminck V 2013 Physical model of differential Mueller matrix for depolarizing uniform media *J. Opt. Soc. Am.* A **30** 2196–204
[24] Simon R 1982 The connection between Mueller and jones matrices of polarization optics *Opt. Commun.* **42** 293–7
[25] Kim K, Mandel L and Wolf E 1987 Relationship between Jones and Mueller matrices for random media *J. Opt. Soc. Am.* A **4** 433–7
[26] Cloude S R 1986 Group theory and polarisation algebra *Optik* **75** 26–36
[27] Han D, Kim Y and Noz M E 1997 Stokes parameters as a minkowskian four-vector *Phys. Rev.* E **56** 6065
[28] Pellat-Finet P and Bausset M 1992 What is common to both polarization optics and relativistic kinematics? *Optik* **90** 101–6
[29] Morales J A and Navarro E 2003 Minkowskian description of polarized light and polarizers *Phys. Rev.* E **67** 026605
[30] Simon B N, Simon S, Mukunda N, Gori F, Santarsiero M, Borghi R and Simon R 2010 A complete characterization of pre-Mueller and Mueller matrices in polarization optics *J. Opt. Soc. Am.* A **27** 188–99
[31] Lakshminarayanan V, Calvo M L and Alieva T 2012 *Mathematical Optics: Classical Quantum, and Computational Methods* (Boca Raton, FL: CRC Press)
[32] Tudor T 2015 On a quasi-relativistic formula in polarization theory *Opt. Lett.* **40** 693–6
[33] Franssens G R 2015 Relativistic kinematics formulation of the polarization effects of Jones–Mueller matrices *J. Opt. Soc. Am.* A **32** 164–72
[34] Réfrégier P, Goudail F, Chavel P and Friberg A 2004 Entropy of partially polarized light and application to statistical processing techniques *J. Opt. Soc. Am.* A **21** 2124–34
[35] Jones R C 1948 A new calculus for the treatment of optical systems: VII. properties of the *n*-matrices *J. Opt. Soc. Am.* **38** 671–85
[36] Azzam R 1978 Propagation of partially polarized light through anisotropic media with or without depolarization: a differential 4×4 matrix calculus *J. Opt. Soc. Am.* **68** 1756–67
[37] Lounesto P 2001 *Clifford Algebras and Spinors* (Cambridge: Cambridge University Press)
[38] Gallier J 2011 *Geometric Methods and Applications: For Computer Science and Engineering* (Berlin: Springer)
[39] Muller R H 1969 Definitions and conventions in ellipsometry *Surf. Sci.* **16** 14–33
[40] Ortega-Quijano N, Haj-Ibrahim B, Garcia-Caurel E, Arce-Diego J L and Ossikovski R 2012 Experimental validation of Mueller matrix differential decomposition *Opt. Express* **20** 1151–63
[41] Kumar S, Purwar H, Ossikovski R, Vitkin I A and Ghosh N 2012 Comparative study of differential matrix and extended polar decomposition formalisms for polarimetric characterization of complex tissue-like turbid media *J. Biomed. Opt.* **17** 105006
[42] Ortega-Quijano N, Fanjul-Vélez F and Arce-Diego J L 2014 Polarimetric study of birefringent turbid media with three-dimensional optic axis orientation *Biomed. Opt. Express* **5** 287–92
[43] Ellingsen P G, Aas L M S, Hagen V S, Kumar R, Lilledahl M B and Kildemo M 2014 Mueller matrix three-dimensional directional imaging of collagen fibers *J. Biomed. Opt.* **19** 026002
[44] Villiger M and Bouma B E 2014 Practical decomposition for physically admissible differential Mueller matrices *Opt. Lett.* **39** 1779–82
[45] Ossikovski R and Devlaminck V 2014 General criterion for the physical realizability of the differential Mueller matrix *Opt. Lett.* **39** 1216–9
[46] Ortega-Quijano N, Fanjul-Vélez F and Arce-Diego J L 2015 Physically meaningful depolarization metric based on the differential Mueller matrix *Opt. Lett.* **40** 3280–3
[47] Ossikovski R and De Martino A 2015 Differential Mueller matrix of a depolarizing homogeneous medium and its relation to the Mueller matrix logarithm *J. Opt. Soc. Am.* A **32** 343–8
[48] Agarwal N, Yoon J, Garcia-Caurel E, Novikova T, Vanel J-C, Pierangelo A, Bykov A, Popov A, Meglinski I and Ossikovski R 2015 Spatial evolution of depolarization in homogeneous turbid media within the differential Mueller matrix formalism *Opt. Lett.* **40** 5634–7
[49] Cloude S R 1990 Conditions for the physical realisability of matrix operators in polarimetry *Proc. SPIE* **1166** 177–85
[50] Ortega-Quijano N and Arce-Diego J L 2011 Depolarizing differential Mueller matrices *Opt. Lett.* **36** 2429–31
[51] Ortega-Quijano N and Arce-Diego J L 2011 Mueller matrix differential decomposition *Opt. Lett.* **36** 1942–4
[52] Ossikovski R 2011 Differential matrix formalism for depolarizing anisotropic media *Opt. Lett.* **36** 2330–2
[53] Ossikovski R and Arteaga O 2014 Statistical meaning of the differential Mueller matrix of depolarizing homogeneous media *Opt. Lett.* **39** 4470–3
[54] Marinopoulos A G, Reining L, Rubio A and Vast N 2003 Optical and loss spectra of carbon nanotubes: depolarization effects and intertube interactions *Phys. Rev. Lett.* **91** 046402
[55] Devlaminck V, Terrier P and Charbois J-M 2013 Physically admissible parameterization for differential Mueller matrix of uniform media *Opt. Lett.* **38** 1410–2
[56] Devlaminck V, Terrier P and Charbois J-M 2013 Differential matrix physically admissible for depolarizing media: the case of diagonal matrices *Opt. Lett.* **38** 1497–9
[57] Gil J J and Bernabeu E 1986 Depolarization and polarization indices of an optical system *J. Mod. Opt.* **33** 185–9

[58] Cloude R S and Pottier E 1995 Concept of polarization entropy in optical scattering *Opt. Eng., Bellingham* **34** 1599–610
[59] Tomamichel M 2015 *Quantum Information Processing with Finite Resources: Mathematical Foundations* vol 5 (Berlin: Springer)
[60] Rao A G, Mallesh K and Sudha 1998 On the algebraic characterization of a Mueller matrix in polarization optics: I. Identifying a Mueller matrix from its *n* matrix *J. Mod. Opt.* **45** 955–87
[61] Rao A G, Mallesh K and Sudha 1998 On the algebraic characterization of a Mueller matrix in polarization optics: II. Necessary and sufficient conditions for Jones-derived Mueller matrices *J. Mod. Opt.* **45** 989–99
[62] Bolshakov Y, van der Mee C V, Ran A C, Reichstein B and Rodman L 1996 Polar decompositions in finite dimensional indefinite scalar product spaces: special cases and applications *Recent Developments in Operator Theory and its Applications* (Berlin: Springer) pp 61–94

Depolarization Remote Sensing by Orthogonality Breaking

Julien Fade and Mehdi Alouini
Institut de Physique de Rennes, Université de Rennes 1, CNRS, Campus de Beaulieu, 35042 Rennes, France
(Received 18 February 2012; published 26 July 2012)

A new concept devoted to sensing the depolarization strength of materials from a single measurement is proposed and successfully validated on a variety of samples. It relies on the measurement of the orthogonality breaking between two orthogonal states of polarization after interaction with the material to be characterized. Due to orthogonality preservation between the two states after propagation in birefringent media, this measurement concept is shown to be perfectly suited to depolarization remote sensing through fibers, opening the way to real-time depolarization endoscopy.

DOI: 10.1103/PhysRevLett.109.043901 PACS numbers: 42.25.Ja, 07.07.Df, 07.60.Vg, 42.62.−b

The interaction of electromagnetic radiation with natural objects has long been the subject of intensive investigations. Most significant advances in terms of understanding and applications of the physics are in the microwave domain where the amplitude, the phase, and the polarization of the field are routinely used, for instance, in long-range sensing systems in order to optimize the information extracted from a given scene [1–4]. Conversely, in the optical domain where common sensors are based on quadratic detection, it is usual to cope with the intensity of the backscattered field. In particular, in the case of polarimetric imaging, the determination of the state of polarization of the backscattered light involves the Stokes vector whose four elements correspond to measured intensities [5]. A rigorous analysis of the depolarization nature of a given material implies the determination of its Mueller matrix which linearly couples the backscattered Stokes vector to the illumination Stokes vector, thus requiring 16 measurements [6]. Consequently, this common approach is very stringent since it implies a perfect control of the polarization states of the emitted light as well as a precise projection of the backscattered electric field on the four analysis states of polarization. Moreover, this approach is very restrictive in terms of wavelength tuning and applies only to free space propagation, forbidding the use of fibers as part of the polarimetric apparatus.

Although some techniques have been recently proposed in the context of biomedical imaging to perform polarimetric measurements through fibers [7,8], they are again based on the same principle, namely, illuminating the object with a diversity of states of polarization and analyzing the backscattered signal with a polarization-sensitive detector. In Ref. [7], it is demonstrated that the degree of polarization of a given material can be recovered statistically but at the expense of a large and time consuming number of realizations. In this context, we felt that, as far as the depolarization strength (degree of polarization) of a material is the parameter of interest, the usual approaches are not optimal from an experimental point of view. Indeed, as far as one parameter has to be determined, it should be possible in principle to retrieve it from a single measurement. More importantly, if such a single measurement is achievable experimentally, then it automatically solves the problem of polarimetric remote sensing through fibers. In this Letter we propose to revisit the way of performing depolarization measurements in the optical domain using the optical electric field rather than its intensity. To this aim, we propose a novel polarimetric sensing modality which involves the concept of polarization orthogonality breaking. We show theoretically and confirm experimentally that this new sensing modality is able to provide the depolarization nature of a material and is by essence insensitive to propagation through fibers. These results thus open the way for high-sensitivity real-time endoscopic polarimetric imaging, a very promising tool in biomedical optics for *in vivo* and *in situ* marker-free diagnosis [7,8]. Although limited so far to free-space measurements, polarization-sensitive imaging techniques have indeed proven efficient in the diagnosis of a number of skin pathologies [9–12] and precancerous lesions [12–14].

In a majority of applications, including biomedical diagnosis, polarimetric imaging end-users are mainly interested in revealing polarization contrasts which may not appear on standard intensity images [5,9–15]. In such a context, characterizing the full Mueller matrix or the Stokes vector $\mathbf{S}$ provides superfluous information, as evidenced by the variety of simplified polarimetric imaging designs available [9,15–17]. In most applications, a relevant contrast parameter to consider is the degree of polarization (DOP) $\mathcal{P} = [1–4\det(\Gamma_{\text{out}})/\text{tr}(\Gamma_{\text{out}})^2]^{1/2}$, with $\Gamma_{\text{out}} = \langle \mathbf{E}_{\text{out}} \mathbf{E}_{\text{out}}^{\dagger} \rangle$ denoting the polarization matrix of the backscattered light which can be bijectively derived from $\mathbf{S}$ [5], and with $\langle\rangle$ denoting a statistical (ensemble) average. However, a majority of materials can be considered as purely depolarizing [15,18], i.e., their Mueller matrix is well approximated by a diagonal matrix of rank 2. In that case, $\mathcal{P}$ can be evaluated from only two intensity measurements through orthogonal polarizers $\mathcal{P} = (I_{\parallel} - I_{\perp})/(I_{\parallel} + I_{\perp})$, when the samples are illuminated with linearly polarized light. In general, the action of a purely

depolarizing material on an incident state of polarization $|\mathbf{E}_{\text{in}}\rangle$ can be phenomenologically modeled by a partial projection of the incident state onto the orthogonal polarization direction denoted $|\mathbf{E}_{\text{in}}^{\perp}\rangle$, i.e., $|\mathbf{E}_{\text{out}}\rangle = \sqrt{\rho}(|\mathbf{E}_{\text{in}}\rangle + \alpha|\mathbf{E}_{\text{in}}^{\perp}\rangle)$, where $\alpha = \sqrt{1-\mathcal{P}}/\sqrt{1+\mathcal{P}}$. Using Jones matrix formalism, such a relation reads

$$|\mathbf{E}_{\text{out}}\rangle = J_{\mathbf{m}}|\mathbf{E}_{\text{in}}\rangle = \sqrt{\rho}[\mathbf{R}_{|\mathbf{E}_{\text{in}}\rangle}]^{\dagger}\begin{pmatrix}1 & \alpha\\ \alpha & 1\end{pmatrix}\mathbf{R}_{|\mathbf{E}_{\text{in}}\rangle}|\mathbf{E}_{\text{in}}\rangle, \quad (1)$$

where the unitary matrix $\mathbf{R}_{|\mathbf{E}_{\text{in}}\rangle} \in SU(2)$ corresponds to the generalized polarization rotation mapping the transverse field eigenbasis $\{|\mathbf{e}_1\rangle, |\mathbf{e}_2\rangle\} \triangleq \{|\mathbf{e}_{\text{in}}\rangle, |\mathbf{e}_{\text{in}}^{\perp}\rangle\}$ into the standard linear transverse field basis $\{|\mathbf{e}_X\rangle, |\mathbf{e}_Y\rangle\}$.

From Eq. (1), it is seen that a nonnull off-diagonal term α leads to a superposition of the two orthogonal states of the electromagnetic field. Assuming that these two eigenstates $|\mathbf{e}_1\rangle$ and $|\mathbf{e}_2\rangle$ are nondegenerate, that is, they have two distinct eigenfrequencies, a coherence oscillation at the difference of the eigenfrequencies is expected, as illustrated in Fig. 1(a). Moreover, the amplitude of the coherence oscillation is directly linked to the depolarization value $\mathcal{P}$ through α. Thus, the depolarization strength of a given material can be recovered from the way this material breaks the orthogonality of a properly prepared state of the electromagnetic field. To illustrate this property, let us consider a light source emitting two distinct frequencies along two orthogonal polarization states

$$|\mathbf{E}_{\text{in}}(\boldsymbol{r}, t)\rangle = \frac{E_0}{\sqrt{2}}[\psi_1(\boldsymbol{r}, t)|\mathbf{e}_1\rangle + \psi_2(\boldsymbol{r}, t)|\mathbf{e}_2\rangle], \quad (2)$$

with $\psi_k(\boldsymbol{r}, t) = M_k(\boldsymbol{r})e^{-2j\pi\nu_k t}$. Such a state is a physical implementation of a nonquantum entangled state [19,20]. For the sake of simplicity, we consider the case of orthogonal states of equal intensities, which can be shown to be the best compromise in terms of detection performance, and we restrict ourselves to the case of plane waves, i.e., $M_k(\boldsymbol{r}) = 1$. In the most general case, the eigenstates $|\mathbf{e}_1\rangle$ and $|\mathbf{e}_2\rangle$ can be elliptical with orthogonal azimuth directions and equal ellipticity. The polarization matrix Γ_{in} of such an illumination field can be decomposed into two

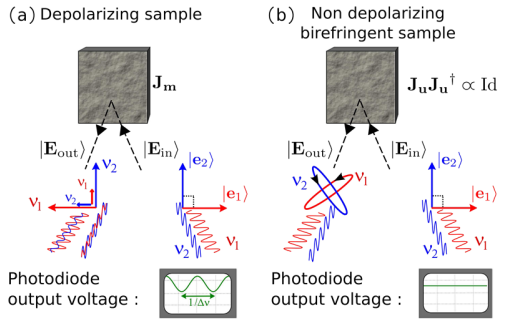

FIG. 1 (color online). Principle of depolarization sensing by orthogonality breaking (DSOB).

terms $\Gamma_{\text{in}} = \Gamma^0 + \Gamma^{\Delta\nu}e^{-j2\pi\Delta\nu t}$. The first term Γ^0 accounts for the continuous part of second-order correlations between the field transverse components, whereas $\Gamma^{\Delta\nu}$ describes interference terms, oscillating at the beat note frequency $\Delta\nu = \nu_2 - \nu_1$. From the above definitions, one can easily derive the input field continuous intensity $I_{\text{in}}^0 = \text{tr}(\Gamma^0) = |E_0|^2$, while the amplitude of the beat note intensity modulation $I_{\text{in}}^{\Delta\nu} = \text{tr}(\Gamma^{\Delta\nu}) = 0$, since the two orthogonal input states do not interfere.

When such a field interacts with an object characterized by its Jones matrix $\mathbf{J}$, the value of the beat note intensity modulation of the resulting field $I_{\text{out}}^{\Delta\nu} = \text{tr}(\mathbf{J}\Gamma^{\Delta\nu}\mathbf{J}^{\dagger})$ provides direct information on the depolarization properties of the object. As illustrated in Fig. 1(a), the loss of orthogonality induced by the interaction with a depolarizing sample gives rise to an interference intensity component oscillating at a frequency $\Delta\nu$ whose amplitude is bijectively related to the material depolarization strength. If the depolarizing sample is described by $\mathbf{J_m}$ given in Eq. (1), one indeed has

$$C_{\text{out}}^{\Delta\nu,\,0} \triangleq \frac{P_{\text{out}}^{\Delta\nu}}{P_{\text{out}}^{0}} = \frac{4\alpha^2}{(1+\alpha^2)^2} = 1 - \mathcal{P}^2. \quad (3)$$

The DOP of the sample can thus be directly retrieved from a single measurement of the beat note optical power $P_{\text{out}}^{\Delta\nu}$ (normalized by the cw optical power P_{out}^{0}). This quantity can be measured by heterodyne detection, thus enabling fast ($< 1\ \mu$s for $\Delta\nu = 1$ GHz), highly-sensitive depolarization measurements.

On the other hand, nondepolarizing media (isotropic, birefringent or optically active media) are characterized by unitary trace-preserving Jones matrices. Such a matrix verifies $\mathbf{J_u}\mathbf{J_u}^{\dagger} \propto \text{Id}$, where Id is the identity matrix, and thus $I_{\text{out}}^{\Delta\nu} = 0$, demonstrating that orthogonality between the two illumination states is preserved when light propagates through such media. This property, illustrated in Fig. 1(b), is valid provided no significant dispersion appears between frequencies ν_1 and ν_2. This is very unlikely to occur in practice since $\Delta\nu$ will not exceed tens of gigahertz for the beat note to be detectable on a photodetector. A consequence of this result is that the depolarization sensing by orthogonality breaking (DSOB) technique proposed in this Letter is in essence insensitive to birefringence and polarization rotation, thus enabling remote sensing through optical fibers, in which stress- or torsion-induced birefringences are usually highly detrimental to usual polarimetric measurements [7].

In order to experimentally illustrate and validate the DSOB principle, we have implemented the setup depicted in Fig. 2(a). In this setup, the probe field state is prepared using a single laser source which inherently produces the two orthogonal states with shifted frequencies. This laser consists of an (Er,Yb)-doped glass 4-cm-long external cavity laser emitting at 1550 nm. Single-longitudinal-mode oscillation is obtained with an intracavity 40-μm-thick

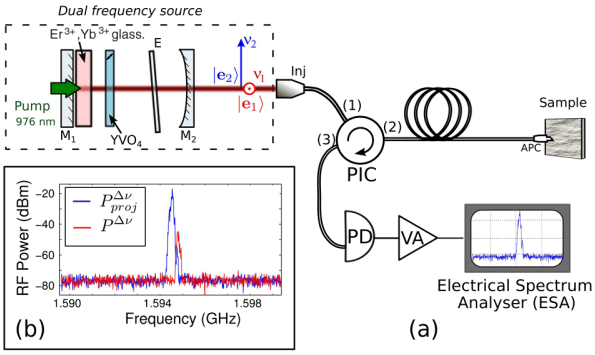

FIG. 2 (color online). (a) Schematic representation of the depolarization remote-sensing setup. Dashed box: description of the (Er,Yb)-doped glass laser producing the two orthogonally polarized and frequency shifted fields. (b) Measurement of the rf contrast obtained on a fibered mirror ($\Delta\nu = 1.254$ GHz).

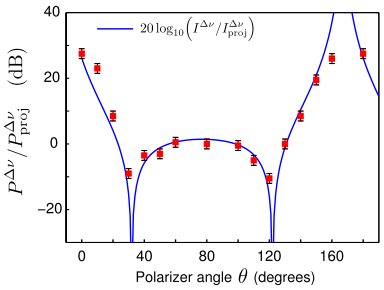

FIG. 3 (color online). Polarimetric orthogonality contrast measured with the setup of Fig. 2(a) on a rotating polarizer and mirror. Radio-frequency power was measured with an ESA.

silica etalon both sides of which are coated for 40% reflection at 1550 nm. Moreover, a 500-μm-thick YVO_4 crystal, cut at 45° of its optical axis, is inserted into the laser cavity in order to, at the same time, define two linear polarization eigenstates, lift the frequency degeneracy, and finally ensure a slight polarization walk-off (50 μm) in the active medium. This walk-off reduces the nonlinear coupling between the two eigenstates [21], leading to robust and simultaneous oscillation of the two polarization eigenstates. The active medium is diode pumped at 976 nm. Lateral positioning of the pump beam enables equalization between the two eigenstates intensities. By slightly tilting the etalon and the YVO_4 crystal, it is possible to set the frequency difference $\Delta\nu = \nu_2 - \nu_1$ to a value compatible with the detection setup, namely within the radio-frequency range, i.e., $\Delta\nu < 2$ GHz. With this configuration, the laser provides an output power of 1.8 mW with a pump power of approximately 130 mW.

We emphasize that the depolarization measurement concept we propose here is expected to be well suited for remote sensing. In order to validate this expectation, the laser output is injected into, and guided along, a 2 m-long single-mode optical fiber (SMF28) before illuminating the sample. The backscattered light is backpropagated into the same fiber, extracted with a polarization-insensitive circulator (PIC) and directed on a high-band pass (16 GHz) photodiode (PD). The detected rf signal is amplified with a high-gain (60 dB, 2 GHz cutoff frequency) voltage amplifier and analyzed on a 40 GHz band pass electrical spectrum analyzer (ESA). It is worth noticing that this measurement setup does not require any component to be inserted at the distal fiber end and may thus be directly adapted to commercial endoscopes. More importantly, no polarizing or birefringent elements are needed, and the spectral range of the setup is therefore only limited by the source, the photodiode, and the fiber spectral excursions. As a consequence, the DSOB technique could easily provide spectrally resolved polarimetric measurements, which can be interesting for materials characterization or biomedical diagnosis [22].

To calibrate and test this experimental setup, we first evaluated the maximum "polarimetric orthogonality contrast" available with such a measurement scheme. This was done by comparing the residual beat note power $P^{\Delta\nu}$ (caused by imperfect orthogonality between the polarization states) to the maximum beat note power available $P^{\Delta\nu}_{\text{proj}}$, obtained by inserting a polarizer (transmission $T_p = 85\%$) at a 45° angle with respect to the illumination polarization directions at the laser output. This contrast was derived from the corresponding spectra analyzed around frequency $\Delta\nu$ on the ESA, as illustrated in Fig. 2(b). After injection into the fiber, we measured a high contrast of -34 ± 1 dB. After propagation through a 20 km-long single-mode optical fiber, a reduced but still high contrast of -25 ± 1 dB was measured, showing that orthogonality is fairly well maintained during propagation over tens of kilometers. It was also observed that the circulator was rather detrimental to orthogonality, since a contrast of -28 ± 1 dB has been measured at the output port (2) of this component, and -27 ± 1 dB at the output port (3) after reflection on a fibered mirror. At this level, it is interesting to note that such a setup providing measurement dynamics of 25 dB makes it possible to measure values of $\mathcal{P}$ up to 99.5% (99.95% with 30 dB dynamics). The new DSOB technique addressed in this Letter may therefore be a very efficient tool when slight depolarization contrasts have to be characterized.

Further calibration was also conducted by using the setup of Fig. 2(a) and a fibered collimator to illuminate a rotating polarizer (axis $\theta_0 = 32°$) followed by a mirror. The polarimetric contrast of the light backpropagated into the fiber was analyzed on the spectrum analyzer for various orientations θ of the polarizer. The obtained results are plotted in Fig. 3 and are in fair agreement with our theoretical predictions, showing that in the experimental configuration considered, one has

$$\frac{I^{\Delta\nu}}{I^{\Delta\nu}_{\text{proj}}} = \left| \frac{2\{\sin[2(\theta - \theta_0)] + K_0\}}{T_p\{1 + K_0 + \sin[2(\theta - \theta_0)]\}} \right|, \qquad (4)$$

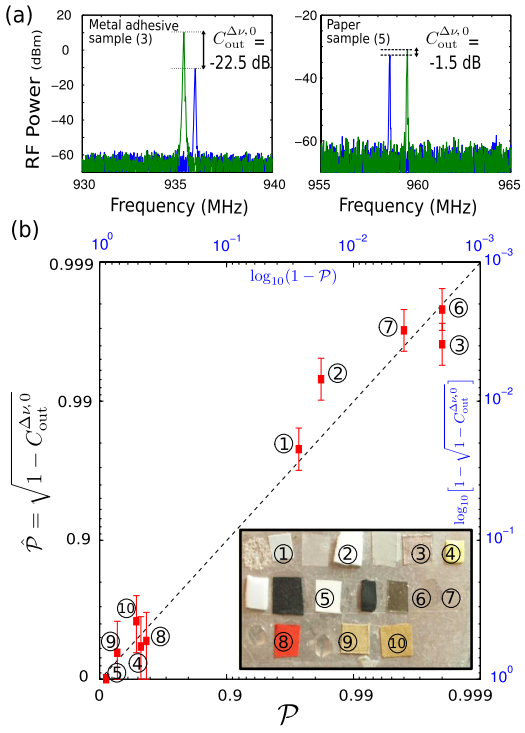

FIG. 4 (color online). (a) Evaluation of the rf polarimetric contrast on a nondepolarizing (left) and a depolarizing (right) sample with $\Delta\nu \simeq 950$ MHz. (b) The DOP estimated ($\hat{\mathcal{P}}$) from the rf beat note power measurement is in fair agreement with the DOP of the samples characterized at $\lambda = 1.55$ μm with a standard free-space Stokes measurement setup.

with $K_0 = 0.3\%$ denoting the amount of intensity reflected at the fiber or collimator end.

Once calibrated, the setup of Fig. 2(a) was tested on a variety of materials [see inset of Fig. 4(b)] to validate experimentally the DSOB technique. To match endoscopic application requirements, we considered a challenging experimental configuration where the materials under investigation were placed in the vicinity of the ferule connector-angled physical contact (FC-APC) fiber-end connector without any collimation optics. In such conditions, a very weak proportion of the illumination optical power was backscattered into the fiber mode and propagated to the detector: $\simeq 10$ μW on a metallic adhesive sample (sample 3) and only $\simeq 0.7$ μW on a diffusive paper sheet (sample 5). However, the heterodyne detection scheme involved in DSOB enables a very high sensitivity after amplification of the detected signal and analysis on the ESA. A natural improvement of this setup would be to use a lock-in detection to measure precisely the output electrical power at frequency $\Delta\nu$. Indeed, the ESA used here for the proof of concept is not required and could be advantageously replaced by a demodulation circuit since the frequency of interest $\Delta\nu$ is known.

The results obtained are reported in Fig. 4. It can first be checked in Fig. 4(a) that the relative beat note optical power is low ($C_{\text{out}}^{\Delta\nu,0} = -22.5 \pm 1$ dB) on a nondepolarizing medium (metal adhesive, $\mathcal{P} = 0.99$), whereas it considerably increases ($C_{\text{out}}^{\Delta\nu,0} = -1.5 \pm 1$ dB) on a diffusive and depolarizing sample (white paper, $\mathcal{P} = 0.11$). For the sake of experimental convenience, $C_{\text{out}}^{\Delta\nu,0}$ was determined here by normalizing the rf output power $P_{\text{out}}^{\Delta\nu}$ (blue dark curves) by $P_{\text{out,proj}}^{\Delta\nu}$ (green light curves), i.e., the rf power obtained with projected polarization states at the laser output, which provides the overall optical power backscattered by the sample (up to a factor $T_p/2$). Then, on a variety of ten samples with distinct depolarization properties, the relative beat note optical power $C_{\text{out}}^{\Delta\nu,0}$ was measured and injected in Eq. (3) to provide an estimation of the DOP. The estimated values of $\hat{\mathcal{P}}$ are plotted in Fig. 4(b) and are in good agreement with the DOP of the samples, characterized independently with standard Stokes free-space measurements performed at 1.55 μm. These experimental results validate the concept of remote depolarization sensing by polarization orthogonality breaking, as well as the DSOB setup proposed.

In this Letter, we introduced a new polarimetric measurement technique, based on the concept of orthogonality breaking, that allows one to measure the depolarization strength of a material from a single measurement in a few tens of milliseconds. In addition, the DSOB technique is *per se* insensitive to propagation through a fiber and is easily implemented without requiring any specific component at the distal end of the fiber, or in front of the detector, thus paving the way for depolarization remote-sensing of biological tissues with conventional endoscopes. Based on a heterodyne detection setup, the proposed method is highly sensitive and therefore perfectly suited for biomedical applications where biological tissues are often slightly depolarizing and prone to photodamage. A first step toward applying the DSOB technique to real-time polarization-sensitive endoscopic imaging would be working on improving the source control and implementing a demodulation circuit. On a wider scope, the DSOB principle may find applications in a number of fields, such as remote sensing and radar, materials characterization, fibre-based sensors, or any other physical measurement resorting to the orthogonality breaking principle.

[1] M. P. M. Hall, S. M. Cherry, J. W. F. Goddard, and G. R. Kennedy, Nature (London) **285**, 195 (1980).
[2] R. Dalidaouch, J. P. Armstrong, S. Schulz, P. M. Platzman, and S. L. McCall, Nature (London) **354**, 53 (1991).
[3] D. Coulson, R. G. Crittenden, and N. G. Turok, Phys. Rev. Lett. **73**, 2390 (1994).
[4] C. Plassard, E. Bourillot, J. Rossignol, Y. Lacroute, E. Lepleux, L. Pacheco, and E. Lesniewska, Phys. Rev. B **83**, 121409 (2011).
[5] J. E. Solomon, Appl. Opt. **20**, 1537 (1981).

[6] J. L. Pezzaniti and R. A. Chipman, Opt. Eng. (Bellingham, Wash.) **34**, 1558 (1995).
[7] J. Desroches, D. Pagnoux, F. Louradour, and A. Barthélémy, Opt. Lett. **34**, 3409 (2009).
[8] W. Y. Oh, B. J. Vakoc, S. H. Yun, G. J. Tearney, and B. E. Bouma, Opt. Lett. **33**, 1330 (2008).
[9] W. Groner, J. W. Winkelman, A. G. Harris, C. Ince, G. J. Bouma, K. Messmer, and R. G. Nadeau, Nature Med. **5**, 1209 (1999).
[10] S. M. Milner, S. Bhat, S. Gulati, G. Gherardini, C. E. Smith, and R. J. Bick, Burns, including thermal injury **31**, 316 (2005).
[11] F. Boulvert, B. Boulbry, G. Le Brun, B. Le Jeune, S. Rivet, and J. Cariou, J. Opt. A **7**, 21 (2005).
[12] I. Semenovitch, F. Sicuro, O. Lupi, and E. Bouskela, Arch. Dermatol. Res. **303**, 475 (2011).
[13] N. Ortega-Quijano, F. Fanjul-Vlez, J. de Cos-Prez, and J. L. Arce-Diego, Opt. Commun. **284**, 4852 (2011).
[14] Z. Tannous, M. Al-Arashi, S. Shah, and A. N. Yaroslavsky, Lasers Surg. Med. **41**, 10 (2009).
[15] S. Breugnot and P. Clémenceau, in *Laser Radar Technology and Applications IV*, edited by G. W. K. C. Werner, Proceedings of SPIE Vol. 3707 (SPIE-International Society for Optical Engineering, Bellingham, WA, 1999), pp. 449–460.
[16] S. L. Jacques, J. C. Ramella-Roman, and K. Lee, J. Biomed. Opt. **7**, 329 (2002).
[17] J. Fade, M. Roche, and M. Alouini, Opt. Lett. **37**, 386 (2012).
[18] S. Y. Lu and R. A. Chipman, J. Opt. Soc. Am. A **13**, 1106 (1996).
[19] B. N. Simon, S. Simon, F. Gori, M. Santarsiero, R. Borghi, N. Mukunda, and R. Simon, Phys. Rev. Lett. **104**, 023901 (2010).
[20] X.-F. Qian and J. H. Eberly, Opt. Lett. **36**, 4110 (2011).
[21] G. Baili, L. Morvan, M. Alouini, D. Dolfi, F. Bretenaker, I. Sagnes, and A. Garnache, Opt. Lett. **34**, 3421 (2009).
[22] E. Salomatina, B. Jiang, J. Novak, and A. N. Yaroslavsky, J Biomed. Opt. **11**, 064026 (2006).

Journal of the Optical Society of America A
OPTICS, IMAGE SCIENCE, AND VISION

Orthogonality-breaking sensing model based on the instantaneous Stokes vector and the Mueller calculus

Noé Ortega-Quijano,[1,*] Julien Fade,[1] Muriel Roche,[2] François Parnet,[1] and Mehdi Alouini[1]

[1]Institut de Physique de Rennes, CNRS, Université de Rennes 1, Campus de Beaulieu, 35042 Rennes, France
[2]Aix-Marseille Université, CNRS, Centrale Marseille, Institut Fresnel, UMR 7249, 13013 Marseille, France
*Corresponding author: noe.ortega@univ-rennes1.fr

Received 27 July 2015; revised 13 November 2015; accepted 23 January 2016; posted 25 January 2016 (Doc. ID 246794); published 3 March 2016

Polarimetric sensing by orthogonality breaking has been recently proposed as an alternative technique for performing direct and fast polarimetric measurements using a specific dual-frequency–dual-polarization (DFDP) source. Based on the instantaneous Stokes–Mueller formalism to describe the high-frequency evolution of the DFDP beam intensity, we thoroughly analyze the interaction of such a beam with birefringent, dichroic, and depolarizing samples. This allows us to confirm that orthogonality breaking is produced by the sample diattenuation, whereas this technique is immune to both birefringence and diagonal depolarization. We further analyze the robustness of this technique when polarimetric sensing is performed through a birefringent waveguide, and the optimal DFDP source configuration for fiber-based endoscopic measurements is subsequently identified. Finally, we consider a stochastic depolarization model based on an ensemble of random linear diattenuators, which makes it possible to understand the progressive vanishing of the detected orthogonality-breaking signal as the spatial heterogeneity of the sample increases, thus confirming the insensitivity of this method to diagonal depolarization. The fact that the orthogonality-breaking signal is exclusively due to the sample dichroism is an advantageous feature for the precise decoupled characterization of such an anisotropic parameter in samples showing several simultaneous effects.

OCIS codes: (110.5405) Polarimetric imaging; (120.5410) Polarimetry; (260.2130) Ellipsometry and polarimetry; (100.1930) Dichroism.

http://dx.doi.org/10.1364/JOSAA.33.000434

1. INTRODUCTION

Polarimetric imaging systems are of growing interest for many applications like remote sensing [1], astronomy [2], defense [3,4], biomedicine [5–8], synthetic-aperture radar [9], and machine or enhanced vision [10,11]. Active polarimetric techniques allow valuable information of a given scene or sample to be retrieved from the measure of its anisotropic and depolarizing properties. Mueller polarimetry is the most exhaustive active technique, as it completely characterizes the polarimetric parameters of an object. This technique typically implies registering 16 images using different approaches to modulate the measurement in the spatial, temporal, and/or spectral domain [12–17]. However, the complexity of the system and the loss of performance entailed by the different multiplexing methods have led to proposals for several simplified polarimetric techniques that optimize the measurement of some specific polarimetric properties at high performance [18–21].

In this context, the implementation of fiber-guided polarimetric imaging systems constitutes a challenging issue, due to the fact that the state of polarization of the illuminating beam is modified by the optical waveguide in an uncontrolled way. This is a remarkable aspect to be addressed for endoscopic applications, where the optical fiber stress-induced birefringence is the dominant effect on beam polarization [22]. The feasibility of a multimodal endoscopic system including cross-polarized imaging has been demonstrated for Barrett's metaplasia imaging [23]. However, such a technique provides an orientation-dependent contrast, which entails some drawbacks for *in vivo* applications. Moreover, the fact that the polarimetric elements and the CCD camera are placed in the distal end of the endoscope is quite restrictive in terms of miniaturization. Regarding Mueller polarimetry, a narrow band 3×3 Mueller polarimetric endoscope was presented and validated *ex vivo* on a Sprague Dawley rat [24]. However, the use of a rigid endoscope is unfeasible for most practical applications. Finally, a full Mueller endoscopic polarimeter, based on a first characterization of the optical fiber using a micro-switchable mirror before every Mueller matrix acquisition, was proposed in [25].

1084-7529/16/040434-13$15/0$15.00

Recently, this novel technique has been combined with spectral encoding of polarimetric channels to significantly reduce the acquisition time [26].

Recently, we proposed a novel polarimetric imaging modality based on the orthogonality-breaking sensing principle [27]. This technique uses a dual-frequency–dual-polarization (DFDP) coherent source, and is based on the measurement of the detected intensity component at the radio-frequency beat note after interaction with the sample or scene under analysis. This technique enables a subset of its polarimetric properties to be determined from a single acquisition at both high speed and high dynamic range. The first implementation of a polarimetric contrast microscope by orthogonality breaking was presented in [28]. A modified source architecture, enabling the linear diattenuation and optical axis of the sample to be completely characterized, was subsequently described and validated in [29]. Though insensitive to birefringence effects, which are predominant in biological tissues, this technique provides an alternative method to characterize biological anisotropic structures. Indeed, biological tissues usually show both birefringence and dichroism sharing the same anisotropy axis [30,31]. As a result, biological anisotropic structures can nonetheless be addressed by measuring their diattenuation properties, provided the measurement dynamics is high enough. However, all these previous works on orthogonality-breaking imaging [27–29] were focused on specific examples and particular measurement configurations. The in-depth analysis of the physical origin of the orthogonality-breaking signal amplitude and phase, in relation with the polarimetric properties of the sample and the characteristics of the illumination system, is still an open question.

In this work, we develop a comprehensive theoretical model of orthogonality-breaking sensing based on the instantaneous Stokes vector and the Mueller calculus. This approach makes it possible to describe the interaction of the DFDP beam with anisotropic depolarizing samples. Based on this method, we develop a thorough analysis of the orthogonality-breaking signal characteristics for both free-space and fiber-guided measurements. The results are presented for the basic types of optical elements, namely, isotropic absorbers, elliptical, circular, and linear retarders and diattenuators, and diagonal depolarizers. This theoretical analysis is then completed with a detailed discussion, based on both simulations and experimental measurements, which allows us to conclude that the orthogonality-breaking technique is definitely not sensitive to diagonal depolarization. Throughout this work, a special emphasis is placed on the practical implications of each configuration for experimental polarimetry.

This paper is organized as follows: the instantaneous Stokes vector description of a polarized light beam is reviewed in Section 2, before applying it to the specific characterization of the DFDP source in Section 3. Using the instantaneous Stokes–Mueller formalism, we then thoroughly study in Section 4 how this type of laser source can be used for free-space polarimetric sensing by the orthogonality-breaking principle. The influence of an optical waveguide on orthogonality-breaking sensing is then investigated in Section 5 to analyze the potential of this technique for endoscopic applications. Last, a discussion on the sensitivity of this technique to depolarization is presented in Section 6 using a stochastic model of linear diattenuation with random optical axis orientation, before the conclusion of this work is given in Section 7.

2. INSTANTANEOUS STOKES VECTOR

First, we consider a fluctuating optical plane wave described by its transverse electric field. The reference frame is set so that propagation is along the z axis in a right-handed Cartesian coordinate system xyz, and thus the complex electric field at a specific point z_0 can be resolved into a pair of orthogonal polarization states:

$$\vec{\mathbf{E}}(t) = \begin{bmatrix} E_1(t) \\ E_2(t) \end{bmatrix}. \tag{1}$$

The corresponding instantaneous Stokes vector is a four-element real vector,

$$\vec{\mathbf{S}}(t) = \begin{bmatrix} S_0(t) \\ S_1(t) \\ S_2(t) \\ S_3(t) \end{bmatrix}, \tag{2}$$

whose elements are the instantaneous Stokes parameters, defined in terms of the complex electric field components as [32]

$$S_0(t) = E_1(t)E_1^*(t) + E_2(t)E_2^*(t), \tag{3}$$

$$S_1(t) = E_1(t)E_1^*(t) - E_2(t)E_2^*(t), \tag{4}$$

$$S_2(t) = E_1(t)E_2^*(t) + E_1^*(t)E_2(t), \tag{5}$$

$$S_3(t) = i[E_1(t)E_2^*(t) - E_1^*(t)E_2(t)]. \tag{6}$$

The first component $S_0(t) = \vec{\mathbf{E}}(t)^\dagger \vec{\mathbf{E}}(t)$ is the instantaneous intensity of the field, with † denoting the Hermitian conjugate.

The instantaneous Stokes vector completely characterizes the state of polarization (SOP) of a partially polarized light beam, except its absolute phase. The conventional Stokes parameters are the ensemble averages of the instantaneous Stokes parameters. Assuming stationarity and ergodicity, the conventional Stokes vector is

$$\vec{\mathbf{S}} = \langle \vec{\mathbf{S}}(t) \rangle = \begin{bmatrix} \langle S_0(t) \rangle \\ \langle S_1(t) \rangle \\ \langle S_2(t) \rangle \\ \langle S_3(t) \rangle \end{bmatrix}, \tag{7}$$

which involves the following time average:

$$\langle X(t) \rangle = \lim_{T \to \infty} \frac{1}{T} \int_0^T X(t) \mathrm{d}t. \tag{8}$$

It is worth recalling that the conventional Stokes parameters are defined in this way simply because, in most experimental setups, the fluctuations of the electric field are produced at optical frequencies that are obviously many orders of magnitude higher than those achievable by the fastest photodetector (so far, ultrafast optical measurements can only be performed by specific techniques like nonlinear optical gating or interferometric detection, which are able to indirectly measure light intensity as well as its time delay). However, in the next section, it is shown

that the instantaneous Stokes vector is a very useful way to characterize DFDP sources.

3. DFDP SOURCE

A. General Equations

Assuming a DFDP source whose two orthogonal modes propagate along the z axis, its transversal electric field can be expressed as

$$\vec{\mathbf{E}}(t) = \frac{E_0}{\sqrt{2}} e^{-i2\pi\nu t}\left(\begin{bmatrix} a_1 \\ b_1 \end{bmatrix} + \sqrt{\gamma} e^{-i2\pi\Delta\nu t}\begin{bmatrix} a_2 \\ b_2 \end{bmatrix}\right), \tag{9}$$

where $\Delta\nu$ is the frequency shift between the two modes, and γ accounts for a possible intensity unbalancing between them. Taking into account the orthogonality condition between the SOPs of the two polarization modes, the components a_i and b_i in the Cartesian basis can be parameterized in the following general form:

$$\begin{aligned} a_1 &= \cos\alpha\cos\varepsilon - i\sin\alpha\sin\varepsilon, \\ b_1 &= \sin\alpha\cos\varepsilon + i\cos\alpha\sin\varepsilon, \end{aligned} \tag{10}$$

and

$$\begin{aligned} a_2 &= -\sin\alpha\cos\varepsilon + i\cos\alpha\sin\varepsilon, \\ b_2 &= \cos\alpha\cos\varepsilon + i\sin\alpha\sin\varepsilon, \end{aligned} \tag{11}$$

where α is the polarization ellipse azimuth and ε is its ellipticity [32]. These equations verify the polarization orthogonality condition $a_1 a_2^* + b_1 b_2^* = 0$. We set $\alpha = 0$ without loss of generality, as we later consider optical elements with arbitrary azimuth. From Eqs. (2)–(6), the instantaneous Stokes vector of a general DFDP source is

$$\vec{\mathbf{S}}(t) = I_0\begin{bmatrix} 1 \\ \frac{1-\gamma}{1+\gamma}\cos(2\varepsilon) - 2\frac{\sqrt{\gamma}}{1+\gamma}\sin(2\varepsilon)\sin(\Delta\omega t) \\ 2\frac{\sqrt{\gamma}}{1+\gamma}\cos(\Delta\omega t) \\ \frac{1-\gamma}{1+\gamma}\sin(2\varepsilon) + 2\frac{\sqrt{\gamma}}{1+\gamma}\cos(2\varepsilon)\sin(\Delta\omega t) \end{bmatrix}, \tag{12}$$

where $I_0 = |\vec{\mathbf{E}}(t)|^2 = (1+\gamma)E_0^2/2$, and with $\Delta\omega = 2\pi\Delta\nu$ denoting the angular frequency that corresponds to the interference between the two modes. The frequency shift $\Delta\nu$ can be tuned to values within the radio-frequency (RF) range, typically from several megahertz up to tens of gigahertz. It can be observed that the instantaneous intensity $S_0(t)$ of this DFDP illumination is constant and equal to I_0.

B. Linear and Circular DFDP Source

On the one hand, if the DFDP source provides two purely linear orthogonal SOPs, then $\varepsilon = 0$ and the instantaneous Stokes vector is

$$\vec{\mathbf{S}}_{\mathbf{L}}(t) = I_0\begin{bmatrix} 1 \\ \frac{1-\gamma}{1+\gamma} \\ 2\frac{\sqrt{\gamma}}{1+\gamma}\cos(\Delta\omega t) \\ 2\frac{\sqrt{\gamma}}{1+\gamma}\sin(\Delta\omega t) \end{bmatrix}. \tag{13}$$

Moreover, if a perfectly balanced source is used ($\gamma = 1$), $\vec{\mathbf{S}}_{\mathbf{L}}(t)$ simplifies to

$$\vec{\mathbf{S}}_{\mathbf{L}}(t) = I_0\begin{bmatrix} 1 \\ 0 \\ \cos(\Delta\omega t) \\ \sin(\Delta\omega t) \end{bmatrix}, \tag{14}$$

which corresponds to an instantaneous Stokes vector continuously oscillating at an angular frequency $\Delta\omega$ from a linear $\pm 45°$ SOP to a purely circular one, as shown in the Poincaré sphere representation included in Fig. 1(a).

On the other hand, if we consider a circular DFDP source, $\varepsilon = \pi/4$ and the instantaneous Stokes vector is given by

$$\vec{\mathbf{S}}_{\mathbf{C}}(t) = I_0\begin{bmatrix} 1 \\ -2\frac{\sqrt{\gamma}}{1+\gamma}\sin(\Delta\omega t) \\ 2\frac{\sqrt{\gamma}}{1+\gamma}\cos(\Delta\omega t) \\ \frac{1-\gamma}{1+\gamma} \end{bmatrix}, \tag{15}$$

which reduces to the following expression for a balanced source:

$$\vec{\mathbf{S}}_{\mathbf{C}}(t) = I_0\begin{bmatrix} 1 \\ -\sin(\Delta\omega t) \\ \cos(\Delta\omega t) \\ 0 \end{bmatrix}. \tag{16}$$

It can be observed that the latter instantaneous Stokes vector oscillates along all the possible linear SOPs, as depicted in Fig. 1(b). The advantages of each of these sources for polarimetric measurements are analyzed in the next sections.

4. FREE-SPACE ORTHOGONALITY-BREAKING SENSING

In this section, we focus on free-space orthogonality-breaking sensing, in which the source beam directly impinges on the sample. According to the Mueller calculus, the output Stokes vector $\vec{\mathbf{S}}_{\mathbf{out}}(t)$ after interaction with an anisotropic depolarizing medium is given by

$$\vec{\mathbf{S}}_{\mathbf{out}}(t) = \mathbf{M}\vec{\mathbf{S}}_{\mathbf{in}}(t), \tag{17}$$

where $\mathbf{M}$ is the Mueller matrix of the sample and $\vec{\mathbf{S}}_{\mathbf{in}}(t)$ is the input Stokes vector. It is worth recalling that this equation is valid for both the instantaneous and the conventional Stokes vector. All the subsequent results assume that the propagation direction is kept constant, so the measurement is made in transmission. The procedure can be equivalently developed for the reverse direction (reflection or backscattering configuration)

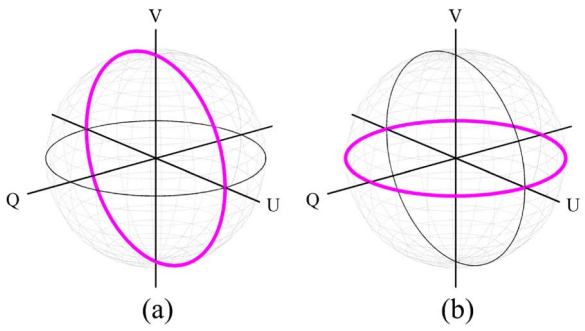

Fig. 1. Poincaré sphere representation of the instantaneous Stokes vector at the output of (a) the linear DFDP balanced source and (b) the circular DFDP balanced source.

provided that $\mathbf{M}$ is replaced by its corresponding Mueller matrix for the reverse direction:

$$\hat{\mathbf{M}} = \mathbf{O}\mathbf{M}^T\mathbf{O}^{-1}, \tag{18}$$

where $\mathbf{O} = \mathrm{diag}(1, 1, -1, 1)$ if the reversal coordinate system $\hat{x}\hat{y}\hat{z}$ is set as $\hat{x} = -x$, $\hat{y} = y$, and $\hat{z} = -z$ [32] (or, alternatively, $\hat{x} = x$, $\hat{y} = -y$, and $\hat{z} = -z$).

In the remainder of this paper we will focus on the study of the detected intensity signal $I_{\mathrm{out}}(t)$, which is a linear combination of the input instantaneous Stokes vector determined by the first row of the Mueller matrix:

$$I_{\mathrm{out}}(t) = [M_{11}M_{12}M_{13}M_{14}]\vec{\mathbf{S}}_{\mathbf{in}}(t). \tag{19}$$

A. Isotropic Absorber

The Mueller matrix of an isotropic absorber is the identity matrix weighted by the isotropic absorption coefficient ρ such that $\mathbf{M}_{\mathbf{abs}} = \rho\mathbf{I}$, and, hence, the output intensity is simply $I_{\mathrm{out}}(t) = \rho I_0$. In this trivial case, it is straightforward to verify that the orthogonality between the two SOPs generated by a general DFDP source is unaltered by the sample, and, consequently, the measured intensity remains constant in time.

B. Elliptical Retarder

A sample with elliptical birefringence presents a Mueller matrix of the following form [33]:

$$\mathbf{M}_{\mathbf{ER}} = \begin{bmatrix} 1 & \vec{0}^T \\ \vec{0} & \mathbf{M}_{3\times3} \end{bmatrix}, \tag{20}$$

where $\mathbf{M}_{3\times3}$ is the 3×3 retardance submatrix, and $\vec{0} = [0 \quad 0 \quad 0]^T$. It can be readily observed that the beam intensity is unaltered by such a sample:

$$I_{\mathrm{out}}(t) = I_0, \tag{21}$$

as expected for unitary polarization elements [32]. As a result, the polarimetric orthogonality between the two SOPs provided by the DFDP source is preserved during propagation through birefringent samples. This is the property that was originally used to make orthogonality-breaking measurements insensitive to propagation through fibers.

C. Diagonal Depolarizer

The general expression of the Mueller matrix of a diagonal depolarizer sample is [32]

$$\mathbf{M}_{\boldsymbol{\Delta}} = \begin{bmatrix} 1 & 0 & 0 & 0 \\ 0 & P_{L1} & 0 & 0 \\ 0 & 0 & P_{L2} & 0 \\ 0 & 0 & 0 & P_C \end{bmatrix}. \tag{22}$$

Diagonal depolarizers are thus defined by the three depolarization parameters P_{L1}, P_{L2}, and P_C. Such depolarizers are the most usual ones. In the particular situation of isotropic linear depolarization (like the one produced by a turbid medium with randomly located nearly spherical particles [34]), $P_{L1} = P_{L2}$. Furthermore, if completely homogeneous depolarization is assumed, the sample is usually called a pure depolarizer, and it can be quantified by a single parameter as $P_{L1} = P_{L2} = P_C$.

In any case, the elements of the first row of $\mathbf{M}_{\boldsymbol{\Delta}}$ satisfy $M_{1j} = 0$ for $j \neq 1$, so, according to Eq. (19), such a sample does not modify the orthogonality of the two orthogonally polarized SOPs, and the beam intensity is expected to remain constant in time as $I_{\mathrm{out}}(t) = I_0$.

As a result, the instantaneous Stokes–Mueller calculus detailed in this article indicates that the orthogonality-breaking sensing principle is not able to provide a measurement of diagonal depolarization. This is in contradiction with what was claimed in an earlier work [27], and with some experimental results obtained in the same reference, which actually seemed to corroborate the possibility of characterizing depolarization. This aspect is analyzed and discussed in detail in Section 6.

D. Diattenuator

1. Linear Diattenuator

The Mueller matrix of a sample showing linear dichroism is

$$\mathbf{M}_{\mathbf{LD}} = \rho \begin{bmatrix} 1 & d\cos(2\phi) & d\sin(2\phi) & 0 \\ d\cos(2\phi) & \frac{1+T}{2} + \frac{1-T}{2}\cos(4\phi) & \frac{1-T}{2}\sin(4\phi) & 0 \\ d\sin(2\phi) & \frac{1-T}{2}\sin(4\phi) & \frac{1+T}{2} - \frac{1-T}{2}\cos(4\phi) & 0 \\ 0 & 0 & 0 & T \end{bmatrix}, \tag{23}$$

where $\rho = (T_{\max} + T_{\min})/2$ accounts for the isotropic absorption, $d = (T_{\max} - T_{\min})/(T_{\max} + T_{\min})$ is the diattenuation coefficient, and $T = 2[T_{\max}T_{\min}]^{\frac{1}{2}}/(T_{\max} + T_{\min})$. Parameters $T_{\max}$ and $T_{\min} \leq T_{\max}$ are the maximum and minimum transmittances, respectively, both of them bounded between 0 and 1, so $0 \leq d \leq 1$. Finally, the parameter ϕ is the linear dichroism angle, i.e., the azimuth of the maximum transmittance axis. We note that $\mathbf{M}_{\mathbf{LD}}$ can be obtained from the Mueller matrix of an elliptical diattenuator (explicitly derived in Appendix A for the sake of generality) by setting $\epsilon = 0$. An ideal polarizer corresponds to a perfect linear dichroic sample showing $T_{\max} = 1$ and $T_{\min} = 0$, so $\rho = 1/2$, $d = 1$, and $T = 0$.

In this section and in the remainder of this article we will consider a perfectly balanced source ($\gamma = 1$). Indeed, the equations of the output intensity for a linear diattenuator using a nonbalanced linear and circular DFDP source have been included in Appendix B for the sake of completeness, and they show that the balanced configuration is actually the most advantageous one for characterizing the sample properties with the highest dynamics.

According to Eq. (19), if a linear diattenuator is illuminated with a balanced linear DFDP source, the first element of the instantaneous output Stokes vector is

$$I_{\mathrm{out}L}(t) = \rho I_0[1 + d\,\sin(2\phi)\cos(\Delta\omega t)], \tag{24}$$

where the subscript L indicates the use of linear illumination states. This equation shows the essential characteristic of the orthogonality-breaking sensing principle, namely, an AC component in the output intensity. This is because the diattenuator partially projects the two SOPs onto each other, making them interfere. Provided that the source can be tuned to set the frequency difference to a value that lies within the bandwidth of

commercially available detectors, it is then perfectly possible to observe the intensity beat note with a fast photodiode.

According to the previous equation, the DC and AC components of the output intensity are, respectively,

$$I^{0}_{\mathrm{out}L} = \rho I_0, \tag{25}$$

$$I^{\Delta\omega X}_{\mathrm{out}L} = \rho I_0 d\ \sin(2\phi), \tag{26}$$

where the superscript X accounts for the in-phase component of the beat-note signal at $\Delta\omega$.

The orthogonality-breaking contrast (OBC) is a scalar parameter defined from the DC and AC components of the detected signal as

$$\mathrm{OBC} = \frac{\overline{I^{\Delta\omega}_{\mathrm{out}}}}{I^{0}_{\mathrm{out}}}, \tag{27}$$

where $\overline{I^{\Delta\omega}_{\mathrm{out}}} = \sqrt{(I^{\Delta\omega X}_{\mathrm{out}})^2 + (I^{\Delta\omega Y}_{\mathrm{out}})^2}$ is the amplitude of the detected beat-note signal. In this case, the quadrature component $I^{\Delta\omega Y}_{\mathrm{out}L}$ is null, so $\overline{I^{\Delta\omega}_{\mathrm{out}L}} = |I^{\Delta\omega X}_{\mathrm{out}L}|$ and the OBC is thus

$$\mathrm{OBC}_L = d|\sin(2\phi)|. \tag{28}$$

Concerning the phase of the AC signal, in this case it is obviously zero as $\angle I^{\Delta\omega}_{\mathrm{out}L} = \arctan(I^{\Delta\omega Y}_{\mathrm{out}L}/I^{\Delta\omega X}_{\mathrm{out}L})$. Consequently, when a linear DFDP source is used, the beat-note component does not undergo any phase delay while interacting with the dichroic sample, and the beat-note intensity depends on both the diattenuation coefficient d and the linear dichroism angle ϕ. It can be observed that the OBC takes a maximum value of d for a linear diattenuator oriented at $\phi = 45°$. This property has been used in previous works to calibrate the measurement system [27,28].

If a circular DFDP source is now considered, the different components of the output intensity are

$$I^{0}_{\mathrm{out}C} = \rho I_0, \tag{29}$$

$$I^{\Delta\omega X}_{\mathrm{out}C} = \rho I_0 d\ \sin(2\phi), \tag{30}$$

$$I^{\Delta\omega Y}_{\mathrm{out}C} = -\rho I_0 d\ \cos(2\phi), \tag{31}$$

where the subscript C denotes circular illumination states. In this case the OBC and the beat-note signal phase are, respectively,

$$\mathrm{OBC}_C = d, \tag{32}$$

$$\angle I^{\Delta\omega}_{\mathrm{out}C} = 2\phi - \pi/2. \tag{33}$$

From the latter equation, the linear dichroism orientation can be readily obtained by

$$\phi = \frac{1}{2}(\angle I^{\Delta\omega}_{\mathrm{out}C} + \pi/2). \tag{34}$$

As a result, under circular illumination, the amplitude of the beat-note signal is independent of the dichroism orientation, giving access directly and without ambiguity to the sample dichroism. Moreover, the linear dichroism angle can be directly retrieved by the phase measurement. Such a feature is actually quite advantageous for linear dichroism sensing, as has been recently demonstrated in a microscopic imaging setup [29].

2. Elliptical/Circular Diattenuator

The complete equations of the detected intensity when the sample presents elliptical dichroism are included in Appendix C. For the sake of conciseness, we shall consider here only the very specific case of a circular diattenuator whose Mueller matrix is

$$\mathbf{M_{CD}} = \rho \begin{bmatrix} 1 & 0 & 0 & d \\ 0 & T & 0 & 0 \\ 0 & 0 & T & 0 \\ d & 0 & 0 & 1 \end{bmatrix}, \tag{35}$$

which is obtained by setting $\varepsilon = \pi/4$ in the Mueller matrix of an elliptical diattenuator (Appendix A), T and d still corresponding to their initial definition given after Eq. (23). If the sample is illuminated with a linear DFDP source, the resulting OBC and phase are

$$\mathrm{OBC}_L = d, \tag{36}$$

$$\angle I^{\Delta\omega}_{\mathrm{out}L} = \pi/2. \tag{37}$$

These equations show that such a configuration is actually sensitive to circular dichroism, which is directly characterized by the OBC, while the phase of the beat-note signal is constant. This latter information actually provides additional information about the dichroism properties when a linear DFDP source is used, as it is 0 for linear dichroism, $\pi/2$ for circular dichroism, and takes intermediate values for elliptical dichroism.

However, if a circular DFDP source is used, the OBC completely vanishes:

$$\mathrm{OBC}_C = 0, \tag{38}$$

which means that such a sample does not break the orthogonality between the circular SOPs. This is because they are precisely the eigenstates of a circular diattenuator. Consequently, there is no beat-note signal in this case.

5. ORTHOGONALITY-BREAKING SENSING THROUGH A WAVEGUIDE

In this section, orthogonality-breaking sensing through a monomode waveguide is considered. It is thus assumed that the source beam is delivered through a waveguide with Mueller matrix $\mathbf{M_{wg1}}$, when it impinges on the sample still described by its Mueller matrix $\mathbf{M}$, and is finally collected by a second waveguide with Mueller matrix $\mathbf{M_{wg2}}$ (which is not necessarily the same as the illumination one for the sake of generality), so the output instantaneous Stokes vector is

$$\vec{\mathbf{S}}_{\mathbf{out}}(t) = \mathbf{M_{wg2}} \mathbf{M} \mathbf{M_{wg1}} \vec{\mathbf{S}}_{\mathbf{in}}(t). \tag{39}$$

We define the intermediate Stokes vector $\vec{\mathbf{S}}_{\mathbf{out}'}(t) = \mathbf{M}\mathbf{M_{wg1}}\vec{\mathbf{S}}_{\mathbf{in}}(t)$ as the instantaneous Stokes vector after interaction of the fiber-guided DFDP beam with the sample. In general, it can be assumed that an optical waveguide behaves as a retarder [25] (with possible isotropic loss, but with no dichroic effects). We thus model it by the Mueller matrix of a birefringent element. If we denote $I_{\mathrm{out}'}$ the first element of the intermediate Stokes vector, one can readily verify that $I_{\mathrm{out}} = I_{\mathrm{out}'}$, as the Mueller matrix of a unitary optical element does not modify the beam intensity. A remarkable implication of this fact is that the collecting fiber does not modify the beat-note

signal possibly produced by the sample, because such information is exclusively carried by the intensity. This means that we can focus our analysis on the effect of the illuminating waveguide—while light collection can be performed by any nondichroic optical waveguide.

Concerning the illuminating fiber, its effect is a modification of the orthogonal SOPs provided by the source, so it obviously has to be taken into account. The results for isotropic absorbers, elliptical retarders, and diagonal depolarizers are not discussed in this section, as the conclusions obtained in the previous section are valid regardless of the SOPs of the DFDP illuminating beam. Moreover, if we focus on biomedical applications, circular dichroism is extremely unusual in biological samples [6,35], so we will exclusively analyze fiber-guided orthogonality-breaking sensing of linearly dichroic samples.

A. Waveguide Acting as a Circular Retarder

Let us first consider a waveguide acting as a circular retarder, whose Mueller matrix is

$$\mathbf{M_{CR}} = \begin{bmatrix} 1 & 0 & 0 & 0 \\ 0 & \cos(2\theta) & \sin(2\theta) & 0 \\ 0 & -\sin(2\theta) & \cos(2\theta) & 0 \\ 0 & 0 & 0 & 1 \end{bmatrix}, \tag{40}$$

θ being the optical rotation angle. If such a waveguide is used to illuminate a linear diattenuator with a DFDP source, it is easily shown that the results obtained in the previous section hold, up to a rotation angle of value θ, due to optical rotation in the waveguide. Typically, one has $\mathrm{OBC}_L = d|\sin(2(\phi+\theta))|$ with a linear DFDP source, whereas $\mathrm{OBC}_C = d$ and $\angle I^{\Delta\omega}_{\mathrm{out}C} = 2(\phi+\theta) - \pi/2$ with a circular DFDP source.

From these results, it is interesting to note that, with circular DFDP illumination states, the presence of an illuminating waveguide acting as a rotator does not prevent us from measuring the diattenuation coefficient, while the phase can be determined up to an additive term depending on the fiber.

B. Waveguide Acting as a Linear Retarder

More typically, an optical waveguide behaves as a linear retarder, whose general Mueller matrix is

$$\mathbf{M_{LR}} = \begin{bmatrix} 1 & 0 & 0 & 0 \\ 0 & \cos\delta\sin^2(2\psi)+\cos^2(2\psi) & (1-\cos\delta)\cos(2\psi)\sin(2\psi) & -\sin\delta\sin(2\psi) \\ 0 & (1-\cos\delta)\cos(2\psi)\sin(2\psi) & \cos\delta\cos^2(2\psi)+\sin^2(2\psi) & \sin\delta\cos(2\psi) \\ 0 & \sin\delta\sin(2\psi) & -\sin\delta\cos(2\psi) & \cos\delta \end{bmatrix}, \tag{41}$$

with ψ denoting the linear birefringence orientation, whereas δ stands for the retardation introduced between the birefringence slow and fast axes [32].

Illuminating a linear diattenuator through a linearly birefringent waveguide gives a lengthy expression of the output intensity that can be simplified to

$$I^0_{\mathrm{out}L} = \rho I_0, \tag{42}$$

$$I^{\Delta\omega X}_{\mathrm{out}L} = I_0\rho d[\sin(2\psi)\cos(2(\phi-\psi)) + \cos(2\psi)\sin(2(\phi-\psi))\cos\delta], \tag{43}$$

$$I^{\Delta\omega Y}_{\mathrm{out}L} = I_0\rho d\,\sin(\delta)\sin(2(\phi-\psi)). \tag{44}$$

It can be checked that, when the linear birefringence axis of the waveguide is parallel to the linear dichroism ($\psi = \phi$), the previous equations are exactly the same as the results obtained without the waveguide [Eqs. (25) and (26)], i.e., $I^{\Delta\omega}_{\mathrm{out}L,\delta\neq0}(t) - I^{\Delta\omega}_{\mathrm{out}L,\delta=0}(t) = 0$. However, in general, the linear birefringence introduced by the waveguide can modify the calculated parameters, and produces an intricate expression of the OBC. Let us define the bias of the measurement as

$$B_L(t) = \frac{I^{\Delta\omega}_{\mathrm{out}L,\delta\neq0}(t) - I^{\Delta\omega}_{\mathrm{out}L,\delta=0}(t)}{I^0_{\mathrm{out}L}}. \tag{45}$$

With a linear DFDP source, the bias due to a linear birefringent waveguide then reads

$$B_L(t) = 2d\,\sin\left(\frac{\delta}{2}\right)\left[-\cos(2\psi)\sin\left(\frac{\delta}{2}\right)\cos(\Delta\omega t) + \cos\left(\frac{\delta}{2}\right)\sin(\Delta\omega t)\right]\sin(2(\phi-\psi)). \tag{46}$$

If we consider the particular case of a slightly birefringent fiber ($\delta \ll 1$), the series expansion of $B_L(t)$ in δ leads at first order in δ to

$$B_L(t) = d\,\sin(2(\phi-\psi))\sin(\Delta\omega t)\delta + O(\delta). \tag{47}$$

If a circular DFDP source is now taken into account, the output intensity components are

$$I^0_{\mathrm{out}C} = \rho I_0, \tag{48}$$

$$I^{\Delta\omega X}_{\mathrm{out}C} = I^{\Delta\omega X}_{\mathrm{out}L}, \tag{49}$$

$$I^{\Delta\omega Y}_{\mathrm{out}C} = -I_0\rho d[\cos(2\psi)\cos(2(\phi-\psi)) - \sin(2\psi)\sin(2(\phi-\psi))\cos\delta]. \tag{50}$$

Again, it can be verified that these equations coincide with the free-space sensing ones for the particular case in which the fiber optical axis is parallel to the sample linear dichroism ($\psi = \phi$). Nonetheless, any other situation leads to a modification of the results by the retarding action of the waveguide. Applying the bias defined in Eq. (45) to the circular DFDP source using Eqs. (49) and (50), one gets

$$B_C(t) = 2d\,\sin\left(\frac{\delta}{2}\right)^2\sin(2(\phi-\psi))\cos(\Delta\omega t - 2\psi). \tag{51}$$

If a slightly birefringent fiber is again considered, it can be verified that the bias is null at first order in δ, and that

$$B_C(t) = d\,\sin(2(\phi-\psi))\cos(\Delta\omega t - 2\psi)\frac{\delta^2}{2} + O(\delta^2). \tag{52}$$

The bias in this case is actually at order 2 in δ. This is an interesting result, showing that the circular DFDP source is more

advantageous for orthogonality-breaking sensing through a linear birefringent waveguide, since the measured OBC is less prone to be biased by a slight birefringence in the waveguide.

6. DISCUSSION

In this last section, we complement the preceding description of the orthogonality-breaking signatures on various optically anisotropic samples by a discussion on the ability of this technique to sense depolarization. Indeed, even though calculations using the instantaneous Mueller–Stokes formalism in Section 4 show that the technique yields no orthogonality-breaking contrast on a diagonal depolarizer, previous experimental results [27] seemed to be in contradiction with this statement.

To clarify this essential aspect, we first performed a verification measurement using a linear DFDP blue source at $\lambda = 488$ nm whose development was detailed in a previous work [28]. The measurements were performed in free space for two different diffusing samples, namely, a blue paper and a red paper. The detector was fixed in a reflection configuration, with an incidence angle of roughly 45° on the sample. This measurement configuration was kept identical for both samples. As explained in detail in a previous work dealing with spectropolarimetric imaging of diffuse objects [36], illuminating both samples with a visible blue source yields two different situations. On the one hand, the main contribution to the backscattered light when the blue paper is measured comes from volume multiple scattering, as the incoming light is weakly absorbed. This type of scattering is very depolarizing, and its Mueller matrix corresponds to a diagonal depolarizer. On the other hand, when the red paper is used as a sample, the incident blue light beam is strongly absorbed by the red pigments. Consequently, the fraction of light reflected toward the detector mostly results from surface scattering, which implies much weaker depolarization and possible anisotropy of the reflection coefficients.

The measurements are presented in Fig. 2, which shows the AC component of the detected intensity for both samples using the linear DFDP source with the states oriented in two different ways, namely, along the 0°–90° and the ±45° directions. In the first configuration, the two linear states of the DFDP beam, respectively, correspond to the so-called *s*- and *p*-polarization components at the surface, whereas, in the second configuration, both linear states have partial projections on the *s* and *p* directions. It can be observed that the AC component for the blue paper is almost zero regardless of linear state orientation (dotted light blue curve and dashed dark blue curve, respectively). In this case, the dominant effect is volume multiple scattering, as mentioned above, which constitutes an initial verification of the fact that diagonal depolarization due to the sample does not produce an orthogonality-breaking signal. Regarding the red paper, one can note that there is a significant variation from roughly no AC signal when the linear modes are oriented at 0°–90° (dashed–dotted light red curve), to a substantial AC component when the modes are along ±45° (solid dark red curve). This result is in agreement with the expected behavior, as in this case surface effects are not masked by volume scattering, and, thus, slight differences in the reflectance coefficients for the *s* and *p* components of the incident light beam can result in dichroic effects in the polarized fraction of the detected backscattered light.

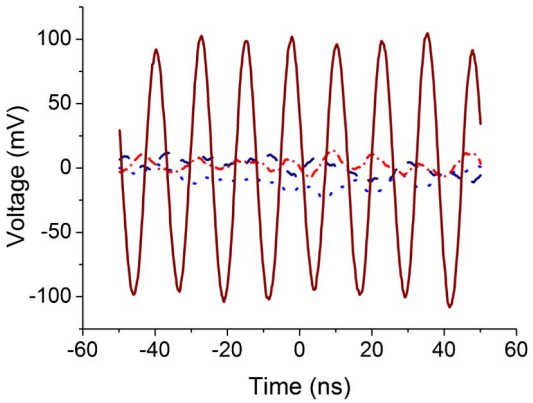

Fig. 2. AC component of the detected backscattered light under blue illumination for a blue paper and linear modes along the 0°–90° directions (dotted light blue curve) and the ±45° directions (dashed dark blue curve), and for a red paper along the same directions (dashed–dotted light red curve and solid dark red curve, respectively).

An appropriate interpretation of the aforementioned discrepancy between these results and some of our previous ones requires a deeper insight into the physical origins of depolarization. In the most general case, this generic notion must obviously encompass (i) the optical anisotropic properties of the sample considered, but must also include (ii) its local structural organization, including spatial randomization effects, (iii) the properties of the illumination field (e.g., spectral bandwidth), and (iv) the characteristics of the detection setup (e.g., numerical aperture [37] and spatial/spectral resolution). Describing a depolarizing medium with the Mueller matrix of a diagonal depolarizer [as $\mathbf{M}_\Delta$ in Eq. (22)] implicitly assumes full incoherent averaging over at least one of the above aspects. However, in a broad range of experimental setups, the characteristics of the sensing/imaging system lead to an only partial averaging operation. As a result, the description of the sample by a diagonal depolarizing Mueller matrix is no longer physically appropriate in such cases.

In the remainder of this section, we propose to use a simple stochastic model of the Mueller matrix of a depolarizing anisotropic medium consisting of the action of random linear dichroic elements. It must be noted that this description does not represent a fully comprehensive model of depolarization, as many physical parameters involved in light depolarization are neglected. However, it is shown that it successfully allows us to characterize the progressive transition from a deterministic anisotropic sample to a strongly random one (characterized by a Mueller matrix of a diagonal depolarizer) as the averaging conditions evolve. We then analyze the polarimetric properties of the resulting "macroscopic" depolarizing Mueller matrix obtained, and we characterize the orthogonality-breaking signatures produced by such a sample and physical sensing conditions. A simple experimental validation using a synthetic depolarizing sample is also included. These results and discussions finally allow us to validate the calculations presented in this work, and to understand how the subtle aspects discussed

regarding the measurement conditions were actually involved in our previous experimental measurements.

A. Stochastic Depolarization Model of an Ensemble of Random Linear Diattenuators

We consider the specific case of a dichroic depolarizing medium in which depolarization is due to the heterogeneity of its anisotropy properties. For that purpose, we consider that the incoming beam undergoes random local dichroic interactions, each polarization transformation having a diattenuation coefficient d_μ, linear dichroism angle ϕ_μ, isotropic absorption ρ_μ, and transmission parameter T_μ, where μ denotes one realization of a random event. The effect of a given random event on a DFDP illumination beam is obviously strictly equivalent to the one studied in Section 4, and can consequently be represented by a single Mueller matrix $\mathbf{M}_{\mathbf{LD}\mu}$ with the same form as that given in Eq. (23). Consequently, the Mueller matrix of a single random event is not depolarizing (Mueller–Jones matrix), as the individual polarization transformation is purely deterministic. In this case, there is a well-known one-to-one relationship between $\mathbf{M}_{\mathbf{LD}\mu}$ and its corresponding Jones matrix, as stated in Eq. (A3) of Appendix A [38,39].

The macroscopic Mueller matrix of the sample that determines the detected intensity now implies averaging over random events, i.e., $\mathbf{M}_{\mathbf{LD}}^{\Delta} = \langle \mathbf{M}_{\mathbf{LD}\mu} \rangle_\mu$. For the sake of simplicity, let us assume that the random variable ϕ_μ is independent from d_μ and ρ_μ. Regarding its probability density function, we propose adopting a convenient statistical model for angular random variables, namely, the wrapped-Gaussian distribution (WGD), with average value $\overline{\phi}$ and variance σ_ϕ^2 [40]. The definition and main properties of WGDs, which basically correspond to normal probability distributions "wrapped" around the unit circle, are recalled in Appendix D. Using these properties, the ensemble-averaged Mueller matrix of the sample is

$$\mathbf{M}_{\mathbf{LD}}^{\Delta} = \langle \mathbf{M}_{\mathbf{LD}\mu} \rangle_\mu = \overline{\rho} \begin{bmatrix} 1 & \overline{d}\cos 2\overline{\phi} e^{-2\sigma_\phi^2} & \overline{d}\sin 2\overline{\phi} e^{-2\sigma_\phi^2} & 0 \\ \overline{d}\cos 2\overline{\phi} e^{-2\sigma_\phi^2} & \frac{1+\langle T\rangle}{2} + \frac{1-\langle T\rangle}{2}\cos 4\overline{\phi} e^{-8\sigma_\phi^2} & (1-\langle T\rangle)\cos 2\overline{\phi}\sin 2\overline{\phi} e^{-8\sigma_\phi^2} & 0 \\ \overline{d}\sin 2\overline{\phi} e^{-2\sigma_\phi^2} & (1-\langle T\rangle)\cos 2\overline{\phi}\sin 2\overline{\phi} e^{-8\sigma_\phi^2} & \frac{1+\langle T\rangle}{2} - \frac{1-\langle T\rangle}{2}\cos 4\overline{\phi} e^{-8\sigma_\phi^2} & 0 \\ 0 & 0 & 0 & \langle T\rangle \end{bmatrix}, \tag{53}$$

where, for the sake of generality, random variables $T_{\min}$ and $T_{\max}$ are simply assumed to admit average values $\overline{T}_{\min}$ and $\overline{T}_{\max}$, hence $\overline{\rho} = (\overline{T}_{\max} + \overline{T}_{\min})/2$, and we set $\overline{d} = (\overline{T}_{\max} - \overline{T}_{\min})/2\overline{\rho}$.

From this matrix, the output intensity can be obtained from Eq. (19) (in the same way as the calculations detailed in Sections 4 and 5), and it is quite straightforwardly shown that the orthogonality-breaking contrast obtained for this sample is

$$\mathrm{OBC}_L = \overline{d} e^{-2\sigma_\phi^2} |\sin 2\overline{\phi}|, \tag{54}$$

in the case of linear input polarization states, whereas circular states would yield

$$\mathrm{OBC}_C = \overline{d} e^{-2\sigma_\phi^2}, \quad \text{and} \quad \angle I_{\mathrm{out}C}^{\Delta\omega} = 2\overline{\phi} - \frac{\pi}{2}. \tag{55}$$

These results are very similar to the case of deterministic transformations of the state of polarization [Eq. (28) and Eqs. (32) and (33)], up to a "fading" factor of the beat-note amplitude equal to $e^{-2\sigma_\phi^2}$. As a result, a strong dispersion of the dichroism orientations would blur the orthogonality-breaking signal produced by the diattenuation properties of the sample. Once again, one can note that using circular input states is more favorable, since the mean value of the diattenuation orientation $\overline{\phi}$ can be retrieved from the measurement of the beat-note phase, provided the beat-note amplitude is not completely attenuated.

To further analyze the previous results, let us now assume that the diattenuation angle ϕ_μ is the only random parameter, d, ρ, and T being now considered as deterministic. On the one hand, it can be immediately observed that when $\sigma_\phi \to 0$, $\mathbf{M}_{\mathbf{LD}\sigma_\phi\to 0}^{\Delta} = \mathbf{M}_{\mathbf{LD}}$, which corresponds to the trivial case of a deterministic sample, whose measurement using the orthogonality-breaking technique obviously yields the same results as those obtained in the previous sections. On the other hand, when the angular distribution becomes strongly randomized (i.e., $\sigma_\phi \gg 1$), the Mueller matrix tends to the form of a diagonal depolarizer:

$$\mathbf{M}_{\mathbf{LD}\sigma_\phi\gg 1}^{\Delta} = \rho\,\mathrm{diag}[1, (1+T)/2, (1+T)/2, T]. \tag{56}$$

We recall that if dichroism is perfect ($d = 1$), then $T = 0$ and the previous matrix corresponds to a sample that completely depolarizes the fourth element of the Stokes vector, and reduces by 0.5 the degree of polarization of any linear input SOP. For other values of T, the depolarization strength of such a diagonal depolarizer for each Stokes vector element varies. In any case, it is verified that the resulting intensity is constant $I_{\mathrm{out}}(t) = \rho I_0$ (in agreement with the results obtained in Section 4.C for diagonal depolarizers), so no orthogonality-breaking signal appears. Apart from that, we note that $\mathbf{M}_{\mathbf{LD}\sigma_\phi\gg 1}^{\Delta}$ turns out to be proportional to the identity matrix (isotropic absorption) when $T \to 1$ (or, equivalently, $d \to 0$). These features confirm that the presented approach makes it possible to simply model the continuous transition from a nondepolarizing sample characterized by a deterministic polarization transformation on the one hand, to a fully depolarizing sample depending on the statistical properties of the random diattenuation parameters on the other hand.

The polarimetric properties of the stochastic Mueller matrix obtained above can now be quantified by several parameters. The first one is the diattenuation coefficient, which can be calculated from $\mathbf{M}_{\mathbf{LD}}^{\Delta}$ (assuming again that ϕ_μ is the only random parameter) by [33]

$$D = \frac{\sqrt{\sum_{j=2}^{4} (\mathbf{M}_{\mathbf{LD}}^{\Delta})_{1j}^2}}{(\mathbf{M}_{\mathbf{LD}}^{\Delta})_{11}} = d e^{-2\sigma_\phi^2}, \tag{57}$$

showing that it scales exactly as the OBC with the angular dispersion. As a result, on this sample, the orthogonality-breaking

technique using circular states, for instance, would provide a direct measure of the *effective* linear diattenuation of the sample (as $\mathrm{OBC}_C = D = de^{-2\sigma_\phi^2}$), and of the average diattenuation orientation $\overline{\phi}$. The evolution of the effective dichroism D is plotted in Fig. 3(a) as a function of σ_ϕ and of $\log_{10} T_{\max}/T_{\min}$ (which is 0 for an isotropic sample and tends to infinity for a perfect polarizer). It can be seen that the effective linear dichroism rapidly decreases with σ_ϕ, whereas it increases for higher $\log_{10} T_{\max}/T_{\min}$ as expected. The evolution of D for $\sigma_\phi = 0$ corresponds to the diattenuation coefficient of a linear diattenuator with a fixed deterministic orientation.

It is now interesting to analyze the depolarizing properties of the $\mathbf{M}_{\mathbf{LD}}^{\mathbf{\Delta}}$ matrix. There are several depolarization metrics that can be used to quantify the depolarizing properties of a sample [33,41–45]. In this work we use Cloude entropy, which is a well-established metric to characterize the overall depolarizing nature of a given Mueller matrix [41]. Cloude entropy is given by $\mathcal{S} = -\sum_{i=1}^{4} \lambda_i' \log_4 \lambda_i'$, where $\lambda_i' = \lambda_i / \sum_{j=1}^{4} \lambda_j$ are the normalized eigenvalues of the 4×4 Cloude coherency matrix [41], whose derivation from $\mathbf{M}_{\mathbf{LD}}^{\mathbf{\Delta}}$ is detailed in Appendix E. Cloude entropy $\mathcal{S}$ is plotted in Fig. 3(b) as a function of σ_ϕ and of $\log_{10} T_{\max}/T_{\min}$. To facilitate the physical interpretation, the evolution of parameters D and $\mathcal{S}$ with $\log_{10} T_{\max}/T_{\min}$ for three different values of σ_ϕ (namely, 0, 1/2, and 2) are, respectively, plotted in Figs. 3(c) and 3(d).

It can be seen in Fig. 3(b) that Cloude entropy $\mathcal{S}$ increases with σ_ϕ, thus evidencing that depolarization is stronger as the angular dispersion grows. On the other hand, Cloude entropy increases with $\log_{10} T_{\max}/T_{\min}$. The Mueller matrix of the sample at $\sigma_\phi = 0$ or $\log_{10} T_{\max}/T_{\min} = 0$ corresponds to a deterministic Mueller matrix, hence leading to a null entropy. Cloude entropy reaches a maximum at $\mathcal{S} = 0.75$ for high values of σ_ϕ and significant anisotropy ($\log_{10} T_{\max}/T_{\min} \neq 0$). It can be noted that the maximum Cloude entropy does not reach unity, simply because the stochastic model of the sample considered does not lead to a complete depolarization of any input SOP, as we have only considered the subset of random linearly dichroic events without including elliptical dichroism.

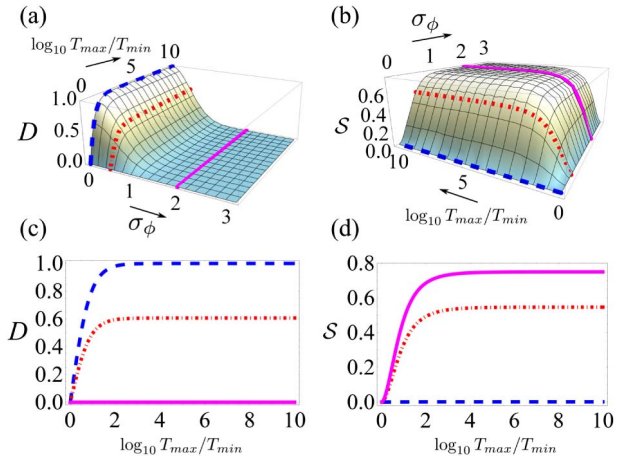

Fig. 3. (a) Evolution of the effective diattenuation coefficient D as a function of angular dispersion σ_φ and of $\log_{10} T_{\max}/T_{\min}$. (b) Evolution of Cloude entropy $\mathcal{S}$ as a function of angular dispersion σ_φ and of $\log_{10} T_{\max}/T_{\min}$. Evolution of (c) diattenuation coefficient D and of (d) Cloude entropy $\mathcal{S}$ as a function of $\log_{10} T_{\max}/T_{\min}$ for $\sigma_\varphi = 0$ (blue dashed), $\sigma_\varphi = 1/2$ (red dashed–dotted), and $\sigma_\varphi = 2$ (magenta solid).

More generally, the joint analysis of the plots in Figs. 3(a) and 3(b) clearly confirms the gradual evolution of $\mathbf{M}_{\mathbf{LD}}^{\mathbf{\Delta}}$ from a deterministic Mueller matrix of a diattenuator ($\mathcal{S} = 0$, $D \neq 0$) to a depolarizing Mueller matrix (maximum $\mathcal{S}$, $D \to 0$) when the angular dispersion σ_ϕ increases, as predicted by Eq. (53). In other words, we observe that the intrinsic dichroic properties of the sample gradually vanish as more orientations of the dichroism are taken into account by increasing σ_ϕ, providing the sample with a "macroscopic" depolarizing nature.

B. Interpretation of Experimental Results

The previous results can be easily confirmed by a simple laboratory experiment. For that purpose, we used the DFDP visible source ($\lambda = 488$ nm) emitting linear polarization states to shine a sample composed of two orthogonally oriented linear Polaroid film sheets placed in juxtaposition to each other. A sketch of the sample is presented in the inset of Fig. 4. The position of the laser beam is then displaced along the sample, whose Mueller matrix $\mathbf{M}_{\mathbf{s}}$ can be written

$$\mathbf{M}_{\mathbf{s}} = A\mathbf{M}_{\mathbf{LD}\phi=0} + (1-A)\mathbf{M}_{\mathbf{LD}\phi=\pi/2}, \tag{58}$$

where A is the fraction of the laser spot area lying on the horizontal polarizer. In the central position $A = 1/2$, so the two polarizers equally contribute to the detected intensity, and the resulting Mueller matrix is

$$\mathbf{M}_{\mathrm{scenter}} = \rho\,\mathrm{diag}[1, 1, T, T]. \tag{59}$$

It is readily observed that such a Mueller matrix corresponds to a diagonal depolarizer. The commercial Polaroid films used satisfy $T \simeq 0$, so when the laser spot is centered in the middle of the synthetic sample proposed in this section (i.e., $x_b = 0$), it behaves as a diagonal depolarizer that completely depolarizes the third and fourth elements of the input Stokes vector, without altering the second one apart from the isotropic absorption. As a result, such a sample provides an OBC that evolves from a maximum value when the spot entirely lies on

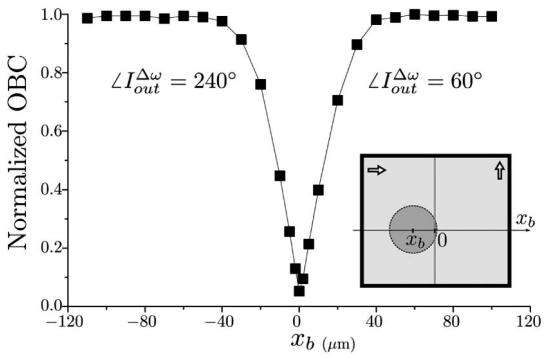

Fig. 4. Evolution of the OBC and phase as a function of beam position. Inset: sketch of the synthetic sample composed of a juxtaposition of two orthogonally oriented Polaroid film sheets. The illumination beam centered in x_b is made to horizontally scan across the sample, $x_b = 0$ corresponding to the juxtaposition edge of the two polarizing films.

a single polarizing film, to a null value when it is placed at the center. The same conclusion can be reached by separately calculating the output intensities for $\phi = 0$ and $\phi = \pi/2$ using Eq. (26) and adding them, which results in a destructive interference between the two beat-note signals in the central position since they show a relative phase of π.

The OBC for this sample was measured using the previously reported setup in transmission [29]. The evolution of the OBC as a function of the beam position is plotted in Fig. 4. This experimental curve follows the expected behavior, evidencing how the maximum orthogonality-breaking contrast obtained on a perfectly dichroic sample (extremal positions of the sample) is gradually lost as the beam simultaneously interacts with two orthogonally oriented polarizers. Indeed, it is confirmed that when the beam is centered, the contributions from each half of the beam destructively interfere on the detector, resulting in a null beat-note amplitude.

In light of all the above results, we are now able to provide an interpretation of the discrepancy between the theoretical predictions presented in Section 4 and the experimental observations at $\lambda = 1.55$ μm reported in [27]. In that work, orthogonality-breaking measurements were carried out in a fibered configuration, and then compared to the control values determined with a standard free-space Stokes polarimeter at $\lambda = 1.55$ μm. According to the discussions presented in this section, the difference in the experimental conditions of the two measurements can have strong consequences on the measured depolarization. Indeed, the standard Stokes polarimetry measurements were carried out in free space, with a relatively high spot size on the sample and high numerical aperture for the light collection. Such an experimental configuration effectively implies a spatial averaging operation over the sample surface and over several spatial coherence areas (speckle grains) as discussed in [37]. However, the orthogonality-breaking signals detected on the same samples were collected through a standard single-mode SMF28 optical fiber whose FC-APC connector end was placed in the vicinity of the samples. Under such conditions, the spatial or angular averaging is very moderate, which presumably corresponds to an intermediate position in the aforementioned transition from a nondepolarizing sample to a depolarizing one. In that case, both the diattenuation coefficient and the sample depolarization lie between their respective maximum and minimum values, as shown in Fig. 3. Therefore, in light of the thorough modelization proposed in this work and of the discussion detailed in this section, we can conclude that the OBC measured in [27] was most likely due to a moderate spatial averaging of the local diattenuation properties of the samples rather than pure depolarization.

7. CONCLUSION

In this work, the instantaneous Stokes–Mueller formalism has been applied to conveniently describe the DFDP beam used in the polarimetric sensing by the orthogonality-breaking technique, and to model the interaction of such a beam with anisotropic depolarizing media. Based on this formalism, we have thoroughly analyzed the characteristics of the orthogonality-breaking signal after interacting with birefringent, dichroic, and depolarizing samples. It has thus been confirmed that this measurement technique provides a direct characterization of dichroic samples, and that using a circular DFDP source makes it possible to readily determine the diattenuation magnitude and orientation from the amplitude and the phase of the detected intensity. Moreover, the insensitivity of this technique to birefringence has been confirmed. This constitutes an interesting property for remote polarimetric measurements, especially for endoscopic applications involving optical fibers. We have consequently characterized the influence of a birefringent waveguide on the detected beat-note component, showing that the OBC is affected by a slight bias at order 2 in the residual fiber birefringence when a circular DFDP source is used.

Last, we have proposed a simple stochastic model of a depolarizing sample composed of randomly oriented linear diattenuators. Such an analytical model, along with the results of a simple and meaningful laboratory experiment, clearly illustrates the gradual OBC vanishing as the orientation randomization of the sample increases, due to the destructive interference of the dephased individual orthogonality-breaking beat notes. All these considerations have led us to reinterpret our first experimental results [27], in which the observed OBC was most likely due to the effective diattenuation of the samples rather than to their depolarizing properties. Consequently, in light of the comprehensive model and the experimental measurements presented in this work, it is concluded that the orthogonality-breaking technique is insensitive to diagonal depolarization. This is an important property to be highlighted. Indeed, most polarimetric techniques are influenced by depolarization, which encompasses many physical aspects, including the structural properties of the sample, the detection geometry, and the source and detector bandwidth. Being exclusively sensitive to dichroism, the orthogonality-breaking technique is thus remarkably advantageous for characterizing such a parameter without being affected by other sample properties, hence potentially leading to a more specific and robust sample characterization.

The general method presented in this work provides an in-depth analysis on the physical origin of the detected signals in different measurement configurations. These results allow orthogonality-breaking sensing to be adequately modeled, which paves the way for the optimal design of orthogonality-breaking imaging systems with the capacity to perform direct and fast polarimetric measurements at high dynamics. The future development of this technique includes a systematic comparative study with standard polarimetric imaging techniques in various application contexts, and its extension to remote endoscopic measurements through fiber bundles for biomedical applications.

APPENDIX A

A characteristic property of the Jones matrix of a general dichroic sample is that its two eigenvalues are real and take the form $\lambda_1 = T_{\max}^{1/2}$ and $\lambda_2 = T_{\min}^{1/2}$, where $T_{\max}$ and $T_{\min}$ are, respectively, the maximum and minimum transmittances. If we consider the eigenvector $\vec{\mathbf{E}}_{\mathbf{eig}}$ corresponding to the greatest eigenvalue,

$$\vec{\mathbf{E}}_{\mathbf{eig}} = \begin{bmatrix} a \\ b \end{bmatrix}, \tag{A1}$$

the Jones matrix of any elliptic dichroic sample is, according to Ref. [46],

$$\mathbf{J_{ED}} = \begin{bmatrix} \lambda_1 aa^* + \lambda_2 bb^* & (\lambda_1 - \lambda_2)ab^* \\ (\lambda_1 - \lambda_2)ba^* & \lambda_2 aa^* + \lambda_1 bb^* \end{bmatrix}. \tag{A2}$$

If a and b are parameterized according to the general expressions given in Eq. (10), the Mueller matrix $\mathbf{M_{ED}}$ of an elliptical diattenuator can be readily obtained by applying the well-known relationship between a Jones matrix and its equivalent Mueller–Jones matrix:

$$\mathbf{M} = \mathbf{T}(\mathbf{J} \otimes \mathbf{J}^*)\mathbf{T}^{-1}, \tag{A3}$$

where $\otimes$ stands for Kronecker product and matrix $\mathbf{T}$ is

$$\mathbf{T} = \begin{pmatrix} 1 & 0 & 0 & 1 \\ 1 & 0 & 0 & -1 \\ 0 & 1 & 1 & 0 \\ 0 & i & -i & 0 \end{pmatrix}, \tag{A4}$$

which satisfies $\mathbf{T}^{-1} = 1/2\mathbf{T}^{\dagger}$ [39]. From the previous equations, the explicit form of $\mathbf{M_{ED}}$ is found to be

$$\mathbf{M_{ED}} = \rho \begin{bmatrix} 1 & dC_{2\phi}C_{2\varepsilon} & dS_{2\phi}C_{2\varepsilon} & dS_{2\varepsilon} \\ dC_{2\phi}C_{2\varepsilon} & \frac{1+3\,T}{4} + \frac{1-T}{4}[C_{4\varepsilon} + 2C_{4\phi}S_{2\varepsilon}^2] & \frac{1-T}{2}S_{4\phi}C_{2\varepsilon}^2 & \frac{1-T}{2}C_{2\phi}S_{4\varepsilon} \\ dS_{2\phi}C_{2\varepsilon} & \frac{1-T}{2}S_{4\phi}C_{2\varepsilon}^2 & \frac{1+3\,T}{4} + [C_{4\varepsilon} - 2C_{4\phi}S_{2\varepsilon}^2] & \frac{1-T}{2}S_{2\phi}S_{4\varepsilon} \\ dS_{2\varepsilon} & \frac{1-T}{2}C_{2\phi}S_{4\varepsilon} & \frac{1-T}{2}S_{2\phi}S_{4\varepsilon} & \frac{1+T}{2} - \frac{1-T}{2}C_{4\varepsilon} \end{bmatrix}, \tag{A5}$$

where the compact notation $C_{k\phi}^n = \cos^n(k\phi)$ and $S_{k\phi}^n = \sin^n(k\phi)$ has been used. The well-known matrix of an ideal elliptical diattenuator [38] results from substituting $T_{\max} = 1$ and $T_{\min} = 0$, so $\rho = 1/2$, $d = 1$, and $T = 0$ in the previous equation.

APPENDIX B

We shall consider a linear diattenuator illuminated by a nonbalanced linear DFDP source, whose instantaneous Stokes vector is given in Eq. (13). The output intensity shows the following DC and in-phase AC components:

$$I_{\text{out}L}^0 = \rho I_0 + d\frac{1-\gamma}{1+\gamma}\cos(2\phi), \tag{B1}$$

$$I_{\text{out}L}^{\Delta\omega X} = 2\rho I_0 \frac{\sqrt{\gamma}}{1+\gamma} d\,\sin(2\phi). \tag{B2}$$

It can be shown that the calculation of the OBC parameter according to Eq. (27) does not provide useful information for characterizing the sample dichroism, as the sample parameters ρ, d, and ϕ are strongly mixed. If a nonbalanced circular DFDP source is instead used, the DC, in-phase, and quadrature components of the output intensity are

$$I_{\text{out}C}^0 = \rho I_0, \qquad I_{\text{out}C}^{\Delta\omega X} = I_{\text{out}L}^{\Delta\omega X}, \tag{B3}$$

$$I_{\text{out}C}^{\Delta\omega Y} = -2\rho I_0 d\frac{\sqrt{\gamma}}{1+\gamma}\cos(2\phi). \tag{B4}$$

In this case, the OBC and the beat-note signal phase are, respectively,

$$\text{OBC}_C = 2d\frac{\sqrt{\gamma}}{1+\gamma}, \quad \text{and} \quad \angle I_{\text{out}C}^{\Delta\omega} = 2\phi - \pi/2. \tag{B5}$$

It should be noted that the OBC is directly the diattenuation coefficient if $\gamma = 1$. Therefore, a balanced source constitutes the most appropriate choice for our purposes. Regarding the phase of the beat-note signal, it enables the linear dichroism orientation to be readily obtained, as discussed in Section 4.

APPENDIX C

We shall now consider a sample with elliptic dichroism, whose Mueller matrix $\mathbf{M_{ED}}$ has been derived in Appendix A. Using a linear DFDP source, the output is

$$I_{\text{out}L}^0 = \rho I_0, \tag{C1}$$

$$I_{\text{out}L}^{\Delta\omega X} = \rho I_0 d\,\cos(2\varepsilon)\sin(2\phi), \tag{C2}$$

$$I_{\text{out}L}^{\Delta\omega Y} = \rho I_0 d\,\sin(2\varepsilon), \tag{C3}$$

which results in the following parameters:

$$\text{OBC}_L = d\sqrt{\sin^2(2\varepsilon) + \cos^2(2\varepsilon)\sin^2(2\phi)}, \tag{C4}$$

$$\angle I_{\text{out}L}^{\Delta\omega} = \arctan\left[\frac{\tan(2\varepsilon)}{\sin(2\phi)}\right]. \tag{C5}$$

Using a circular DFDP source, the results are

$$I_{\text{out}C}^0 = \rho I_0, \qquad I_{\text{out}C}^{\Delta\omega X} = I_{\text{out}L}^{\Delta\omega X}, \tag{C6}$$

$$I_{\text{out}C}^{\Delta\omega Y} = -\rho I_0 d\,\cos(2\varepsilon)\cos(2\phi), \tag{C7}$$

which leads to

$$\text{OBC}_C = d|\cos(2\varepsilon)|, \tag{C8}$$

$$\angle I_{\text{out}C}^{\Delta\omega} = 2\phi - \pi/2. \tag{C9}$$

We can highlight two aspects of this configuration. The first one is that the measured diattenuation coefficient d diminishes as a function of the dichroism ellipticity, completely vanishing in the case of circular dichroism. The second one is that the phase of the beat-note signal is the same regardless of the sample ellipticity, so it can be extracted in the same way as in Eq. (34).

APPENDIX D

Let θ be a random variable distributed according to a WGD with probability density function (pdf) [40]

$$f_{\text{WG}}(\theta;\mu,\sigma) = \frac{1}{\sqrt{2\pi}\sigma}\sum_{k=-\infty}^{+\infty} e^{-\frac{(\theta-\mu+2k\pi)^2}{2\sigma^2}}, \tag{D1}$$

where the parameters μ and σ, respectively, identify with the mean and standard deviation of θ. Such a WGD verifies the following property:

$$\langle z^n \rangle = \int_\Gamma e^{\mathrm{i}n\theta} f_{\mathrm{WG}}(\theta;\mu,\sigma)\mathrm{d}\theta = e^{\mathrm{i}n\mu} e^{-\frac{n^2\sigma^2}{2}}, \tag{D2}$$

where $z = e^{i\theta}$, and Γ is an integration interval of length 2π. As a result, the first moments of z are thus $\langle z \rangle = e^{i\mu} e^{-\frac{\sigma^2}{2}}$ and $\langle z^2 \rangle = e^{2i\mu} e^{-2\sigma^2}$, and one has

$$\langle \sin\theta \rangle = e^{-\frac{\sigma^2}{2}} \sin\mu, \langle \cos\theta \rangle = e^{-\frac{\sigma^2}{2}} \cos\mu. \tag{D3}$$

APPENDIX E

The Cloude coherency matrix $\mathbf{CM}$ of a Mueller matrix $\mathbf{M}$ can be straightforwardly derived from the relations given in [41]: $\mathbf{CM} = (\sum_{j,k=1}^{4} \mathbf{M}_{jk}\boldsymbol{\eta}_{jk})/4$, with $\boldsymbol{\eta}_{jk} = \mathbf{T}(\sigma_j \otimes \sigma_k^*)\mathbf{T}^\dagger$, where the $\boldsymbol{\sigma}_{i,i\in[1,4]}$ stand for the standard Pauli matrices, and where $\mathbf{T}$ is given in Eq. (A4). Using these relations, one obtains the Cloude coherency matrix of $\mathbf{M}_{\mathbf{LD}}^{\mathbf{\Delta}}$ [Eq. (53)], as

$$\mathbf{CM}_{\mathbf{LD}}^{\mathbf{\Delta}} = \rho \begin{bmatrix} \mathbf{CM}_{\mathbf{LD},3\times3}^{\mathbf{\Delta}} & \vec{0} \\ \vec{0}^T & 0 \end{bmatrix}, \tag{E1}$$

where the upper 3×3 matrix $\mathbf{CM}_{\mathbf{LD},3\times3}^{\mathbf{\Delta}}$ reads

$$\rho \begin{bmatrix} 1+\langle T\rangle & \overline{d}C_{2\overline{\phi}}e^{-2\sigma_\phi^2} & \overline{d}S_{2\overline{\phi}}e^{-2\sigma_\phi^2} \\ \overline{d}C_{2\overline{\phi}}e^{-2\sigma_\phi^2} & \frac{1-\langle T\rangle}{2}[1+C_{4\overline{\phi}}e^{-8\sigma_\phi^2}] & \frac{1-\langle T\rangle}{2}S_{4\overline{\phi}}e^{-8\sigma_\phi^2} \\ \overline{d}S_{2\overline{\phi}}e^{-2\sigma_\phi^2} & \frac{1-\langle T\rangle}{2}S_{4\overline{\phi}}e^{-8\sigma_\phi^2} & \frac{1-\langle T\rangle}{2}[1-C_{4\overline{\phi}}e^{-8\sigma_\phi^2}] \end{bmatrix}. \tag{E2}$$

It can be clearly seen that this matrix is of rank three as soon as $\sigma_\phi \neq 0$, whereas it is of rank one (independently of σ_ϕ) when $\langle T \rangle = 1$ (isotropic case), thus leading to null Cloude entropy ($\mathcal{S} = 0$).

Funding. Agence Nationale de la Recherche (ANR) (ANR-13-ASTR-0001); Direction Générale de l'Armement (DGA).

Acknowledgment. F.P.'s Ph.D. is supported by the DGA-MRIS scholarship and by Région Bretagne.

REFERENCES

1. J. S. Tyo, D. L. Goldstein, D. B. Chenault, and J. A. Shaw, "Review of passive imaging polarimetry for remote sensing applications," Appl. Opt. **45**, 5453–5469 (2006).
2. J. Tinbergen, *Astronomical Polarimetry* (Cambridge University, 1996).
3. F. Goudail and Ph. Réfrégier, "Target segmentation in active polarimetric images by use of statistical active contours," Appl. Opt. **41**, 874–883 (2002).
4. S. G. Demos and R. R. Alfano, "Optical fingerprinting using polarisation contrast improvement," Electron. Lett. **33**, 582–584 (1997).
5. J. M. Bueno, J. J. Hunter, C. J. Cookson, M. L. Kisilak, and M. C. W. Campbell, "Improved scanning laser fundus imaging using polarimetry," J. Opt. Soc. Am. A **24**, 1337–1348 (2007).
6. N. Ghosh and I. A. Vitkin, "Tissue polarimetry: concepts, challenges, applications, and outlook," J. Biomed. Opt. **16**, 110801 (2011).
7. M. H. Smith, P. D. Burke, A. Lompado, E. A. Tanner, and L. W. Hillman, "Mueller matrix imaging polarimetry in dermatology," Proc. SPIE **3911**, 210–216 (2000).
8. A. Pierangelo, A. Benali, M.-R. Antonelli, T. Novikova, P. Validire, B. Gayet, and A. De Martino, "*Ex vivo* characterization of human colon cancer by Mueller polarimetric imaging," Opt. Express **19**, 1582–1593 (2011).
9. J. S. Lee, M. R. Grunes, and E. Pottier, "Quantitative comparison of classification capability: fully polarimetric versus dual and single-polarization SAR," IEEE Trans. Geosci. Remote Sens. **39**, 1347–1351 (2001).
10. F. Meriaudeau, M. Ferraton, C. Stolz, O. Morel, and L. Bigue, "Polarization imaging for industrial inspection," Proc. SPIE **6813**, 681308 (2008).
11. J. Fade, S. Panigrahi, A. Carré, L. Frein, C. Hamel, F. Bretenaker, H. Ramachandran, and M. Alouini, "Long-range polarimetric imaging through fog," Appl. Opt. **53**, 3854–3865 (2014).
12. J. S. Tyo, "Design of optimal polarimeters: maximization of signal-to-noise ratio and minimization of systematic error," Appl. Opt. **41**, 619–630 (2002).
13. A. De Martino, Y.-K. Kim, E. García-Caurel, B. Laude, and B. Drévillon, "Optimized Mueller polarimeter with liquid crystals," Opt. Lett **28**, 616–618 (2003).
14. S. Jiao, M. Todorovic, G. Stoica, and L. V. Wang, "Fiber-based polarization-sensitive Mueller matrix optical coherence tomography with continuous source polarization modulation," Appl. Opt. **44**, 5463–5467 (2005).
15. C. F. LaCasse, R. A. Chipman, and J. S. Tyo, "Band limited data reconstruction in modulated polarimeters," Opt. Express **19**, 14976–14989 (2011).
16. A. S. Alenin and J. S. Tyo, "Generalized channeled polarimetry," J. Opt. Soc. Am. A **31**, 1013–1022 (2014).
17. A. Le Gratiet, S. Rivet, M. Dubreuil, and Y. Le Grand, "100 kHz Mueller polarimeter in reflection configuration," Opt. Lett. **40**, 645–648 (2015).
18. G. Anna, H. Sauer, F. Goudail, and D. Dolfi, "Fully tunable active polarization imager for contrast enhancement and partial polarimetry," Appl. Opt. **51**, 5302–5309 (2012).
19. T. T. Tower and R. T. Tranquillo, "Alignment maps of tissues: II. Fast harmonic analysis for imaging," Biophys. J. **81**, 2964–2971 (2001).
20. Ph. Réfrégier, J. Fade, and M. Roche, "Estimation precision of the degree of polarization from a single speckle intensity image," Opt. Lett. **32**, 739–741 (2007).
21. Z. Nan, J. Xiaoyu, H. Yonghong, and M. Hui, "Linear polarization difference imaging and its potential applications," Appl. Opt. **48**, 6734–6739 (2009).
22. T. C. Wood and D. S. Elson, "Polarization response measurement and simulation of rigid endoscopes," Biomed. Opt. Express **1**, 463–470 (2010).
23. N. Thekkek, M. C. Pierce, M. H. Lee, A. D. Polydorides, R. M. Flores, S. Anandasabapathy, and R. R. Richards-Kortum, "Modular video endoscopy for *in vivo* cross-polarized and vital-dye fluorescence imaging of Barrett's-associated neoplasia," J. Biomed. Opt. **18**, 026007 (2013).
24. J. Qi, M. Ye, M. Singh, N. T. Clancy, and D. S. Edson, "Narrow band 3×3 Mueller polarimetric endoscopy," Biomed. Opt. Express **4**, 2433–2449 (2013).
25. S. Manhas, J. Vizet, S. Deby, J.-C. Vanel, P. Boito, M. Verdier, A. De Martino, and D. Pagnoux, "Demonstration of full 4×4 Mueller polarimetry through an optical fiber for endoscopic applications," Opt. Express **23**, 3047–3054 (2015).
26. J. Vizet, J. Brevier, J. Desroches, A. Barthélémy, F. Louradour, and D. Pagnoux, "One shot endoscopic polarization measurement device based on a spectrally encoded polarization states generator," Opt. Express **23**, 16439–16448 (2015).
27. J. Fade and M. Alouini, "Depolarization remote sensing by orthogonality breaking," Phys. Rev. Lett. **109**, 043901 (2012).
28. E. Schaub, J. Fade, N. Ortega-Quijano, C. Hamel, and M. Alouini, "Polarimetric contrast microscopy by orthogonality breaking," J. Opt. **16**, 122001 (2014).
29. N. Ortega-Quijano, J. Fade, E. Schaub, F. Parnet, and M. Alouini, "Full characterization of dichroic samples from a single measurement by circular polarization orthogonality breaking," Opt. Lett. **40**, 1270–1273 (2015).
30. S. Jiao, W. Yu, G. Stoica, and L. V. Wang, "Contrast mechanisms in polarization-sensitive Mueller-matrix optical coherence tomography and application in burn imaging," Appl. Opt. **42**, 5191–5197 (2003).

31. B. H. Park, M. C. Pierce, B. Cense, and J. F. de Boer, "Jones matrix analysis for a polarization-sensitive optical coherence tomography system using fiber-optic components," Opt. Lett. **29**, 2512–2514 (2004).
32. C. Brosseau, *Fundamentals of Polarized Light: A Statistical Optics Approach* (Wiley, 1998).
33. S.-Y. Lu and R. A. Chipman, "Interpretation of Mueller matrices based on polar decomposition," J. Opt. Soc. Am. A **13**, 1106–1113 (1996).
34. M. I. Mishchenko, J. W. Hovenier, and L. D. Travis, *Light Scattering by Nonspherical Particles* (Academic, 2000).
35. V. V. Tuchin, L. V. Wang, and D. A. Zimnyakov, *Optical Polarization in Biomedical Applications* (Springer, 2006).
36. M. Alouini, F. Goudail, N. Roux, L. Le Hors, P. Hartemann, S. Breugnot, and D. Dolfi, "Active spectro-polarimetric imaging: signature modeling, imaging demonstrator and target detection," Eur. Phys. J. Appl. Phys. **42**, 129–139 (2008).
37. L. Pouget, J. Fade, C. Hamel, and M. Alouini, "Polarimetric imaging beyond the speckle grain scale," Appl. Opt. **51**, 7345–7356 (2012).
38. R. A. Chipman, "Mueller matrices," in *Handbook of Optics*, M. Bass, ed. (McGraw-Hill, 2010), Vol. I.
39. D. G. M. Anderson and R. Barakat, "Necessary and sufficient conditions for a Mueller matrix to be derivable from a Jones matrix," J. Opt. Soc. Am. A **11**, 2305–2319 (1994).
40. K. V. Mardia and P. E. Jupp, *Directional Statistics* (Wiley, 1999).
41. S. R. Cloude, "Group theory and polarisation algebra," Optik **75**, 26–36 (1986).
42. J. J. Gil and E. Bernabeu, "A depolarization criterion in Mueller matrices," Opt. Acta **32**, 259–261 (1985).
43. R. A. Chipman, "Depolarization index and the average degree of polarization," Appl. Opt. **44**, 2490–2495 (2005).
44. R. Ossikovski, "Alternative depolarization criteria for Mueller matrices," J. Opt. Soc. Am. A **27**, 808–814 (2010).
45. N. Ortega-Quijano, F. Fanjul-Vélez, and J. L. Arce-Diego, "Physically meaningful depolarization metric based on the differential Mueller matrix," Opt. Lett. **40**, 3280–3283 (2015).
46. D. S. Kliger, J. W. Lewis, and C. E. Randall, *Polarized Light in Optics and Spectroscopy* (Academic, 1990).

Full characterization of dichroic samples from a single measurement by circular polarization orthogonality breaking

Noé Ortega-Quijano,* Julien Fade, Emmanuel Schaub, François Parnet, and Mehdi Alouini

Institut de Physique de Rennes, CNRS, Université de Rennes 1, Campus de Beaulieu, 35 042 Rennes, France
**Corresponding author: noe.ortega@univ-rennes1.fr*

Received November 20, 2014; revised February 11, 2015; accepted February 18, 2015;
posted February 20, 2015 (Doc. ID 227228); published March 19, 2015

We report a novel method to unambiguously determine the magnitude and orientation of linear dichroism in a simultaneous way. It is based on the use of a dedicated dual-frequency dual-polarization coherent source providing two orthogonal circularly polarized modes at the output. We show that the interaction of such a beam with dichroic media gives rise to a beatnote signal whose amplitude and phase enable the full determination of the diattenuation coefficient and axis orientation, respectively. The application of this method to polarimetric imaging provides single-shot sample characterization by its diattenuation coefficient and optical axis angle, with potential applications in biomedical imaging. © 2015 Optical Society of America

OCIS codes: (110.5405) Polarimetric imaging; (120.5410) Polarimetry; (120.0120) Instrumentation, measurement, and metrology; (100.1930) Dichroism.
http://dx.doi.org/10.1364/OL.40.001270

Polarimetry is a widely used technique to enhance contrast and perform beam and/or sample characterization in many different fields like atmospheric remote sensing, target detection, astronomy, and biomedical diagnostics [1]. Active polarimetric imaging is based on illuminating and analyzing a given scene or sample using controlled states of polarization (SOPs). The number of required SOPs depends on the specific polarimetric technique. Complete Mueller polarimetry enables the anisotropic and depolarizing optical properties of a sample to be fully characterized, but requires to perform a minimum of 16 measurements that can be multiplexed either spatially, temporally, or spectrally [2]. Incomplete polarimetric techniques make it possible to diminish the number of measurements to the detriment of the measurable information about the sample. For instance, scalar polarimetric contrast images are commonly achieved from only two intensity measurements in the family of two-channel imaging systems [3–5], and degree-of-polarization maps can be estimated from a single-image acquisition under coherent illumination [6].

Polarimetric sensing by orthogonality breaking is a recently proposed measurement principle that enables the direct characterization of the sample dichroism and/or depolarization in a single measurement (i.e., using a single signal acquisition without either temporal or spatial multiplexing), with a high dynamic range and acquisition speed [7]. Its essential aspects are the use of a specific dual-frequency dual-polarization coherent source and the fact that the polarimetric information is carried by a radio-frequency (RF) intensity beatnote induced by the sample dichroism/depolarization. Being inherently insensitive to birefringence effects, orthogonality breaking sensing is specially adapted for endoscopic applications, and for biomedical imaging in general. Indeed, biological tissues show both birefringence and dichroism sharing the same optical axis [8–10], so the characterization of its anisotropic structure (including its pathological alterations) can be advantageously performed by measuring its linear diattenuation. In that perspective, we have recently reported the development of a polarimetric contrast microscope based on this technique [11]. Nevertheless, as far as dichroism is the measurement purpose, one can wonder whether the orthogonality breaking principle upgraded with a dedicated arrangement can bring a simple and elegant solution to fully characterize linear dichroism.

In this Letter, we present a novel dual-frequency dual-polarization source configuration that enables the anisotropy parameters (magnitude and orientation angle) of a linear dichroic sample to be fully characterized in a simultaneous way. Specifically, we show that generating two orthogonal circularly polarized modes with a detuning frequency between them makes it possible to extract the dichroism parameters from the measurement of the RF beatnote signal after interaction with the sample. The source architecture is described and a concise model of the light-sample interaction is presented. These theoretical developments are then validated on several test samples. Finally, the potential of this technique to perform real-time dichroism imaging is explored on a synthetic imaging scenario using a laser scanning imaging setup.

Let us consider a specific dual-frequency dual-circular-polarization (DF-DCP) laser source. Assuming plane waves propagation along z, the beam at a given distance can be denoted, up to a propagation phase factor, by

$$\mathbf{E}_{\text{in}}(t) = \frac{E_0}{\sqrt{2}} e^{-j(2\pi\nu t)} [\mathbf{e}_R + e^{-j2\pi\Delta\nu t}\mathbf{e}_L], \tag{1}$$

where $\mathbf{e}_{L,R} = [1 \pm j]^T/\sqrt{2}$ stands for the Jones vector of a left (respectively right) circularly polarized light beam. The initial intensity of the generated DF-DCP beam is $I_0 = |E_0|^2$. When such probe beam is used to illuminate a sample showing linear dichroism with optical axis orientation ϕ, the Jones formalism allows us to easily write the output field as

0146-9592/15/071270-04$15.00/0

$$\mathbf{E}_{\text{out}}(t) = \mathbf{J}_{d,\phi}\mathbf{E}_{\text{in}}(t) = R[-\phi]\mathbf{J}_d R[\phi]\mathbf{E}_{\text{in}}(t), \tag{2}$$

where $R[\phi]$ is the standard rotation matrix, and $\mathbf{J}_d$ is the Jones matrix of a dichroic element along the x axis:

$$\mathbf{J}_d = \sqrt{\rho}\begin{pmatrix} \sqrt{1+d} & 0 \\ 0 & \sqrt{1-d} \end{pmatrix}, \tag{3}$$

where $\rho = (T_{\min} + T_{\max})/2$ stands for its isotropic absorption, and $d = (T_{\max} - T_{\min})/(T_{\max} + T_{\min})$ is the diattenuation coefficient, $T_{\min}$ and $T_{\max}$ respectively being the minimum and maximum transmittances. It can be noted that the orientation angle of such dichroic sample is defined up to a π angle, since $\mathbf{J}_{d,\phi} = \mathbf{J}_{d,\phi+\pi}$.

The output intensity which can be measured by a fast photodetector after interaction of the DF-DCP beam with the sample is given by $I_{\text{out}} = \mathbf{E}_{\text{out}}^{\dagger}\mathbf{E}_{\text{out}}$, where $\dagger$ is the complex conjugate transpose. Its calculation leads to the decomposition of the output intensity into a DC term (I_{out}^{0}) and a RF term at the beatnote frequency $\Delta\nu$ between the two modes ($I_{\text{out}}^{\Delta\nu}(t)$). These intensity components are given by

$$I_{\text{out}}^{0} = \rho I_0, \tag{4}$$

$$I_{\text{out}}^{\Delta\nu}(t) = \rho d I_0 \cos(2\pi\Delta\nu t + 2\phi + p\pi), \tag{5}$$

where the π phase shift depends on the experimental configuration ($p = 0$ for transmission measurements, whereas $p = 1$ for the reflection/backscattering configuration). These equations show that measuring the DC and the RF beatnote components of the output intensity directly gives access to all sample parameters. Firstly, the orthogonality breaking contrast parameter, already introduced in our previous work [11], is readily found to equal the sample diattenuation:

$$\text{OBC} = |I_{\text{out}}^{\Delta\nu}(t)|/I_{\text{out}}^{0}(t) = d. \tag{6}$$

Regarding the optical axis orientation, it can be observed that ϕ is directly given by the beatnote signal phase, up to a π term, as $\arg[I_{\text{out}}^{\Delta\nu}(t)] = 2\phi + p\pi$. Finally, isotropic absorption ρ is directly calculated from the DC intensity, as in conventional non-polarimetric techniques. We highlight that all these parameters are obtained in an uncoupled and straightforward way, which considerably simplifies the sample characteristics determination and analysis. It should be noted that in more complex situations involving multiple anisotropic effects like circular birefringence (e.g., in multilayered samples or fiber-guided measurement systems), the implementation of this method would require a more detailed analysis, which is out of the scope of this work.

The first experimental setup used to validate the presented method is shown in Fig. 1(a). It is composed of a 40-mW commercial 488-nm source that is introduced into a polarization splitting/combining Mach–Zehnder architecture. One of the arms has an acousto-optical modulator that introduces a fixed frequency shift of $\Delta\nu =$ 80 MHz. A pinhole is used to spatially filter the two

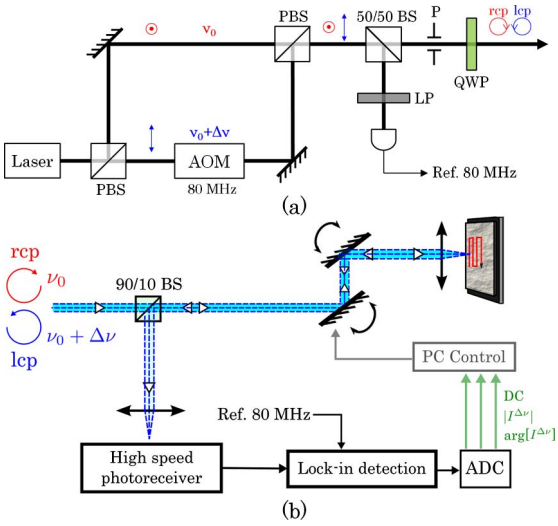

Fig. 1. (a) Dual-frequency dual-circular-polarization source architecture at $\lambda = 488$ nm. (b) Complete imaging setup in reflection configuration.

orthogonal linearly polarized modes at the output and to ensure perfect superposition of their respective wave vectors. Then a quarter wave plate (QWP) oriented at 45 degrees with respect to the linear polarization directions turns them into two orthogonal right and left circular SOPs. Note that a fraction of the output signal is taken at the exit of the Mach–Zehnder interferometer architecture, before the pinhole and the QWP. It is sent on a linear polarizer at 45 degrees followed by a fast Si PIN photodiode that provides us with a beatnote reference signal. Such 80-MHz reference is used for signal demodulation instead of the AOM driver output to avoid any drift between the phases of the reference and the measured beatnote signal that might be induced by optical path depth residual fluctuations in the interferometer. Moreover, it enables the measurement of the maximum beatnote amplitude achievable by our system, which is subsequently used to normalize the measurements.

We first performed a free-space single-point measurement of several control samples in transmission. Optical elements with different diattenuation coefficients were chosen, namely a VIS polarizer (LP-VIS-A, Thorlabs) and a NIR polarizer (LP-NIR, Thorlabs). First, the diattenuation coefficient was determined from the conventional measurement of the minimum and maximum transmittances, with a result of 0.99 and 0.45, respectively, in agreement with manufacturer's specifications at $\lambda =$ 488 nm. Subsequently, the diattenuation magnitude and orientation angle were determined following the approach detailed above using an oscilloscope. The measurements were repeated for multiple sample orientations. The calculated diattenuation is shown in Fig. 2(a). It can be observed that the measured coefficient for the VIS polarizer is around 0.97, which is approximately constant independently of the sample orientation as expected. We note that the presence of a small modulation arises from the fact that the generated SOPs were not perfectly circularly polarized. This residual modulation could be easily calibrated out in an operational system. Regarding the NIR polarizer, its diattenuation coefficient

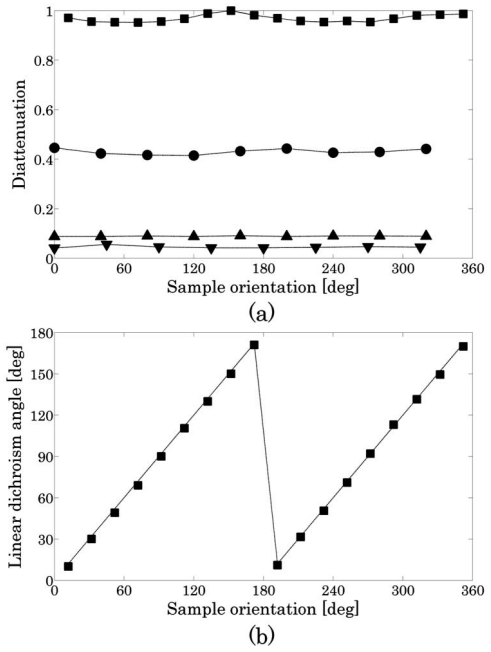

Fig. 2. (a) Linear diattenuation coefficient of a visible linear polarizer (■), a near-infrared polarizer (•), a neutral density filter (▲), and a $\lambda/2$@850-nm waveplate (▼) as a function of the sample orientation angle. (b) Control (dotted line) and measured (■) linear dichroism angle of the visible linear polarizer.

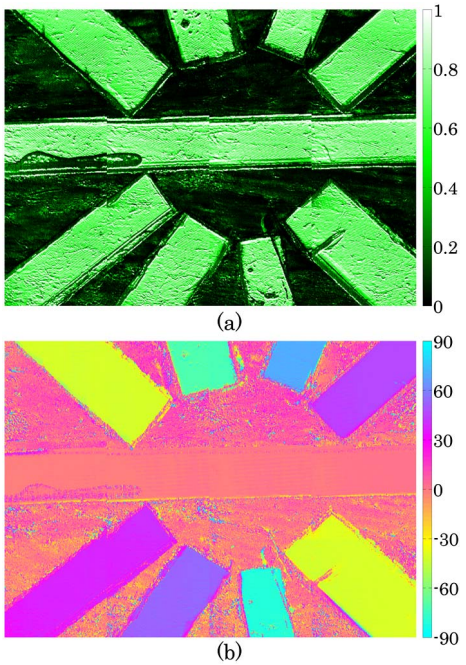

Fig. 3. Linear diattenuation magnitude (a) and orientation (b) of the measured sample. Each image is 10×7.5 mm.

yields an almost constant value of around 0.43, which shows a good agreement with the expected value. The optical axis orientation was retrieved from the phase shift between the signal and the reference, after an initial calibration on a polarizer of known orientation to compensate the phase delay due to the electrical wires length. It is worth noting that this compensation has to be performed only once and remains valid for all the subsequent measurements. The orientation angle of the VIS polarizer has been plotted in Fig. 2(b). The measured angles are in fair agreement with the control values (which are the known orientation angles directly read from the VIS polarizer graduated rotation mount). Finally, a neutral density filter and a half wave plate (at $\lambda = 850$ nm) were measured. Ideally, the diattenuation of these elements is null. The measured diattenuation was respectively 0.09 and 0.045, as shown in the lower part of Fig. 2(a). These small deviations from 0 are explained by the presence of a residual systematic signal at 80 MHz (mainly due to unperfect electronic shielding of the AOM RF driver and of the photodiode wiring) that introduces a slight bias in the measurements.

The previous results validate the proposed method for single point measurements, enabling its application to a polarimetric contrast imaging system. We have previously reported the implementation of a microscopic imager in which the sample was moved using a motorized translation stage, which considerably limited the acquisition speed [11]. In this work, we have used the galvanometric mirror capability of our 4PI microscope prototype (PIXEL facility of the University of Rennes 1) for laser beam scanning. Such new arrangement acquires a 256×256 pixels image of a 2.5-mm side sample in about 4 s only. The system is sketched in Fig. 1(b). The DF-DCP beam is delivered using a polarization-maintaining fiber (that replaces the pinhole used in the previous measurement) and focused on the sample using a conventional lens (LA1608, Thorlabs), and the reflected light is collected by a 90:10 beamsplitter cube after passing back through the scanning mirrors (descanned detection mode). The beam is detected by a high-speed photoreceiver whose signal is connected to a RF lock-in amplifier (SR844, Stanford Research Systems).

We have used a controlled dichroic sample made of several polaroid rectangular cuts radially placed around a central one. Each polaroid stripe was cut along its dichroic axis and mounted between a mirror and a coverslip, using microscope objective oil as the mounting medium. The region of interest was about 10×7.5 mm, so a mosaic of several individual images was made to have a proper rendering of the full sample. The diattenuation magnitude and orientation were directly obtained from the DC intensity and the 80-MHz beatnote amplitude and phase, which were measured simultaneously in a single laser scan following the method described above. The measured diattenuation magnitude is shown in Fig. 3(a). The most relevant characteristic is that the contrast is effectively constant all over each polaroid stripe, as the measured diattenuation is unaffected by the relative orientation of the dichroic axis. Diattenuation is actually close to 1 for each polaroid fragment, and almost 0 elsewhere, as expected. The linear dichroism angle is presented in Fig. 3(b). It can be observed that the measured parameter successfully discriminates the orientation of each dichroic segment. The value in each of them is almost constant, the uniformity of the results being indeed greater than that observed in the diattenuation magnitude image. This behavior is a consequence of the fact that phase is usually less prone to be affected by noise and other fluctuations than amplitude.

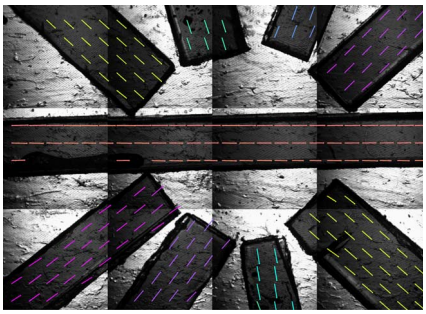

Fig. 4. Mean intensity I_{out}^{0} (background) and local estimation of the linear dichroism angle (colored lines).

Another interesting feature of these results is that the calculated parameters are not affected by variations in the sample illumination. The background of Fig. 4 shows the DC intensity, where there is an apparent inhomogeneity in the sample illumination for each individual image. The beatnote amplitude mosaic (not included) shows a similar pattern. Intensity fluctuations are cancelled in the diattenuation parameters calculation, so the diattenuation magnitude and orientation images (which are presented without any image processing) are unaffected by illumination inhomogeneities.

Additionally, we present a reconstruction of the orientation angles to further check the validity of the results. In order to do that, the dichroism angle image is divided into a set of 30×30 pixels subimages. A threshold is fixed so that only the pixels with a diattenuation coefficient greater than 0.5 are taken into account. The average angle is subsequently estimated for all the valid pixels of each subimage. The estimated local angle is graphically indicated by the oriented lines in Fig. 4, where the color corresponds to the colorbar in Fig. 3(b). It can be observed that the measured orientation angle is indeed aligned with the polaroid fragments, being constant in each polaroid stripe as stated above.

In conclusion, we have presented a method for determining diattenuation magnitude and orientation with a single-shot and fast measurement. Our approach is based on a specific DF-DCP source. It has then been predicted that the measurement of the beatnote signal that results from the interaction of such beam with dichroic samples enables linear dichroism (magnitude and angle) to be fully characterized in a straightforward and decoupled way. When applied to polarimetric imaging, this leads to a uniform contrast independently of the sample orientation, which is very useful for real-time applications. The potentially high dynamic range of this method and its ability to characterize dichroism in a single shot entail a high potential for biomedical applications. Moreover, the fact that orthogonality breaking sensing is easily adaptable to endoscopic systems makes the presented approach an interesting technique for minimally invasive tissue characterization.

This work was partly funded by the French National Defense Agency (DGA) project RADIO LIBRE (ANR-13-ASTR-0001) and by Région Bretagne. The PIXEL facility was supported by Région Bretagne, Rennes Métropole, Conseil Général d'Ille-et-Vilaine, and the European Regional Development Fund.

References

1. F. Snik, J. Craven-Jones, M. Escuti, S. Fineschi, D. Harrington, A. De Martino, D. Mawet, J. Riedi, and J. S. Tyo, Proc. SPIE **9099**, 90990B (2014).
2. A. S. Alenin and J. S. Tyo, J. Opt. Soc. Am. A **31**, 1013 (2014).
3. J. S. Tyo, D. L. Goldstein, D. B. Chenault, and J. A. Shaw, Appl. Opt. **45**, 5453 (2006).
4. F. Goudail and A. Bénière, Opt. Lett. **34**, 1471 (2009).
5. M. Richert, X. Orlik, and A. De Martino, Opt. Express **17**, 14199 (2009).
6. J. Fade, M. Roche, and M. Alouini, Opt. Lett. **37**, 386 (2012).
7. J. Fade and M. Alouini, Phys. Rev. Lett. **109**, 043901 (2012).
8. S. Jiao and L. V. Wang, Opt. Lett. **27**, 101 (2002).
9. S. Jiao, W. Yu, G. Stoica, and L. V. Wang, Appl. Opt. **42**, 5191 (2003).
10. B. H. Park, M. C. Pierce, B. Cense, and J. F. de Boer, Opt. Lett. **29**, 2512 (2004).
11. E. Schaub, J. Fade, N. Ortega-Quijano, C. Hamel, and M. Alouini, J. Opt. **16**, 122001 (2014).

Two-pixel polarimetric camera by compressive sensing

Julien Fade, Estéban Perrotin, and Jérôme Bobin

***Abstract*—We propose an original concept of compressive sensing (CS) polarimetric imaging based on a digital micro-mirror (DMD) array and two single-pixel detectors. The polarimetric sensitivity of the proposed setup is due to an experimental imperfection of reflecting mirrors which is exploited here to form an original reconstruction problem, including a CS problem and a source separation task. We show that a two-step approach tackling each problem successively is outperformed by a dedicated combined reconstruction method, which is explicited in this article and preferably implemented through a reweighted FISTA algorithm. The combined reconstruction approach is then further improved by including physical constraints specific to the polarimetric imaging context considered, which are implemented in an original constrained GFB algorithm. Numerical simulations demonstrate the efficiency of the 2-pixel CS polarimetric imaging setup to retrieve polarimetric contrast data with significant compression rate and good reconstruction quality. The influence of experimental imperfections of the DMD are also analyzed through numerical simulations, and 2D polarimetric imaging reconstruction results are finally presented.**

***Index Terms*—compressed sensing, polarimetric imaging, sparse signal modeling, proximal algorithms**

I. Introduction

In various application domains such as biomedical diagnosis, defence or remote sensing, standard intensity imaging techniques sometimes fail to reveal relevant contrasts or to gather sufficient information. In these domains, polarimetric approaches have proved efficient to enhance the estimation or detection capabilities of the imaging systems [1], [2], [3], [4], [5], [6], [7]. Mostly often, the polarimetric information is provided by a scalar polarization contrast image, which offers complementary constrast information with respect to the conventional intensity image. This polarization contrast image usually corresponds to the map of the degree of polarization (DOP) of the light backscattered at each location of the scene. Four polarimetric measurements are theoretically needed to determine such a DOP image [8]. However, to reduce both cost and acquisition time, simplified 2-channel imaging modalities are usually preferred in active polarimetric imaging, such as in Orthogonal States Contrast (OSC) imaging. This approach consists of computing a contrast map $\mathrm{OSC} = (\mathbf{x}_S - \mathbf{x}_P)/(\mathbf{x}_S - \mathbf{x}_P)$ between two polarimetric images ($\mathbf{x}_S$ and $\mathbf{x}_P$) of the scene, acquired through a linear polarizer oriented along two orthogonal directions, denoted S and P throughout the article where S denotes the polarization direction of the illumination source. Owing to its instrumental simplicity, which can be further improved using voltage-controlled electro-optics devices [9], [10] or appropriate optical design [11], and due to the fact that OSC provides a good estimate of the DOP (under the assumption that the imaged objects are purely depolarizing [4], [12]), OSC imaging is today widely used in many applications [12].

On the other hand, compressive sensing (CS) and CS-derived original imaging concepts such as the single-pixel camera (SPC) have attracted much attention these past years [13], [14]. With this approach, the measurement process relies on the spatial sampling of the image of interest with a Digital Micromirror Device (DMD), and on numerical reconstruction of the image from intensity measurements on a single photodetector for different sampling patterns on the DMD, allowing a compressed version of the image to be recovered from the photocurrent signal acquired. More recently, the concept of SPC has been applied to a number of domains including, among others, multi/hyperspectral imaging [15], [16], [17], [18], THz imaging [14], or random media-assisted CS [19]. However, despite the swarming interest in CS, only few attempts were reported so far to perform polarimetric CS imaging [16], [20], [21], [22], [23]. The imaging setups proposed in these references are all directly based on the SPC concept, where polarimetric sensitivity was simply gained by detecting the optical signals through appropriate polarization analyzing devices during sequential acquisitions, or with a unique acquisition on several detectors after appropriate beam splitting of the light reflected by the DMD. In these references, the reconstruction process consisted of solving as many CS reconstruction problems as polarimetric channels were considered (2 or 4). More precisely, in [20], [21], the SPC scheme was readily improved by adding a rotating polarizer in front of the detector. These techniques can operate as polarimetric imaging systems only at the expense of a two-fold (respectively four-fold) increase in the measurement time, while at the same time suffering from the loss in intensity due to the use of a polarization analyzer. In references [22], [23], the measurement time was limited, but the complexity of the imaging system was largely increased, to the expense of important losses in the imaging setup.

In this article, we revisit the problem of 2-channel polarimetric CS by proposing an original polarimetric imaging architecture using two single-pixel detectors. The proposed setup is still inspired from the initial concept of SPC, but does not require any polarization analyzing element as it relies on imperfections of the DMD itself. Contrarily to previous attempts in polarimetric CS, the polarimetric information is obtained through a single temporal data acquisition on the two photodetectors, and the polarimetric channels are recovered

J. Fade and E. Perrotin are with the FOTON Institute, University of Rennes 1, CNRS, Campus de Beaulieu, Rennes, France.

J. Bobin is with the CEA, IRFU, Service d'Astrophysique-SEDI, Gif-sur-Yvette, France.

Manuscript received ???.

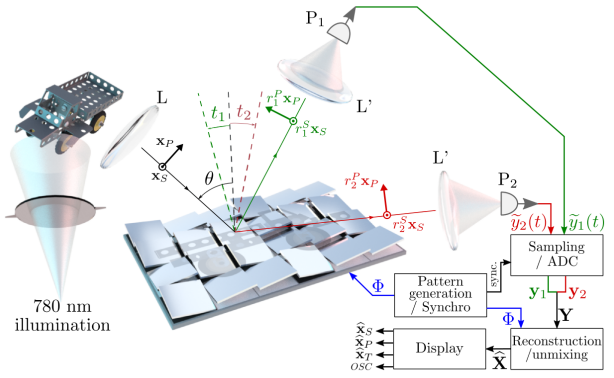

Fig. 1. Sketch of the 2-pixel CS polarimetric imaging setup proposed. It is inspired from the concept of SPC where the image is first spatially sampled by a DMD which reflects light in two directions, and where the total photon flux is detected on a single photodetector in each direction.

simultaneously from a single reconstruction step. It also offers in principle the best detectivity tradeoff, as all the light directed towards the DMD is involved in the imaging process without passing through any polarization analysis component.

This article is organized as follows: in Section II, the principle and the optical setup proposed to achieve CS polarimetric imaging are detailed. Then in Section III, various algorithms are presented to tackle this original CS inverse problem, along with several possible algorithmic optimizations such as reweighted approaches or constrained algorithms that can be implemented to improve the reconstruction results. The performance of the algorithms and of the 2-pixel polarimetric CS imaging approach are finally discussed in Section IV through numerical simulations on 1D and 2D test signals. In this section, the influence of experimental imperfections on the reconstruction quality is also analyzed, before conclusions and perspectives of the article are provided in Section V.

II. Principle of 2-pixel CS polarimetric imaging

A. 2-pixel CS polarimetric imaging setup

The polarimetric CS imaging approach proposed relies on the SPC imaging architecture. As will be demonstrated, it makes it possible to perform standard intensity and polarimetric contrast imaging using CS, without requiring any polarization analysis component. The corresponding experimental setup is sketched in Fig. 1. In the context of active imaging, we assume that the scene or object of interest is enlightened by an horizontally polarized light source. An image of the scene is formed through a lens L onto the surface of the DMD, which spatially samples it by applying a controlled binary pattern on the micromirrors. The detection setup is strictly similar to the SPC architecture, with a first photodetector (P_1) used to detect light reflected in the first reflection direction through a lens (L'). However, the light reflected in the second direction of the tilted mirrors is directed towards a second photodetector (P_2) via a lens (L'), instead of being discarded as in the original SPC scheme. By applying a series of different patterns on the DMD, the detection of the total light intensity reflected in directions 1 and 2 by photodetectors P_1 and P_2 provides two temporal signals that are sampled and digitized on a Analog to Digital Converter (ADC), before they can be used for numerical inversion of the intensity and polarimetric contrast images.

Throughout this article, we will denote the total intensity image of the scene by a single dimensional row vector $\mathbf{x}_T = \{x_{T_i}\}_{i=1,\dots,N}$ of length N. We assume that the total intensity image can be written as the sum of two polarimetric components, i.e., $\mathbf{x}_T = \mathbf{x}_S + \mathbf{x}_P$. Subscripts S and P denote two orthogonal linear polarization directions w.r.t. the orientation of the DMD surface and to the direction of linear polarization of the illuminating beam (S), as sketched in Fig. 1. We assume that these two components are compressible in the same sparse representation $\{\Psi_k\}_{k=1,\dots,N'}$, i.e., they can be written as $\mathbf{x}_{S,P} = \mathbf{s}_{S,P}\,\mathbf{\Psi}$, where $\mathbf{\Psi} = [\Psi_1, \dots, \Psi_{N'}]$ is a $N' \times N$ matrix with $N' \geq N$, and $\mathbf{s}_{S,P}$ are $N' \times 1$ column vectors containing the expansion coefficients. In the compressed sensing framework, compressibility means that most of these expansion coefficients have a small amplitude. Only the few large-amplitude coefficients code for the salient information of the polarimetric signals. This assumption generally refers to the approximately sparse signal model in the CS literature [24].

Upon reflection on the DMD surface, the polarimetric components of the original image $\mathbf{x}_T$ are altered by the Fresnel's reflection coefficients (in intensity) of the mirror, depending on the reflection angle. Let us denote by r_i^S and r_i^P the Fresnel's reflection coefficients (in intensity) of the mirror for each tilt direction $i = 1, 2$ and respectively for the S and P polarimetric components of the image formed on the DMD surface. Neglecting absorption effects, these coefficients are real and verify $r_{1,2}^{S,P} \in [0, 1]$. With such notations, the images respectively reflected towards detectors P_1 and P_2 read $\widetilde{\mathbf{y}}_1^\circ = r_1^S \mathbf{x}_S + r_1^P \mathbf{x}_P$ and $\widetilde{\mathbf{y}}_2^\circ = r_2^S \mathbf{x}_S + r_2^P \mathbf{x}_P$, which can be rewritten in a compact form as

$$\widetilde{\mathbf{Y}}^\circ = \begin{bmatrix} \widetilde{\mathbf{y}}_1^\circ \\ \widetilde{\mathbf{y}}_2^\circ \end{bmatrix} = \begin{bmatrix} r_1^S & r_1^P \\ r_2^S & r_2^P \end{bmatrix} \begin{bmatrix} \mathbf{x}_S \\ \mathbf{x}_P \end{bmatrix} = \widetilde{\mathbf{A}}\mathbf{X}. \quad (1)$$

When a given pattern indexed by k is applied on the DMD to spatially sample the image, the total intensity reflected towards direction 1 and integrated on detector P_1 can be denoted by $\widetilde{y}_1^{(k)} = \widetilde{\mathbf{y}}_1^\circ \varphi^{(k)}$, where $\varphi^{(k)}$ is a binary valued N-dimensional column vector encoding the set of orientations of the individual mirrors (DMD pattern). Similarly, $\widetilde{y}_2^{(k)} = \widetilde{\mathbf{y}}_2^\circ \overline{\varphi}^{(k)}$, where $\overline{\varphi}^{(k)} = \mathbf{1}_N - \varphi^{(k)}$ is the complement of vector $\varphi^{(k)}$. Then, when M measurements are accumulated with various sets of pseudo-random configurations of the DMD, the detected intensities $\{\widetilde{y}_i^{(1)} \dots \widetilde{y}_i^{(M)}\}_{i=1,2}$ organized in a $2 \times M$ measurement matrix read

$$\widetilde{\mathbf{Y}} = \begin{bmatrix} \widetilde{\mathbf{y}}_1^\circ \boldsymbol{\varphi} \\ \widetilde{\mathbf{y}}_2^\circ \overline{\boldsymbol{\varphi}} \end{bmatrix}, \quad (2)$$

with sensing matrix $\boldsymbol{\varphi} = [\varphi^{(1)} \dots \varphi^{(M)}]$ and $\overline{\boldsymbol{\varphi}} = [\overline{\varphi}^{(1)} \dots \overline{\varphi}^{(M)}]$.

Under the above assumptions, we will show that such a simple setup suffices to retrieve a compressive measurement of the polarimetric components $\mathbf{x}_S$ and $\mathbf{x}_P$, and thus

of the intensity image $\mathbf{x}_T = \mathbf{x}_S + \mathbf{x}_P$, and OSC image $\text{OSC} = (\mathbf{x_S} - \mathbf{x_P})/\mathbf{x}_T$. It is worth noting here that all the available light incoming from the scene is detected, thereby offering optimal energy balance, and that no polarimetric optical component has been inserted in the setup. Indeed, to achieve polarimetric sensitivity, this CS imaging setup relies on the slight variation of the Fresnel coefficients for the S and P-polarized components of light as a function of the angle of incidence of the incoming light beam. As sketched in Fig. 1, the angle of incidence on the mirror is denoted by $\theta_1 = \theta - t_1$ (respectively $\theta_2 = \theta - t_2$) for tilt direction 1 (respectively direction 2), where θ is the angle of incidence with respect to the DMD surface, and where t_1 and t_2 denote the tilt angle of the mirrors (typically $t_1 = 12°$ and $t_2 = -12°$ on most DMDs [25]). This dependency with θ is illustrated in Fig. 2.a, where we plotted the evolution of the four reflection coefficients $r_{1,2}^{S,P}$ at wavelength 780 nm for aluminum mirrors when θ varies from 17° to 65°. The influence of the value of these coefficients on the CS reconstruction problem is discussed below in Section II-C and their calculation is recalled in Appendix A. At this level, it is interesting to note that polarization vision mechanisms in some animal species rely on such polarization sensitivity of the Fresnel reflection or refraction coefficients[26].

B. Description of the CS inverse problem

With the above notations, we will now describe this imaging process as a CS inverse problem. We first rewrite the binary sensing matrix $\boldsymbol{\varphi}$ as $\boldsymbol{\varphi} = (\mathbf{1}_{N,M} + \boldsymbol{\Phi})/2$, and consequently, $\overline{\boldsymbol{\varphi}} = (\mathbf{1}_{N,M} - \boldsymbol{\Phi})/2$, where the elemets of $\boldsymbol{\Phi}$ take on -1 and $+1$ values. We impose that, for all DMD configurations, 50 % of the micromirrors are oriented towards direction 1 such that $\sum_{i=1}^{N} \Phi_i^{(k)} = 0$. In such a case, the measurement matrix can then be rewritten as $\widetilde{\mathbf{Y}} = \overline{\mathbf{Y}} + \mathbf{Y}$, with $\overline{\mathbf{Y}} = \widetilde{\mathbf{Y}}^{\circ}\mathbf{1}_{N,M}/2$, and

$$\mathbf{Y} = \frac{1}{2}\begin{bmatrix} \widetilde{\mathbf{y}}_1^{\circ}\boldsymbol{\Phi} \\ -\widetilde{\mathbf{y}}_2^{\circ}\boldsymbol{\Phi} \end{bmatrix} = \frac{\mathbf{Q}\widetilde{\mathbf{Y}}^{\circ}\boldsymbol{\Phi}}{2}, \quad \text{with} \quad \mathbf{Q} = \begin{bmatrix} 1 & 0 \\ 0 & -1 \end{bmatrix}. \tag{3}$$

For the sake of simplicity, we will assume in the following that the constant term $\overline{\mathbf{Y}}$ can be easily estimated and subtracted out from the measured data, e.g. by averaging the acquisitions over all M DMD pattern realizations considered. In this case, the CS problem that must be solved is given in Eq. (3) and reads $\mathbf{Y} = \mathbf{Q}\widetilde{\mathbf{Y}}^{\circ}\boldsymbol{\Phi}/2 = \mathbf{Q}\widetilde{\mathbf{A}}\mathbf{X}\boldsymbol{\Phi}/2$. For the sake of clarity, and taking into account an additive noise contribution $\mathbf{b}$ on the detected intensities, we propose to rewrite it with simplified notations as

$$\mathbf{Y} = \mathbf{A}\mathbf{X}\boldsymbol{\Phi} + \mathbf{b}, \quad \text{with} \quad \mathbf{A} = \frac{\mathbf{Q}\widetilde{\mathbf{A}}}{2} = \frac{1}{2}\begin{bmatrix} r_1^S & r_1^P \\ -r_2^S & -r_2^P \end{bmatrix}. \tag{4}$$

We also introduce $\mathbf{Y}^{\circ} = \mathbf{A}\mathbf{X}$, such that $\mathbf{Y} = \mathbf{Y}^{\circ}\boldsymbol{\Phi}$.

As a result, the N-dimensional polarimetric components of the image contained in $\mathbf{X}$ can be in principle recovered from a number of measurements $M \ll N$ provided the problem described in the above equation can be solved. Contrarily to most CS inverse problems that have been considered so far, we are facing an additional difficulty in this particular situation, as the signals to recover are strongly mixed in the measurement process via the mixing matrix $\mathbf{A}$. Indeed, as illustrated in Fig. 2.a, the reflection coefficients on metals are usually quite similar for polarization directions S and P, causing a strong crosstalk between the two components of interest. As a consequence, the signals detected at photodetectors P_1 and P_2 are almost perfectly anticorrelated, the polarimetric information lying in the tiny discrepancies between these two signals. This is illustrated in Fig. 3, where simulated intensity signals are plotted. As will be shown in Section III, several approaches can be used to tackle this unmixing/CS reconstruction problem, either by considering the two problems independently, or by solving them simultaneously in the recovery process.

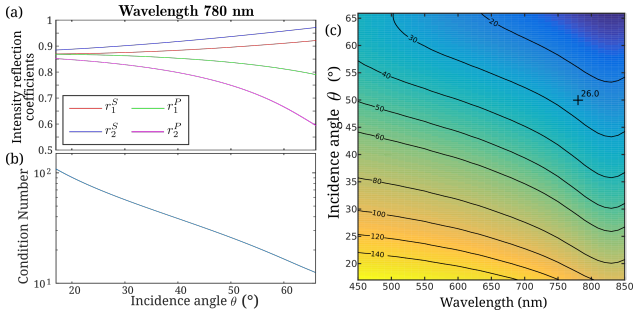

Fig. 2. (a) Evolution of the reflection coefficients in intensity for two tilt directions and two polarimetric components S and P, as a function of incidence angle θ on the DMD surface at wavelength 780 nm. (b) Evolution of the condition number $\kappa(\mathbf{A})$ of matrix $\mathbf{A}$ as a function of θ at 780 nm. (c) Contour plot of $\kappa(\mathbf{A})$ as a function of θ and wavelength. The black cross indicates the physical situation addressed in the numerical experiments.

C. Experimental parameters and imperfections

Before we detail the reconstruction algorithms used to achieve polarimetric CS imaging with the 2-pixel camera setup proposed, let us analyze the possible influence of some experimental parameters on the reconstruction quality, and how these parameters can be optimized.

Obviously, an important parameter that will control the difficulty of the unmixing problem is the mixing matrix $\mathbf{A}$, which depends on the wavelength and bandwidth of the illuminating source, on the incidence angles θ_1 and θ_2 on the two tilt positions, and on the optical coating of the reflective surface of the micromirrors. Sticking to the specifications of commercially available DMDs [25], we have simulated the values of the $r_{1,2}^{S,P}$ coefficients for aluminum-coated metallic micromirrors with tilt angles $\pm 12°$, for varying wavelengths over the spectral bandwidth of commercially available DMDs (450-850 nm), and for varying incidence angle θ. The expression of the Fresnel's intensity reflection coefficients on metals is recalled in Appendix A. The evolution of parameters $r_{1,2}^{S,P}$ with θ is plotted in Fig. 2.a for a wavelength of 780 nm, showing that the four reflection coefficients considered do not differ much (typically, less that 15% difference for reasonable incidence angles). The unmixing step in the reconstruction problem consisting basically of an "inversion" of matrix $\mathbf{A}$, the condition number $\kappa(\mathbf{A}) = \|\mathbf{A}^{-1}\|_2 \cdot \|\mathbf{A}\|_2$ naturally gives

an indication about the difficulty of such inversion procedure. We have thus plotted in Fig. 2.b the evolution of $\kappa(\mathbf{A})$ as a function of θ, which confirms that high incidence angles may be favored. We further analyzed the evolution of $\kappa(\mathbf{A})$ with θ and with the illumination wavelength. The contour plot in Fig. 2.c shows that the condition number can vary by a factor of 5 across the range of wavelength and incidence angle considered, higher wavelengths being best adapted to maximize the polarimetric sensitivity of the reflection on aluminum mirrors. As a result, owing to the availability of laser and LED sources at such wavelength, and to keep reasonable incidence angles, we will consider throughout the remainder of this article the situation of a monochromatic illumination at 780 nm, with incidence angle $\theta = 50°$ (black cross in Fig. 2), yielding a reasonably low condition number of $\kappa(\mathbf{A}) = 26$.

It can be noted here that dielectric coated micromirrors could offer stronger polarization dependence of the reflection coefficients, but to the expense of totally revisiting the fabrication process of DMDs. For the sake of simplicity, we will neglect in this article the influence of the anti-reflection coated cover slit that protects the DMD surface [25]. We also neglect the dispersion of the values of coefficients $r_{1,2}^{S,P}$ with the source spectral bandwidth and with the slight variation of incidence angle when the image of the scene is formed on the DMD surface. All these possible sources of imperfections can be neglected here to study the principle of 2-pixel polarimetric camera, but may be addressed in further work to achieve the experimental validation of this CS imaging scheme.

Nevertheless, we shall analyze in our simulations how a bias in the estimated incidence angle θ can have an impact on reconstruction quality. Indeed, it is quite obvious that a bias on θ will lead to using an incorrect mixing matrix in the inversion process, hence hindering the recovery of a satisfactory polarization contrast image. Moreover, we also consider the influence of possible individual random errors in the tilt angles of each micromirror of the DMD. Indeed, the typical individual tilt error is about $\pm 1°$ to $\pm 2°$ according to standard DMD's specifications [25], thus its consequences on the reconstruction process may not be negligible. If global angle bias on θ and individual tilt errors can affect the reconstruction, their influence on image quality is likely to be very different. Global bias on θ can be basically treated as a calibration error, whereas individual tilt errors would rather behave as additional random noise on the inversion process.

Lastly, we will consider that the only source of noise is the photodetectors electronic noise, and we assume statistical independence between the noise at photodetectors P_1 and P_2, and between noise realizations as the DMD patterns are varied. In the above inverse problem, noise vector $\mathbf{b}$ can thus be modeled by a centered Gaussian distribution of variance σ^2, i.e., $\forall i \in \{1, 2\}, \forall j \in [1, M], \mathbf{b}_{ij} \sim \mathcal{N}(0, \sigma^2)$.

III. Reconstruction algorithms

In this section, we describe different strategies to reconstruct the polarimetric data $\mathbf{X}$ from the compressed measurements $\mathbf{Y} = \mathbf{AX\Phi} + \mathbf{b}$. In the framework of compressed sensing, the signal recovery problem is generally described as a "large p, small n" problem, where the number of unknown, i.e. the number of samples in the polarimetric components, can be much larger than the number of measurements in $\mathbf{Y}$. Hence, it is essential to enforce additional constraints on the signal to be recovered, which eventually boils down to solving a minimization problem of the form

$$\widehat{\mathbf{X}} = \text{Argmin}_{\mathbf{X}} \quad \mathcal{P}(\mathbf{X}) + \frac{1}{2} \|\mathbf{Y} - \mathbf{AX\Phi}\|_F^2, \tag{5}$$

where the first term is a penalization term that favors solutions with certain desired properties, and the second term is a data fidelity term that measures the discrepancy between the data $\mathbf{Y}$ and the model $\mathbf{AX\Phi}$. The Frobenius norm is defined as $\|\mathbf{Y}\|_F^2 = \text{Trace}\left(\mathbf{YY}^T\right)$.
In the context of CS [27], [28], it is customary to enforce the sparsity of the unknown variable $\mathbf{X}$ in some signal representation $\mathbf{\Psi}$ that is chosen a priori. In the following sections, we describe and compare several strategies that are precisely dedicated to solve the two-pixel polarimetric compressed sensing recovery problem.

A. 2-stage reconstruction approach

The recovery problem in Eq. (5) can described as the combination of two classical inverse problems: a compressed sensing problem and a source separation problem. A first straightforward approach consists in tackling alternately both problems. Then, recovering the polarimetric components can be performed with the following 2-stage approach.

- **Compressed sensing:** denoting the non-compressed mixed polarimetric components by $\mathbf{Y}^\circ = \mathbf{AX}$, the actual measurements $\mathbf{Y}$ can be defined as $\mathbf{Y} = \mathbf{Y}^\circ\mathbf{\Phi}$. Recovering $\mathbf{Y}^\circ$ then boils down to a standard compressed sensing recovery problem. This step is customarily solved by finding the minimum of the problem

$$\widehat{\mathbf{Y}^\circ} = \text{Argmin}_{\mathbf{Y}^\circ} \quad \left\|\mathbf{\Lambda} \odot \left(\mathbf{Y}^\circ\mathbf{\Psi}^T\right)\right\|_{\ell_1} + \frac{1}{2}\|\mathbf{Y} - \mathbf{Y}^\circ\mathbf{\Phi}\|_F^2, \tag{6}$$

  where the 1-norm $\|\,.\,\|_{\ell_1}$ enforces the sparsity of $\mathbf{Y}^\circ$ in $\mathbf{\Psi}$ and $\mathbf{\Lambda}$ stands for the regularization parameters, which is composed of strictly positive entries (see section III-D for details about the parameters' selection). This optimization problem is solved using the reweighting FISTA algorithm. This algorithm is referred to as Algorithm 2 and is detailed in Appendix B.

- **Source separation:** once the mixed polarimetric components $\mathbf{Y}^\circ$ are estimated, retrieving $\mathbf{X}$ from $\mathbf{Y}^\circ = \mathbf{AX}$ is equivalent to a source separation or unmixing problem, which can be tackled by minimizing the Euclidean distance between $\mathbf{Y}^\circ$ and the model $\mathbf{AX}$ as follows

$$\widehat{\mathbf{X}} = \text{Argmin}_{\mathbf{X}} \quad \left\|\widehat{\mathbf{Y}^\circ} - \mathbf{AX}\right\|_F^2. \tag{7}$$

  Since $\mathbf{A}$ is invertible, the solution of this problem is given by $\widehat{\mathbf{X}} = \mathbf{A}^{-1}\widehat{\mathbf{Y}^\circ}$.

B. Combined sparse reconstruction

Despite its simplicity, this two-stage approach suffers from a major drawback: the mixed components $\mathbf{Y}^{\circ}$ won't be perfectly estimated, especially when only few measurements in $\mathbf{Y}$ are available and when noise contaminates the data. These mis-estimation errors will be amplified in the unmixing stage. Since the mixing matrix $\mathbf{A}$ is likely to be ill-conditioned, this errors will largely impact the reconstruction accuracy of the reconstruction process.

A more effective strategy consists in jointly tackling both the compressed sensing recovery and unmixing problems. Extending standard reconstruction procedures yields the following optimization problem

$$\widehat{\mathbf{X}} = \text{Argmin}_{\mathbf{X}} \quad \left\| \mathbf{\Lambda} \odot \left(\mathbf{X} \mathbf{\Psi}^T \right) \right\|_{\ell_1} + \frac{1}{2} \left\| \mathbf{Y} - \mathbf{A}\mathbf{X}\mathbf{\Phi} \right\|_F^2, \quad (8)$$

where the $2 \times N$ matrix $\mathbf{\Lambda}$ stands for the same weight matrix we introduced in the 2-stage approach (see section III-D). In the next, we make use of the reweighted FISTA algorithm (see Appendix B) to solve (8).

C. Constrained sparse reconstruction

Further improving the accuracy of the components' recovery requires imposing additional, more physical, constraints on $\mathbf{X}$. In the context of polarimetric data, each component $\mathbf{x}_S$ and $\mathbf{x}_P$ has naturally non-negative samples. As well, under active polarized illumination, and assuming purely depolarizing samples, the components must verify the following inequality: $\mathbf{x}_S \succeq \mathbf{x}_P$. In this section, we propose extending the reweighted FISTA algorithm to enforce these additional constraints. The optimization problem to tackle is described as follows

$$\begin{aligned} \text{Argmin}_{\mathbf{X}} \quad & \left\| \mathbf{\Lambda} \odot \left(\mathbf{X} \mathbf{\Psi}^T \right) \right\|_{\ell_1} + i_{\mathbf{X} \succeq 0}(\mathbf{X}) \\ & + i_{\mathbf{D}\mathbf{X} \succeq 0}(\mathbf{X}) + \frac{1}{2} \left\| \mathbf{Y} - \mathbf{A}\mathbf{X}\mathbf{\Phi} \right\|_F^2, \end{aligned} \quad (9)$$

where $i_{\mathbf{X} \succeq 0}(\mathbf{X})$ stands for the characteristic function of the positive orthant $\{\mathbf{X};\ \forall i,j,\ [\mathbf{X}]_{ij} \geq 0\}$ and $i_{\mathbf{D}\mathbf{X} \succeq 0}(\mathbf{X})$ for the characteristic function of the convex set $\{\mathbf{X};\ \forall i,j,\ [\mathbf{D}\mathbf{X}]_{ij} \geq 0\}$ where $\mathbf{D} = [1, -1]$.

In contrast to the standard problem in Eq. (8), the problem in Eq. (9) is composed of a sum of convex penalizations that cannot be tackled with the FISTA algorithm. For that end, the Generalized Forward Backward (GFB) algorithm [29] is the perfect algorithm to solve such an optimization problem. The application of the GFB to Eq. (9) is described in Alg. 1, where γ stands for the gradient path length used in the algorithm, and L denotes the maximum iteration number.

Algorithm 1:

Combined GFB

Choose $\mathbf{\Lambda}$ (see III-D), $\gamma < \frac{1}{\|\mathbf{A}\|_2^2}$, $\{\mu_i\}_{i=1,\cdots,3}$ such that $\sum_{i=1}^3 \mu_i = 1$, $\mathbf{X}^{(0)}$, $\{\mathbf{U}_i\}_{i=1,\cdots,3}$

while $l < L_{outer}$ **do**

while $t < L$ **do**

- Gradient of the data fidelity term:

$$\mathbf{G} = -\mathbf{A}^T \left(\mathbf{Y} - \mathbf{A}\mathbf{X}^{(t)}\mathbf{\Phi} \right) \mathbf{\Phi}^T$$

- Sparsity penalization $\mathbf{U}_1$:

$$\mathbf{U}_1^{(t+1)} = \mathbf{U}_1^{(t)} + \text{prox}_{\gamma \| \mathbf{\Lambda}^{(l)} \odot (.\, \mathbf{\Psi}^T) \|_{\ell_1}} \left(2\mathbf{X}^{(t)} - \mathbf{U}_1^{(t)} - \gamma \mathbf{G} \right) - \mathbf{X}^{(t)}$$

- Positivity constraint variable $\mathbf{U}_2$:

$$\mathbf{U}_2^{(t+1)} = \mathbf{U}_2^{(t)} + \text{prox}_{i_{\mathbf{X} \succeq 0}(.)} \left(2\mathbf{X}^{(t)} - \mathbf{U}_2^{(t)} - \gamma \mathbf{G} \right) - \mathbf{X}^{(t)}$$

- Components' inequality $\mathbf{U}_3$:

$$\mathbf{U}_3^{(t+1)} = \mathbf{U}_3^{(t)} + \text{prox}_{i_{\mathbf{D}\mathbf{X} \succeq 0}(.)} \left(2\mathbf{X}^{(t)} - \mathbf{U}_3^{(t)} - \gamma \mathbf{G} \right) - \mathbf{X}^{(t)}$$

- Polarimetric components $\mathbf{X}$:

$$\mathbf{X}^{(t+1)} = \sum_{i=1}^{3} \mu_i \mathbf{U}_i^{(t+1)}$$

Update the weights $\mathbf{\Lambda}^{(l)}$ - see section III-D.

end

In this algorithm, the application of each penalization or constraint is performed independently on distinct intermediate variables $\{\mathbf{U}_i\}_{i=1,\cdots,3}$. Updating each of these variables only requires the current estimate of the polarimetric components $\mathbf{X}^{(t)}$, the gradient of the quadratic data fidelity term $\mathbf{G} = -\mathbf{A}^T \left(\mathbf{Y} - \mathbf{A}\mathbf{X}^{(t)}\mathbf{\Phi} \right) \mathbf{\Phi}^T$ as well as the so-called proximal operator of the penalization or constraint. The proximal operators required in the above algorithms are defined in Appendix B.

The convergence of the GFB algorithm is guaranteed as long as the gradient path length verifies $\gamma < \frac{1}{\|\mathbf{A}\|_2^2}$, where the spectral norm of $\mathbf{A}$ is defined as its largest singular value. The scalar weights $\{\mu_i\}_{i=1,\cdots,3}$ must be strictly positive and have to sum to 1. Hence, the final update of the polarimetric components is a weighted average of the different intermediate variables. In the remainder of this paper, these weights will all be set equal to $1/3$. The proposed GFB-based algorithm is initialized with the polarimetric signals provided by the reweighted FISTA algorithm described in the above section. Since the problem 9 is convex, this initialization does not change the solution but it dramatically reduces its computational cost.

D. Optimization of algorithm parameters

The three above signal recovery approaches require tuning a certain number of parameters, whose setting is essential for an accurate estimation:

- **Sparse signal representation:** the choice of the sparse signal representation $\mathbf{\Psi}$ highly depends on the geometrical content of the components $\mathbf{X}$. For instance, if the signal $\mathbf{X}$ is assumed to be composed of oscillatory structures, it is customary to choose $\mathbf{\Psi}$ as a discrete cosine transform or its localized variant. In case $\mathbf{X}$ mainly contains local anisotropic contour-like features, the curvelet transform is a good fit. In this framework, redundant wavelets are a generic choice that generally provides good recovery results for most reconstruction problems that involve natural images. In this article, $\mathbf{\Psi}$ will be chosen as an undecimated wavelet frame [30]. Strictly speaking, undecimated wavelet frames are not orthogonal representations, which entails that the proximal operator defined in Eq. (12) of Appendix B is an approximation. Nevertheless, it is customary to use Eq. (12) along with undecimated wavelets. Indeed, in that specific case, the Gram matrix of the representation $\mathbf{\Psi}^T\mathbf{\Psi}$ is diagonally dominant, which makes it close to an isometry.
- **Regularization parameters:** whether it is in the 2-step reconstruction approach, or in the combined reconstruction approaches including the reweighted FISTA or the proposed constrained GFB, the regularization parameters contained in matrix $\mathbf{\Lambda}$ aim at balancing between the sparsity constraint and the data fidelity term. These parameters define thresholds that are applied to the expansion coefficients of $\mathbf{X}$ in the sparse representation $\mathbf{\Psi}$, which eventually act as a denoising procedure. Therefore, in practice, these parameters are chosen so as to reject noise-dominated coefficients in $\mathbf{\Psi}$. For that purpose, the weight matrix is built so that each of its elements are the product of two terms: $[\mathbf{\Lambda}]_{ij} = \lambda_i w_{ij}$ where $\lambda_i > 0$ and $0 < w_{ij} \leq 1$.
The first term defines the global threshold per polarimetric component and its value is derived straight from the derivative of the data fidelity term:

$$\forall i \in \{1,2\}; \quad \lambda_i = \tau \,.\, \text{mad}\left([\mathbf{G}\mathbf{\Psi}^T]_i\right),$$

where the median absolute deviation (mad) is a robust empirical estimator of a Gaussian noise standard deviation, $\mathbf{G}$ is the gradient of the data fidelity term, and τ is a scalar that is generally chosen between 2 and 3. This choice holds true for the three reconstruction approaches. The extra parameters $\{w_{ij}\}$ are the standard parameters that are defined in reweighted ℓ_1 techniques. Following [31], these parameters are chosen based on some estimate $\widehat{\mathbf{X}}$ of the polarimetric components

$$\forall i,j; \quad w_{ij} = \frac{\epsilon}{\epsilon + \frac{|[\widehat{\mathbf{X}}\mathbf{\Psi}^T]_{ij}|}{\|\widehat{\mathbf{X}}\mathbf{\Psi}^T\|_\infty}}, \tag{10}$$

where ϵ is a small scalar. This procedure is applied to the reweighted FISTA algorithm as well as the constrained GFB.

- **Number of iterations, reweighted steps and stopping criterion :** In the next, the maximum number of iterations is fixed to $L = 20000$, except specified otherwise. For the reweighted algorithms, two reweighted steps ($L_{outer} = 2$) taking place respectively after 2000 and 4000 iterations were sufficient to maximize reconstruction quality. Lastly, for all reconstruction algorithms, the stopping criterion is based on the relative variation of the solution $\widehat{\mathbf{X}}$ between two consecutive iterations: $\|\widehat{\mathbf{X}}^{(t+1)} - \widehat{\mathbf{X}}^{(t)}\|_F / \|\widehat{\mathbf{X}}^{(t)}\|_F < \epsilon$, where $\epsilon = 10^{-9}$.

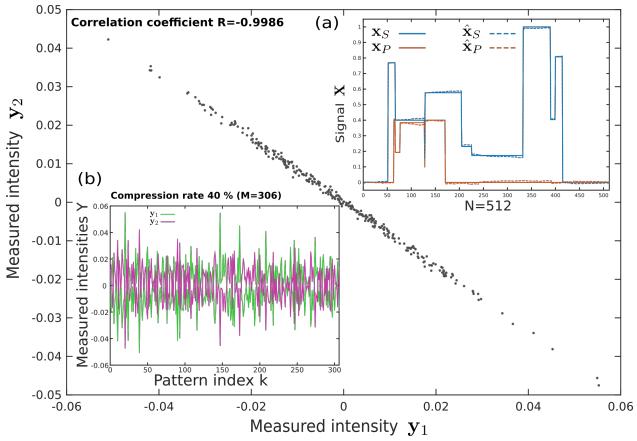

Fig. 3. Inset (a): Synthetic 1D polarimetric test signal used to assess recontruction algorithms performance. An example of reconstructed signal is also given (see text for details). Inset (b): example of measured intensities on photodetectors P_1 and P_2 for $M = 306$ (compression 40 %) different binary patterns (Hadamard) applied on the DMD. Main figure: plot of intensity $\mathbf{y}_2$ as a function of $\mathbf{y}_1$ revealing strong anticorrelation between the two detected signals.

IV. Numerical results

In this section, we analyze the performance of the reconstruction algorithms and regularization procedures described above. These algorithms will also be compared in terms of robustness to some of the experimental imperfections mentioned in Section II. This analysis will be conducted on a 1D test signal for the sake of computation speed. The quality of the reconstructed signals will be standardly evaluated throughout this section by computing the Peak Signal to Noise Ratio (PSNR) of a concatenated vector of the reconstructed polarimetric components, i.e., $[\widehat{\mathbf{x}}_S\ \widehat{\mathbf{x}}_P]$. Then, we will present some polarimetric imaging numerical results on 2D signals that demonstrate the ability of this concept of 2-pixel polarimetric camera to provide satisfactory compressed polarization contrast images at low cost and low complexity.

A. Comparison of algorithms performance and robustness

1) Description of 1D test signal: In order to optimize computation resources, we generated a synthetic polarimetric 1D data sample of length $N = 512$, that will be used throughout this subsection to compare the performance of the above algorithms. The corresponding signals $\mathbf{x}_S$ and $\mathbf{x}_P$ are plotted in the inset (a) of Fig. 3, respectively with blue and red solid lines. The simulated polarimetric components verify the positivity constraint $\mathbf{x}_S \succeq \mathbf{x}_P$, and it can be noted that their supports are not joint, for the sake of generality. In the inset (b) of Fig. 3, we plot a set of simulated detected intensity

signals $\mathbf{y}_1$ and $\mathbf{y}_2$, with 40 % compression rate ($M = 306$), and SNR = 40 dB. The mixing matrix A used to generate the data has been calculated as detailed in Appendix A, assuming an incidence angle $\theta = 50°$ and wavelength of 780 nm (i.e., the optimal conditions identified in Section II-C). The patterns used on the DMD to sample the image were generated from a randomly scrambled Hadamard transform of the signal $\mathbf{X}$ of size $N = 512$. Unless otherwise specified, the same experimental conditions will be assumed for all numerical results presented in this article. In Fig. 3, $\mathbf{y}_2$ is plotted as a function of $\mathbf{y}_1$, evidencing the strong anticorrelation existing between the two detected signals. Lastly, in the inset (a) of Fig. 3, we show an example of reconstructed signals $\hat{\mathbf{x}}_S$ and $\hat{\mathbf{x}}_P$ obtained with the reweighted FISTA algorithm, and yielding PSNR = 37.7 dB. As for all reconstructions of the 1D signal presented below, the reconstruction process makes use of the unidimensional undecimated wavelet transform with the Haar filter, which is well suited to sparesely represent piecewise constant signals. It can be checked in the inset (a) of Fig. 3 that the algorithm has not been constrained to ensure positivity of either $\hat{\mathbf{x}}_S$, $\hat{\mathbf{x}}_P$ or $\hat{\mathbf{x}}_S - \hat{\mathbf{x}}_P$.

2) Algorithms performance: Using this 1D test signal, we are now able to compare the performance of the various algorithms as a function of the different parameters involved in the imaging process. Let us first analyze the influence of the data SNR on the reconstruction quality, for an intermediate compression rate of 40 %. The evolution of the PSNR of $\hat{\mathbf{X}}$ as a function of the SNR is given in Fig. 4. All the data points in Fig. 4 have been obtained from 30 realizations of the numerical experiments, with the error bars indicating the interquartile range, i.e., distance between the first to the third quartile of the data series.

It can first be seen that all the algorithms asymptotically exhibit a linear evolution of their PSNR as a function of the SNR. Then, it is interesting to note that for intermediate values of SNR (10 dB<SNR<50 dB), the 2-step approach underperforms with respect to the simplest implementation of the combined reconstruction approach (denoted by combined-FISTA). However, as soon as a reweighted procedure is implemented, solving the CS and the unmixing problems simultaneously (algorithm denoted as combined-rFISTA) provides an asymptotical gain of about 12 dB in PSNR with respect to the 2-step algorithm. Lastly, imposing physical positivity constraints on $\hat{\mathbf{x}}_S$, $\hat{\mathbf{x}}_P$ and $\hat{\mathbf{x}}_S - \hat{\mathbf{x}}_P$ through the implementation of the GFB algorithm (denoted as combined-GFB) does not bring any additional gain in performance for highest values of SNR. However, in noisy situations, for SNR < 50 dB, the positivity constraints prove efficient to improve the reconstruction quality. A maximum gain of almost 10 dB is obtained for SNR = 0 dB, a situation where the unconstrained rFISTA approach fails to surpass the reconstruction quality obtained with the 2-step procedure.

We now analyze the influence of the compression rate and of the incidence angle θ on the PSNR of the reconstructed signals. As discussed in Section II-C, the incidence angle controls the condition number $\kappa(\mathbf{A})$ of the mixing matrix, and hence the difficulty of the unmixing problem. For this

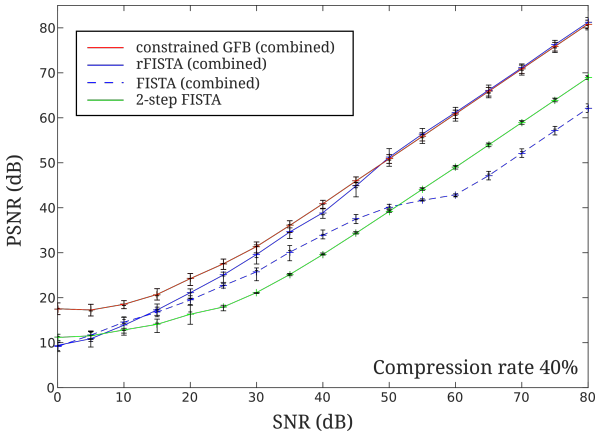

Fig. 4. Evolution of the PSNR of the signal $\hat{\mathbf{X}}$ reconstructed with the 4 compared algorithms as a function of detected signal SNR for a compression rate of 40 %. The symbols represent the mean PSNR over 30 realizations with error bars indicating the interquartile range. The lines are only guides for the eyes.

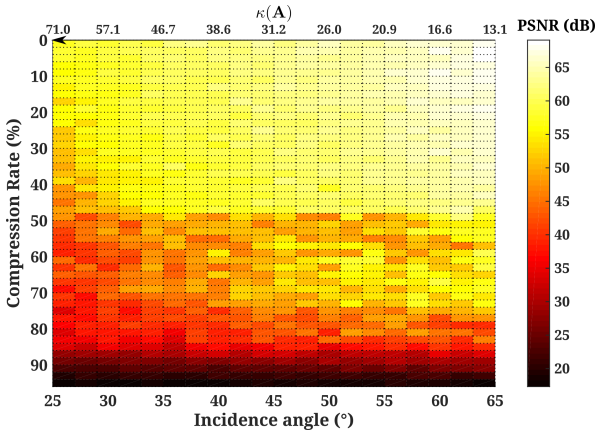

Fig. 5. 2D map of the PSNR (averaged over 10 realizations) of $\hat{\mathbf{X}}$ reconstructed with the combined-reweighting FISTA algorithm, as a function of incidence angle θ, and compression rate. The corresponding condition number $\kappa(\mathbf{A})$ is indicated as a function of θ.

numerical experiment, we consider only the combined-rFISTA algorithm (plotted in blue solid line in the previous figure), with fixed number of iterations ($L = 10^4$), and with a SNR of 60 dB. A 2D-plot of the average PSNR obtained over 10 realizations of each numerical experiment is provided in Fig. 5, for 40 values of θ ranging between 25° to 65°, and 49 values of compression rate between 0 % (no compression) to 96 %. It can be observed that the reconstruction quality obeys a classical "phase transition" behaviour frequenty observed in CS problems, with three main domains which can be identified. Firstly, for compression rates below 50 %, the reconstruction is almost perfect (PSNR $\geq$ 55 dB), whatever be the value of θ. Only for highest values of $\kappa(\mathbf{A})$ (i.e., for $\theta \leq 30°$), the algorithm fails is reaching a PSNR of 50 dB, but remains above 45 dB. Then, for intermediate values of compression rate between 50 % and 80 %, the reconstruction quality gradually decreases while remaining above 35 dB. In that regime, the influence of the condition number $\kappa(\mathbf{A})$

appears clearly on the reconstruction quality. Lastly, a sharp transition occurs around 85 % compression rate, above which no satisfactory reconstruction can be obtained regardless of θ. This 2D-map is rather encouraging towards possible experimental implementations of the 2-pixel polarimetric CS camera. Indeed, it shows that provided a good SNR can be ensured (here 60 dB), polarimetric signals can be retrieved at relatively high compression rates ($\leq 80\%$), and for reasonable incidence angles on the DMD.

3) Robustness to incidence angle bias and tilt errors: Before presenting results on a polarimetric imaging scenario with 2D test signals, we report a last numerical experiment conducted on the 1D test signal to assess the robustness of the various algorithms to experimental imperfections, such as a bias on the incidence angle θ, and random errors on the micromirrors tilt angles.

The influence of a bias in θ has been analyzed as follows. Measurement vector $\mathbf{Y}$ was generated assuming a SNR of 80 dB, and an incidence angle $\theta = 50°$, as in Fig. 4. However, the reconstruction procedure was run with an incorrect mixing matrix $\mathbf{A}$, assuming a wrong incidence angle of $\theta + \delta\theta$. This way, we mimicked an experimental bias $\delta\theta$ comprised between $0.05°$ and $10°$ on the incidence angle. The reconstruction PSNR obtained with different algorithms is plotted in Fig. 6 in solid lines for a compression rate of 0 %. It can be seen that the presence of a bias in reconstruction angle leads to a linear degradation of the PSNR in a log-log scale for all three algorithms tested. Even for a very small bias ($\delta\theta = 0.05°$), a significant drop of more than 20 dB in reconstruction quality can be observed for all three algorithms with respect to unbiased reconstruction, but still offering satisfactory recovery quality (PNSR ≥ 55 dB). Applying physical constraints in the reconstruction procedure with the GFB algorithm seems to alleviate the degradation, for any magnitude of $\delta\theta$, as far as simple angular bias is considered. However, the PSNR value of the reconstructed vector $\hat{\mathbf{X}}$ which is used to gauge reconstruction quality is not satisfactory here: it has indeed been observed on reconstructed signals that applying constraints with an erroneous mixing matrix often leads to singular results, where second polarimetric component $\mathbf{x}_P$ is forced to zero, thus yielding null polarimetric contrast. This is interpreted by the fact that the physical constraints applied can be no longer valid for the measured data with an incorrect matrix $\mathbf{A}$.

Concerning the influence of random tilt errors on the micromirrors, we simulated this effect by computing individual mixing matrices A for all N micromirrors simulated, assuming that the tilt angles t_1 and t_2 were affected by a random error. For the sake of computational speed, we assumed a uniform distribution over 11 values of the tilt error between $\pm 1°$. The PSNR of the reconstructed signal with angular bias and uniform tilt error is also plotted in Fig. 6 in dashed lines for 0 % compression. On the one hand, the additional random tilts do not modify significantly the results for highest values of angular bias ($\delta\theta \geq 1°$) where the incorrect "average" matrix A is responsible for most of the quality degradation. On the other hand, for very low values of $\delta\theta$, the PSNR reaches a limit upper value of about 35-40 dB, due to the presence of random

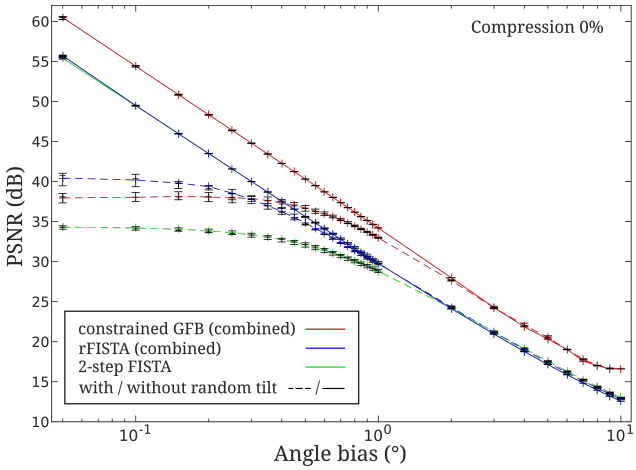

Fig. 6. Influence of the bias on incidence angle θ in the reconstruction quality (PSNR) for 0 % compression (solid lines). PSNR of the reconstructed signal in the presence of bias and random tilt error on individual micromirrors (dashed line).

tilt errors which seems to affect more strongly the constrained version of the algorithm. Despite such degradation of reconstruction quality, these numerical experiments evidence that with imperfect experimental configurations, using a combined recovery approach instead of a 2-step reconstruction procedure can be advantageous. Correct PSNR values (≥ 35 dB) can be reached with the rFISTA or GFB algorithms with small angular biases ($\leq 1°$) and in the presence of random tilt errors.

B. Numerical polarimetric imaging results on 2D signals

In this last section, we analyze the ability of the 2-pixel polarimetric CS camera to retrieve polarimetric contrast images from simulated 2D data. Owing to its performance and its simple implementation with respect to constrained GFB, we only consider in this section the reweighted FISTA algorithm implementing a combined reconstruction procedure. We first consider in the next subsection a simple imaging scenario to study the influence of polarimetric contrast on the reconstuction quality, before a more realistic example of polarimetric image reconstruction is given in Section IV-B2.

1) Influence of polarimetric contrast: For this first imaging scenario, we consider a square object with high total intensity value over a dark background, forming an image of $N = 128 \times 128$ pixels. This intensity image $\mathbf{x}_T$, plotted in Fig. 7 is supposed to be the sum of two polarimetric image components $\mathbf{x}_S$ and $\mathbf{x}_P$, yielding a true OSC map also plotted in Fig. 7. In this scenario, we assume that a first object (smaller square) cannot be distinguished from the second object (bigger square) on the intensity image $\mathbf{x}_T$, while OSC map allows the two objects to be clearly identified. The background is assumed totally depolarizing (OSC = 0). The smaller square object is always supposed slightly depolarizing (OSC = 0.8) whereas the OSC of the second object (bigger square) is varied between 0 and 1 in the following numerical experiments. Fig. 7 shows an example of reconstruction of the total intensity and the OSC map with the combined-rFISTA algorithm (with

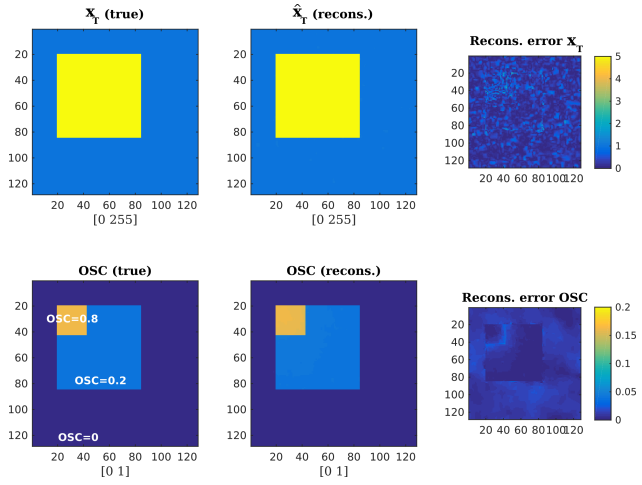

Fig. 7. Simulated polarimetric imaging scenario containing two objects over constant background. First row: total intensity image $\mathbf{x}_T$ (true), $\hat{\mathbf{x}}_T$(reconstruction) and reconstruction error map. The two objects are indistinguishable in the total intensity image. Second row: true and reconstructed OSC image, and reconstruction error map.

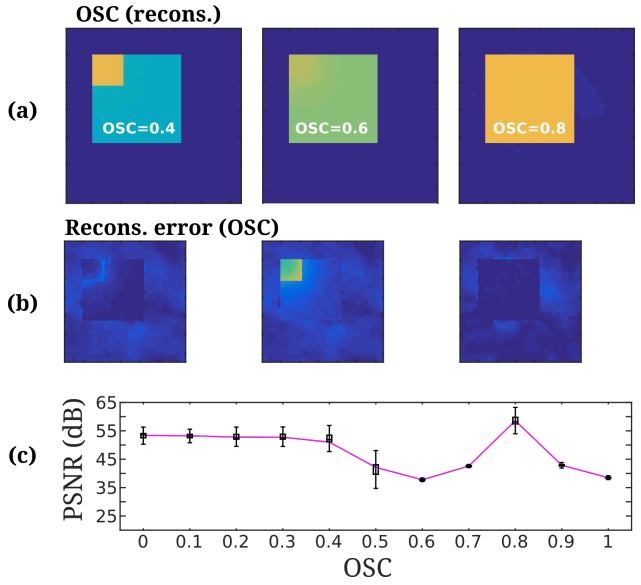

Fig. 8. (a) Reconstructed OSC image (a) and reconstruction error map (b) for various values of the OSC of the second object. (c) Evolution of the reconstruction PSNR of $\mathbf{X}$ when the OSC of the second object is varied between 0 and 1.

Haar wavelets) for SNR = 40 dB, compression rate 40%, incidence angle $\theta = 50°$ and without bias or uncertainty on the tilt directions. The reconstruction quality is visually very good (PSNR = 52.8 dB), as evidenced by the reconstruction error map of the total intensity and OSC shown in Fig. 7. This simple example demonstrates the possibility of providing relevant polarimetric information from the proposed concept of 2-pixel polarimetric CS camera.

In the first row (a) of Fig. 8, we plotted the reconstructed OSC maps for three other values of the OSC of the second object (bigger square). The reconstruction error map is given in the second row (b), while the evolution of the PSNR with the OSC of the second object is plotted in Fig. 8.c. These results evidence the fact that the reconstruction quality naturally decreases when the polarimetric contrast between the two objects is reduced, i.e., when the reconstruction problem becomes more difficult. This can be easily understood as the smallest variations of contrast are likely to be burried in the noise and totally filtered out by the regularization process. This is clearly seen for OSC = 0.6, where the sharpest features of the first object disappear in the reconstructed OSC map. Obviously, reconstruction quality is maximimed when the OSC of the second object reaches 0.8, i.e., a single object is to be identified in the image, thus yielding a simpler reconstruction problem.

2) Example of reconstruction on realistic image data: Laslty, we present an example of reconstructed polarimetric image on a more realistic imaging scenario. For that purpose, we considered a true intensity image $\mathbf{x}_T$ of the *cameraman* with size $N = 512 \times 512$, as plotted in Fig. 9. Appropriate polarimetric components $\mathbf{x}_S$ and $\mathbf{x}_P$ were generated so that a true OSC map would reveal 4 hidden objects (3 in the grass, 1 in the buildings) over a depolarizing background, as can be seen in Fig. 9. The reconstruction results with Symmlet wavelet transform are also displayed in Fig. 9, along with reconstruction error maps. The total intensity image is almost perfectly reconstructed, as would be the case with a SPC imaging system. However, the 4 hidden objects remain of course invisible in the reconstructed image $\hat{\mathbf{x}}_T$. Contrarily, the reconstructed OSC map makes it possible to identify the presence of the 4 hidden objects by revealing their polarimetric contrast over the background. The analysis of the reconstruction error map of OSC shows that the polarimetric information about the 4 hidden objects is fairly retrieved. However one can notice significant reconstruction errors in the darkest regions of the image (cameraman and tripod). These imperfections could be lowered in the future by refining regularization parameters and constraints in the algorithm implementation.

V. Conclusion and Perspectives

In this article, we have proposed a new concept of CS polarimetric imaging inspired from the SPC principle. Relying on the tiny differences in reflection coefficients of mirrors with incidence angle and polarization direction, the setup proposed allows intensity and polarimetric contrast informations to be recovered from the temporal acquisition on two single-pixel detectors, and without requiring any polarization analysis optical component. We have shown that this recovery problem could be analyzed as a joint CS and source separation tasks, that can be tackled independantly and successively using standard approaches (respectively ℓ_1 minimization and direct matrix inversion), or optimally treated in an original combined reconstruction approach. For that purpose, we have presented different versions of a combined algorithm, including FISTA implementation of the combined optimization problem, with potential reweighted steps that have proved efficient to increase the reconstruction quality. Moreover, to enforce additional physical constraints on the measured data, we have proposed

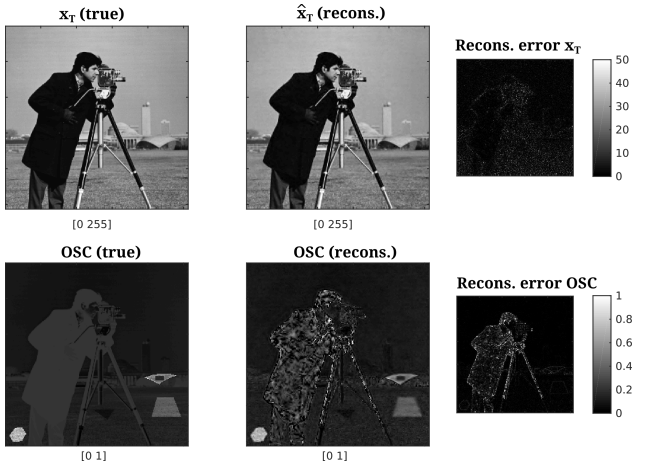

Fig. 9. Example of numerical polarimetric imaging experiment on realistic 512×512 pixels image data. First row: total intensity image $\mathbf{x}_T$, reconstruction $\hat{\mathbf{x}}_T$ and error map. The total intensity image is the standard cameraman test image, where the 4 hidden objects are totally hidden. Second row: true OSC image, reconstructed OSC image and error map. The 4 hidden objects are revealed by their polarimetric contrast over depolarizing background on the OSC images.

a constrained sparse reconstruction method based on the GFB algorithm, allowing the reconstruction quality to be improved in low SNR conditions.

Numerical simulations have permitted to validate these approaches and to analyze the influence of experimental conditions, such as incidence angle, SNR, micromirrors tilt errors, etc. Generally speaking, these results are encouraging towards the experimental implementation of such an imaging setup as good reconstruction quality was obtained for reasonable incidence angles on the mirror, even in the presence of a small bias or randomness in the mirrors tilt direction. Significant compression rates could be achieved while still offering sufficient reconstruction quality, as illustrated on the 2D simulation results presented.

Experimental implementation of this computational imaging approach appears as a natural perspective to this work. Another interesting research track is the design of a blind calibration method so as to compensate possible mis-estimation of the mixing matrix $\mathbf{A}$ involved in the reconstruction process. More generally, applying CS concepts to more sophisticated multichannel polarimetric imaging techniques which are characterized by very specific algebraic constraints is likely to raise interesting reconstruction issues.

APPENDIX A
COMPUTATION OF THE REFLECTION COEFFICIENTS

We consider a mirror with complex refraction index $\tilde{n} = n + jk$, which can be conveniently rewritten $\tilde{n} = n(1 + j\kappa)$ [32]. We consider the reflection of a beam propagating in an input medium consisting of air ($n_a = 1$). For an incidence angle θ on the mirror, one has from the generalized Snell's law $n_a \sin\theta = \tilde{n} \sin\tau$, with τ the refraction angle. Setting $u = n\cos r$ and $v = n\kappa\cos r$, one has $\tilde{n}\cos r = u + jv$.

It can be shown [32] that with such notations the reflection coefficient in intensity for TE waves (S-polarized) can be written [32]

$$r^S(\theta) = \frac{(n_a\cos\theta - u)^2 + v^2}{(n_a\cos\theta + u)^2 + v^2} = \frac{(\cos\theta - u)^2 + v^2}{(\cos\theta + u)^2 + v^2},$$

whereas for the TM (P-polarized) waves, one has

$$r^P(\theta) = \frac{(n^2(1-\kappa^2)\cos\theta - u)^2 + (2n^2\kappa\cos\theta - v)^2}{(n^2(1-\kappa^2)\cos\theta + u)^2 + (2n^2\kappa\cos\theta + v)^2}, \quad (11)$$

with $u = \sqrt{(\mathcal{A} + \sqrt{\mathcal{B}})/2}$ and $v = \sqrt{(-\mathcal{A} + \sqrt{\mathcal{B}})/2}$, and $\mathcal{A} = n^2(1-\kappa^2) - \sin^2\theta$ and $\mathcal{B} = \mathcal{A}^2 + 4n^4\kappa^2$.

From these equations, we were able to compute the micromirrors reflection coefficients for any incidence and any wavelength. The complex refraction index was obtained from a recent evaluation of aluminum reflection coefficients in Reference [33].

APPENDIX B
RECONSTRUCTION ALGORITHMS

A. Forward-backward splitting algorithm

Whether it is in the 2-step or in the combined sparse reconstruction approach, recovering the polarimetric signal $\mathbf{X}$ requires solving optimization problems of the form

$$\min_{\mathbf{X}} \quad \mathcal{P}(\mathbf{X}) + \mathcal{L}(\mathbf{X}),$$

where the data fidelity term $\mathcal{L}(\mathbf{X})$ is a quadratic norm that is differentiable and whose gradient is Lipschitz with some constant L_i, and $\mathcal{P}(\mathbf{X})$ is a convex but non-smooth penalization. Minimization problem can be carried out efficiently with recent proximal algorithms [34], and more precisely with the Forward-Backward Splitting (FBS) algorithm [35]. The FBS algorithm is an iterative procedure that can be described with the following update rule at iteration t

$$\mathbf{X}^{(t+1)} = \text{prox}_{\gamma\mathcal{P}}\left(\mathbf{X}^{(t)} - \gamma\nabla\mathcal{L}(\mathbf{X}^{(t)})\right)$$

where $\nabla\mathcal{L}(\mathbf{X}^{(t)})$ stands for the derivative of $\mathcal{L}$ in $\mathbf{X}^{(t)}$ and γ is the gradient path length. The proximal operator $\text{prox}_{\gamma\mathcal{P}}$ is defined by the solution to the problem

$$\text{prox}_{\gamma\mathcal{P}}(\mathbf{Z}) = \text{Argmin}_{\mathbf{X}}\gamma\mathcal{P}(\mathbf{X}) + \frac{1}{2}\|\mathbf{Z} - \mathbf{X}\|_F^2.$$

While the proximal operator of the penalization function is defined as the solution of an optimization problem, standardly used proximal operators admit a closed form expression (see Appendix B-B).

In this article, the term $\mathcal{P}$ will penalize non sparse solutions and will be based on the ℓ_1 norm. Introduced in [31], the reweighted ℓ_1 norm further introduces weights $\mathbf{\Lambda}$ that aim at reducing the bias induced by the standard ℓ_1 norm. Consequently, the penalization term used in this article will take the generic form

$$\mathcal{P}(\mathbf{X}) = \left\|\mathbf{\Lambda} \odot \left(\mathbf{X}\mathbf{\Psi}^T\right)\right\|_{\ell_1}$$

where $\mathbf{\Psi}$ is the signal representation where sparsity is modeled. The final optimization procedure then alternates between

updates of $\mathbf{X}$ for fixed weights $\mathbf{\Lambda}$ and updates of these weights, which has been showed to dramatically improves the accuracy of the reconstruction.

In the proposed reweighted algorithm, updates of the polarimetric signals are carried out using an accelerated version of the FBS algorithm coined FISTA [36]. The generic description of the reweighted FISTA algorithm is given in Algorithm 2

Algorithm 2:

Reweighted FISTA algorithm

Choose initial point $\mathbf{X}^{(0)}$ and set the weights to 1.

while $l < L_{outer}$ **do**

  Update the polarimetric components with starting point $\mathbf{W}^{(0)} = \mathbf{X}^{(l-1)}$ and $\mathbf{Z}^{(0)} = \mathbf{X}^{(l-1)}$. Fix $\rho^{(0)} = 1$.

  while $t < L$ **do**

$\mathbf{W}^{(t+1)} = \text{prox}_{\gamma \|\mathbf{\Lambda} \odot (\,.\,\mathbf{\Psi}^T)\|_{\ell_1}} \left(\mathbf{Z}^{(t)} - \gamma \nabla \mathcal{L}(\mathbf{Z}^{(t)})\right)$

$\rho^{(t+1)} = \frac{1+\sqrt{1+4\rho^{(t)\,2}}}{2}$

$\mathbf{Z}^{(t)} = \mathbf{W}^{(t+1)} + \frac{\rho^{(t)}-1}{\rho^{(t+1)}}(\mathbf{W}^{(t+1)} - \mathbf{W}^{(t)})$

  Fix $\mathbf{X}^{(l)} = \mathbf{Z}^{(L)}$

  Update the weights $\mathbf{\Lambda}^{(l)}$ - see Section III-D.

end

This procedure generally increases the accuracy of the reconstruction process with few updates of the weights $\mathbf{\Lambda}$, typically L_{outer} between 3 to 5. Details about practical parameter tuning are given in Section III-D.

B. Useful proximal operators

Hereafter, we described different proximal operators that are used in the proposed reconstruction algorithms.

Reweighted ℓ_1: Assuming that the sparse signal representation $\mathbf{\Psi}$ is an orthogonal matrix, the proximal operator of $\left\|\mathbf{\Lambda} \odot \left(\mathbf{X}\mathbf{\Psi}^T\right)\right\|_{\ell_1}$ is defined as

$$\text{prox}_{\|\mathbf{\Lambda} \odot (\,.\,\mathbf{\Psi}^T)\|_{\ell_1}}(\mathbf{Z}) = \mathbf{\Psi}\mathcal{S}_{\mathbf{\Lambda}}\left(\mathbf{Z}\mathbf{\Psi}^T\right) \tag{12}$$

where the weighted soft-thresholding operator $\mathcal{S}_{\mathbf{\Lambda}}$ is defined as

$$\forall i,j; \quad \mathcal{S}_{\mathbf{\Lambda}}(\mathbf{Z}_{ij}) = \begin{cases} \mathbf{Z}_{ij} - \mathbf{\Lambda}_{ij}\text{sign}(\mathbf{Z}_{ij}) \text{ if } |\mathbf{Z}_{ij}| > \mathbf{\Lambda}_{ij} \\ 0 \text{ otherwise} \end{cases} \tag{13}$$

Positivity constraint: The proximal operator of the positivity constraint is defined as the orthogonal projector onto the non-negative orthant:

$$\forall i,j; \quad \text{prox}_{i_{\mathbf{X} \succeq 0}(.)}(\mathbf{Z}_{ij}) = \begin{cases} \mathbf{Z}_{ij} \text{ if } \mathbf{Z}_{ij} > 0 \\ 0 \text{ otherwise} \end{cases} \tag{14}$$

Inequality constraint: The inequality constraint $x_s \succeq x_p$ can be recast as $\mathbf{DX} \succeq 0$, where $\mathbf{D} = [1, -1]$. Its proximal operator is defined as the orthogonal projector onto the convex set $\{\mathbf{Z};\ \forall i,j,\ [\mathbf{DZ}]_{ij} \geq 0\}$, which is defined as

$$\text{prox}_{i_{\mathbf{D}\,.\,\succeq 0}}(\mathbf{Z}) = \text{Argmin}_{\mathbf{DX} \succeq 0} \quad \frac{1}{2}\|\mathbf{Z} - \mathbf{X}\|_F^2.$$

This expression can be more conveniently recast in a Lagragian formulation by introducing the Lagrange multipliers $\boldsymbol{\pi}$

$$\text{prox}_{i_{\mathbf{D}\,.\,\succeq 0}}(\mathbf{Z}) = \text{Argmin}_{\mathbf{X}} \quad < \mathbf{DX}, \boldsymbol{\pi} > + \frac{1}{2}\|\mathbf{Z} - \mathbf{X}\|_F^2.$$

Its optimum is obtained for $\mathbf{X} = \mathbf{Z} - \mathbf{D}^T\boldsymbol{\pi}$, which should verify the constraint $\mathbf{DX} \succeq 0$. This entails

$$\mathbf{DZ} - 2\boldsymbol{\pi} \succeq 0.$$

Consequently, the Lagrange multipliers must take the values

$$\forall j; \quad \boldsymbol{\pi}_j = \begin{cases} \frac{1}{2}[\mathbf{DZ}]_j \text{ if } [\mathbf{DZ}]_j < 0 \\ 0 \text{ otherwise} \end{cases} \tag{15}$$

From this expression of the Lagrange multipliers, the proximal operator is then defined as

$$\text{prox}_{i_{\mathbf{D}\,.\,\succeq 0}}(\mathbf{Z}) = \mathbf{Z} - \mathbf{D}^T\boldsymbol{\pi}. \tag{16}$$

ACKNOWLEDGMENTS

The authors would like to thank Anthony Carré for his help in the 3D rendering of Fig. 1. This work is supported by the European Research Council through the grant LENA (contract no. 678282).

REFERENCES

[1] W. Groner, J. W. Winkelman, A. G. Harris, C. Ince, G. J. Bouma, K. Messmer, and R. G. Nadeau, "Orthogonal polarization spectral imaging: A new method for study of the microcirculation," *Nature Medicine*, vol. 5, no. 10, pp. 1209–1213, 1999.

[2] F. Boulvert, B. Boulbry, G. Le Brun, B. Le Jeune, S. Rivet, and J. Cariou, "Analysis of the depolarizing properties of irradiated pig skin," *Journal of Optics A: Pure and Applied Optics*, vol. 7, no. 1, p. 21, 2005.

[3] M. Anastasiadou, A. D. Martino, D. Clement, F. Lige, B. Laude-Boulesteix, N. Quang, J. Dreyfuss, B. Huynh, A. Nazac, L. Schwartz, and H. Cohen, "Polarimetric imaging for the diagnosis of cervical cancer," *physica status solidi (c)*, vol. 5, no. 5, pp. 1423–1426, 2008.

[4] S. Breugnot and P. Clémenceau, "Modeling and performances of a polarization active imager at lambda=806 nm," in *Laser Radar technology and applications IV*, G. W. K. C. Werner, Ed., vol. 3707. Proc. SPIE, 1999, pp. 449–460.

[5] M. Alouini, F. Goudail, A. Grisard, J. Bourderionnet, D. Dolfi, A. Bénière, I. Baarstad, T. Løke, P. Kaspersen, X. Normandin, and G. Berginc, "Near-infrared active polarimetric and multispectral laboratory demonstrator for target detection," *Appl. Opt.*, vol. 48, no. 8, pp. 1610–1618, 2009.

[6] J. Fade, S. Panigrahi, A. Carré, L. Frein, C. Hamel, F. Bretenaker, H. Ramachandran, and M. Alouini, "Long-range polarimetric imaging through fog," *Applied optics*, vol. 53, no. 18, pp. 3854–3865, 2014.

[7] F. Snik, J. Craven-Jones, M. Escuti, S. Fineschi, D. Harrington, A. De Martino, D. Mawet, J. Riedi, and J. S. Tyo, "An overview of polarimetric sensing techniques and technology with applications to different research fields," in *SPIE Sensing Technology+ Applications*. International Society for Optics and Photonics, 2014, pp. 90 990B–90 990B.

[8] C. Brosseau, *Fundamentals of polarized light - A statistical Optics approach*. John Wiley, 1998.

[9] N. Gupta, R. Dahmani, and S. Choy, "Acousto-optic tunable filter based visible- to near-infrared spectropolarimetric imager," *Optical Engineering*, vol. 41, no. 5, pp. 1033–1038, 2002.

[10] G. Anna, H. Sauer, F. Goudail, and D. Dolfi, "Fully tunable active polarization imager for contrast enhancement and partial polarimetry," *Applied optics*, vol. 51, no. 21, pp. 5302–5309, 2012.

[11] A. Bénière, M. Alouini, F. Goudail, and D. Dolfi, "Design and experimental validation of a snapshot polarization contrast imager," *Appl. Opt.*, vol. 48, no. 30, pp. 5764–5773, 2009.

[12] F. Goudail and P. Réfrégier, *Statistical image processing techniques for noisy images: an application oriented approach*. New York: Kluwer, 2004.

[13] R. G. Baraniuk, "Single-pixel imaging via compressive sampling," *IEEE Signal Processing Magazine*, 2008.
[14] W. L. Chan, K. Charan, D. Takhar, K. F. Kelly, R. G. Baraniuk, and D. M. Mittleman, "A single-pixel terahertz imaging system based on compressed sensing," *Applied Physics Letters*, vol. 93, no. 12, p. 121105, 2008.
[15] A. Wagadarikar, R. John, R. Willett, and D. Brady, "Single disperser design for coded aperture snapshot spectral imaging," *Applied optics*, vol. 47, no. 10, pp. B44–B51, 2008.
[16] A. Asensio Ramos and A. López Ariste, "Compressive sensing for spectroscopy and polarimetry," *arXiv*, vol. 509, p. A49, Jan. 2010.
[17] V. Studer, J. Bobin, M. Chahid, H. S. Mousavi, E. Candes, and M. Dahan, "Compressive fluorescence microscopy for biological and hyperspectral imaging," *Proceedings of the National Academy of Sciences*, vol. 109, no. 26, pp. E1679–E1687, 2012.
[18] Y. August and A. Stern, "Compressive sensing spectrometry based on liquid crystal devices," *Optics letters*, vol. 38, no. 23, pp. 4996–4999, 2013.
[19] A. Liutkus, D. Martina, S. Popoff, G. Chardon, O. Katz, G. Lerosey, S. Gigan, L. Daudet, and I. Carron, "Imaging With Nature: A Universal Analog Compressive Imager Using a Multiply Scattering Medium," *ArXiv e-prints*, Sep. 2013.
[20] V. Durán, P. Clemente, M. Fernández-Alonso, E. Tajahuerce, and J. Lancis, "Single-pixel polarimetric imaging," *Optics letters*, vol. 37, no. 5, pp. 824–826, 2012.
[21] F. Soldevila, E. Irles, V. Durán, P. Clemente, M. Fernández-Alonso, E. Tajahuerce, and J. Lancis, "Single-pixel polarimetric imaging spectrometer by compressive sensing," *Applied Physics B*, vol. 113, no. 4, pp. 551–558, 2013.
[22] S. S. Welsh, M. P. Edgar, R. Bowman, B. Sun, and M. J. Padgett, "Near video-rate linear stokes imaging with single-pixel detectors," *Journal of Optics*, vol. 17, no. 2, p. 025705, 2015.
[23] C. Fu, H. Arguello, B. M. Sadler, and G. R. Arce, "Compressive spectral polarization imaging by a pixelized polarizer and colored patterned detector," *J. Opt. Soc. Am. A*, vol. 32, no. 11, pp. 2178–2188, Nov 2015.
[24] Y. C. Eldar and G. Kutyniok, *Compressed sensing: theory and applications*. Cambridge University Press, 2012.
[25] *DLP6500-0.65-1080p Datasheet*, Texas Instruments, october 2016, rev. B. [Online]. Available: http://www.ti.com/product/DLP6500FYE/datasheet
[26] I. N. Flamarique, C. W. Hawryshyn, and F. I. Hárosi, "Double-cone internal reflection as a basis for polarization detection in fish," *JOSA A*, vol. 15, no. 2, pp. 349–358, 1998.
[27] E. Candès and M. Wakin, "People hearing without listening: An introduction to compressive sampling," *IEEE Signal Processing Magazine*, March 2008, 21–30.
[28] E. Candès, "Compressive sampling," *International Congress of Mathematics, Madrid*, 2006.
[29] H. Raguet, J. Fadili, and G. Peyre, "A Generalized Forward-Backward Splitting," *SIAM Journal on Imaging Sciences*, vol. 6, no. 3, pp. 1199–1226, 2013. [Online]. Available: http://hal.archives-ouvertes.fr/hal-00613637/
[30] J.-L. Starck, J. Fadili, and F. Murtagh, "The undecimated wavelet decomposition and its reconstruction," *IEEE Transactions on Image Processing*, vol. 16, 2007, 297–309.
[31] E. J. Candes, M. B. Wakin, and S. P. Boyd, "Enhancing sparsity by reweighted L1 minimization," *Journal of Fourier Analysis and Applications*, vol. 14, no. 5, 2008, 877–905.
[32] M. Born and E. Wolf, "Principles of optics, 7-th ed," *Cambridge University, Cambridge*, pp. 752–754, 1999.
[33] A. D. Rakić, A. B. Djurišić, J. M. Elazar, and M. L. Majewski, "Optical properties of metallic films for vertical-cavity optoelectronic devices," *Applied optics*, vol. 37, no. 22, pp. 5271–5283, 1998.
[34] N. Parikh and S. Boyd, "Proximal algorithms," *Foundations and Trends in Optimization*, vol. 1, no. 3, 2014.
[35] P. L. Combettes and V. R. Wajs, "Signal recovery by proximal forward-backward splitting," *Multiscale Modeling & Simulation*, vol. 4, no. 4, 2005, 1168–1200.
[36] A. Beck and M. Teboulle, "Fast iterative shrinkage-thresholding algorithm for linear inverse problems," *SIAM journal on imaging science*, vol. 2, 2009, 183–202.

PLACE PHOTO HERE

Julien Fade Biography text here.

PLACE PHOTO HERE

Estéban Perrotin Biography text here.

PLACE PHOTO HERE

Jérôme Bobin Biography text here.

Computational polarization imaging from a single speckle image

Julien Fade,[1,*] Muriel Roche,[2] and Mehdi Alouini[1,3]

[1]*Institut de Physique de Rennes, Université de Rennes 1, CNRS, Campus de Beaulieu, 35042 Rennes, France*

[2]*Institut Fresnel, Aix-Marseille Université, Ecole Centrale Marseille, CNRS, Campus Saint-Jérôme, 13013 Marseille, France*

[3]*Thales Research and Technology, RD 128, 91767 Palaiseau Cedex, France*

**Corresponding author: julien.fade@univ-rennes1.fr*

Received September 14, 2011; revised November 22, 2011; accepted December 5, 2011; posted December 6, 2011 (Doc. ID 154575); published January 30, 2012

We experimentally demonstrate that imaging of the degree of polarization (DOP) can be achieved from a single intensity image acquired under coherent illumination. This computational technique is based on the analysis of the speckle characteristics in a statistically homogeneous neighborhood of the pixel. Over a variety of samples obtained experimentally, we show that a simple calibration step allows this method to quickly and simply provide correct estimated values of the DOP, with precision in agreement with theoretical predictions. It is shown that unlike linear polarimetric contrast imaging, this method remains valid on birefringent samples. © 2012 Optical Society of America

OCIS codes: 120.5410, 030.4280, 120.6150, 030.6600.

Polarimetric imaging is a promising and widely investigated technique in many different fields of application, such as military, medical, or robotics domains [1,2]. In particular, imaging the degree of polarization (DOP) of the light backscattered by a scene can reveal contrasts that do not appear in standard intensity images [2]. Four polarimetric measurements are actually needed to determine the polarization state of light, but simplified imaging modalities have been proposed to reduce both costs and acquisition times, such as orthogonal states contrast (OSC) imaging, requiring only two measurements [2]. Recently, theoretical studies [3–7] have shown that an alternative DOP imaging technique, using a single-image acquisition under coherent active illumination and without a polarizing element, could lead to estimation performance compatible with potential applications. This computational approach is based on the analysis of the speckle statistics in the image, which contain information on the DOP of the reflected light [8]. In addition to its simplicity, this technique is applicable at any wavelength and is not affected by image registration issues, which are in general detrimental to the quality of polarimetric imaging devices. In this Letter, we experimentally demonstrate the applicability of such a technique over a variety of samples, and we analyze its precision in comparison to theoretical characterizations [5] and to standard methods.

The experimental setup used is sketched in Fig. 1(a). The sample is illuminated with a 5 cm diameter spot from a collimated 633 nm He:Ne laser beam of 15 mW power. A polarizer (P_1) ensures a vertical direction of the illumination polarization. Imaging of the sample is operated with a 12-bit Basler A312f CCD camera (782 pixels × 582 pixels pixels) and a 50 mm objective, whose line of sight is almost aligned with the illumination beam axis (to avoid undesirable specular reflections). The camera has been selected for its good noise properties under low illumination, when the objective aperture is shrunk to obtain at least a speckle grain per pixel on average. Four Stokes images can be recorded with the appropriate configurations of a polarization analyzer (P_2) and a quarter-wave plate [see Fig. 1(a)]. The image of the DOP in each pixel of the scene can then be classically obtained from these four Stokes measurements [9]. In addition, the OSC image can also be derived from $\mathrm{OSC} = (I_{\parallel} - I_{\perp})/(I_{\parallel} + I_{\perp})$, where $I_{\parallel}$ and $I_{\perp}$ denote the first two Stokes images acquired. OSC is often used in polarimetric imaging applications, since it is equal to the DOP over a majority of materials (purely depolarizing materials) [2].

In addition to these four Stokes measurements, a fifth image denoted I_T is recorded without any polarimetric component in front of the camera objective. As detailed in [3–7], the square DOP, denoted $\mathcal{P}^2$, can be retrieved very simply from this bare speckle intensity image, by computing the following estimator: $\widehat{\mathcal{P}^2} = 2[\langle I_T^2\rangle_\chi / \langle I_T\rangle_\chi^2 - 1]/\kappa - 1$, where $\langle . \rangle_\chi$ denotes statistical averaging over a homogeneous neighborhood χ of the considered pixel. Previous theoretical work [5] has shown that

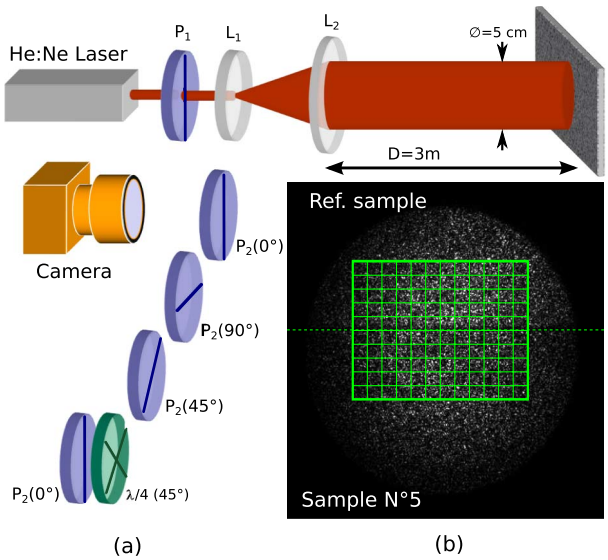

Fig. 1. (Color online) (a) Experimental setup, (b) example of an intensity image of the reference sample and sample 5 (green paint).

0146-9592/12/030386-03$15.00/0

statistically homogeneous neighborhoods of typically a few hundred pixels are needed for such a method to provide satisfactory estimation precision (about 10%). In the previous equation, the parameter κ is directly linked to the speckle order $L = 1/\kappa$, which characterizes the average number of speckle grains contained in one pixel of the imaging system [5]. This computational method must therefore be calibrated to characterize the value of the parameter κ, which will be detailed in the following.

In the first experiment reported here, we have considered eight different polarimetric scenes [see Fig. 1(b)] comprising an identical reference material (beige painted cardboard slab) in the upper part of the image and eight different test materials, described in Table 1, in the lower part of the image. To avoid illumination inhomogeneities, regions of interest of 240 pixels × 100 pixels are selected in the upper and lower parts of the images. These regions are then further partitioned into 60 subregions of 400 pixels each [see Fig. 1(b)]. Indeed, performing the estimation on such regions of limited size appears more realistic (homogeneous regions $>10^4$ pixels are unlikely to occur in real conditions), and smaller regions ensure good illumination uniformity. Lastly, it allows a statistical analysis of the estimation precision to be carried out from the 60 realizations.

As mentioned previously, a precise characterization of the parameter κ is needed before the estimator $\widehat{\mathcal{P}^2}$ can be applied on a single intensity image. For a fixed wavelength and experiment geometry, κ is inversely proportional to the objective aperture and does not depend on the sample considered. Computing the ratio of the variance to the square mean intensity of a fully polarized speckle pattern is a simple way to determine this parameter experimentally [8]. We thus calibrated the estimator $\widehat{\mathcal{P}^2}$ on the reference sample by computing κ on the four Stokes images acquired (which are fully polarized). Very similar results were obtained on each Stokes image and along the eight experiments, finally leading to the estimated value $\hat{\kappa} = 0.808 \pm 0.003$, which corresponds to a speckle order of $L = 1.24$.

Once the parameter κ is characterized, the estimator $\widehat{\mathcal{P}^2}$ can be applied on the image I_T acquired without a polarimetric component. Estimation results are plotted with blue diamond symbols in Fig. 2(a) for the reference sample and for the eight test samples. It can be immediately checked that except for test sample 8, the estimator $\widehat{\mathcal{P}^2}$ provides the correct value of the square DOP, in agreement (at least within the estimated error bar) with the results obtained with standard Stokes measurements (red squares) or OSC (green triangles). This experimentally demonstrates the applicability of the computational technique addressed here. Furthermore, this result shows that the value of κ estimated on the reference sample remains valid on other materials. Unfortunately, this might not be always the case, for instance, with samples showing a nonuniform reflectivity distribution or with textured materials. We suspect such a situation occurs with sample 8, for which $\widehat{\mathcal{P}^2}$ leads to irrelevant values ($\widehat{\mathcal{P}^2} = 1.2$). It has been checked that the parameter κ was equal to 0.95 on this black plastic slab, which can be interpreted as follows: since the sample is very dark, light mainly undergoes surface backscattering (and hence very low depolarization [10]) on the smooth, glossy plastic surface, making it difficult to avoid a detrimental contribution from specular backscattering.

As stated previously, the precision of the single-image computational estimation method can be evaluated from the 60 homogeneous regions of 400 pixels on which the estimation was operated. In Fig. 2(a), one can see that a larger standard deviation is of course the price to pay for a simplification of the imaging system. It must, however, be noticed that even on samples of limited size (20 pixels × 20 pixels), the computational estimation method allows materials of distinct polarimetric properties to be discriminated, with a 10% precision on $\mathcal{P}^2$. Previous theoretical results can be used to assess the variance of $\widehat{\mathcal{P}^2}$ for various speckle models [5]. This can be checked in Fig. 2(b), where the experimental variance of $\widehat{\mathcal{P}^2}$ is compared with theoretical predictions obtained when a so-called standard (respectively, compound) speckle model is considered, i.e., when the intensity distribution for $\mathcal{P} = 1$ is assumed to follow a gamma distribution (respectively, a $\mathcal{K}$ distribution) [8], with an

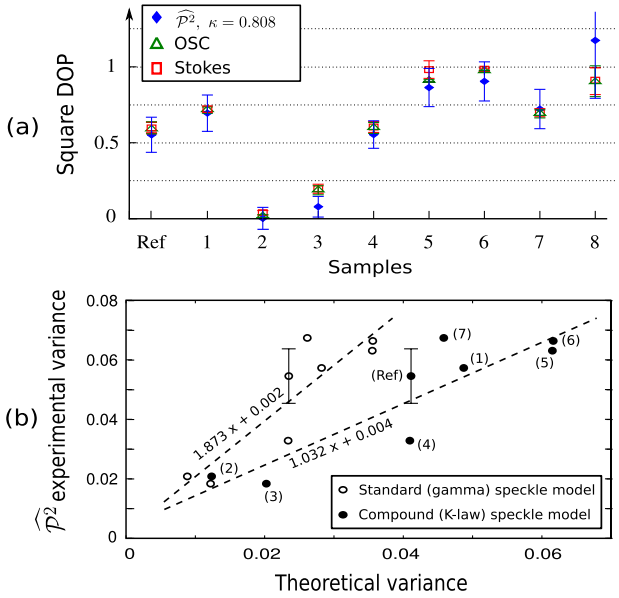

Fig. 2. (Color online) (a) Values of the square DOP estimated on homogeneous regions of 400 pixels on the nine samples, (b) comparison between experimental variance of $\widehat{\mathcal{P}^2}$ and theoretical predictions for distinct speckle models. Sample 8, leading to an erroneous estimated value of $\mathcal{P}$, is not represented in this figure. The error bar on experimental variance is estimated from the eight experiments conducted on the reference sample.

Table 1. Description of the Samples

Reference: Beige cardboard [0.61]	
1: Black paper [0.72]	2: White paper [0.04]
3: Cream plastic [0.20]	4: Gray paint [0.60]
5: Green paint [0.98]	6: Aluminum [0.98]
7: Sandblasted aluminum [0.70]	8: Black plastic [0.91]

Bracketed figures correspond to the values of $\mathcal{P}^2$ estimated from Stokes measurements.

Table 2. Estimated Values of the Square DOP for Metal and Cardboard Samples for Different Speckle Orders

Sample	$f/$	κ	$\widehat{\mathcal{P}^2_{\mathrm{OSC}}}$	$\widehat{\mathcal{P}^2}$
Metal	$f/16$	0.7 [0.1][a]	0.94 [0.01]	0.9 [0.3]
	$f/4$	0.12 [0.02]	0.96 [0.01]	0.8 [0.3]
Cardboard	$f/16$	0.66 [0.07]	0.05 [0.02]	0.04 [0.1]
	$f/4$	0.14 [0.02]	0.06 [0.01]	−0.03 [0.1]

[a]Bracketed numbers are the estimation standard deviation.

appropriate shape parameter equal to $L = 1/\kappa$. As can be seen from the linear fit parameters, fair agreement between experiments and theory can be observed, especially with a compound speckle model, which seems to be more relevant in the conditions of our experiment.

To check the validity of the method when the speckle order varies, a second experiment has been conducted with a green 532 nm frequency-doubled Nd:YVO_4 laser of 10 mW power. Two samples have been imaged (a metal slab and a cardboard sheet) for two distinct objective apertures ($f/16$ and $f/4$), leading to different parameters κ (see Table 2). Both measurements of κ and $\mathcal{P}^2$ have been carried out on 100 homogeneous regions of 10 pixels × 10 pixels. In this experiment, the calibration procedure has been performed on the cardboard reference sample. The results are summarized in Table 2. It can be seen that the single-image computational technique remains valid for different values of the parameter κ, provided it has been carefully characterized.

A last experiment is reported in this Letter to check the applicability of the single-image computational technique on non-purely depolarizing materials (e.g., birefringent samples). The experimental configuration is similar to the one described in the previous paragraph, but we added a tunable Babinet–Soleil (BS) compensator within the path of the backscattered light, with slow and fast axes oriented at a 45° angle from the illumination polarization direction. With the metallic sample, we were thus able to obtain an almost fully polarized backscattered speckle field ($\mathcal{P}^2 = 0.93$ from Stokes measurements), with a polarization state varying between a vertical linear polarization and a circular polarization, when the BS compensator retardation angle φ was varied between 0 and $\pi/2$. In Fig. 3, we plotted the estimation results obtained with the computational method (blue diamonds) and with the OSC (green triangles). It can first be checked on this figure that the OSC is unable to correctly evaluate the DOP in the presence of birefringent samples, while estimator $\widehat{\mathcal{P}^2}$ remains valid for any polarization state. It can be also noted that estimation precision does not depend on the polarization state ellipticity, in

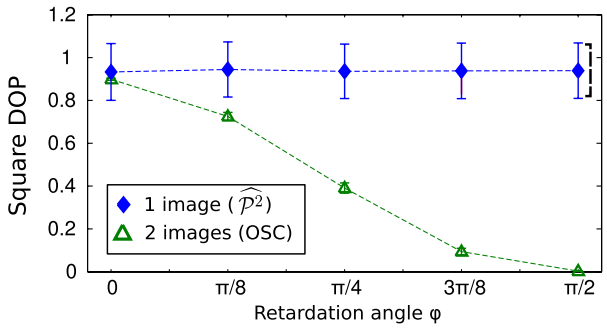

Fig. 3. (Color online) Square DOP estimated from two images (OSC) and one image (estimator $\widehat{\mathcal{P}^2}$), as a function of the retardation φ imposed by the BS compensator.

agreement with theoretical predictions plotted with a dashed error bar for a compound speckle model.

In this Letter, a computational technique involving single-image acquisition has been tested successfully on a variety of nontextured materials to achieve DOP estimation with precision in agreement with theory [5]. The applicability of such a technique at different wavelengths, on birefringent materials, and for distinct speckle orders has also been demonstrated. Too add perspective to this work, other experiments should be conducted to validate previous theoretical predictions that showed that this computational technique should be quite robust to photon noise [6] and detector noise [7], thus enabling low-flux real-time polarimetric imaging.

The authors thank Pr. Ph. Réfrégier for fruitful discussions.

References

1. J. S. Tyo, D. L. Goldstein, D. B. Chenault, and J. A. Shaw, Appl. Opt. **45**, 5453 (2006).
2. S. Breugnot and P. Clémenceau, Proc. SPIE **3707**, 449 (1999).
3. T. J. Schulz, Proc. SPIE **5888**, 58880N (2005).
4. P. Réfrégier, J. Fade, and M. Roche, Opt. Lett. **32**, 739 (2007).
5. J. Fade, M. Roche, and P. Réfrégier, J. Opt. Soc. Am. A **25**, 483 (2008).
6. J. Fade, P. Réfrégier, and M. Roche, J. Opt. A: Pure Appl. Opt. **10**, 115301 (2008).
7. W. Wang and T. J. Schulz, J. Opt. Soc. Am. A **27**, 1274 (2010).
8. J. W. Goodman, in *Speckle Phenomena in Optics: Theory and Applications* (Roberts, 2007), Chap. 3.
9. E. Collett, *Polarized Light: Fundamentals and Applications* (Dekker, 1993).
10. M. Alouini, F. Goudail, N. Roux, L. Le Hors, P. Hartemann, S. Breugnot, and D. Dolfi, Eur. Phys. J. Appl. Phys. **42**, 129 (2008).

Selection of publications - Part II

- Julien Fade, Swapnesh Panigrahi, Anthony Carré, Ludovic Frein, Cyril Hamel, Fabien Bretenaker, Hema Ramachandran, Mehdi Alouini. "Long-range polarimetric imaging through fog". Applied Optics, 53 (18), pp. 3854-3865 (2014).

- Julien Fade, Swapnesh Panigrahi, Mehdi Alouini. "Optimal estimation in polarimetric imaging in the presence of correlated noise fluctuations". Optics Express, 22 (5), pp. 4920-4931 (2014).

- Swapnesh Panigrahi, Julien Fade, Mehdi Alouini. "Adaptive polarimetric image representation for contrast optimization of a polarized beacon through fog". Journal of Optics, 17, pp. 065703 (2015).

- Swapnesh Panigrahi, Julien Fade, Hema Ramachandran, Mehdi Alouini. "Theoretical optimal modulation frequencies for scattering parameter estimation and ballistic photon filtering in diffusing media". Optics Express, 24 (14), pp. 16066-16083 (2016).

- Julien Fade, Sidonie Lefebvre, Nicolas Cézard. "Minimum description length approach for unsupervised spectral unmixing of multiple interfering gas species". Optics Express, 19 (15), pp. 13862-13872 (2011).

- Julien Fade. "Stochastic complexity-based model selection with false alarm rate control in optical spectroscopy". Pattern Recognition Letters, 65, pp. 152-156 (2015).

Long-range polarimetric imaging through fog

Julien Fade,[1,*] Swapnesh Panigrahi,[1] Anthony Carré,[1] Ludovic Frein,[1] Cyril Hamel,[1] Fabien Bretenaker,[2] Hema Ramachandran,[3] and Mehdi Alouini[1]

[1]Institut de Physique de Rennes, CNRS, Université de Rennes 1, Campus de Beaulieu, 35 042 Rennes, France

[2]Laboratoire Aimé Cotton, CNRS, Université Paris-Sud 11, 91 405 Orsay, France

[3]Raman Research Institute, CV Raman Avenue, Sadashivanagar, 560 080 Bangalore, India

*Corresponding author: julien.fade@univ-rennes1.fr

Received 6 March 2014; revised 6 May 2014; accepted 7 May 2014;
posted 9 May 2014 (Doc. ID 206232); published 13 June 2014

We report an experimental implementation of long-range polarimetric imaging through fog over kilometric distance in real field atmospheric conditions. An incoherent polarized light source settled on a telecommunication tower is imaged at a distance of 1.3 km with a snapshot polarimetric camera including a birefringent Wollaston prism, allowing simultaneous acquisition of two images along orthogonal polarization directions. From a large number of acquisitions datasets and under various environmental conditions (clear sky/fog/haze, day/night), we compare the efficiency of using polarized light for source contrast increase with different signal representations (intensity, polarimetric difference, polarimetric contrast, etc.). With the limited-dynamics detector used, a maximum fourfold increase in contrast was demonstrated under bright background illumination using polarimetric difference image.

OCIS codes: (110.0113) Imaging through turbid media; (110.5405) Polarimetric imaging; (010.7295) Visibility and imaging; (110.4280) Noise in imaging systems.

http://dx.doi.org/10.1364/AO.53.003854

1. Introduction

Imaging of objects and light sources hidden behind a turbid medium has wide applications in areas pertaining to medical diagnostics [1,2], remote sensing [3], and transport and navigation [4]. More specifically, imaging through nebulous media encountered in nature, like fog, rain, and light haze, is still a topical issue that attracts a lot of attention. Enhanced vision in such weather conditions has indeed tremendous applications for assistance in navigation of all modes of vehicular transport. Vision systems that can offer enhanced visibility during such weather conditions can be used to provide visual assistance by means of augmented reality displays that can efficiently detect and isolate light sources hidden beyond foggy intervening media. Besides, with the advent of autonomous vehicles, both airborne and terrestrial, this problem becomes increasingly important in the field of machine vision and vehicular safety as well.

In general, the photons traveling through any random medium can be classified into ballistic, *snake*, and diffused photons. The diffused photons undergo maximum scattering as they travel through the medium, whereas ballistic and snake photons undergo predominantly forward scattering. As a result, the diffused photons randomly take longer paths and times to reach the detector. Consequently, in the process, they are received as noise over the ballistic photons that retain the spatial and temporal information of the source (signal). Various approaches have been studied to discriminate and record only the ballistic and snake photons in order to attain a better contrast of signal over the noise. For instance, time-gated imaging, using a gated camera synchronized to a pulsed illumination source, is shown to be an

1559-128X/14/183854-12$15.00/0

efficient way to recover the information carried by ballistic photons [1,5]. Other approaches have also been studied such as spatial filtering techniques [6,7], intensity modulation schemes [8,9] or laser optical feedback imaging [10,11].

An alternative approach, such as polarization-gated imaging [12–16], involves this time light polarization. It is based on the preservation of the state of polarization of light (linear or circular) during propagation through thick scattering media, such as heavy fog conditions, with minor depolarization. This so-called *polarization memory effect* has been analyzed in numerous references, both for linearly polarized [17] and circularly polarized light [18,19]. As a result, such an effect can be exploited using a polarization-sensitive imaging device to enhance the visibility of a source provided this latter emits polarized light. These approaches have already proved efficient and been reported in a number of laboratory experiments [12–16], with simulated turbidity conditions on very short distances using artificial scatterers like aerosols.

In case of light traveling through fog, photons undergo scattering by a cloud of randomly distributed particles with sizes in the order of 5–50 μm and varying number density [20]. Moreover, depending on the environmental conditions, the scatterers in the intervening medium may not retain a perfect spheroid shape due to drag (as in case of large rain drops) or may have ice crystals with preferred orientations [21].

Although these overall studies on polarized light propagation bring very useful elements of understanding, they remain quite difficult to exploit for sizing an outdoor imaging system because they are carried out in well-established and well-controlled conditions. Indeed, the combined effects of sun illumination, surrounding artificial illumination, visibility evolution, change of scatterers density and size, and varying atmospheric conditions are extremely difficult to mimic or anticipate in a laboratory. In addition, unless resorting to numerical scattering simulations, long-range propagation is a phenomenon that cannot be easily simulated by a laboratory experiment, even with a scaling approach.

Keeping in mind the aforementioned applications and requirement of study of such vision systems in real atmospheric conditions, we report in this paper the design, implementation, and operation of an imaging experiment we developed to investigate the polarimetric contrasts of a scene including a polarized light source in a real foggy environment over a kilometric distance. Such distance corresponds to a reasonable range requirement for transport safety applications. We also analyze the efficiency of several representations of the polarimetric information obtained with our imaging installation in various environmental conditions (clear sky/fog/haze, day/night).

This article is organized as follows: in the next section, we recall some basics of polarimetric imaging and the corresponding experimental techniques. Then, in Section 3, we detail the long-range polarimetric imaging setup used in this experiment, as well as calibration procedures in Section 4. Two representative datasets are then extensively analyzed in Section 5, among numerous datasets acquired during experimental campaigns. The efficiency of different polarimetric signal representations to increase visual contrast of a polarized light source in fog over long distances is discussed for varying environmental conditions. Then, a general discussion and conclusion on the experiment is eventually provided in Section 6.

2. Polarimetric Contrast Imaging

Polarization-sensitive imaging has proved efficient in the context of enhanced vision through turbid media [22], industrial quality control [23,24], and machine vision [25]. To probe the complete polarimetric properties of a light source, one needs to measure the Stokes vector S given by

$$S = \begin{pmatrix} S_0 \\ S_1 \\ S_2 \\ S_3 \end{pmatrix} = \begin{pmatrix} I_x + I_y \\ I_x - I_y \\ I_{+45^\circ} - I_{-45^\circ} \\ I_R - I_L \end{pmatrix}, \tag{1}$$

from which the degree of polarization (DOP) of the source can be obtained using the relation $\mathrm{DOP} = \sqrt{S_1^2 + S_2^2 + S_3^2}/S_0$. Hitherto, various techniques have been employed to fully or partially measure the Stokes vectors of an image and obtain the polarimetric information of the scene of interest. Most often, rotating polarizers and/or moving birefringent plates are used. Other schemes including prisms [26], Savart plates [27], polarization gratings [28], liquid crystal modulators [29], or microgrid division-of-focal-plane polarimetric imagers [30] have been used with varying degrees of compromise toward mechanical reliability and real-time acquisition and processing. Measuring the full Stokes vector at each pixel can be a slow and storage-heavy task and hence not very suitable for imaging moving objects, thus limiting their application in real-time scenarios. In the experiment presented here, we consider a highly polarized source with *a priori* known linear polarization state with the intervening medium being nonbirefringent. Therefore, it is not necessary to measure the full Stokes vector but only the first two components of the Stokes vector to define the so-called orthogonal states contrast (OSC) given by Eq. (2):

$$\mathrm{OSC} = \frac{S_1}{S_0} = \frac{I_\parallel - I_\perp}{I_\parallel + I_\perp}, \tag{2}$$

where $I_\parallel$ and $I_\perp$ are the intensities obtained through orthogonally aligned analyzers or through a polarization splitting Wollaston prism. In the case considered here of a linearly polarized light propagating through a nonbirefringent medium, the OSC is

equal to the DOP of the source after passing through the atmosphere and fog. The intensity measures recorded by a pixel of a camera are of course affected by various noise sources, for instance, (1) the Gaussian electronic noise induced by the electronic readout circuit of the CCD array sensor and (2) optical noise due to photon noise, atmospheric turbulence, and fluctuations introduced by spatial/temporal evolutions of the intermediate foggy medium. As will be seen later, the computation of the OSC may be strongly affected by this noise, especially in low illumination conditions, since the division by total intensity ($I_T = I_{\parallel} + I_{\perp}$) may lead to unbounded values.

3. Long-Range Experimental Setup

The experiment presented here is designed to implement a long-range polarimetric imaging system over kilometric distances and in real-field outdoor conditions. Such an experiment allows us to assess the benefits of using polarized light for improved detectability of a lightmark through turbid atmosphere over long distances. Such a system can have practical applications in aviation or navigation at sea in poor visibility conditions. The setup mainly consists of a polarized light emitter and a polarimetric imaging system that simultaneously acquires two images of a scene corresponding to the two orthogonal directions of polarization. These elements, which are extensively described in this section, are located on the Beaulieu campus of University of Rennes 1 and are separated by 1.27 km. The source is located on the top of a telecommunication tower owned by the TDF company. The detection setup is located in a laboratory building as illustrated in Fig. 1. The various parts of the setup are described in detail in the following subsections.

A. Polarized Source

The source used is a 300 W halogen incandescent lamp with a linear polarizer, both placed inside a weatherproof steel housing as shown in Fig. 1. The light from the incandescent lamp is polarized using an adhesive dichroic polymer polarizing sheet glued to a glass plate and oriented such that the polarization axis is vertical. Half the optical power provided by the lamp being absorbed by the polarizer, it turned out that standard polaroid sheets are subject to deterioration after a few minutes of illumination. For this reason, we use polarizing sheets specifically designed for the LCD projector industry, thus ensuring high durability under high power operation conditions. Before installing the source, we conducted durability tests in indoor conditions with a 300 W lamp. The lamp was allowed to run continuously during daytime. In these conditions, it was noticed that the polarimetric contrast of the sheet was reduced by 57.4% in a period of five days with continuous daytime usage. In light of this, a weather-proof steel housing was designed, such that the polarizing sheet glued on a glass plate is placed sufficiently far (20 cm) from the lamp. Moreover, holes have been drilled in the bottom and top of the housing to enable air flow between the lamp and the glass plate. This air flow is stimulated by convection when the temperature of the glass plate increases, allowing the hot air in between to be removed, thus providing an efficient heat dissipation. Such a mechanical design ensures a reasonable lifetime of almost one year in outdoor conditions before requiring replacement.

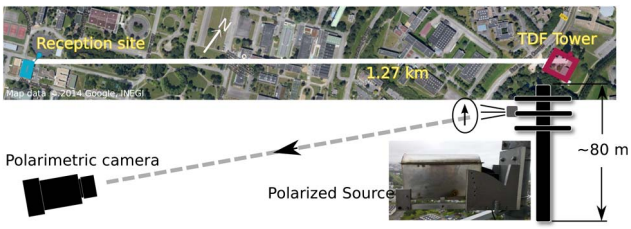

Fig. 1. Long-range polarimetric imaging experimental setup. The source and the camera are separated by 1.27 km with the camera placed in the University of Rennes 1 campus and the source located on a telecommunication tower of the TDF company. The photograph shows the polarized light source settled on the telecommunication tower.

The telecommunication tower is about 80 m in height and provides a suitable location for the source. The distance of the tower from the laboratory site in the University of Rennes 1 is optimal for various applications where long-range imaging through fog may be crucial. The tower is also the tallest structure in the surrounding area and is in line of sight from the laboratory buildings. The polarized source is connected to a Global system for mobile telecommunications (GSM) switch, enabling easy remote control of the emission part of the experiment.

B. Snapshot Polarimetric Camera

The detection system consists of a snapshot polarimetric imaging setup and a computer dedicated for control and image acquisition. The detection system is housed on a mezzanine floor of a laboratory building in the line of sight of the emitter. The schematic of the imaging setup is shown in Figs. 2(a) and 2(b). The imaging setup consists of a telescopic arrangement of lenses L1 (50 mm, F/2.8 camera objective) and L2 (25 mm, F/2.1 camera objective) which creates a collimated beam of light that is incident on a Wollaston prism (WP). The WP is a calcite birefringent prism with a 5° splitting angle which introduces an angular separation between the vertical and horizontal polarization components of the incident beam. These ordinary and extraordinary beams are then focused onto the camera using a third lens L3 (25 mm, F/2.1 camera objective), thus creating two images $I_{\parallel}$ and $I_{\perp}$ on the CCD. This setup allows us to simultaneously record a scene along orthogonal polarization directions using a single camera. This has a huge advantage in real-time processing of moving objects and has proved to be efficient in the presence of turbulence and relative motion of the scene [26], such as fog in our case. It has been demonstrated that this configuration suffers from lower geometrical

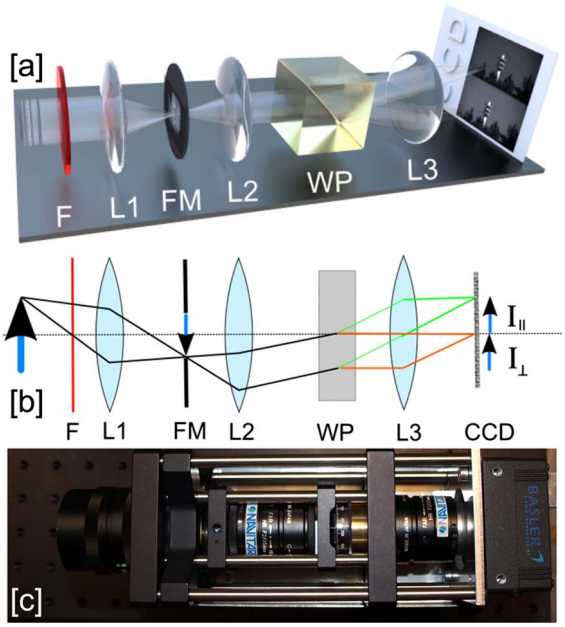

Fig. 2. Polarimetric imaging setup: The WP angularly separates the incident beam into two orthogonal polarization components forming two images $I_{\parallel}$ and $I_{\perp}$ on the CCD. The illustration in (a) shows a orthographic view of the polarimetric imager while the schematic in (b) geometrically indicates the working principle of the imaging setup. A top view photograph of the imaging setup is shown in (c).

aberration as well [26]. In order to avoid chromatic aberrations due to the WP, we use a selective red filter (F) with a central wavelength of 612 nm and a linewidth of 12 nm. The two images produced on the CCD have considerable overlap because of the small splitting angle of the WP. To prevent this overlap, a stainless-steel slit painted with dark matte paint of dimension 3 mm × 18 mm is used as a field mask (FM) and is placed in the intermediate image plane existing between lenses L1 and L2. The CCD camera is a 12 bit, 782 × 582 pixels resolution camera (Basler A312f) with pixel size of 8 μm and average dark count of 23 e^{-}/s with standard deviation of 0.6 e^{-}/s. The camera was selected for its low noise properties in low light conditions, which as we will see is preferable while performing arithmetic on the acquired polarimetric images.

C. Control Program

The camera is controlled through an IEEE 1394a interface by a custom acquisition program developed using LabVIEW. A number of features are implemented in the program that suit the experiment and provide automation of acquisition using a user-friendly interface. One of the features implemented is what we will refer to as auto-exposure mode (AEM). We had to implement such an AEM because the imaging system is by essence operated for long time periods under varying weather conditions. Under this mode, the exposure time of the camera is automatically changed depending on the illumination of a given predefined pixel. This pixel can be chosen to be the pixel representing the source on the camera (we will refer to this pixel as the source pixel for brevity in further sections), thereby avoiding saturation or underexposure of the source pixel with respect to the surrounding scene. It is also possible to feed this control loop with the average brightness of a region of interest (ROI) or of the overall scene. The advantage of this mode is most apparent during twilight and in foggy conditions when the illumination of the scene varies strongly in time. Using dynamically controlled exposure time, one obtains a time series of frames, which can be normalized to their respective exposure times (which are stored in a data file by the program) so as to continually exploit the full dynamic range of the camera. We also implement a so-called cumulative grab mode (CGM) to avoid recording the 100 Hz intensity fluctuations due to the 50 Hz modulation of the electrical supply network. This mode is automatically activated for exposures smaller than 10 ms, that is, when the source blinking becomes apparent. Under CGM mode, a frame having maximum gray-level value of the source pixel is chosen from a sample of N_{CGM} frames where N_{CGM} depends on the exposure time T_{exp} in milliseconds as $N_{\mathrm{CGM}} = 20\ (\mathrm{ms})/T_{\mathrm{exp}}$. The program also displays the calculated OSC of the source pixel in real time and allows for compensation of the ambient light contribution, in which case the OSC reads

$$\mathrm{OSC}_A = \frac{(I^s_{\parallel} - I^a_{\parallel}) - (I^s_{\perp} - I^a_{\perp})}{(I^s_{\parallel} - I^a_{\parallel}) + (I^s_{\perp} - I^a_{\perp})}. \tag{3}$$

In Eq. (3), $I^s_{\parallel}$ (respectively $I^s_{\perp}$) denotes the average intensity over a 3 × 3 pixels area enclosing the pixel corresponding to the source location (source pixel) in $I_{\parallel}$ (respectively $I_{\perp}$). On the other hand, $I^a_{\parallel}$ (respectively $I^a_{\perp}$) estimates the ambient illumination by averaging a 3 × 3 pixels area in the vicinity of the source pixel but strictly distinct from the source spatial extent. With such definition, the OSC is computed taking into account intensity measures $I^a_{\parallel}$ and $I^a_{\perp}$ of a reference area close to the source representing the ambient illumination.

Using such control software with AEM allows us to acquire images at predefined intervals over long periods of time with strongly varying illumination conditions (i.e., clear sky, obstructed vision, daytime/nighttime and twilight).

4. Experiment Calibration

In this section, we first describe the camera calibration and image registration procedures which have to be implemented so as to provide reliable polarimetric images and measurements. Then, we report some experimental results which allowed us to validate the experimental system (emission and acquisition) and laboratory calibration on real field conditions.

A. Imaging Setup Calibration

The frames obtained in the experiment described above are binary values obtained from the camera. Processing of the frames to extract the images is at this step carried out in a post-acquisition stage. The post-processing includes fixed pattern dark frame subtraction, pixel nonuniformity correction, image registration and optical distortion correction. The latter processing steps are organized in the following manner.

1. *Detector Calibration*

For a camera sensor there are mainly three calibrations to be performed in order to record an image that closely corresponds to the scene being imaged, namely dark pattern calibration, nonuniformity of pixel gain, and removal of hot and dead pixels. Each pixel has different dark noise properties at a particular temperature and exposure time. After averaging over a number of dark frames acquired in total darkness, one obtains the fixed pattern dark frame (I_{FPD}) that can be subtracted from the images of interest. It must be noted that this correction depends on the exposure time. We thus averaged 500 dark frames to obtain the I_{FPD} for different exposure times. Another important correction to be made is the nonuniformity in pixel gain. Owing to the fabrication process, each pixel in the sensor may not have the same sensitivity/gain. This nonuniformity is estimated by illuminating the sensor with spatially uniform white light and recording the resulting pattern. This image is normalized by dividing by the mean gray level to create a gain nonuniformity image I_{GNU}. Using the above two calibration images, a raw image recorded is systematically corrected using $I_{\mathrm{corr}} = (I_{\mathrm{raw}} - I_{\mathrm{FPD}})/I_{\mathrm{GNU}}$.

2. *Image Registration and Distortion Calibration*

Once the above calibrations and corrections are performed on the bare detector itself (without any image forming optics), the polarimetric optical imaging system is mounted. When the system is assembled and images are recorded, one has to extract the two images corresponding to orthogonal polarization directions from a single frame. It is required that the two extracted images have a one-to-one correspondence between pixels such that they map the same scene. This process is straightforward if there is no geometrical distortion or if both the images share the same geometrical distortion. However, the WP used in the polarimetric imaging setup does introduce astigmatism and anamorphic distortion in the resulting images [31]. The distortion is nonsymmetrical with respect to the two image channels, and hence a perfect image registration is not possible by merely translating one of the image to match the other. The difference in distortion in the two images can be reduced by a nonlinear coordinates transformation on $I_{\perp}$ to match the distortion in $I_{\parallel}$.

To perform such corrections, a grid of equally spaced dots (printed black dots on white paper with no specific polarization orientation) was imaged through the system, and the acquired images were used to calibrate the two image registration methods, namely simple translation and nonlinear coordinates transformation. The correction by translation was obtained by a maximum correlation technique where one of the image channels, say $I_{\perp}$, was translated in the x and y directions over 21×21 pixels, and correlation values with $I_{\parallel}$ were recorded for each translation position. Then, a best match was found by looking for the maximum correlation value and translating $I_{\perp}$ accordingly. The inset in Fig. 3 shows the correlation map, and Fig. 3(b) shows the difference image $I_{\Delta} = I_{\parallel} - I_{\perp}$ after correction by translation. This shows a great improvement in comparison to uncorrected images [Fig. 3(a)], but it can be observed that pixel registration is imperfect in the outer regions of the image.

Therefore, to digitally remove the residual mismatch caused by the nonsymmetrical aberrations in both channels, we resort to a nonlinear coordinates transformation on the pixels of image $I_{\perp}$ to match the distortion in $I_{\parallel}$. This is performed by extracting the coordinates of the centroids of the dots in two thresholded polarimetric images and finding the coefficients of a two-dimensional polynomial of degree 3 for the x–y coordinates transformation. The coefficients of the polynomial are found using a least squares optimization procedure. A polynomial of degree 3 has been found to be sufficient to describe the nonlinear transformation as the higher order coefficients of the polynomial are negligible compared

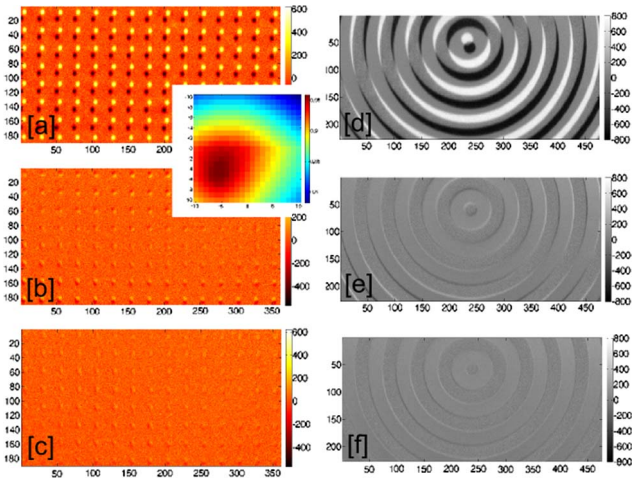

Fig. 3. Difference image ($I_{\parallel} - I_{\perp}$) of the calibration target (grid of dots) (left) and test object (right). The top images correspond to the difference images formed with approximate extraction of the two image channels. The middle row is the result of image registration correction by pixel linear translation, and the bottom row corresponds to the difference images created after applying the distortion correction algorithm. The inset shows the correlation map obtained by translating the $I_{\perp}$ over 21×21 pixels and finding maximum correlation with $I_{\parallel}$.

to the lower order coefficients. By applying this nonlinear coordinates transformation to the pixels of $I_{\perp}$, we obtain a distorted version of the latter, which now shares the same geometrical distortions as $I_{\parallel}$. For further processing of the polarimetric images, it is lastly necessary to resample the resulting image on the same regular (square) set of pixels locations as $I_{\parallel}$, which is done by a Matlab implementation of a standard bicubic interpolation algorithm. The result of this geometrical correction procedure can be observed in the difference image after correction given in Fig. 3(c).

A comparison of the effectiveness of the calibration and of the image registration using simple translation and nonlinear correction is given in Figs. 3(d)–3(f) on a test object (plain white paper with circular pattern in black). In comparison to approximate extraction [Fig. 3(d)], simple translation allows for a reduction by 63% of the span of extreme values in the difference image [Fig. 3(e)], whereas with the nonlinear distortion correction, a further reduction by 30% is obtained [Fig. 3(f)].

It must be noted that the nonlinear correction method is computationally slower than finding linear translation parameters by the maximum correlation method. The calculation of parameters for nonlinear correction is a one-time calibration procedure that takes about a minute for completion on a standard computer (Matlab on 2.60 GHz processor). This time is acceptable even though it is 25 times slower than finding the maximum correlation in a small neighborhood of 21×21 pixels. However, the computational time required to correct each frame becomes very stringent for real-time applications. In this case, the simple translation is four orders of magnitude faster than the nonlinear correction, which takes about 2 s to process because of interpolation of a large number of pixel values. As a consequence, for applications requiring high processing speed and where only a small region of the image is of interest, it is sufficient to use only linear translation. Thus, in the remainder of this article, as we shall consider a small ROI around the source location, we will limit ourselves to simple translation registrations for the sake of computational effectiveness on long time series experiments.

3. *Intensity Asymmetry*

It is important to take note of any transmission asymmetry in the two image channels introduced by the WP. In our case a 2.7% asymmetry in intensity was observed after imaging a uniformly illuminated depolarizing object (plain white paper observed with different orientations) through the system. The measured average intensity ratio ($I_{\parallel}/I_{\perp} = 1.027$) was used to correct this asymmetry. This ratio was seen to be constant over a large central region including the ROI.

B. *In Situ* Verification

Along with the above calibration procedures, further alignment of the detection system with the polarization direction of the source is done while mounting the detection system. The polarimetric camera setup and the control/acquisition computer are settled in a mezzanine floor of a building facing the telecommunication tower. It has first been checked that the spread of the light source was close to our expectancies (1×1 pixel with the selected 50 mm focal length objective lens), with an actual horizontal spread of 1.5 pixels and vertical spread of about 2 pixels. The main discrepancy in the vertical direction is due to the influence of the WP.

The whole setup is placed on a stable mechanical mount with adjustable angle (pitch) so that the imaging system can be aligned in line of sight with the source on the tower. In addition, the tilt angle (roll) must be well aligned so that the polarization axis of the imager is strictly aligned with the polarization direction of the source. This calibration is preferably done during nighttime in clear sky with the polarized lightmark turned on. It is indeed easier to minimize and even nullify the intensity at the source location in the perpendicular polarization image ($I_{\perp}$) in dark background. After such calibration, we observed an OSC of 0.97 for the source pixel which increased to a value of 1.00 when OSC was computed taking into account the low intensity background contribution, as in Eq. (3).

During these preliminary calibration acquisitions, it was checked on the acquired frames that the daytime clear sky is polarized to some extent, depending on sun location, and that the ambient light backscattered on the tower structures and imaged on the camera can partly retain polarization. However, we observed that the imaged scene is almost totally depolarized as soon as a thin layer of fog or haze is present in the atmosphere or when the weather is covered by (even very thin) clouds. As a result, the difference image of the two image channels is expected to provide an obvious advantage over intensity imaging due to its ability to cancel the unpolarized background and isolate the polarized source.

5. Experimental Results: Signal Contrast in Foggy Condition

Once the imaging system described in previous sections was settled, optimized, and calibrated, and using the above-mentioned control program, we were able to acquire numerous series of frames of the source at different times of the day (dawn, daytime, dusk, nigthtime) with varying atmospheric conditions (clear sky, thin haze, fog, cloud, rain, snow, etc.). The corresponding time series acquisitions were recorded during years 2011 and 2012 with various time periods (10 images/min to 6 images/h) over long time spans of several hours or tens of hours.

During these long-term acquisitions, the dynamically varying exposure time in AEM was recorded for each acquisition, and the frames were normalized to their respective exposure times during postacquisition analysis. From each raw frame, we then extracted the two subimages $I_{\parallel}^{j}$ and $I_{\perp}^{j}$ (with j

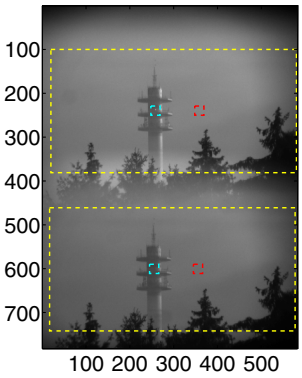

Fig. 4. Raw image obtained from the camera with 782 × 582 pixels. Extraction of two image channels after applying image registration process is demarcated in the yellow dashed box. The ambient illumination is obtained by averaging over the region shown in red-dashed lines, and the region shown in blue dashed lines is the 21 × 21 pixel ROI that includes the source at its center.

corresponding to the jth image in the time series). One raw image extracted from a time series is represented in Fig. 4, with an overlay indicating the image registration (rectangles in yellow) from which ROIs corresponding to $I_{\parallel}^{j}$ and $I_{\perp}^{j}$ are extracted. The example of ROI shown in light blue in Fig. 4 is a 21 × 21 pixels rectangle surrounding the source location.

A. Principle of the Measurement

These numerous acquisitions were used to gauge the effectiveness of polarimetric imaging under various atmospheric conditions. The analysis of the experimental results led us to retain four main different scenarios, associating clear sky/foggy conditions and daytime/nighttime. The conditions in daytime with fog are indeed such that the intensity of the pixels around the source are nearly uniform, making it difficult to identify the source from the background in a simple intensity image. In clear sky conditions, the background consists of the telecommunication tower structures and installations. On the other hand, in nighttime we have conditions where the source is brighter and the background is dark with unpolarized and localized bright light sources (for instance, the red aircraft warning lights on the tower) or sometimes, during heavy fog, a uniformly lit background because of scattering of city lights.

In all these conditions, we are interested in maximizing the visual contrast of the source with respect to its background. Polarimetric imaging provides us with two data sets ($I_{\parallel}$ and $I_{\perp}$) for the same image and thus allows us to create various representations of the image with different visual contrasts. We thus propose to consider four simple *signal representations* of the available data, generally referred to as γ, and compare their visual contrast under various environmental conditions. These four signal representations correspond to a simple intensity image (γ_I), a polarimetric difference image (γ_Δ), the OSC image (γ_{OSC}), and a polarimetric ratio image (γ_{ratio}) and are given in Table 1, along with their respective symbols and mathematical definitions.

Table 1. Signal Representations of Polarimetric Data, with $\langle\rangle_{\chi_k}$ Denoting Spatial Averaging over a Square Neighborhood χ_k of the Central Pixel of Size N_k Pixels

Signal Representation	Symbol	Definition
Intensity	γ_I	$I_{\parallel} + I_{\perp}$
Polarimetric difference	γ_Δ	$I_{\parallel} - I_{\perp}$
OSC	γ_{OSC}	$\frac{I_{\parallel}-I_{\perp}}{I_{\parallel}+I_{\perp}}$
Polarimetric ratio	γ_{ratio}	$\frac{I_{\parallel}}{\langle I_{\perp}\rangle_{\chi_k}}$

It is obviously seen that the absolute values of these signal representations are different. However, we will be interested in the remainder of this section in comparing the visual contrast of the polarized source that can be obtained with these different representations. We must therefore provide a fair comparison between the contrasts obtained in different representations. For this purpose we define a contrast-to-noise ratio (CNR) such that the CNR value is insensitive to the scale of these four representations. The CNR is defined for a central pixel denoted s (signal γ_s) with respect to its surrounding square neighborhood χ_k of size N_k pixels as

$$\mathrm{CNR} = \frac{\gamma_s - \langle\gamma\rangle_{\chi_k}}{\sqrt{\frac{1}{N_k - 1}\sum_{i\in\chi_k}\left(\gamma_i - \langle\gamma\rangle_{\chi_k}\right)^2}}, \tag{4}$$

where $\langle\gamma\rangle_{\chi_k} = \sum_{i=1}^{N_k}\gamma_i/N_k$ is the spatial average over χ_k. It must be noted that the evaluation of the spatial averages is carried out for a sample of pixels defined by the region χ_k that excludes the 2 × 2 central region centered on the source pixel to prevent the spatial extent of the light source from perturbing computation of the background statistical properties. With the above definition, the CNR is basically the measure of how many standard deviations away the signal pixel lies from the distribution of its surrounding pixels. The CNR values computed on the data provide a more quantitative evaluation of the contrast than a visual analysis of the polarimetric images plotted in subsequent figures. Moreover, in an applicative context, the CNR would be directly linked to the performance of automated detection of polarized sources of unknown number and locations in a scene. In the presence of a structured background and/or unpolarized spurious sources, a high CNR would warrant good detection probability along with low false alarm rate.

In the following subsections, we provide a thorough data analysis performed on two particular time-series acquisitions, allowing one to observe clear sky and foggy conditions in daytime (Section 5.B) and nighttime (Section 5.C). These two experimental data series are representative of the wide variability of environmental conditions that were made possible to address with the experimental facility described in this article.

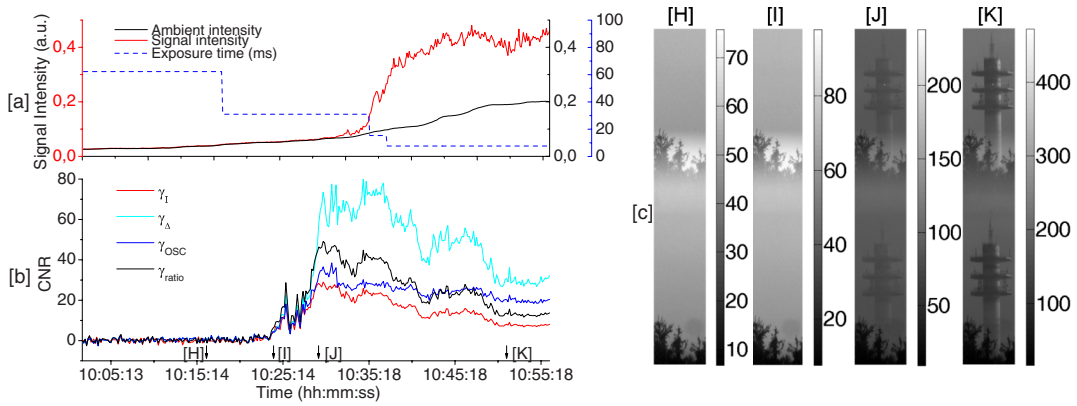

Fig. 5. (a) Time evolution of the source (signal) intensity, ambient intensity, and camera exposure time across daytime experiment. (b) Time evolution of the CNR of four polarimetric signal representations. (c) Raw images of four frames labeled H, I, J, and K, corresponding to various visibility conditions across daytime experiments.

B. Daytime Measurement

This first data acquisition series that we will focus on has been recorded on October 17, 2011, between 10:02 a.m. and 10:57 a.m. During this 55 min acquisition, an image has been recorded every 10 s, making it possible to observe rapid rising of a thick fog and evolution of its density within a period of 30 min. The evolution of the experimental conditions can be observed in Fig. 5. In Fig. 5(a), the intensity of the pixel corresponding to the location of the polarized source (signal pixel) is plotted as the red curve as a function of time. In addition, the evolution of the ambient intensity is represented by the black curve. This quantity was estimated from a spatial averaging of the total intensity $I = I_{\parallel} + I_{\perp}$ in a homogeneous 21×21 pixels sky region, marked in Fig. 4 with a red square. The camera exposure time during the whole experiment was controlled by the software in AEM so as to prevent underexposure or saturation of the signal pixel. The evolution of the exposure time is also provided in Fig. 5(a) by the dotted blue curve, revealing the smooth evolution of the fog density and background illumination during the experiment.

Across this experimental dataset (330 images), four instants will be considered, labeled H, I, J, and K in Fig. 5(b). The corresponding raw images acquired by the imager are, respectively, plotted in Fig. 5(c). They correspond to different interesting situations of visibility of the source through fog. The first situation H corresponds to high fog density where the source is completely embedded in the background illumination, as can be checked in Fig. 5(a) by comparing the levels of the signal and background intensities. Acquisition I is the first image recorded on which the light source begins to be detectable over the background. Then, acquisition J corresponds to an intermediate situation of a light haze limiting the visibility of the source, whereas the last measurement K has been acquired in clear sky but with a significantly higher background illumination than in the J situation.

Let us now analyze the CNRs associated with the four signal representations considered in this article and defined in Table 1. The evolution of the CNRs across the whole dataset is given in Fig. 5(b). In Fig. 6, we also provide the contrast images computed for each signal representation and for each situation H through K on a 21×21 pixels neighborhood of the central signal pixel. The numerical values indicated in Fig. 6 correspond to the CNR of the central pixel estimated on this neighborhood. As can be seen from these results, the source is hidden behind heavy fog until 10:13 a.m., and all CNR values remain close to zero in this situation. It can be indeed checked in Fig. 6 that the source is not distinguishable on any of the four signal representations studied.

Measurements performed after 10:13 a.m. are more interesting. Indeed, they first allowed us to observe that, as soon as the light emitted by the source is visible over the background, it retains a very high

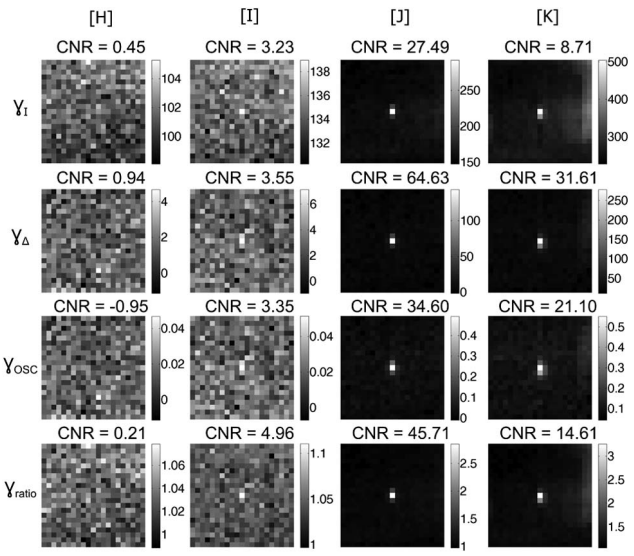

Fig. 6. CNR images of the 21×21 ROI around the polarized light source, extracted at times indicated by H, I, J, and K in Fig. 5. Rows 1 to 4 correspond to the CNR obtained with intensity image, difference image, OSC image, and contrast ratio image, respectively. The corresponding CNRs for the central source pixel are also given as numerical figures for comparison.

polarization degree, with no detectable depolarization induced by turbid atmosphere nor partially depolarized halo in the vicinity of the source location. Following a similar interpretation as in prior laboratory experiments [12–17] on short distances, this result can be understood by considering properties of Mie scattering on large particle size in fog droplets [16,32]. In our case, since we are working at a very long distance, the light emitted by the source can be almost totally absorbed by a thin fog, which in return cannot be considered as a strongly diffusive medium and hence cannot induce strong depolarization. In addition, the low numerical aperture of the imaging system at such a distance acts as a spatial filter [6,7], thus preventing most of the scattered and snake photons (slightly scattered) from entering the imaging system.

Then, the results given in Figs. 5 and 6 reveal that, as soon as the intensity coming from the source is detectable, all polarimetric signal representations (γ_Δ, γ_{OSC}, and γ_{ratio}) provide CNR values significantly higher than the CNR obtained with a standard nonpolarimetric intensity measurement (γ_I). This general result thus confirms the interest of polarimetric measurements for enhanced vision through poor visibility conditions. The analysis can be however refined so as to identify the best signal representation in a given situation. In very low visibility conditions (acquisition I), it appears that γ_{ratio} gives the best improvement in terms of CNR (60% increase) with respect to an intensity measurement γ_I.

On the other hand, when visibility increases, the best signal representation corresponds to a difference image γ_Δ, allowing the CNR to be enhanced up to a factor of almost 4 (acquisition K). The efficiency of the difference image is due to its ability to suppress the background contribution. This enhancement is either due to diffused light in the turbid atmosphere, as in acquisition J, or due to the surrounding scene, as in acquisition K, on which elements of the telecommunication tower can be identified on the intensity image. Indeed, as has been noticed in Section 4.B, the ambient light does not exhibit noticeable polarization as soon as the sky is covered by clouds or when a thin layer of haze or fog is obscuring the atmosphere. Hence, the contributions of this ambient background on the two polarimetric images $I_\parallel$ and $I_\perp$ are strictly identical and can be suppressed on a difference image.

Lastly, it is interesting to note that γ_{OSC} never appears to be the best representation, contrary to anterior work on active polarimetric imaging [33,34] (where, due to the reflection geometry of imaging, the background has a significant polarized component). Indeed, in the present context of an active polarized source and passive totally unpolarized background, OSC implies a normalization of γ_Δ by the total intensity γ_I, which, on the dark background image γ_Δ obtained, increases the relative noise in the final image and thus decreases the CNR. In the next section, it will be shown that such normalization can be much more detrimental to signal quality in nighttime conditions. Therefore, this normalization must be avoided when it comes to locating or detecting a target in poor visibility conditions, unless one wants to assess the DOP of the light source.

C. Nighttime Measurement

A similar experiment was conducted during nighttime on October 14, 2011, between 1:53 a.m. and 7:17 a.m. During this 324 min acquisition, a raw frame has been recorded every minute. As in the previous section, the evolution of signal pixel and background intensities are plotted, respectively, in red and black curves in Fig. 7(a). The evolution of the exposure time over this long time period is given in Fig. 7(a) by the dotted blue curve (logarithmic scale). This curve shows the strong variations of the exposure time at night with atmospheric conditions, ranging from 7 ms to a maximum value of 4 s authorized by the camera used. From the observation of these curves, it can be noted that a dense fog cloud has totally obscured the visibility of the source between 3:40 a.m. and 4:55 a.m., leading to a maximum

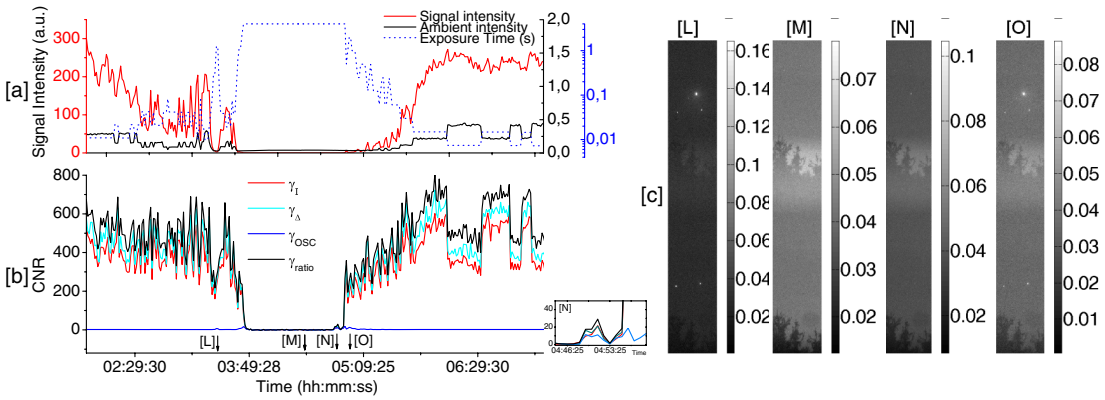

Fig. 7. Same as Fig. 5 for nighttime experiment. The inset shows a magnified part of the plot where the fog is thinning and the CNRs are comparable for all signal representations. Four frames labeled L, M, N, and O have been selected to be representative of visibility conditions during night experiments. The display dynamics in (c) has been expanded by a factor of 20 for all night situations so that the background becomes visible.

exposure time in total darkness, as in situation labeled M in Fig. 7. On the other hand, the beginning and end of the acquisition correspond to almost clear sky conditions (as in situations labeled L and O). The strong signal intensity variations observed in clear sky conditions are mainly due to atmospheric turbulence which causes flicker of the location of the signal pixel on the images and can also be partly due to an imperfect smoothing of the source intensity modulation at 100 Hz. In the conditions of the experiment, one other situation labeled N has retained our attention since it corresponds to one of the rare instants of fog setting/rising in which the source is partly visible. The raw images corresponding to these four situations are also plotted in Fig. 7(c).

As in Fig. 5, the CNRs associated with the four signal representations are plotted in Fig. 7(a) across the whole dataset. The contrast images obtained at each particular situation analyzed, L, M, N, and O, are given in Fig. 8. These experimental results first confirm that OSC is not a relevant signal representation due to noise amplification occurring with normalization. The corresponding CNR is indeed always close to zero, and the noise amplification can be clearly observed in Fig. 8. This effect is particularly enhanced in night conditions since background values are very close to or equal to zero [since the exposure time is limited in clear sky to prevent saturation of the source pixel; see Fig. 7(a)], thus leading to nonnumerical values in the final image, which are not taken into account in the computation of CNR.

The comparison of the three other signal representations considered in this paper is more informative. It can first be noted that between 3:40 a.m. and 4:55 a.m., none of the representations allows the source to be significantly detected over the background due to total absorption of the emitted light when propagating through dense fog. In clear sky conditions, however (situations L and O), or partially reduced visibility (situation N), it can be observed that the simple intensity image and polarimetric difference image share comparable CNR values. This confirms the fact that γ_Δ only outperforms a simple intensity image in the presence of significant background contribution, as observed above in daytime conditions. In nighttime conditions, the very dark background is strongly affected by camera dark noise, and a difference image could, in some configurations of noise realization, lead to a degradation of the CNR with respect to an intensity detector. Only the ratio representation γ_{ratio} allows improving the CNR values by a factor comprised between 10% and 35%, which can be explained by the noise reduction induced by the spatial averaging of the background in the expression of γ_{ratio}.

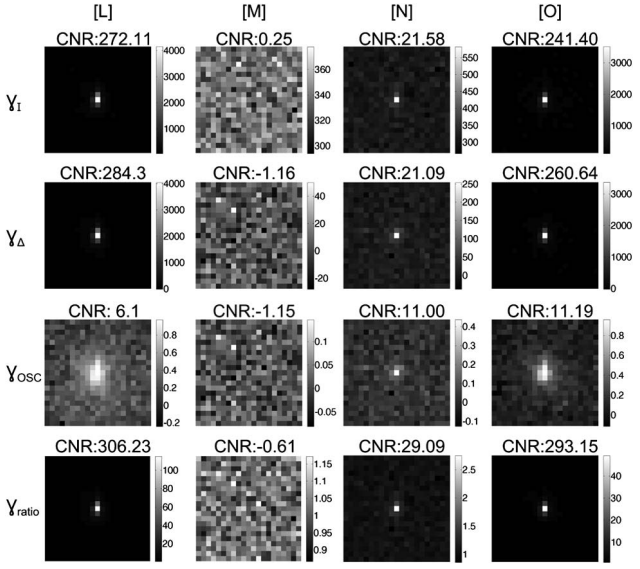

Fig. 8. Same as Fig. 6 for nighttime experiments. The OSC image is observed to be noisy and has the least signal contrast as a result.

These results, which seem to soften the interest of polarimetric imaging for vision enhancement through turbid atmosphere in night conditions, actually reveal the limitations of the sensor used for these experiments. These nocturnal acquisitions indeed allow us to identify two ways of improvement for our detection system, which are (1) the minimization of the dark noise and most importantly (2) the increase in detector dynamics. Reducing the dark noise would limit the level of noise in the dark background in nighttime conditions for polarimetric signal representations, as stated above. Moreover, it can be observed in Fig. 7(b) that between 6:00 a.m. and 7:10 a.m., strong variations in all the CNR values occur, following the same abrupt "steps" at each modification of the exposure time. This is a confirmation that in these situations, the dark image background is perturbed with camera dark noise. Usually, the dark noise level increases with the acquisition time. However, the Basler A312f camera used implements a Sony ICX 415AL sensor, whose hole-accumulation diode technology makes it possible to inhibit the increase of dark noise level with integration time. As a result, the noise contribution is thus artificially doubled in our measurements relatively to the signal pixel value when exposure time is divided by two, hence leading to a strong decrease in terms of CNR. This also confirms that adapting the exposure time cannot increase the dynamics of a detector when the illumination variations across the scene exceed the actual sensor dynamics. It would thus be highly beneficial to use a high dynamics sensor to improve these results and potentially increase the range of environmental conditions for which polarimetric imaging could be advantageous for vision enhancement through turbid atmosphere over long distances.

6. Conclusion

In this paper, we have reported an experimental setup allowing us to perform snapshot polarimetric contrast imaging of a light emitter through turbid atmosphere over kilometric distances. With this setup it has been possible to acquire long time series of measurements in various real environmental

conditions of weather and visibility. The results reported in the article have permitted us to assess the benefits of using a polarized light source and a polarization-sensitive camera to increase visual contrast or detectability of such a light source in degraded visibility conditions and at a distance compatible with potential applications, such as navigation assistance for airborne, maritime, or terrestrial transportation. It can be concluded from these results that for the purpose of detecting a polarized source embedded in an unpolarized background, using polarized beacons and polarimetric cameras can lead to a significant improvement of the contrast. This is particularly true in the presence of high background illumination levels, which are likely to occur in daytime conditions, or in nighttime situations, due to scattering of unpolarized ambient light by the atmosphere itself. This is indeed beneficial, as computing a simple polarization-difference image would make it possible to isolate the target from ambient light and hence provide higher contrast in foggy situations in real time.

Another result of this article is that no significant depolarization of the polarized source nor depolarized halo could be detected during propagation through fog over a kilometer with a standard dynamics camera such as the one used in this experiment. This observation, unreported to our best knowledge at a kilometric distance, thus confirms the interest of conducting such experiments in real-field conditions over long distances. This behavior, similar to the one observed in short distance laboratory experiments, was not an entirely predictable result. It is indeed difficult to mimic the physical conditions that were encountered during these experiments with in-laboratory short distance measurements using highly diffusive water or gas tanks.

As a perspective to this work, we are currently implementing in our setup a new camera with a higher dynamics range and lower noise level so as to refine the first analyses presented in this article. Such a camera will make it possible to analyze situations in which observations were limited by the detector itself. More importantly, it is also expected that a high dynamics sensor will increase the range of application of polarimetric imaging in terms of visibility distance for beacon detection or localization in turbid atmosphere. Other important perspectives to this work can be enumerated, among which is the definition of clear figures of merit that link image contrast ratios with visibility range. Another important field of research that will be addressed is the definition of optimal signal representation as a function of environmental or instrumental conditions for various image processing tasks, such as estimation or detection. Recent results have evidenced the potential of polarimetric imaging contrast when relevant statistical parameters, such as partial correlation between measurements, are considered [35]. Applying these theoretical results to experimental data will necessitate a more thorough analysis of the images in terms of statistical properties, which will also be enabled with the use of a better camera. Then, the implementation of these optimal estimators/detectors on field-programmable gate array (FPGA) boards for in-line real-time image processing and display is also an interesting perspective to this work.

The authors are grateful to the TDF company, and in particular to A. Lecluse and P. Gelebart, for providing a location for the emitter on the telecommunication tower. This work has been partly funded by the CEFIPRA (project no. 4604-4).

References

1. S. Andersson-Engels, R. Berg, S. Svanberg, and O. Jarlman, "Time-resolved transillumination for medical diagnostics," Opt. Lett. **15**, 1179–1181 (1990).
2. N. Zeng, X. Jiang, Q. Gao, Y. He, and H. Ma, "Linear polarization difference imaging and its potential applications," Appl. Opt. **48**, 6734–6739 (2009).
3. M. Dubreuil, P. Delrot, I. Leonard, A. Alfalou, C. Brosseau, and A. Dogariu, "Exploring underwater target detection by imaging polarimetry and correlation techniques," Appl. Opt. **52**, 997–1005 (2013).
4. W. R. Watkins, D. H. Tofsted, V. G. CuQlock-Knopp, J. B. Jordan, and J. O. Merritt, "Navigation through fog using stereoscopic active imaging," Proc. SPIE **4023**, 20–28 (2000).
5. L. Wang, P. Ho, C. Liu, G. Zhang, and R. Alfano, "Ballistic 2-d imaging through scattering walls using an ultrafast optical Kerr gate," Science **253**, 769–771 (1991).
6. Q. Z. Wang, X. Liang, L. Wang, P. P. Ho, and R. R. Alfano, "Fourier spatial filter acts as a temporal gate for light propagating through a turbid medium," Opt. Lett. **20**, 1498–1500 (1995).
7. E. Leith, B. Hoover, S. Grannell, K. Mills, H. Chen, and D. Dilworth, "Realization of time gating by use of spatial filtering," Appl. Opt. **38**, 1370–1376 (1999).
8. M. Oleary, D. Boas, B. Chance, and A. Yodh, "Refraction of diffuse photon density waves," Phys. Rev. Lett. **69**, 2658–2661 (1992).
9. L. Mullen, A. Laux, B. Concannon, E. P. Zege, I. L. Katsev, and A. S. Prikhach, "Amplitude-modulated laser imager," Appl. Opt. **43**, 3874–3892 (2004).
10. E. Lacot, R. Day, and F. Stoeckel, "Laser optical feedback tomography," Opt. Lett. **24**, 744–746 (1999).
11. E. Belin and V. Boucher, "An imaging system based on laser optical feedback for fog vision applications," Proc. SPIE **7088**, 70880N (2008).
12. J. Schmitt, A. Gandjbakhche, and R. Bonner, "Use of polarized light to discriminate short-path photons in a multiply scattering medium," Appl. Opt. **31**, 6535–6546 (1992).
13. H. Horinaka, K. Hashimoto, K. Wada, Y. Cho, and M. Osawa, "Extraction of quasi-straightforward-propagating photons from diffused light transmitting through a scattering medium by polarization modulation," Opt. Lett. **20**, 1501–1503 (1995).
14. O. Emile, F. Bretenaker, and A. Floch, "Rotating polarization imaging in turbid media," Opt. Lett. **21**, 1706–1708 (1996).
15. H. Ramachandran and A. Narayanan, "Two-dimensional imaging through turbid media using a continuous wave light source," Opt. Commun. **154**, 255–260 (1998).
16. S. Mujumdar and H. Ramachandran, "Imaging through turbid media using polarization modulation: dependence on scattering anisotropy," Opt. Commun. **241**, 1–9 (2004).
17. J. S. Ryan and A. I. Carswell, "Laser beam broadening and depolarization in dense fogs," J. Opt. Soc. Am. **68**, 900–908 (1978).
18. M. Xu and R. Alfano, "Circular polarization memory of light," Phys. Rev. E **72**, 065601 (2005).
19. R. Nothdurft and G. Yao, "Applying the polarization memory effect in polarization-gated subsurface imaging," Opt. Express **14**, 4656–4661 (2006).

20. J. A. Garland, "Some fog droplet size distributions obtained by an impaction method," Q. J. Roy. Meteor. Soc. **97**, 483–494 (1971).
21. M. Hayman, S. Spuler, B. Morley, and J. VanAndel, "Polarization lidar operation for measuring backscatter phase matrices of oriented scatterers," Opt. Express **20**, 29553–29567 (2012).
22. S. Demos and R. Alfano, "Optical polarization imaging," Appl. Opt. **36**, 150–155 (1997).
23. P. Terrier, V. Devlaminck, and J. Charbois, "Segmentation of rough surfaces using a polarization imaging system," J. Opt. Soc. Am. A **25**, 423–430 (2008).
24. O. Morel, C. Stolz, F. Meriaudeau, and P. Gorria, "Active lighting applied to three-dimensional reconstruction of specular metallic surfaces by polarization imaging," Appl. Opt. **45**, 4062–4068 (2006).
25. M. Yamada, K. Ueda, I. Horiba, and N. Sugie, "Discrimination of the road condition toward understanding of vehicle driving environments," IEEE Trans. Intell. Transp. Syst. **2**, 26–31 (2001).
26. A. Bénière, M. Alouini, F. Goudail, and D. Dolfi, "Design and experimental validation of a snapshot polarization contrast imager," Appl. Opt. **48**, 5764–5773 (2009).
27. H. Luo, K. Oka, D. Edward, M. Kudenov, J. Schiewgerling, and E. Dereniak, "Compact and miniature snapshot imaging polarimeter," Appl. Opt. **47**, 4413–4417 (2008).
28. M. W. Kudenov, M. J. Escuti, N. Hagen, E. L. Dereniak, and K. Oka, "Snapshot imaging Mueller matrix polarimeter using polarization gratings," Opt. Lett. **37**, 1367–1369 (2012).
29. S. Alali, T. Yang, and I. Vitkin, "Rapid time-gated polarimetric Stokes imaging using photoelastic modulators," Opt. Lett. **38**, 2997–3000 (2013).
30. V. Gruev, R. Perkins, and T. York, "CCD polarization imaging sensor with aluminum nanowire optical filters," Opt. Express **18**, 19087–19094 (2010).
31. M. C. Simon, "Wollaston prism with large split angle," Appl. Opt. **25**, 369–376 (1986).
32. D. Bicout, C. Brosseau, A. Martinez, and J. Schmitt, "Depolarization of multiply scattered waves by spherical diffusers: influence of the size parameter," Phys. Rev. E **49**, 1767–1770 (1994).
33. M. Alouini, F. Goudail, N. Roux, L. Le Hors, P. Hartemann, S. Breugnot, and D. Dolfi, "Active spectro-polarimetric imaging: signature modeling, imaging demonstrator and target detection," Eur. Phys. J. Appl. Phys. **42**, 129–139 (2008).
34. A. Bénière, F. Goudail, D. Dolfi, and M. Alouini, "Target detection in active polarization images perturbed with additive noise and illumination nonuniformity," J. Opt. Soc. Am. A **26**, 1678–1686 (2009).
35. J. Fade, S. Panigrahi, and M. Alouini, "Optimal estimation in polarimetric imaging in the presence of correlated noise fluctuations," Opt. Express **22**, 4920–4931 (2014).

Optimal estimation in polarimetric imaging in the presence of correlated noise fluctuations

Julien Fade,* Swapnesh Panigrahi, and Mehdi Alouini

Institut de Physique de Rennes, Université de Rennes 1, CNRS, Campus de Beaulieu, 35042 Rennes, France

*julien.fade@univ-rennes1.fr

Abstract: We quantitatively analyze how a polarization-sensitive imager can overcome the precision of a standard intensity camera when estimating a parameter on a polarized source over an intense background. We show that the gain is maximized when the two polarimetric channels are perturbed with significantly correlated noise fluctuations. An optimal estimator is derived and compared to standard intensity and polarimetric estimators.

OCIS codes: (110.5405) Polarimetric imaging; (110.4280) Noise in imaging systems; (110.3055) Information theoretical analysis; (030.6600) Statistical optics; (110.0113) Imaging through turbid media.

References and links

1. M. P. Rowe, J. S. Tyo, N. Engheta, and E. N. Pugh, "Polarization-difference imaging: a biologically inspired techniquefor observation through scattering media," Opt. Lett. **20**, 608–610 (1995).
2. S. Demos, H. Savage, A. S. Heerdt, S. Schantz, and R. Alfano, "Time resolved degree of polarization for human breast tissue," Opt. Commun. **124**, 439–442 (1996).
3. O. Emile, F. Bretenaker, and A. L. Floch, "Rotating polarization imaging in turbid media," Opt. Lett. **21**, 1706–1708 (1996).
4. H. Ramachandran and A. Narayanan, "Two-dimensional imaging through turbid media using a continuous wave light source," Opt. Commun. **154**, 255–260 (1998).
5. J. Guan and J. Zhu, "Target detection in turbid medium using polarization-based range-gated technology," Opt. Express **21**, 14152–14158 (2013).
6. G. D. Lewis, D. L. Jordan, and P. J. Roberts, "Backscattering target detection in a turbid medium by polarization discrimination," Appl. Opt. **38**, 3937–3944 (1999).
7. P. Réfrégier, M. Roche, and F. Goudail, "Cramer-Rao lower bound for the estimation of the degree of polarization in active coherent imagery at low photon levels," Opt. Lett. **31**, 3565–3567 (2006).
8. A. Bénière, F. Goudail, M. Alouini, and D. Dolfi, "Degree of polarization estimation in the presence of nonuniform illumination and additive gaussian noise," J. Opt. Soc. Am. A **25**, 919–929 (2008).
9. M. Boffety, F. Galland, and A.-G. Allais, "Influence of polarization filtering on image registration precision in underwater conditions," Opt. Lett. **37**, 3273–3275 (2012).
10. M. Dubreuil, P. Delrot, I. Leonard, A. Alfalou, C. Brosseau, and A. Dogariu, "Exploring underwater target detection by imaging polarimetry and correlation techniques," Appl. Opt. **52**, 997–1005 (2013).
11. A. Bénière, M. Alouini, F. Goudail, and D. Dolfi, "Design and experimental validation of a snapshot polarization contrast imager," Appl. Opt. **48**, 5764–5773 (2009).
12. N. Hautiere and D. Aubert, "Contrast restoration of foggy images through use of an onboard camera," in *Proceedings of 2005 IEEE Intelligent Transportation Systems* (2005), pp 601–606.
13. N. Gracias, S. Negahdaripour, L. Neumann, R. Prados, and R. Garcia, "A motion compensated filtering approach to remove sunlight flicker in shallow water images," in *OCEANS 2008*, (2008), pp. 1–7.
14. M. Darecki, D. Stramski, and M. Sokólski, "Measurements of high-frequency light fluctuations induced by sea surface waves with an underwater porcupine radiometer system," J. Geophys. Res. **116**, C00H09 (2011).
15. F. A. Sadjadi and C. L. Chun, "Automatic detection of small objects from their infrared state-of-polarization vectors," Opt. Lett. **28**, 531–533 (2003).

#200923 - $15.00 USD Received 8 Nov 2013; revised 22 Dec 2013; accepted 23 Dec 2013; published 24 Feb 2014

16. B. Laude-Boulesteix, A. D. Martino, B. Drévillon, and L. Schwartz, "Mueller polarimetric imaging system with liquid crystals," Appl. Opt. **43**, 2824–2832 (2004).
17. J. Jaffe, "Computer modeling and the design of optimal underwater imaging systems," IEEE J. Oceanic Eng. **15**, 101–111 (1990).
18. P. Garthwaite, I. Jolliffe, and B. Jones, *Statistical Inference* (Prentice Hall, 1995).
19. J. Fade, N. Treps, C. Fabre, and P. Réfrégier, "Optimal precision of parameter estimation in images with local sub-Poissonian quantum fluctuations," Eur. Phys. J. D **50**, 215–227 (2008).

1. Introduction and posing of the problem

1.1. Introduction

Polarimetric-sensitive detectors (PSD) have long been implemented and have proved efficient in many application fields, such as biomedical imaging [1, 2], and vision/contrast enhancement through turbid media [3–5]. In this context, the benefits of polarimetric imaging have been thoroughly investigated by considering various imaging architectures and noise models [6–9]. However, the gain in measurement precision that can be reached when a PSD is used instead of a standard intensity detector (ID), in the presence of significantly correlated noise fluctuations in each polarimetric channel, is still unexplored to the best of our knowledge. Indeed, for practical reasons it is usually assumed that these noise fluctuations are uncorrelated. As a result, considering the most favorable situation of a perfectly polarized source (or polarizing object) embedded in unpolarized background, the polarimetric channel which offers the best contrast is the one corresponding to the polarization state of the source. In this channel, the mean intensity level of the source is thus preserved, whereas that of the unpolarized background is reduced by a factor of two, leading to a doubling of contrast as compared to standard intensity detection [1, 10]. Nevertheless, the assumption of uncorrelated noise fluctuations is not representative of most real field scenarios especially when the polarimetric channels are acquired simultaneously [11]. For instance, a polarized source appearing through fog or haze is a situation where the background mean level is time-varying [12] especially when the imaging system is moving or vibrating. More generally, similar situations might be encountered when imaging objects through turbid media, as in the fields of underwater imaging [13, 14], or infrared target detection [15]. Imaging a static scene might also be subject to intensity fluctuations of the illuminating source, as often encountered in polarimetric microscopy [16]. Thus, one can wonder whether the noise correlation properties of the different polarimetric channels could be properly exploited in order to optimize, in terms of contrast, the representation of the polarimetric image.

In this article, we intend to rigorously quantify the gain in measurement precision that can be reached when a PSD is used in the presence of significantly correlated noise fluctuations in each polarimetric channel. This article is organized as follows: in the remainder of the first Section, we describe the general polarimetric image formation model addressed, as well as the correlated-noise statistical model considered throughout this article. Within the theoretical framework of information theory, the benefit of using PSD instead of a standard ID is then derived in Section 2, for a general estimation problem consisting in measuring a parameter (intensity, absorbance, location, etc.) on a polarized source over an intense background. The expression of this gain in optimal estimation precision is then thoroughly analyzed in Section 3 in relation with realistic experimental imaging conditions. Lastly, optimal estimation procedures are derived and discussed in Section 4, before providing conclusions of the article in Section 5.

#200923 - $15.00 USD Received 8 Nov 2013; revised 22 Dec 2013; accepted 23 Dec 2013; published 24 Feb 2014

1.2. Image formation model

We will consider a general framework consisting in the estimation of a given parameter (intensity, location, etc.) from a polarized signal contribution, denoted s_i at location i, with a degree of polarization (DOP) denoted by $P \in [0,1]$, which is either emitted by an active source or backscattered by an object of interest. Using a simple classical but realistic illumination model [9, 10, 17], the intensity X_i^I detected at location i is assumed to also comprise a background contribution b_i, with a DOP denoted by $\beta \in [0,1]$. This background contribution is due to ambient light scattering through a turbid medium (atmosphere, water, or biological tissue). For the sake of generality, we shall analyze any couple of polarization parameters P and β which can correspond to many different experimental conditions. Although in most experiments the signal contribution is highly polarized in comparison to an unpolarized background ($P \gg \beta$), some situations can involve opposite physical conditions ($\beta \gg P$), such as underwater imaging as mentioned in [10].

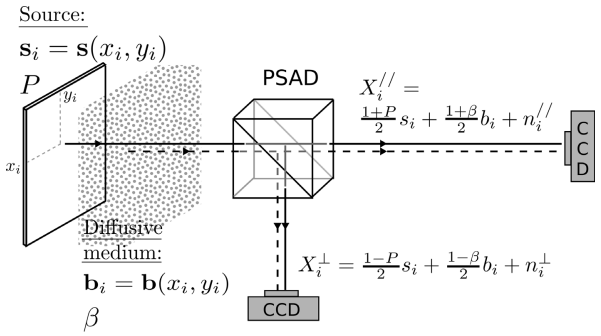

Fig. 1. Sketch of the image formation model: a polarization-splitting analyzing device (PSAD) can be any suitable birefringent crystal in case of simultaneous acquisitions of images $\mathbf{X}^{//}$ and $\mathbf{X}^{\perp}$ [11], or a rotating polarizer or liquid crystal device for sequential acquisitions. Image formation optics are not represented for the sake of clarity.

A non-polarimetric ID with N pixels gives access to a sample $\mathbf{X}_i^I = \{X_i^I\}_{i=1,\ldots,N}$, with $\langle X_i^I \rangle = s_i + b_i$, whereas a PSD provides a bidimensional vector $\mathbf{X}_i^P = \left[X_i^{//},\ X_i^{\perp}\right]^T$ at each location i of the detector, obtained from the intensities recorded along two orthogonal polarization directions [11], as sketched in Fig. 1. With the above illumination model, the average value of $\mathbf{X}_i^P$ is simply given by

$$\langle \mathbf{X}_i^P \rangle = \begin{bmatrix} \frac{1+P}{2} s_i + \frac{1+\beta}{2} b_i \\ \frac{1-P}{2} s_i + \frac{1-\beta}{2} b_i \end{bmatrix}. \tag{1}$$

1.3. Noise model

Throughout this article, we shall consider a Gaussian noise model, which makes it possible to take into account various sources of noise in realistic situations. In addition, such model provides closed-form expressions which is in favour of physical interpretation. At a given location i, the second order statistical properties of the bidimensional measurement vector $\mathbf{X}_i^P$ are modeled by a covariance matrix $\Gamma_i = \left\langle \delta\mathbf{X}_i^P \left(\delta\mathbf{X}_i^P\right)^T \right\rangle$, with $\delta\mathbf{X}_i^P = \mathbf{X}_i^P - \langle \mathbf{X}_i^P \rangle$, of the following form:

$$\Gamma_i = \begin{bmatrix} \sigma_{//,i}^2 & c_i \\ c_i & \sigma_{\perp,i}^2 \end{bmatrix} = \begin{bmatrix} \frac{1+\beta}{2}\varepsilon_i^2 + \sigma_0^2 & \rho\frac{\sqrt{1-\beta^2}}{2}\varepsilon_i^2 \\ \rho\frac{\sqrt{1-\beta^2}}{2}\varepsilon_i^2 & \frac{1-\beta}{2}\varepsilon_i^2 + \sigma_0^2 \end{bmatrix}.$$

#200923 - $15.00 USD Received 8 Nov 2013; revised 22 Dec 2013; accepted 23 Dec 2013; published 24 Feb 2014

The Gaussian probability density function of a $N-$pixels measurement sample is then given by $P_{\mathbf{X}}(\mathbf{X}^P) = \prod_{i=1}^{N} \exp\{-\frac{1}{2}(\delta\mathbf{X}_i^P)^T \Gamma_i^{-1} \delta\mathbf{X}_i^P\}/2\pi\sqrt{\det[\Gamma_i]}$.

Table 1. List and description of symbols and acronyms. Dependency in scene location *i* has been omitted for the sake of concision.

Symbols:		**Acronyms:**	
s / b	Source / background mean value	PSD	Polarization-sensitive detector
P / β	Source / background DOP		
$\mathbf{X}^I$ / $\mathbf{X}^P$	Intensity / polarimetric sample measured	ID	Intensity detector
$X^{//}$ / $X^{\perp}$	Orthogonal polarimetric measures	DOP	Degree of polarization
Γ	Covariance matrix of $\mathbf{X}^P$	PSAD	Polarization-splitting analyzing device
$\sigma_{//}^2$ / $\sigma_{\perp}^2$	Noise variance on polarimetric channels		
σ_0^2	Detector electronic noise variance	FI / I_F	Fisher information
ε^2	Optical multiplicative noise variance	CRB	Cramer-Rao bound
ω^2	Ratio of noise variances ($\omega^2 = \varepsilon^2/\sigma_0^2$)	SNR	Signal-to-noise ratio
ρ	Correlation parameter	ML	Maximum likelihood
μ / μ_∞	Gain / asymptotic gain in optimal estimation precision		
$\hat{s}_{ML}^I$ / $\hat{s}_{ML}^P$	Intensity / polarimetric ML estimator		
$\hat{s}_{\Delta}^P$	Polarimetric difference estimator		

Let us focus on the parallel channel: through this statistical description, we assume that the noise variance can be written $\sigma_{//,i}^2 = (1+\beta)\varepsilon_i^2/2 + \sigma_0^2$, with the detector electronic noise contribution σ_0^2 being rationally independent from the location i in the image, and from the illumination level or polarization properties. The first term in the expression of $\sigma_{//,i}^2$ accounts for a multiplicative "optical" noise, introduced by background optical intensity fluctuations, and hence depends on the background DOP β. This noise contribution, proportional to the background average level b_i, can model the effect of turbulence or variations of scatterers density, as well as photon noise in the high background intensity limit.

Due to these scene-dependent optical fluctuations, the intensity measurements in the two polarimetric channels are likely to be correlated, especially in the case of simultaneous acquisition of the polarimetric images with a polarization-splitting analyzing device (PSAD), as sketched in Fig. 1 or as extensively described in [11]. Such partial correlation will be modeled by a non-null covariance term c_i in Γ_i. We assume that the scene-dependent noise contributions only are partially correlated through a correlation parameter ρ, whereas the detector noise is assumed to be uncorrelated between the two channels.

2. Gain in optimal estimation performance

2.1. Principle

To characterize the gain in terms of estimation precision when PSDs are used instead of classical IDs, we propose to resort to information theory, by determining and comparing the Fisher Information (FI) associated to each imaging modality. The FI characterizes the amount of information available in a sample $\mathbf{X}$ for the estimation of a parameter y, and is defined as [18]

$$\mathrm{I_F}(y) = -\left\langle \frac{\partial^2 \ln P_{\mathbf{X}}(\mathbf{X})}{\partial y^2} \right\rangle. \tag{2}$$

According to the well-known Cramer-Rao theorem, its inverse value $\mathrm{I_F}^{-1}(y)$ defines a lower bound (Cramer-Rao bound (CRB)) on the minimum variance expectable for estimating param-

#200923 - $15.00 USD Received 8 Nov 2013; revised 22 Dec 2013; accepted 23 Dec 2013; published 24 Feb 2014

eter y with an unbiased estimation procedure [18]. In the following, we shall limit ourselves to the estimation of the mean signal intensity s_i at location i for the sake of simplicity but without loss of generality. Indeed, it is possible to extrapolate the results of this article to other physical situations since one has $\mathrm{I_F}(z) = \mathrm{I_F}(y)\left[dy/dz\right]^2$ from simple variable transformation relations. For instance, for the estimation of an atmospheric transmittance τ such that $s = e^{-L\tau}$, the FI is directly obtained with $\mathrm{I_F}(\tau) = L^2 s^2 \mathrm{I_F}(s)$, which simply involves the FI for the estimation of the mean signal intensity $\mathrm{I_F}(s)$. Another illutration is the interesting case of image registration addressed in [9], in which a translation parameter η is to be estimated over the whole image such that $\mathbf{s} = \{s(x_i - \eta)\}_{i=1,\ldots,N}$. In this latter case, the above relation yields $\mathrm{I_F}(\eta) = \sum_{i=1}^{N} [s'(x_i - \eta)]^2 \mathrm{I_F}(s_i)$, which again only involves the FI for the estimation of the mean intensity at each location i.

2.2. Expression of the gain

The FI in the case of polarimetric and intensity measurements are derived in Appendix A, and are not recalled here for the sake of concision. We propose to define a gain in optimal precision by comparing the FI available with a polarimetric setup over the FI available with a standard intensity detector, for given experimental conditions. This definition, which has been used in other references [9, 19], yields:

$$\mu(\omega, P, \beta, \rho) = \frac{\mathrm{I_F}^P(s)}{\mathrm{I_F}^I(s)} = \frac{(1+\omega^2)\left[\frac{1+P^2}{2} + \frac{Q}{4}\omega^2\right]}{1 + \omega^2 + \frac{(1-\rho^2)(1-\beta^2)}{4}\omega^4}, \tag{3}$$

where

$$Q = (1 - 2\beta P + P^2) - \rho(1 - P^2)\sqrt{1-\beta^2}, \tag{4}$$

and with $\omega^2 = \varepsilon^2/\sigma_0^2$. This last parameter ω^2 gives the relative value of the noise contributions variances, allowing one to identify the dominant noise term. Thus, "optical" noise ε^2 dominates when $\omega^2 \gg 1$, whereas electronic fluctuations are the main source of noise when $\omega^2 \ll 1$. As an illustration, the evolution of the gain $\mu(\omega, P, \beta, \rho)$ given in Eq. (3) is plotted in Fig. 2 as a function of ρ for various values of ω, and for a partially polarized source ($P = 0.4$) and background ($\beta = 0.1$). It can be immediately checked that the gain does not depend on ρ when electronic noise dominates ($\omega \ll 1$), and that it increases as ω increases.

As will be shown in the following, such definition of a gain in optimal estimation precision can provide insightful results on the physical estimation problem at hands, regardless of the actual estimation procedure used, since derived from information theory. In addition, it can have practical implications if optimal estimators can be identified, as will be shown in Section 4.

3. Physical analysis of the gain $\mu(\omega, P, \beta, \rho)$

In this section, we derive and analyze a number of properties of the gain in optimal precision $\mu(\omega, P, \beta, \rho)$ defined above. These results will allow us to study the benefits of using PSDs for estimation tasks in the presence of intense background and potentially correlated measurements.

3.1. Influence of ambient illumination level

Let us first study how the gain evolves as a function of the ambient background illumination level b. For that purpose, we analyze the behaviour of the gain $\mu(\omega, P, \beta, \rho)$ as a function of $\omega = \varepsilon/\sigma_0$, since ε has been assumed proportional to b. A tractable but tedious calculus sketched in Appendix B leads to this first property:

#200923 - $15.00 USD Received 8 Nov 2013; revised 22 Dec 2013; accepted 23 Dec 2013; published 24 Feb 2014

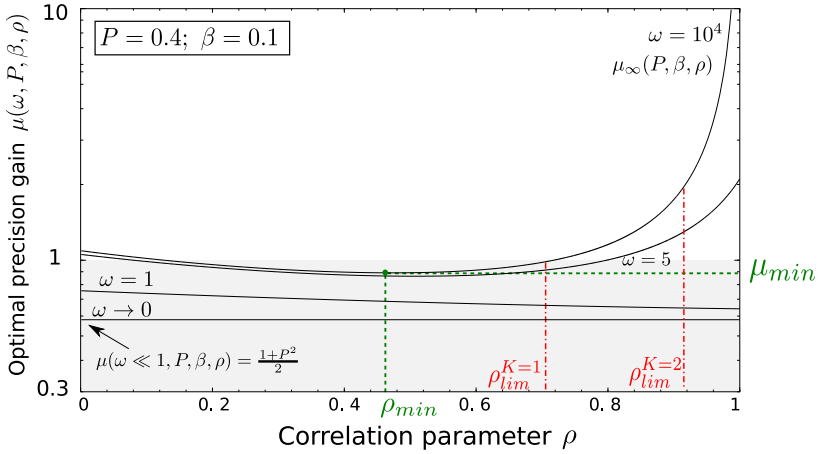

Fig. 2. Evolution of $\mu(\omega,P,\beta,\rho)$ for $P = 0.4$ and $\beta = 0.1$ as a function of ρ for $\omega = \{10^{-3},1,5,10^4\}$.

Property 1 *The gain $\mu(\omega,P,\beta,\rho)$ is a monotonically increasing function of ω.*

This is an interesting result, showing that increasing the relative amount of "optical" noise with respect to electronic noise tends to favour a polarimetric setup in terms of estimation performance, even if the polarimetric measurements are totally uncorrelated ($\rho \to 0$).

When electronic noise dominates, the gain falls down below unity, since $\mu(\omega \ll 1,P,\beta,\rho) \to (1+P^2)/2 \leq 1$. Indeed, for a given amount of light energy entering the imaging system, the PSAD reduces the signal-to-noise ratio (SNR) on the detectors in comparison to a standard ID since energy is splitted into two polarization channels. This property can be checked in Fig. 2 where $\mu(\omega,P,\beta,\rho)$ is plotted as a function of ρ, when $P = 0.4$ and $\beta = 0.1$.

3.2. Asymptotic behaviour in the high intensity regime

Focusing on the high intensity regime by setting $\omega \to \infty$, we obtain a simpler expression

$$\mu_\infty(P,\beta,\rho) = \mu(\omega \gg 1,P,\beta,\rho) = \frac{Q}{(1-\rho^2)(1-\beta^2)}, \tag{5}$$

which will be referred to as *asymptotic gain* subsequently.

Let us analyze the evolution of the asymptotic gain as a function of the correlation between polarimetric channels. Surprisingly, it can be shown that $\mu_\infty(P,\beta,\rho)$ is not a monotonically increasing function of the correlation parameter ρ, as can be observed in Fig. 2. The following property can indeed be demonstrated (see Appendix C):

Property 2 *The asymptotic gain $\mu_\infty(P,\beta,\rho)$ reaches a minimum value $\mu_{\infty,min}$ for a correlation parameter ρ_{min}, such that*

$$\begin{cases} \mu_{\infty,min} = \frac{(1+P)^2}{2(1+\beta)} & \text{and} \quad \rho_{min} = \frac{1-P}{1+P}\sqrt{\frac{1+\beta}{1-\beta}}, \quad \text{if} \quad \beta \leq \frac{2P}{1+P^2} \\ \mu_{\infty,min} = \frac{(1-P)^2}{2(1-\beta)} & \text{and} \quad \rho_{min} = \frac{1+P}{1-P}\sqrt{\frac{1-\beta}{1+\beta}}, \quad \text{otherwise} \end{cases} \tag{6}$$

This property is rather counter-intuitive but can be interpreted as follows. First, when the two acquired polarimetric images are uncorrelated ($\rho \simeq 0$), gain in estimation precision only occurs

#200923 - $15.00 USD Received 8 Nov 2013; revised 22 Dec 2013; accepted 23 Dec 2013; published 24 Feb 2014

if SNR reduction caused by intensity splitting between the two polarization channels is compensated by the increase in size of the statistical sample considered (Two sets of N measures with a PSD, instead of one in an standard ID). Though, as soon as $\rho \neq 0$, the polarimetric measures are no longer independent, and thus the available FI is necessarily lower than the one available with two independent sets of N measurements. This remains true for smaller values of ρ. However, for values of $\rho > \rho_{min}$, the strongly correlated noise perturbing each polarization channel can be partly cancelled out by taking profit of the two acquired images, leading to a potentially strong increase in the gain. This is indeed possible if signal and background contributions exhibit different relative intensity levels on the two acquired images. In this case, an optimal estimation procedure, such as the one described in Section 4, can take profit of this relative contrast mismatch to estimate the desired parameter on the signal contribution with a high precision.

Using the expression of the asymptotic gain given in Eq. (5), let us now analyze in which physical conditions one should favour using a PSD rather than a standard ID. For that purpose, the two following properties can be established. A sketch of the demonstration of these properties is given in Appendix D.

Property 3 *For a given value of P, the asymptotic gain $\mu_\infty(P,\beta,\rho)$ is greater or equal to a minimum gain value K (with $K \geq 1$) for any value of the correlation parameter ρ provided*

$$\beta \leq \frac{(1+P)^2}{2K} - 1, \quad \textit{if} \quad \beta \leq P, \tag{7}$$

$$\beta \geq 1 - \frac{(1-P)^2}{2K} \quad \textit{if} \quad \beta \geq P. \tag{8}$$

Property 4 *When the conditions of Property 3 are not verified, the asymptotic gain $\mu_\infty(P,\beta,\rho)$ is greater or equal to a minimum gain value K (with $K \geq 1$) provided the correlation parameter ρ verifies*

$$\rho \geq \rho_{lim}^K = \frac{1-P^2}{2K\sqrt{1-\beta^2}} + \sqrt{\Phi}, \tag{9}$$

where

$$\Phi = \left[1 - \frac{1}{2K}\frac{(1-P)^2}{1-\beta}\right] \times \left[1 - \frac{1}{2K}\frac{(1+P)^2}{1+\beta}\right]. \tag{10}$$

3.3. Discussion

The previous properties provide conditions on the physical parameters at hand in order to ensure a minimum gain K when using PSDs instead of standard imagers. In this subsection, we propose to quantitatively analyze these theoretical results.

We obviously start focusing on the case of unitary gain (i.e., $K = 1$) which delimitates situations in which polarimetric imaging systems can bring an improvement in estimation precision. In this case, the conditions of Eqs. (7) and (8) respectively read $\beta \leq (1+P)^2/2 - 1$ when $\beta \leq P$, and $\beta \geq 1 - (1-P)^2/2$ when $\beta \geq P$. For a fully depolarized background ($\beta = 0$), for instance, this means that a polarimetric imaging system can improve the quality of estimation, whatever be the value of ρ, as long as a moderately polarized source is used with a minimum value of $P = \sqrt{2} - 1 \simeq 0.414$. On the other hand, when the source is totally unpolarized, a gain can be expected for any value of ρ provided $\beta \geq 1/2$. In the two-dimensional plot of Fig. 3(a) as a function of polarization parameters P and β, the conditions of Eqs. (7) and (8) for $K = 1$ are represented with continuous green curves and delimitate two regions. When the conditions hold (greyed region in Fig. 3(a)), the values of $\mu_{\infty,min}$ and ρ_{min} are represented in contour plots,

#200923 - $15.00 USD Received 8 Nov 2013; revised 22 Dec 2013; accepted 23 Dec 2013; published 24 Feb 2014

10 March 2014 | Vol. 22, No. 5 | DOI:10.1364/OE.22.004920 | OPTICS EXPRESS 4926

respectively in blue dashed lines and green dot-dashed lines. In the second region, i.e., when the inequalities of Eqs. (7) and (8) are not verified, the correlation parameter ρ has to be greater than a minimum value denoted $\rho_{lim}^{K=1}$ so as to ensure $\mu_\infty(P,\beta,\rho) \geq 1$. The values of $\rho_{lim}^{K=1}$ are plotted in Fig. 3(a) in red continuous lines, as a function of P and β.

The same graphical representation has been used in Fig. 3(b)-3(d) in the case of $K = \{2,5,10\}$ respectively, to plot the values of ρ_{min} and $\mu_{\infty,min}$ when the relation of Eq. (8) holds, and the values of ρ_{lim}^{K} otherwise. It is interesting to notice that when $P \geq \beta$, a limit value $\rho_{lim}^{K} > 0$ always has to be ensured for any couple of parameters P and β as long as $K \geq 2$ since condition of Eq. (7) cannot be fulfilled in this case. On the other hand, when a highly polarized background is considered and $\beta \geq P$, a high asymptotic gain value K can be reached with uncorrelated measurements (i.e., $\rho = 0$) provided P is small enough. This property can be understood by noticing that a high value of β implies a low background contribution on one of the two acquired images, thus facilitating estimation of a parameter on the low polarized signal contribution. This result must be however mitigated since the detector noise has been neglected to derive Properties 3 and 4, but should be taken into account in this latter case involving low background illumination levels.

In terms of practical application, the charts given in Fig. 3 provide insightful information about the expectable gain in precision using a PSD for a given set of physical parameters P, β and ρ. As could be expected, the best performance gain is obtained when a high polarimetric contrast can be observed between the background and signal contributions (high P and low β, or high β and low P). However, these charts clearly evidence that the gain in performance increases also when the measurements are significantly correlated. Yet, these charts may be of great use to assess the optimal performance of a real field polarimetric imaging system, in which all intermediate situations are likely to occur. For instance, the degradation of the DOP of a highly polarized source could be taken into account in the dimensioning of an experiment. The influence of unwanted or unexpected polarization/depolarization of the background could be also analyzed with the above results.

4. Optimal estimation procedure

The relevance of the above results is however conditioned to the definition of *efficient* estimation procedures, i.e., estimators ensuring unbiased estimation and a minimum variance which reaches the CRB studied above. Let us thus consider estimators of s in the maximum likelihood (ML) sense, since ML estimators are known to be *efficient* under Gaussian fluctuations [18], which is the noise model considered throughout this article. Limiting ourselves to the high intensity regime ($\omega \to \infty$), and assuming that the background mean value b is *a priori* known, the ML estimator of s using a standard intensity detector is simply given by $\hat{s}_{ML}^{I} = \hat{X}^{I} - b$. When a polarimetric imager is used, the derivation of the ML estimator of s is detailed in Appendix E and leads to

$$\hat{s}_{ML}^{P} = \frac{U\hat{X}^{//} + V\hat{X}^{\perp} + Z}{W}, \tag{11}$$

where U, V, W and Z are functions of P, β, ρ and b, which parameters are assumed *a priori* known. These functions can be easily derived from Appendix E with appropriate changes of variable, but are not detailed here for brevity reasons. Both ML estimators are unbiased, i.e., $\langle \hat{s}_{ML}^{P} \rangle = \langle \hat{s}_{ML}^{I} \rangle = s$, and their variances are easily compared using the above characterization of the FIs since they respectively reach the CRBs computed above in the cases of polarimetric and intensity measurements. As a result, the gain studied in the previous section corresponds to the ratio of the variances of these two ML estimators: $\mu_\infty(P,\beta,\rho) = \mathrm{var}(\hat{s}_{ML}^{I})/\mathrm{var}(\hat{s}_{ML}^{P})$.

For a fair comparison, the estimation samples should involve the same number of pixels. Thus, a PSD with N pixels in each polarimetric channels must be compared to a $2N$-pixels

#200923 - $15.00 USD Received 8 Nov 2013; revised 22 Dec 2013; accepted 23 Dec 2013; published 24 Feb 2014

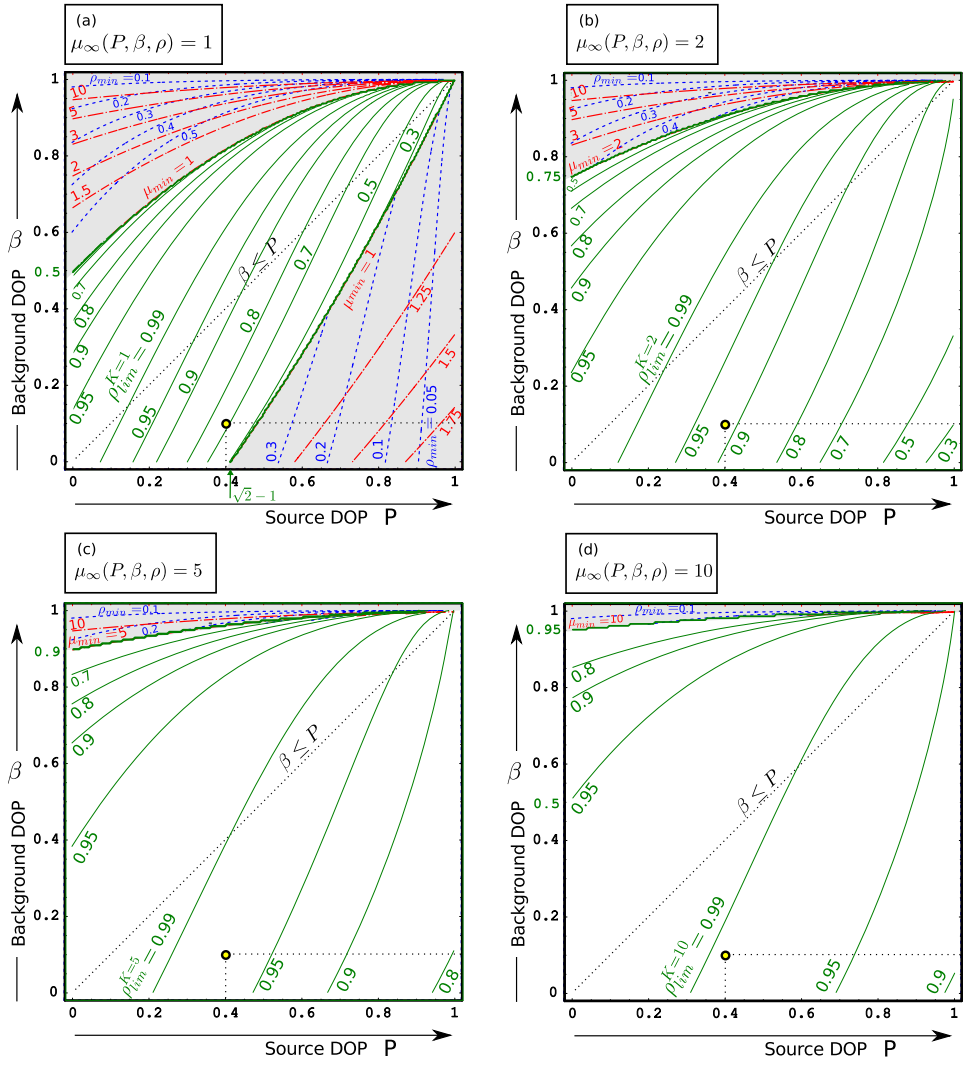

Fig. 3. Contour plots of ρ_{lim}^{K} for various values of K as a function of P and β. Additional contour plots of ρ_{min} and $\mu_{\infty,min}$ are provided when relations (7) and (8) hold. The yellow circles correspond to the situation addressed in Fig. 2 ($P=0.4$ and $\beta=0.1$).

standard ID. In this case, the relative performance of the two estimators can be directly assessed from the chart plotted in Fig. 3(b), which gives conditions for a minimum gain value of $\mu_\infty(P,\beta,\rho)\geq K=2$. The analyzis of this chart interestingly shows that PSDs are not systematically preferable to standard ID if the correlation between the fluctuations lies below a lower limit $\rho_{lim}^{K=2}$ determined above. As a result, the chart plotted in Fig. 3(b) turns out to be a useful tool for determining the optimal estimation procedure, depending on the experimental conditions.

Lastly, it can be interesting to compare the ML estimator with other estimation procedures which are classically used in polarimetric imaging. For instance, when polarimetric measure-

#200923 - $15.00 USD Received 8 Nov 2013; revised 22 Dec 2013; accepted 23 Dec 2013; published 24 Feb 2014

10 March 2014 | Vol. 22, No. 5 | DOI:10.1364/OE.22.004920 | OPTICS EXPRESS 4928

ments along orthogonal polarization directions are available, a simple *difference* image is classically obtained by substraction of the two polarimetric channels [1]. For the estimation of the parameter s, such *difference* estimator would simply read $\hat{s}^P_\Delta = [\hat{X}^{//} - \hat{X}^{\perp} - \beta b]/P$. However, it can be shown that this standard estimator is not optimal, in general, in the situation addressed in this article. Its variance, derived in Appendix F, is indeed greater that $\mathrm{var}(\hat{s}^P_{ML})$ (and thus greater than the CRB) except when $\rho = (1-\beta P)/(1-\beta^2)$, in which case the difference estimator $\hat{s}^P_\Delta$ identifies with $\hat{s}^P_{ML}$.

5. Conclusion

As a conclusion, the theoretical results derived in this article quantitatively demonstrate that polarimetric imagers can significantly improve the estimation precision, provided noise fluctuations in each polarimetric channels are significantly correlated. Hence, this confirms the interest of snapshot polarimetric imagers as described in [11] since they may favour correlated background/noise fluctuations in the two polarimetric channels, which are acquired simultaneously. In these conditions, we have also shown that the optimal estimation procedure differs from a natural *difference* image, but can be simply implemented. These results can be useful for the design of polarimetric imaging systems involving estimation through turbid media, or in other fields of application, for post-processing of polarimetric images exhibiting temporally or spatially correlated fluctuations.

Appendix

To derive the expressions presented in this article, it is interesting to introduce the following simplified notations: $a = (1+P)/2$ and $\alpha = (1-P)/(1+P)$ on the one hand, and, on the other hand, $c^2 = (1+\beta)/2$ and $\gamma^2 = (1-\beta)/(1+\beta)$. In a single pixel configuration ($N=1$) for the sake of simplicity, the polarimetric measurement considered is $\mathbf{X}^P = [X^{//},\ X^{\perp}]^T$, such that $\langle \mathbf{X}^P \rangle = [as + c^2 b,\ \alpha as + \gamma^2 c^2 b]^T$ and

$$\Gamma = \langle \delta\mathbf{X}\delta\mathbf{X}^T \rangle = c^2 \begin{bmatrix} \varepsilon^2 + \varsigma^2 & \rho\gamma\varepsilon^2 \\ \rho\gamma\varepsilon^2 & \gamma^2\varepsilon^2 + \varsigma^2 \end{bmatrix},$$

with $\varsigma^2 = 2\sigma_0^2/(1+\beta)$. It is easily checked that the conditions $P \in [0,1]$, $\beta \in [0,1]$ and $\beta \leq P$ are equivalent to $\alpha \in [0,1]$, $\gamma \in [0,1]$ and $\gamma^2 \geq \alpha$.

A. Fisher informations calculations

With the Gaussian noise model used in this article, the loglikelihood of the polarimetric measure $\mathbf{X}^P$ can be written $\ell(\mathbf{X}^P) = \ln P_{\mathbf{X}}(\mathbf{X}^P) = -\left(\delta\mathbf{X}^P\right)^T \Gamma^{-1} \delta\mathbf{X}^P/2$ up to an additive term independent of s. An application of Eq. (2) leads to the FI for the estimation of s, which reads $\mathrm{I_F}^P(s) = \left[\langle\mathbf{X}\rangle'^P\right]^T \Gamma^{-1} \langle\mathbf{X}\rangle'^P$, with $\langle\mathbf{X}\rangle'^P = \partial\langle\mathbf{X}\rangle^P/\partial s = \langle\partial\mathbf{X}^P/\partial s\rangle = [a,\ a\,\alpha]^T$. A direct calculation gives:

$$\mathrm{I_F}^P(s) = \frac{a^2}{c^2\varepsilon^2} \cdot \frac{(\alpha^2 - 2\rho\alpha\gamma + \gamma^2) + (1+\alpha^2)u^{-2}}{\gamma^2(1-\rho^2) + (1+\gamma^2)u^{-2} + u^{-4}}, \tag{12}$$

with $u^2 = \varepsilon^2/\varsigma^2 = (1+\beta)\,\omega^2/2$.

The FI for the estimation of s from the total intensity of the beam (non-polarimetric measurement) is a standard result under Gaussian fluctuations hypothesis. One has

$$\mathrm{I_F}^I(s) = \frac{a^2}{c^2\varepsilon^2} \cdot \frac{(1+\alpha)^2}{(1+\gamma^2) + u^{-2}} = \frac{\sigma^{-2}}{1+\omega^2}. \tag{13}$$

#200923 - $15.00 USD Received 8 Nov 2013; revised 22 Dec 2013; accepted 23 Dec 2013; published 24 Feb 2014

The gain $\mu(u,\alpha,\gamma,\rho) = {I_F}^P(s)/{I_F}^I(s)$ can then be easily derived, leading to Eq. (3) with appropriate changes of variables.

B. Monotonicity of $\mu(u,\alpha,\gamma,\rho)$ as a function of u

To demonstrate Property 1, let us first rewrite $\mu(u,\alpha,\gamma,\rho)$ as

$$\mu(u,\alpha,\gamma,\rho) = \frac{Au^2+B}{Du^4+Cu^2+1} \times \frac{Cu^2+1}{E}, \tag{14}$$

with $A=(\alpha^2-2\rho\alpha\gamma+\gamma^2)$, $B=1+\alpha^2$, $C=1+\gamma^2$, $D=\gamma^2(1-\rho^2)$ and $E=(1+\alpha)^2$, all these expressions being greater or equal to zero. Let us notice that $\mu(0,\alpha,\gamma,\rho)=B/E=(1+P^2)/2$.

The derivative of $\mu(u,\alpha,\gamma,\rho)$ as a function of u is thus

$$\frac{\partial[\mu(u,\alpha,\gamma,\rho)]}{\partial u} = \frac{2u\mathscr{H}(u)}{\left[1+Cu^2+Du^4\right]^2 E}, \tag{15}$$

with $\mathscr{H}(u) = A+2(AC-BD)u^2+(AC^2-AD-BCD)u^4$.

The function $\mu(u,\alpha,\gamma,\rho)$ is monotonically increasing on $u\in[0;\infty[$ if $\partial[\mu(u,\alpha,\gamma,\rho)]/\partial u \geq 0 \Leftrightarrow \mathscr{H}(u)\geq 0,\ \forall u\in[0;\infty[$. Noticing that $\mathscr{H}(0)=A\geq 0$, and that $\mathscr{H}(u)$ is a second-order polynomial in u^2, we can compute the discriminant

$$\Delta = 4D(A^2+DB^2-ABC) = -4\gamma^2(1-\rho^2)\left[\alpha(1-\gamma^2)-\rho\gamma(1-\alpha^2)\right]^2, \tag{16}$$

which is negative. As a consequence, $\mathscr{H}(u)$ does not admit real root on $u\in[0;\infty[$, and hence, $\mathscr{H}(u)$ is positive on $u\in[0;\infty[$. As a result, $\mu(u,\alpha,\gamma,\rho)$ is a positive, monotonically increasing function of u for $u\in[0;\infty[$.

C. Minimum value of the asymptotic gain $\mu_\infty(\alpha,\gamma,\rho)$:

The asymptotic gain is obtained by setting $u\to\infty$:

$$\mu_\infty(\alpha,\gamma,\rho) = \frac{(\alpha^2-2\rho\alpha\gamma+\gamma^2)(1+\gamma^2)}{\gamma^2(1-\rho^2)(1+\alpha)^2} \tag{17}$$

It is easily shown that $\mu_\infty(\alpha,\gamma,\rho)$ reaches a minimum if $(\alpha\rho-\gamma)(\alpha-\rho\gamma)=0$. Since $\rho\in[0,1]$, the only admissible root is $\rho_{min}=\alpha/\gamma$ when $\gamma\geq\alpha$ and thus $\mu_{\infty,min}(\alpha,\gamma)=(1+\gamma^2)/(1+\alpha)^2$. When $\gamma\leq\alpha$, the only admissible root is $\rho_{min}=\gamma/\alpha$, and in this case $\mu_{\infty,min}(\alpha,\gamma)=\alpha^2(1+\gamma^2)/\gamma^2(1+\alpha)^2$. The expressions of ρ_{min} and $\mu_{\infty,min}(P,\beta)$ given in the article can be recovered with an appropriate change of variables.

From the above results, the conditions for $\mu_{\infty,min}(\alpha,\gamma)\geq K$ are directly derived as

$$\gamma^2 \geq K(1+\alpha)^2-1 \quad \text{when} \quad \gamma\geq\alpha \tag{18}$$

$$\gamma^2 \leq \alpha^2/\left[K(1+\alpha)^2-\alpha^2\right] \quad \text{when} \quad \gamma\leq\alpha. \tag{19}$$

D. Condition for minimum gain $\mu_\infty(\alpha,\gamma,\rho)=K$:

Solving $\mu_\infty(\alpha,\gamma,\rho)=K$ leads to two roots $\rho^K_{1/2}=\left[\alpha(1+\gamma^2)\mp\sqrt{\Phi}\right]/K\gamma(1+\alpha)^2$ verifying $\rho^K_{1/2}\in[0,1]$, with $\Phi=\left[1+\gamma^2-K(1+\alpha)^2\right]\left[\alpha^2(1+\gamma^2)-K(1+\alpha)^2\gamma^2\right]$, or with the notations of Appendix B, $\Phi=\left[C-KE\right]\left[\alpha^2C-KE\gamma^2\right]$.

Let us focus on the greatest root, denoted $\rho^K_{lim}=\rho^K_2$ in the following, and which defines the minimum value of ρ such that $\mu_\infty(\alpha,\gamma,\rho)\geq K,\ \forall\rho\geq\rho^K_{lim}$. It can first be checked that

#200923 - $15.00 USD Received 8 Nov 2013; revised 22 Dec 2013; accepted 23 Dec 2013; published 24 Feb 2014

the expressions of ρ_{lim}^K and Φ respectively given in the Eqs. (9) and (10) of Property 4 can be retrieved with appropriate changes of variables. In particular, one has $\Phi = \Psi/\left[K^2\gamma^2(1+\alpha)^4\right]$.

Let us now study in which conditions this upper root ρ_{lim}^K actually defines a real-valued limit on the correlation parameter ρ. It is clear that ρ_{lim}^K is imaginary if $\Phi \leq 0$, which occurs when one of the two following inequalities is verified: (a): $\alpha^2 C/\gamma^2 E \leq K \leq C/E$; or (b): $\alpha^2 C/\gamma^2 E \geq K \geq C/E$. When $\gamma \geq \alpha$, inequality (b) is impossible, and (a) is verified if $\gamma^2 \geq K(1+\alpha)^2 - 1$. When $\gamma \leq \alpha$, inequality (a) is impossible, and (b) is verified if $\gamma^2 \leq \alpha^2/\left[K(1+\alpha)^2 - \alpha^2\right]$. These conditions obviously correspond to those derived above in Appendix C in Eqs. (18) and (19) for ensuring $\mu_{\infty,min}(\alpha,\gamma) \geq K$.

For the sake of physical interpretation, we can rewrite these conditions as

$$\gamma^2 \geq K(1+\alpha)^2 - 1, \quad \text{if} \quad \alpha \leq \gamma^2, \quad \text{and} \tag{20}$$

$$\gamma^2 \leq \alpha^2/\left[K(1+\alpha)^2 - \alpha^2\right], \quad \text{if} \quad \alpha \geq \gamma^2, \tag{21}$$

which allows relations (7) and (8) of Property 3 to be retrieved by appropriate change of variables. Indeed, it can be checked that none of the conditions of Eqs. (18) and (19) apply when $\gamma^2 \leq \alpha \leq \gamma$.

E. ML estimator $\hat{s}_{ML}^P$

We derive the ML estimator in a situation of negligible detector noise, i.e., $u \to \infty$ (or $\omega \to \infty$). From the expression of $\ell(\mathbf{X}^P)$ given in Appendix A, we derive $\hat{s}_{ML}^P$ by solving $\partial\ell(\mathbf{X}^P)/\partial s = 0$, leading to equation $\left(\delta\mathbf{X}^P\right)^T\Gamma^{-1}\langle\mathbf{X}\rangle' + \left(\langle\mathbf{X}\rangle'\right)^T\Gamma^{-1}\delta\mathbf{X}^P = 0$. A straightforward but tedious calculation finally gives the expression of Eq. (11), with $U = \gamma[\gamma - \alpha\rho]$, $V = [\alpha - \gamma\rho]$, $Z = bc^2\gamma[\rho(\alpha+\gamma^2) - \gamma(1+\alpha)]$, and $W = a[\alpha^2 - 2\rho\alpha\gamma + \gamma^2]$. It is easily checked that this estimator is unbiased $\langle\hat{s}_{ML}^P\rangle = s$, since $\langle\hat{X}^{//}\rangle = as + c^2 b$ and $\langle\hat{X}^{\perp}\rangle = a\alpha s + c^2\gamma^2 b$. Moreover, the variance of this estimator necessarily reaches the CRB since ML estimator is efficient under Gaussian fluctuations [18]. This can be checked by noticing that $\mathrm{var}(\hat{s}_{ML}^P) = \left[U^2\,\mathrm{var}(\hat{X}^{//}) + V^2\,\mathrm{var}(\hat{X}^{\perp}) + UV\,\mathrm{cov}(\hat{X}^{//},\hat{X}^{\perp})\right]/W^2$ which, after a simplification step, is equal to $\lim_{u\to\infty}\{1/\mathrm{I_F}^P(s)\}$.

F. Difference image estimator $\hat{s}_{\Delta}^P$

With the notations used in this appendix, the estimator $\hat{s}_{\Delta}^P$ given in Section 4 reads $\hat{s}_{\Delta}^P = \left[(\hat{X}^{//} - \hat{X}^{\perp}) - bc^2(1-\gamma^2)\right]/\left[a(1+\alpha^2)\right]$. One easily checks that it is unbiased and that $\mathrm{var}(\hat{s}_{\Delta}^P) = \left[\mathrm{var}(\hat{X}^{//}) + \mathrm{var}(\hat{X}^{\perp}) - 2\mathrm{cov}(\hat{X}^{//},\hat{X}^{\perp})\right]/\left[a^2(1+\alpha)^2\right]$, which is equal to $\mathrm{var}(\hat{s}_{\Delta}) = c^2\varepsilon^2\left[1+\gamma^2-2\rho\gamma\right]/\left[a^2(1+\alpha)^2\right]$.

Lastly, it can be shown that $\mathrm{var}(\hat{s}_{\Delta}^P) = \mathrm{var}(\hat{s}_{ML}^P)$ if $\alpha + \gamma^2 - \rho(1+\alpha)\gamma = 0$, i.e., if $\rho = (\alpha+\gamma^2)/\gamma(1+\alpha) = (1-\beta P)/(1-\beta^2)$, in which case $\hat{s}_{\Delta}^P = \hat{s}_{ML}^P$.

Acknowledgments

This work has been supported by the TDF company and by Rennes Metropole through Dr. J. Fade's *AIS* grant.

#200923 - $15.00 USD Received 8 Nov 2013; revised 22 Dec 2013; accepted 23 Dec 2013; published 24 Feb 2014

IOP Publishing Journal of Optics
J. Opt. 17 (2015) 065703 (7pp) doi:10.1088/2040-8978/17/6/065703

Adaptive polarimetric image representation for contrast optimization of a polarized beacon through fog

Swapnesh Panigrahi, Julien Fade and Mehdi Alouini

Institut de Physique de Rennes, CNRS, Université de Rennes 1, Campus de Beaulieu, F-35042 Rennes, France

E-mail: julien.fade@univ-rennes1.fr

Received 29 January 2015, revised 19 March 2015
Accepted for publication 20 March 2015
Published 1 May 2015

Abstract

We present a contrast-maximizing optimal linear representation of polarimetric images obtained from a snapshot polarimetric camera for enhanced vision of a polarized light source in obscured weather conditions (fog, haze, cloud) over long distances (above 1 km). We quantitatively compare the gain in contrast obtained by different linear representations of the experimental polarimetric images taken during rapidly varying foggy conditions. It is shown that the adaptive image representation that depends on the correlation in background noise fluctuations in the two polarimetric images provides an optimal contrast enhancement over all weather conditions as opposed to a simple difference image which underperforms during low visibility conditions. Finally, we derive the analytic expression of the gain in contrast obtained with this optimal representation and show that the experimental results are in agreement with the assumed correlated Gaussian noise model.

Keywords: polarimetric imaging, imaging through turbid media, image processing

1. Introduction

Polarimetric imaging produces multi-dimensional pixel data that is either interpreted in terms of polarimetric properties of the imaged objects, or quite often, processed into a single image revealing specific contrasts which may not appear on standard reflectance images. In simplified polarimetric imaging systems, a pair of monochromatic images are acquired along two orthogonal polarization directions. The two-dimensional (2D) pixel data obtained can then be presented by either color encoding or by a combination of the two components so as to enhance contrast between objects in a scene sharing different polarimetric properties. Such contrast-maximizing representation of the polarimetric information can prove helpful in underwater polarimetric imaging [1] and imaging through turbid media [2] (like colloids [3], tissues [4] and fog [5]). In most laboratory based imaging experiments [6, 7], the scene is static and the object of interest is usually embedded in a uniform background, thus allowing for processing over multiple frames acquired over a period of time. However, in real-world scenarios with fast moving scene and/or camera, it is often desirable to reach real-time imaging and processing. This requires the identification and use of computationally simple and optimal representations of the polarimetric images that are adapted to the experimental scenarios at hand.

In this article, we address the specific issue of contrast enhancement of an intentionally polarized beacon of light (or semaphore), imaged at a long distance through obscured atmosphere with a polarization-sensitive camera. Such situation is of great interest for applications in transportation safety. In this context, we demonstrate, both analytically and experimentally, that an optimal processing of the polarimetric images allows such contrast maximization under all experimental conditions encountered. The optimal polarimetric representation derived differs from commonly used polarimetric contrasts, but remains computationally compatible with real-time processing at video rate, which is a stringent constraint in the applicative context considered here.

This article is organized as follows: in section 2, the experimental setup is described, as well as the statistical measure used to assess the contrast of the source in the image.

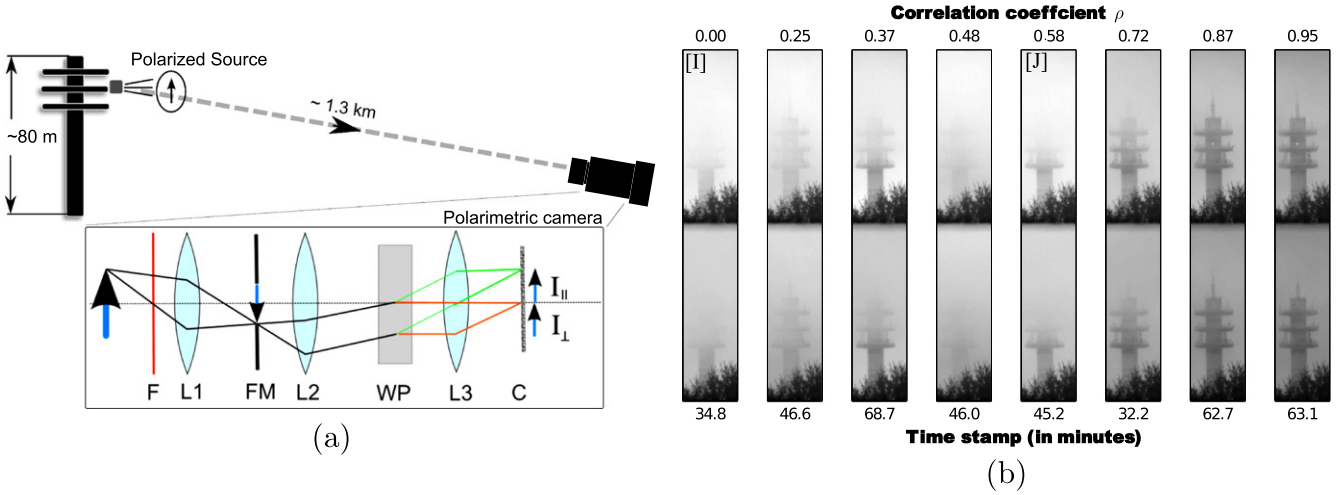

Figure 1. (a) The schematic shows the long range imaging setup. The polarimetric camera consists of the arrangement of lenses L1 and L2 after a monochromatic filter F (at 612 nm, FWHM = 12 nm). The image is partly masked by a slit (FM) and passed through a Wollaston prism (WP) to produce two images $I_{\|}$ and $I_{\perp}$ on a single camera (C) using lens L3. (b) A subset of the raw images from the polarimetric camera, showing the tower and the source with varying conditions of fog density and visibility. The eight images are sorted in increasing order of background correlation (ρ) estimated over a small ROI surrounding the source pixel. The time stamp of acquisition is indicated below each image.

Then, the numerical and theoretical derivation of an optimal polarimetric representation is reported in section 3. The efficiency of this optimal representation to enhance contrast of a polarized source through fog is then discussed on experimental data in section 4, allowing us to confirm theoretical predictions in real field conditions. Conclusion and perspectives of this article are finally given in section 5.

2. Long distance polarimetric imaging experiment through fog

The long distance polarimetric imaging experiment described in the following has been set up in the vicinity of the campus of University of Rennes 1 to gather experimental data on real atmospheric conditions. The imaging experiment covers a kilometric distance which is the typical range of distance one aims at for transportation safety applications like air and sea transport. A thorough description of this experimental facility and of the snapshot polarimetric imager designed is reported in [5], along with a detailed depiction of the experiment control and calibration procedure.

2.1. Experimental setup

The experiment basically consists of a highly linearly polarized source of incoherent light, placed on a telecommunication tower (about 80 m in height and 1.3 km far from the detection site at the laboratory), and a Wollaston-prism based polarimetric camera for imaging. The experimental setup reported in [5] is improved here using a higher dynamics, low noise camera (Andor NEO sCMOS 5.5 Mpixels, 16 bit, 0.015 e-/pixel/s dark noise at −30 °C sensor temperature) which is more suitable for this experiment. Such high-dynamics detector enables finer sampling of intensity levels and noise statistics in the acquired images. The entire imaging system has been thoroughly re-calibrated with this new camera. As mentioned before and shown in the schematic in figure 1(a), the source is imaged from a distance of about 1.3 km, and the snapshot polarimetric imager enables the simultaneous acquisition of two images on the camera (namely, $I_{\|}$ and $I_{\perp}$) corresponding to the two orthogonal polarization directions, with $I_{\|}$ aligned with the direction of polarization of the source. For the purpose of illustration in this article, we pick a dataset of images taken during an experiment conducted on 24-01-2014 between 1:00 p.m. and 2:20 p.m. (at a time interval of 1 frame/10 s). During this 80 min acquisition, successive passing fog layers obscured the source intermittently, causing the visibility of the source to evolve rapidly and significantly. An example of eight frames acquired by the polarimetric camera can be observed in figure 1(b).

2.2. Polarimetric contrast image

Using the image registration method described in [5], the two images can be extracted to form a set of 2D pixels, such that the ith pixel $X_i^P = [x_{\|,i}, x_{\perp,i}]^T$ is a part of the polarimetric image $I_P = \{X_i^P\}_{i\in[1,N]} = [I_{\|}, I_{\perp}]^T$. In practice, this 2D data is processed to provide the end-user with a final contrast image, or to feed a higher-level image processing algorithm (detection and tracking, segmentation, etc). For that purpose, the recorded 2D data can be represented by a linear combination of both images $I_{\|}$ and $I_{\perp}$, i.e., as a projection of the individual vectors X_i^P over a row vector $W = [u, v]$. Thus, a linear representation denoted generically by γ can be written as

$$\gamma = WI_P = u\, I_{\|} + v\, I_{\perp}. \quad (1)$$

In each such representation, the source will have different contrast and with different overall scaling depending on the

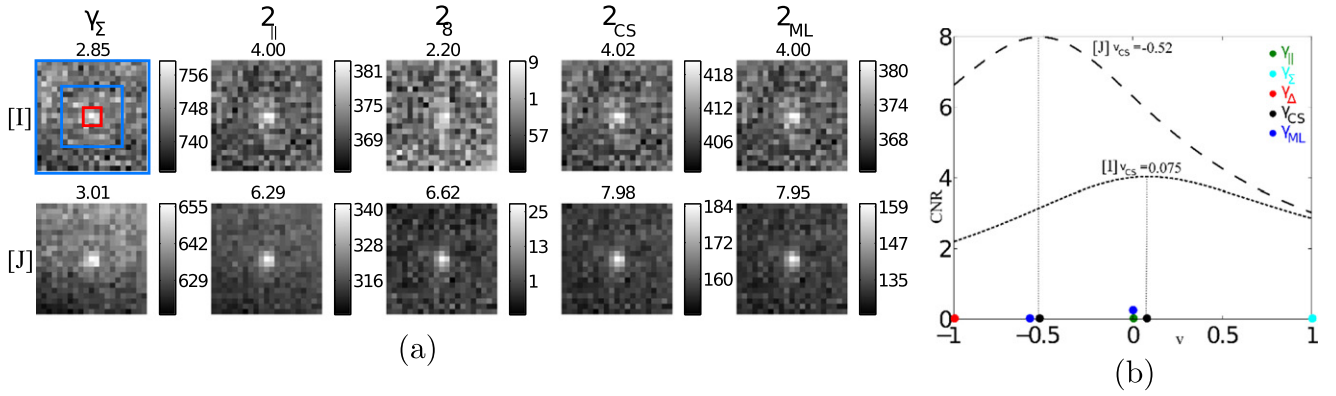

Figure 2. (a) Comparison of the contrasts obtained for three representations of the polarimetric images for frames labeled as [I] and [J] in figure 1(b). The source region, $\mathcal{S}$ is bounded by the 3 × 3 pixels red square and $\mathcal{B}$ is the background region between the two blue squares of sizes 11 × 11 pixels and 21 × 21 pixels. (b) CNR-maximizing 1D search over values of v keeping $u = 1$ for the two frames.

values of u and v. As a result, we resort to a contrast-to-noise ratio (CNR) in order to fairly compare the contrast of the source in each representation. Using a local region of interest (ROI) of size 21 × 21 pixels around the source, we identify two sets of pixels (shown as colored squares in figure 2(a) and described in the caption) denoted by $\mathcal{B}$ (*background*) and $\mathcal{S}$ (*source*), and we define the CNR of the source in a general representation γ as

$$C(\gamma) = \left| \frac{\langle \gamma \rangle_{\mathcal{S}} - \langle \gamma \rangle_{\mathcal{B}}}{\hat{\sigma}_{\mathcal{B}}(\gamma)} \right|, \tag{2}$$

where

$$\langle \gamma \rangle_\chi = \sum_{i \in \chi} \frac{\gamma_i}{N_\chi} \quad \text{and} \quad \hat{\sigma}^2_\chi(\gamma) = \frac{1}{N_\chi - 1} \sum_{i \in \chi} \left(\gamma_i - \langle \gamma \rangle_\chi \right)^2$$

respectively stand for the empirical mean and variance over region χ, with cardinality N_χ. This contrast measure returns the local contrast of a central pixel w.r.t. its immediate background and remains invariant under scaling of the gray levels in the image, i.e., for different values of $[u, v]$. In a general case, the intervening medium may be birefringent and thus the values of u and v can range between $[-1, 1]$. However, for non-birefringent medium, where no rotation of polarization is observed, the weight (u) of $I_\parallel$ remains non-zero and thus can be scaled out so that the representation depends only on the weight (v) of $I_\perp$. Further, for a generic representation γ, we define a gain in contrast with respect to an intensity-summed image ($\gamma_\Sigma = I_\parallel + I_\perp$) which would be acquired with a standard camera. For brevity, we denote this gain as

$$g^\Sigma = \frac{C(\gamma)}{C(\gamma_\Sigma)}. \tag{3}$$

3. Derivation of an optimal polarimetric representation

Several combinations of the acquired polarimetric images can be envisaged for producing a final contrast image. In the context of this article, we aim at maximizing the CNR of a polarized light source over a background. This naturally raises the question of finding the optimal representation that provides the best contrast independent of the atmospheric situation, while remaining computationally efficient to match real-time requirements. Before deriving such optimal representation, let us first recall standard polarimetric representations which are commonly used in the literature for various applications in polarimetric imaging.

3.1. Standard polarimetric representations

From the two acquired polarimetric images $I_\parallel$ and $I_\perp$, most simple and standard representations are:

Intensity-summed image ($\gamma_\Sigma = [1, 1]\, I_P$): such combination qualitatively provides the image that would be acquired with a standard, polarization-insensitive camera. Thus, other representations can be compared as a gain with respect to the intensity-summed image.

Polarization filtered image ($\gamma_\parallel = [1, 0]\, I_P$): another very simple approach is to use a polarization-filtered image, which can be obtained on our setup by retaining only the polarimetric image corresponding to the direction of polarization of the light source.

Polarization-difference image ($\gamma_\Delta = [1, -1]\, I_P$): computing a difference image by subtracting the two polarimetric frames acquired is a very standard technique, widely used in polarimetric imaging [8, 12] for its efficiency in contrast enhancement. In the first experiments conducted with the imaging system described above, it was indeed noticed that the difference image performs generally better than the other standard representations [5]. Nevertheless, it was also observed that γ_Δ does not always provide the best possible contrast in the context of polarimetric imaging through fog considered in this article.

Orthogonal states contrast image (OSC = $\gamma_\Delta/\gamma_\Sigma$): this polarimetric contrast is obtained by normalizing the difference image by the intensity-summed image. It is widely used and has proved efficient in active polarimetric

Table 1. Polarimetric representations and gains in CNR.

Representation	Symbol	W	$g^{\Sigma} = C(\gamma)/C(\gamma_{\Sigma})$
Intensity-summed	γ_{Σ}	[1, 1]	1
Pol. filtered	$\gamma_{\parallel}$	[1, 0]	$\sqrt{2(1+\rho)}$
Pol. difference	γ_{Δ}	[1, −1]	$\sqrt{(1+\rho)/(1-\rho)}$
Computational	γ_{CS}	[1, v_{CS}]	—
Max. Likelihood	γ_{ML}	[1, $-\rho$]	$\sqrt{2/(1-\rho)}$

imaging for its ability to provide an estimate of the degree of polarization of light scattered by an object (or an imaged scene) [10, 11]. However, it was shown that such normalization tends to increase the noise in the final image due to possible low intensity values in the intensity-summed image [5]. For that reason, and due to the fact that the OSC cannot be written as a linear combination of $I_{\parallel}$ and $I_{\perp}$, this representation will not be considered in the remainder of this article.

In the next subsections, we derive an optimal polarimetric representation, which in general differs from the most classical ones, whose expressions are summarized in table 1.

3.2. Computational representation: numerical maximization of CNR

It is possible to determine the optimal projection numerically for each acquired frame by a simple grid search over possible coefficient vectors W. As a result, the optimal representation, denoted $W_{\mathrm{CS}} = [u_{\mathrm{CS}}, v_{\mathrm{CS}}]$ in the following, is obtained by computationally solving $W_{\mathrm{CS}} = \underset{W}{\mathrm{argmax}}\{C(WI_P)\}$, for $u \in [0, 1]$ and $v \in [-1, 1]$ and obtaining an image $\gamma_{\mathrm{CS}} = W_{\mathrm{CS}} I_P$.

On the resulting processed images of two individual frames in figure 2(a), on the ROI defined above, it can be checked that a significant contrast enhancement can be obtained over the difference image γ_{Δ} and the intensity-summed image γ_{Σ}, which indicates that the optimal representation γ_{CS} differs, in these cases, from both γ_{Δ} and γ_{Σ}. It can be observed that for the frame labeled [I], the optimal representation is very close to a polarization-filtered image $\gamma_{\parallel}$. On the other hand, for the frame [J], the computational search leads to optimal weight of v_{CS} corresponding to an intermediate situation between representations γ_{Δ} and $\gamma_{\parallel}$.

3.3. Optimal representation: theoretical maximization of CNR

As observed in the previous subsection, the optimum linear combination of the polarimetric images for contrast enhancement may differ from the commonly used polarimetric representations, and may vary from frame to frame. Accordingly, identifying the physical parameter that influences the weights of the optimum linear combination would make it possible to implement an adaptive representation of polarimetric image that provides the best contrast for any weather condition. However, in such a long distance imaging setup, there is no a priori knowledge of the properties of the intervening medium, and thus we rely on the noise properties of the image. We hypothesize a correlated Gaussian noise model treating each pixel X_i^P as a bivariate random variable having a mean of $\langle X^P \rangle_{\mathcal{S}} = [s + b/2, b/2]^T$ at the source location and $\langle X^P \rangle_{\mathcal{B}} = [b/2, b/2]^T$ outside the source location. Here, s and b denote the mean intensities of the highly polarized source and the depolarized background, respectively. The second-order statistical properties of X^P are modeled by the covariance matrix Γ_i defined as

$$\Gamma_i = \left\langle \left(X_i^P - \left\langle X_i^P \right\rangle\right)\left(X_i^P - \left\langle X_i^P \right\rangle\right)^T \right\rangle = \frac{\epsilon_i^2}{2}\begin{pmatrix} 1 & \rho \\ \rho & 1 \end{pmatrix}, \quad (4)$$

where ϵ_i stands for the standard deviation of the overall multiplicative optical noise, which is likely to be partially correlated in polarimetric channels especially in snapshot imaging. The correlation coefficient is denoted by ρ. With such statistical noise model, the theoretical expression of the CNR of a generic representation γ has been derived in the appendix. The obtained expression can be easily and analytically maximized w.r.t. ρ, which indeed leads to the following linear representation $\gamma_{\mathrm{ML}} = W_{\mathrm{ML}} I_P$ with $W_{\mathrm{ML}} = [1, -\rho]$. This provides a simple adaptive representation where the background noise correlation coefficient, ρ, can in practice be estimated locally over the region $\mathcal{B}$ using the following empirical estimator

$$\widehat{\rho} = \sum_{i \in \mathcal{B}} \frac{\left(X_i^{\parallel} - \langle X^{\parallel} \rangle_{\mathcal{B}}\right)\left(X_i^{\perp} - \langle X^{\perp} \rangle_{\mathcal{B}}\right)}{\widehat{\sigma_{\mathcal{B}}}\left(X^{\parallel}\right)\widehat{\sigma_{\mathcal{B}}}\left(X^{\perp}\right)}, \quad (5)$$

where $\mathcal{B}$ still denotes the background region comprised between the two blue squares of sizes 11 × 11 pixels and 21 × 21 pixels depicted in figure 2(a). This representation is denoted as γ_{ML} (for maximum likelihood) since, for the experimental conditions at hand (with highly polarized source and completely depolarized background), its form could be equivalently derived from a likelihood maximizing approach [9]. Using this representation on the same dataset, it can be seen in figure 2(a) that γ_{CS} and γ_{ML} consistently provide enhanced contrast compared to other simple polarimetric representations. As can be observed in figure 2(b), these representations are almost equivalent, the small discrepancy between each other being due to numerical errors in the computation of the estimators and/or to possible deviation of the actual statistics from a Gaussian model. This result is verified over the entire dataset and further discussed in the next section.

4. Results and discussion

4.1. Experimental results

In figure 3, we plot the time evolution of the gain in CNR defined in equation (3) for each representation. For reference, the CNR $C(\gamma_{\Sigma})$ is shown as black-dotted line in the bottom of figure 3. The comparison confirms that the difference image γ_{Δ} (solid red lines) is not always the best representation and in

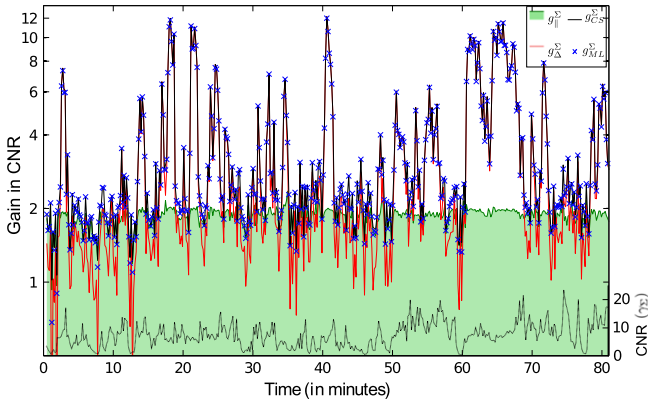

Figure 3. Gain in contrast (log scale) reached by the difference image γ_Δ (red solid lines) and γ_{CS} representation (black solid line) w.r.t the intensity-summed image γ_Σ. The blue crosses show the gain obtained with γ_{ML} representation, which can be seen to follow the maximum attainable contrast. The green filled curve shows the gain of the $\gamma_\parallel$ image with respect to the intensity-summed image.

many cases is outperformed by a simple 'polarization-filtered' image $\gamma_\parallel$, i.e., the raw $I_\parallel$ image (solid, filled green). Furthermore, γ_{CS} (solid black), presents the best contrast gain, and in general differs from both γ_Δ and $\gamma_\parallel$. It can be clearly observed that the gain in source contrast in the ML representation (γ_{ML}) closely follows the best possible gain obtained with γ_{CS}, i.e., with a computational search over all possible linear combinations. As a result, this simple analytical representation behaves adaptively to present the best source contrast in the final image for all fog density conditions. These experimental results also quantify the advantage in using a polarimetric camera for long distance contrast-enhancement of a polarized beacon through fog, as the CNR gain rises from two-fold to a maximum of 12-fold compared to an intensity-summed image which is qualitatively similar to an image obtained from a standard intensity camera. It must be noticed at this level that the noise statistics of an intensity-summed image may differ in general from the ones obtained with a true intensity imager. As shown in appendix, a fair comparison with a true intensity imager would imply a gain comprised between two and six-fold, for the noise model considered.

4.2. Influence of ρ and theoretical gains in CNR

As stated in the previous section, the derivation of the ML representation allowed us to identify the background correlation, ρ, as a crucial factor in determining the optimal contrast linear representation. In the above framework it is straightforward to calculate the theoretical CNR for each representation and thus compute the functional dependence of the gain in contrast with the correlation parameter (see appendix). The theoretical forms are tabulated in table 1 and plotted as solid lines in figure 4(a). Furthermore, the experimentally generated contrast gains are plotted alongside (scattered symbols) as a function of locally estimated background correlation. The plot shows that the CNR gain for each representation depends on ρ in an orderly fashion which was not obvious in the 'noisy' time-series data in figure 3. It is interesting to notice that the difference image γ_Δ gives the best CNR with high values of ρ, but is outperformed by the polarization-filtered image $\gamma_\parallel$ as the value of ρ falls bellow 0.5. The performance of $\gamma_\parallel$ remains linear with ρ, with a maximum gain of 2 for high values of ρ, while that of γ_Δ rises steeply when $\rho \to 1$. Again, the optimality of the ML representation is clearly seen, as it corresponds to the best contrast representation for all values of ρ.

The ρ-dependant performance of the studied representations (particularly γ_Δ and γ_{ML}) can be interpreted by noting that, in the present context, ρ is a measure of the visibility of background structure in the local scene or local non-uniformity in reflectance. This can also be checked on the frames shown in figure 1(b) that are sorted in increasing order of ρ. As a result, the main benefit of γ_Δ relies in its ability to suppress highly structured (and thus correlated) background in the final image. This property is retained by the γ_{ML}, which identifies with γ_Δ for $\rho \to 1$. On the other hand, with uncorrelated background ($\rho = 0$), the perpendicular image $I_\perp$ does not bring any further information, making $\gamma_\parallel$ optimal during very low visibility conditions. The experiment also quantifies the advantage in using a polarimetric camera as we observe a maximum CNR gain of 12-fold compared to the intensity-summed image which is qualitatively similar to an image obtained from standard intensity camera.

4.3. Implementation of optimal representations

Finally, we briefly discuss the implementation and some generic issues associated with computing such contrast-maximizing representations in realistic field conditions. For instance, in the context of assistance to navigation in foggy weather, the camera and the beacons may be in relative motion. As a result, the number and location of the beacons that have to be identified in the foggy images are unknown, and must be retrieved on a frame-to-frame basis to be displayed to the user, or to an automated detection algorithm. According to the previous results, computing the optimal polarimetric representation at each location of each frame (using a sliding window) will provide a contrast-maximized image that reveals the presence of a source embedded in fog, or that better isolates the polarized source from the rest of the image as compared to a standard intensity image, as illustrated in figure 4(b).

To obtain the contrast-maximized image (or a pixel-wise CNR map of this contrast-maximized image), the estimation of local statistics over a sliding window can be replaced with a convolution approach which performs quickly by using fast Fourier transforms. For computing γ_{CS}, multiple CNR images must be generated and the maximum value at each pixel must be chosen to form the final image. In contrast, for the ML representation one would need fewer Fourier transforms to calculate the local correlation coefficients, thus providing γ_{ML} a noticeable time advantage over γ_{CS}. However, with fast computers or FPGA based embedded system, both techniques should remain within real-time requirement. Another parameter of importance is the size and shape of ROI, which

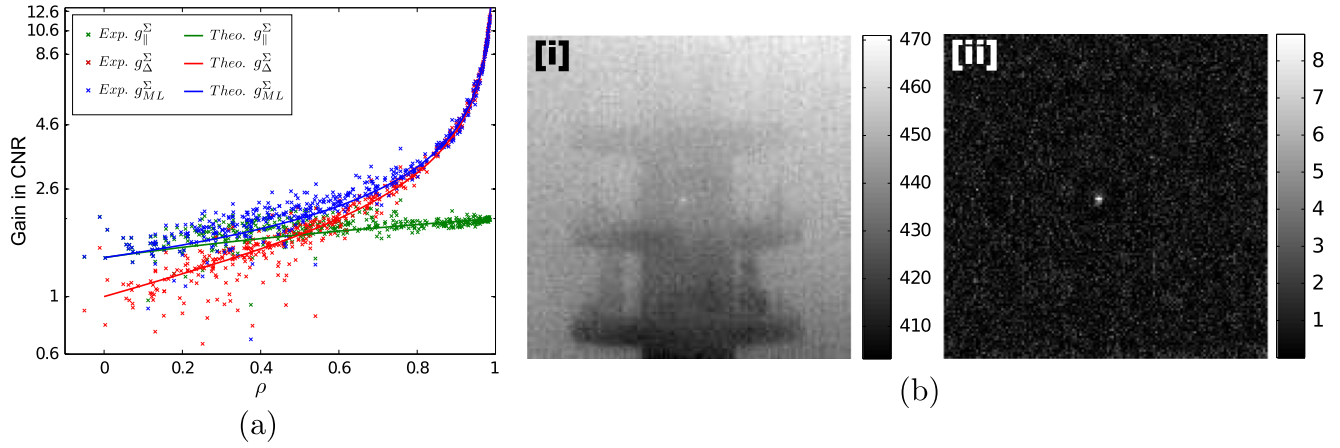

Figure 4. (a) The experimentally obtained gain in CNR (scattered points) for each representation is plotted in log scale along-side the corresponding functional forms (solid lines) of the gain listed in table 1. (b) Comparison of the intensity-summed image obtained with a standard camera (left, (i)) with a processed CNR map of γ_{ML} (right, (ii)) that can be provided as a final contrast enhanced image to the end-user or to a higher-level image processing unit.

should also be varied to maximize the CNR over multiple scales, especially when the spread of the source is unknown and may evolve in time. The ML method remains specifically suitable in this case as only a 1D maximization over scale is required as opposed to a search over both scale and linear weighting of polarimetric images.

5. Conclusion

In this article, we first showed experimentally that when performing real field polarimetric imaging, two polarimetric channels acquired along two orthogonal polarization directions can have intensity fluctuations that are significantly correlated. Moreover, experiments reveal that the contrast of a polarized light source under any visibility condition can be maximized using a linear combination of the two acquired polarimetric images, which differs in general from the standard polarimetric representations used in literature. Under a correlated Gaussian noise hypothesis, we also demonstrated that the optimal representation is simply related to the noise correlation coefficient, which is also observed experimentally. As a result, such computationally-efficient representation can replace a numerical search of the optimal weighting coefficients, and could thus be easily implemented in real-time applications as a pre-processing task for automated detection/localization on wide field images. Lastly, the results presented here could be easily generalized to any case of partially polarized source and background with finite detector noise, which could be of interest for underwater imaging or imaging in biological tissues.

Acknowledgments

This work has been partly funded by the CEFIPRA (project N° 4604-4). The authors would like to thank Prof Hema Ramachandran for fruitful discussions. The authors acknowledge the TDF company and Rennes Métropole for supporting this work, and L Frein, C Hamel, A Carré and S Bouhier for technical assistance.

Appendix

As noted above, the polarimetric pixel can be written as a 2D random vector $X^P = [x^{\parallel}, x^{\perp}]^T$, where the dependency in pixel location i is omitted in the appendix for the sake of clarity. Assuming a correlated Gaussian noise model and keeping the same notations as in section 2.2, we derive the expression for CNR for a generic polarimetric representation γ. Its mean value at a given location in the image is directly given by $\langle\gamma\rangle = W\langle X^P\rangle$, and its variance reads $\sigma^2(\gamma) = W\Gamma W^T$. From the definition of the CNR in equation (2), a straightforward calculation yields

$$C(\gamma) = \frac{s}{\epsilon}\sqrt{\frac{2u^2}{u^2 + 2\rho uv + v^2}}.$$

As a result, the gain in CNR with respect to the intensity-summed representation γ_Σ reads

$$g^{\Sigma} = \frac{C(\gamma)}{C(\gamma_\Sigma)} = \sqrt{\frac{2u^2(1+\rho)}{u^2 + 2\rho uv + v^2}},$$

from which the gain expressions of table 1 are easily derived.

If one now considers a true intensity imager, and given the notations above, the intensity level X^I recorded at a given pixel would have a mean value of $\langle X^I\rangle_S = s + b$ at the source location, and $\langle X^I\rangle_B = b$ in the background region, with variance $\sigma^2(X^I) = \epsilon^2$. The CNR is thus $C(X^I) = s/\epsilon$, and as a result,

$$g^I = \frac{C(\gamma)}{C\left(X^I\right)} = \frac{C(\gamma)}{C(\gamma_\Sigma)}\frac{C(\gamma_\Sigma)}{C\left(X^I\right)} = \frac{g^{\Sigma}}{\sqrt{1+\rho}}. \qquad (A.1)$$

This shows that the gain with respect to a true intensity imager is equivalent to the gain with respect to the intensity-summed image only when the correlation parameter ρ tends to 0, and is lower by a factor of 2 when ρ approaches unity.

References

[1] Boffety M, Galland F and Allais A G 2012 Influence of polarization filtering on image registration precision in underwater conditions *Opt. Lett.* **37** 3273–5

[2] Ramachandran H and Narayanan A 1998 Two-dimensional imaging through turbid media using a continuous wave light source *Opt. Commun.* **154** 255–60

[3] Demos S G and Alfano R R 1997 Optical polarization imaging *Appl. Opt.* **36** 150–5

[4] Nan Z, Xiaoyu J, Qiang G, Yonghong H and Hui M 2009 Linear polarization difference imaging and its potential applications *Appl. Opt.* **48** 6734–9

[5] Fade J, Panigrahi S, Carré A, Frein L, Hamel C, Bretenaker F, Ramachandran H and Alouini M 2014 Long range polarimetric imaging through fog *Appl. Opt.* **53** 3854–65

[6] Horinaka H, Hashimoto K, Wada K, Cho Y and Osawa M 1995 Extraction of quasi-straightforward-propagating photons from diffused light transmitting through a scattering medium by polarization modulation *Opt. Lett.* **20** 1501–3

[7] Emile O, Bretenaker F and Floch A L 1996 Rotating polarization imaging in turbid media *Opt. Lett.* **21** 1706–8

[8] Tyo J S, Rowe M P, Pugh E N and Engheta N 1996 Target detection in optically scattering media by polarization-difference imaging *Appl. Opt.* **35** 1855–70

[9] Fade J, Panigrahi S and Alouini M 2014 Optimal estimation in polarimetric imaging in the presence of correlated noise fluctuations *Opt. Express* **22** 4920–31

[10] Bénière A, Alouini M, Goudail F and Dolfi D 2009 Design and experimental validation of a snapshot polarization contrast imager *Appl. Opt.* **48** 5764–73

[11] Sankaran V, Schönenberger K, Walsh J T and Maitland D J 1999 Polarization discrimination of coherently propagating light in turbid media *Appl. Opt.* **38** 4252–61

[12] Rowe M P, Pugh E N, Tyo J S and Engheta N 1995 Polarization-difference imaging: a biologically inspired technique for observation through scattering media *Opt. Lett.* **20** 608–10

Research Article | Vol. 24, No. 14 | 11 Jul 2016 | OPTICS EXPRESS 16066

Optics EXPRESS

Theoretical optimal modulation frequencies for scattering parameter estimation and ballistic photon filtering in diffusing media

SWAPNESH PANIGRAHI,[1,*] JULIEN FADE,[1] HEMA RAMACHANDRAN,[2] AND MEHDI ALOUINI[1]

[1]*Institut de Physique de Rennes, CNRS, UniversitÃl' de Rennes 1, Campus de Beaulieu, 35 042 Rennes, France*

[2]*Raman Research Institute, CV Raman Avenue, Sadashivanagar, 560 080 Bangalore, India*

[*]*swapnesh.panigrahi@univ-rennes1.fr*

Abstract: The efficiency of using intensity modulated light for the estimation of scattering properties of a turbid medium and for ballistic photon discrimination is theoretically quantified in this article. Using the diffusion model for modulated photon transport and considering a noisy quadrature demodulation scheme, the minimum-variance bounds on estimation of parameters of interest are analytically derived and analyzed. The existence of a variance-minimizing optimal modulation frequency is shown and its evolution with the properties of the intervening medium is derived and studied. Furthermore, a metric is defined to quantify the efficiency of ballistic photon filtering which may be sought when imaging through turbid media. The analytical derivation of this metric shows that the minimum modulation frequency required to attain significant ballistic discrimination depends only on the reduced scattering coefficient of the medium in a linear fashion for a highly scattering medium.

OCIS codes: (110.0113) Imaging through turbid media; (170.5270) Photon density waves; (170.4090) Modulation techniques; (170.5280) Photon migration; (290.1990) Diffusion.

References and links

1. D. Boas, D. Brooks, E. Miller, C. DiMarzio, M. Kilmer, R. Gaudette, and Q. Zhang, "Imaging the body with diffuse optical tomography," IEEE Signal Proc. Mag. **18**, 57–75 (2001).
2. Y. Y. Schechner and N. Karpel, "Clear underwater vision," in *Proceedings of the IEEE Computer Society Conference on Computer Vision and Pattern Recognition,* (CVPR IEEE 2004) pp. I-536-I-543 Vol.1.
3. H. Ramachandran and A. Narayanan, "Two-dimensional imaging through turbid media using a continuous wave light source," Opt. Commun. **154**, 255–260 (1998).
4. W. R. Watkins, D. H. Tofsted, V. G. CuQlock-Knopp, J. B. Jordan and J. O. Merritt, "Navigation through fog using stereoscopic active imaging," Proc. SPIE **4023**, Enhanced and Synthetic Vision 2000, 20 (2000).
5. N. Hautiere, J. P. Tarel and D. Aubert, "Towards Fog-Free In-Vehicle Vision Systems through Contrast Restoration," in *Proceedings of the IEEE Computer Society Conference on Computer Vision and Pattern Recognition,* (IEEE, 2007), pp. 1–8.
6. S. R. Arridge, "Optical tomography in medical imaging," Inverse Probl. **15**, R41–R93 (1999).
7. M. Brewster and Y. Yamada, "Optical properties of thick, turbid media from picosecond time-resolved light scattering measurements," Int. J. Heat Mass Tran. **38**, 2569 – 2581 (1995).
8. B. J. Tromberg, N. Shah, R. Lanning, A. Cerussi, J. Espinoza, T. Pham, L. Svaasand, and J. Butler, "Non-Invasive In Vivo Characterization of Breast Tumors Using Photon Migration Spectroscopy," Neoplasia **2**, 26–40 (2000).
9. S. B. Colak, M. B. Van Der Mark, G. W. Hooft, J. H. Hoogenraad, E. S. Van Der Linden, and F. A. Kuijpers, "Clinical optical tomography and NIR spectroscopy for breast cancer detection," IEEE J. Sel. Top. Quant. **5**, 1143–1158 (1999).
10. G. Strangman, D. A. Boas, and J. P. Sutton, "Non-invasive neuroimaging using near-infrared light," Biol. Psychiat. **52**, 679–693 (2002).
11. T. J. Farrell, M. S. Patterson, and B. Wilson, "A diffusion theory model of spatially resolved, steadyâĂŘstate diffuse reflectance for the noninvasive determination of tissue optical properties in vivo," Med. Phys. **19(4)** (1992).
12. M. Ghijsen, B. Choi, A. Durkin, S. Gioux, and B. Tromberg, "Real-time simultaneous single snapshot of optical properties and blood flow using coherent spatial frequency domain imaging (cSFDI)," Biomed. Opt. Express **7**, 870–882 (2016).
13. D. A. Benaron and D. K. Stevenson, "Optical time-of-flight and absorbance imaging of biologic media," Science **259**, 1463–1466 (1993).

#264066 http://dx.doi.org/10.1364/OE.24.016066
Journal © 2016 Received 26 Apr 2016; revised 9 Jun 2016; accepted 9 Jun 2016; published 8 Jul 2016

Optics EXPRESS

14. R. Cubeddu, A. Pifferi, P. Taroni, A. Torricelli, and G. Valentini, "Time-resolved imaging on a realistic tissue phantom: μ(s)' and μ(a) images versus time-integrated images," Appl. Opt. **35**, 4533–4540 (1996).
15. E. Gratton, S. Fantini, M. a. Franceschini, G. Gratton, and M. Fabiani, "Measurements of scattering and absorption changes in muscle and brain," Philos. Trans. R. Soc. B Biol. Sci. **352**, 727–735 (1997).
16. B. J. Tromberg, L. O. Svaasand, T.-T. Tsay, and R. C. Haskell, "Properties of photon density waves in multiple-scattering media," Appl. Opt. **32**, 607 (1993).
17. H. Jiang, K. D. Paulsen, U. L. Osterberg, B. W. Pogue, and M. S. Patterson, "Simultaneous reconstruction of optical absorption and scattering maps in turbid media from near-infrared frequency-domain data," Opt. Lett. **20**, 2128–2130 (1995).
18. B. W. Pogue and M. S. Patterson, "Frequency-domain optical absorption spectroscopy of finite tissue volumes using diffusion theory," Phys. Med. Biol. **39**, 1157–1180 (1994).
19. S. Farsiu, J. Christofferson, B. Eriksson, P. Milanfar, B. Friedlander, A. Shakouri, and R. Nowak, "Statistical detection and imaging of objects hidden in turbid media using ballistic photons," Appl. Opt. **46**, 5805–5822 (2007).
20. L. Wang, P. P. Ho, C. Liu, G. Zhang, and R. R. Alfano, "Ballistic 2-d imaging through scattering walls using an ultrafast optical kerr gate," Science **253**, 769–771 (1991).
21. D. Sedarsky, E. Berrocal, and M. Linne, "Quantitative image contrast enhancement in time-gated transillumination of scattering media," Opt. Express **19**, 1866–1883 (2011).
22. R. Berg, O. Jarlman, and S. Svanberg, "Medical transillumination imaging using short-pulse diode lasers," Appl. Opt. **32**, 574 (1993).
23. O. Emile, F. Bretenaker, and A. L. Floch, "Rotating polarization imaging in turbid media," Opt. Lett. **21**, 1706–1708 (1996).
24. L. Mullen, A. Laux, B. Concannon, E. P. Zege, I. L. Katsev, and A. S. Prikhach, "Amplitude-modulated laser imager," Appl. Optics **43**, 3874–3892 (2004).
25. S. Sudarsanam, J. Mathew, S. Panigrahi, J. Fade, M. Alouini, and H. Ramachandran, "Real-time imaging through strongly scattering media: seeing through turbid media, instantly," Sci. Rep. **6**, 25033 (2016).
26. M. S. Patterson, B. Chance, and B. C. Wilson, "Time resolved reflectance and transmittance for the non-invasive measurement of tissue optical properties," Appl. Opt. **28**, 2331–2336 (1989).
27. D. Contini, F. Martelli, and G. Zaccanti, "Photon migration through a turbid slab described by a model based on diffusion approximation. I. Theory," Appl. Opt. **36**, 4587 (1997).
28. J. B. Fishkin and E. Gratton, "Propagation of photon-density waves in strongly scattering media containing an absorbing semi-infinite plane bounded by a straight edge," J. Opt. Soc. Am. A. **10**, 127–140 (1993).
29. S. L. Jacques and B. W. Pogue, "Tutorial on diffuse light transport," J. Biomed. Opt. **13**, 041302 (2008).
30. S. T. Flock, M. S. Patterson, B. C. Wilson, and D. R. Wyman, "Monte Carlo modeling of light propagation in highly scattering tissues. I. Model predictions and comparison with diffusion theory," IEEE T. Biomed Eng. **36**, 1162–1168 (1989).
31. L. V. Wang, H. Wu, *Biomedical Optics: Principles and Imaging* (Wiley, 2007).
32. A. Ishimaru, *Wave Propagation and Scattering in Random Media* (Wiley, 1999).
33. R. Lange and P. Seitz, "Solid-state time-of-flight range camera," IEEE J. Quantum Elect. **37**, 390–397 (2001).
34. F. Mufti and R. Mahony, "Statistical analysis of signal measurement in time-of-flight cameras," ISPRS J. Photogramm. **66**, 720–731 (2011).
35. P. H. Garthwaite, I. T. Jolliffe, B. Jones, *Statistical Inference* (Oxford University, 2002).
36. H. K. Kim, U. J. Netz, J. Beuthan, and A. H. Hielscher, "Optimal source-modulation frequencies for transport-theory-based optical tomography of small-tissue volumes," Opt. Express **16**, 18082–18101 (2008).
37. X. Gu, K. Ren, and A. H. Hielscher, "Frequency-domain sensitivity analysis for small imaging domains using the equation of radiative transfer," Appl. Opt. **46**, 1624–1632 (2007).
38. V. Toronov, E. D'Amico, D. Hueber, E. Gratton, B. Barbieri, and A. Webb, "Optimization of the signal-to-noise ratio of frequency-domain instrumentation for near-infrared spectro-imaging of the human brain," Opt. Express **11**, 2717–2729 (2003).
39. WMO-No. 8, "Guide to Meteorological Instruments and Methods of Observation," 7^{th} edition, World Meteo., (2008).
40. J. B. Fishkin, S. Fantini, M. J. vandeVen, and E. Gratton, "Gigahertz photon density waves in a turbid medium: Theory and experiments," Phys. Rev. E **53**, 2307–2319 (1996).

1. Introduction

Imaging through and within turbid media is an area of interest that has tremendous application in medical diagnostics [1], underwater vision [2], imaging through colloids [3] and transportation and navigational aids [4,5]. Light traveling through a complex medium with randomly distributed positions and refractive indices undergoes absorption and random scattering and loses the spatial and temporal information of its source. The photons that undergo such multiple scattering are labeled as diffused photons. A small fraction of the total photons called ballistic and quasi-

Optics EXPRESS

ballistic photons, undergo no or very few forward scattering events before they reach the detector, and they retain the information of its source (direction, polarization state, modulation,...). It is of wide interest to discriminate the ballistic/quasi-ballistic photons from the diffused photons for resolution enhanced imaging through turbid media. However, the diffuse light that strongly depends on the properties of the scattering medium can be used to deduce various parameters related to the medium itself. Thus, imaging in turbid media can be classified into two broad categories: parameter estimation using only diffused light to obtain image of heterogeneities in the turbid media and filtering of ballistic photons from diffused light for high resolution imaging through turbid media.

Parameter estimation In parameter estimation, the physical properties of the intervening media are of interest and controlled light sources may be used to estimate the scattering and absorption parameters [6, 7]. Diffuse optical imaging which has been widely studied and applied in medical imaging [8] is used to estimate the scattering and absorption coefficient in the intervening media for detection of malignant tissues in breast [9] or for brain imaging [10]. Various methodologies have been developed that utilize the diffusion equation to model light transport through tissues to estimate its scattering parameters. Steady-state solution is generally used in case where continuous wave light sources are used [11] or when patterned light source is used as in case of spatial frequency domain imaging [12]. Diffusion approximation is also commonly used to model the transport of pulsed light [13, 14] or modulated light [15–18] through the scattering media. The precision of estimation of the parameters is crucial in this case. In practice, intensity modulated light with diffusion theory are widely used in frequency-domain photon migration measurements, where an intensity modulated light with modulation frequencies of a few hundred MHz is transmitted through a diffusing medium. According to the time dependent solution of the diffusion theory, at these frequencies, the wave number of the density wave traveling through the medium is dependent on the scattering and absorption properties of the medium. As a result, the detected modulated light has reduced modulation index and an additional phase, both of which depend on the scattering properties of the medium and its thickness. As the diffusion theory provides an analytical model for the change of modulation index and phase of the modulated light, the parameters of the intervening medium could be estimated by using a single or multiple modulation frequencies.

Ballistic discrimination On the other hand, ballistic filtering is used when the spatial resolution of objects embedded in scattering media is of interest [19, 20]. For instance, for industrial applications where it is required to image objects embedded in colloidal system, or in navigation where vision through fog can be efficiently achieved with ballistic filtering. The problem of imaging through such media has been addressed using various techniques that essentially rely on discriminating ballistic/quasi-ballistic photons from multiply scattered (diffuse) photons traversing through a turbid medium. For example, time gated imaging [21, 22], polarization gated imaging [23], intensity modulation imaging [24] etc., where information carried by the ballistic/quasi-ballistic photons is filtered from the diffuse light. It is challenging to efficiently detect the ballistic photons that have low signal to noise ratio as compared to the diffused photons, especially in highly scattering media. Ballistic photon filtering could also be achieved with an intensity modulation imaging scheme by discriminating them from the diffused light that arrives with reduced modulation index and additional phase. One of the purposes of this article is to theoretically study the feasibility of such an approach, which is currently the topic of active research [25].

In this article, we analyze the widely used diffusion approximation for transport of modulated light, from an information theoretical point of view for efficient parameter estimation and for ballistic photons discrimination. Assuming a general scheme of optical quadrature demodulation

Optics EXPRESS

detection and a corresponding noise model, this approach provides a rigorous insight into the maximal precision of estimation of parameters using the diffusion equation, thereby providing a robust theoretical argument for choosing the frequency of modulation suited to the experiment at hand. Similarly, for ballistic filtering, we will present an information theoretic performance metric and study the optimum ballistic discrimination efficiency that can be achieved under this imaging scheme.

In section 2, we provide a brief description of the use of diffusion equation, the transport of modulated light in diffusing media and the imaging scheme along with the parameters that will be used in the theoretical analysis. In section 3, a generalized demodulation scheme is defined and a noise model is presented. Then, in section 4, the noise model and the diffusion theory are used to calculate the Cramer-Rao bound for parameter estimation. Finally, in section 5, the ballistic filtering efficiency is analyzed and discussed with respect to real field situations.

2. Imaging scheme and diffusion model

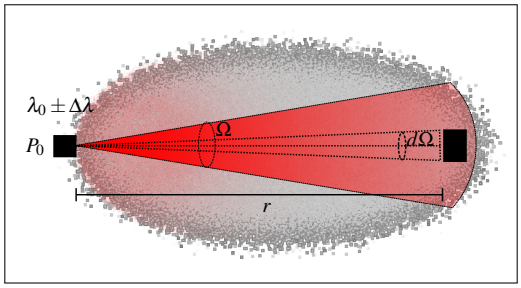

Fig. 1. Imaging scheme: A directional source of light with power, P_0, forward cone solid angle, Ω, having a limited spectral width ($\lambda \pm \Delta\lambda$) is detected at a distance r by a detector that subtends an angle $d\Omega$ from the source.

The diffusion theory for photon transport provides a simple, fast and analytical method for modeling the light propagation through various turbid media. The properties of intensity modulated light through a diffusing medium have been well studied and reviewed [15, 26–28]. Here, we present a brief introduction underlining concepts that are relevant in the context of this article. We will follow the modeling of the intensity modulated light in diffusing media as derived in several references [16, 28, 29] in the context of diffuse optical imaging. We will use the formulations previously derived by the cited authors to parameterize our detection scheme and then use information theoretical tools to derive simple rules for choosing frequency operating points to efficiently use intensity modulation light depending on the properties of the medium.

2.1. Diffusion model

The diffusion model arises when the photons are allowed to perform a random walk, diffusing from high photon density regions to low photon density regions. The theory has proved efficient when modeling light in a predominantly scattering medium where the source and the detector are far from boundaries of the medium and when detection is carried out sufficiently away from a point source, in a supposed infinite geometry. The efficiency of the diffusion theory has been studied alongside Monte-Carlo simulation and shown to have well acceptable accuracy in the domain of its validity [30]. Let us now identify some parameters that are important for describing light transport in a scattering medium. First, the absorption coefficient, denoted by μ (in units of m^{-1}), corresponds to the inverse of the mean distance traveled by a photon before it is absorbed. Similarly, the scattering coefficient μ_s (m^{-1}) is the inverse mean distance before a photon is

Optics EXPRESS

scattered in the medium. We shall also consider the *reduced* scattering coefficient, denoted by σ in this work, and classically defined as $\sigma = \mu_s(1-g)$, where g is the (dimensionless) anisotropy factor, defined as the mean cosine of the scattering phase function [31, 32]. Such a reduced scattering coefficient allows anisotropic scattering media to be easily described (notably through diffusion equation), and may be interpreted as the inverse of the scattering length for a fictitious isotropically scattering ($g = 0$) medium having the same macroscopic light-transport parameters as the real anisotropically scattering ($g \neq 0$) medium. Within this framework, an important length scale is the transport mean free path ($TMFP$) denoted by l_*, which is the mean distance traveled by photons before they lose their initial directional information and is equal to $[\mu+\sigma]^{-1}$. The diffusion theory also includes two other constants: the diffusion length (D) defined as $D = l_*/3$ and the optical penetration depth (δ), which is the inverse of the effective attenuation coefficient ($\sqrt{\mu/D}$) in diffusing medium.

In addition, for the analysis in the following sections we will use various dimensionless constants that are also given in the right side of Table 1. For instance, the dimensionless parameter $R_\delta = r/\delta$ corresponds to the effective optical attenuation of diffused light. The parameter q is related to the angular frequency of modulation and the non-trivial form of the reparameterization will be justified in following sections. For ease of reading, the corresponding definitions of all these parameters are tabulated in Table 1.

2.2. Imaging scheme

Table 1. Left column: definitions, symbols and units of experimental parameters and diffusing medium parameters. Right column: definition of dimensionless reduced parameters.

Meaning	Symbol	Unit	Param.	Defn.
Distance of propagation	r	(m)	–	–
Mean Free Path (MFP)	$MFP = 1/(\mu+\mu_s)$	(m)	R_b	r/MFP
Transport MFP (TMFP)	$l_* = 1/(\mu+\sigma)$	(m)	R_*	r/l_*
Diffusion length	$D = l_*/3$	(m)	–	–
Optical penetration depth	$\delta = [D/\mu]^{\frac{1}{2}}$		R_δ	r/δ
	$= [3\mu(\mu+\sigma)]^{-\frac{1}{2}}$	(m)		
Angular modulation frequency	ω	(rad/s)	q	$\sqrt{\frac{1+\sqrt{1+(\omega/\mu c)^2}}{2}}$
Effective refractive index	n	-		
Speed of light in medium	c	(m/s)	–	–

The imaging scheme considered in this article includes a directional point source of light with a forward cone solid angle Ω and that subtends a solid angle of $d\Omega$ at the detector which is placed at a distance r from the source. For the sake of simplicity, we shall consider a source of limited spectral range $\lambda_0 \pm \Delta\lambda$, so that the above diffusion parameters can be considered as constant over the considered spectral range. The schematic in Fig. 1 illustrates the scenario. In the presence of an intervening scattering medium, the net intensity of ballistic photons reaching the detector of collection area $d\Omega r^2$ is proportional to the total power P_0 emitted by the source. It is given by the Bouguer-Beer-Lambert's law as $I_B = \xi P_0\, e^{-(\mu+\mu_s)r}\frac{d\Omega r^2}{\Omega r^2} = \xi P_0\, e^{-(\mu+\mu_s)r}\frac{d\Omega}{\Omega}$ [31], with an extinction coefficient $\mu+\mu_s$, (equal to the inverse MFP, see Table 1) allowing us to define $R_b = r/MFP$ as the effective optical attenuation of ballistic light. The scaling factor ξ represents the overall detector efficiency on the considered spectral range. Similarly, according to the steady state solution of the diffusion theory, the diffuse photon intensity reaching the detector is also proportional to the total power emitted by source, such that $I_D = \xi P_0\, e^{-r/\delta}\frac{d\Omega r^2}{4\pi D r} = \xi P_0\, e^{-r/\delta}\frac{d\Omega}{4\pi}\frac{r}{D}$ [16, 29]. The expressions for the intensities of ballistic and diffused light show that there are

Optics EXPRESS

clearly two important length scales to be considered, namely, the TMFP (l_*) and the optical penetration depth (δ). Considering only the above two classes of photons, it is possible to obtain an order of magnitude value of the ratio (α) of ballistic photons to diffuse photons reaching the detector as

$$\alpha = \frac{I_B}{I_D} = \Omega' \frac{D}{r}\, e^{-r(\mu+\mu_s-1/\delta)} = \Omega' \frac{e^{R_\delta - R_b}}{3R_*}, \tag{1}$$

where we use dimensionless variables R_*, R_δ, R_b and $\Omega' = 4\pi/\Omega$.

2.3. Modulated light in diffusing media

The propagation of sinusoidally modulated light through a scattering medium has been modeled using diffusion theory and it has been shown that the transport of modulated light behaves as photon density waves whose properties are dependent on the properties of the medium [15, 16, 27, 28]. In this article, we consider an intensity modulated source of light having modulation angular frequency ω and amplitude modulation index M (also classically termed *modulation depth*), which describes the amplitude of the periodic fluctuation of light intensity around its unmodulated level. In that case, the instantaneous intensity reads $i(t) = I_0(1 + M\cos[\omega t])$. The ballistic light that follows Bouguer-Beer-Lambert's law, is only attenuated and reaches the detector with instantaneous intensity $i_b(t) = I_B(1 + m_B\cos[\omega t])$ without any change in received modulation index, $m_B = M$.

However, the time dependent solution of the photon diffusion theory shows that the modulated light traversing through a scattering medium is received at the detector with reduced modulation index and additional phase [16]. Then, the instantaneous diffuse light intensity received at the detector is $i_d(t) = I_D(1 + m_D\cos[\omega t + \Delta\phi])$. Without derivation, we present the expression of the reduced modulation index m_D and the phase $\Delta\phi$ which is identically reported in [16, 29] for an infinite medium:

$$m_D = M\exp\left[-r\sqrt{3\mu(\mu+\sigma)}\left(\sqrt{\frac{1+\sqrt{1+(\omega/\mu c)^2}}{2}}-1\right)\right] = M\, e^{-R_\delta(q-1)},$$

$$\Delta\phi = r\sqrt{3\mu(\mu+\sigma)}\sqrt{\frac{-1+\sqrt{1+(\omega/\mu c)^2}}{2}} = R_\delta\sqrt{q^2-1}. \tag{2}$$

where the parameter $q = \sqrt{(1+\sqrt{1+(\omega/\mu c)^2})/2}$, is related to the angular frequency of modulation and ranges between $[1,\infty)$ when $\omega \in [0,\infty)$. Although the physical interpretation of this parameter is not straightforward, we will see later that qR_δ can be identified as a dimensionless, frequency-dependent, effective attenuation of the diffused light. In the remainder of this article, we define $\beta = m_B/m_D$ as the ratio of the modulation indices of ballistic light to diffuse light. The expressions of the intensity, phase and modulation index of ballistic and diffuse light components are recalled in Table 2.

It is quite straightforward to see that using the above equations, the parameters R_δ and q can be estimated when the modulation index and phase of the diffuse light are accurately detected. The model can indeed be inverted as shown in Eq. (2.3):

$$R_\delta = \frac{\Delta\phi^2 - 2(\ln[\beta])^2}{4\ln[\beta]}, \tag{3}$$

$$q = \frac{\Delta\phi^2 + 2(\ln[\beta])^2}{\Delta\phi^2 - 2(\ln[\beta])^2}. \tag{4}$$

Optics EXPRESS

Table 2. Expressions of intensity, modulation index and relative phase for the ballistic and diffuse components of the detected light.

Detection	Ballistic photons	Diffuse photons	Ratio (Ballistic/Diffuse)
Relative phase ($\Delta\phi$)	0	$R_\delta\sqrt{2(q^2-1)}$	–
Modulation index	$m_B = M$	$m_D = Me^{-R_\delta(q-1)}$	$\beta = e^{R_\delta(q-1)}$
Intensity	$I_B = \xi\frac{d\Omega}{\Omega}P_0\, e^{-R_b}$	$I_D = \xi\frac{d\Omega}{4\pi}3P_0R_*\, e^{-R_\delta}$	$\alpha = \Omega'\frac{e^{R_\delta - R_b}}{3R_*}$

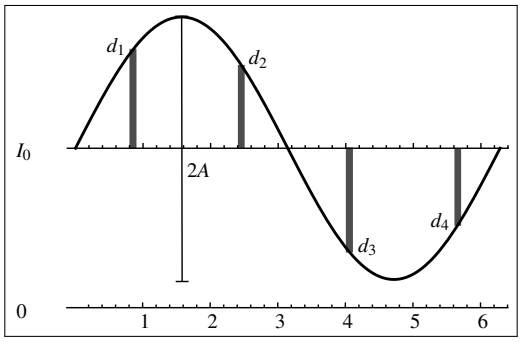

Fig. 2. Illustration of the optical signal received at the detector. As an example, four samples are shown here to form the quadrature components which, consequently, can be used for estimation of amplitude and phase of the signal.

Thus, the above formulation provides a simple analytical method for estimation of the scattering and absorption parameters of the scattering medium using only diffuse light and a modulated light source. In practice, especially in diffuse optical imaging, the modulation frequency is scanned to obtain corresponding values of modulation index and phase. Then, a non-linear fit of the theoretical prediction with the data provides the estimates for the scattering and absorption properties of the medium [16]. The effect of scattering media on modulation index and phase can also be exploited to attain discrimination of ballistic photons that retain the modulation index and phase. These application scenarios can be analyzed from an information theoretical point of view for a well-defined detection technique. The detection of the modulation index and the phase can be performed in various ways. Generally in a demodulation scheme, the amplitude, phase and mean intensity are recorded and then the modulation index can be easily estimated. Quadrature demodulation is one of the simplest and the most widely used scheme for demodulation. It avoids, in particular, phase tracking of the incoming signal which brings additional noise contributions. In the following section we look at a quadrature detection scheme and derive the noise model for the detection.

3. Quadrature detection scheme and noise model

Demodulation of a sinusoidally modulated signal can be performed by product detection, where the signal is continuously multiplied with a sine and cosine of the same frequency to obtain the quadrature amplitudes. This quadrature detection can be interpreted as follows. Let us consider a detection system where a sinusoidal signal of angular frequency ω, modulation index M and mean intensity I_0 is sampled N times in a period producing photon count or grey level data d_i ($i = 1$ to N). Then the quadrature components can be estimated by applying sinusoidal weighting of the data points and computing the two quadratures $U = \sum_{i=1}^{N} d_i \cos[\omega t_i + \phi] = A\cos[\phi]$ and $V = \sum_{i=1}^{N} d_i \sin[\omega t_i + \phi] = A\sin[\phi]$, for $N \geq 2$, where ϕ denotes the relative phase difference

Optics EXPRESS

between the signal and the demodulating waveforms. From the obtained variables U and V, estimates of the amplitude $A = MI_0/2$ and relative phase ϕ of the demodulated signal are respectively given by $\hat{A} = \sqrt{U^2+V^2}$ and $\hat{\phi} = tan^{-1}[V/U]$.

The intensity statistics of the random variables U and V can be derived by knowing that the photon count within an infinitesimal sampling window at time t_i may follow Poisson distribution with mean and variance equal to the intensity received at the sampling window, which is d_i in the current notation. Then, a weighted addition of the Poisson distributed data is also Poissonian, indicating that U and V will also be distributed as Poisson random variables with variance $I_0/2$ (see Appendix A.1). For high intensities, the Poisson distribution can be well approximated by a Gaussian distribution ($\mathcal{N}$) with variance equal to the mean. Thus, we approximate that U and V are distributed as $\mathcal{N}(A\cos[\phi], \Lambda^2)$ and $\mathcal{N}(A\sin[\phi], \Lambda^2)$, respectively, with $\Lambda^2 = I_0/2$ and $\mathcal{N}(\bar{x}, var(x))$ denoting the normal distribution with mean $\bar{x}$ and variance $var(x)$. Knowing the distribution of the quadrature components, it is then possible to derive the joint probability density function (PDF) of the random variables, $Z = \sqrt{U^2+V^2}$ and $\Psi = tan^{-1}(V/U)$, respectively associated with the modulation amplitude A and relative phase ϕ, by applying the appropriate change of variables to the Gaussian distribution, as given in the Appendix A.2. The expected values of the random variables Z, Ψ and their variance form the parameter vector $\theta' = [A, \phi, \Lambda^2]$, where $2A = MI_0$ is the peak-to-peak amplitude as shown in the schematic of Fig. 2. Then, the joint PDF of the amplitude and phase is

$$P_{Z,\Psi}(z, \psi | A, \phi, \Lambda^2) = \frac{z}{2\pi\Lambda^2} \exp\left[-\frac{1}{2\Lambda^2}(z^2 + A^2 - 2zA\cos[\psi - \phi])\right]. \tag{5}$$

Quadrature demodulation cameras are in widespread use, especially in 3D imaging. For instance, novel demodulation cameras like time-of-flight (TOF) cameras collect four samples per period to obtain the quadratures $U = d_1 - d_3$ and $V = d_2 - d_4$ at frequencies up to 20 MHz [33]. Information theoretical studies have been made to accurately determine the phase which contains the depth information of a scene using the above PDF [34]. In the following, we will use Fisher information (FI) and Cramer-Rao bound (CRB) to analyze how well the diffusion parameters of the scattering medium can be estimated using modulated light and the quadrature detection technique.

3.1. Fisher information

Fisher information (FI) is a useful and efficient method of quantifying the precision with which the unknown parameters in a data model can be estimated. It can be further used to analyze the behavior of the covariance of estimators and its dependency on other parameters. FI is ultimately related to the minimum covariance bound on the unbiased estimation of the unknown parameters. Here, we will use the FI to quantitatively derive simple rules that must be taken into account when using intensity modulated light in diffusion approximation for estimation of scattering properties of a medium and for ballistic filtering applications.

The expected Fisher information matrix (FIM) for a parameter vector (η) is defined as $\mathscr{F}(\eta)_{ij} = -\left\langle \frac{\partial^2 \ln[P(\mathbf{x}|\eta)]}{\partial\eta_i \partial\eta_j} \right\rangle$, where $\langle . \rangle$ denotes the expectation value. We present below the FIM for the detection procedure described above with respect to the parameter vector $\theta' = [A, \phi, \Lambda^2]$. It is straightforward to show that the FI reads in that case

$$\mathscr{F}(\theta') = \begin{array}{c} \begin{matrix} (A) & (\phi) & (\Lambda^2) \end{matrix} \\ \begin{pmatrix} \frac{1}{\Lambda^2} & 0 & 0 \\ 0 & \frac{A^2}{\Lambda^2} & 0 \\ 0 & 0 & \frac{1}{\Lambda^4} \end{pmatrix} \end{array} \begin{matrix} (A) \\ (\phi) \\ (\Lambda^2) \end{matrix}, \tag{6}$$

Optics EXPRESS

where the bracketted grey symbols are a guide for the reader to better identify the pair of parameters addressed by each element of the FIM.

The above FIM is diagonal, which shows that the three parameters in θ' can be estimated independently. Moreover, the precision in estimation of the phase increases with the amplitude of the signal. The detection technique described in the preceding section is not limited to detector arrays, but is generally adopted in lock-in detection. In this detection scheme, the recorded amplitude and phase of the diffuse light through a scattering media can be modeled by the diffusion theory as presented in preceding sections. Using this model, the noise model of the detection can be reparametrized as shown below and consequently, estimation precision of the parameters can be calculated.

3.2. Reparametrization of noise model using diffusion theory

Let us consider the effect of diffused light only, and obtain the FIM with respect to the new set of parameters $\theta = [M, R_\delta, R_*]$ to deduce some insight into the precision of estimation of each respective parameter and its dependency on other parameters. The FI with respect to the new parameters can be obtained by calculating the Jacobian matrix, $J_{\mathscr{D}}$, of the transformation $\theta' \rightarrow \theta$ in the presence of diffuse light only, as denoted by the subscript $\mathscr{D}$. The i^{th}, j^{th} component of this matrix is $\left[J_{\mathscr{D}}\right]_{i,j} = \frac{\partial \theta'_i}{\partial \theta_j}$. Given the modulation index, phase and the intensity expected for diffuse light from the diffusion model, the amplitude, phase and variance can be written as $A_D = m_D I_D/2$, $\Delta\phi = R_\delta \sqrt{2(q^2-1)}$ and $\Lambda_D^2 = I_D/2 = 3S_0 R_* \, e^{-R_\delta}/2$, where we have set $S_0 = \xi d\Omega P_0/4\pi$. The Jacobian is then calculated to obtain the FIM with respect to parameter vector θ using the transformation $\mathscr{F}_{\mathscr{D}}(\theta) = J_{\mathscr{D}}^T \mathscr{F}(\theta') J_{\mathscr{D}}$. Both, the Jacobian and the FIM $\mathscr{F}_{\mathscr{D}}(\theta)$ are shown in Appendices B and C, for reference. It is worth mentioning here that in applications where the SNR of the amplitude and phase are important, the noise model presented here can be used to obtain the SNR of detected amplitude and phase as a function of frequency by using the above relations. However, we will focus on deriving and analyzing the minimum variance bounds on estimation of scattering parameters as presented in the following section.

4. Maximal precision in estimation of scattering parameters in diffuse optical imaging

4.1. Lower bound on estimation variance

The above re-parameterization allows us to study the variance bound in estimation of θ with respect to the frequency of modulation represented by the variable q. According to the Cramer-Rao theorem, for any unbiased estimator $\hat{\theta}$ of the parameter vector θ, and for any row vector w having the same dimension as θ, one has $w\left\langle \hat{\theta}\hat{\theta}^T \right\rangle w^T \geq w\mathscr{F}(\theta)^{-1} w^T$. Thus, the Cramer-Rao bound (CRB) provides a minimum covariance bound that can be reached by an efficient estimation technique. Generically, it is not guaranteed that such an efficient estimator always exists, however, Maximum Likelihood (ML) estimators has been shown to be asymptotically unbiased and efficient for a large collection of data, with optimality strictly proved in the case of exponential family of distributions [35]. The exact forms of ML estimators in this case are solutions to transcendental equations and remain out of the scope of this article. Instead, let us analyze the lower covariance bound to reveal some simple conclusions and rules for the estimation problem. We provide the bound as $CRB_{\mathscr{D}}(\theta) = \mathscr{F}_{\mathscr{D}}(\theta)^{-1}$ for the invertible matrix

Optics EXPRESS

$\mathscr{F}_{\mathscr{D}}(\theta)$ which is shown in the Appendix C:

$$CRB_{\mathscr{D}}(\theta) = \begin{bmatrix} (M) & (R_\delta) & (R_*) \\ M^2 + \frac{4e^{(-1+2q)R_\delta} q}{3(1+q)R_* S_0} & \frac{2e^{(-1+2q)R_\delta}}{3M(1+q)R_* S_0} & -MR_* + \frac{2e^{(-1+2q)R_\delta}}{3M(1+q)S_0} \\ \frac{2e^{(-1+2q)R_\delta}}{3M(1+q)R_* S_0} & \frac{2e^{(-1+2q)R_\delta}}{3M^2(-1+q^2)R_* S_0} & \frac{2e^{(-1+2q)R_\delta}}{3M^2(-1+q^2)S_0} \\ -MR_* + \frac{2e^{(-1+2q)R_\delta}}{3M(1+q)S_0} & \frac{2e^{(-1+2q)R_\delta}}{3M^2(-1+q^2)S_0} & R_*^2 + \frac{2e^{(-1+2q)R_\delta} R_*}{3M^2(-1+q^2)S_0} \end{bmatrix} \begin{matrix} (M) \\ (R_\delta) \\ (R_*) \end{matrix}, \quad (7)$$

where again the bracketed grey symbols are a guide for the reader to identify the pair of parameters addressed by each element of the CRB matrix.

It is clearly seen that the variances are functions of the frequency of modulation (represented by q). Let us first look at the variance in estimation for the parameters R_δ and R_*. The variance of R_* increases with its mean value and has an additional frequency dependent term, while the variance of R_δ decreases with R_*. The dependence of both the parameters on frequency is the same and has a functional form $e^{(-1+2q)R_\delta}/(-1+q^2)$. A simple calculus shows that this function reaches a minimum at $q_{opt} = \left(1+\sqrt{1+4R_\delta^2}\right)/2R_\delta$. This indicates that there exists an optimal angular frequency ω_{opt} around which the variance of the estimation is minimum. This optimal angular frequency depends only on R_δ and is given by the following expression

$$\frac{\omega_{opt}}{\mu c} = \frac{\sqrt{2}\left[1+\left[1+4R_\delta^2\right]^{\frac{1}{2}} + R_\delta^2\left(3+\left[1+4R_\delta^2\right]^{\frac{1}{2}}\right)\right]^{\frac{1}{2}}}{R_\delta^2}, \quad (8)$$

whose evolution is plotted in Fig. 3(a). It can be readily seen that in the small-R_δ limit, the optimal frequency behaves like $\omega_{opt}/\mu c = 2/R_\delta^2$, whereas it evolves as $\omega_{opt}/\mu c = 2/\sqrt{R_\delta}$ when $R_\delta \to \infty$. In the next subsection we analyze the properties and evolution of the optimal frequency ω_{opt} obtained for the estimation of scattering parameters.

4.2. Optimal operating frequency

The expression for the variance-minimizing optimal angular frequency ω_{opt} has a non-trivial form that depends on the normalized optical attenuation $R_\delta = r/\delta$, which basically represents the inverse of an overall visibility factor for the diffuse photons. The existence of an optimal operating point has interesting consequences, especially in the context of diffused optical imaging, where the SNR of the images is an important limiting factor. Generally, in such applications, the operating frequency, denoted here by ω_a, is chosen such that $\omega_a/\mu c = 1$ [29]. This is indeed a reasonable choice of operating frequency, justified by the fact that at smaller frequencies the phase change due to diffusion is too small to be detected, while at much higher frequencies, the change in phase becomes comparatively insensitive to further increase in frequency, thereby not bringing any further improvement in the estimation of the medium parameters [29].

To understand the loss incurred by an imperfect choice of operating frequency, we compare the performance of estimation provided by the two frequencies, ω_{opt} and ω_a. We plot the ratio of the variance in the estimation of R_δ obtained when using ω_{opt} against ω_a in Fig. 3(b). The figure provides a quantitative study of the loss in optimal precision in using ω_a as opposed to using ω_{opt}. The precision of estimation are equal only when $R_\delta = 5.3$, at which point $\omega_{opt} = \omega_a$, as indicated by the dashed lines in the figures. For example, taking typical values of scattering parameters valid in tissues, such that $\mu = 0.1$ cm^{-1} and $\sigma = 10$ cm^{-1}, the two operating points are the same only for a detector placed as distance of 3 cm. The standard operating frequency ω_a is independent of the propagation distance r and of σ, depending only on the absorption coefficient μ. As illustrated in Fig. 3(a), for a detection carried out at a distance higher than

Optics EXPRESS

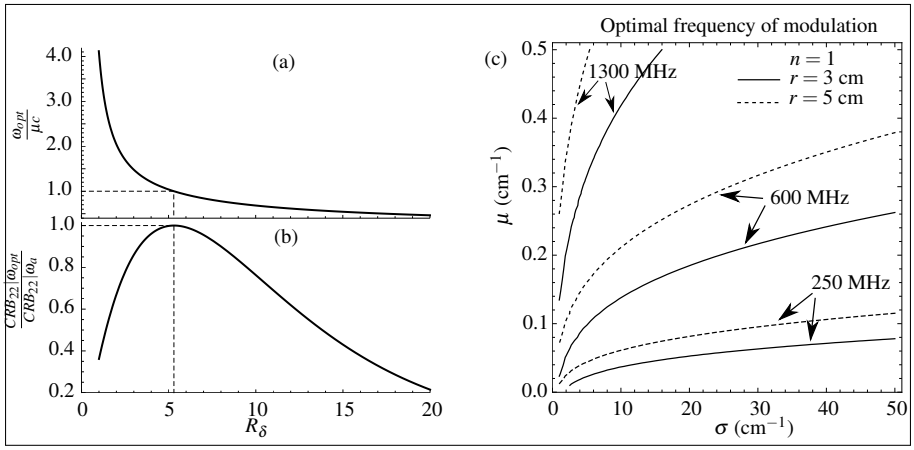

Fig. 3. (a) Ratio of the optimal frequency ω_{opt} to standard operating frequency $\omega_a = \mu c$ as a function of the normalized optical attenuation R_δ. (b) Loss in precision in the estimation of R_δ using modulation angular frequency ω_a as opposed to ω_{opt} as a function of R_δ. (c) Contours of optimal frequency of modulation as a function of absorption coefficient μ and reduced scattering coefficient σ and the detection distance r for an intervening medium having refractive index 1. The frequencies can be scaled down by a factor of n for a medium with refractive index n.

3 cm, the optimal frequency is in fact smaller, which may reduce the cost and complexity of the electronics required at high frequencies while providing better results. On the other hand, if the detection is carried out closer than 3 cm, operating frequencies higher than the standard operational frequency are suggested.

Similarly, since R_δ is a function of σ, μ and r, the dependency of the optimal modulation frequency on these three parameters can be analyzed from the contour plot shown in Fig. 3(c). Firstly, for fixed values of σ and μ, the optimal operating frequency decreases with increase in r. Secondly, for fixed values of r and μ, the optimal frequency is seen to decrease with the increase in σ. The above two dependencies can be interpreted by noticing that longer distance of travel or higher scattering coefficient would allow for a larger amount of multiple scattering events leading to greater modification of the phase and the modulation index of the diffused light, for a given coefficient μ.

Finally, the optimal frequency is seen to increase with the increase in μ, for fixed values of r and σ. An increase in absorption would lead to smaller amplitude of modulation at the detector. To compensate for this loss that occurs at a rate of μc, the photon density arrival rate should be increased leading to a increase in optimal frequency of operation. It can also be noticed that the change of optimal operating frequency is more sensitive to a change in absorption coefficient than to a change in σ or r. The above conclusions can also be easily obtained by noticing that equation Eq. (8) can be approximated to $\omega_{opt} = 2\mu c/\sqrt{R_\delta} = 2\sqrt{\mu}c[r\sqrt{3(1+\sigma/\mu)}]^{-1/2}$, for sufficiently large value of R_δ, as noted above. It is interesting to notice at this level that the above analytical deductions about the existence of an optimal operating frequency and its evolution with scattering parameters are qualitatively in very good agreement with previous numerical simulations and experimental studies presented in [36–38].

More generally, the above results show that our analysis, based on a diffusion model for the propagation of photons coupled with an information theoretical approach, makes it possible to account for several competing phenomena involved in light diffusion. For instance, the noise variance Λ^2 observed with the quadrature detection scheme described in Section 3 decreases

Optics EXPRESS

with R_δ but is independent of ω, whereas the modulation index and the phase depend on R_δ but with rates of change that are functions of the angular frequency). This analysis is able to provide the functional dependence of the optimal operating frequency with respect to properties of the medium under consideration and practical indications concerning the optimal experimental parameters for the estimation task considered. The conclusion obtained appears to be more specific than the usual rule of thumb used in similar experiments, as it reveals the optimal operating frequency and provides insight into the various competing phenomena that produce it.

It is possible to extend such an information theoretical analysis towards another problem, namely, ballistic photon filtering in diffusing media, where the goal is to efficiently discriminate the ballistic photons from the diffused photons. In the next section we will introduce a performance metric for ballistic discrimination and present the optimal operating point based on the information theoretical approach coherent with the previous discussions.

5. Ballistic filtering

The importance of ballistic discrimination has been discussed in the introduction section, for instance when imaging objects embedded in nebulous media like fog. As noted above, when high-frequency modulated light propagates in a turbid medium, the ballistic photons and diffused photons have different transport properties in terms of modulation index and phase, which can be exploited by a demodulating detector to attain discrimination of ballistic photons.

By contrast, such a physical ballistic filtering effect cannot be obtained with a standard intensity camera, or with low-frequency modulation/lock-in detection. In both cases, detection of an extremely small ballistic contribution over a spatially uniform diffuse illumination would be possible only at the expense of a dramatic increase in the detector dynamics or acquisition time.

In this section, we investigate the conditions required to obtain significant ballistic filtering with modulated light in a turbid medium. More particularly, we derive the minimum modulation frequency required to attain ballistic filtering irrespective of photon budget and exposure time.

5.1. Gain definition for ballistic filtering efficiency

We will again resort to FI to define a ballistic filtering efficiency as the gain in information provided by the ballistic light for the estimation of the modulation index M of the light source. Let us consider a quadrature demodulation camera that receives ballistic light over the diffused light on a set of pixels denoted $\mathscr{B}\oplus\mathscr{D}$ and another set of pixels that receive only diffused light at a region denoted by $\mathscr{D}$. In most cases, the contrast between these two regions is marginal because fewer ballistic photons reach the detector. To quantify this contrast in a demodulation scheme, we define the ballistic discrimination efficiency (or gain) as the ratio of FIs in the estimation of the actual modulation index M of the source when using data from region $\mathscr{B}\oplus\mathscr{D}$ as opposed to $\mathscr{D}$. The gain in information, denoted by $\mathscr{G}_{bf}$ is thus defined as

$$\mathscr{G}_{bf} = \frac{[\mathscr{F}_{\mathscr{B}\oplus\mathscr{D}}(\theta)]_{11}}{[\mathscr{F}_{\mathscr{D}}(\theta)]_{11}}, \tag{9}$$

where $[\mathscr{F}_{\mathscr{D}}(\theta)]_{11} = [J_{\mathscr{D}}^T \mathscr{F}(\theta') J_{\mathscr{D}}]_{11}$ is the first (upper left) term of the FIM $\mathscr{F}_{\mathscr{D}}(\theta)$ given in Appendix C when only diffused light is considered, whereas $[\mathscr{F}_{\mathscr{B}\oplus\mathscr{D}}(\theta)]_{11} = [J_{\mathscr{B}\oplus\mathscr{D}}^T \mathscr{F}(\theta') J_{\mathscr{B}\oplus\mathscr{D}}]_{11}$ stands for the first term of $[\mathscr{F}_{\mathscr{B}\oplus\mathscr{D}}(\theta)]_{11}$ obtained when ballistic and diffused light are simultaneously taken into account. In the above expressions, $J_{\mathscr{B}\oplus\mathscr{D}}$ is the Jacobian of the transformation $\theta' \to \theta$ in the presence of ballistic and diffuse light. Here, we do not need to compute either the entire Jacobian $J_{\mathscr{B}\oplus\mathscr{D}}$ or the entire FIM $\mathscr{F}_{\mathscr{B}\oplus\mathscr{D}}(\theta)$, as our problem is restricted to finding the first term in the FIM, which provides a limiting but reasonable condition for achieving ballistic filtering when other parameters like R_δ and R_* are already known or assumed to be known.

Optics EXPRESS

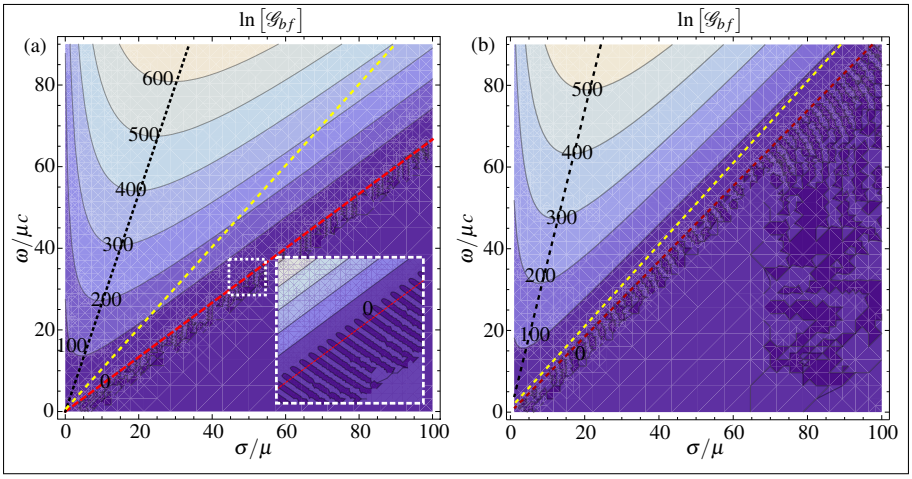

Fig. 4. (a) Contour plot of $\ln[\mathscr{G}_{bf}]$ for range $\sigma/\mu \in [1,100]$ and $\omega/\mu c \in [0.01,90]$, with anisotropy factor $g = 0$. (Inset) Shows a zoomed in section of the plot where the effect of the cosine term is clearly visible. The cosine term makes it difficult to analytically obtain the contour of unity gain but the condition of Eq. (13) for expecting a gain is displayed as red dashed line. The diffusion approximation remains valid in the region below the yellow dashed line. (b) Same contour plot as (a) for anisotropy factor $g = 0.15$.

Consequently, the gain can be calculated as

$$\mathscr{G}_{bf} = \frac{\frac{1}{\Lambda^2_{\mathscr{B}\oplus\mathscr{D}}}\left(\frac{\partial A_{\mathscr{B}\oplus\mathscr{D}}}{\partial M}\right)^2}{\frac{1}{\Lambda^2_{\mathscr{D}}}\left(\frac{\partial A_{\mathscr{D}}}{\partial M}\right)^2}, \tag{10}$$

where the $A_{\mathscr{B}\oplus\mathscr{D}}$ and $A_{\mathscr{D}}$ are the amplitudes received at the regions $\mathscr{B}\oplus\mathscr{D}$ and $\mathscr{D}$, respectively (see Appendix D). Finally, the expression for the gain $\mathscr{G}_{bf}$ can be written as

$$\mathscr{G}_{bf} = \frac{1}{1+\alpha}\left(1+\alpha^2\beta^2+2\alpha\beta\cos\Delta\phi\right) \tag{11}$$

$$= \frac{1+\frac{\Omega'^2\, e^{\tau}\left(1+\frac{6R_*}{\Omega'}e^{-\tau/2}\cos\sqrt{2(q^2-1)}R_\delta\right)}{9R_*^2}}{1+\alpha}, \tag{12}$$

where $\tau = 2(qR_\delta - R_b)$, $\beta = e^{R_\delta(q-1)}$ and $\alpha = I_B/I_D$ is the ratio of received ballistic light over diffused light.

5.2. Condition for ballistic filtering gain

The contour plot of the $\ln[\mathscr{G}_{bf}]$ as a function of the normalized angular modulation frequency ($\omega/\mu c$) and of σ/μ is shown in Fig. 4 for two values of the anisotropy coefficient g, taking $\Omega' = 1$ (isotropic emitter) and $r\mu = 10$. In Figs. 4(a) and 4(b), the domain of validity of the diffusion approximation is delimited by the region below the yellow dashed line (see Section 5.4). It can be seen that a gain much greater than unity can be obtained for angular frequencies that lie above a roughly linear contour. Thus, the minimum angular frequency required for ballistic filtering depends roughly linearly on the scattering properties (through μ_s, σ and/or g) of the medium. The analytical expression of the contour for unity gain is not easily computed because

Optics EXPRESS

of the oscillating cosine term in Eq. (11), as can be seen in the inset of Fig. 4. Taking a closer look at the expression of ballistic gain, it can be noticed that a significant gain can be obtained only when $\tau > 0$, which allows exponential increase in gain and at the same time makes it possible to neglect the cosine term inside the bracketed expression. Moreover, it can be easily checked that it is a sufficient condition to ensure that $\mathscr{G}_{bf}$ of Eq. (11) is greater than unity. The above simple condition can be rewritten as $qR_\delta > R_b$, which interestingly suggests that qR_δ effectively behaves as a frequency-dependent attenuation for diffused light, which should be greater than the effective attenuation experienced by ballistic light (R_b) in order to achieve efficient ballistic filtering. The above inequality leads to a condition in terms of minimum frequency of operation which can be written as

$$q > R_b/R_\delta = \frac{(1-g)+\frac{\sigma}{\mu}}{(1-g)\sqrt{3(1+\frac{\sigma}{\mu})}}, \tag{13}$$

which interestingly appears to be independent of the propagation distance r. When expressed in terms of angular frequency ω, this gain condition can be plotted as the red dashed line on the contour maps in Fig. 4 and seems to provide a well-defined condition for attaining ballistic gain. Further simplification holds under the validity conditions of the diffusion theory, where $\sigma > 10\mu$. In this case, the condition for achieving ballistic filtering reduces to

$$\frac{\omega}{c} > \frac{2}{3}\frac{\sigma}{(1-g)^2}, \tag{14}$$

and is insensitive to the value of the absorption coefficient μ. This clearly indicates that filtering of ballistic photons using an imaging demodulation technique will be more difficult, and hence require higher modulation frequency, in forward anisotropically scattering media with $g > 0$. Indeed, this can be physically understood, as diffused photons will be less likely to deviate from the ballistic path in a significantly forward scattering medium.

As a result, the above equation provides a simple rule of thumb for achieving ballistic filtering in the context of intensity modulation and quadrature detection. It must be noted that the effect of Ω' and $r\mu$ (that are set as constants in Fig. 4) is only on the value of the gain and they do not affect the above condition for efficient ballistic discrimination. Identification of this minimum modulation frequency for ballistic filtering is also important from a practical point of view as it is easier to design electronic or electro-optic devices that work at low modulation and demodulation frequencies. According to the above results, ballistic filtering in biomedical applications would, however, require very high (if not unrealistic) modulation frequencies, as for typical values of $\sigma = 10$ cm^{-1}, refraction index $n = 1.33$, and a propagation distance $r = 5$ cm, one obtains f_{min}=23.9 GHz (respectively f_{min}=597 GHz) when $g = 0$ (respectively $g = 0.8$)!

The expression derived above can also serve conversely to provide the range of visibilities that can be handled by a ballistic filtering device working at any fixed modulation-demodulation frequency. For instance, for transport safety in foggy weather, if we consider $r = 1$ km, $n = 1.33$, and a modulation frequency of f=10 MHz, the above rule of thumb indicates that ballistic filtering can be obtained when $\mu_s \leq 0.42$ m^{-1} (respectively $\mu_s \leq 0.084$ m^{-1}) when $g = 0$ (respectively $g = 0.8$). According to the World Meteorological Organization's recommendations [39], such values of μ_s correspond to very low visibilities (meteorological optical range $MOR = 3/\mu_s$) of 7.5 m (respectively 36 m), still assuming a homogeneous, mostly scattering medium ($\mu_s \gg \mu$).

5.3. Maximum expectable gain

Lastly, we can estimate the maximum expectable gain under the condition of highly diffusing medium with reduced ballistic contribution ($\alpha \ll 1$). The gain values derived below may not be quantitatively relevant for practical experiments because many phenomena have been neglected in our analysis so far, such as detector noise, turbulence, spurious ambient illumination, limited

Optics EXPRESS

dynamics of the detector, etc. Under the above conditions, the maximal expected gain using an intensity modulation scheme and a quadrature demodulation technique is roughly driven by the exponential term, i.e., $\ln[\mathscr{G}_{bf}] \sim \tau$, which allows one to fairly retrieve the gain values plotted in Fig. 4. As noted above, the value of the maximum expectable gain depends not only on ω and σ but also on r and μ.

The evolution of the maximum gain with the physical parameters involved can be analyzed from the expression of τ. It is obvious to see that $\mathscr{G}_{bf}$ naturally increases with ω, but also with r. This can be interpreted by noticing that increasing the number of spatial periods along the propagation must increase the efficiency of the ballistic filtering. It is also quite straightforward to show that $\mathscr{G}_{bf}$ increases with the absorption coefficient μ when the diffusion approximation is valid ($\sigma/\mu > 10$). Though difficult to interpret, it is also possible to demonstrate from the expression of τ that $\ln[\mathscr{G}_{bf_{max}}]$ increases with σ when $\omega/\mu c > 8\sigma/3\mu(1-g)^2$ (which condition is satisfied on the left side of the dotted black lines plotted in Figs. 4(a) and 4(b)), otherwise it should decrease with σ.

5.4. Limitations and validity of the study

However, it is important to note here that the diffusion equation for modulated photon transport is admitted to be valid for frequencies lower than $\omega/c < \mu + \sigma$ [40], which correspond in Fig. 4 to the region lying below the yellow dashed line. More generally, it is easy to check that when $g > 1 - \sqrt{2/3} = 0.1835$, the minimum frequency derived above $\omega_{min}/c = 2\sigma/3(1-g)^2$ lies outside the domain of validity of the diffusion approximation. This restricts our analysis to situations of quasi-isotropic diffusion regime, in fair agreement with primal premises of the diffusion equation approximation for photon transport.

Finally, we would like to stress again that the quantitative gain values retrieved from Fig. 4 are highly unlikely to be achieved in a practical experiment because we have neglected all sources of experimental imperfections in our work, and, for very high frequencies, the extrapolated gains are obtained from the diffusion approximation beyond its validity. However, the above study makes it possible to understand the interplay of the main physical parameters at stake in ballistic filtering for contrast enhancement.

6. Conclusion

We have used the photon diffusion theory and its predictions for transport of intensity modulated light in a diffusing medium along with the noise model for quadrature demodulation scheme, to derive optimal operating points for two application scenarios: scattering parameter estimation as used in diffuse optical imaging and ballistic photon filtering as used in ballistic photon imaging. In the case of estimation of scattering parameters using only diffused light, the Cramer-Rao lower bound on the estimation of scattering parameters was derived and was shown to have a minimum at an optimal modulation frequency. The derived optimal frequency of modulation that achieves minimum variance of estimation depends on the optical penetration depth and the distance of propagation. The evolution of this optimal operating frequency was analytically shown to be increasing with higher absorption coefficient and decreasing with increase in distance of detection and/or the scattering coefficient of the medium. The loss in estimation precision incurred when using a non-optimal operating frequency was quantified. These results pave way for better design of diffuse optical imaging setups that are used in medical instruments. Indeed, given the average scattering parameters of the tissue under test, an optimal frequency can be inferred from the above analytical expressions, and used in the setup to optimize its performance when estimating the parameters of the scattering inhomogeneities.

In the case of ballistic photon imaging using intensity modulated light, an information theoretical metric was introduced to quantify the efficiency of discriminating ballistic photons from diffused photons. A minimum operating angular frequency was derived which appeared to be

Optics EXPRESS

essentially a linear function of the scattering coefficient of the intervening medium only: it was shown that a significant gain in ballistic filtering can be expected when the angular frequency of modulation $\omega > 2\sigma c/3(1-g)^2$. According to this rule of thumb, ballistic filtering using modulated imaging seems within reach for transport safety applications. On the other hand, the minimum frequencies derived for typical parameters and propagation lengths encountered in biomedical applications seem hardly compatible with available imaging systems, thereby motivating the search for high frequency demodulation imaging systems.

In this approach, diffusion theory of photon transport and noise model of a quadrature demodulation scheme were tied together using information theoretical tools to provide minimumvariance operating points and to derive the expression of expected gains by taking into account various competing phenomena in the system. It must, however, be kept in mind that the analysis is valid within the applicability of the diffusion approximation, which is supposed to breaks down at large angular modulation frequencies close to $\omega/c = \mu + \sigma$. Moreover, the extremely high numerical values of gain presented in the article are only limited by physical photon noise that is carried forward to the detection scheme. The properties of the detector, like detection noise and detector dynamics were ignored so far to limit the calculations and to focus on the physical limits and optimal operation of such a scheme. However, in real life application, additive detector noise and source phase noise must be taken into account. Incorporating such additional noise factors in our approach is a clear perspective to this work, which will indeed limit the attainable gain values to more realistic values.

Appendix

A. Noise model

A.1. Noise variance

At each time slice t_i the photons received at the detector can be modeled as having Poisson noise with variance equal to the mean. Then, the optical noise variance at each slice is $I(t_i) = I_0(1+M\cos[2\pi t_i/T])$. The quadrature components are obtained by weighting each slice with sine and cosine of same frequency. Thus, the total noise variance will propagate as var(V) = $\sum_{i=0}^{nT} \sin[2\pi t_i/T+\phi_r]^2 I(t)$
$= \frac{I_0}{2} + I_0 M \sum_{i=0}^{nT} (\sin[2\pi t_i/T+\phi_r](\sin[4\pi t_i/T+\phi_r] + \sin[\phi_r]))$
$= \frac{I_0}{2}$ Similarly, one shows var$(U) = \frac{I_0}{2}$.

A.2. Joint PDF of amplitude and phase

Let us consider quadrature components $[U,V]^T$ as joint Gaussian random variables with mean $[A\cos[\phi], A\sin[\phi]]^T$ and covariance matrix $\Sigma = \text{Diag}\,[\Lambda^2,\Lambda^2]$. Then, the joint distribution of the random variables U and V is

$$P_{U,V}(u,v|A,\phi,\Lambda^2) = \frac{1}{2\pi\Lambda^2}\exp\left[-\frac{(u-A\cos[\phi])^2+(v-A\sin[\phi])^2}{2\Lambda^2}\right]. \tag{15}$$

For a change of variables, such that $Z = \sqrt{U^2+V^2}$ and $\Psi = tan^{-1}[V/U]U = Z\cos[\Psi], V = Z\sin[\Psi]$, changed PDF can be obtained by noting that

$$P_{Z,\Psi}(z,\psi|A,\phi,\Lambda^2) = P_{U,V}(u,v|A,\phi,\Lambda^2)\left|J_{u,v}^{z,\psi}\right| = \frac{z}{2\pi\Lambda^2}\exp\left[-\frac{1}{2\Lambda^2}(z^2+A^2-2zA\cos[\psi-\phi])\right], \tag{16}$$

where, $J_{u,v}^{z,\psi}$ is the Jacobian of the transformation $\{u,v\} \to \{z,\psi\}$ and $|.|$ is the determinant.

Optics EXPRESS

B. Jacobian matrix of the transformation $\theta' \to \theta$ for diffuse light only

The Jacobian matrix for $\theta' \to \theta$

$$J_{\mathscr{D}} = \begin{bmatrix} \frac{3}{2}e^{-qR_\delta}R_* S_0 & -\frac{3}{2}e^{-qR_\delta}MqR_* S_0 & \frac{3}{2}e^{-qR_\delta}MS_0 \\ 0 & \sqrt{-1+q^2} & 0 \\ 0 & -\frac{3}{2}e^{-R_\delta}R_* S_0 & \frac{3}{2}e^{-R_\delta}S_0 \end{bmatrix}. \tag{17}$$

C. Fisher information $\mathscr{F}_{\mathscr{D}}(\theta)$

In the presence of diffused light only, the FIM for a change of coordinates $\theta' \to \theta$ is simply calculated by $\mathscr{F}_{\mathscr{D}}(\theta) = J_{\mathscr{D}}^T \, \mathscr{F}(\theta') \, J_{\mathscr{D}}$

$$\mathscr{F}(\theta) = \begin{bmatrix} \frac{3}{2}e^{(1-2q)R_\delta}R_* S_0 & -\frac{3}{2}e^{(1-2q)R_\delta}MqR_* S_0 & \frac{3}{2}e^{(1-2q)R_\delta}MS_0 \\ -\frac{3}{2}e^{(1-2q)R_\delta}MqR_* S_0 & 1+\frac{3}{2}e^{(1-2q)R_\delta}M^2\left(-1+2q^2\right)R_* S_0 & -\frac{1}{R_*}-\frac{3}{2}e^{(1-2q)R_\delta}M^2 qS_0 \\ \frac{3}{2}e^{(1-2q)R_\delta}MS_0 & -\frac{1}{R_*}-\frac{3}{2}e^{(1-2q)R_\delta}M^2 qS_0 & \frac{2+3e^{(1-2q)R_\delta}M^2 R_* S_0}{2R_*^2} \end{bmatrix}. \tag{18}$$

D. Amplitude detected at ballistic and diffused regions

Diffused region $\mathscr{D}$ When the detector (or a pixel) receives only diffused light, the quadrature components detected are given by $\mathrm{u}_D = \int I_D(1+m_D\cos[\omega t-\phi_D])\cos[\omega t+\delta\phi]\,dt$ $= \frac{I_D m_D}{2}\cos[\phi_D+\delta\phi]$
$\mathrm{v}_D = \int I_D(1+m_D\cos[\omega t-\phi_D])\sin[\omega t+\delta\phi]\,dt$ $= \frac{I_D m_D}{2}\sin[\phi_D+\delta\phi]$.

Ballistic + Diffused region $\mathscr{B}\oplus\mathscr{D}$ When the detector (or a pixel) receives both contributions of diffused light and ballistic light, the quadrature components detected have the following expressions

$$\begin{aligned} u_{\mathscr{B}\oplus\mathscr{D}} = \; & \int [I_D(1+m_D\cos[\omega t-\phi_D])+I_B(1+m_B\cos[\omega t-\phi_B])] \\ & \times\cos[\omega t+\delta\phi]\,dt \\ & = \tfrac{I_D m_D}{2}\cos[\phi_D+\delta\phi]+\tfrac{I_B m_B}{2}\cos[\delta\phi] \end{aligned}$$

Similarly,

$$v_{\mathscr{B}\oplus\mathscr{D}} = \frac{I_D m_D}{2}\sin[\phi_D+\delta\phi]+\frac{I_B m_B}{2}\sin[\delta\phi].$$

Amplitudes As a consequence of the above derivations, the amplitudes estimated on detectors that receive only diffused light and detectors that receive both ballistic and diffused light respectively read

$$A^2_{\mathscr{D}} = \tfrac{I_D^2 m_D^2}{4}$$

$$A^2_{\mathscr{B}\oplus\mathscr{D}} = \frac{I_D^2 m_D^2}{4}+\frac{I_B^2 m_B^2}{4}+\frac{I_D I_B m_D m_B}{2}\cos[\phi_D] = \frac{I_D^2 m_D^2}{4}\left(1+\alpha^2\beta^2+2\alpha\beta\cos[\phi_D]\right).$$

Optics EXPRESS

Acknowledgment

This work is funded by CEFIPRA under the project RITFOLD 4604-4 as a collaboration between Institut de Physique de Rennes, Université de Rennes 1, France and Raman Research Institute, Bangalore, India.

We would like to thank Prof. Afshin Daryoush for fruitful discussions. We also acknowledge two anonymous reviewers for their thoughtful suggestions to improve this article.

Minimum Description Length approach for unsupervised spectral unmixing of multiple interfering gas species

Julien Fade,[1,2,*] **Sidonie Lefebvre,**[1] **and Nicolas Cézard**[1]

[1] *French Aerospace Lab (ONERA), Chemin de la Hunière, 91 761 Palaiseau, France*
[2] *Institut de Physique de Rennes UMR CNRS 6251, Université de Rennes 1, Campus de Beaulieu, 35 042 Rennes, France*
[*] *julien.fade@univ-rennes1.fr*

Abstract: We address an original statistical method for unsupervised identification and concentration estimation of spectrally interfering gas components of unknown nature and number. We show that such spectral unmixing can be efficiently achieved using information criteria derived from the Minimum Description Length (MDL) principle, outperforming standard information criteria such as AICc or BIC. In the context of spectroscopic applications, we also show that the most efficient MDL technique implemented shows good robustness to experimental artifacts.

OCIS codes: (070.4790) Spectrum analysis; (300.0300) Spectroscopy; (010.1030) Absorption; (010.0280) Remote sensing and sensors; (280.1120) Air pollution monitoring.

References and links

1. P. Weibring, C. Abrahamsson, M. Sjholm, J. N. Smith, H. Edner, and S. Svanberg, "Multi-component chemical analysis of gas mixtures using a continuously tuneable lidar system," Appl. Phys. B **79**, 525–530 (2004).
2. J. R. Quagliano, P. O. Stoutland, R. R. Petrin, R. K. Sander, R. J. Romero, M. C. Whitehead, C. R. Quick, J. J. Tiee, and L. J. Jolin, "Quantitative chemical identification of four gases in remote infrared (9-11 μm) differential absorption lidar experiments," Appl. Opt. **36**, 1915–1927 (1997).
3. G. Wysocki, R. Lewicki, R. Curl, F. Tittel, L. Diehl, F. Capasso, M. Troccoli, G. Hofler, D. Bour, S. Corzine, R. Maulini, M. Giovannini, and J. Faist, "Widely tunable mode-hop free external cavity quantum cascade lasers for high resolution spectroscopy and chemical sensing," Appl. Phys. B: Lasers and Optics **92**, 305–311 (2008).
4. U. Platt and J. Stutz, *Differential Optical Absorption Spectroscopy* (Springer, 2008).
5. R. A. Hashmonay, R. M. Varma, M. Modrak, R. H. Kagann, and P. D. Sullivan, "Simultaneous measurement of vaporous and aerosolized threats by active open path FTIR," Unclassified Technical Report ADA449529, Arcadis Geraghty and Miller Research Triangle Park NC (2004).
6. J. Kasparian, M. Rodriguez, G. Méjean, J. Yu, E. Salmon, H. Wille, R. Bourayou, S. Frey, Y. André, A. Mysyrowicz, R. Sauerbrey, J. Wolf, and L. Wöste, "White-light filaments for atmospheric analysis," Science **301**, 61–64 (2003).
7. D. M. Brown, K. Shi, Z. Liu, and C. R. Philbrick, "Long-path supercontinuum absorption spectroscopy for measurement of atmospheric constituents," Opt. Express **16**, 8457–8471 (2008).
8. P. S. Edwards, A. M. Wyant, D. M. Brown, Z. Liu, and C. R. Philbrick, "Supercontinuum laser sensing of atmospheric constituents," Proc. SPIE **7323**, 73230S (2009).
9. E. R. Warren, "Optimum detection of multiple vapor materials with frequency-agile lidar," Appl. Opt. **35**, 4180–4193 (1996).
10. S. Yin and W. Wang, "Novel algorithm for simultaneously detecting multiple vapor materials with multiple-wavelength differential absorption lidar," Chin. Opt. Lett. **4**, 360–363 (2006).
11. J. Fade and N. Cézard, "Supercontinuum lidar absorption spectroscopy for gas detection and concentration estimation," in "Proc. 25th International Laser and Remote-sensing Conference,"(2010), pp. 798–801.
12. J. Rissanen, *Information and Complexity in Statistical Modeling* (Springer, 2007).

#144366 - $15.00 USD Received 31 Mar 2011; revised 6 May 2011; accepted 9 May 2011; published 6 Jul 2011

13. R. A. Stine, "Model selection using information theory and the MDL principle," Sociolog. Methods Res. **33**, 230–260 (2004).
14. C. D. Giurcaneanu, "Stochastic complexity for the detection of periodically expressed genes," in "Proc. of IEEE International Workshop on Genomic Signal Processing and Statistics,"(2007), pp. 1–4.
15. H. Chen, T. Kirubarajan, Y. Bar-Shalom, and K. R. Pattipati, "MDL approach for multiple low-observable track initiation," Proc. SPIE **4728**, 477–488 (2002).
16. M. Hansen and B. Yu, "Model selection and the principle of minimum description length," J. Am. Stat. Assoc. **96**, 746–774 (2001).
17. C. L. Mallows, "Some comments on c_p," Technometrics **15**, 661–675 (1973).
18. H. Akaike, "A new look at the statistical model identification," IEEE Trans. Autom. Control **19**, 716–723 (1974).
19. G. Schwartz, "Estimating the dimension of a model," Ann. Stat. **9**, 461–464 (1978).
20. D. P. Foster and E. I. G., "The risk inflation criterion for multiple regression," Ann. Stat. **22**, 1947–1975 (1994).
21. J. Rissanen, *Stochastic Complexity in Statistical Inquiry, Series in Computer Science* (World Scientific, 1989), Vol. 15.
22. J. Rissanen, "Fisher information and stochastic complexity," IEEE Trans. Inform. Theory **42**, 48–54 (1996).
23. M. Duhant, W. Renard, G. Canat, F. Smektala, J. Troles, P. Bourdon, and C. Planchat, "Improving mid-infrared supercontinuum generation efficency by pumping a fluoride fiber directly into the anomalous regime at 1995nm," in CLEO/Europe and EQEC 2011 Conference Digest, (2011), p. CD9_1. (to be published)
24. A. Berrou, M. Raybaut, A. Godard, and M. Lefebvre, "High-resolution photoacoustic and direct absorption spectroscopy of main greenhouse gases by use of a pulsed entangled cavity doubly resonant OPO," Appl. Phys. B **98**, 217–230 (2010).
25. R. Tibshirani, "Regression shrinkage and selection via the lasso," J. R. Stat. Soc. Ser. B **58**, 267–288 (1996).
26. E. J. Candès and Y. Plan, "Near-ideal model selection by ℓ_1 minimization," Ann. Stat. **37**, 2145–2177 (2009).

1. Introduction

Air pollution monitoring in the atmosphere has motivated the development of many active optical instruments based on absorption spectroscopy. Ideally, a single instrument should be able to detect and quantify numerous gas species. It is therefore appropriate to use an illumination source that can cover a large spectral range. Two kinds of sources can be used, which are: i) narrow-line lasers with broad tunability, and ii) instantaneous broadband sources. Both families have demonstrated high potential for measurement of multi-components gas mixtures in the atmosphere. Narrow-line tunable lasers have been used in multi-wavelength systems like DIfferential Absorption Lidars (DIAL) [1, 2] and Tunable-Diode Laser Absorption Spectroscopy (TD-LAS) [3]. Instantaneous broadband sources have been used in various experiments schemes such as Differential Optical Absorption Spectroscopy (DOAS) [4], open-path active Fourier-Transform InfraRed (FTIR) spectroscopy [5], white-light filament-induced spectroscopy [6], and more recently, supercontinuum fiber laser spectroscopy [7, 8]. These various techniques share a common experimental design which is sketched in Fig. 1.

All these techniques provide multi-spectral absorption data that can be processed by multivariate statistical analysis in order to characterize the gas mixture. When the number and nature of the chemicals are a priori known, efficient algorithms can be designed to estimate their concentrations [9–11]. However, in many practical cases, the number, nature, and concentration of gas components are all unknown. In such situations, the same algorithms are inclined to overfit signal noise by assigning non-zero concentrations to many gas species in the fixed list of expectable gases (all of them being estimated at the same time). This results in complex and often unrealistic gas diagnosis. To avoid this, it is necessary to design unsupervised methods enabling simultaneous gas selection and concentration estimation. In this paper, we use the powerful concept of Minimum Description Length (MDL) principle to tackle this problem. We illustrate the potential of the method for spectral unmixing of several chemicals in the mid-infrared range. This spectral range is of particular interest for air pollution monitoring, as many industrial and greenhouse gases exhibit strong absorption lines in this band.

In broad outline, the MDL principle is based on the idea that the best model describing the measured data must minimize the code length needed to describe the data and to encode the

#144366 - $15.00 USD Received 31 Mar 2011; revised 6 May 2011; accepted 9 May 2011; published 6 Jul 2011

model itself [12]. Such a principle has already been applied in various domains, such as social sciences [13], biology [14] or radar signal processing [15] for instance. For the first time to the best of our knowledge, we show that this principle can be used for spectroscopic applications. More precisely, the approach presented in this paper allows unsupervised spectral unmixing of gas mixtures to be simply operated, with detection performances that outperform standard information criteria.

This paper is organized as follows: in the next section, we present the physical situation considered, and the principle of the MDL-based spectral unmixing algorithm is detailed. In section 3, we present and analyze some simulation results, allowing us to quantitatively compare the performance of the MDL-based approaches with standard methods. We also analyze the robustness of the proposed method when experimental outliers occur in the measurement process. Finally, the conclusion and perspectives of the paper are given in Section 4.

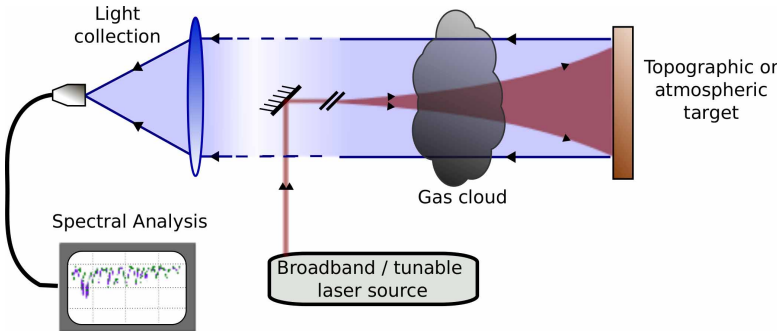

Fig. 1. Illustration of an absorption spectroscopy experiment using an active broadband illumination or tunable laser source.

2. Principle of unsupervised spectral unmixing algorithm

2.1. Posing of the problem

Before presenting the principle of the unsupervised spectral unmixing method addressed in this paper, let us detail the physical model that will be considered in the following. In most of absorption spectroscopy experiments, one is interested in measuring a vector $\mathbf{X}$ containing intensity measures on M spectral slits (or wavelengths) not necessarily adjacent. In the presence of absorbing gas species, these spectral measurements reveal specific absorption patterns depending on the nature and concentration of the chemicals encountered by the probe light beam. These spectral absorption patterns are superimposed with the spectral baseline of the active illumination source. The vector $\mathbf{X}$ of the measured intensities is linked to the K-dimensional vector $\mathbf{c}$ containing the gases concentrations $\mathbf{c} = [c_1, \ldots, c_K]^T$ through the following equation

$$\mathbf{X} = \left(\mathbf{a}_{0\mathrm{u}} e^{-\mathbf{H_u c}}\right) * g, \tag{1}$$

where g denotes the spectral slit (or laser linewidth) convolution function, which is assumed known in the following. In this equation, $\mathbf{a}_{0\mathrm{u}}$ denotes the baseline spectrum, and the $M \times K$ matrix $\mathbf{H_u} = [\mathbf{h}_{\mathbf{u}1}, \mathbf{h}_2, \ldots, \mathbf{h}_{\mathbf{u}K}]$ contains the unconvolved high-resolution absorption spectra of the K gas species. For the sake of simplicity, we will only consider in this paper the case of small absorption optical depths (i.e., $\mathbf{H_u c} \ll 1$). Moreover, we assume that the baseline $\mathbf{a}_0$ is varying slowly with respect to both the absorption lines and the convolution function widths. In such conditions, the measured intensities can be written,

$$\mathbf{X} = \mathbf{a}_0 e^{-\mathbf{Hc}}, \tag{2}$$

#144366 - $15.00 USD Received 31 Mar 2011; revised 6 May 2011; accepted 9 May 2011; published 6 Jul 2011

where the matrix $\mathbf{H} = [(\mathbf{h}_{\mathbf{u}1} * g), (\mathbf{h}_{\mathbf{u}2} * g), \ldots, (\mathbf{h}_{\mathbf{u}K} * g)]$ contains the convolved absorption spectra of the K gas species, and where the convolved spectral baseline $\mathbf{a}_0$ is assumed known, either from instrumental calibration or with a precise radiometric model of the illumination source. More accurate models involving deconvolution procedures, as well as the influence of a possible resolution mismatch between the instrument and the model are outside the scope of this paper, but could deserve investigation in future work.

The noisy experimental intensity measures over the M spectral slits, obtained for instance with a dispersive spectrometer or a FTIR spectrometer, will be denoted $\tilde{\mathbf{X}}$ in the remaining of this paper. It is a common procedure to use the logarithm of the measured data so as to obtain a linear regression model of the following form:

$$\tilde{\mathbf{Y}} = \ln \tilde{\mathbf{X}} = \mathbf{b}_0 - \mathbf{H} \cdot \mathbf{c} + \mathbf{n}, \tag{3}$$

with $\mathbf{b}_0 = \ln \mathbf{a}_0$, and where the M-dimensional zero-mean random vector $\mathbf{n}$ allows us to model the experimental noise. We assume that the noise contribution to the measured signal $\tilde{\mathbf{Y}}$ can be correctly accounted for with a Gaussian additive model. We also assume independence between the noise affecting two distinct spectral slits, i.e., $\langle \mathrm{n}_i \, \mathrm{n}_j \rangle = 0$ if $i \neq j$. For such a linear regression model, the usual estimator is $\hat{\mathbf{c}} = (\mathbf{H}\mathbf{H}^T)^{-1}\mathbf{H}^T(\tilde{\mathbf{Y}} - \mathbf{b}_0)$ and is usually referred to as the Minimum Mean Squared Error (MMSE) estimator since it minimizes the Residual Sum of Squares $RSS = (\tilde{\mathbf{Y}} - \hat{\mathbf{Y}})^T(\tilde{\mathbf{Y}} - \hat{\mathbf{Y}})$, with $\hat{\mathbf{Y}} = \mathbf{b}_0 - \mathbf{H}\hat{\mathbf{c}}$.

Under the hypothesis of Gaussian fluctuations and if the noise variance is not assumed *a priori* known during the estimation procedure, it can be shown [16] that this quantity is related to the loglikelihood $\ell_{\tilde{\mathbf{Y}}}(\tilde{\mathbf{Y}}|\mathbf{H})$ of the observed data through the following equation

$$\ell_{\tilde{\mathbf{Y}}}(\tilde{\mathbf{Y}}|\mathbf{H}) = \ln P_{\tilde{\mathbf{Y}}}(\tilde{\mathbf{Y}}|\mathbf{H}) = -\frac{M}{2} \ln RSS + ct, \tag{4}$$

where ct denotes an additive constant independent of the measured data. It can be noted that this last equation shows that the MMSE is also the Maximum Likelihood (ML) estimator under Gaussian fluctuations.

2.2. Model selection

The issue of model selection arises in many practical situations. For the problem at hand, two questions have to be answered: how many gas components (regressors) do we need to describe the experimental data, and which regressors have to be selected in the linear regression model of Eq. (3) to best explain the observations ? Without any model selection step, the most exhaustive regression model would include any gas species presenting characteristic absorption lines within the spectral range considered, and may lead to misleading and imprecise (if not incorrect) results, mostly due to overfitting of the noise. To avoid such undesirable situations, many penalization methods have been proposed among which we can cite the Akaike Information Criterion (AIC) [18], the Bayesian Information Criterion (BIC) [19], the Risk Inflation Criterion (RIC) [20], etc. These so-called *information criteria* make it possible to introduce sparsity constraints in the regression model, by selecting the solution (i.e., the regressor matrix $\mathbf{H}$) which minimizes $-\ell_{\tilde{\mathbf{Y}}}(\tilde{\mathbf{Y}}|\mathbf{H}) + \mathscr{C}$, with a different penalization term $\mathscr{C}$ depending on the information criterion considered. It can be noted however that since the loglikelihood is proportional to the logarithm of the RSS, up to an additive constant independent of the selected regression model [16], the model selection can be operated equivalently by minimizing $M/2 \ln RSS + \mathscr{C}$.

Let us briefly recall two of the classical information criteria, which will be used in the remaining of the paper as benchmarks to assess the quality of the proposed MDL-based methods. The simplest is the Akaike Information Criterion (AIC) [18], which introduces a penalization

#144366 - $15.00 USD Received 31 Mar 2011; revised 6 May 2011; accepted 9 May 2011; published 6 Jul 2011

term equal to the number K of regressors included in the model. In the case of samples of limited size, this penalization term can be refined and is usually referred to as AICc and will be denoted $\mathscr{C}^{(a)}$ in the following, with [16]

$$\mathscr{C}^{(a)} = \frac{M}{2}\frac{1+K/M}{1-(K+2)/M}. \tag{5}$$

We shall also consider the well-known Bayesian Information Criterion (BIC) [19], whose penalization term reads

$$\mathscr{C}^{(b)} = \frac{K}{2}\ln M. \tag{6}$$

Other information criteria can be found in abundance in the literature, which may suggest that an appropriate "most efficient" criterion at hand can be designed for a given statistical problem. Among various attempts to build a general theoretical framework to interpret model complexity, the Minimum Description Length (MDL) principle introduced by Rissanen [12] is an interesting and fruitful approach. The MDL principle is based on the underlying idea that the best description of the data will be given by the model leading to the shortest code length (expressed in bits or in *nats* (1 *nat*= $\ln 2$ bits)) needed to both describe the data given the model, and to encode the model itself [12, 16].

It is interesting to note that one of the simplest forms of the MDL, the so-called *two-stage description length*, is intimately related to the BIC. Indeed, assuming a M-dimensional data described with a probability density function (Pdf) parametrized with a K-dimensional vector θ, it can be shown that the code length (in *nats*) needed to describe the data is given by the negative loglikelihood ($-\ell(\tilde{\mathbf{Y}}|\theta)$) [12, 16]. In addition, the code length needed to describe such a model with K parameters can be shown to be equal to approximately $K/2\ln M$ [12, 16]. From this result, it can thus be seen that minimizing the two-stage MDL boils down to applying a BIC penalization.

More recently, sophisticated forms of the MDL principle have been proposed, with a constant effort towards loosening the assumptions held on the observed data. We shall focus in the following on two MDL approaches whose expressions are recalled below. Detailed theoretical foundings of these MDL theories can be found in Refs [12, 16, 21].

Mixture MDL and g-prior (gMDL): Within the framework of *mixture* MDL [21], a prior distribution is assigned to the vector parameter θ. With a specific choice of the prior distribution (Zellner's g-prior), one obtains the so-called *gMDL* for which the criterion to minimize has the following closed form expression [16]:

$$\min\begin{cases} \frac{M}{2}\ln RSS + \mathscr{C}^{(g)} & \text{if } F > 1 \\ \frac{M}{2}\ln(\tilde{\mathbf{Y}}-\mathbf{b}_0)^T(\tilde{\mathbf{Y}}-\mathbf{b}_0) & \text{otherwise,} \end{cases} \tag{7}$$

where $F = (M-K)\left[(\tilde{\mathbf{Y}}-\mathbf{b}_0)^T(\tilde{\mathbf{Y}}-\mathbf{b}_0) - RSS\right]/K\,RSS$ is the standard F-ratio for testing the null model containing the spectral baseline only. The penalization term $\mathscr{C}^{(g)}$ in Eq.(7) is given in [16] and can be written

$$\mathscr{C}^{(g)} = \frac{K}{2}\ln F + \frac{M}{2}\ln\frac{M}{M-K}. \tag{8}$$

Normalized Maximized Likelihood (nMDL): Lastly, we shall be interested in the recently proposed Normalized Maximized Likelihood form of the MDL [22]. This approach has proved efficient in various practical problems and has shown several optimality properties [12, 16]. For the statistical problem considered in this paper, the nMDL theory suggests to introduce the following penalization terms [12]:

#144366 - $15.00 USD Received 31 Mar 2011; revised 6 May 2011; accepted 9 May 2011; published 6 Jul 2011

- For a model including the baseline only:

$$\mathscr{C}^{(n)} = \frac{M}{2}\ln\frac{2\pi}{M} + \frac{1}{2}\ln\frac{M}{2} + \ln\ln\frac{b}{a}. \tag{9}$$

- In any other cases:

$$\mathscr{C}^{(n)} = \frac{K}{2}\ln F + \frac{1}{2}\ln K(M-K) + \frac{K}{2}\ln M + \frac{M}{2}\ln\frac{2\pi}{M-K} + 2\ln\ln\frac{b}{a} - \ln 2 + \mathscr{L}_c, \tag{10}$$

where $\mathscr{L}_c$ denotes the code length needed for encoding the model. Following Rissanen, we use the code length

$$\mathscr{L}_c = \min\left\{K_{max}, \left[\ln\frac{K!(K_{max}-K)!}{K_{max}!} + \ln K + \log_2\ln(eK_{max})\right]\right\} \tag{11}$$

for a selection among K_{max} potential regressors contained in the spectral database.

It must be noted that the nMDL approach requires the hyperparameters a and b to be estimated. According to Rissanen's indications [12], the estimator of the hyperparameter a is given by the RSS obtained with the most exhaustive model (i.e. K_{max} regressors included) while the estimator of the hyperparameter b is the RSS obtained with the less exhaustive model (i.e. baseline only).

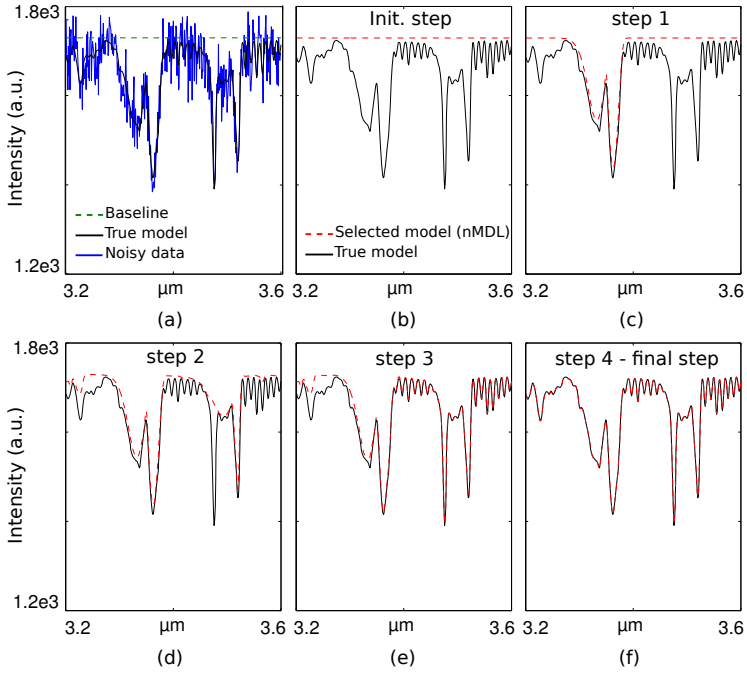

Fig. 2. (a) Example of simulated noisy data with S-SNR=6.3 dB (blue curve) superimposed with the true spectrum (black curve) and baseline (green dashed curve). (b)-(f) Comparison of the reconstructed signal after various steps of nMDL-based stepwise model selection (red dotted curve) with the true spectrum (black curve).

#144366 - $15.00 USD Received 31 Mar 2011; revised 6 May 2011; accepted 9 May 2011; published 6 Jul 2011

2.3. Stepwise algorithm for unsupervised spectral unmixing

Whatever the criterion selected, the determination of the optimal model requires an exhaustive search among all possible models which is computationally intensive if the number of potential regressors K_{max} is important. Instead of carrying out extensive operational research techniques such as *branch & bound* for instance, we implement a stepwise search algorithm for the sake of computation rapidity. We use a forward stepwise algorithm with an initialization state containing the baseline only. At each step of the algorithm, the regressor (i.e., the gas species) that most diminishes the criterion is included in the model, until any further increase in the model complexity leads to an increase of the criterion. An example of iterative model selection is illustrated in Fig. 2. At each step of the algorithm implementing nMDL criterion, the corresponding reconstructed signal is plotted in red dashed curve, and can be compared with the signal obtained with the true model (black curve).

Since we are concerned with absorption spectroscopy applications, we also implement a modified version of the algorithm so as to include a positivity constraint in the estimation results by rejecting models leading to physically unwanted negative concentration values.

It can be noted that this algorithm could be further refined for future developments by including backward elimination steps to reduce the risk of reaching local minima. Nevertheless, as will be shown in the next section, the algorithm implemented here is sufficient to compare the quality of the MDL approaches and standard information criteria such as AICc and BIC for unsupervised spectral unmixing of gas components.

3. Implementation and comparison of MDL-based information criteria

3.1. Simulated absorption spectroscopy experiment

We simulated a typical absorption spectroscopy experiment by numerically generating spectral measurements over $M = 400$ adjacent spectral slits, spanning between 3.2 and 3.6 μm, with a simulated instrumental spectral resolution of 2.3 nm (Gaussian slit function). The physical situation considered in this experiment consisted of a spectrally uniform illumination propagated through a gas mixture with 4 components: O_3 (6000 ppm.m), NO_2 (500 ppm.m), CH_4 (70 ppm.m) and H_2CO (30 ppm.m), where the numerical values in brackets correspond to their respective path-length integrated concentration.

The model selection was operated with the stepwise algorithm presented above from a spectral database containing $K_{max} = 16$ gas species, including the 4 gases of the "true" model and 12 spectrally interfering species (such as H_2O, N_2O, NH_3, HCl, etc.) with significant absorption strength within the spectral range considered. The strong spectral overlap of the database species can be checked in Fig. 3, where the absorption spectra of 8 gas species (among 16 in the spectral database) are plotted. In this figure, the spectra are convolved with a Gaussian kernel to match the spectral resolution of the instrument considered in the simulated experimental data.

To account for experimental/detection noise, M statistically independent realizations of Gaussian random noise with variance σ^2 were added to the absorption spectra generated over M spectral slits. Varying the noise variance allowed us to simulate experiments with different values of the Signal to Noise Ratio (SNR), usually defined in the context of additive Gaussian noise as the ratio of the flat baseline value to the noise standard deviation σ. However, this quantity is poorly adapted to assess the difficulty of the estimation problem considered, since it only depends on the active illumination power, and does not depend on the absorption strength of the gas mixture to be detected. We thus introduce another figure of merit, denoted S-SNR for *spectral* SNR, and defined as:

$$\text{S-SNR} = \frac{\sqrt{\frac{1}{M}(\mathbf{b}_0 - \mathbf{Y})^T(\mathbf{b}_0 - \mathbf{Y})}}{\sigma} = \frac{\sqrt{\frac{1}{M}\mathbf{c}^T\mathbf{H}^T\mathbf{H}\mathbf{c}}}{\sigma}. \tag{12}$$

#144366 - $15.00 USD Received 31 Mar 2011; revised 6 May 2011; accepted 9 May 2011; published 6 Jul 2011

In this expression, the numerator can be interpreted as the root mean square of the absorption signal $\mathbf{b}_0 - \mathbf{Y} = \mathbf{Hc}$ from which the nature and concentration of the gas components have to be estimated. An increase of the gas mixture concentrations accentuates the spectral absorption patterns in the measured spectrum, thus leading to an easier identification/estimation. In that case, it can be seen from the above definition that the S-SNR value is correspondingly increased. An example of simulated noisy data is given in Fig.2(a) for a S-SNR=6.3 dB.

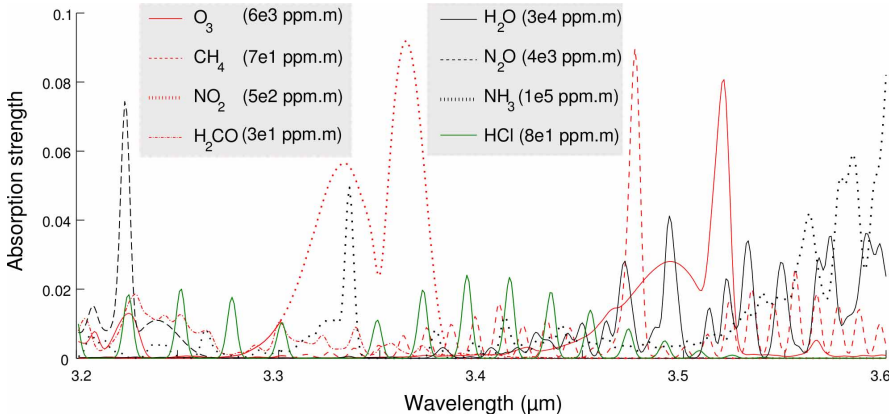

Fig. 3. Absorption spectra of the 4 gas components present in the mixture (red curves) and of 4 other chemicals of the spectral database (black and green curves) with resolution 2.3 nm. The green curve corresponds to the absorption spectrum of HCl, which is used in section 3.4 to simulate anomalous measurements (outliers).

3.2. Simulation results

The results of the numerical simulations are summarized in Table 1, where the percentage of correct model selections is given for the 4 information criteria compared in this paper and for different SNRs. For each physical situation considered, this percentage is evaluated over $R = 5.10^3$ realizations of the selection/estimation task on statistically independent simulated data. Two situations were considered according to whether light has undergone absorption from the gas mixture or not.

This table clearly reveals that in the context of unsupervised spectral unmixing, the MDL approaches implemented outperform the classical information criteria such as AICc or BIC, for reasonably high values of the SNR. This general result can be refined by observing that when the gas mixture is present, the nMDL is by far the most efficient criterion, with less than 2% erroneous selected models when S-SNR $\geq$ 6.3 dB, while the standard BIC selects approximately 17% erroneous models in the same conditions and AICc is strongly ineffective, leading to a large majority of erroneous selections. For lower values of the signal to noise ratio (S-SNR $<$4.3 dB) however, the percentage of correct models selected by nMDL strongly diminishes, and better performance is obtained with BIC. As for the gMDL approach, it can be noted that this criterion outperforms BIC for high SNRs (S-SNR$\geq$ 9.8 dB), but the advantage quickly drops out as the SNR decreases.

To complement this analysis, it is interesting to focus on the distribution of the size of the selected models. In Fig. 4.a, the histogram of the selected models sizes is plotted for the 4 criteria and for a S-SNR=6.3 dB. This figure reveals a clear tendency for AICc to overfit the noise patterns, thus leading to strongly overestimated model sizes. If the size distributions for BIC and gMDL are very similar, with approximately 16% of overestimated models ($K = 5$),

#144366 - $15.00 USD Received 31 Mar 2011; revised 6 May 2011; accepted 9 May 2011; published 6 Jul 2011

Table 1. Percentage of Correct Models Selected by the Stepwise Algorithm with Four Information Criteria (AICc, BIC, gMDL, nMDL) and for Various Values of the SNR

	With gas mixture				No gas mixture			
S-SNR	AICc	BIC	gMDL	nMDL	AICc	BIC	gMDL	nMDL
20.3 dB	16.5	83.6	96.0	>99.9	11.1	81.5	98.8	93.6
14.3 dB	18.6	83.7	92.8	99.9	11.0	80.3	99.2	93.1
9.8 dB	18.5	83.8	87.6	99.8	10.3	81.7	99.0	93.6
6.3 dB	17.7	83.1	80.8	98.9	10.6	82.0	99.0	92.3
4.3 dB	18.0	82.5	76.6	90.0	10.0	81.8	99.0	94.0
2.0 dB	16.4	74.0	63.5	53.5	10.8	81.7	98.9	92.8

it is however interesting to note that nMDL appears very efficient at avoiding overfitting, with only 1% of overestimated selections and 0.4% of selections with only $K = 3$ components. This property has already been addressed in Ref. [12] and remains valid in the less favorable situations of low SNRs where nMDL is outperformed by BIC: when S-SNR=2 dB, nMDL leads to only 53.5% of correct models but more than 99% of the remaining selections have an underestimated size ($K = 3$) and the "missing" gas component is always H_2CO. In the context of absorption spectroscopy, this behavior seems interesting since it decreases the probability of erroneously detecting a gas component in excess and thus strengthens the confidence in the components selected with nMDL.

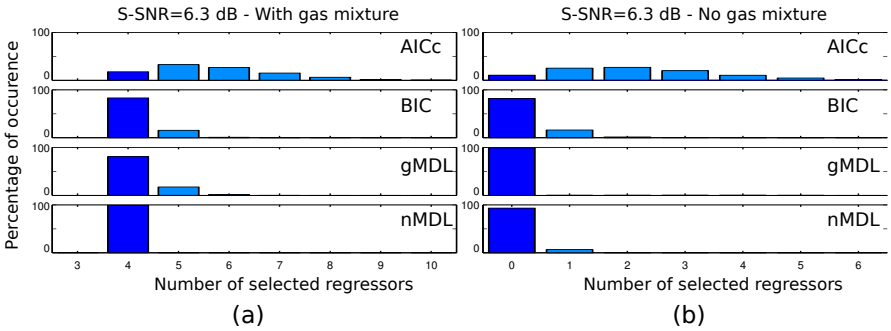

Fig. 4. Histograms of the number of regressors selected by AICc, BIC, gMDL and nMDL criteria for S-SNR=6.3 dB, (a): with a 4-components gas mixture; (b): without gas mixture.

Let us now analyze the second physical situation considered in the simulations where the illumination beam does not undergo any absorption. In this situation, it appears clearly again that MDL approaches lead to better results, when compared with standard criteria such as AICc and BIC. Once again, this result can be interpreted from the ability of MDL approaches to avoid overfitting, which can also be checked on the histograms of Fig.4.b. With approximately 99% of correct models, the gMDL criterion leads to the lowest probability of false alarm Pfa $\simeq 1 - 0.99 = 1\%$, which we define as the probability of detecting any gas mixture when there is not. On this particular point, the nMDL criterion appears less efficient with a Pfa $\simeq 6.5\%$.

From the above results, an interesting strategy for a practical implementation could be to use the *gMDL* criterion to test the null hypothesis. In case this hypothesis is rejected, the algorithm could switch to the nMDL criterion, which showed the best performance for model selection. In the next subsection, we analyze how a positivity-constrained implementation of the stepwise algorithm influences the previous results.

#144366 - $15.00 USD Received 31 Mar 2011; revised 6 May 2011; accepted 9 May 2011; published 6 Jul 2011

3.3. *Influence of a positivity constraint*

As stated in section 2.3, we also implemented a positivity-constrained version of the stepwise algorithm to provide physically acceptable results in the context of absorption spectroscopy. As can be checked in Table 2, such a constraint noticeably improves the quality of model selection with all the criteria considered. For instance, with a S-SNR=6.3 dB, the positivity-constrained algorithm selects 42.4% of correct models with AICc, 91.2% with BIC, 90.2% with gMDL and 99.3% with nMDL. When there is no gas mixture, the proportion of erroneous rejection of the null model hypothesis also diminishes whatever the criterion considered.

Table 2. Percentage of Correct Models Selected by the Stepwise Algorithm Implementing a Positivity Constraint on the Regression Coefficients (i.e., on the Gas Components Concentrations)

	With gas mixture				No gas mixture			
S-SNR	AICc	BIC	gMDL	nMDL	AICc	BIC	gMDL	nMDL
20.3 dB	40.0	92.6	98.4	>99.9	31.2	89.2	99.4	96.9
6.3 dB	42.4	91.2	90.2	99.3	28.6	89.3	99.50	97.0
4.3 dB	40.8	90.4	87.0	90.6	29.2	88.0	99.4	97.1
2.0 dB	41.6	81.8	77.6	57.3	29.1	88.8	98.4	96.9

It can be noticed however that the performance of nMDL is less influenced by this constraint than the other criteria. This property may indicate that the nMDL criterion is intrinsically efficient at avoiding non-physical results in the context addressed here, even if no positivity-constraint is applied to the algorithm.

3.4. *Influence of outliers*

To complete our analysis, we study the influence of measurement outliers. In practical situations of in-field experiments, many sources of measurement artifacts may exist, and it is likely that some amount of anomalous measures may occur. It is thus interesting to check the robustness of the implemented methods to the occurrence of outliers.

For that purpose, simulations were carried out in the same physical conditions as in the previous section, but the simulated data were generated in that case from the averaging of $N = 20$ independent measures. Among these $N = 20$ measures, we included a varying proportion of outliers, corresponding to the simulated noisy absorption spectrum of a single interferent gas species (HCl [80 ppm.m]), whose absorption spectrum is represented in green curve in Fig. 3.

Table 3. Percentage of Correct Models Selected by the Stepwise Algorithm with a S-SNR=6.3 dB for a Varying Proportion of Measurement Outliers

	With gas mixture				No gas mixture			
% outliers	AICc	BIC	gMDL	nMDL	AICc	BIC	gMDL	nMDL
0 %	17.7	83.1	80.8	98.9	10.6	82.0	99.0	92.3
5%	13.7	80.0	75.7	97.4	8.3	77.1	98.1	93.8
20 %	7.3	62.2	53.6	90.1	5.2	59.7	92.4	93.9

The results obtained are summarized in Table 3, where the percentage of correct models is given for a S-SNR=6.3 dB on the averaged signal. Once again, it can be clearly seen that in the context of spectral unmixing of interfering gas species, the nMDL criterion outperforms the other methods, with still 90% of correct models for a significant amount of outliers (20%). It can also be noted that the inclusion of outliers does not influence the Pfa obtained with nMDL

#144366 - $15.00 USD Received 31 Mar 2011; revised 6 May 2011; accepted 9 May 2011; published 6 Jul 2011

(approximately $1 - 0.933 \simeq 6,7\%$) while this quantity noticeably decreases when other criteria are implemented.

4. Conclusion

In this paper, we presented an original technique for unsupervised spectral unmixing of multiple gas species. More precisely, we have shown that two Minimum Description Length approaches can be successfully implemented in a stepwise model selection algorithm. Applied on spectroscopic data, this algorithm allows one to estimate the number, nature and concentration of the components of an unknown gas mixture without requiring ajustment of any parameter.

In the context addressed in this paper, numerical simulations have demonstrated that the MDL approaches outperform the standard information criteria tested (AICc, BIC). When a gas mixture is present within the path of the illumination beam, the gMDL approach does not provide great improvement in comparison to classical BIC, but we illustrated its efficiency in avoiding false alarms when no gas mixture is present. However, the most promising results for a practical implementation were obtained with the Normalized Maximized Likelihood (nMDL) approach, which seems to be a very interesting alternative to standard criteria, and can still be implemented with a simple algorithm. The nMDL criterion strongly outperforms the other methods for reasonable values of the SNR and provides the best robustness to measurements artifacts.

A promising perspective to this work is the opportunity to apply this method to experimental spectroscopic data due to recent development in our laboratories of appropriate mid-infrared powerful sources with broadband spectrum [23], or with highly tunable operating wavelength [24]. It must be noted that this approach is not limited to the case of absorption spectroscopy, and could be also applied in many situations requiring spectral unmixing (Raman spectroscopy, hyperspectral data processing, etc.). A further analysis of the influence of the spectral resolution and of the noise model would be also a useful theoretical continuation of this work, as well as the study of detection performances. A comparison of the MDL-based model selection techniques presented in this paper with other parsimonious model selection methods such as the *lasso* approaches [25, 26] is another interesting perspective.

#144366 - $15.00 USD Received 31 Mar 2011; revised 6 May 2011; accepted 9 May 2011; published 6 Jul 2011

Pattern Recognition Letters 65 (2015) 152–156

Contents lists available at ScienceDirect

Pattern Recognition Letters

journal homepage: www.elsevier.com/locate/patrec

Stochastic complexity-based model selection with false alarm rate control in optical spectroscopy☆

Julien Fade*

Institut de Physique de Rennes, Université de Rennes 1, CNRS, Campus Beaulieu, Rennes 35042, France

ARTICLE INFO

Article history:
Received 14 March 2015
Available online 31 July 2015

Keywords:
model selection
stochastic complexity
hypothesis testing

ABSTRACT

Stochastic complexity-based penalization criteria can prove efficient and robust in spectroscopy applications for unsupervised identification and concentration estimation of spectrally interfering chemical components. It is shown here how the so-called Normalized Maximized Likelihood (nMDL) introduced in [17] can be tailored to provide control of the detection performances in terms of probability of false alarm. Numerical experiments conducted on realistic simulated optical spectroscopy signals evidence that the nMDL approach outperforms standard information criteria in terms of model selection performances. Moreover, the ability to control false alarm rates with the proposed modified nMDL criterion is demonstrated on simulations.

1. Introduction

Model selection is a very common issue in the field of data analysis and regression. Many questions usually have to be answered simultaneously: does the data reveals the presence of a significant feature (regressor), or not? If so, how many and which regressors must be selected in the linear regression model to better explain the observations? Without any model selection step, the most exhaustive regression model would include all potential regressors, and may lead to misleading and imprecise (if not incorrect) results, mostly due to overfitting of the noise. This can have harmful consequences in some situations, for instance in the context of trace gas detection by optical spectroscopy as addressed by this paper as an illustration.

To avoid such undesirable situations, and to provide unsupervised model selection strategies, many penalized regression methods have been proposed using various penalization criteria, such as the classical information criteria (Mallow's C_p [13], Akaike's AIC and variants [1,10], Schwarz's BIC [20], RIC [5], etc.). However, many "best" penalization criteria have been introduced in the literature to refine these standard selection rules, so as to optimize the quality of model selection depending on the problem at hand [22]. This raises the question of the generality of such penalization strategies. In that context, since its introduction by Rissanen's seminal work [15], the Minimum Description Length (MDL) principle is an interesting and fruitful attempt to build a general theoretical framework to interpret model complexity and to provide unsupervised model selection rules. The MDL principle states that the best description of the data must be given by the model leading to the shortest code length, or stochastic complexity (SC) (expressed in bits or in *nats* (1 *nat*= ln 2 bits)) required to describe both the model and the data [9,15,18]. The MDL principle has found wide applicability in very distinct contexts, such as model selection [9], data clustering [8], but also radar signal processing [3] or image segmentation [6].

In this paper, we focus on a sophisticated form of the SC, referred to as Normalized Maximized Likelihood (nMDL) [17]. We show how this penalization criterion can be modified so as to provide probability of false alarm (Pfa) control in the context of model selection, and we illustrate this property on realistic numerical simulations of an unsupervised optical spectroscopy experiment. The paper is organized as follows: in Section 2, the expression of the nMDL criterion is first recalled, and a modified version of this criterion is derived, allowing to control the Pfa in the model selection procedure. Then, a simulated experiment of optical spectroscopy is described in Section 3 and numerical simulation results allow us to compare the quality of the standard nMDL criterion with respect to more standard information criteria. The possibility of Pfa control using the proposed modified nMDL criterion is finally illustrated on simulated data, before the conclusion of the paper is given in Section 4.

2. Normalized-Maximized Likelihood (nMDL) criterion and false alarm rate control

Throughout this paper, we shall consider the simple problem of linear regression, with m-dimensional observation vector $\tilde{\mathbf{y}}$ modeled as

$$\tilde{\mathbf{y}} = \mathbf{H} \cdot \mathbf{c} + \mathbf{n}, \tag{1}$$

☆ This paper has been recommended for acceptance by Dr. G. Moser.

* Tel.: +33 223 235 215; fax: +33 223 236 717.
E-mail address: julien.fade@univ-rennes1.fr

http://dx.doi.org/10.1016/j.patrec.2015.07.022
0167-8655/

with $m \times k$ regressor matrix $\mathbf{H}$ and unknown parameters vector $\mathbf{c}$. We further assume the m components of the additive noise vector $\mathbf{n}$ to be independent realizations of a centered Gaussian random variable. Under this hypothesis, applying a penalized criterion in the model selection procedure corresponds to minimize the following quantity:

$$-\ell_{\tilde{\mathbf{y}}}(\tilde{\mathbf{y}}; \mathbf{H}) + \mathcal{C}, \tag{2}$$

where the expression of $\mathcal{C}$ depends on the penalization criterion used (AIC, BIC, etc.), and where the log-likelihood is directly related to the regression residual sum of squares (RSS) through $\ell_{\tilde{\mathbf{y}}}(\tilde{\mathbf{y}}; \mathbf{H}) = -(m/2) \ln \mathrm{RSS}$.

2.1. nMDL criterion

The Normalized Maximized Likelihood (nMDL) is a recently introduced form of SC [17] which has proved efficient in various practical problems [4,9,18] and which presents various optimality properties [18]. The nMDL theory suggests the following penalization terms to be introduced in the criterion given in Eq. (2), depending on the hypothesis considered [18]:

$$\mathcal{C}^{(n)}_{|\mathcal{H}_0} = \frac{m}{2} \ln \pi - \ln \Gamma\left(\frac{m}{2}\right) + \ln \ln \frac{b}{a} \tag{3}$$

and

$$\mathcal{C}^{(n)}_{|\mathcal{H}_1^{(k)}} = \frac{k}{2} \ln \frac{kF}{m-k} + \frac{m}{2} \ln \pi - \ln \left[\Gamma\left(\frac{k}{2}\right) \Gamma\left(\frac{m-k}{2}\right) \right] + \mathcal{L}_k + 2 \ln \ln \frac{b}{a}, \tag{4}$$

where hypothesis $\mathcal{H}_0$ refers to the null-model (no regressor) and hypothesis $\mathcal{H}_1^{(k)}$ to a selected model containing k regressors among K_m potential regressors. In this last equation, F denotes the standard F-ratio, which depends on the RSS of the regression through $F = (m-k)[\tilde{\mathbf{y}}^T \tilde{\mathbf{y}} - RSS]/(k\,RSS)$. The code length $\mathcal{L}_k$ needed for encoding model $\mathcal{H}_1^{(k)}$ is given by $\mathcal{L}_k = \ln \binom{K_m}{k} + \ln k + \log_2 \ln (e\,K_m)$ [18]. Lastly, it must be noted that the nMDL approach requires two hyperparameters a and b to be estimated. According to indications in [18], they can be respectively estimated with the regression sum of squares (i.e., $\tilde{\mathbf{y}}^T \tilde{\mathbf{y}} - RSS$) obtained with the most exhaustive model $\mathcal{H}_1^{(K_m)}$ and the regression sum of squares under null hypothesis $\mathcal{H}_0$.

As with standard information criteria, model selection is finally carried out by identifying the set of regressors which minimizes the penalized criterion. This operation can be performed by exhaustive search, or by appropriate stepwise procedures, in which the number of regressors is gradually increased until no further decrease of the criterion can be reached. Such a stepwise method will be used in Section 3.

In the remainder of this section, we show and illustrate how the nMDL criterion can be tailored so as to provide control of the false alarm rate (Pfa) in a model selection procedure.

2.2. Pfa control and model selection

The link between detection performance and model selection is a known result for standard information criteria. For instance, it is quite straightforward to understand that using the AIC or BIC criteria for model selection is equivalent to applying a standard generalized likelihood ratio test (GLRT) with given threshold depending on the penalization considered [23]. For example, to discriminate between hypothesis $\mathcal{H}_0$ and hypothesis $\mathcal{H}_1$ (at least one regressor included in the selected model), this decision rule can be summarized as

$$\ell_{glrt}(\tilde{\mathbf{y}}) = \ln \left[\frac{P(\tilde{\mathbf{y}}|\mathcal{H}_1)}{P(\tilde{\mathbf{y}}|\mathcal{H}_0)} \right] = \ell_{\tilde{\mathbf{y}}}(\tilde{\mathbf{y}}; \mathcal{H}_1) - \ell_{\tilde{\mathbf{y}}}(\tilde{\mathbf{y}}; \mathcal{H}_0) \underset{\mathcal{H}_0}{\overset{\mathcal{H}_1}{\gtrless}} \tau, \tag{5}$$

where the value of the threshold τ fixes the Pfa. For a Gaussian noise model, one simply has

$$\ell_{glrt}(\tilde{\mathbf{y}}) = \frac{m}{2} \ln \frac{\mathrm{RSS}_0}{\mathrm{RSS}_1}. \tag{6}$$

A similar property has been recently analyzed in the case of the nMDL criterion in [7], where the authors evidenced that the application of the nMDL criterion is formally equivalent to a GLRT with fixed threshold. In the following, we show how to exploit this property so as to control the Pfa in a model selection procedure. This is made possible by introducing a slightly modified version of the nMDL criterion.

2.3. Thresholded nMDL criterion for Pfa control

Although one of the main concerns that underlies MDL approaches is to minimize the number of user-defined parameters in the criterion, we propose to introduce a fixed threshold in the application of the nMDL criterion. Meanwhile, this avoids resorting to the hyperparameters a and b included in the former criterion, which is easily obtained by setting $a = be$ in Eqs. (3) and (4). Such modified nMDL criterion for discrimination between null/non-null hypotheses leads to the following decision rule:

$$\begin{aligned} \Delta\mathcal{C}^{(n)}(\tilde{\mathbf{y}}, m, k) &= -\ell_{\tilde{\mathbf{y}}}(\tilde{\mathbf{y}}; \mathcal{H}_1^{(k)}) + \mathcal{C}^{(n)}_{|\mathcal{H}_1^{(k)}} + \ell_{\tilde{\mathbf{y}}}(\tilde{\mathbf{y}}; \mathcal{H}_0) - \mathcal{C}^{(n)}_{|\mathcal{H}_0} \underset{\mathcal{H}_1}{\overset{\mathcal{H}_0}{\gtrless}} \delta_{\mathrm{Pfa}} \\ \Leftrightarrow\ \Delta\mathcal{C}^{(n)}(\tilde{\mathbf{y}}, m, k) &= -\ell_{glrt}(\tilde{\mathbf{y}}) + \mathcal{C}^{(n)}_{|\mathcal{H}_1^{(k)}} - \mathcal{C}^{(n)}_{|\mathcal{H}_0} \underset{\mathcal{H}_1}{\overset{\mathcal{H}_0}{\gtrless}} \delta_{\mathrm{Pfa}}, \end{aligned} \tag{7}$$

illustrating that the nMDL criterion will reject hypothesis $\mathcal{H}_0$ if $\Delta\mathcal{C}^{(n)}(\tilde{\mathbf{y}}, m, k)$ is lower than a given threshold.

Let us now analyze the relationship between the Pfa and the value of the user-defined threshold δ_{Pfa}. First, by noticing that $\ell_{glrt} = m/2 \ln[1 + kF/(m-k)]$, a few calculation steps allow us to show that the quantity $\Delta\mathcal{C}^{(n)}$ can be rewritten as a function of the generalized log-likelihood test (GLRT) ℓ_{glrt} as (see [7])

$$\Delta\mathcal{C}^{(n)}(\ell_{glrt}, m, k) = g(\ell_{glrt}, m, k) + \eta(m, k) + \mathcal{L}_k, \tag{8}$$

with $\eta(m,k) = -\ln B[k/2, (m-k)/2]$, where the Beta function reads $B(x,y) = [\Gamma(x)\,\Gamma(y)]/\Gamma(x+y)$, and with

$$g(x, m, k) = -x + \frac{k}{2} \ln[e^{2x/m} - 1]. \tag{9}$$

$\mathcal{L}_k$ still denotes the code length needed to encode the model. Using Stirling's approximation of the Beta function, this modified nMDL criterion can be rewritten $\Delta\mathcal{C}'^{(n)}(\ell_{glrt}, m, k) = g(\ell_{glrt}, m, k) + \eta'(m, k) + \mathcal{L}_k$, with

$$\eta'(m,k) = \frac{1}{2}\left[f(m) - f(m-k) - f(k) + \ln \left[\frac{k(m-k)}{4\pi m} \right] \right] \tag{10}$$

and $f(x) = x \ln(x)$.

From this expression, it can first be observed that $\Delta\mathcal{C}'^{(n)}(\ell_{glrt}, m, k)$ does not evolve monotonously as a function of ℓ_{glrt}. Nevertheless, following a similar reasoning as in [7], it can be shown that the function $\Delta\mathcal{C}'^{n}(\ell_{glrt}, m, k)$ is concave and takes on positive values when ℓ_{glrt} lies within an interval $[\ell^-_{glrt}, \ell^+_{glrt}]$ (see Fig. 1), $\forall\, k \in [1; m]$, as soon as $K_m > 2$. It is now quite obvious that the application of the modified (thresholded) nMDL decision rule given in Eq. (7) corresponds to a fixed value of the false alarm rate, which is equal to the probability that ℓ_{glrt} lies outside the interval $[\ell^-_{\delta_{\mathrm{Pfa}}}; \ell^+_{\delta_{\mathrm{Pfa}}}]$ when hypothesis $\mathcal{H}_0$ is true, i.e.,

$$\mathrm{Pfa} = \Pr(\ell_{glrt} < \ell^-_{\delta_{\mathrm{Pfa}}} | \mathcal{H}_0) + \Pr(\ell_{glrt} > \ell^+_{\delta_{\mathrm{Pfa}}} | \mathcal{H}_0). \tag{11}$$

This is illustrated in Fig. 1 where the obtained Pfa corresponds to the darkened areas under the red dashed curve representing the probability density function (pdf) of the log-likelihood ratio ℓ_{glrt} under hypothesis $\mathcal{H}_0$. From this last relation, it is now clear that provided the

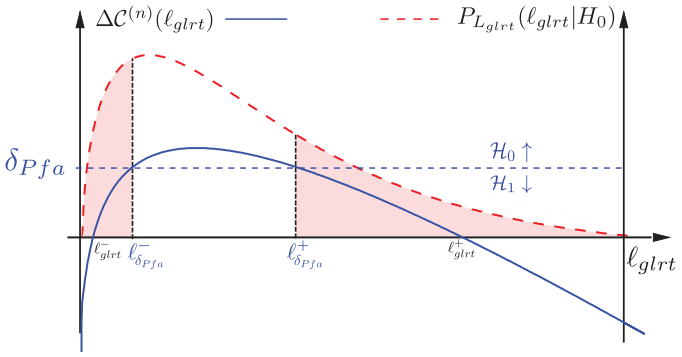

Fig. 1. Evolution of the modified nMDL criterion as a function of the log-likelihood ratio test ℓ_{glrt} (blue solid curve). A possible probability density function (Pdf) of ℓ_{glrt} under hypothesis $\mathcal{H}_0$ is plotted in red dashed curve for illustration. (For interpretation of the references to color in this figure legend, the reader is referred to the web version of this article.)

GLRT pdf under the null model hypothesis $P_L(\ell_{glrt}|\mathcal{H}_0)$ is known, one can determine (at least numerically) the appropriate threshold δ_{Pfa} so as to provide the desired value of the Pfa.

3. Application to model selection in optical spectroscopy

3.1. Model selection for unsupervised optical spectroscopy

Let us now apply the previous model selection procedures to the practical case of unsupervised optical spectroscopy. In that context, we assume that the intensities of the analyzed light detected on m distinct spectral slits form a vector $\mathbf{x}$. This vector is linked to the k-dimensional vector $\mathbf{c}$ containing the concentrations of the gas components $\mathbf{c} = [c_1 \dots c_k]^T$ through the following equation

$$\mathbf{x} = \mathbf{a}_0 e^{-\mathbf{Hc}}, \tag{12}$$

where $\mathbf{a}_0$ denotes the baseline spectrum. The $m \times k$ regressors matrix $\mathbf{H} = [\mathbf{h}_1, \mathbf{h}_2, \dots, \mathbf{h}_k]$ contains the absorption spectra $\mathbf{h}_i$ of the k components of the regression model. We assume that the $\mathbf{h}_i$ are known on the m spectral slits considered, with a resolution adapted to the spectral resolution of the spectrometer used in the measurement. For the sake of simplicity, we shall also assume that the spectral baseline $\mathbf{a}_0$ is known, either by instrumental calibration or with an accurate radiometric model of the illumination source, which can be passive or active using for instance a supercontinuum laser [2].

Let $\tilde{\mathbf{x}}$ denote the measurement vector containing experimental intensity measurements over the m spectral slits (obtained for instance with a dispersive spectrometer or an optical spectrum analyzer). It is a standard procedure in spectroscopic measurements to use the logarithm of the measured data $\tilde{\mathbf{x}}$, so as to obtain a linear regression model of the form of Eq. (1) with $\tilde{\mathbf{y}} = \ln \mathbf{a}_0 - \ln \tilde{\mathbf{x}}$ and where the vector $\mathbf{n}$ allows us to model the influence of experimental noise. We assume that the noise can still be considered as Gaussian and we hypothesize independence between the noise affecting two distinct spectral slits, i.e., $\langle n_i\, n_j \rangle = 0$ if $i \neq j$. In the presence of intense spectral baseline and of limited absorption strengths, such assumptions are realistic and are quite common in spectroscopy for other standard linear model selection techniques such as Least Squares, or Partial Least Squares approaches [14,24]. For such a classical linear regression model, the estimator minimizing the RSS $= \tilde{\mathbf{y}}^T(\mathbf{Id} - \mathbf{W})\tilde{\mathbf{y}}$ is referred to as Minimum Mean Squared Error (MMSE) estimator and reads $\hat{\mathbf{c}} = (\mathbf{H}^T\mathbf{H})^{-1}\mathbf{H}^T\tilde{\mathbf{y}} = \mathbf{H}^{-1}\mathbf{W}\tilde{\mathbf{y}}$, with $\mathbf{W}$ being the projection matrix. Under the hypothesis of Gaussian fluctuations with unknown variance, this estimator identifies with the Maximum Likelihood (ML) estimator.

In the context of optical spectroscopy considered in this paper, the Pfa will correspond to the probability of erroneously selecting a model including at least one gas component, when there is actually no gas mixture to be detected. This corresponds to an important practical situation for noxious trace gas detection in industrial or military context, in which optical spectroscopy in the mid-infrared proves efficient.

3.2. Numerical implementation and simulation results

3.2.1. Other penalization criteria

In this last section, we shall consider two classical information criteria and a different MDL penalization form as benchmarks to assess the quality of the nMDL method explored. The simplest penalization is the Akaike Information Criterion (AIC) [1], which is equal to the number k of regressors included in the model. In the case of samples of limited size, this criterion can be refined, and is usually referred to as AICc [10], which we will denote $\mathcal{C}^{(a)}$ in the following and which reads $\mathcal{C}^{(a)} = m(m-k)/2(m-k-2)$. We shall also consider the well-known Bayesian Information Criterion (BIC) [20], whose penalization term reads $\mathcal{C}^{(b)} = (k/2)\ln m$.

In addition, we also consider the so-called gMDL criterion, introduced in [16], within the framework of *mixture* MDL. In this approach, a prior distribution is assigned to the pdf parameters vector, and the gMDL criterion corresponds to a specific choice of the prior distribution, namely Zellner's g-prior, and can be written in the following form :

$$\min \begin{cases} \frac{m}{2}\ln \text{RSS} + \mathcal{C}^{(g)} & \text{if } F > 1 \\ \frac{m}{2}\ln \tilde{\mathbf{y}}^T\tilde{\mathbf{y}} & \text{otherwise.} \end{cases} \tag{13}$$

By taking the penalization term $\mathcal{C}^{(g)}$ in Eq. (13) equal to

$$\mathcal{C}^{(g)} = \frac{k}{2}\ln F + \frac{m}{2}\ln\frac{m}{m-k}, \tag{14}$$

this form of the gMDL is strictly equivalent to the criterion given in [9], up to the code length of two hyperparameters that can be reasonably neglected according to [16].

3.2.2. Model selection implementation

We considered a realistic optical spectroscopy scenario within the mid-infrared range (3.2–3.6 μm), with simulated absorption spectra on $M = 400$ spectral slits, obtained from the high-resolution Hi-Tran spectral database [19], and convolved with a Gaussian kernel to match an instrumental spectral resolution of 2.4 nm. We assumed that the incoming light from a flat spectral baseline was absorbed by a mixture of $k = 4$ gas, among a simulated spectral database containing $K_m = 16$ components. The individual spectra of the 4 gas components are plotted in red curves Fig. 2, and the figures in brackets denote their respective concentrations (indicated in ppm.m) in the simulated mixture. The spectra of 4 other "interfering" gas species of the spectral database (but not included in the actual simulated mixture) are also plotted to show the potentially strong overlap between the gas species of the database. The simulated optical spectrum intensity obtained with the considered gas mixture is plotted in magenta continuous curve in Fig. 2, and a simulated noisy experimental spectrum is given in blue continuous curve. The noise model is Gaussian with variance σ^2 on the M spectral slits.

The model selection has been performed with various penalization criteria (AICc, BIC, gMDL, nMDL) using an approximate forward stepwise search algorithm, with initial state containing the spectral baseline only (hypothesis $\mathcal{H}_0$). Without loss of generality, we considered in the experiments simulated datasets of $N = 20$ independent measurement outcomes, which corresponds to reasonable signal averaging in a field experiment. Two situations have been considered, corresponding to the following hypotheses: (a) the 4-components gas mixture described above was present on the path of the light (hypothesis $\mathcal{H}_1^{(4)}$) and, (b) no gas mixture were present (hypothesis $\mathcal{H}_0$).

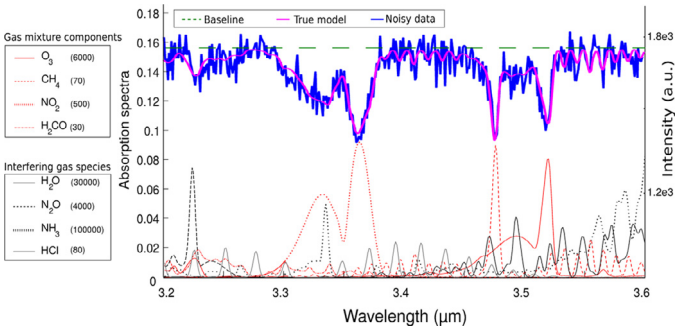

Fig. 2. Absorption spectra of the 4 components of the simulated gas mixture (red curves) and of 4 interfering gas species in the simulated spectral database (black and gray curves). The intensity spectrum corresponding to the actual gas mixture model is plotted in magenta curve, along with the flat spectral baseline (dashed green curve) and a realization of a noisy signal acquisition is represented in blue curve. (For interpretation of the references to color in this figure legend, the reader is referred to the web version of this article.)

Table 1
Percentage of correct/incorrect model sizes selected by the stepwise algorithm with four information criteria (AICc, BIC, gMDL, nMDL) for a SNR of 6.3 dB.

	With gas mixture ($\mathcal{H}_1$)				No gas mixture ($\mathcal{H}_0$)		
	=	+1	+2	≥ 3	=	+1	≥ 2
AICc	**17.7**	32.6	26.5	23.2	**10.6**	25.3	64.1
BIC	**83.2**	15.6	1.2	–	**82.0**	16.2	1.8
gMDL	**80.9**	17.4	1.6	0.1	**99.0**	0.2	0.8
nMDL	**95.9**	3.9	0.2	–	**93.3**	6.7	–

$R = 5000$ realizations of each model selection experiment have been carried out to statistically assess the performance of each penalization criterion.

3.2.3. Simulation results

Table 1 summarizes the results obtained on the two considered scenarios with various penalization criteria, and for a low SNR of 6.3 dB, with SNR $= ||\mathbf{Hc}||/\sqrt{M}\sigma$, as defined in [4]. These results illustrate the efficiency of the nMDL approach for unsupervised model selection, since it leads to a significantly higher percentage of correctly selected models under hypothesis $\mathcal{H}_1$. Moreover, as pointed out in previous works [4,18], it tends to avoid model overfitting, which is a strong benefit in the context of trace gas detection.

Under hypothesis $\mathcal{H}_0$, it can first be noted that the MDL approaches outperform the standard AICc and BIC criteria. It is nevertheless observed that the nMDL leads to a greater probability of false alarm (6.7%) than gMDL (1%), where the Pfa is defined here as the proportion of non-null models selected by the algorithm under the $\mathcal{H}_0$ hypothesis. Since we consider a forward stepwise selection algorithm, such definition identifies with the Pfa defined in Section 2.3.

It appears from these simulation results that using the nMDL criterion can be very beneficial in the context of unsupervised optical spectroscopy. As noted in previous work [4], it also gathers interesting properties for real-field experimental implementation, such as being quite robust to measurement outliers.

3.3. False alarm rate control with nMDL criterion

In this last subsection, we illustrate the potentiality of Pfa control using the modified nMDL criterion introduced in Section 2.3, in the physical context of unsupervised optical spectroscopy. For that purpose, new simulations have been carried out to implement the modified nMDL criterion. Since we used a stepwise algorithm, the decision between a null model ($\mathcal{H}_0$) and a non-null model ($\mathcal{H}_1$) is operated during the first step of the model selection algorithm. In that case,

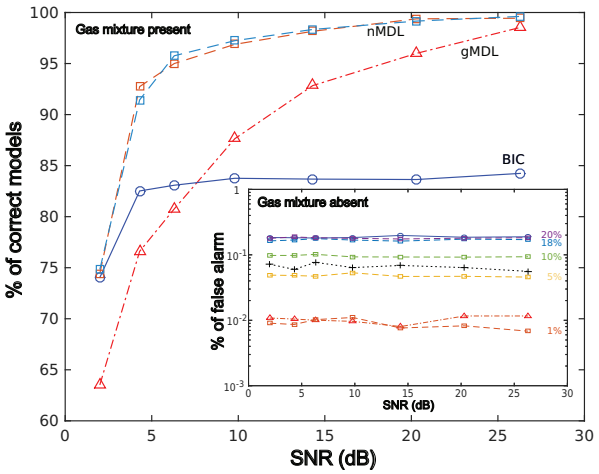

Fig. 3. Evolution of the percentage of correct model selections as a function of the SNR with a gas mixture. Comparison between BIC (blue circles), gMDL (red triangles) and nMDL with Pfa fixed to 18% (light blue squares) and to 1% (orange squares). Inset: Comparison of the Pfa as a function of SNR, obtained with BIC (blue circles), gMDL, (red triangles), original nMDL (black crosses) and modified nMDL with various fixed values of Pfa (1, 5, 10, 18 and 20% in square symbols). (For interpretation of the references to color in this figure legend, the reader is referred to the web version of this article.)

and with the Gaussian model of fluctuations considered, it is well-known that $P_L(\ell_{glrt}|\mathcal{H}_0)$ corresponds to a centered χ^2-law with one degree of freedom [11].

Moreover, it is also a well-known result that the multiple hypotheses test involved in a stepwise algorithm naturally results in an excessive false alarm rate [12]. This can be understood by noting that testing a larger number of hypotheses reduces the power for rejecting all of them, i.e., reduces the probability for selecting the correct model $\mathcal{H}_0$. This unwanted situation can nevertheless be easily avoided by applying a classical Bonferroni correction [12,21]. In our case, this correction simply consists of implementing the algorithm with a threshold $\delta_{\mathrm{Pfa}/K_m}$, calculated for a false alarm rate of Pfa/K_m, where K_m is the number of potential regressors in the initial spectral database.

With this precaution taken into account, the numerical results presented in Fig. 3 allow us to check the validity of the proposed approach for Pfa control. We considered the same physical situation as in Section 3.2.2, and the percentage of correctly selected models under hypothesis $\mathcal{H}_1^{(4)}$ in the presence of the gas mixture is plotted as a function of the SNR, for the standard BIC (blue circle symbols), the gMDL (red triangle symbols) and the modified nMDL. For this last criterion, two thresholds have been considered so as to provide a false alarm rate of 18% (respectively, 1%) similar to the Pfa obtained with the BIC (respectively, the gMDL), and the corresponding results are plotted with light blue square symbols (respectively, orange square symbols). This can be checked in the inset of Fig. 3, where the probabilities of false alarm are plotted for BIC (blue circle symbols), gMDL (red triangle symbols), and nMDL with appropriate thresholds so as to match the Pfas of BIC (blue square symbols) or gMDL (orange square symbols). The Pfas obtained with the modified nMDL for three other values of the threshold are also displayed in square symbols, as well as the Pfa that would be obtained with the standard unconstrained nMDL (black crosses symbols) for comparison. This demonstrates the ability to control the Pfa with the modified nMDL criterion.

In addition, the results obtained allow us to confirm the conclusions of section 3.2.3, showing that the nMDL criterion strongly outperforms a standard information criterion such as BIC, for sufficiently high values of the SNR (typically > 5 dB). The comparison with the gMDL approach shows that the nMDL is less sensitive to a degradation of the SNR, and is thus better adapted for practical implementation in real field scenarios. It can be noticed in Fig. 3 that the nMDL

criterion leads to similar percentages of correct models for distinct values of the threshold δ_{Pfa}. Indeed, when at least one regressor has been included in the model, the next selection steps of the stepwise algorithm are operated by applying the nMDL criterion of Eq. (4) between non-null models of varying number of regressors $k > 1$, in which cases the constant threshold δ_{Pfa} no longer plays a role in the decision.

4. Conclusion

In this paper, we have shown that a modified nMDL penalization criterion could ensure Pfa control in a model selection procedure. This property relies on the fact, evidenced by Giurcaneanu and Razavi [7], that the nMDL criterion in model selection is formally equivalent to applying a GLRT for rejecting the null hypothesis. To manage Pfa control, we proposed in this paper to introduce an additional parameter in the nMDL criterion, whose value can be linked to the desired Pfa. We illustrated this property on simulated data, in the context of unsupervised optical spectroscopy which is a current environmental issue for air pollution monitoring and detection. These numerical simulations have permitted to confirm that nMDL penalization outperforms standard information criteria, reinforcing the interest of MDL approaches for model selection tasks.

The perspectives of this work will be to apply this approach and the Pfa control ability to real field optical spectroscopy experiments. These interesting properties could also be useful in other applications, in which unsupervised model selection is required.

References

[1] H. Akaike, A new look at the statistical model identification, IEEE Trans. on Autom. Control 19 (1974) 716–723.
[2] N. Cezard, A. Dobroc, G. Canat, M. Duhant, W. Renard, C. Alhenc-Gelas, S. Lefebvre, J. Fade, Supercontinuum laser absorption spectroscopy in the mid-infrared range for identification and concentration estimation of a multi-component atmospheric gas mixture, in: Proceedings of SPIE Remote Sensing, International Society for Optics and Photonics, 2011, p. 81820V.
[3] H. Chen, T. Kirubarajan, Y. Bar-Shalom, K.R. Pattipati, MDL approach for multiple low-observable track initiation, Proc. SPIE 4728 (2002) 477–488.
[4] J. Fade, S. Lefebvre, N. Cézard, Minimum description length approach for unsupervised spectral unmixing of multiple interfering gas species, Optics Express 19 (2011) 13862–13872.
[5] D.P. Foster, E.I. G., The risk inflation criterion for multiple regression, Annals of Stat. 22 (1994) 1947–1975.
[6] F. Galland, N. Bertaux, P. Réfrégier, Minimum description length synthetic aperture radar image segmentation, IEEE Trans. Image Process 12 (2003) 995–1006.
[7] C.D. Giurcaneanu, S.A. Razavi, New insights on stochastic complexity, in: Proceedings of the 17th European Signal Processing Conference, 2009, pp. 2479–5475.
[8] P.D. Grünwald, I.J. Myung, M.A. Pitt, Advances in Minimum Description Length: Theory and Applications, MIT Press, Cambridge, 2005.
[9] M. Hansen, B. Yu, Model selection and the principle of minimum description length, J. Am. Stat. Assoc. 96 (2001) 746–774.
[10] C.M. Hurvich, C.L. Tsai, Regression and time series model selection in small samples, Biometrika 76 (1989) 297–307.
[11] S.M. Kay, Fundamentals of Statistical Signal Processing - Volume II : Detection Theory, Prentice-Hall, Upper Saddle River, 1998, pp. 186–247.chapter Statistical decision theory II
[12] L.L. Kupper, J.R. Stewart, K.A. Williams, A note on controlling significance levels in stepwise regression, Am. J. Epidemiol. 103 (1976) 13–15.
[13] C.L. Mallows, Some comments on c_p, Technometrics 15 (1973) 661–675.
[14] U. Platt, J. Stutz, Differential Optical Absorption Spectroscopy, Springer, Berlin / Heidelberg, 2008.
[15] J. Rissanen, Modeling by shortest data description, Automatica 14 (1978) 465–471.
[16] J. Rissanen, Stochastic Complexity in Statistical Inquiry, in: Series in Computer Science, vol. 15, World Scientific, Singapore, 1989.
[17] J. Rissanen, Fisher information and stochastic complexity, IEEE Trans. Inform. Theory 42 (1996) 48–54.
[18] J. Rissanen, Information and Complexity in Statistical Modeling, Springer, New-York, 2007.
[19] L.S. Rothman, D. Jacquemart, A. Barbe, D.C. Benner, M. Birk, L. Brown, M. Carleer, C. Chackerian, K. Chance, L.e.a. Coudert, et al., The hitran 2004 molecular spectroscopic database, J. Quant. Spectrosc. Radiat. Transf. 96 (2005) 139–204.
[20] G. Schwartz, Estimating the dimension of a model, Annals of Stat. 9 (1978) 461–464.
[21] J.P. Shaffer, Multiple hypothesis testing, Annu. Rev. Psychol. 46 (1995) 561–584.
[22] P. Stoica, Y. Selen, Model-order selection: a review of information criterion rules, Signal Process. Mag. IEEE 21 (2004) 36–47.
[23] P. Stoica, Y. Selen, J. Li, On information criteria and the generalized likelihood ratio test of model order selection, IEEE Signal Process. Lett. 11 (2004) 794–797.
[24] S. Verboven, M. Hubert, P. Goos, Robust preprocessing and model selection for spectral data, J. Chemom. 26 (2012) 282–289.

Équipe DOP, Institut Foton Université de Rennes 1 - CNRS Bat 11B - Campus de Beaulieu, 35 042 Rennes Cedex